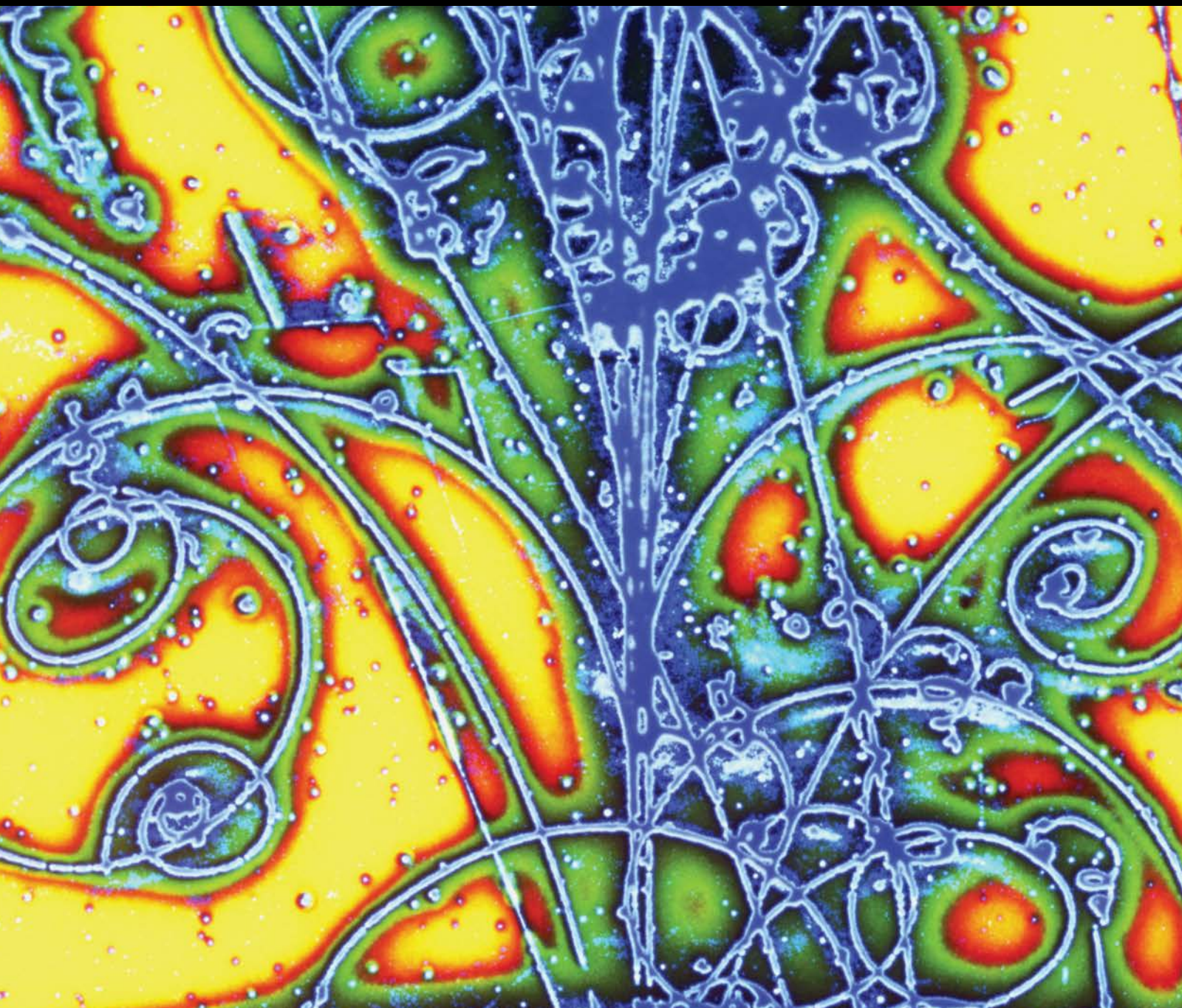


Advances in High Energy Physics

# Neutrino Masses and Oscillations 2015

Guest Editors: Vincenzo Flaminio, Mauro Mezzetto, Leslie Camilleri,  
Srubabati Goswami, and Seon-Hee Seo





---

# **Neutrino Masses and Oscillations 2015**

Advances in High Energy Physics

---

## **Neutrino Masses and Oscillations 2015**

Guest Editors: Vincenzo Flaminio, Mauro Mezzetto,  
Leslie Camilleri, Srubabati Goswami, and Seon-Hee Seo



---

Copyright © 2017 Hindawi Publishing Corporation. All rights reserved.

This is a special issue published in "Advances in High Energy Physics." All articles are open access articles distributed under the Creative Commons Attribution License, which permits unrestricted use, distribution, and reproduction in any medium, provided the original work is properly cited.

## Editorial Board

L. A. Anchordoqui, USA  
T. Asselmeyer-Maluga, Germany  
M. Battaglia, Switzerland  
Botio Betev, Switzerland  
L. Bianchini, Switzerland  
Burak Bilki, USA  
Adrian Buzatu, UK  
Rong-Gen Cai, China  
Duncan L. Carlsmith, USA  
Ashot Chilingarian, Armenia  
Anna Cimmino, Belgium  
Andrea Coccaro, Switzerland  
Shi-Hai Dong, Mexico  
Edmond C. Dukes, USA  
Amir H. Fatollahi, Iran

F. Filthaut, Netherlands  
Chao-Qiang Geng, Taiwan  
Philippe Gras, France  
Xiaochun He, USA  
Filipe R. Joaquim, Portugal  
K. K. Joo, Republic of Korea  
Aurelio Juste, Spain  
Michal Kreps, UK  
Ming Liu, USA  
Enrico Lunghi, USA  
Piero Nicolini, Germany  
Seog H. Oh, USA  
Sergio Palomares-Ruiz, Spain  
Giovanni Pauletta, Italy  
Yvonne Peters, UK

Anastasios Petkou, Greece  
Alexey A. Petrov, USA  
Thomas Rössler, Sweden  
J. José Sanz-Cillero, Spain  
Edward Sarkisyan-Grinbaum, USA  
Sally Seidel, USA  
George Siopsis, USA  
Luca Stanco, Italy  
S. Thoudam, Netherlands  
S. Triambak, South Africa  
Elias C. Vagenas, Kuwait  
Nikos Varelas, USA  
Yau W. Wah, USA

# Contents

## **Neutrino Masses and Oscillations 2015**

Vincenzo Flaminio, Mauro Mezzetto, Leslie Camilleri, Srubabati Goswami, and Seon-Hee Seo  
Volume 2017, Article ID 6590489, 3 pages

## **The Opportunity Offered by the ESSnuSB Project to Exploit the Larger Leptonic CP Violation Signal at the Second Oscillation Maximum and the Requirements of This Project on the ESS Accelerator Complex**

E. Wildner, E. Baussan, M. Blennow, M. Bogomilov, A. Burgman, E. Bouquerel, C. Carlile, J. Cederkäll, P. Christiansen, P. Cupial, H. Danared, M. Dracos, T. Ekelöf, M. Eshraqi, R. Hall-Wilton, J.-P. Koutchouk, M. Lindroos, M. Martini, R. Matev, D. McGinnis, R. Miyamoto, T. Ohlsson, H. Öhman, M. Oivegård, R. Ruber, H. Schönauer, J. Y. Tang, R. Tsenov, G. Vankova-Kirilova, and N. Vassilopoulos  
Volume 2016, Article ID 8640493, 16 pages

## **T2K and Beyond**

M. G. Catanesi  
Volume 2016, Article ID 5496103, 17 pages

## **The Use of Low Temperature Detectors for Direct Measurements of the Mass of the Electron Neutrino**

A. Nucciotti  
Volume 2016, Article ID 9153024, 41 pages

## **Neutrinoless Double Beta Decay: 2015 Review**

Stefano Dell’Oro, Simone Marcocci, Matteo Viel, and Francesco Vissani  
Volume 2016, Article ID 2162659, 37 pages

## **The Results of MINOS and the Future with MINOS+**

A. Timmons  
Volume 2016, Article ID 7064960, 25 pages

## **Current Status and Future Prospects of the SNO+ Experiment**

S. Andringa, E. Arushanova, S. Asahi, M. Askins, D. J. Auty, A. R. Back, Z. Barnard, N. Barros, E. W. Beier, A. Bialek, S. D. Biller, E. Blucher, R. Bonventre, D. Braid, E. Caden, E. Callaghan, J. Caravaca, J. Carvalho, L. Cavalli, D. Chauhan, M. Chen, O. Chkvorets, K. Clark, B. Cleveland, I. T. Coulter, D. Cressy, X. Dai, C. Darrach, B. Davis-Purcell, R. Deen, M. M. Depatie, F. Descamps, F. Di Lodovico, N. Duhaime, F. Duncan, J. Dunger, E. Falk, N. Fatemighomi, R. Ford, P. Gorel, C. Grant, S. Grullon, E. Guillian, A. L. Hallin, D. Hallman, S. Hans, J. Hartnell, P. Harvey, M. Hedayatipour, W. J. Heintzelman, R. L. Helmer, B. Hreljac, J. Hu, T. Iida, C. M. Jackson, N. A. Jelley, C. Jillings, C. Jones, P. G. Jones, K. Kamdin, T. Kaptanoglu, J. Kaspar, P. Keener, P. Khaghani, L. Kippenbrock, J. R. Klein, R. Knapik, J. N. Kofron, L. L. Kormos, S. Korte, C. Kraus, C. B. Krauss, K. Labe, I. Lam, C. Lan, B. J. Land, S. Langrock, A. LaTorre, I. Lawson, G. M. Lefevre, E. J. Leming, J. Lidgard, X. Liu, Y. Liu, V. Lozza, S. Maguire, A. Maio, K. Majumdar, S. Manecki, J. Maneira, E. Marzec, A. Mastbaum, N. McCauley, A. B. McDonald, J. E. McMillan, P. Mekarski, C. Miller, Y. Mohan, E. Mony, M. J. Mottram, V. Novikov, H. M. OŠKeeffe, E. OŠullivan, G. D. Orebi Gann, M. J. Parnell, S. J. M. Peeters, T. Pershing, Z. Petriw, G. Prior, J. C. Prouty, S. Quirk, A. Reichold, A. Robertson, J. Rose, R. Rosero, P. M. Rost, J. Rumleskie, M. A. Schumaker, M. H. Schwendener, D. Scislowski, J. Secrest, M. Seddighin, L. Segui, S. Seibert, T. Shantz, T. M. Shokair, L. Sibley, J. R. Sinclair, K. Singh, P. Skensved, A. Sörensen, T. Sonley, R. Stainforth, M. Strait, M. I. Stringer, R. Svoboda, J. Tatar, L. Tian, N. Tolich, J. Tseng, H. W. C. Tseung, R. Van Berg, E. Vázquez-Jáuregui, C. Virtue, B. von Krosigk, J. M. G. Walker, M. Walker, O. Wasalski, J. Waterfield, R. F. White, J. R. Wilson, T. J. Winchester, A. Wright, M. Yeh, T. Zhao, and K. Zuber  
Volume 2016, Article ID 6194250, 21 pages



---

**The Antineutrino Energy Structure in Reactor Experiments**

Pau Novella

Volume 2015, Article ID 364392, 12 pages

**Measurement of Atmospheric Neutrino Oscillations with Very Large Volume Neutrino Telescopes**

J. P. Yáñez and A. Kouchner

Volume 2015, Article ID 271968, 24 pages

**The Deep Underground Neutrino Experiment**

Maury Goodman

Volume 2015, Article ID 256351, 9 pages

**Partial Quark-Lepton Universality and Neutrino CP Violation**

Jiajun Liao, D. Marfatia, and K. Whisnant

Volume 2015, Article ID 561910, 5 pages

**Quasi-Classical Gravity Effect on Neutrino Oscillations in a Gravitational Field of a Heavy Astrophysical Object**

Jonathan Miller and Roman Pasechnik

Volume 2015, Article ID 381569, 15 pages

**Constraints on the Nonstandard Interaction in Propagation from Atmospheric Neutrinos**

Shinya Fukasawa and Osamu Yasuda

Volume 2015, Article ID 820941, 13 pages

## Editorial

# Neutrino Masses and Oscillations 2015

**Vincenzo Flaminio,<sup>1</sup> Mauro Mezzetto,<sup>2</sup> Leslie Camilleri,<sup>3</sup>  
Srubabati Goswami,<sup>4</sup> and Seon-Hee Seo<sup>5</sup>**

<sup>1</sup>Physics Department and INFN, Pisa University, Largo B. Pontecorvo, 56127 Pisa, Italy

<sup>2</sup>Physics Department and INFN, Padova University, Via Marzolo, 35131 Padova, Italy

<sup>3</sup>Nevis Labs, Columbia University, P.O. Box 137, Irvington, NY 10533, USA

<sup>4</sup>Physical Research Laboratory, Navrangpura, Ahmedabad 380009, India

<sup>5</sup>Department of Physics and Astronomy, Seoul National University, 1 Gwanak-ro, Gwanak-gu, Seoul 08826, Republic of Korea

Correspondence should be addressed to Vincenzo Flaminio; [vincenzo.flaminio@cern.ch](mailto:vincenzo.flaminio@cern.ch)

Received 25 February 2016; Accepted 25 February 2016; Published 13 February 2017

Copyright © 2017 Vincenzo Flaminio et al. This is an open access article distributed under the Creative Commons Attribution License, which permits unrestricted use, distribution, and reproduction in any medium, provided the original work is properly cited. The publication of this article was funded by SCOAP<sup>3</sup>.

This volume follows the one published in 2014, on the occasion of the 100th anniversary of the birth of Bruno Pontecorvo.

The last two years have witnessed an impressive progress in our understanding of the phenomenon of neutrino oscillations.

The field of neutrino oscillations has moreover acquired worldwide resonance after the 2015 Physics Nobel Prize awarded to Takaaki Kajita and Arthur B. McDonald “for the discovery of neutrino oscillations, which shows that neutrinos have mass.”

In parallel, the construction of new detectors aimed at a direct measurement of the mass of the electron neutrino and of neutrinoless double beta decay has been completed or is approaching completion.

Reactor antineutrino experiments have improved by large amounts the precision in the determination of the oscillation parameters, notably those of  $\sin^2 2\theta_{13}$  and  $\Delta m_{ee}^2$ .

Thanks to a big increase in the sensitivity of both reactor and accelerator experiments, a determination of the CP violating parameter  $\delta$  seems within reach now.

Recent, accurate measurements of the electron antineutrino flux from nuclear reactors have been reported by the experiments Daya Bay, Double Chooz, and RENO. These have confirmed the previous hints for an electron antineutrino flux lower than previously assumed, with a visible anomaly around 5 MeV. This will have implications not only for the determination of the neutrino oscillation parameters

but also for the possible existence of the so-called *sterile neutrinos*.

It should moreover be recalled that in 2015-2016 the first observation has taken place of neutrinos of astrophysical origin, by the IceCube experiment. This experiment and its European counterpart, ANTARES, have provided a detailed measurement of the flux and energy distribution of atmospheric neutrinos, used to obtain independent information on neutrino oscillations, as shown in one of the contributions to this volume.

Following the discovery of neutrino oscillations that require neutrinos to be massive but can only provide information on neutrino mass differences, the efforts to measure the absolute neutrino masses have become even more topical. The paper “*The Use of Low Temperature Detectors for Direct Measurements of the Mass of the Electron Neutrino*” by A. Nucciotti describes extensively the progress in the use of low temperature detectors now being used and planned to reach sub-eV sensitivity. Progress in the energy resolution and scalability of these detectors has made this technique competitive with the more traditional tritium beta decay magnetic/electrostatic spectrometer method.

The article “*T2K and Beyond*” by M. G. Catanesi describes the detector and the results of the T2K experiment in Japan on the measurement of angle  $\theta_{13}$ . The paper then goes on to summarize the future prospects of the project for the measurement of  $\theta_{13}$  and of the CP phase  $\delta$  with the already approved running and also following possible upgrades of the beam line

and reduction of the measurement systematics which could lead to a first observation of a nonzero value of  $\delta$ . The synergy of T2K with the NOvA experiment in the USA is also covered.

The European Spallation Source is currently being built in Sweden. The article “*The Opportunity Offered by the ESSnuSB Project to Exploit the Larger Leptonic CP Violation Signal at the Second Oscillation Maximum and the Requirements of this Project on the ESS Accelerator Complex*,” by E. Wildner and collaborators describes the possibility of using it for the production of a very intense 0.4 GeV neutrino beam. The paper then summarizes how this beam, when coupled with a large underground water Cerenkov detector placed at the second oscillation maximum 540 km from the neutrino source, could lead to the discovery of CP violation at  $5\sigma$  level over a significant fraction of the range of the CP violation phase.

The article “*Current Status and Future Prospects of the SNO+ Experiment*” by S. Andringa et al. describes the many physics targets that can be reached by that experiment, ranging from neutrinoless double beta decay to neutrino oscillations and supernova neutrinos.

The experiment is located at a depth of about 5900 meters of water equivalent, at the site of SNOLAB (Sudbury, Canada). Neutrinoless double beta decay will be the main object of the experiment and certainly the one that will be tackled initially. To this purpose the detector will be filled with about 780 tons of ultrapure liquid scintillator, loaded with 800 kg of  $^{130}\text{Te}$ . The corresponding effective Majorana neutrino sensitivity is expected to fall in the range 55–133 meV.

SNO+ aims in addition to measure reactor antineutrino oscillations, with neutrinos coming from reactors located at various distances from the detector, both in Canada and in the USA.

SNO+ also aims at the detection of geoneutrinos and solar neutrinos and of supernova neutrinos.

The article “*Measurement of atmospheric neutrino oscillations with very large volume neutrino telescopes*” by J. P. Yanez and A. Kouchner discusses the recent results obtained by the IceCube and ANTARES experiments for atmospheric neutrino oscillations. These are mainly sensitive to  $\nu_\mu \rightarrow \nu_e$  oscillations and mainly to the large mass splittings. The article discusses in detail the geometry of the experiments and the event reconstruction and analysis.

The results obtained so far are still not competitive with those provided by accelerator experiments, but with the increase in statistics and detector improvements they will provide substantially more precise determinations.

The article also discusses the results that will be obtained by the forthcoming extensions of both experiments: PINGU at the South Pole and ORCA in the Mediterranean.

The article “*The Antineutrino Energy Structure in Reactor Experiments*” by P. Novella summarizes the current status of the 5 MeV excess ( $\sim 4$  sigma) seen in the visible energy spectrum of the electron antineutrinos in the three reactor neutrino experiments: Daya Bay, Double Chooz, and RENO. All three experiments showed a consistent result for the 5 MeV excess, which is not explained by the reactor neutrino model most widely used. The possible causes of the 5 MeV excess are studied but such excess is most likely due to an incomplete

or inaccurate model and to the associated uncertainty on the spectrum as predicted by the model. This article suggests possible future directions in the study of the reactor antineutrino spectrum that could hopefully explain the excess.

The article “*The Results of MINOS and the Future with MINOS+*” by A. Timmons describes the achievements of the long baseline MINOS experiment. The experiment, using the Fermilab NuMI muon neutrino-antineutrino beam, having energies between 0 and 15 GeV and a near and a far detector located about 700 km away from each other, has measured the disappearance of muon neutrinos and antineutrinos, made a search for the appearance of electron neutrinos, and measured the neutral-current interaction rate. The latter has confirmed oscillations between only three neutrino flavours, thus placing limits on the so-called sterile neutrinos. MINOS will continue as MINOS+ in an upgraded beam with increased energy and intensity, allowing precision tests of the three-flavour neutrino oscillation picture, in particular a very sensitive search of sterile neutrinos.

The article “*The Deep Underground Neutrino Experiment (DUNE)*,” by M. Goodman, discusses the status and perspectives of the next-generation long baseline neutrino experiment that will use a beam generated at Fermilab. The collaboration plans to build a staged 40 kt liquid argon detector at the Sanford Underground Research Facility in South Dakota, a high precision near detector, and a powerful neutrino beam line generated by a 1.2 MW proton beam produced by the PIP-II upgrade, evolving to a power of 2.3 MW by 2030. The paper describes the oscillation physics goals and the status of the collaboration.

The neutrinoless double beta decay process violates lepton number by two units and thus its observation would imply the Majorana nature of the neutrinos, underscoring the importance of this process. In the review article “*Neutrinoless Double Beta Decay: 2015 Review*” by S. Dell’Oro et al. a comprehensive review on the status of this process is presented.

The review discusses various aspects of the experiments searching for this rare process and the role of nuclear physics including salient features of the different models for calculating nuclear matrix element uncertainties as well as implications for neutrino mass models.

In the article “*Quasi-Classical Gravity Effect on Neutrino Oscillations in a Gravitational Field of a Heavy Astrophysical Object*” by J. Miller and R. Pasechnik, implications of quantum gravity effects on neutrino oscillations are explored.

The authors compare the decoherence in the neutrino propagation states due to quantum gravity effects with the one induced by the Earth matter effect. This enables them to propose a new way for detecting quantum gravity effects through the measurement of the flavour composition of astrophysical neutrinos.

The article “*Partial Quark-Lepton Universality and Neutrino CP Violation*” by J. Liao et al. presents a model with partial quark-lepton universality. Such models can naturally arise in the context of grand unified theories. The constraint on the model parameters in terms of the Dirac CP phase is discussed.

In the article “*Constraints on the Nonstandard Interaction in Propagation from Atmospheric Neutrinos*” by S. Fukasawa and O. Yasuda, the effect of nonstandard interactions on the

propagation of atmospheric neutrinos is studied assuming only the electron and the tau neutrinos are affected by such interactions. Constraints on parameters characterizing this effect are obtained from SuperKamiokande data and predictions for the future HyperKamiokande experiment are also made.

*Vincenzo Flaminio*  
*Mauro Mezzetto*  
*Leslie Camilleri*  
*Srubabati Goswami*  
*Seon-Hee Seo*

## Research Article

# The Opportunity Offered by the ESSnuSB Project to Exploit the Larger Leptonic CP Violation Signal at the Second Oscillation Maximum and the Requirements of This Project on the ESS Accelerator Complex

**E. Wildner,<sup>1</sup> E. Baussan,<sup>2</sup> M. Blennow,<sup>3</sup> M. Bogomilov,<sup>4</sup>  
A. Burgman,<sup>5</sup> E. Bouquerel,<sup>2</sup> C. Carlile,<sup>6</sup> J. Cederkäll,<sup>5</sup> P. Christiansen,<sup>5</sup>  
P. Cupial,<sup>7</sup> H. Danared,<sup>8</sup> M. Dracos,<sup>2</sup> T. Ekelöf,<sup>6</sup> M. Eshraqi,<sup>8</sup>  
R. Hall-Wilton,<sup>8</sup> J.-P. Koutchouk,<sup>1,6</sup> M. Lindroos,<sup>8</sup> M. Martini,<sup>1</sup>  
R. Matev,<sup>4</sup> D. McGinnis,<sup>8</sup> R. Miyamoto,<sup>8</sup> T. Ohlsson,<sup>3</sup> H. Öhman,<sup>6</sup>  
M. Olvegård,<sup>6</sup> R. Ruber,<sup>6</sup> H. Schönauer,<sup>1</sup> J. Y. Tang,<sup>9</sup> R. Tsenov,<sup>4</sup>  
G. Vankova-Kirilova,<sup>4</sup> and N. Vassilopoulos<sup>9</sup>**

<sup>1</sup>CERN, 1211 Geneva 23, Switzerland

<sup>2</sup>IPHC, Université de Strasbourg, CNRS/IN2P3, 67037 Strasbourg, France

<sup>3</sup>Department of Theoretical Physics, School of Engineering Sciences, KTH Royal Institute of Technology, AlbaNova University Center, 106 91 Stockholm, Sweden

<sup>4</sup>Department of Atomic Physics, St. Kliment Ohridski University of Sofia, 1164 Sofia, Bulgaria

<sup>5</sup>Department of Physics, Lund University, P.O. Box 118, 221 00 Lund, Sweden

<sup>6</sup>Department of Physics and Astronomy, Uppsala University, P.O. Box 516, 75120 Uppsala, Sweden

<sup>7</sup>AGH University of Science and Technology, Aleja Mickiewicza 30, 30-059 Krakow, Poland

<sup>8</sup>European Spallation Source, ESS ERIC, P.O. Box 176, 221 00 Lund, Sweden

<sup>9</sup>Institute of High Energy Physics, CAS, Beijing 100049, China

Correspondence should be addressed to E. Wildner; [elena.wildner@cern.ch](mailto:elena.wildner@cern.ch) and T. Ekelöf; [tord.ekelof@physics.uu.se](mailto:tord.ekelof@physics.uu.se)

Received 3 September 2015; Revised 18 December 2015; Accepted 29 December 2015

Academic Editor: Leslie Camilleri

Copyright © 2016 E. Wildner et al. This is an open access article distributed under the Creative Commons Attribution License, which permits unrestricted use, distribution, and reproduction in any medium, provided the original work is properly cited. The publication of this article was funded by SCOAP<sup>3</sup>.

The European Spallation Source (ESS), currently under construction in Lund, Sweden, is a research center that will provide, by 2023, the world's most powerful neutron source. The average power of the proton linac will be 5 MW. Pulsing this linac at higher frequency will make it possible to raise the average total beam power to 10 MW to produce, in parallel with the spallation neutron production, a very intense neutrino Super Beam of about 0.4 GeV mean neutrino energy. This will allow searching for leptonic CP violation at the second oscillation maximum where the sensitivity is about 3 times higher than at the first. The ESS neutrino Super Beam, ESSnuSB operated with a 2.0 GeV linac proton beam, together with a large underground Water Cherenkov detector located at 540 km from Lund, will make it possible to discover leptonic CP violation at  $5\sigma$  significance level in 56% (65% for an upgrade to 2.5 GeV beam energy) of the leptonic CP-violating phase range after 10 years of data taking, assuming a 5% systematic error in the neutrino flux and 10% in the neutrino cross section. The paper presents the outstanding physics reach possible for CP violation with ESSnuSB obtainable under these assumptions for the systematic errors. It also describes the upgrade of the ESS accelerator complex required for ESSnuSB.

## 1. Overview

An ultimate goal of the long baseline neutrino experiments now being planned is the discovery and high precision measurement of the leptonic CP violation through measurement of the  $\nu_\mu \rightarrow \nu_e$  oscillation probability. Such a discovery and measurement would shed new light on the fundamental problem of how to explain the dominance of matter over antimatter in the Universe. The discovery and measurement in 2012 of a nonzero value as large as ca.  $9^\circ$  of the neutrino mixing angle  $\theta_{13}$ , corresponding to a value of  $\sin^2 2\theta_{13}$  of ca. 0.095 [1–4], confirmed the possibility of discovering and measuring a nonzero value of the Dirac leptonic CP violating angle  $\delta_{CP}$ . Before 2012 a significantly smaller value for  $\theta_{13}$  was assumed when planning for future long base neutrino experiments. See, for example, [5], in which a range of values for  $\sin^2 2\theta_{13}$  between 0.01 and 0.09 are used, with 0.04 as the standard value, to evaluate the performance of a proposed experiment. The large value of  $\theta_{13}$  implies that the sensitivity to CP violation is three times higher at the second neutrino oscillation maximum as compared to the first.

The European Spallation Source (ESS) [6] under construction in Lund, Sweden, since the fall of 2014, is a research center that will have the world's most powerful neutron source. It is based on a 2.0 GeV superconducting linac (with space available for an upgrade to the originally planned energy of 2.5 GeV), providing 2.86 ms long proton pulses at 14 Hz for the spallation neutron facility with 5 MW average power on target (Figure 1). By pulsing the linac at higher frequency, additional beam pulses can be interleaved to provide a total average beam power of 10 MW. The extra pulses, providing  $1.5 \cdot 10^{16}$  protons per second on target, corresponding to  $2.7 \cdot 10^{23}$  protons on target per year, can be used to obtain a neutrino beam of unprecedented intensity. The uniquely high intensity of the ESS linac allows for sufficient event statistics to be collected with a Megaton neutrino detector positioned at the second neutrino oscillation maximum, where the relative CP violation sensitivity is about three times higher than at the first maximum, where the DUNE experiment in the USA [7] and the Hyper-K experiment in Japan [8] have their respective detectors positioned.

In a first publication [9] the European Spallation Source neutrino Super Beam (ESSnuSB) collaboration proposes searching for leptonic CP violation by making use of the Super Beam described above and a Megaton water Cherenkov detector placed in the 1200 m deep Garpenberg mine located at a distance of 540 km from the neutrino source in Lund, near the second neutrino oscillation maximum. In the present paper we report on some further progress made in the study of the ESSnuSB project, in particular regarding its performance for CP violation discovery and measurement, the proton accumulator ring, and the Near Detector. Table 1 shows an overview of the parameters of the facility. The ESSnuSB Design Study is taking advantage of many of the results obtained in the FP7 Design Study EUROnu [10] on future neutrino facilities. The results from the now terminated EUROnu project of the study of the 4.5 GeV/5 MW neutrino Super Beam from the CERN Superconducting Proton Linac

TABLE 1: Main parameters of the ESSnuSB neutrino facility.

Parameter	Value
Average neutrino energy	0.36 GeV
Baseline	540 km
Detector technology	Water Cherenkov
Fiducial volume	500 kt
PMTs	240k 8"
10-year reach ( $2\nu + 8\bar{\nu}$ )	60% of $\delta_{CP}$ range ( $5\sigma$ )
$L/E$ (2nd oscillation max.)	1500 km/GeV

TABLE 2: Current main parameters of the ESS linac.

Parameter	Value
Average beam power	5 MW
Ion kinetic energy	2 GeV
Average macro pulse current	62.5 mA
Average macro pulse length	2.86/4 ms
Pulse repetition rate	14 Hz
Maximum accelerating cavity surface field	45 MV/m
Linac length	352.5 m
Reliability	95%
Annual operating period	5000 h

SPL [11, 12] and of the MEMPHYS large water Cherenkov detector in the Fréjus tunnel have served as very useful references in the ESSnuSB Design Study [13, 14].

The purpose of ESS is the production and use of spallation neutrons. The use of the ESS linac for neutron and neutrino production simultaneously, not reducing neutron production, will decrease considerably the cost of the proposed neutrino project as compared to constructing a dedicated proton driver for generating the neutrino beam. The current main parameters of the ESS proton driver are listed in Table 2.

With presently available technology, the horn-type hadron collector cannot handle 2.86 ms long pulses due to the excessive ohmic heating of the magnet-system current-leads. Therefore, the linac pulse has to be accumulated in a multiturn injection storage ring that can deliver, through single turn extraction, pulses of a few  $\mu$ s length to the neutrino production target and horn assembly. There is space available on the ESS site to implement such a proton accumulator and its transfer lines from the linac to the target station as well as for the implementation of the target station itself and a Near Detector. To inject protons from the linac into the accumulator with satisfactory efficiency, charge exchange injection will be necessary. Therefore, the ESS linac has to be further equipped such that it can be used to accelerate  $H^-$  pulses of the same length and intensity as the proton pulses.

A preliminary study of the modifications of the ESS linac that are required to allow simultaneous acceleration of  $H^+$  and  $H^-$  ions at an average power of 5 + 5 MW has been made [15]. It is proposed that some of these modifications be made already during the current linac construction phase, such that it will later be possible to upgrade the linac with only minor interventions during the operation of the linac for

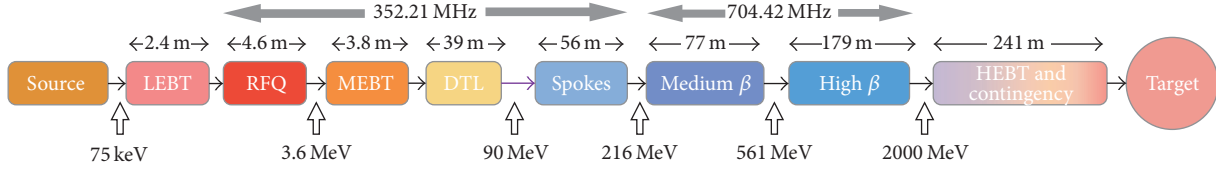


FIGURE 1: The ESS superconducting linac.

spallation neutron production. These modifications, which will increase the initial construction cost of the linac by ca. 10%, will significantly reduce the cost of the subsequent upgrade of the linac to enable the production of a neutrino beam.

The proposed upgrade of the accelerator complex will significantly increase the potential and options also for other future developments of the ESS. One example of this is that the accumulator studies aim at a design allowing the accumulator to satisfy the requirements for the production of both short neutrino pulses of a few  $\mu\text{s}$  length through single turn extraction and short neutron pulses of the order of 100  $\mu\text{s}$  length through multiturn extraction, thus also providing, as a future option, the production of short, uniquely intense neutron pulses [16].

The EUROnu studies identified some key elements of the SPL Super Beam for which further R&D would be necessary, such as the proton target, the hadron collector, and its pulse generator. These items will be further studied to prove their feasibility for the ESS based neutrino project. Simulation studies have resulted in the choice of the 1200 m deep Garpenberg mine in the Swedish Dalarna county, 540 km from ESS in Lund, as the optimal location for the Far Neutrino Detector. The Near Detector will contain a water Cherenkov detector and possibly other types of detectors. Results from the European FP7 LAGUNA Design Study [17] provide useful information for the design of the detectors and the needed infrastructure.

## 2. The Significant Advantage of Measuring Leptonic CP Violation at the Second Oscillation Maximum

The following expression describes the probability for the  $\nu_\mu \rightarrow \nu_e$  oscillation [19]:

$$\begin{aligned}
 P(\nu_\mu \rightarrow \nu_e) &= \sin^2 \theta_{23} \sin^2 2\theta_{13} \sin^2 \left( \frac{\Delta_{31} L}{2} \right) \\
 &+ \cos^2 \theta_{23} \sin^2 2\theta_{12} \sin^2 \left( \frac{\Delta_{21} L}{2} \right) \\
 &+ \tilde{J} \cos \left( \delta_{\text{CP}} - \frac{\Delta_{31} L}{2} \right) \sin \left( \frac{\Delta_{21} L}{2} \right) \sin \left( \frac{\Delta_{31} L}{2} \right),
 \end{aligned} \tag{1}$$

where  $\tilde{J} \equiv \cos \theta_{13} \sin 2\theta_{12} \sin 2\theta_{23} \sin 2\theta_{13}$  and  $\Delta_{ij} \equiv \Delta m_{ij}^2 / 2E_\nu$ . The sign of  $\delta_{\text{CP}}$  is the opposite for antineutrinos.

The first two terms in this expression are generally referred to as the ‘‘atmospheric’’ term and the ‘‘solar’’ term,

respectively. The third is the ‘‘CP interference’’ term which is the only term that depends on the CP violating angle  $\delta_{\text{CP}}$ .

Plots for two different values of the mixing angle,  $\theta_{13} = 1^\circ$  and  $\theta_{13} = 10^\circ$ , of the three terms in the  $\nu_\mu \rightarrow \nu_e$  oscillation probability expression are shown in Figure 2 as a function of the variable  $L/E$ , the ratio between the accelerator-detector distance  $L$  (the baseline) and the neutrino energy  $E$ . The CP violating term is calculated without the factor  $\cos(\delta_{\text{CP}} - \Delta_{31} L/2)$ ; that is, what is shown is the maximum value this term could take on. The first and second neutrino oscillation maxima are clearly seen in the atmospheric term to be at around  $L/E = 500 \text{ km/GeV}$  and  $1500 \text{ km/GeV}$ .

The information on  $\delta_{\text{CP}}$  is thus contained in the CP interference term. As can be seen in Figure 2(a), for a value of the neutrino mixing angle  $\theta_{13}$  that is small, like  $1^\circ$ , which lies within the range of values used in the long baseline neutrino study projects before 2012, the CP interference term at  $L/E = 500 \text{ km/GeV}$  is somewhat larger than both the solar and the atmospheric term, whereas at  $L/E = 1500 \text{ km/GeV}$  the CP interference term is much smaller than the dominant solar term. Had the value of  $\theta_{13}$  indeed been small, the sensitivity to  $\delta_{\text{CP}}$  would thus have been much higher at  $L/E = 500 \text{ km/GeV}$  than at  $L/E = 1500 \text{ km/GeV}$ . This is certainly one reason why some proposed projects, which were designed well before 2012, have their respective detectors placed at a distance from the accelerator approximately corresponding to  $L/E = 500 \text{ km/GeV}$ , that is, at the first maximum. However, when in 2012  $\theta_{13}$  was measured and found to be about  $9^\circ$  [1–4], the relation between the three terms was drastically changed as shown in Figure 2(b). For  $\theta_{13} = 10^\circ$ , the CP interference term at  $L/E = 500 \text{ km/GeV}$  is much smaller than the dominant atmospheric term, whereas it has about the same amplitude as the dominant atmospheric term at  $L/E = 1500 \text{ km/GeV}$ . From these considerations it is thus clear that the sensitivity to  $\delta_{\text{CP}}$  indeed is significantly higher at the second neutrino oscillation maximum than at the first.

The conceptual design of ESSnuSB [9] was made in 2012 and in view of the, at the time, newly measured high value of  $\theta_{13}$ , the detector was located at the second neutrino oscillation maximum. For an ESSnuSB proton energy of 2.0 GeV the mean neutrino energy is about 360 MeV and the distance of the second maximum from the  $\nu_\mu$  source is of the order of 540 km. Figure 3 shows, for this baseline, the number of electron neutrinos detected in two years, running with positive polarity in the horn, as a function of neutrino energy  $E$  for four different values of  $\delta_{\text{CP}}$ : 0 and  $\pi$ , which correspond to no CP violation, and  $\pi/2$  and  $3\pi/2$ , which correspond to maximum CP violation of opposite signs, respectively. The parameters used in the GLOBES calculation to obtain this plot are  $\Delta m_{21}^2 = 7.5 \cdot 10^{-5} \text{ eV}^2$ ,  $\Delta m_{31}^2 = 2.47 \cdot 10^{-3} \text{ eV}^2$ ,  $\theta_{12} = 0.58$ ,

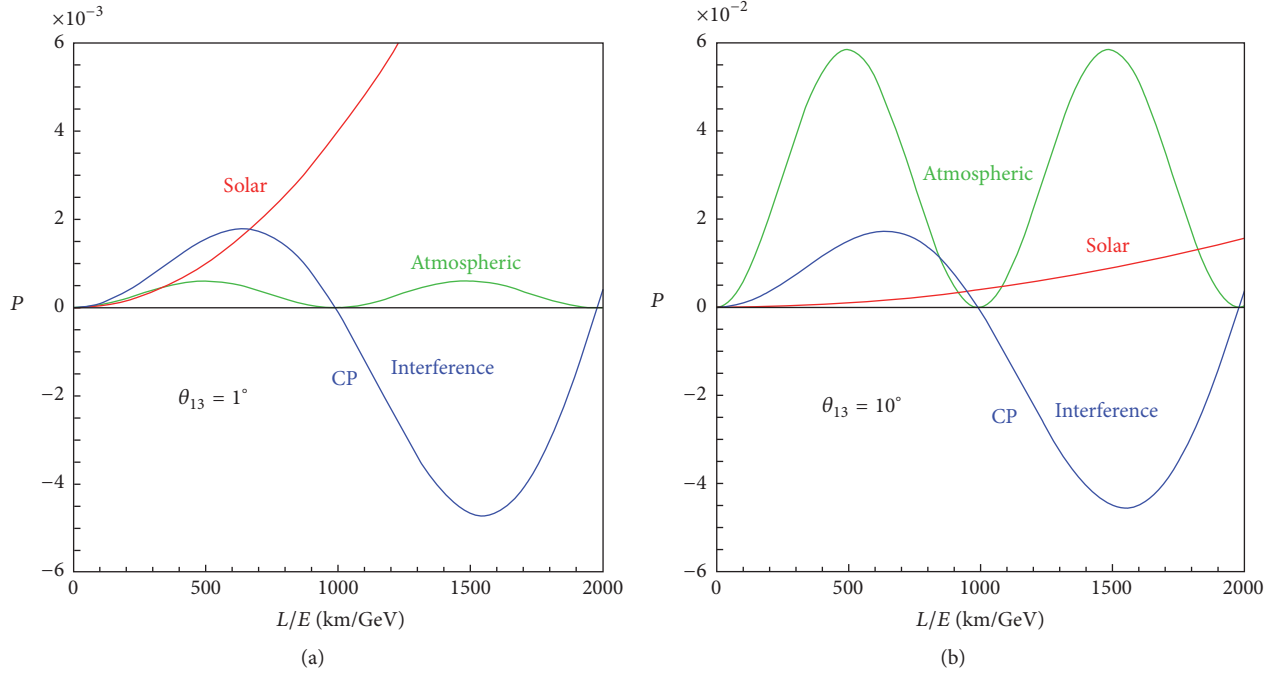


FIGURE 2: Plots showing, for two different values of the neutrino mixing angle  $\theta_{13} = 1^\circ$  (a) and  $\theta_{13} = 10^\circ$  (b), the three terms in the expression for the  $\nu_\mu \rightarrow \nu_e$  oscillation probability as a function of the ratio between the accelerator-to-detector distance  $L$  (the baseline) and the neutrino energy  $E$  [19]. The CP violating term is calculated without the factor  $\cos(\delta_{\text{CP}} - \Delta_{31}L/2)$ ; that is, what is shown is the maximum value this term could take on.

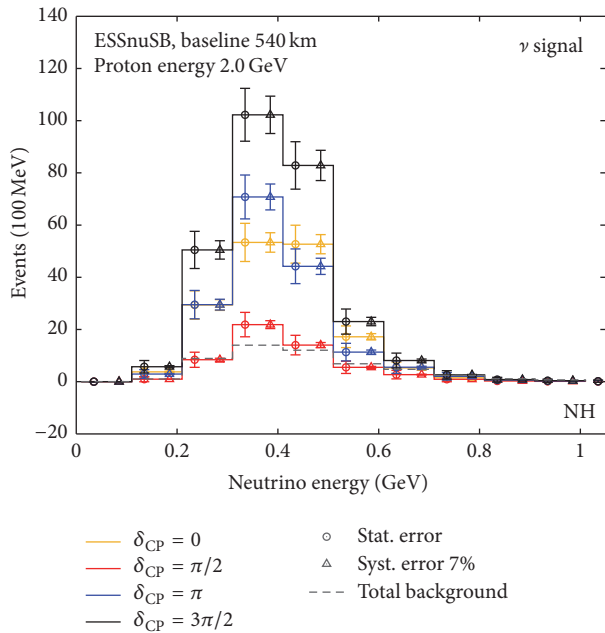


FIGURE 3: Histograms showing, for a baseline of 540 km and a proton energy of 2.0 GeV, the energy distribution for the electron neutrinos detected during 2 years of data taking for three different values of  $\delta_{\text{CP}}$ .

$\theta_{13} = 0.15$ , and  $\theta_{23} = 0.70$ . These parameters are included assuming prior knowledge with an accuracy of 3% for  $\theta_{12}$ , 0.02 for  $\sin^2 2\theta_{23}$ , 0.005 for  $\sin^2 2\theta_{13}$ , 4% for  $\Delta m_{31}^2$ , and 3%

for  $\Delta m_{21}^2$  at  $1\sigma$  level. The neutrino mass hierarchy is assumed to be unknown. The same parameters have been used for all results of ESSnuSB calculations shown in this paper.

Figure 4 shows the same type of comparison, this time between DUNE and Hyper-K, designed to measure at the first maximum, and ESSnuSB, designed to measure at the second maximum. A comparison of the left and right panels shows that almost all of the events in the Hyper-K and DUNE experiments are located within the region of the first oscillation maximum whereas for ESSnuSB almost all of the events are located within the region of the second maximum. In particular, there is no increase in the signal count rate visible for Hyper-K or DUNE in the energy region of the second maximum. The ratio between the numbers of electron neutrinos with  $\delta_{\text{CP}} = 3\pi/2$  and with  $\delta_{\text{CP}} = \pi/2$  can be seen to be about 1.5 for DUNE, 1.6 for Hyper-K, and as high as about 4.8 for ESSnuSB, implying an about three times higher sensitivity to the value of  $\delta_{\text{CP}}$  as compared to the other two experiments.

The four bins in Figure 5 show the total number of events detected at the second maximum for neutrinos and antineutrinos and for a proton energy of 2 GeV and 2.5 GeV, respectively. The data collection time is 2 years with neutrinos and 8 years with antineutrinos in order to detect (very) approximately equal numbers of electron neutrinos and antineutrinos. For a proton energy of 2.5 GeV the total number of events can be seen to be somewhat higher than for a 2.0 GeV proton energy, indicating that the energy originally planned for the ESS project of 2.5 GeV would be more favorable for ESSnuSB than the recently downscoped value of 2.0 GeV.

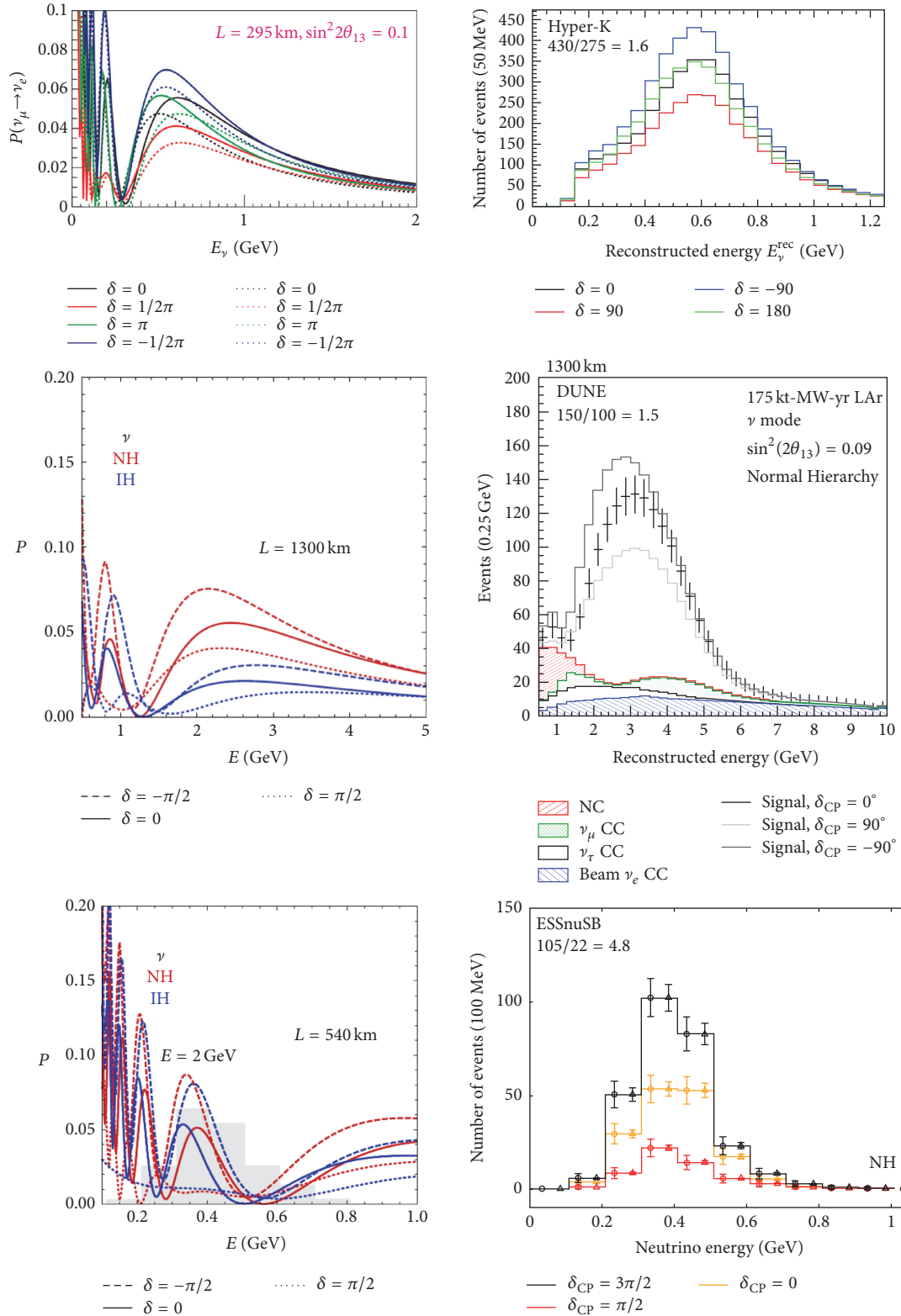


FIGURE 4: The histograms in the panels in the right hand part of the figure show, for the three different neutrino beam projects Hyper-K [8], DUNE [20, 21], and ESSnuSB, the number of detected electron neutrinos as a function of neutrino energy  $E$  for three different values of  $\delta_{\text{CP}}$ : 0, which corresponds to no CP violation, and  $\pi/2$  and  $3\pi/2$ , which correspond to maximum CP violation of opposite signs, respectively. The left panels show the calculated probability for the electron neutrino oscillation for the same three  $\delta_{\text{CP}}$  values and for Normal Hierarchy (NH, red) and Inverted Hierarchy (IH, blue) [8, 21]. The shaded histogram in the left ESSnuSB panel shows the profile of the unoscillated (muon) neutrino energy distribution. The ratio between the numbers of electron neutrinos with  $\delta_{\text{CP}} = 3\pi/2$  and with  $\pi/2$  is 4.8 for ESSnuSB and 1.6 and 1.5, respectively, for Hyper-K and LBNE/DUNE, as noted under the experiment acronym in each histogram graph.

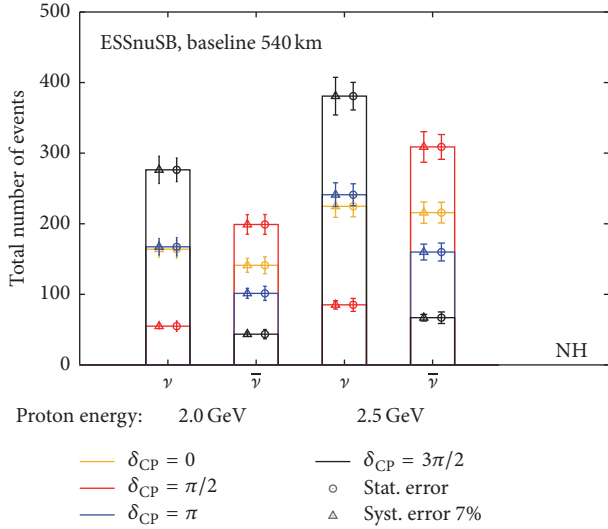


FIGURE 5: The bins show the total numbers of electron neutrinos and antineutrinos, respectively, detected in ESSnuSB after 2 years of data taking with a neutrino beam and 8 years with an antineutrino beam and for a proton energy of 2.0 GeV and for 2.5 GeV, respectively, with the detector placed at the second maximum.

The T2K experiment [22] has, after 4 years of operation and data analysis, managed to reduce its systematic uncertainties for the electron (muon) neutrino signal to a level of 6.3% (7.4%). Figure 3 shows, for each 100 MeV bin, the statistical errors as well as a 7% systematic error. The statistical error is seen to be larger than the systematic one. However, as shown by the leftmost bar in Figure 5, which represents the total numbers of events in the histograms in Figure 3, for the total number of events the statistical and systematic errors are in balance. This raises the question of how much information is contained in the relative shape of the histograms in Figure 3, as this information is not taken into account when considering only the total number of events. The answer to this question may be deduced from the four different histograms in Figure 6, which have been obtained by dividing the four histograms of Figure 3 by their respective total numbers of events. There is some difference between the curves in Figure 6 but these differences are comparable in magnitude to the statistical errors.

Described so far is what could be done with ESSnuSB neutrino beam data collected during 2 years. However, a major goal is to compare the neutrino and antineutrino beam data shown in Figure 5, which provides additional and very sensitive information on  $\delta_{CP}$ . Figure 7 shows for ESSnuSB the normalized difference between the total numbers of electron neutrinos, collected during 2 years, and of electron antineutrinos, collected during 8 years  $(N_{\nu_e} - N_{\bar{\nu}_e}) / (N_{\nu_e} + N_{\bar{\nu}_e})$  for a proton energy of 2.0 GeV and 2.5 GeV, respectively, at the first maximum (a) and the second maximum (b). The normalization takes into account the difference in the production as well as the detection cross sections between the neutrinos and the antineutrinos. The variation of the asymmetry with  $\delta_{CP}$  can be seen to be significantly bigger at the second maximum as compared to the first maximum and

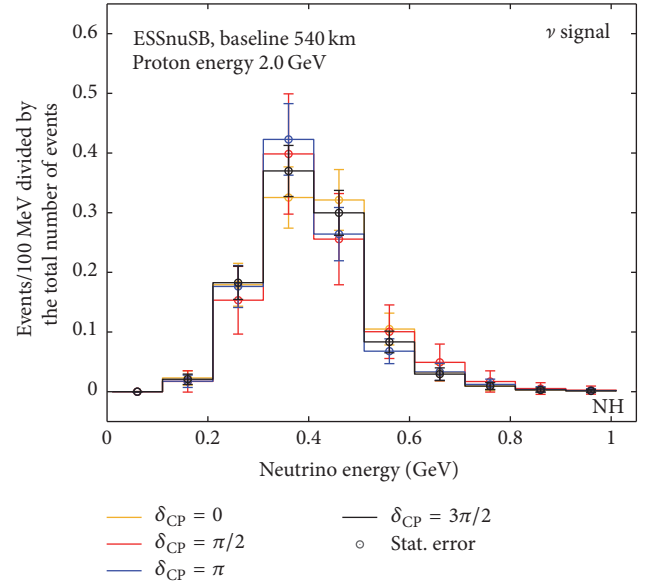


FIGURE 6: The 4 different histograms in this figure have been obtained by dividing each of the four different histograms in Figure 3 by their respective total numbers of events, so that the difference in relative shape between the histograms can be seen.

the statistical and systematic errors are well balanced. Other investigations of the sensitivity of the neutrino-antineutrino asymmetry to the value of  $\delta_{CP}$  have shown that the probability  $P(\bar{\nu}_\mu \rightarrow \bar{\nu}_e)$  varies with  $\delta_{CP}$  between 1/2 and 2 times the probability  $P(\nu_\mu \rightarrow \nu_e)$  at the first maximum and between 1/7 and 7 times the probability  $P(\nu_\mu \rightarrow \nu_e)$  at the second maximum [23].

By fitting simulated [24, 25] ESSnuSB data collected during 2 years with a neutrino beam and 8 years with an antineutrino beam one may calculate the fraction of the total range of possible values for  $\delta_{CP}$  for which CP violation can be discovered with  $5\sigma$  and  $3\sigma$  significance level, respectively. In Figure 8 the result of such global calculations is plotted for different distances between the accelerator and the detector  $L$  from 100 km to 1000 km (horizontal axis), for the three different proton beam energies 2.0, 2.5, and 3.0 GeV (blue, green, and red lines, resp.), and with the mixing angle  $\theta_{13} = 8.73^\circ$ . From these curves one may see that the highest potential for discovery is at the second maximum. One can also see that the potential is somewhat higher for a proton beam energy of 2.5 GeV (and 3.0 GeV) as compared to 2.0 GeV. The systematic errors used to produce these plots are those shown in the left column (SB Def.) of Table 3 [18].

With the exceptionally high power of the ESS linac it is possible to profit from the significantly higher sensitivity to  $\delta_{CP}$  at the second maximum, rendering ESSnuSB about three times less sensitive to systematic errors as compared to experiments measuring at the first maximum.

Figure 9 shows, for ESSnuSB using a 540 km baseline and a proton energy of 2.0 GeV ((a) current ESS design) and 2.5 GeV ((b) originally planned linac energy for which upgrade space is available in the linac tunnel), respectively, the dependence of the fraction of values of  $\delta_{CP}$  for which

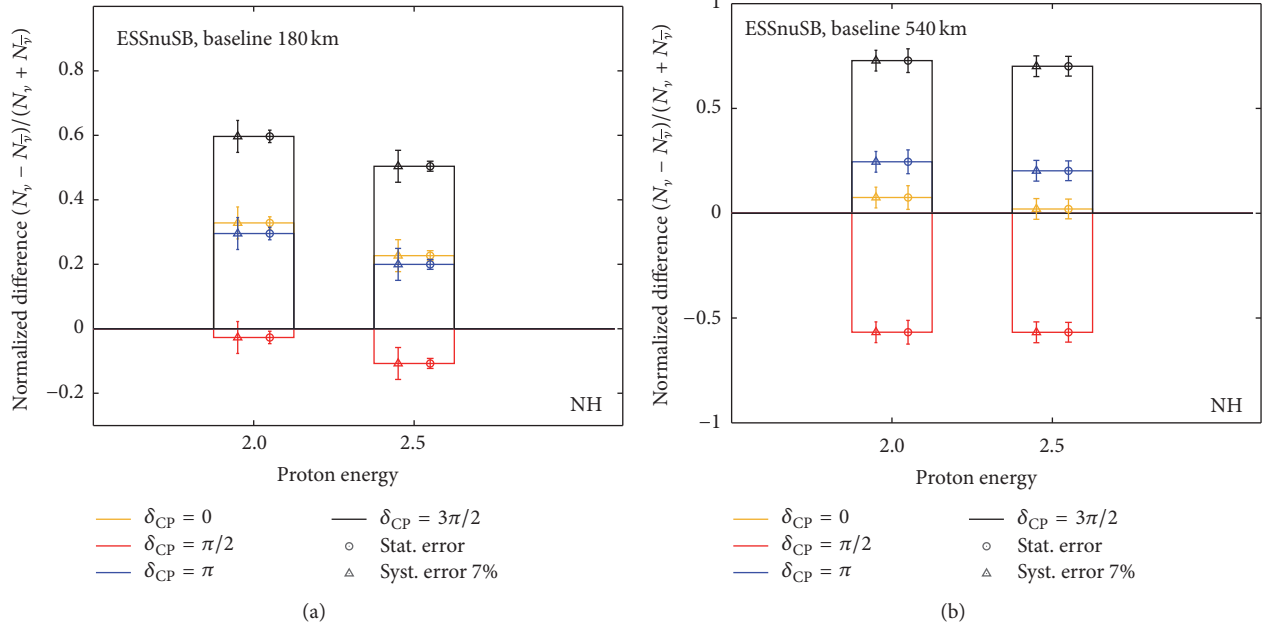


FIGURE 7: The towers show the normalized difference between the total numbers of electron neutrinos and of electron antineutrinos  $(N_{\nu_e} - N_{\bar{\nu}_e})/(N_{\nu_e} + N_{\bar{\nu}_e})$  for a proton energy of 2.0 GeV and 2.5 GeV, respectively, at the first maximum (180 km (a)) and the second maximum (540 km (b)).

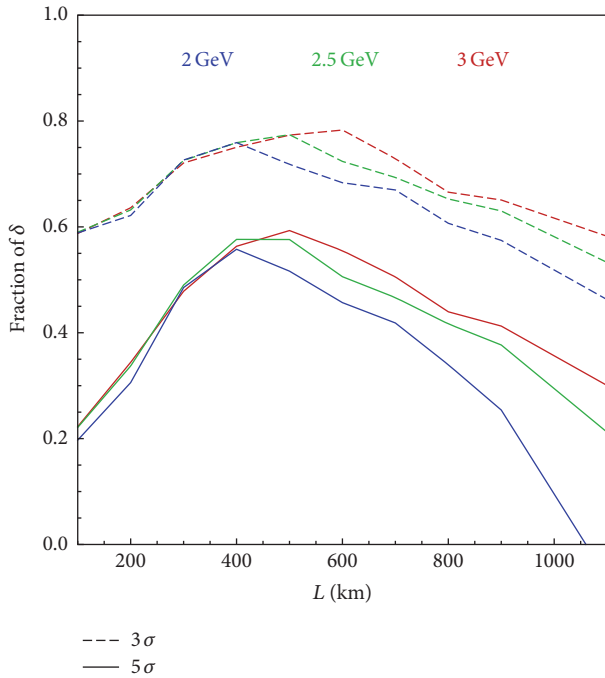


FIGURE 8: The curves show the fraction of the total range of possible values for  $\delta_{CP}$  for which CP violation can be discovered with 5 $\sigma$  and 3 $\sigma$  significance level, respectively, as a function of the distance  $L$  between the accelerator and the detector (the baseline), with  $L$  ranging from 100 km to 1000 km (horizontal axis) for three different proton beam energies 2.0, 2.5, and 3.0 GeV (blue, green, and red curves) and for a value of the mixing angle  $\theta_{13} = 8.73^\circ$ . The systematic errors used to produce these plots are those listed in the left column (SB Def.) of Table 3.

TABLE 3: The different sources of uncertainty that contribute to the total systematic uncertainty in the determination of the CP violating angle  $\delta_{CP}$ . This table is an extraction of information from a table used in [18]. Here, only the uncertainties for the Super Beam cases “SB Def.” (for default) are used to obtain the results shown in Figures 8 and 10 and “SB Opt.” (for optimistic) to obtain the results shown in Figure 9.

Error source	SB Def.	SB Opt.
Fiducial volume ND	0.5%	0.2%
Fiducial volume FD	2.5%	1.0%
Flux error signal $\nu$	7.5%	5%
Flux error background $\nu$	15%	10%
Flux error signal $\bar{\nu}$	15%	10%
Flux error background $\bar{\nu}$	30%	20%
Background uncertainty	7.5%	5%
Cross sections $\times$ eff. QE	15%	10%
Cross sections $\times$ eff. RES	15%	10%
Cross sections $\times$ eff. DIS	7.5%	5%
Effec. ratio $\nu_e/\nu_\mu$ QE	11%	3.5%
Effec. ratio $\nu_e/\nu_\mu$ RES	5.4%	2.7%
Effec. ratio $\nu_e/\nu_\mu$ DIS	5.1%	2.5%
Matter density	2%	1%

a CP violation discovery at 5 $\sigma$  and 3 $\sigma$ , respectively, can be made as a function of event statistics, or as it is called in this figure “exposure.” The “nominal exposure” corresponds to 10 years of data taking: 2 years with a neutrino beam and 8 years with an antineutrino beam. The systematic errors that have been used are shown in the right column (SB Opt.) of

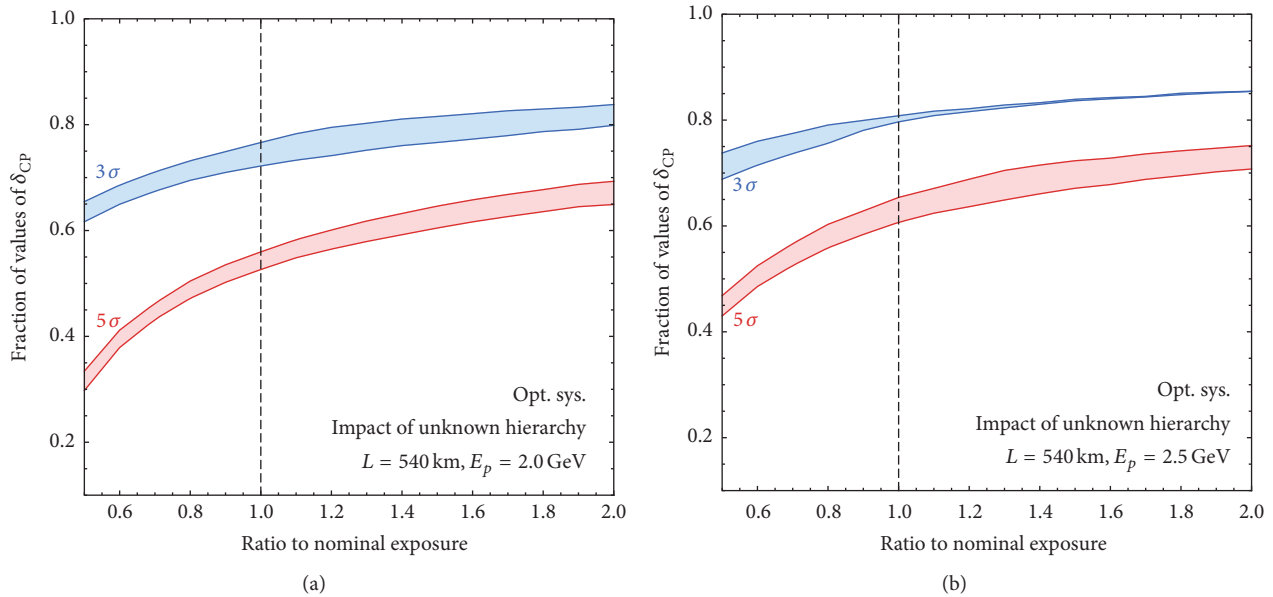


FIGURE 9: Curves showing the dependence of the fraction of values of  $\delta_{CP}$  for which a CP violation discovery at  $5\sigma$  and  $3\sigma$ , respectively, can be made as a function of event statistics, or exposure, where the nominal exposure corresponds to 10 years of data taking. (a) is for a proton energy of 2.0 GeV (current ESS design) and (b) for 2.5 GeV. The upper boundaries of the colored bands were obtained assuming the hierarchy to be known (NH) and the lower boundaries assuming the hierarchy to be unknown; that is, it is marginalized over. The systematic errors used to produce these plots are those shown in the right column (SB Opt.) of Table 3 [18].

Table 3. The upper boundary of the colored bands assumes the neutrino hierarchy to be known and the lower boundary to be unknown. For the nominal exposure, assuming the neutrino hierarchy to be known, CP violation can be discovered at  $5\sigma$  in about 56% and 65% of the total range of possible values, for a 2.0 GeV and a 2.5 GeV linac proton energy, respectively. Doubling the exposure to 4 years with a neutrino beam and 16 years with an antineutrino beam will lead to an increase of the fraction of the total range of possible  $\delta_{CP}$  covered to 69% and 71%, respectively. The comparatively small difference in this fraction when doubling the exposure, assuming the hierarchy to be known and unknown, illustrates the comparatively weak dependence on this parameter at the low neutrino energies of ESSnuSB.

In order for DUNE to reach a similar performance, a 2% systematic error in the signal normalization for  $\nu_e$  is required [7]. For Hyper-K the corresponding requirement is a total systematic error of 4% in the energy region of maximal flux 0.55–0.65 GeV [8]. The current systematic error in the T2K measurement of  $\nu_e$  appearance is 6.3% [22]. It is quite clear that the systematic errors shown in the ‘‘SB Opt.’’ column of Table 3, in which the neutrino flux systematic error is 5% and the neutrino cross section systematic error is 10% (at the low neutrino energies of ESSnuSB the QE cross section dominates), are considerably more readily obtainable as compared to the total systematic error levels of 2% and 4% required for DUNE and Hyper-K, respectively.

Conversely, assuming the systematic errors to be on the same level for all three experiments as for ESSnuSB, the potential for CP discovery is higher for ESSnuSB due to

the approximately three times higher signal at the second maximum. This was confirmed already in 2013 by global calculations, made by the theory group at the Snowmass Study in the USA [26], in which the expected performances of the different proposals for international neutrino beam projects were compared, using the same systematic errors for all experiments, in this case the systematic errors shown in the left column (SB Def.) of Table 3. Figure 10(a) shows the  $1\sigma$  error in the determination of  $\delta_{CP}$  (horizontal axis) as a function of the covered fraction of  $\delta_{CP}$  (vertical axis). One can see that, among the accelerator based projects shown, the resolution attainable with ESSnuSB is surpassed only by the Neutrino Factory project (IDS-NF). Figure 10(b) shows with which level of significance, in terms of number of standard deviations  $\sigma$ , CP violation can be discovered (vertical axis) versus the fraction of the total range of possible values for  $\delta_{CP}$  for which CP violation (horizontal axis) can be discovered. From these plots ESSnuSB can be seen to have the widest discovery coverage of the  $\delta_{CP}$  range among the Super Beam experiments investigated. Admittedly, the systematic errors chosen for these studies made in 2013 are quite conservative; for example, the error for the  $\nu_e$  signal is 7.5%, but this is to our knowledge the only comparison made under the assumption of equal systematic errors for all experiments. There is in principle no reason why there should be a significant difference in the systematic errors between the future long baseline experiments, at least not between Hyper-K and ESSnuSB which are planned to have similar neutrino beam energies and neutrino detectors. The ca. three times higher CP signal in ESSnuSB does however represent a significant difference.

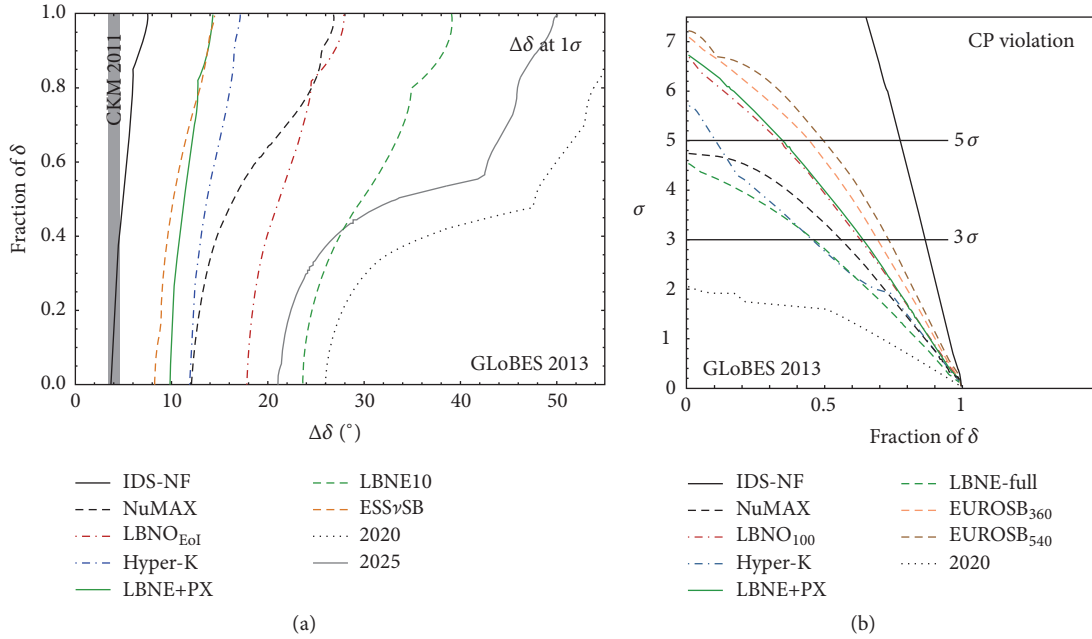


FIGURE 10: In (a) the  $1\sigma$  error in the determination of  $\delta_{CP}$  is shown (horizontal axis) as a function of the  $\delta_{CP}$  fraction for which this accuracy can be reached (vertical axis) [26]. (b) shows with what level of significance in terms of number of standard deviations  $\sigma$  that leptonic CP violation can be discovered (vertical axis) versus the fraction of the total range of possible values for  $\delta_{CP}$  (horizontal axis) [9]. The systematic errors used to produce these plots are those shown in the left column (SB Def.) of Table 3.

### 3. The Required Upgrades and Additions to the ESS Accelerator Facility

The 2.86 ms long proton pulses at ESS will be sent directly to the spallation target for neutron production. However, for neutrino production the requirement to have a few  $\mu$ s short pulses on target makes it necessary to compress the proton pulses using an accumulator ring. The injection of many turns into this ring cannot be made efficiently if the injected beam consists of the same particles as the circulating beam. By accelerating  $H^-$  ions in the linac, an efficient injection system can be designed based on the use of stripping foils or a laser beam, thus producing a circulating proton beam in the accumulator. From this follows the fact that the linac must be able to accelerate interleaved pulses of protons and  $H^-$ . In particular the linac magnets must be designed such that it will be possible to switch between two different optics settings for the two different linac beams.

At the US Spallation Neutron Source (SNS), at Oakridge National Laboratory [27], the linac also accelerates  $H^-$  pulses that are compressed through multiturn injection into an accumulator, to get shorter pulses for their neutron production target. The beam power at SNS is about 1.5 MW on target [27] and foil stripping is used. Due to the similar context and requirements, we have used the SNS accumulator as a model for our first studies of the ESS accumulator.

A second ion source, for the production of  $H^-$ , will be needed at ESS, as well as additional equipment in an  $H^-$  injector line for beam transport up to the point where the  $H^-$  beam goes into ESS linac. The optimal place for merging the two lines remains to be identified on the basis of the beam transport efficiency from the source.

$H^-$  ions in the linac beam will lose electrons due to phenomena such as collisions with residual gas, with black-body photons, and by intrabeam stripping. This will lead to some additional beam loss which needs to be minimized. Lorentz stripping in the magnetic fields can be reduced by careful choice of the optics for the  $H^-$  beam. Considering the experience of SNS it has been concluded that the losses in the ESS linac for the  $H^+$  case would be around 0.1 W/m. To avoid complicating the service work for the linac, the total losses for both beams in the linac, both  $H^-$  and  $H^+$ , should be maximum 1.0 W/m and this total limit will have to be guaranteed by the design of the transport of the  $H^-$  beam and by the collimation system.

The  $H^-$  linac pulse will be chopped in the medium energy beam transport line (3.6 MeV) to have regular gaps in the pulse such that when the beam is fully injected in the accumulator, there is a gap in the circulating beam. This is needed in order to avoid beam loss during the radio frequency (rf) beam capture in the accumulator and for the extraction of the beam to the production target. These gaps are seen by the accelerating cavities in the linac. The resulting higher order resonance modes (HOMs) are not expected to be an issue; however, this will be verified by calculations. The fact that there is no beam in the gaps represents a loss of about 10% of the particles on the production target.

The baseline energy of the linac beam is 2.0 GeV. Contingency space is available in the linac tunnel for upgrade to higher energies. As mentioned in Section 2, higher energies are beneficial for the physics reach of the ESSnuSB facility. The extraction of the H-beam will be made in the contingency region of the linac tunnel (see Figure 1), at the point where 2.5 GeV can be reached by adding more accelerating modules,

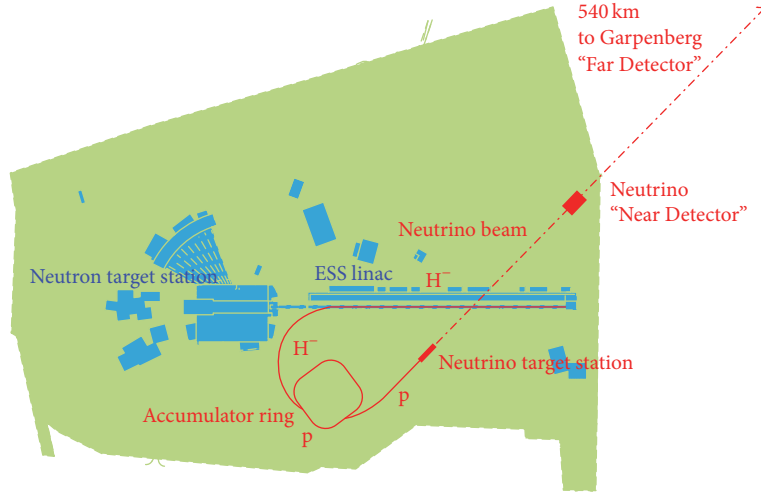


FIGURE 11: The proposed layout on the ESS site (courtesy of K. Hedin, ESS). The  $H^-$  beam in the linac, the accumulator and the transfer lines, the neutrino target station, and the neutrino beam are shown in red.

such that it will be possible to profit from a future linac upgrade to this energy. Due to space limitations around the neutron target hall, the transfer line from the linac to the accumulator cannot be designed for a beam energy higher than 2.5 GeV. This limitation is due to the requirement that the radius of the  $H^-$  beam transfer lines must be large enough so that the induced radioactivity by Lorentz stripping can be kept within allowed limits. With a 66% dipole filling factor in the transfer line and 2.5 GeV beam energy, the radius must not be smaller than about 110 m [28]. A first layout for the accumulator, the target, the transfer lines, and the neutrino beam direction is shown in Figure 11. The target station would need to be located at a depth of 25 m (see Section 4), and the neutrino beam will therefore pass below the linac.

There are several additional important items in the inventory of upgrades that need to be made during the linac construction phase for the future additional 5 MW  $H^-$  beam, such as the extra infrastructure and space that will be required for additional cabling and electrical equipment, for extra power transformers, for the additional  $H^-$  source, and for the beam equipment of the  $H^-$  beam transport at low energy. The water cooling plant, the cryogenic liquids plant, the cooling channels in the radio frequency power sources, and the accelerating cavities need to be designed for increased dynamic heat load [15]. It has to be possible to adjust the strengths of the linac focusing and steering magnets with the linac pulsing frequency. It is essential that these comparatively modest preparatory modifications be made during the linac build-up phase 2017–2023 in order to reduce the cost and time required for the subsequent linac upgrade and, in particular, to reduce the disruption in the linac operation for neutron production to an acceptable level.

**3.1. The Accumulator.** To fill the accumulator with as many as  $1.1 \cdot 10^{15}$  protons is a challenging task. This number could be reduced by splitting the 2.86 ms linac pulse in shorter and more frequent linac pulses of the same current, still maintaining the 5 MW total power for the neutrinos [29].

TABLE 4: Summary of lattice parameters for the accumulator.

Parameter	Value
Circumference	376 m
Number of dipoles	64
Number of quadrupoles	84
Injection region	12.5 m
Revolution time	1.32 $\mu$ s

The first case under study is to reduce the maximum intensity in the ring to 1/4. One 2.86 ms long pulse would be sent to the neutron target and 4 pulses, 0.72 ms long, to the accumulator, respectively. This can be achieved by increasing the pulsing rate of the linac from 28 Hz to 70 Hz; see the lower part of Figure 12. The neutron pulse frequency would still be 14 Hz. Alternatively, the 2.86 ms pulse could be injected sequentially into four stacked accumulator rings using a switchyard at injection as proposed in [9]. Also in this configuration the intensity in each ring would be 1/4 of the total intensity.

Studies are ongoing to evaluate effects of the high intensities using a first design of an accumulator with 376 m circumference and 1.32  $\mu$ s revolution time. The main parameters are shown in Table 4 and the lattice layout in Figure 13. The studies will indicate the intensity limit of the ring and possible improvements of the design. The aim is to have as few rings and as low linac pulsing frequency as possible. Having only one ring needs careful design of the stripping foil, which has to accept higher pulse rates than in the case of four stacked rings. The option with several stacked rings is subject to Lorentz stripping in the injection switchyard that distributes the linac beam into the four rings. Beam loss from this beam switching would have to be evaluated [30].

Increasing the number of pulses leads to increased power consumption in the cavities because of the power losses when ramping up and down the radio frequency field strength in the cavities for each pulse. 5 MW beam power needs 13.3 MW

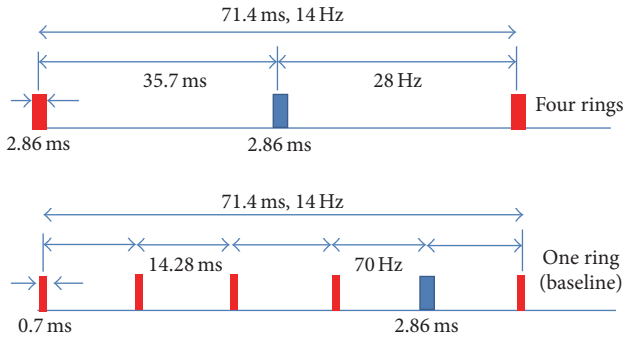


FIGURE 12: Pulse distribution for the case with four stacked accumulators and for the one-ring options: the upper part of the figure shows the 28 Hz pulsing of the linac with one proton (blue) and one  $H^-$  (red) pulse interleaved and the lower part shows the case of four 0.72 ms long pulses of  $H^-$  for neutrinos which are followed by one 2.86 ms proton pulse for the neutrino spallation target. The upper case needs a switching system and gaps in the  $H^-$  pulse to distribute the particles in the four stacked rings.

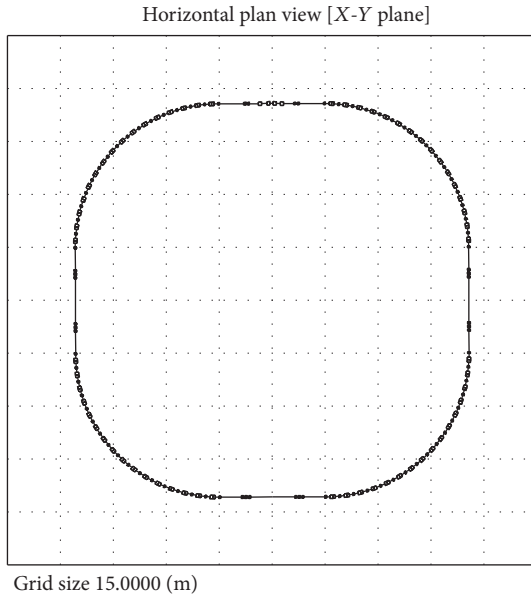


FIGURE 13: The layout of the lattice for the ESS accumulator.

wall plug power for 14 pulses of 2.86 ms per second. In the case of one accumulator ring and 70 Hz pulse frequency (see Figure 12) 13.3 MW + 17.0 MW wall plug power will be needed. The cost of the additional 3.7 MW, essentially being the overhead to fill and empty the cavities, will have to be weighed against the cost of the construction, the power consumption, the operation of three additional accumulators, and the impact on the target pulsing. Ongoing testing of the cavities at the FREIA Laboratory [31] at Uppsala University and future operational experience of the ESS linac will show how many pulses per second can be safely produced. The choice of linac pulsing has impact also on the powering and pulsing of the target focusing system. From the EUROnu studies we have a design of a power supply that can be pulsed

at 56 Hz. 70 Hz needs development or an additional power supply.

**3.1.1. Lattice.** To store  $2.7 \cdot 10^{14}$  protons in the accumulator requires a well chosen magnetic field structure (the lattice). The circumference and the beam pipe aperture are critical; the cost of investment and operation of the accumulator will critically depend on its design. The design concept of the accumulator ring at the SNS [27], in which the magnet fields in the original 1 GeV lattice are rather moderate, has been used as a starting point for the design of the ESSnuSB accumulator. The lattice is a square lattice with four long straight sections for rf, instrumentation, injection, and extraction; see Figure 13. It is possible to adopt the SNS 30 m injection straight section unchanged for 2.0 GeV. However, in view of the large apertures required, the bending fields in the arcs are kept as conservative as in the SNS; hence the arc lengths have tentatively been doubled considering that collective effects are more important at lower energies and that this would be conservative for 2.5 GeV. The circumference is increased from 248 to 376 m, which reduces the number of injection turns per fill, which is an advantage for the foil temperature.

Different lattice types will be designed to study space charge effects. The first simulations have been made using the SNS FODO lattice [29]. A FODO lattice is flexible and robust and gives a compact beam size for high energy machines with, however, a relatively large variation around the ring in the transverse beam size [32]. Doublet lattices give more space in the lattice and are optimal for the focusing of highly nonspherical beams (mini- $\beta$  in electron colliders) and can lead to large variations in the transverse beam size. Triplets give a smooth variation of the beam size and, in particular, small variations of the ratio between the two transverse sizes (e.g., small  $\beta$  in proton colliders) and an almost uniformly distributed space charge field.

**3.1.2. Injection.** To start the design procedure, a total final charge in the accumulator of 1/4 of the original  $1.1 \cdot 10^{15}$  protons has been assumed. This intensity gives negative space charge tune shifts of values less than 0.2 for an accumulator of 376 m having  $100\pi$  normalized (95%) emittance fully injected beam, which is a value considered as conservative. The accumulator radio frequency system will keep the protons confined in an rf “bucket” and prevent the protons from filling the gap in the circulating beam in such a way that the beam can be extracted with low beam loss. As mentioned above, this gap will be generated in the linac medium energy section by chopping a part of the pulse corresponding to the gap duration. The gap duration will be determined by the extraction kicker rise time, which is between 50 and 100 ns, the exact value depending on the design of the lattice and the angle of extraction.

Charge exchange injection by foil stripping is proposed as initial implementation, since this technology is well known. The SNS accumulator uses foil stripping in operation for a beam power of more than 1 MW. Laser stripping is envisaged at the SNS [33]. A future SNS laser stripping realization could ultimately be ported to the ESS accumulator with limited

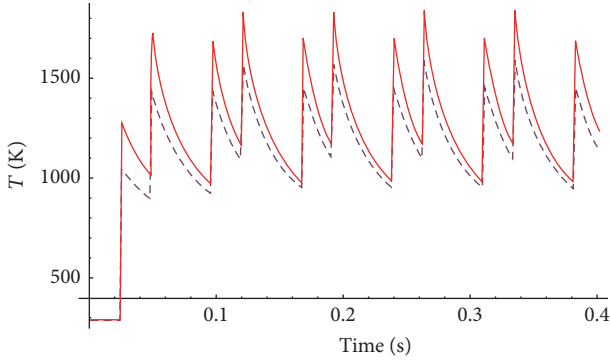


FIGURE 14: Evolution of maximum foil temperatures [K] at the  $H^-$  spot peak (dashed) and the combined  $H^-$  and circulating protons peak (red). Two injections into the accumulator per linac pulse.

modifications, provided the SNS-like injection lattice is kept for the ESSnuSB accumulator design.

The injection process is presently being studied by tracking particles from the linac using the ESS linac beam parameters derived from simulations. The idea is to “paint” the phase space at injection in a way such as to minimize space charge effects, while keeping a limited beam size. After the beam pulse (550 turns) is injected, the beam is extracted in one turn to the target.

Stripping foil temperatures were computed using several different methods [29, 34] giving very similar results. Calculations are based on ground-laying work made for the SNS injection [35]. Minimizing the number of foil passes of the circulating beam requires a local increase of its transverse size. Promising results were obtained by changing the injection optics to increase the linac spot size on the foil. A maximum temperature of 1550 K on the foil was obtained. For this case the average number of foil passes of the circulating beam was found to be about 4.8 and the emittance of the circulating beam was  $200\pi$  (95%) normalized. The maximum temperature on the foil for SNS operation does not exceed 1600 K. Further simulations show that, even for  $100\pi$  (95%) normalized emittance, foil temperatures can be kept at levels likely to be acceptable, with the hottest spots at 1650 K [36].

The case of filling the ring only twice with a linac pulse of 1.5 ms each time, instead of four times with a pulse of 0.7 ms, has been calculated. This configuration would reduce the linac pulsing frequency or the number of stacked accumulators, respectively. Peak temperatures of 1560 K for the  $H^-$  beam alone and 1850 K for the sum of the effects of  $H^-$  and  $H^+$  beams are reached. The maximum space charge tune shifts remain below  $-0.16$ , which is a clearly acceptable value. The temperature profiles on the foil resulting from this calculation are shown in Figure 14. The normalized emittance of the fully injected beam is in this case  $200\pi$ . However, the final beam emittance in the ring will be constrained by the requirements to have efficient extraction of the beam from the accumulator and efficient transport of the beam from the accumulator, through the switchyard [37] up to the four targets, still keeping the temperature of the foil within limits.

## 4. The Target Station

The main elements of the secondary neutrino beam are the target station with the four-horn/target systems to produce and focus the charged mesons, the 25 m long decay tunnel to produce the neutrinos from the meson decay, and the beam dump to absorb the undecayed mesons. The apparatus will be heavily shielded with iron and concrete due to the high radiation produced.

The target station design and the short pion-decay tunnel have already been studied for the Super Beam within the EUROnu [10] project with further optimizations for the ESSnuSB project [38]. In order to mitigate the detrimental effects of the high power beam, four targets and horns are needed; each target will be hit by a 1.25 MW proton beam. The target is placed inside the inner conductor of the horn for maximum particle collection while the shape of the inner conductor is optimized such as to produce the best possible neutrino beam for the discovery of CP violation [38].

The target is made of a bed of 3 mm diameter titanium spheres packed in an about 530 mm long canister with 30 mm diameter and cooled with helium gas. This type of target can be more efficiently cooled and stress development on the spheres is less than on the usual monolithic or segmented solid targets used in the past. Thermal modeling has shown that it is possible to cool the packed-bed target in a way to accept more than 1 MW beam power [38].

For the EUROnu Super Beam, a 350 kA pulsed power supply running at 50 Hz frequency was proposed for the four horns [39]. For ESSnuSB, additional studies have shown that modifications could be made in order to comply with 56 Hz and other possible pulsing scenarios [40]. To maintain acceptable stress and deformation on the conductors of the horn that are produced by the pulsed current and the particle-crossing, water jets have been proposed for cooling. The water jet system is able to maintain a constant temperature along the conductors. Preliminary fatigue studies on such a setup, taking into account the thermodynamical analyses performed for the horns, indicate that each horn can withstand a year ( $10^8$  pulses) of operation [38].

Experiments, including vibration tests as well as tests of the cooling capacity of the proposed system, can be made at the high intensity proton irradiation facility at CERN [41].

The region surrounding the four-horn/target system is shielded such as to produce less than  $10 \mu\text{Sv/h}$  prompt effective dose on the areas above, for example, the top floor and the power supply unit room. The region surrounding the decay tunnel and the beam dump is shielded such that the activation of the rock complies with the ESS safety rules. In the preliminary radiation studies of EUROnu a depth of 10 m inside the molasse rock was considered.

The neutrino beam has to point down from the horizontal plane at ESS by  $2.67^\circ$  (46.6 mrad) to get to the Garpenberg mine at 540 km distance, where the Far Detector will be placed. From this follows the fact that the target station will be at 25 m depth, giving space to proton beam extraction equipment and the switchyard. The SPL Super Beam target station was designed to be situated at 18 m depth; thus 25 m

depth for the ESSnuSB should be compatible with radiation safety and civil engineering constraints.

## 5. Design Considerations for the Near Detector

In order to achieve the required experimental sensitivity it is important to construct a Near Detector (ND) close to the neutrino production point. The ND should be able to measure the flux of each neutrino species in the beam, directly after production, to precision better than 5%. As the electron neutrino content in the beam is 0.3%, the ND needs to be able to separate Charged Current (CC) muon and electron neutrino events at a level better than  $10^{-4}$ . The preliminary ND design suggested here resulted from a series of simulations. The proposal is to use a cylindrical water Cherenkov detector with a radius,  $R_{\text{ND}} = 5$  m, and a length,  $L_{\text{ND}} = 10$  m, positioned with its central axis aligned with the direction of the neutrino beam,  $z_{\text{ND}} = 500$  m, from the target station. On the outside it is covered with scintillator plates to veto atmospheric muons and to reject events not fully contained in the detector. Further details about the study of this ND design can be found in [42].

The input to the study was a neutrino beam profile obtained using FLUKA 2011.xx (version 2014) [43] and GEANT 3.21 [44]. The calculation was made for a proton beam energy of 2.0 GeV. The neutrino energy distribution, for the case where the horn focuses positively charged particles, is shown by the gray-shaded histogram in Figure 4. The neutrinos from this beam were used to simulate neutrino interaction events in water using the GENIE toolkit [45]. The angular acceptance of the Far Detector (FD) is  $\pm 0.1$  mrad, while for the ND it is  $\pm 10$  mrad. As the ND provides the baseline for the FD measurements, it is important that the neutrino energy spectrum and the flavour composition of the beam are not significantly different for the two detectors. It was verified that when the angle with respect to the beam axis of the produced neutrinos varies from 0 to 10 mrad, the change in neutrino flavour composition and energy distribution is indeed negligible. At an ND distance,  $z_{\text{ND}} = 500$  m, with a radius,  $R_{\text{ND}} = 5$  m, and length,  $L_{\text{ND}} = 10$  m, the muon neutrino CC event rate would be  $260 \text{ s}^{-1}$  and the electron neutrino CC event rate  $1 \text{ s}^{-1}$ .

For ESSnuSB neutrino energies the muons resulting from CC collisions travel less than 3 m in water (the CC electrons travel shorter) before they stop radiating Cherenkov light. This implies that most of the events will be fully contained within the cylindrical ND water volume given above. To explore the conditions for the event reconstruction, an event sample was produced, containing idealized neutrino CC event products in a simplified detector environment. Each event in this sample was initiated with a charged lepton with a predetermined kinetic energy and momentum along the  $z$ -axis. A photodetector wall was placed in the  $x - y$  plane at  $z = 5$  m, where each photon was registered on impact. From the timing and position of the detected photons one can determine the position of the initial vertex, the direction of the charged lepton, its flavour, and its energy. An algorithm, to determine the event vertex coordinates, was developed that iteratively investigates a number of coordinate sets in

the detector using the timing and positions of the detected photons. Using photodetectors with time resolution in the order of 0.1 ns and position resolution in the order of 1 cm, this algorithm can locate the vertex with an accuracy of a few centimeters. Further information concerning the principles for event reconstruction in a water Cherenkov detector is given in, for example, [46].

The simulations also showed that the energy of the lepton could be estimated from the number of detected photons,  $N_\gamma$ , which is assumed to be roughly proportional to  $E_{\text{kin}} - E_{\text{ChTh}}$ , where  $E_{\text{kin}}$  is the lepton kinetic energy and  $E_{\text{ChTh}}$  is the threshold energy for Cherenkov light production. The lepton flavour identification was done by examining the fuzziness of the edge of the produced Cherenkov ring. For this purpose an algorithm was developed, based on a modified version of the circular Hough transform [47] that used filled circles instead of ring contours. Lepton flavour identification was done using this algorithm by fitting a “muon ring” and an “electron ring” to the detected photons of each event, to determine which flavour was most probable to have produced the detector response. The algorithm looks at several parameters and awards each event a number of  $\mu$ -votes and  $e$ -votes. By applying cuts to these votes the lepton flavour is determined. This first trial identification algorithm yielded a misidentification rate of 0.3%. This is still larger than required and further work is thus needed. All misidentified events were muons that had been identified as electrons and were mainly found among lower energy events. Details of the algorithm used and the results obtained can be found in [42].

## 6. Project Time Schedule

The aim of the presently ongoing ESSnuSB Design Study is to produce a Conceptual Design Report by 2018 to be followed by a Technical Design Report by 2020. This assumes that adequate financial support for the Design Study can be secured. Taking into account technical constraints only, the upgrade of the linac and the construction of the accumulator, of the neutrino target station, of the Near Detector, and of the Far Detector could start by 2021. The ESSnuSB build-up period is estimated to take some 7 years (dominated by the construction of the Far Detector) leading up to start of data taking at the earliest by 2027. Taking other funding and organizational constraints into account, 2030 is a more probable date for start of data taking.

A crucial prerequisite for this time schedule is that the comparatively modest modifications of the linac that are described at the end of Section 3 are made during the linac build-up period 2017–2023. To introduce the same modifications once the linac is running for spallation neutron production will be disruptive to the neutron experiments, will take more time, and will be more costly.

## 7. Summary and Conclusions

Leptonic CP violation potentially plays a crucial role for the explanation of matter-antimatter asymmetry in the Universe. The prime opportunity to discover and measure leptonic CP violation is offered by future Super Beam experiments

studying the  $\nu_\mu \rightarrow \nu_e$  oscillation. Following the discovery in 2012 of a large value of the neutrino mixing angle  $\theta_{13}$ , analytical calculations show that a higher sensitivity to CP violation is obtained by measuring at the second neutrino oscillation maximum, as compared to the first.

This fact has been shown in this paper by comparing directly the sensitivities to CP violation of experimental observables, such as the number of detected electron neutrinos and the normalized electron neutrino-antineutrino asymmetry at the first and the second maximum, respectively. The higher sensitivity, using the same conservative assumptions for systematic errors, at the second maximum is also apparent from comparisons previously made between different Super Beam projects on the basis of global simulation calculations. In view of the very high neutrino beam intensity required for measurements at the second maximum, the uniquely high power of the ESS proton driver represents a significant advantage for such measurements.

ESSnuSB is currently the only Super Beam experiment which concentrates on taking its data at the second oscillation maximum. Global calculations show that, taking data with ESSnuSB with a 2.0 GeV (2.5 GeV) ESS proton beam during 10 years using the MEMPHYS Megaton water Cherenkov detector placed in the 1200 m deep Garpenberg mine at the second maximum, 540 km from ESS, the coverage of the range of possible CP violating angle values is 56% (65%) assuming the neutrino hierarchy to be known and the systematic errors to be those shown in the ‘‘SB Opt.’’ column of Table 3, in which the neutrino flux error is 5% and the neutrino cross section error is 10%.

The generation of the neutrino Super Beam using the ESS linac will require acceleration of  $H^-$  pulses. These pulses will be interleaved with the proton pulses accelerated for neutron production in such a way that the linac will deliver a 5 MW  $H^-$  beam simultaneously with the 5 MW proton beam. The  $H^-$  beam will be injected into a 376 m circumference accumulator ring, stripping off the two electrons of each  $H^-$  ion at the entrance to the ring, by multiturn injection and ejected from the ring by single turn extraction, thereby obtaining compression of the pulse length from 2.86 ms to 1.3  $\mu$ s. The ejected  $H^-$  beam will be guided to a neutrino target with a surrounding horn-type hadron collector, downstream of which there is a 25 m long pion-decay tunnel. The very high current required in the horn cannot be maintained for more than a few  $\mu$ s which is what necessitates the strong compression of the linac pulse.

The accumulator ring and the target station can be installed underground on the ESS site without significant interference with the linac construction and operation. The introduction of  $H^-$  pulses in the linac and the doubling of the linac average power can to a large extent be made after the completion of the linac, as presently designed, without major interference with the linac operation provided, however, that certain comparatively modest, but crucial, preparative modifications are made to the linac already during its build-up phase 2017–2023.

The accumulator ring, which will contain an exceptionally high number of protons, represents a challenging design task, in particular its injection scheme and its ring lattice and

collimation. In order to somewhat reduce the complexity of the task, the number of protons per pulse can be reduced by using one of two alternative schemes: by injecting more and shorter  $H^-$  pulses in the compressor ring or by splitting the long  $H^-$  pulses up on more than one compressor ring. Design work of an accumulator ring receiving a sequence of pulses after each 2.86 ms long proton pulse in the linac and of an injection stripping scheme, based on foil stripping, is ongoing. This study will give us an indication of how many particles that can be stored, which will give the number of linac pulses or the number of accumulators that will be needed to handle the full linac beam and send it to the four targets.

The Near Detector plays a crucial role for the determination of the neutrino flux needed in the evaluation of the Far Detector data. The simulation of a cylindrical water Cherenkov detector, 10 m long and 5 m in radius located 500 m downstream of the target, has been used to study how such a detector could match the requirements. Methods for the determination of the position of the initial CC vertex, the direction of the charged lepton, its flavour, and its energy have been designed and evaluated. The results obtained so far are encouraging but need to be worked on further to satisfy the demanding requirement of not more than 5% systematic error in the Far Detector measurements.

The current ESSnuSB Design Study is foreseen to lead to a CDR in 2018 and to a TDR in 2020. Taking into account technical constraints only, construction of all parts could start in 2021 and be completed at the earliest by 2027.

## Competing Interests

The authors declare that they have no competing interests.

## Acknowledgments

The authors are grateful to E. Fernandez-Martinez and P. Coloma who have contributed with calculations and plots for the physics part of this paper, to F. Gerigk and E. Montesinos for their study and report of the modifications of the ESS linac that are required to allow simultaneous acceleration of  $H^+$  and  $H^-$  ions at an average power of 5 + 5 MW, and to B. Holzer and B. Goddard for giving help with aspects related to the accumulator design.

## References

- [1] K. Abe, N. Abgrall, Y. Ajima et al., ‘‘Indication of electron neutrino appearance from an accelerator-produced off-axis muon neutrino beam,’’ *Physical Review Letters*, vol. 107, no. 4, Article ID 041801, 2011.
- [2] Y. Abe, C. Aberle, T. Akiri et al., ‘‘Indication of reactor  $\bar{\nu}_e$  disappearance in the double chooz experiment,’’ *Physical Review Letters*, vol. 108, Article ID 131801, 2012.
- [3] J. K. Ahn, S. Chebotaryov, J. H. Choi et al., ‘‘Observation of reactor electron antineutrinos disappearance in the reno experiment,’’ *Physical Review Letters*, vol. 108, no. 19, Article ID 191802, 2012.

- [4] F. P. An, J. Z. Bai, A. B. Balantekin et al., “Observation of electron-antineutrino disappearance at daya bay,” *Physical Review Letters*, vol. 108, no. 17, Article ID 171803, 2012.
- [5] M. V. Diwan, D. Beavis, M.-C. Chen et al., “Very long baseline neutrino oscillation experiments for precise measurements of mixing parameters and CP violating effects,” *Physical Review D*, vol. 68, no. 1, Article ID 012002, 2003.
- [6] S. Peggs, R. Kreier, C. Carlile et al., Eds., *ESS Technical Design Report*, ESS-doc-274, ESS, Lund, Sweden, 2013, <http://eval.esss.lu.se/cgi-bin/public/DocDB/ShowDocument?docid=274>.
- [7] “Long-baseline neutrino facility (LBNF) and deep underground neutrino experiment (DUNE),” Conceptual Design Report, 2015.
- [8] K. Abe, H. Aihara, C. Andreopoulos et al., “Physics potential of a long-baseline neutrino oscillation experiment using a J-PARC neutrino beam and Hyper-Kamiokande,” *Progress of Theoretical and Experimental Physics*, vol. 2015, Article ID 053C02, 2015.
- [9] E. Baussan, M. Blennow, M. Bogomilov et al., “A very intense neutrino super beam experiment for leptonic CP violation discovery based on the European spallation source linac,” *Nuclear Physics B*, vol. 885, pp. 127–149, 2014.
- [10] T. R. Edgecock, O. Caretta, T. Davenne et al., “High intensity neutrino oscillation facilities in Europe,” *Physical Review Accelerators and Beams*, vol. 16, no. 2, Article ID 021002, 18 pages, 2013.
- [11] F. Gerigk, S. Atieh, I. Aviles Santillana et al., *Conceptual Design of the Low-Power and High-Power SPL: A Superconducting H<sup>-</sup> Linac at CERN*, CERN, Geneva, Switzerland, 2014.
- [12] O. Brunner, S. Calatroni, E. Ciapala et al., “Assessment of the basic parameters of the cern superconducting proton linac,” *Physical Review Accelerators and Beams*, vol. 12, no. 7, Article ID 070402, 24 pages, 2009.
- [13] E. Baussan, J. Bielski, C. Bobeth et al., “Neutrino super beam based on a superconducting proton linac,” *Physical Review Accelerators and Beams*, vol. 17, no. 3, Article ID 031001, 26 pages, 2014.
- [14] L. Agostino, M. Buizza-Avanzini, M. Dracos et al., “Study of the performance of a large scale water-Cherenkov detector (MEMPHYS),” *Journal of Cosmology and Astroparticle Physics*, vol. 2013, article 024, 2013.
- [15] F. Gerigk and E. Montesinos, “Recommended modifications of the ESS baseline architecture for ESSnuSB,” Tech. Rep. CERN-ACC-NOTE-2015-0040, CERN, Geneva, Switzerland, 2015, <http://cds.cern.ch/record/2110681>.
- [16] D. McGinnis, M. Lindroos, and R. Miyamoto, “European spallation source afterburner concept,” in *Proceedings of the 4th International Particle Accelerator Conference (IPAC '13)*, pp. 3924–3926, Shanghai, China, May 2013.
- [17] T. Patzak, “LAGUNA and LAGUNA-LBNO: future megaton neutrino detectors in Europe,” *Nuclear Instruments and Methods in Physics Research Section A: Accelerators, Spectrometers, Detectors and Associated Equipment*, vol. 695, pp. 184–187, 2012.
- [18] P. Coloma, P. Huber, J. Kopp, and W. Winter, “Systematic uncertainties in long-baseline neutrino oscillations for large  $\theta_{13}$ ,” *Physical Review D*, vol. 87, no. 3, Article ID 033004, 12 pages, 2013.
- [19] P. Coloma and E. Fernandez-Martinez, “Optimization of neutrino oscillation facilities for large  $\theta_{13}$ ,” *Journal of High Energy Physics*, vol. 2012, article 89, 2012.
- [20] M. Bass, M. Bishai, D. Cherdack et al., “Baseline optimization for the measurement of CP violation, mass hierarchy, and  $\theta_{23}$  octant in a long-baseline neutrino oscillation experiment,” *Physical Review D*, vol. 91, no. 5, Article ID 052015, 2015.
- [21] R. Aleksan, P. Braun-Munzinger, P. Chomaz et al., “Physics briefing book: input for the strategy group to draft the update of the European strategy for particle physics,” Tech. Rep. CERN-ESG-005, CERN, Geneva, Switzerland, 2013, Open Symposium held in Cracow from 10th to 12th of September 2012.
- [22] C. Bronner, “T2K oscillation results,” in *Proceedings of the 16th International Workshop on Neutrino Factories and Future Neutrino Beam Facilities (NUFACT '14)*, Proceedings of Science, Glasgow, UK, August 2014.
- [23] S. Parke, “Neutrinos: theory and phenomenology,” *Physica Scripta T*, vol. 158, Article ID 014013, 2013.
- [24] P. Huber, M. Lindner, and W. Winter, “Simulation of long-baseline neutrino oscillation experiments with GLOBES: (General Long Baseline Experiment Simulator),” *Computer Physics Communications*, vol. 167, no. 3, pp. 195–202, 2005.
- [25] P. Huber, J. Kopp, M. Lindner, M. Rolinec, and W. Winter, “New features in the simulation of neutrino oscillation experiments with GLOBES 3.0: General Long Baseline Experiment Simulator,” *Computer Physics Communications*, vol. 177, no. 5, pp. 432–438, 2007.
- [26] A. de Gouvea, K. Pitts, K. Scholberg et al., “Working group report: neutrinos,” in *Proceedings of the Community Summer Study: Snowmass on the Mississippi (CSS '13)*, Minneapolis, Minn, USA, August 2013.
- [27] SNS design manual, 2003, <https://neutrons.ornl.gov/sns>.
- [28] A. J. Jason, D. W. Hudgings, and O. B. van Dyck, “Neutralization of H<sup>-</sup> beams by magnetic stripping,” *IEEE Transactions on Nuclear Science*, vol. 28, no. 3, pp. 2703–2706, 1981.
- [29] E. Wildner, J. Jonnerby, J.-P. Koutchouk et al., “The accumulator of the ESSnuSB for neutrino production,” in *Proceedings of the 5th International Particle Accelerator Conference (IPAC '14)*, pp. 2245–2247, Dresden, Germany, June 2014.
- [30] E. Bouquerel, M. Dracos, and F. Osswald, “Preliminary design of a 4 MW proton beam switchyard for a neutrino super beam production facility,” in *Proceedings of the 4th International Particle Accelerator Conference (IPAC '13)*, pp. 1880–1882, Shanghai, China, May 2013.
- [31] M. Olvegård, A. Bhattacharyya, D. Dancila et al., “Progress at the FREIA laboratory,” in *Proceedings of the 6th International Particle Accelerator Conference (IPAC '15)*, pp. 3072–3075, Richmond, VA, USA, May 2015.
- [32] M. Fitterer, *Design study of the large hadron electron collider and a rapid cycling synchrotron as alternative to the PS booster upgrade at CERN [Ph.D. thesis]*, Karlsruhe University, Karlsruhe, Germany, 2013.
- [33] A. V. Aleksandrov, T. V. Gorlov, V. V. Danilov, and Y. Liu, “Status of laser stripping at the SNS,” in *Proceedings of the 24th Particle Accelerator Conference (PAC '11)*, C110328, pp. 2035–2037, New York, NY, USA, March-April 2011.
- [34] M. Martini, “Modelling accumulator stripper foil heating for ESSNUB facility,” Tech. Rep. CERN-ACC-NOTE-2015-0005, CERN, Geneva, Switzerland, 2015.
- [35] M. A. Plum, J. Holmes, R. W. Shaw, and C. S. Feigerle, “SNS stripper foil development program,” *Nuclear Instruments and Methods in Physics Research Section A: Accelerators, Spectrometers, Detectors and Associated Equipment*, vol. 590, no. 1–3, pp. 43–46, 2008.
- [36] E. Wildner, J. Jonnerby, J. P. Koutchouk et al., “The accumulator of the ESSnuSB for neutrino production,” in *Proceedings of the*

- 6th International Particle Accelerator Conference (IPAC '15), pp. 3942–3944, Richmond, Va, USA, May 2015.
- [37] E. Bouquerel, “Design status of the ESS $\nu$ SB switchyard,” in *Proceedings of the 6th International Particle Accelerator Conference (IPAC '15)*, pp. 125–127, Richmond, VA, USA, May 2015.
- [38] E. Baussan, J. Bielski, C. Bobeth et al., “Neutrino super beam based on a superconducting proton linac,” *Physical Review Special Topics—Accelerators and Beams*, vol. 17, no. 3, Article ID 031001, 26 pages, 2014.
- [39] E. Baussan, E. Bouquerel, M. Dracos et al., “Study of the pulse power supply unit for the four-horn system of the CERN to Fréjus neutrino super beam,” *Journal of Instrumentation*, vol. 8, no. 7, Article ID T07006, 2013.
- [40] N. Vassilopoulos, “ESS $\nu$ SB: update on secondary beam studies,” in *Proceedings of the 16th International Workshop on Neutrino Factories and Future Neutrino Beam Facilities (NUFACT '14)*, Proceedings of Science, Glasgow, UK, August 2014.
- [41] N. Charitonidis, I. Efthymiopoulos, A. Fabich, M. Meddahi, and E. Gianfelice-Wendt, “Status and planned experiments of the HiRadMat pulsed beam material test facility at CERN SPS,” in *Proceedings of the 6th International Particle Accelerator Conference (IPAC '15)*, WEPMN072, Richmond, Va, USA, May 2015.
- [42] A. Burgman, *A neutrino detector design—a simulation study on the design of the cherenkov near detector of the proposed ESS $\nu$ SB [M.S. thesis]*, Lund University, Lund, Sweden, 2015.
- [43] A. Ferrari, P. R. Sala, A. Fassò, and J. Ranft, “FLUKA: a multi-particle transport code (program version 2005),” Tech. Rep. CERN-2005-10; INFN/TC 05/11; SLAC-R-773, CERN, Geneva, Switzerland, 2005.
- [44] S. Agostinelli, J. Allison, K. Amako, J. Apostolakis, H. Araujo, and P. Arce, “Geant4—a simulation toolkit,” *Nuclear Instruments and Methods in Physics Research A: Accelerators, Spectrometers, Detectors and Associated Equipment*, vol. 506, no. 3, pp. 250–303, 2003.
- [45] C. Andreopoulos, A. Bell, D. Bhattacharya et al., “The GENIE neutrino Monte Carlo generator,” *Nuclear Instruments and Methods in Physics Research A*, vol. 614, no. 1, pp. 87–104, 2010.
- [46] K. Abe, Y. Hayato, T. Iida et al., “Solar neutrino results in Super-Kamiokande-III,” *Physical Review D*, vol. 83, no. 5, Article ID 052010, 19 pages, 2010.
- [47] R. O. Duda and P. E. Hart, “Use of the Hough transformation to detect lines and curves in pictures,” *Communications of the ACM*, vol. 15, no. 1, pp. 11–15, 1972.

## Review Article

# T2K and Beyond

**M. G. Catanesi**

*INFN Sezione di Bari, Via Orabona 4, 70125 Bari, Italy*

Correspondence should be addressed to M. G. Catanesi; [gabriella.catanesi@cern.ch](mailto:gabriella.catanesi@cern.ch)

Received 1 November 2015; Revised 22 January 2016; Accepted 10 February 2016

Academic Editor: Leslie Camilleri

Copyright © 2016 M. G. Catanesi. This is an open access article distributed under the Creative Commons Attribution License, which permits unrestricted use, distribution, and reproduction in any medium, provided the original work is properly cited. The publication of this article was funded by SCOAP<sup>3</sup>.

This paper presents the *state of the art* of the T2K experiment and the measurements prospects for the incoming years. After a brief description of the experiment, the most recent results will be illustrated. The observation of the electron neutrino appearance in a muon neutrino beam and the new high-precision measurements of the mixing angle  $\theta_{13}$  by the reactor experiments have led to a reevaluation of the expected sensitivity to the oscillation parameters, relative to what was given in the original T2K proposal. For this reason the new physics potential of T2K for  $7.8 \times 10^{21}$  p.o.t. and for data exposure 3 times larger than that expected to be reachable with accelerator and beam line upgrades in 2026 before the start of operation of the next generation of long-baseline neutrino oscillation experiments will also be described in the text. In particular the last challenging scenario opens the door to the possibility of obtaining, under some conditions, a  $3\sigma$  measurement excluding  $\sin(\delta_{CP}) = 0$ .

## 1. Introduction

In the last 15 years several experimental measurements confirmed the neutrino oscillations hypothesis by attacking the problem on different fronts:

- (i) The observation of a zenith-angle-dependent deficit in muon neutrinos produced by high-energy proton interactions in the atmosphere [1] supported the possibility that a particular neutrino flavor can be transmuted into another one.
- (ii) The *anomalous* solar neutrino flux [2] problem was shown to be due to neutrino oscillation by precise measurements [3–6].
- (iii) Taking advantage of nuclear reactors as intense sources, the disappearance of electron antineutrinos has been firmly established [6–9].

- (iv) The development of high intensity proton accelerators that can produce focused neutrino beams with mean energy from a few hundred MeV to tens of GeV has enabled measurements of the disappearance of muon neutrinos (and muon antineutrinos) [10–12] and appearance of electron neutrinos (and electron antineutrinos) [13–16] and tau-neutrinos [17] over distances of hundreds of kilometres.

As a matter of fact the possibility for a neutrino of a particular flavor to be transmuted into another flavor has profound implications demonstrating that neutrinos have mass. Recently this extraordinary achievement in physics was fully recognized in the scientific community by the awarding of the Nobel Prize 2015 to T. Kajita and A. B. McDonald.

To date, all the experimental results cited above are well described within the three neutrino generations oscillation framework. In this case the unitary mixing

matrix, often referred to as the PMNS (Pontecorvo-Maki-Nakagawa-Sakata) matrix [18], can be written as a  $3 \times 3$  matrix:

$$\begin{aligned}
 U &= \begin{pmatrix} 1 & 0 & 0 \\ 0 & +c_{23} & +s_{23} \\ 0 & -s_{23} & +c_{23} \end{pmatrix} \begin{pmatrix} +c_{13} & 0 & +s_{13}e^{-i\delta_{\text{CP}}} \\ 0 & 1 & 0 \\ -s_{13}e^{i\delta_{\text{CP}}} & 0 & +c_{13} \end{pmatrix} \begin{pmatrix} +c_{12} & +s_{12} & 0 \\ -s_{12} & +c_{12} & 0 \\ 0 & 0 & 1 \end{pmatrix} \\
 &= \begin{pmatrix} c_{12}c_{13} & s_{12}c_{13} & s_{13}e^{-i\delta_{\text{CP}}} \\ -s_{12}c_{23} - c_{12}s_{23}s_{13}e^{i\delta_{\text{CP}}} & c_{12}c_{23} - s_{12}s_{23}s_{13}e^{i\delta_{\text{CP}}} & s_{23}c_{13} \\ s_{12}s_{23} - c_{12}c_{23}s_{13}e^{i\delta_{\text{CP}}} & -c_{12}s_{23} - s_{12}c_{23}s_{13}e^{i\delta_{\text{CP}}} & c_{23}c_{13} \end{pmatrix}, \tag{1}
 \end{aligned}$$

where  $c_{ij} = \cos \theta_{ij}$  and  $s_{ij} = \sin \theta_{ij}$ . In this case four parameters are required to describe the matrix: three angles  $\theta_{12}$ ,  $\theta_{23}$ , and  $\theta_{13}$  and the CP-violating phase  $\delta_{\text{CP}}$ .

In this context the T2K experiment, proposed in 2003 [19] and approved in 2006 to collect data corresponding to  $7.8 \times 10^{21}$  protons-on-target (p.o.t) from a 30 GeV proton beam at the J-PARC accelerator facility in Japan, played an important role and will keep playing it in the future.

T2K is a long-baseline neutrino oscillation experiment designed to achieve the following main physics goals:

- (i) search for  $\nu_{\mu} \rightarrow \nu_e$  appearance and establish  $\theta_{13} \neq 0$  with a sensitivity down to  $\sin^2 2\theta_{13} \sim 0.008$  (90% CL);
- (ii) precision measurement of oscillation parameters in  $\nu_{\mu}$  disappearance mode with  $\delta(\Delta m_{32}^2) \sim 10^{-4} \text{ eV}^2$  and  $\delta(\sin^2 2\theta_{23}) \sim 0.01$ ;
- (iii) search for exotic physics including Lorenz violation and search for sterile components in  $\nu_{\mu}$  ( $\nu_e$ ) disappearance at the near detector and more.

The T2K experiment began the physics data-taking in 2010 [20]. Despite the devastating March 2011 earthquake in eastern Japan, which caused severe damage to the accelerator complex at J-PARC and abruptly discontinued the data-taking run of the experiment, in July 2011 the T2K collaboration announced a first indication of  $\theta_{13} \neq 0$  [13] and in 2013 reached a major physics goal: the discovery of  $\nu_{\mu} \rightarrow \nu_e$  appearance at  $7.3\sigma$  level of significance when a mere 8.4% of the total approved p.o.t. [15] was recorded. This is the first time that explicit flavor appearance has been observed from another neutrino flavor with a significance larger than  $5\sigma$ . This observation opened the door to the search for CP violation (CPV) in the lepton sector.

Following this discovery, the primary physics goal for T2K and, at large, for the neutrino physic community has become a detailed investigation of the three-flavor paradigm; this requires the determination of the unknown CP-violating phase  $\delta_{\text{CP}}$ , the resolution of the mass hierarchy (MH), and the precise measurement of  $\theta_{23}$  to determine the octant.

T2K, along with the Nova [21] experiment that started data-taking one year earlier, will play a major role in the determination of these parameters for at least a decade.

In this paper, after a brief description of the experiment in Section 2, we will describe the most recent results obtained by T2K (Section 3). In Section 4 we will provide a reevaluation of the expected sensitivity to the oscillation parameters, relative to what was given in the original T2K proposal [19], by taking into account the actual observation of the electron neutrino appearance in a muon neutrino beam by T2K and the new high-precision measurements of the mixing angle  $\theta_{13}$  from reactor experiments. In Section 5.1 we will briefly describe the proposed upgrade plan for the J-PARC accelerators and neutrino experimental facility aiming to reach a 1.3 MW beam power [22, 23]. Finally in Section 5.2 we will describe the physics potential of T2K for data exposure 3 times larger than the presently approved one.

## 2. The T2K Experiment

The T2K (Tokai-to-Kamioka) experiment is a second generation LBL (long-baseline) neutrino oscillation experiment to probe physics beyond the Standard Model. T2K uses an almost pure  $\nu_{\mu}$  beam produced using the new MW-class proton synchrotron at J-PARC (Japan Proton Accelerator Research Complex jointly constructed and operated by KEK and JAEA). The neutrino beam is detected first in the near detector *ND280* and then travels 295 km to the far detector *Super-Kamiokande* (see Figure 1).

T2K adopts the off-axis method to generate a narrow-band neutrino beam using the proton synchrotron at J-PARC. In this method the neutrino beam is purposely directed at an angle with respect to the baseline connecting the proton target to the far detector, Super-Kamiokande. The off-axis angle is set at  $2.5^\circ$  so that the narrow-band  $\nu_{\mu}$  beam generated towards the far detector has a peak energy at  $\sim 0.6 \text{ GeV}$  (see Figure 2). Such configuration maximizes the effect of the neutrino oscillation at 295 km and minimizes the background to electron neutrino appearance detection. The angle can be reduced to  $2.0^\circ$ , allowing variation of the peak neutrino energy, if necessary. The J-PARC beamline can also provide to the experiment an antineutrino beam instead of a neutrino beam. As it will be shown in Sections 4 and 5, this aspect is very important to constrain the  $\delta_{\text{CP}}$  phase.



FIGURE 1: The neutrino beam journey in the T2K experiment. The high intensity neutrino beam is produced at J-PARC (Tokai, Mito, Ibaraki Prefecture, Japan) and travels 295 km to the Super-Kamiokande detector (mount Kamioka, close to Hida, Gifu Prefecture, Japan).

**2.1. Near Detectors.** The near detectors were constructed in an underground hall of 33.5 m depth and 17.5 m diameter at 280 m downstream of the target. They are used to measure the neutrino energy spectrum, flavor content, and interaction rates of the unoscillated beam and to predict the neutrino interactions at Super-Kamiokande. Two detectors were installed: an on-axis detector (aimed in the direction of the neutrino beam center) and an off-axis detector (aimed in the direction of SK).

The on-axis detector, namely, the INGRID detector, consists of 16  $1\text{ m} \times 1\text{ m} \times 1\text{ m}$  cubic modules as shown in Figure 3(a). Each module is a “sandwich” of iron/scintillator detectors: 14 of them are arranged so as to form a cross configuration, and the remaining two diagonal modules are positioned off the cross axes. The center of the cross corresponds to the neutrino beam center, defined as  $0^\circ$  with respect to the direction of the primary proton beamline. INGRID is able to measure the on-axis neutrino beam profile and direction with an accuracy of  $\pm 1$  mrad. Note that the monitoring of beam direction with high precision is very important for the *off-axis* configuration. In fact 1 mrad divergence corresponds to a change of 2% in the integral of the neutrino flux expected at SK.

The off-axis detector (named ND280) shown in Figure 3(b) is a magnetized tracking detector. The detector elements are contained inside the refurbished UA1 magnet. Inside the upstream end of magnet sits a  $\pi^0$ -detector (P0D) consisting of tracking planes of scintillating bars alternating with either water target/brass foil or lead foil. Downstream of the P0D is the tracker, composed of three time projection chambers (TPCs) and two fine grained detectors (FGDs) consisting of layers of finely segmented scintillating bars.

The tracker is designed to study charged current interactions in the FGDs. The P0D, TPCs, and FGDs are all surrounded by an electromagnetic calorimeter (ECal) for detecting electrons and photons to better constrain the  $\nu_e$  contamination in the beam and the  $\gamma$  background, while the return yoke of the magnet is instrumented with scintillator slabs to measure the range of the muons (Side Muon Range Detectors, SMRD) escaping from the sides of the off-axis detector.

In addition, the near off-axis detector can also perform accurate cross section measurements on different target materials (carbon, water, oxygen, and argon) to minimize

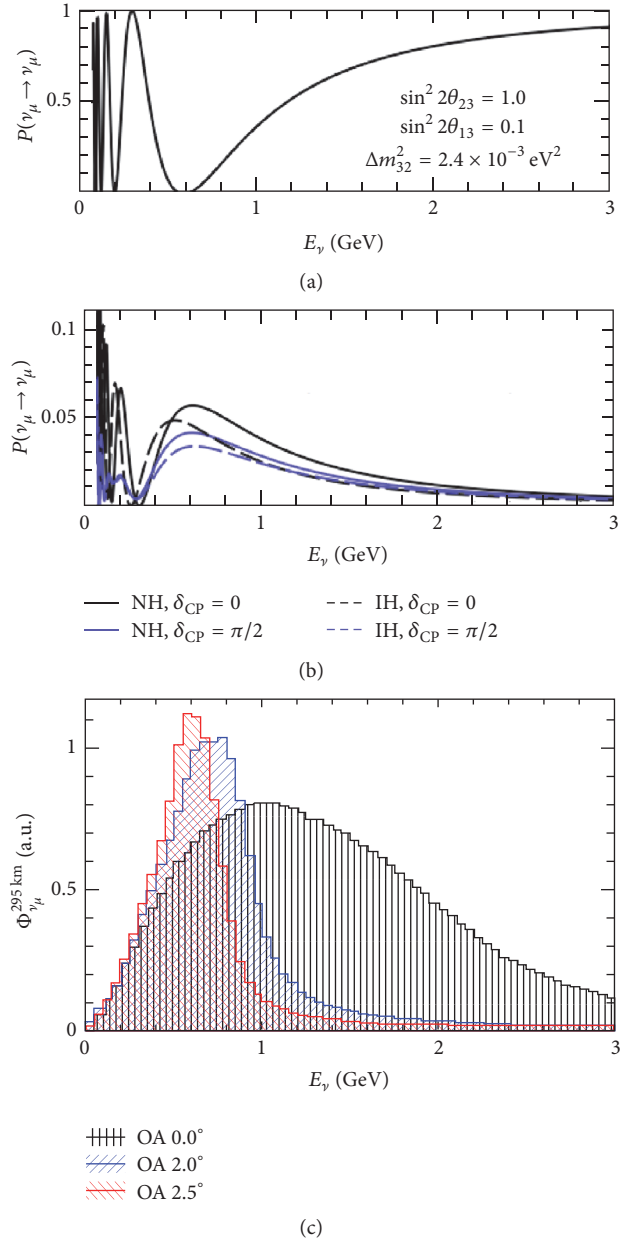


FIGURE 2: The muon neutrino survival probability (a) and electron neutrino appearance probabilities (b) at 295 km and the unoscillated neutrino fluxes for different values of the off-axis angle (OA) (c). The appearance probability is shown for two values of the phase  $\delta_{\text{CP}}$  and for normal (NH) and inverted (IH) mass hierarchies.

the impact of the interaction model uncertainties on the systematic error budget.

**2.2. Super-Kamiokande.** The far detector, Super-Kamiokande (SK), is a 50 kton water Cherenkov detector [26] located 1000 m underground in the Kamioka mine, Japan. Its distance from J-PARC is 295 km. In the inner detector (ID), 22.5 kton of fiducial volume is viewed by 11,129 20-inch diameter PMTs. The outer detector (OD), which surrounds the ID, is also a water Cherenkov detector: it is used to veto events that enter or exit the ID. SK started its operation in April

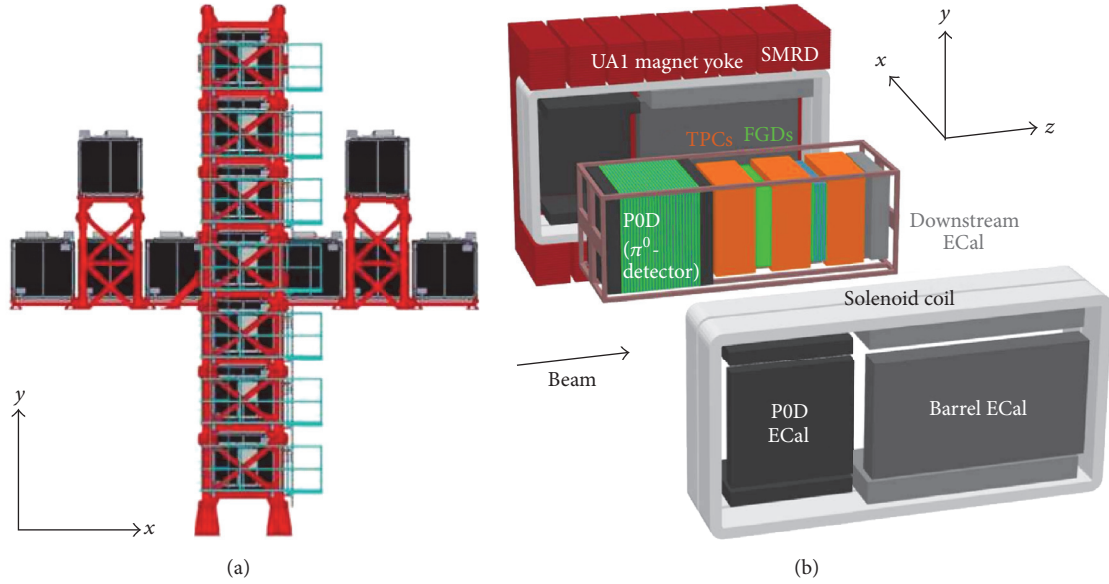


FIGURE 3: Schematic view of the INGRID on-axis detector (a) and the ND280 off-axis detector (b).

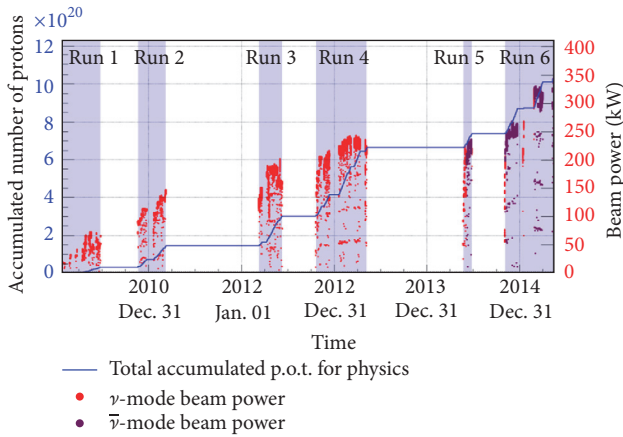


FIGURE 4: The evolution of the primary proton beam intensity and integrated proton delivery in the T2K experiment. Red (violet) dots show averaged beam power per hour in the neutrino (antineutrino) mode beam; the scale is given in the right vertical axis. The blue solid line shows the accumulated number of delivered protons from the beginning of the experiment. The scale is given in the left vertical axis.

1996. After a complete upgrade of its electronics systems in 2008, it was named SK-IV. The most important characteristic of SK, as the far detector of the T2K experiment, is its ability to differentiate between muons and electrons with high efficiency. Considering that the majority of the neutrino interactions in this range of energies are charged current quasielastic (CCQE) interactions, the identification of muons and electrons directly implies the identification of the parent  $\nu_\mu$  ( $\bar{\nu}_\mu$ ) or  $\nu_e$  ( $\bar{\nu}_e$ ). Details about the SK particle identification performances are reported in [27]. It was verified that the probability of misidentification is less than 1%.

**2.3. Data-Taking Status.** The evolution of the proton beam delivery is shown in Figure 4. The physics data-taking started

in January 2010. That year one beam pulse had only six bunches in 5 microseconds. The number of protons per pulse (ppp) was limited to  $2. \times 10^{13}$ , and the beam pulse cycle was at that time 3.52 seconds. Many efforts were made by the J-PARC accelerator group to increase the beam power. To date the number of bunches in each pulse is 8, and the number of protons per pulse is  $1.8 \times 10^{14}$ . In the meantime, the beam cycle time was reduced to 2.48 seconds. The maximum beam power achieved through June 2015 was 371 kW. T2K accumulated  $1.1 \times 10^{21}$  p.o.t. until June 4, 2015. This is about 14% of the final goal of  $7.8 \times 10^{21}$  p.o.t., which can be obtained over five years of beam operation [22, 23, 28].

In June 2014, the direction of the magnetic horn current was reversed and an antineutrino beam run was started. In the next section, results based on  $6.57 \times 10^{20}$  p.o.t. neutrino beam data [12, 15, 29] and  $4.04 \times 10^{20}$  p.o.t. antineutrino beam data recorded until June 2015 will be reported [30].

**2.4. Analysis Strategy.** T2K employs various analysis methods to estimate oscillation parameters. In general, these methods extract oscillation parameters from the data by comparing the observed and predicted  $\nu_e$  and  $\nu_\mu$  interaction rates and energy spectra at the far detector. The rate and spectrum depend on the oscillation parameters, the incident neutrino flux, neutrino interaction cross sections, and the detector response. The initial estimate of the neutrino flux is determined by detailed simulations incorporating proton beam measurements, INGRID measurements, and the pion and kaon production rates measured by the NA61/SHINE [31, 32] experiment.

The ND280 detector measurement of  $\nu_\mu$  charged current (CC) events (unoscillated spectra) is used to constrain the initial flux estimates and parameters of the neutrino interaction models that affect the predicted rate and spectrum of neutrino interactions at both ND280 and Super-K.

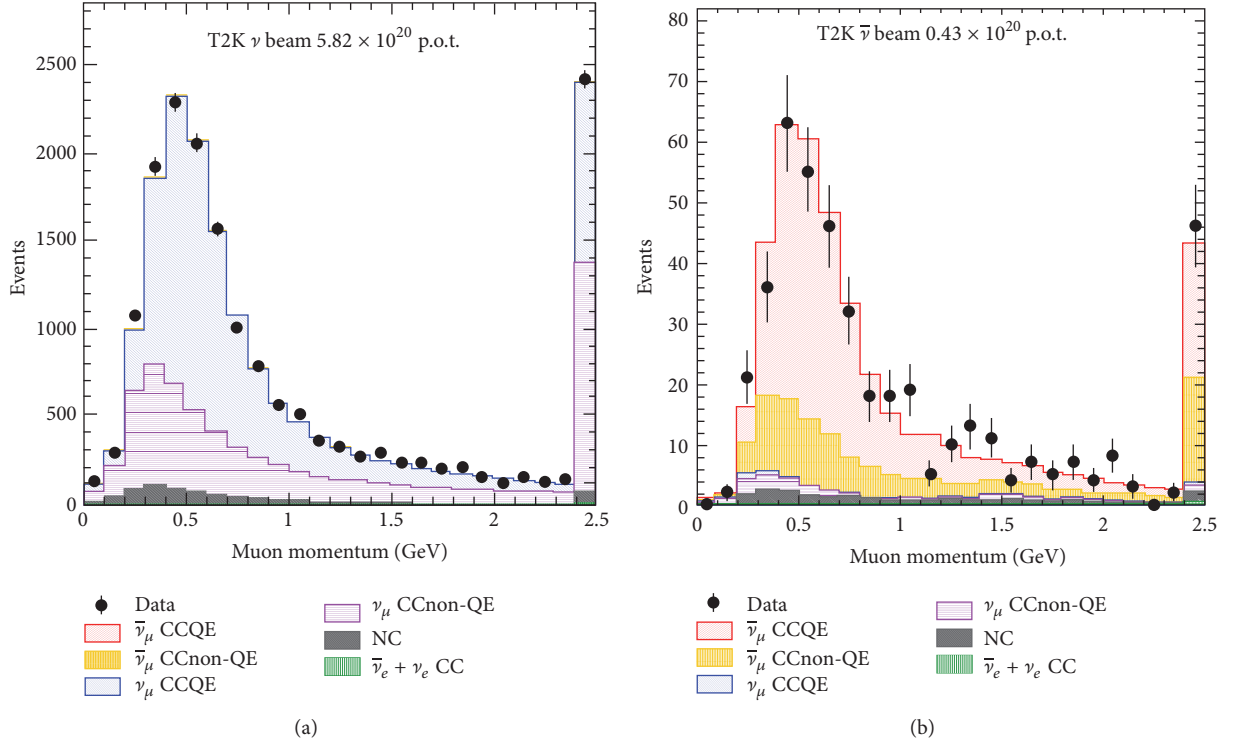


FIGURE 5: Muon momentum distribution of CC  $\nu_\mu$  events (a) and CC  $\bar{\nu}_\mu$  events (b) in ND280. Data points include statistical and systematic errors. After the adjustment of systematic uncertainties, there is agreement between the data and Monte Carlo simulation.

$\nu_\mu$  ( $\bar{\nu}_\mu$ ) CC interactions are selected by requiring that the highest-momentum negative- (positive-) curvature track in an event starts within the upstream FGD (FGD1) fiducial volume (FV) and has an energy deposit in the middle TPC (TPC2) consistent with a muon. The muon PID requirement is based on a truncated mean of measurements of energy loss in the TPC gas [33]. Events with a track in the TPC upstream of FGD1 are rejected and the remaining  $\nu_\mu$  CC candidates are divided into three subsamples according to the number of associated pions:  $\nu_\mu$  CC  $0\pi$ , dominated by CCQE interactions,  $\nu_\mu$  CC  $1\pi^+$ , dominated by CC resonant pion production, and the so-called  $\nu_\mu$  CC *other*, dominated by deep inelastic scattering.

Several control samples are used to assess the uncertainty in the modeling of FGD and TPC response. A detailed description of the systematic errors considered in the analysis and the numerical evaluation of each of them can be found in [13]. All the parameters related to cross sections and neutrino fluxes are adjusted based on the comparison between ND280 data and Monte Carlo. As is shown in Figure 5, after the adjustment [12, 13], the agreement is good.

Thanks to the inputs from the ND280 analysis, the systematic errors on the expected neutrino events at SK are strongly reduced. The effect is illustrated in Figure 6: they decrease from 23.5% to 7.7% for  $\nu_\mu$  candidates and from 26.8% to 6.8% for  $\nu_e$  candidates.

At SK,  $\nu_e$  and/or  $\nu_\mu$  charged current quasielastic (CCQE) events are selected, with efficiencies and backgrounds determined through detailed simulations tuned to control samples,

accounting for final state interactions (FSI) inside the nucleus and secondary hadronic interactions (SI) in the detector material. These combined results are used in a fit to determine the oscillation parameters.

### 3. Recent T2K Results

**3.1. Neutrino Events Selection in SK.** In the years 2010–2013, neutrino events corresponding to  $6.57 \times 10^{20}$  p.o.t. have been recorded in SK. The event selection process comprises two steps. The first is the same for  $\nu_\mu$  and  $\nu_e$ , and it allows accepting only the beam-related Fully Contained Fiducial Volume (FCFV) events. Note that, with the addition of the request that the event time stamp is within a range of 2 to 10  $\mu$ s from the beam spill time recorded in Tokai, the applied cuts are the same as those in the well-established atmospheric neutrino analysis [34].

Applying these conditions, 377 events have been selected as FCFV events. The expected number of background events from non-beam-related sources in accidental coincidence was estimated to be 0.0085.

From this point on, separate conditions have been applied to the  $\nu_\mu$  and  $\nu_e$  samples, allowing the selection of 120  $\nu_\mu$  and 28  $\nu_e$  candidates.

To identify  $\nu_\mu$  CC candidate events the following conditions have been applied:

- (i) There is only one reconstructed Cherenkov ring.
- (ii) The ring is  $\mu$ -like.

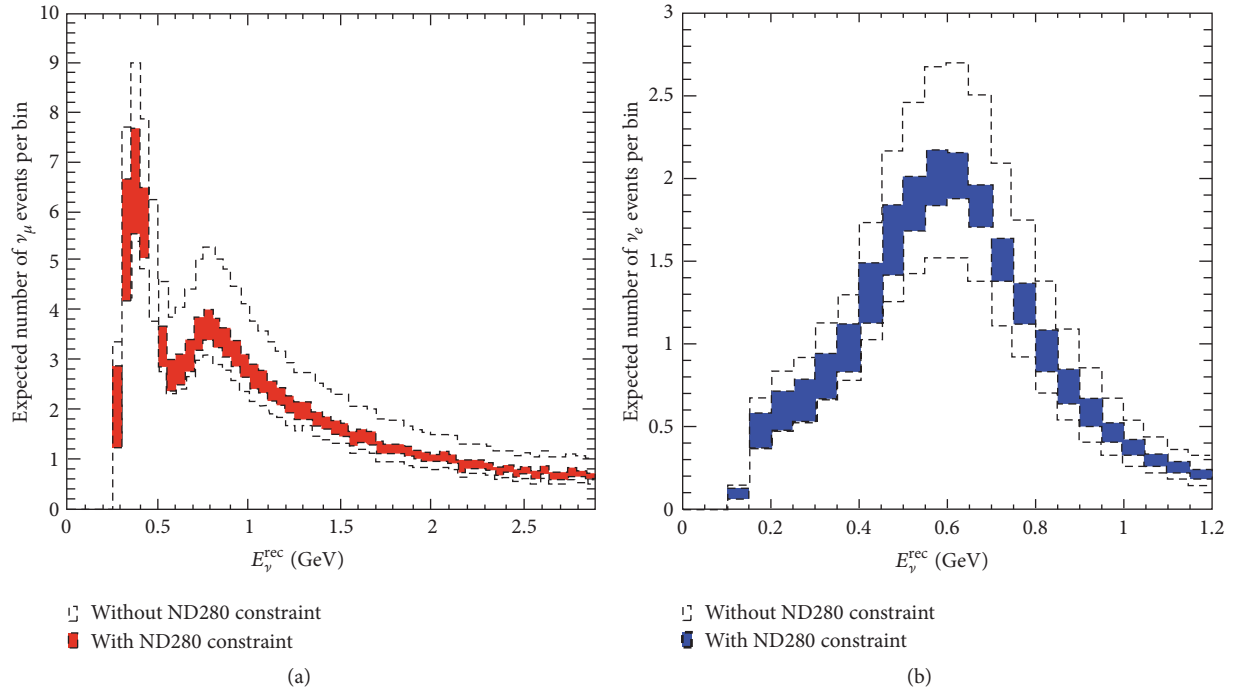


FIGURE 6: Total error envelopes for the reconstructed energy distributions of  $\nu_{\mu}$  CC (a) and  $\nu_e$  CC (b) candidate events at SK, using typical oscillation parameter values, with and without the ND280 constraint applied.

- (iii) The reconstructed momentum is higher than 200 MeV.
- (iv) There are less than two reconstructed Michel electrons.

The momentum cut ( $>200$  MeV) is applied to reject charged pions and misidentified electrons from the decay of unobserved muons and pions. The requirement to have fewer than two Michel electrons rejects events with additional unseen muons or pions.

For the selection of the  $\nu_e$  CC candidate events the criteria listed below have been used:

- (i) There is only one reconstructed Cherenkov ring.
- (ii) The ring is  $e$ -like.
- (iii) The visible energy ( $E_{\text{vis}}$ ) is higher than 100 MeV.
- (iv) There is no reconstructed Michel electron.
- (v) The reconstructed energy ( $E_{\text{rec}}$ ) is less than 1.25 GeV.
- (vi) The event is not consistent with  $\pi_0$  hypothesis.

The  $E_{\text{vis}}$  requirement removes low energy neutral current (NC) interactions and electrons from the decay of unseen parents that are below Cherenkov threshold or fall outside the beam time window. Since above 1.25 GeV the intrinsic  $\nu_e$  beam is dominant, a reconstructed energy below this threshold is also requested.

Finally the same selection criteria have been applied to the corresponding Monte Carlo sample, obtaining the numbers of expected neutrino candidates for the no-oscillation hypothesis: they are  $446 \pm 23$  for  $\nu_{\mu}$  and  $4.9 \pm 0.6$  for  $\nu_e$ , respectively.

**3.2.  $\nu_{\mu}$  Disappearance.** As reported in the previous subsection, 120 muon neutrino candidates have been observed in  $6.57 \times 10^{20}$  p.o.t., to be compared with the  $446 \pm 23$  expected if no oscillation is assumed. The neutrino energy distribution for the selected sample of 120 events is shown in Figures 7(a) and 7(b) together with the ratio of oscillated to unoscillated events as a function of neutrino energy for the data and the best fit spectrum. In Figure 7(a) is also visible the small contribution at low energy from NC as estimated by MC. The disappearance of muon neutrinos events as well as the distortion of the neutrino energy spectrum are evident.

The best fit oscillation parameters measured under those conditions are as follows:  $\sin^2(\theta_{23}) = 0.51 \pm 0.056$  and  $|\Delta m_{32}^2| = 2.51 \pm 0.10 \times 10^{-3} \text{ eV}^2$ , respectively [12].

The constraint in the two-dimensional  $\sin^2(\theta_{23})$ - $\Delta m_{32}^2$  plane for normal and inverted mass hierarchy is shown in Figure 7(c). The T2K results are consistent with those from SK [35] and MINOS [25] and provide the most stringent constraint for  $\sin^2(\theta_{23})$ .

**3.3.  $\nu_e$  Appearance.** As presented in Section 3.1, by analyzing a data sample at SK corresponding to  $6.57 \times 10^{20}$  p.o.t. 28 electron neutrino candidates have been observed, where  $4.9 \pm 0.6$  where expected from a no-oscillation hypothesis. This result [15] confirmed, with higher statistic, previous T2K claims [13, 14] based on  $1.43 \times 10^{20}$  and  $3.01 \times 10^{20}$  p.o.t., respectively.

From a statistical point of view, the significance of the signal corresponds to 7.3 standard deviations. It can be concluded with certainty that for the first time the electron

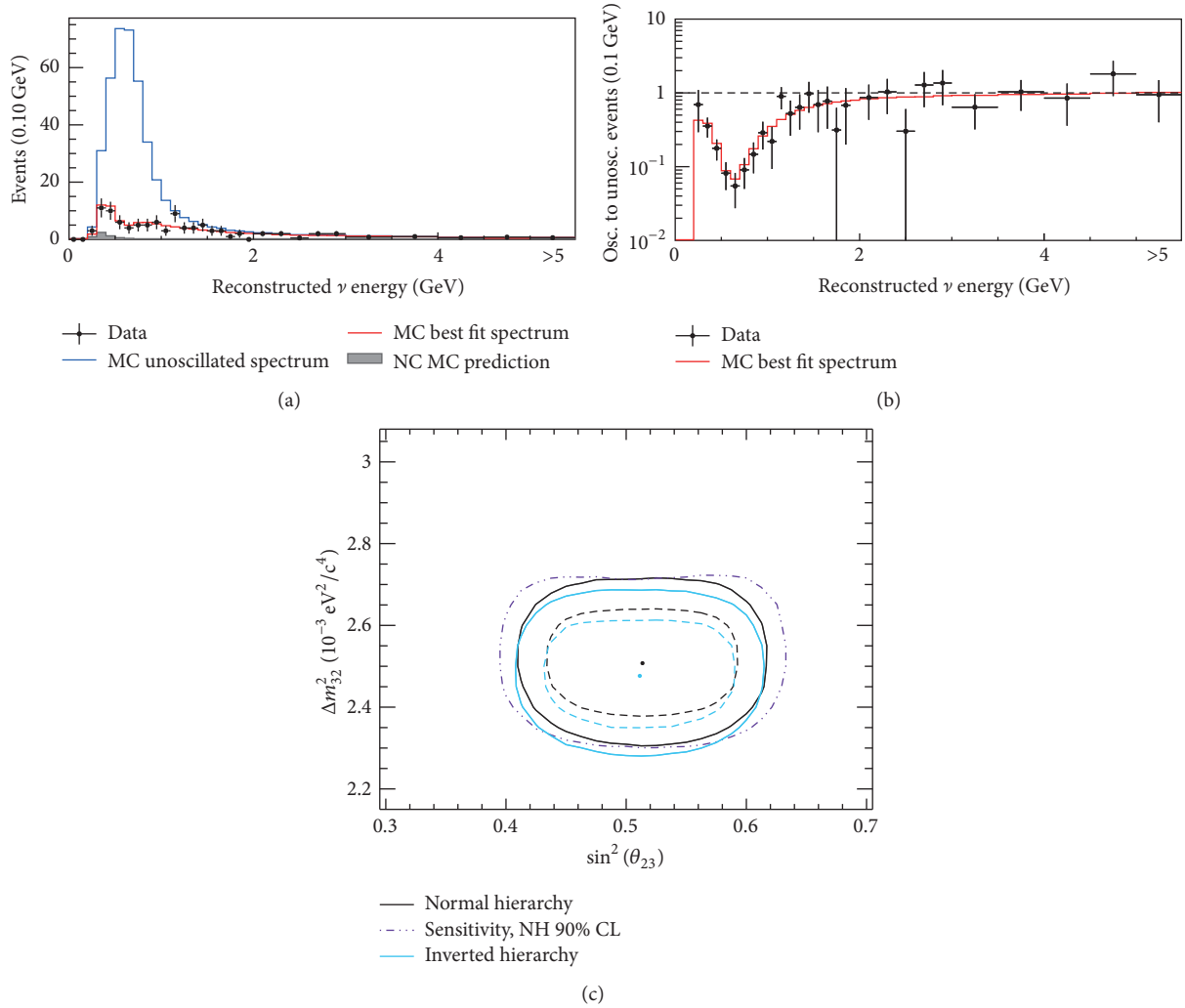


FIGURE 7: (c) The 68% (dashed) and 90% (solid) CL intervals for the  $\nu_\mu$  disappearance analysis assuming normal and inverted mass hierarchies. The 90% CL sensitivity contour for the normal hierarchy is overlaid for comparison. (a) Reconstructed neutrino energy spectrum for data, best fit prediction, and unoscillated prediction. (b) Ratio of oscillated to unoscillated events as a function of neutrino energy for the data and the best fit spectrum.

neutrino appearance has been observed in an almost pure  $\nu_\mu$  beam.

This result is very relevant, in particular because it opens the possibility of new studies in the lepton sector of charge-parity (CP) violation, which provides a distinction in physical processes involving matter and antimatter.

Constraints on oscillation parameters have been carefully calculated by comparing data and expectations. The allowed region in the  $\sin^2 2\theta_{13}$ - $\delta_{\text{CP}}$  plane for normal mass hierarchy and inverted mass hierarchy are shown in Figures 8(a) and 8(b) together with the constraints from reactor experiments [15]. The overlap between T2K and the reactor results indicates that negative  $\delta_{\text{CP}}$  is favoured with a slight preference (67%) for the normal mass hierarchy.

For  $\delta_{\text{CP}} = 0$  and normal (inverted) hierarchy, the best fit value with a 68% CL is  $\sin^2 2\theta_{13} = 0.136(+0.044/-0.033)$  ( $\sin^2 2\theta_{13} = 0.166(+0.051/-0.042)$ ).

At 90% confidence level and including reactor measurements, T2K excludes the region  $\delta_{\text{CP}} = [0.15, 0.83]\pi$  for

normal hierarchy and  $\delta_{\text{CP}} = [-0.08, 1.09]\pi$  for inverted hierarchy.

The T2K and reactor data weakly favour the normal hierarchy with a Bayes Factor of 2.2.

The  $-2\Delta \ln \mathcal{L}$  value as a function of  $\delta_{\text{CP}}$  for normal hierarchy (solid line) and inverted hierarchy (dotted line) is shown in Figure 8(c) [15]. The likelihood is marginalized over  $\sin^2 2\theta_{13}$ ,  $\sin^2 \theta_{23}$ , and  $\Delta m_{32}^2$ . The solid (dotted) line with markers corresponds to the 90% CL limits for normal (inverted) hierarchy, evaluated by using the Feldman-Cousins method. The  $\delta_{\text{CP}}$  regions with values above the lines are excluded at 90% CL.

More recently [36] the T2K collaboration published an analysis that for the first time combines measurements of muon neutrino disappearance and electron neutrino appearance to estimate four oscillation parameters and the mass hierarchy. *Frequentist* and *Bayesian* intervals have been used for combinations of these parameters, with and without the inclusion of recent reactor measurements.

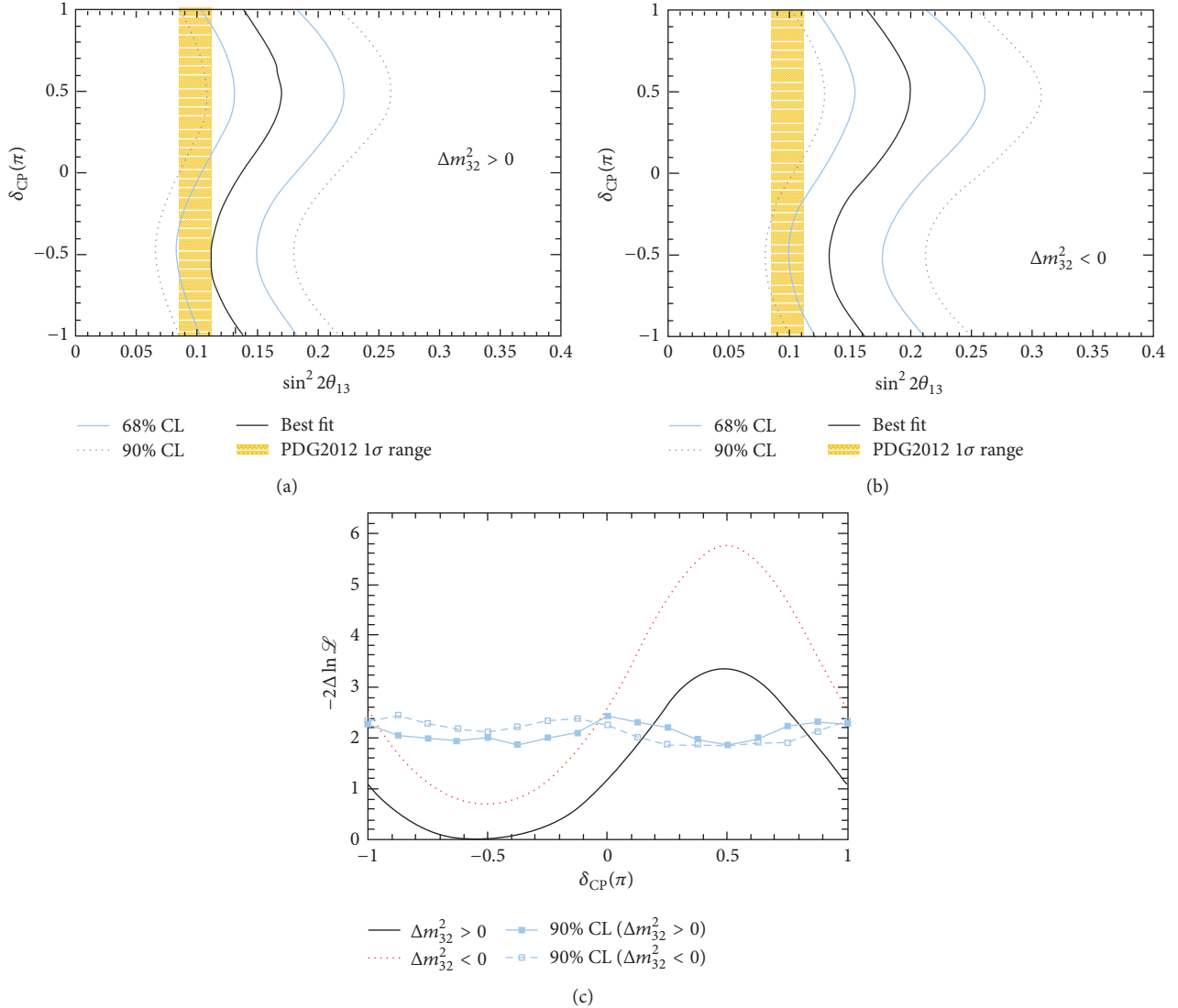


FIGURE 8: (a, b) The 68% and 90% CL allowed regions for  $\sin^2 2\theta_{13}$ , as a function of  $\delta_{\text{CP}}$  assuming normal hierarchy (a) and inverted hierarchy (b). The solid line represents the best fit  $\sin^2 2\theta_{13}$  value for given  $\delta_{\text{CP}}$  values. The values of  $\sin^2 2\theta_{13}$  and  $\Delta m_{32}^2$  are varied in the fit with the constraint from [12]. The shaded region shows the average  $\theta_{13}$  value from the PDG2012 [24]. (c) The  $-2\Delta \ln \mathcal{L}$  value as a function of  $\delta_{\text{CP}}$  for normal hierarchy (solid line) and inverted hierarchy (dotted line). The solid (dotted) line with markers corresponds to the 90% CL limits for normal (inverted) hierarchy, evaluated by using the Feldman-Cousins method. The  $\delta_{\text{CP}}$  regions with values above the lines are excluded at 90% CL.

3.4.  $\bar{\nu}_\mu$  Disappearance (Preliminary). Recently T2K reported [30] an initial measurement of muon antineutrino disappearance using the accelerator-produced off-axis neutrino beam at J-PARC.

The event selection applied at SK is unchanged with respect to the neutrino beam mode previously described.

Using a dataset corresponding to  $4.04 \times 10^{20}$  protons-on-target, 34 fully contained  $\mu$ -like events were observed while 103 events were predicted by Monte Carlo for the unoscillated case.

The best fit oscillation parameters measured under those conditions are  $\sin^2(\bar{\theta}_{23}) = 0.45$  and  $|\Delta \bar{m}_{32}^2| = 2.51 \times 10^{-3} \text{ eV}^2$  with 68% confidence intervals of 0.38–0.64 and 2.26–2.80 ( $\times 10^{-3} \text{ eV}^2$ ), respectively.

Preliminary results from the  $\bar{\nu}_\mu$  disappearance analysis are illustrated in Figure 9.

The distribution of reconstructed neutrino energy for the 34 single ring  $\mu$ -like events, together with expectations for no-oscillation hypothesis, is shown in Figure 9(a). The deficit is clearly seen.

In Figure 9(b), the constraints on oscillation parameters  $|\Delta \bar{m}_{32}^2|$  and  $\sin^2(\bar{\theta}_{23})$  obtained from this analysis are compared with previous results. Clearly they are in agreement with antineutrino measurements from both the MINOS and Super-Kamiokande collaborations and also with precise measurements of neutrino disappearance from T2K.

In spite these results representing only 10% of the expected T2K antineutrino dataset, they are already

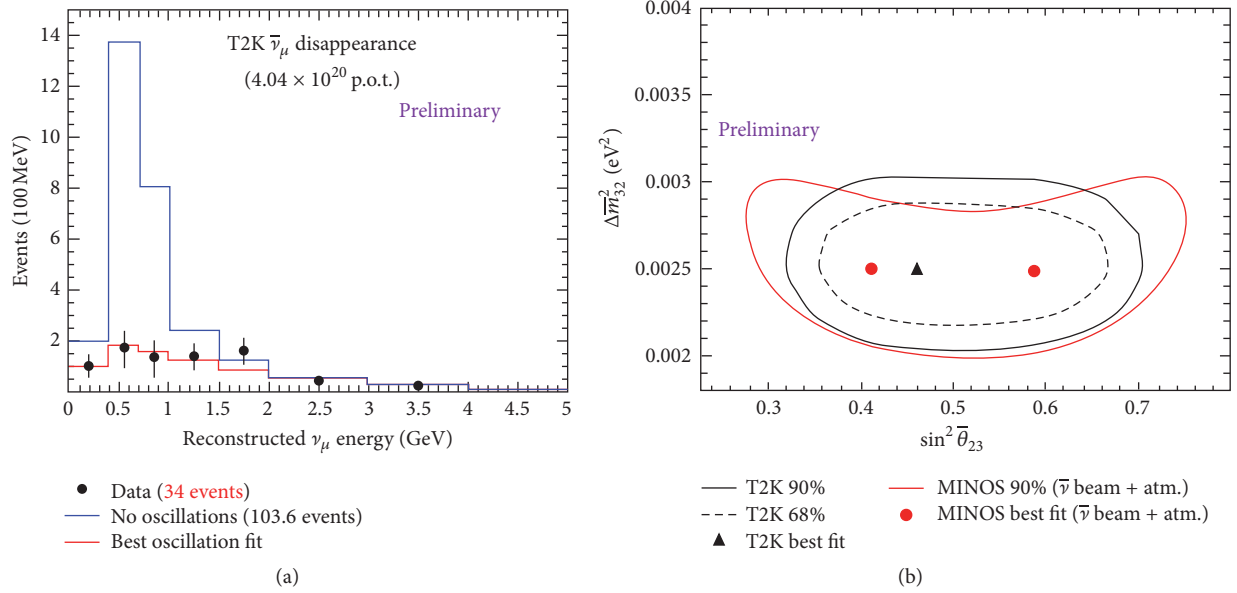


FIGURE 9: (a) Distribution of reconstructed neutrino energy for 34 single ring  $\mu$ -like events observed in antineutrino beam corresponding to  $4.04 \times 10^{20}$  p.o.t. The expectations for no oscillation and for best fit oscillation parameters are also shown. (b) Constraints on oscillation parameters  $|\Delta m_{32}^2|$  and  $\sin^2(\theta_{23})$  obtained from  $\bar{\nu}_\mu$  disappearance. Constraints from the MINOS [25] experiment are also shown.

competitive with both MINOS [25] and SK [37], demonstrating the effectiveness of the off-axis beam technique.

**3.5.  $\bar{\nu}_e$  Appearance (Preliminary).** The selection process of  $\bar{\nu}_e$  candidates in SK is exactly the same as that for neutrino beam data. After all selections, three events remain as possible candidates of the  $\bar{\nu}_e$  appearance signal. The expected number of background events is calculated by Monte Carlo assuming the absence of  $\bar{\nu}_\mu$ - $\bar{\nu}_e$  oscillation. Background events include  $\nu_e$  appearance from  $\nu_\mu$ - $\nu_e$  oscillation, misidentified  $\nu_\mu$  (or  $\bar{\nu}_\mu$ ), and original  $\nu_e$  (or  $\bar{\nu}_e$ ) from the decay of muons in the T2K beam line. The number of background events varies from 1.51 to 1.77, depending on mass hierarchy and  $\delta_{\text{CP}}$ .

Obviously, the observation of three candidates is not significant evidence of  $\bar{\nu}_e$  appearance but the collaboration plans to multiply by factor 3 the statistic in the incoming years.

#### 4. T2K Physics Potential for $7.8 \times 10^{21}$ p.o.t.

The observation of the electron neutrino appearance in a muon neutrino beam by T2K and the high-precision measurement of the mixing angle  $\theta_{13}$  by reactor experiments have led to reevaluation of the physics potential of T2K for the approved dataset ( $7.8 \times 10^{21}$  p.o.t.) that, according to the latest plans of the accelerator group in J-PARC, will be achieved by  $\sim 2020$ .

In particular in [38] the sensitivities for CP violation in neutrinos, nonmaximal  $\sin^2 2\theta_{23}$ , octant of  $\theta_{23}$ , and mass hierarchy have been explored for T2K alone and in combination with NO $\nu$ A and reactor experiments results.

Special care was also taken in studying the effect coming for various combinations of  $\nu$ -mode and  $\bar{\nu}$ -mode data-taking. In fact the probability of  $\nu_\mu \rightarrow \nu_e$  is slightly different from the probability for  $\bar{\nu}_\mu \rightarrow \bar{\nu}_e$  oscillation because of the swap in the sign of the  $\delta_{\text{CP}}$  term. This implies that the antineutrino oscillation probability is larger (smaller) than the neutrino oscillation probability for positive (negative)  $\delta_{\text{CP}}$  by up to 25%. Accordingly, comparison of oscillation probabilities between neutrino mode and antineutrinos mode could help in the determination of the  $\delta_{\text{CP}}$  value.

**4.1. T2K Alone.** A three-flavor analysis combining appearance and disappearance, for both  $\nu$ -mode and  $\bar{\nu}$ -mode, has been performed assuming the expected full statistics of  $7.8 \times 10^{21}$  p.o.t..

The selection of candidate events in SK was done using the same criteria described in Section 3.1.

The study includes either statistical errors only or statistical and systematic errors established for the 2012 oscillation analyses. In addition, signal efficiency and background are taken into account.

It should be emphasized that this evaluation is conservative, considering that the analyses performed on data collected in the years 2013–2015 already showed an improved precision by about 20%, or more, with respect to the numbers quoted in [38].

Reconstructed appearance and disappearance energy spectra generated for the approved full T2K statistics, assuming a data-taking condition of either 100%  $\nu$ -mode or 100%  $\bar{\nu}$ -mode, are shown in Figure 10. All the oscillation parameters have been used in generating the spectra.  $\delta_{\text{CP}}$ ,  $\sin^2 2\theta_{13}$ ,  $\sin^2 \theta_{23}$ , and  $\Delta m_{32}^2$  were left unknown in the fit, while

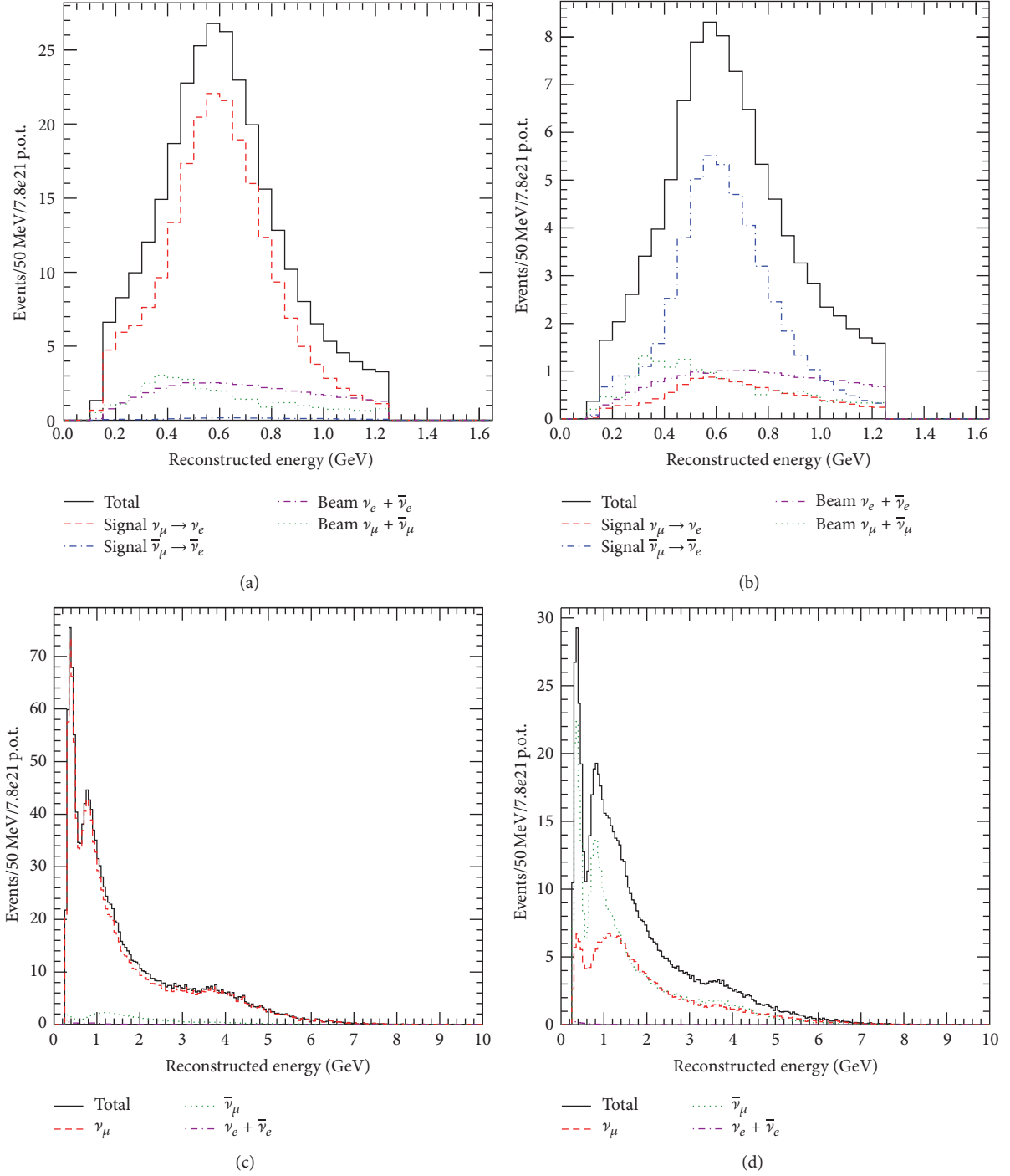


FIGURE 10: (a)  $\nu_e$  appearance reconstructed energy spectrum, 100%  $\nu$ -mode running. (b)  $\bar{\nu}_e$  appearance reconstructed energy spectrum, 100%  $\bar{\nu}$ -mode running. (c)  $\nu_\mu$  disappearance reconstructed energy spectrum, 100%  $\nu$ -mode running. (d)  $\bar{\nu}_\mu$  disappearance reconstructed energy spectrum, 100%  $\bar{\nu}$ -mode running. All the oscillation parameters have been used in generating the spectra.  $\delta_{\text{CP}}$ ,  $\sin^2 2\theta_{13}$ ,  $\sin^2 \theta_{23}$ , and  $\Delta m_{32}^2$  were left unknown in the fit, while  $\sin^2 2\theta_{12}$  and  $\Delta m_{21}^2$  are assumed to be fixed to the values given in Table 1.

$\sin^2 2\theta_{12}$  and  $\Delta m_{21}^2$  are assumed to be fixed to the values given in Table 1. The expected number of  $\nu_e$  or  $\bar{\nu}_e$  appearance events at  $7.8 \times 10^{21}$  p.o.t. obtained from [38] is shown in Table 2 for two different values of  $\delta_{\text{CP}}$  ( $-90^\circ$ ,  $0^\circ$ ). The number of events is broken down into those coming from appearance signal

or intrinsic beam background events that undergo charged current (CC) interactions in SK or beam background events that undergo neutral current (NC) interactions.

The values given in Table 2 indicate that statistics is much more favourable for the  $\nu$ -mode, where a signal 3 times larger

TABLE I: Nominal values of the oscillation parameters.

Parameter	$\sin^2 2\theta_{13}$	$\delta_{\text{CP}}$	$\sin^2 \theta_{23}$	$\Delta m_{32}^2$	Hierarchy	$\sin^2 2\theta_{12}$	$\Delta m_{21}^2$
Nominal value	0.1	0	0.5	$2.4 \times 10^{-3} \text{ eV}^2$	Normal	0.8704	$7.6 \times 10^{-5} \text{ eV}^2$

TABLE 2: Expected numbers of  $\nu_e$  or  $\bar{\nu}_e$  appearance events at  $7.8 \times 10^{21}$  p.o.t.. The number of events is broken down into those coming from appearance signal or intrinsic beam background events that undergo charged current (CC) interactions in SK or beam background events that undergo neutral current (NC) interactions.

	$\delta_{\text{CP}}$	Total	Signal $\nu_\mu \rightarrow \nu_e$	Signal $\bar{\nu}_\mu \rightarrow \bar{\nu}_e$	Beam CC $\nu_e + \bar{\nu}_e$	Beam CC $\nu_\mu + \bar{\nu}_\mu$	NC
100% $\nu$ -mode	$0^\circ$	291.5	211.9	2.4			
100% $\nu$ -mode	$-90^\circ$	341.8	262.9	1.7	41.3	1.4	34.5
100% $\bar{\nu}$ -mode	$0^\circ$	94.9	11.2	48.8			
100% $\bar{\nu}$ -mode	$-90^\circ$	82.9	13.1	34.9	17.2	0.4	17.3

is expected. However, only combining  $\nu$ -mode and  $\bar{\nu}$ -mode will give an advantage in constraining  $\delta_{\text{CP}}$ .

This effect is clearly illustrated in Figure 11.

In this example, (a) and (b) of Figure 11 show  $\delta_{\text{CP}}$  versus  $\sin^2 2\theta_{13}$  90% CL intervals, each given for 50% of the full T2K p.o.t., of  $\nu$ - and  $\bar{\nu}$ -mode at true  $\delta_{\text{CP}} = -90^\circ$  assuming NH and without a reactor constraint (if the fit is assuming the correct mass hierarchy (MH) it is called NH, while if it is assuming the incorrect MH it is called IH).

When the two contours are combined in Figure 11(c), it becomes evident that  $\delta_{\text{CP}}$  can be constrained without any requirement from external data.

However, for other parameters (like  $\theta_{23}$ ) the constraint from the reactor measurements is very important and it is not avoidable if one wishes to discriminate the octant and cancel the degeneracies.

Figure 12 shows, as an example, the 90% CL regions for  $\Delta m_{32}^2$  versus  $\sin^2 \theta_{23}$  at the full T2K statistics for  $\sin^2 \theta_{23} = 0.4$ . In this case the  $\theta_{23}$  octant cannot be resolved only by combining both  $\nu$ -mode and  $\bar{\nu}$ -mode data (Figure 12(a)). In fact the reactor constraint on  $\theta_{13}$  should be included to resolve degeneracies between the oscillation parameters  $\sin^2 \theta_{23}$ ,  $\sin^2 2\theta_{13}$ , and  $\delta_{\text{CP}}$  as clearly illustrated in Figure 12(b).

4.2. *T2K + NO $\nu$ A*. Since the ability of T2K to measure the value of  $\delta_{\text{CP}}$  is greatly enhanced by the knowledge of the mass hierarchy, the same study [38] has also incorporated the impact of expected data from the NO $\nu$ A experiment using the GLOBES tools [39].

The NO $\nu$ A experiment [21], which started operating in 2014, has a longer baseline (810 km) and higher peak neutrino energy ( $\sim 2$  GeV) than T2K. Accordingly, the impact of the matter effect on the predicted far detector event spectra is larger in NO $\nu$ A ( $\sim 30\%$ ) than in T2K ( $\sim 10\%$ ), leading to a better sensitivity to the mass hierarchy.

The study assumes the T2K final statistic ( $7.8 \times 10^{21}$  p.o.t.) [19] and  $1.8 \times 10^{21}$  p.o.t. in  $\nu$ -mode and  $1.8 \times 10^{21}$  p.o.t.  $\bar{\nu}$  for NO $\nu$ A [21]. The result is illustrated in Figures 13 and 14 for the NH and IH case, respectively. The plots on the left assume a data-taking condition of 100%  $\nu$ -mode for T2K and 50%  $\nu$ -

50%  $\bar{\nu}$ -mode for NO $\nu$ A. The plots on the right assume a data-taking condition of 50%  $\nu$ - 50%  $\bar{\nu}$ -mode for both T2K and NO $\nu$ A.

Because of the complementary nature of these two experiments, when T2K data is combined with data from NO $\nu$ A, the region of oscillation parameter space where there is sensitivity to observe a nonzero  $\delta_{\text{CP}}$  is substantially increased compared to when each experiment is analyzed alone.

The results of the studies in [38] are actually used to guide the optimization of the future run plan for T2K.

## 5. T2K Physics Potential for $20 \times 10^{21}$ p.o.t. or More

In summer of 2015 the T2K collaboration has been considering an extension of the data-taking run beyond the approved total  $7.8 \times 10^{21}$  to  $20 \times 10^{21}$  p.o.t. or more ( $25 \times 10^{21}$  p.o.t.). In fact, from studies [40, 41], based on the same considerations described in Section 4.1, an enhancement of the statistics by factor 3 or more could possibly lead to a  $3\sigma$  measurement excluding  $\sin(\delta_{\text{CP}}) = 0$  (depending on the true value of  $\delta_{\text{CP}}$  and on the knowledge of the MH) and showing the first evidence of CP violation in the lepton sector.

In this section we will give a short summary of those recent studies with the *caveat* that all the plots showed below must be considered *work in progress*.

5.1. *J-PARC Beam Update*. The extended T2K p.o.t. projection, based on the latest J-PARC beam schedule (red dots), is shown in Figure 15 together with a new possible J-PARC beam upgraded schedule as envisaged in [28] (blue dots). The extended T2K p.o.t. projection includes the MR (Main Ring) update (recently approved) that will allow reaching power of 750 kW in 2019 and up to 1.3 MW when the repetition cycle will be reduced from 2.4 s to 1.3 s.

The MR beam power time evolution together with the possible data accumulation is shown in Figure 16 [23], where 5-month neutrino beam operation each year and realistic running time efficiency are assumed.

The new projection shown in Figure 15 (blue dots) assumes an effective p.o.t. calculated by also taking into

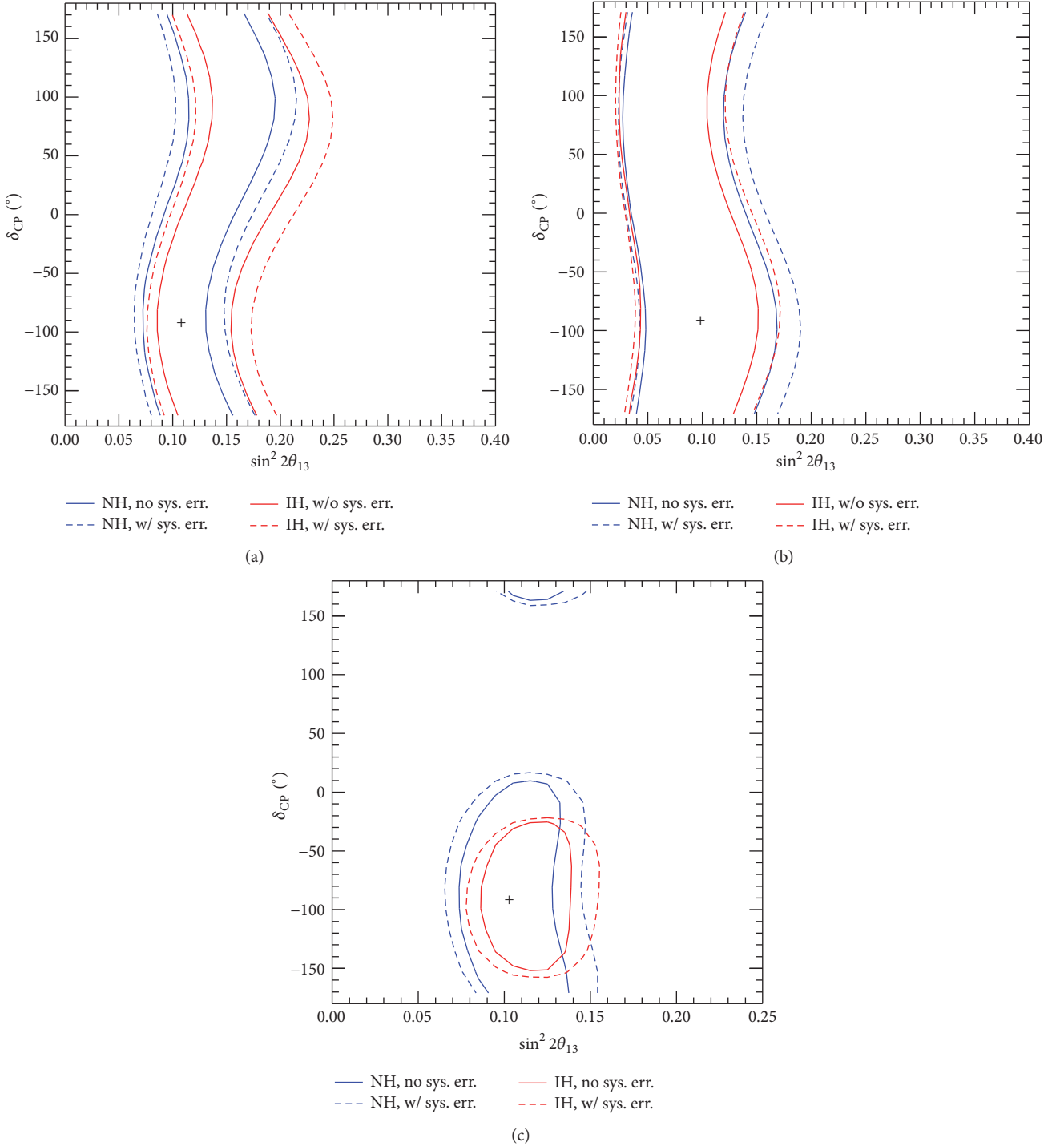


FIGURE 11: Expected  $\delta_{CP}$  versus  $\sin^2 2\theta_{13}$  90% CL intervals, where (a) and (b) are given for neutrino and antineutrino mode running for 50% of the full T2K p.o.t. each and (c) demonstrated the sensitivity of the total T2K p.o.t. with 50%  $\nu$ -mode plus 50%  $\bar{\nu}$ -mode running. Contours are plotted for the case of true  $\delta_{CP} = -90^\circ$  and NH. The blue curves are fits assuming the correct MH(NH), while the red ones are fits assuming the incorrect MH(IH), and contours are plotted from the minimum  $\chi^2$  value for both MH assumptions. The solid contours are with statistical error only, while the dashed contours include the systematic errors used in the 2012 oscillation analysis assuming full correlation between  $\nu$ - and  $\bar{\nu}$ -mode running errors.

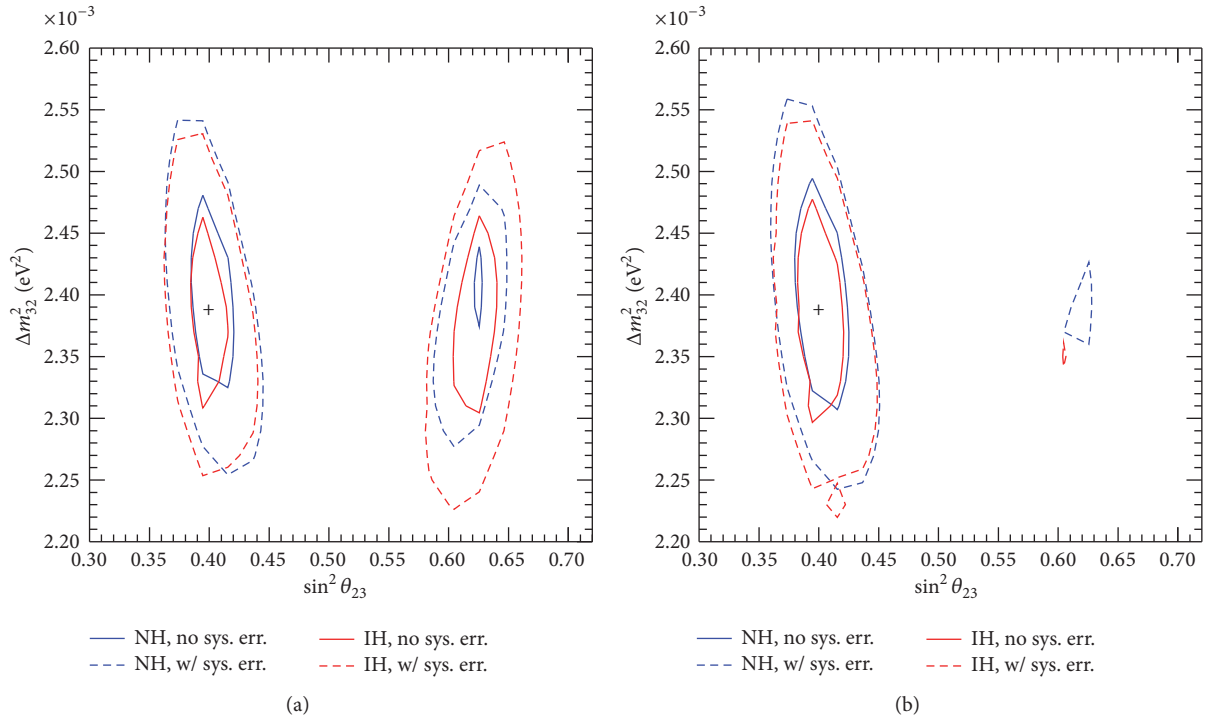


FIGURE 12:  $\Delta m_{32}^2$  versus  $\sin^2 \theta_{23}$  90% CL intervals for  $7.8 \times 10^{21}$  p.o.t. (50%  $\nu$ -mode plus 50%  $\bar{\nu}$ -mode running). Contours are plotted for the case of true  $\delta_{\text{CP}} = 0^\circ$ ,  $\sin^2 \theta_{23} = 0.4$ ,  $\Delta m_{32}^2 = 2.4 \times 10^{-3} \text{ eV}^2$ , and NH. The plot on (a) does not include the reactor constraint; the plot on (b) includes it. The blue curves show fits assuming the correct MH(NH), while the red ones show fits assuming the incorrect MH(IH). The solid contours are with statistical error only, while the dashed contours include the 2012 systematic errors fully correlated between  $\nu$ -mode and  $\bar{\nu}$ -mode.

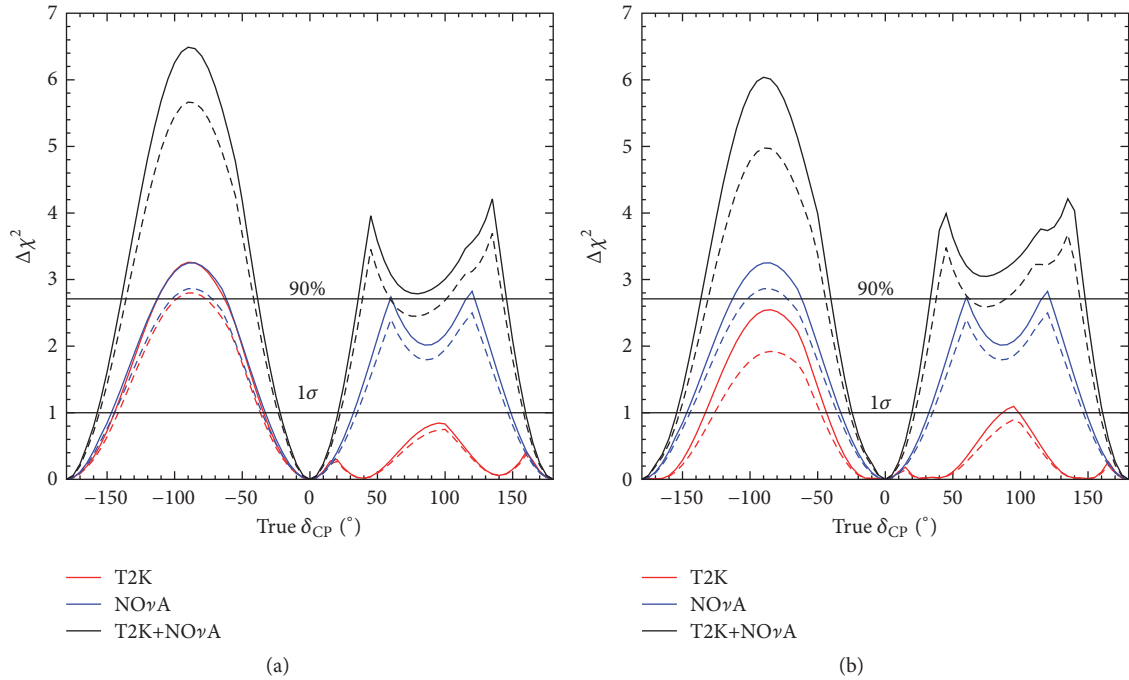


FIGURE 13: The predicted  $\Delta \chi^2$  for rejecting the  $\sin \delta_{\text{CP}} = 0$  hypothesis, as a function of  $\delta_{\text{CP}}$  for T2K (red), NO $\nu$ A (blue), and T2K + NO $\nu$ A (black), assuming NH. Dashed (solid) curves indicate studies where normalization systematics are (not) considered. (a) 1:0 T2K, 1:1 NO $\nu$ A  $\nu$ : $\bar{\nu}$ . (b) 1:1 T2K, 1:1 NO $\nu$ A  $\nu$ : $\bar{\nu}$ .

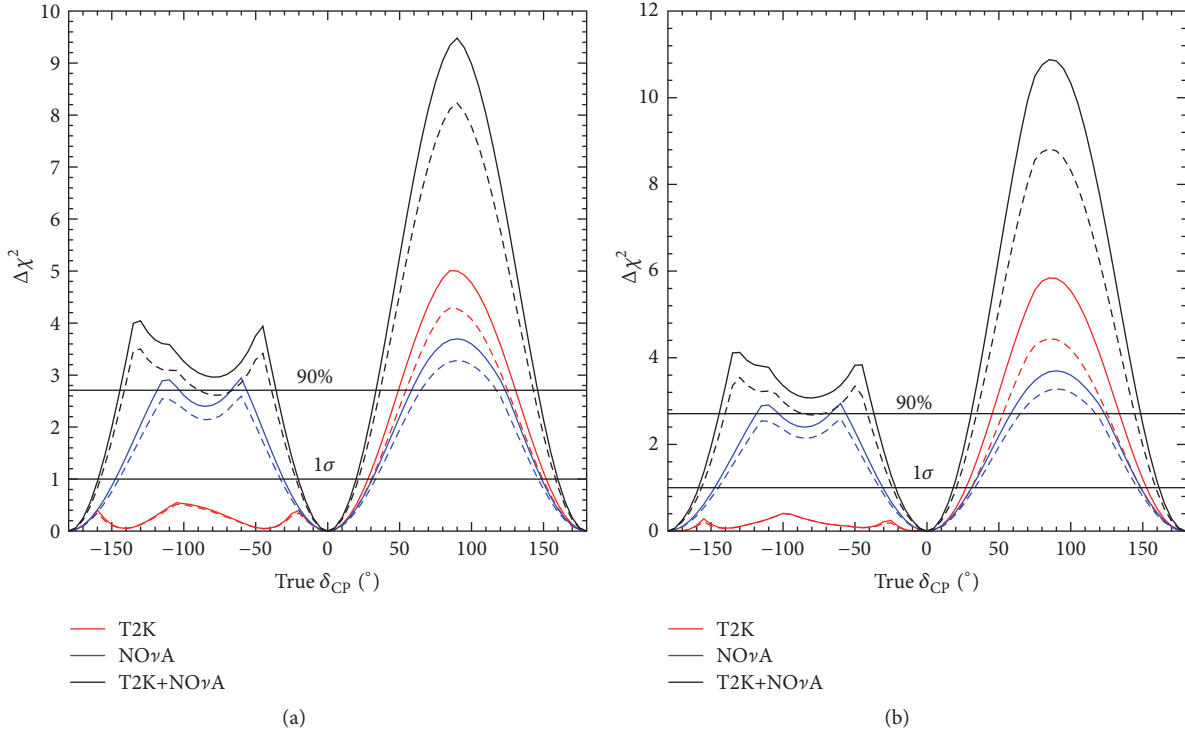


FIGURE 14: The predicted  $\Delta\chi^2$  for rejecting the  $\sin \delta_{CP} = 0$  hypothesis, as a function of  $\delta_{CP}$  for T2K (red), NO $\nu$ A (blue), and T2K + NO $\nu$ A (black), assuming IH. Dashed (solid) curves indicate studies where normalization systematics are (not) considered. (a) 1:0 T2K, 1:1 NO $\nu$ A  $\nu$ : $\bar{\nu}$ . (b) 1:1 T2K, 1:1 NO $\nu$ A  $\nu$ : $\bar{\nu}$ .

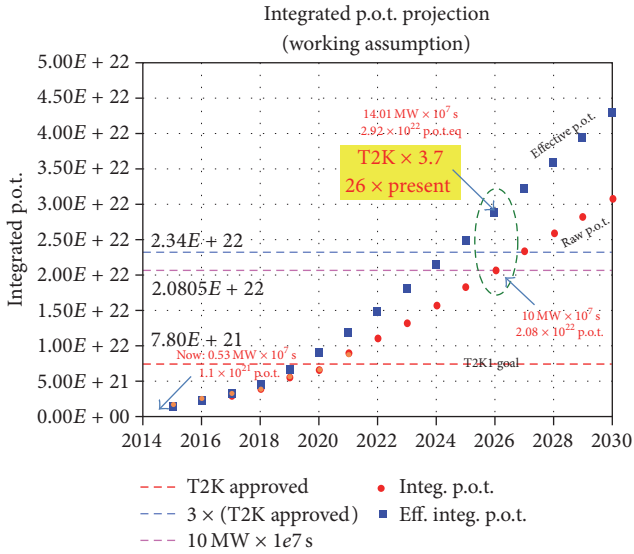


FIGURE 15: The extended T2K p.o.t. projection, based on the last J-PARC beam schedule (red dots) together with a new possible J-PARC beam upgraded schedule as envisaged in [28] (blue dots). The new projection assumes an effective p.o.t., calculated including additional hardware upgrades and analysis improvements in SK.

account additional hardware upgrades and some analysis improvements in SK. The possible hardware improvements include an increase of the horn current from  $\pm 250$  kA to  $\pm 320$  kA. This will lead up to a 10% more neutrino flux

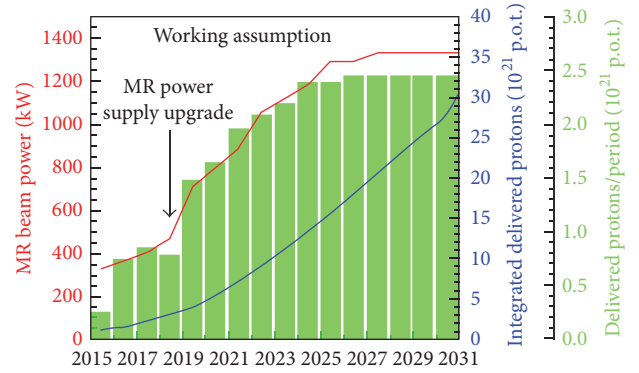


FIGURE 16: Anticipated MR beam power and POT accumulation versus calendar year [23].

at the far detector. The analysis improvements include the expansion of the SK fiducial volume and/or adding new SK event selections. As an example, adding CC  $1\pi$  events will increase the event sample at the far detector by 14%.

According to the projections showed in Figures 15 and 16, T2K will be able to collect neutrino events corresponding to  $20 \times 10^{21}$  p.o.t. ( $25 \times 10^{21}$  p.o.t.) before the year 2026 (2028) (red dots) or 2024 (2025) (blue dots).

Tables 3 and 4 [40, 41] show the expected numbers of  $\nu_e$  or  $\bar{\nu}_e$  appearance events and  $\nu_\mu$  or  $\bar{\nu}_\mu$  disappearance events for two different values of  $\delta_{CP}$  ( $-90^\circ, 0^\circ$ ) at  $7.8 \times 10^{21}$  p.o.t. and  $25 \times 10^{21}$  p.o.t., respectively. A combination of 50%  $\nu$ - + 50%  $\bar{\nu}$ - mode beam running is assumed.

TABLE 3: Expected numbers of  $\nu_e$  or  $\bar{\nu}_e$  appearance events for two different values of  $\delta_{\text{CP}}$  ( $-90^\circ$ ,  $0^\circ$ ) at  $7.8 \times 10^{21}$  p.o.t. and  $25 \times 10^{21}$  p.o.t., respectively. A combination of 50%  $\nu$ - + 50%  $\bar{\nu}$ -mode beam running is assumed.

		$\nu_e$ signal	$\nu_e$ bkg.	$\bar{\nu}_e$ signal	$\bar{\nu}_e$ bkg.
7.8e21 p.o.t.	$0^\circ$	98.2	26.8	25.6	16.3
	$-90^\circ$	121.4	26.4	19.0	17.2
25e21 p.o.t.	$0^\circ$	314	85.9	82.1	52.2
	$-90^\circ$	389	84.6	60.9	55.1

TABLE 4: Expected numbers of  $\nu_\mu$  or  $\bar{\nu}_\mu$  disappearance events assuming or not the oscillation hypothesis at  $7.8 \times 10^{21}$  p.o.t. and  $25 \times 10^{21}$  p.o.t., respectively. A combination of 50%  $\nu$ - + 50%  $\bar{\nu}$ -mode beam running is assumed.

		$\nu_\mu$ -model	$\bar{\nu}_\mu$ -mode
7.8e21 p.o.t.	w/o oscillation	2648	1007
	w/ oscillation	741	342
25e21 p.o.t.	w/o oscillation	8519	3228
	w/ oscillation	2375	1096

5.2. *T2K Sensitivities to the Oscillation Parameters with  $20 \times 10^{21}$  p.o.t.* At the beginning of January 2016 the T2K collaboration has submitted an EoI (Expression of Interest) [42] to the Japanese PAC Committee, aiming to extend the T2K run to  $20 \times 10^{21}$  p.o.t. (T2K-II). For this study T2K systematic errors are encoded into a covariance matrix with bins in reconstructed neutrino energy. Errors on the shape of the reconstructed energy spectra are taken into account. Two hypotheses have been considered on both reconstructed  $\nu_e$  appearance and  $\nu_\mu$  disappearance events: the current (2016) T2K systematic error on the far detector prediction (the total systematic error on the far detector prediction is now 6.8% [36]) and a possible reduction to 4% that seems to be reachable in the next years by T2K.

The T2K sensitivity to a nonzero  $\sin(\delta_{\text{CP}})$  also depends on the true values of the oscillation parameters. In this case all plots assume  $\sin^2 2\theta_{13} = 0.085$  and  $\Delta m_{32}^2 = 2.5 \times 10^{-3}$ .

The updated horn current of  $\pm 320$  kA and a combination of 50%  $\nu$ - + 50%  $\bar{\nu}$ -mode beam running are also assumed.

In Figure 17 the predicted  $\Delta\chi^2$  for rejecting the  $\sin \delta_{\text{CP}} = 0$  hypothesis is plotted versus p.o.t. (assuming  $\delta_{\text{CP}} = -90^\circ$  and true normal mass hierarchy (NH)) for various true values of  $\sin^2 \theta_{23}$  with or without systematic errors. It is clear that not only the improvement in statistics but also the reduction of the T2K systematic errors would be more than beneficial in the case of an extension of T2K.

Also the knowledge of the mass hierarchy is an important element, as it can be seen by looking at Figure 18 where  $\Delta\chi^2$  for rejecting the  $\sin \delta_{\text{CP}} = 0$  is plotted versus true  $\delta_{\text{CP}}$ . In fact, comparing Figure 18(b) (that assumes MH is known) with Figure 18(a) (that assumes MH is unknown), it is clear that the sensitivity to  $\sin \delta_{\text{CP}} = 0$  will be enhanced in the first case. However several experiments (JUNO, NO $\nu$ A, ORCA, and PINGU) are expected or plan to determine the mass

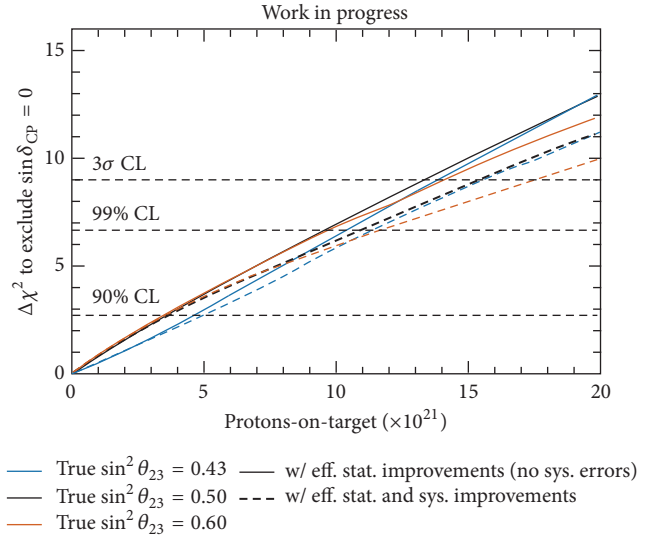


FIGURE 17: Predicted  $\Delta\chi^2$  for rejecting the  $\sin \delta_{\text{CP}} = 0$  hypothesis versus p.o.t. assuming  $\delta_{\text{CP}} = -90^\circ$  and NH for various true values of  $\sin^2 \theta_{23}$  with or without systematic errors.

hierarchy before or during the proposed period of T2K-II [21, 43–45]. In this context the sensitivity shown in Figure 18(b) seems to illustrate a realistic scenario.

## 6. Conclusions

The T2K experiment, proposed in 2003 and approved in 2006 to collect data corresponding to  $7.8 \times 10^{21}$  protons-on-target (p.o.t.) from a 30 GeV proton beam at the J-PARC accelerator facility in Japan, is one of the most important players in the field of neutrino oscillations.

Built to search for  $\nu_\mu \rightarrow \nu_e$  appearance and to make precision measurements of oscillation parameters in  $\nu_\mu$  disappearance, it realized its first goal with just 8.4% of the total approved p.o.t. and at the same time provided the most stringent constraints on  $\sin^2(\theta_{23})$  obtained until now.

The T2K collaboration is now looking to the determination of the unknown CP-violating phase  $\delta_{\text{CP}}$  and to more precise measurements of  $\theta_{23}$  to determine the octant.

Reevaluation of the expected sensitivity to the oscillation parameters that takes into account the observation of the electron neutrino appearance was done considering two different scenarios: the approved data-taking and data exposure 3 times larger.

In the latter case, assuming a combination of 50%  $\nu$ - + 50%  $\bar{\nu}$ -mode beam running, it might be possible to obtain a  $3\sigma$  measurement excluding  $\sin(\delta_{\text{CP}}) = 0$  (assuming  $\delta_{\text{CP}} = -90^\circ$  and NH) around the year 2025, before the next generation of neutrino experiments will start their operation.

## Competing Interests

The author declares that they have no competing interests.

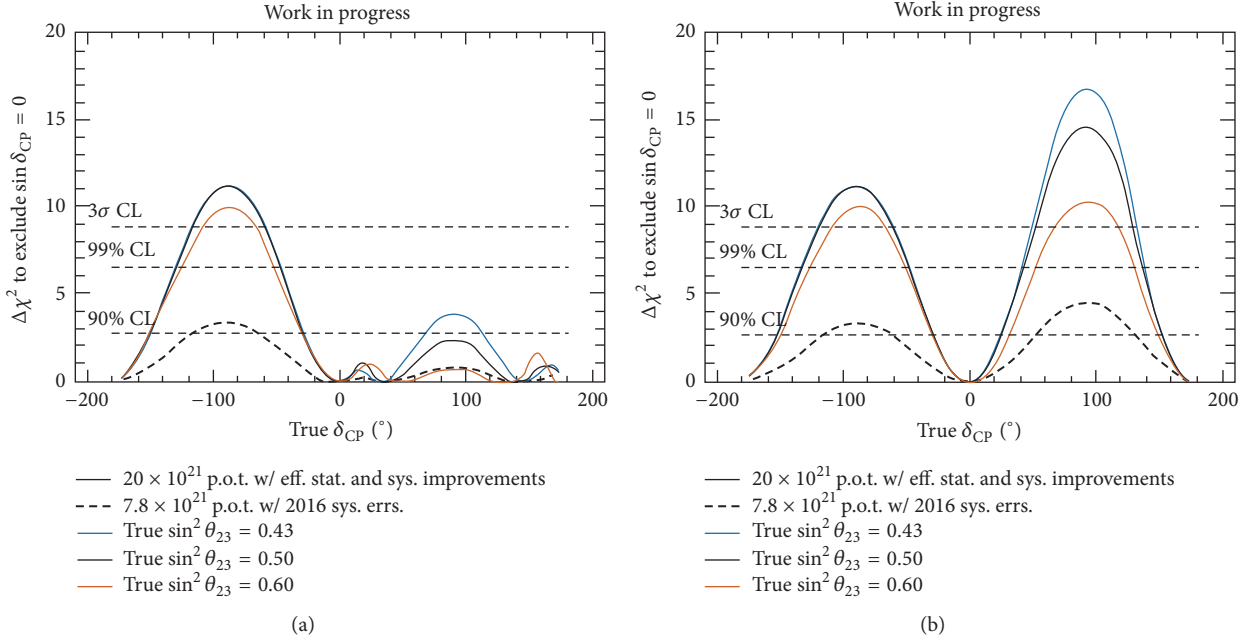


FIGURE 18: Sensitivities to CP violation as a function of true value of  $\delta_{CP}$  for T2K and extended T2K for various true values of  $\sin^2\theta_{23}$  assuming (b) or not (a) that the true MH is the normal MH.

## References

- [1] Y. Fukuda, Super-Kamiokande Collaboration et al., “Evidence for oscillation of atmospheric neutrinos,” *Physical Review Letters*, vol. 81, no. 8, pp. 1562–1567, 1998.
- [2] B. T. Cleveland, T. Daily, R. Davis Jr. et al., “Measurement of the solar electron neutrino flux with the homestake chlorine detector,” *The Astrophysical Journal*, vol. 496, no. 1, pp. 505–526, 1998.
- [3] K. Abe, Y. Hayato, T. Iida et al., “Solar neutrino results in Super-Kamiokande-III,” *Physical Review D*, vol. 83, no. 5, Article ID 052010, 19 pages, 2011.
- [4] B. Aharmim, S. N. Ahmed, A. E. Anthony et al., “Combined analysis of all three phases of solar neutrino data from the Sudbury Neutrino observatory,” *Physical Review C*, vol. 88, no. 2, Article ID 025501, 2013.
- [5] G. Bellini, J. Benziger, D. Bick et al., “First evidence of *pep* solar neutrinos by direct detection in Borexino,” *Physical Review Letters*, vol. 108, no. 5, Article ID 051302, 6 pages, 2012.
- [6] K. Eguchi, S. Enomoto, K. Furuno et al., “First results from KamLAND: evidence for reactor antineutrino disappearance,” *Physical Review Letters*, vol. 90, no. 2, Article ID 021802, 2003.
- [7] F. P. An, J. Z. Bai, A. B. Balantekin et al., “Observation of electron-antineutrino disappearance at Daya Bay,” *Physical Review Letters*, vol. 108, no. 17, Article ID 171803, 7 pages, 2012.
- [8] Y. Abe, C. Aberle, J. C. dos Anjos et al., “Reactor  $\bar{\nu}_e$  disappearance in the Double Chooz experiment,” *Physical Review D*, vol. 86, Article ID 052008, 2012.
- [9] J. K. Ahn, S. Chebotaryov, J. H. Choi et al., “Observation of reactor electron antineutrinos disappearance in the RENO experiment,” *Physical Review Letters*, vol. 108, no. 19, Article ID 191802, 2012.
- [10] P. Adamson, I. Anghel, C. Backhouse et al., “Measurement of neutrino and antineutrino oscillations using beam and atmospheric data in MINOS,” *Physical Review Letters*, vol. 110, no. 25, Article ID 251801, 2013.
- [11] M. H. Ahn, E. Aliu, S. Andringa et al., “Measurement of neutrino oscillation by the K2K experiment,” *Physical Review D*, vol. 74, no. 7, Article ID 072003, 2006.
- [12] K. Abe, J. Adam, H. Aihara et al., “Precise measurement of the neutrino mixing parameter  $\theta_{23}$  from Muon neutrino disappearance in an off-axis beam,” *Physical Review Letters*, vol. 112, no. 18, Article ID 181801, 8 pages, 2014.
- [13] K. Abe, N. Abgrall, Y. Ajima et al., “Indication of electron neutrino appearance from an accelerator-produced off-axis muon neutrino beam,” *Physical Review Letters*, vol. 107, Article ID 041801, 2011.
- [14] K. Abe, M. Kaur, N. Abgrall et al., “Evidence of electron neutrino appearance in a muon neutrino beam,” *Physical Review D*, vol. 88, no. 3, Article ID 032002, 2013.
- [15] K. Abe, J. Adam, H. Aihara et al., “Observation of electron neutrino appearance in a muon neutrino beam,” *Physical Review Letters*, vol. 112, Article ID 061802, 2014.
- [16] P. Adamson, I. Anghel, C. Backhouse et al., “Electron neutrino and antineutrino appearance in the full MINOS data sample,” *Physical Review Letters*, vol. 110, no. 17, Article ID 171801, 2013.
- [17] N. Agafonova, A. Aleksandrov, O. Altinok et al., “Observation of a first  $\nu_T$  candidate event in the OPERA experiment in the CNGS beam,” *Physics Letters B*, vol. 691, no. 3, pp. 138–145, 2010.
- [18] Z. Maki, M. Nakagawa, and S. Sakata, “Remarks on the Unified Model of Elementary Particles,” *Progress of Theoretical Physics*, vol. 28, no. 5, pp. 870–880, 1962.
- [19] “Letter of intent: neutrino oscillation experiment at JHF,” 2003, <http://neutrino.kek.jp/jhfnu/loi/loi.v2.030528.pdf>.
- [20] K. Abe, N. Abgrall, H. Aihara et al., “The T2K experiment,” *Nuclear Instruments and Methods in Physics Research Section A*, vol. 659, no. 1, pp. 106–135, 2011.

- [21] NOvA technical design report, [http://www-nova.fnal.gov/nova\\_cd2\\_review/trd\\_oct\\_23/trd.htm](http://www-nova.fnal.gov/nova_cd2_review/trd_oct_23/trd.htm).
- [22] T. Koseki and K. Hasegawa, "Present status of J-PARC—after the shutdown due to the radioactive material leak accident—," in *Proceeding of the IPAC 2014 Conferences*, Dresden, Germany, 2014.
- [23] F. Naito, Contribution at the PAC meeting: JPARC, July 2015.
- [24] J. Beringer, J.-F. Arguin, R. M. Barnett et al., "Review of particle physics," *Physical Review D*, vol. 86, no. 1, Article ID 010001, 2012.
- [25] P. Adamson, I. Anghel, A. Aurisano et al., "Combined Analysis of  $\nu_\mu$  Disappearance and  $\nu_\mu \rightarrow \nu_e$  Appearance in MINOS Using Accelerator and Atmospheric Neutrinos," *Physical Review Letters*, vol. 112, no. 19, Article ID 191801, 2014.
- [26] S. Fukuda, Y. Fukuda, T. Hayakawa et al., "The Super-Kamiokande detector," *Nuclear Instruments and Methods in Physics Research Section A*, vol. 501, no. 2-3, pp. 418–462, 2003.
- [27] S. Kasuga, T. Hayakawa, S. Joukou et al., "A study on the  $e/\mu$  identification capability of a water Čerenkov detector and the atmospheric neutrino problem," *Physics Letters B*, vol. 374, no. 1-3, pp. 238–242, 1996.
- [28] T. Kobayashi, "Potential J-PARC beam power improvement and beam delivery before 2026," in *Proceedings of the Workshop for Neutrino Programs with Facilities in Japan*, J-PARC, August 2015.
- [29] K. Abe, J. Adam, H. Aihara et al., "Measurements of neutrino oscillation in appearance and disappearance channels by the T2K experiment with  $6.6 \times 10^{20}$  protons on target," *Physical Review D*, vol. 91, no. 7, Article ID 072010, 50 pages, 2015.
- [30] M. Ravonel, "(on behalf of the T2K Collaboration), Talk at European Physical Society HEP 2015," Vienna, 2015.
- [31] N. Abgrall, A. Aduszkiewicz, B. Andrieu et al., "Measurements of cross sections and charged pion spectra in proton-carbon interactions at 31 GeV/c," *Physical Review C*, vol. 84, no. 3, Article ID 034604, 26 pages, 2011.
- [32] N. Abgrall, A. Aduszkiewicz, T. Anticic et al., "Measurement of production properties of positively charged kaons in proton-carbon interactions at 31 GeV/c," *Physical Review C*, vol. 85, no. 3, Article ID 035210, 2012.
- [33] N. Abgrall, B. Andrieu, P. Baron et al., "Time projection chambers for the T2K near detectors," *Nuclear Instruments and Methods in Physics Research Section A: Accelerators, Spectrometers, Detectors and Associated Equipment*, vol. 637, no. 1, pp. 25–46, 2011.
- [34] Y. Ashie, J. Hosaka, K. Ishihara et al., "Measurement of atmospheric neutrino oscillation parameters by Super-Kamiokande I," *Physical Review D*, vol. 71, no. 11, Article ID 112005, 35 pages, 2005.
- [35] A. Himmel and Super-Kamiokande Collaboration, "Recent results from Super-Kamiokande," *AIP Conference Proceedings*, vol. 1604, pp. 345–352, 2014.
- [36] K. Abe, J. Adam, H. Aihara et al., "Measurements of neutrino oscillation in appearance and disappearance channels by the T2K experiment with  $6.6 \times 10^{20}$  protons on target," *Physical Review D*, vol. 91, no. 7, Article ID 072010, 50 pages, 2015.
- [37] K. Abe, Y. Hayato, T. Iida et al., "Search for differences in oscillation parameters for atmospheric neutrinos and antineutrinos at super-kamiokande," *Physical Review Letters*, vol. 107, no. 24, Article ID 241801, 2011.
- [38] K. Abe, J. Adam, H. Aihara et al., "Neutrino oscillation physics potential of the T2K experiment," *Progress of Theoretical and Experimental Physics*, vol. 2015, Article ID 043C01, 4 pages, 2015.
- [39] P. Huber, M. Lindner, W. Winter et al., "Simulation of long-baseline neutrino oscillation experiments with GLOBES: (General Long Baseline Experiment Simulator)," *Computer Physics Communications*, vol. 167, no. 3, pp. 195–202, 2005.
- [40] A. Ichikawa and T2K Collaboration, "Talk at workshop for neutrino programs with facilities in Japan," J-PARC, August 2015.
- [41] The International Workshop on Future Potential of High Intensity Proton Accelerator for Particle and Nuclear Physics (HINT '15), J-PARC, Tokai-Village, Japan, October 2015.
- [42] T2K Collaboration, "Expression of interest for an extended run at T2K to  $20 \times 10^{21}$  POT," PAC Meeting, (JPARC), January 2016.
- [43] F. An, G. An, Q. An et al., "Neutrino physics with JUNO," <http://arxiv.org/abs/1507.05613>.
- [44] M. G. Aartsen, R. Abbasi, M. Ackermann et al., "Letter of intent: the Precision IceCube Next Generation Upgrade (PINGU)," <http://arxiv.org/abs/1401.2046>.
- [45] KM3NET Collaboration, "The ORCA option for KM3NeT," <https://arxiv.org/abs/1402.1022>.

## Review Article

# The Use of Low Temperature Detectors for Direct Measurements of the Mass of the Electron Neutrino

A. Nucciotti<sup>1,2</sup>

<sup>1</sup>*Dipartimento di Fisica, Università di Milano-Bicocca, 20126 Milano, Italy*

<sup>2</sup>*INFN-Sezione di Milano-Bicocca, 20126 Milano, Italy*

Correspondence should be addressed to A. Nucciotti; [angelo.nucciotti@mib.infn.it](mailto:angelo.nucciotti@mib.infn.it)

Received 2 November 2015; Revised 9 February 2016; Accepted 11 February 2016

Academic Editor: Leslie Camilleri

Copyright © 2016 A. Nucciotti. This is an open access article distributed under the Creative Commons Attribution License, which permits unrestricted use, distribution, and reproduction in any medium, provided the original work is properly cited. The publication of this article was funded by SCOAP<sup>3</sup>.

Recent years have witnessed many exciting breakthroughs in neutrino physics. The detection of neutrino oscillations has proved that neutrinos are massive particles, but the assessment of their absolute mass scale is still an outstanding challenge in today particle physics and cosmology. Since low temperature detectors were first proposed for neutrino physics experiments in 1984, there has been tremendous technical progress: today this technique offers the high energy resolution and scalability required to perform competitive experiments challenging the lowest electron neutrino masses. This paper reviews the thirty-year effort aimed at realizing calorimetric measurements with sub-eV neutrino mass sensitivity using low temperature detectors.

## 1. Introduction

Almost two decades ago, the discovery of neutrino flavor oscillations firmly demonstrated that neutrinos are massive particles [1]. This was a crucial breach in the Standard Model of fundamental interactions which assumed massless neutrinos. Flavor oscillations show that the three active neutrino flavor states ( $\nu_e$ ,  $\nu_\mu$ , and  $\nu_\tau$ ) are a superposition of three mass states ( $\nu_1$ ,  $\nu_2$ , and  $\nu_3$ ) and allow the measurement of the difference between the squared masses of the neutrino mass states, but they are not at all sensitive to the absolute masses of the neutrinos.

Today, assessing the neutrino mass scale is still an outstanding task for particle physics, as the absolute value of the neutrino mass would provide an important parameter to extend the Standard Model of particle physics and understand the origin of fermion masses beyond the Higgs mechanism. Furthermore, due to their abundance as Big Bang relics, neutrinos strongly affect the large scale structure and dynamics of the universe by means of their gravitational interactions, which hinder the structure clustering with an effect that is dependent on their mass [2, 3]. In the framework of  $\Lambda$ CDM cosmology (the model with Cold Dark Matter and a cosmological constant  $\Lambda$ ), the scale dependence of

clustering observed in the universe can be indeed used to set an upper limit on the neutrino mass sum  $m_\Sigma = \sum_i m_i$ , where  $m_i$  is the mass of the  $\nu_i$  state. Depending on the model complexity and the input data used, this limit spans in the range between about 0.3 and 1.3 eV [4]; more recently, by combining cosmic microwave background data with galaxy surveys and data on baryon acoustic oscillations, a significantly lower bound on the neutrino mass sum of 0.23 eV has been published [5], although this value is strongly model dependent.

The oscillations discovery and the accurate cosmological observations revived and boosted the interest in neutrino physics (this is also confirmed by the Nobel Prizes in Physics awarded in the years 2002, 2008, and, very recently, 2015), with the start of many ambitious experiments for different high precision measurements and the rate of publishing papers increased by almost an order of magnitude, but in spite of the enhanced experimental efforts very little is known about neutrinos and their properties. Several crucial pieces are still missing, in particular the absolute neutrino mass scale, the neutrino mass ordering (the so-called *mass hierarchy*), the neutrino nature (Dirac or Majorana fermion), the magnitude of the CP (charge and parity) violation phases, and the possible existence of sterile neutrinos.

This paper is devoted to the assessment of the absolute neutrino mass scale and in particular to the direct measurement of the electron neutrino mass via calorimetric experiments. After a brief overview of our present picture for massive neutrinos, I will introduce both the theoretical and the experimental issues involved in the direct determination of the neutrino mass and discuss the past and current calorimetric experiments, with a focus on experiments with low temperature detectors.

## 2. The Neutrino Mass Pattern and Mixing Matrix

Most of the existing experimental data on neutrino oscillations can be explained by assuming a three-neutrino framework, where any flavor state  $\nu_l$  ( $l = e, \mu, \tau$ ) is described as a superposition of mass states  $\nu_i$  ( $i = 1, 2, 3$ ) or

$$|\nu_l\rangle = \sum_i U_{li} |\nu_i\rangle, \quad (1)$$

where  $U_{li}$  is the  $3 \times 3$  Pontecorvo-Maki-Nakagawa-Sakata unitary mixing matrix (see, e.g., [6]). As a consequence, the neutrino flavor is no longer a conserved quantity and for neutrinos propagating in vacuum the amplitude of the process  $\nu_l \rightarrow \nu_{l'}$  is not vanishing.

The mixing matrix  $U_{li}$  is parametrized by three angles, conventionally denoted by  $\Theta_{12}$ ,  $\Theta_{13}$ , and  $\Theta_{23}$ , one CP violation phase  $\delta$ , and two Majorana phases  $\alpha_1$ ,  $\alpha_2$ ; these two have physical consequences only if neutrinos are Majorana particles—that is, identical to their antiparticles—but they do not affect neutrino oscillations. To these six parameters, three angles and three phases, the three mass values  $m_i$  must be added also, for a total of nine unknowns altogether. In the years, oscillation experiments measuring the flux of solar, atmospheric, reactor, and accelerator neutrinos have contributed to the precise determination of many of these unknowns.

The oscillation probabilities depend, in general, on the neutrino energy, on the source-detector distance, on the elements of the mixing matrix, and on the neutrino mass squared differences  $\Delta m_{ij}^2 \equiv m_j^2 - m_i^2$ . At present, the three mixing angles and the two mass splittings, conventionally  $\Delta m_{21}^2$  (from solar neutrino oscillations) and  $\Delta m_{31}^2$  (from atmospheric neutrino oscillations), have been determined with reasonable accuracy [1]. However, the available data are not yet able to discriminate the neutrino mass ordering. While the effect of the interactions of solar neutrinos with matter constituents (known as Mikheyev-Smirnov-Wolfenstein effect) allows the establishment of  $m_1 < m_2$  so that  $\Delta m_{21}^2 > 0$ , we have  $\Delta m_{21}^2 \ll |\Delta m_{31}^2| \cong |\Delta m_{32}^2|$  and we are left with two possibilities: either  $m_1 < m_2 < m_3$  (normal ordering, i.e.,  $\Delta m_{31}^2 > 0$ ) or  $m_3 < m_1 < m_2$  (inverted ordering, i.e.,  $\Delta m_{31}^2 < 0$ ) (compare also with Figure 3). In both schemes, there is a Quasi-Degeneracy (QD) of the three neutrino masses when  $m_1 \simeq m_2 \simeq m_3$ , with  $m_i \gg \sqrt{\Delta m_{31}^2} \simeq 5 \times 10^{-2} \text{ eV}$ . Depending on the value of the lightest mass values, the neutrino mass ordering can also follow

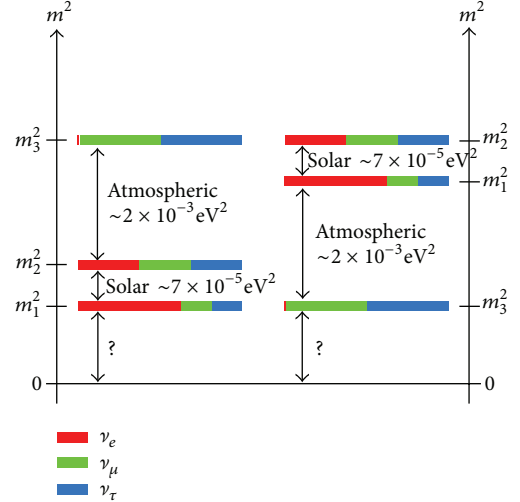


FIGURE 1: In a three-neutrino scheme, the oscillation parameters measured by the various experiments point two possible scenarios regarding the neutrino mass ordering: Normal Hierarchy (left) and Inverted Hierarchy (right). The absolute scale is not accessible by the presently available data.

a Normal Hierarchy (NH), with  $m_1 \ll m_2 \ll m_3$  (in which  $m_2 \simeq \sqrt{\Delta m_{21}^2}$  and  $m_3 \simeq \sqrt{\Delta m_{31}^2}$ ), or an Inverse Hierarchy (IH), with  $m_3 \ll m_1 < m_2$  (in which  $m_1$  and  $m_2$  are quasi-degenerate); see Figure 1. As a final remark, as shown in Figure 3, independent of the mass scheme, oscillation results state that at least two neutrinos are massive, with masses larger than  $\sqrt{\Delta m_{21}^2} \simeq 8.7 \times 10^{-3} \text{ eV}$ .

Most of the oscillation data are well described by the three-neutrino schemes. However, there are a few anomalous indications (the so-called *reactor neutrino anomaly*) [7] that cannot be accommodated within this picture. If confirmed, they would indicate the existence of additional neutrino families, the sterile neutrinos. These neutrinos do not directly participate in the standard weak interactions and would manifest themselves only when mixing with the familiar active neutrinos. Future reactor experiments will test this fascinating possibility.

Assessing the neutrino mass ordering, that is, the sign of  $|\Delta m_{31}^2|$ , is of fundamental importance not only because it would address the correct theoretical extension of the Standard Model, but also because it can impact many important processes in particle physics (like neutrinoless double beta decay). In addition, the phase  $\delta$  governing CP violation in the flavor oscillation experiments remains unknown and a topic of considerable interest [8]. A worldwide research program is underway to address these important open issues in the near future by precise study of the various oscillation patterns.

The oscillation experiments, however, are not able to access the remaining unknown quantities, that is, the absolute mass scale and the two Majorana phases. Their determination is the ultimate goal of nuclear beta decay end-point experiments and neutrinoless double beta decay searches.

The finite neutrino mass manifesting in neutrino oscillations is already an important breach in the Standard Model

of fundamental interactions, but the neutrino sector could hold more surprises. In fact, recent reanalysis of existing data from reactor oscillation experiments together with some anomalies observed in short baseline accelerator oscillation experiments (LSND, MiniBOONE) and in solar experiment calibration with neutrino sources (GALLEX) points to the existence of at least a fourth generation of neutrinos [7]. These hypothetical neutrinos would be *sterile* in the sense that they would feel only gravitational interactions, along with those induced by mixing with the other ordinary neutrinos. Combined analysis of the available data from various sources leads to an additional mass splitting of  $\Delta m_{\text{sterile}}^2 \approx 1 \text{ eV}$ , with a mixing parameter of about  $\sin^2(2\theta) \approx 0.1$ . Sterile right handed neutrinos are indeed introduced naturally when one tries to extend the Standard Model to include the mass of active neutrinos ( $\nu$ MSM) [9]. Moreover, sterile neutrinos in the keV mass range are perfect candidates as Warm Dark Matter (WDM) particles [10].

### 3. Weak Nuclear Decays and Neutrino Mass Scale

Fundamental neutrino properties, in particular its absolute mass and its nature, can be investigated by means of suitable weak decays, where flavor state neutrinos are emitted along with charged leptons and/or pions. There are two complementary approaches for the measurement of the neutrino mass in laboratory experiments: the precise spectroscopy of beta decay at its kinematical *end-point* and the search for neutrinoless double beta decay. Though the expected effective mass sensitivity for neutrinoless double beta decay search is higher, this process implies a strong model-dependence since it requires the neutrino to be a Majorana particle.

Direct neutrino mass measurement, by analyzing the kinematics of electrons emitted in a beta decay, is the most sensitive model independent method to assess the neutrino mass absolute value (analogue measurements involving pion or tau decays give much weaker limits on  $m_{\nu_\mu}$  or  $m_{\nu_\tau}$ ). The beta decay is a nuclear transition involving two nuclides  $(A, Z - 1)$  and  $(A, Z)$ :

$$(A, Z - 1) \longrightarrow (A, Z) + e^- + \bar{\nu}_e, \quad (2)$$

where  $A$  and  $Z$  are, respectively, the mass and atomic numbers of the involved nuclei. Neglecting the nuclear recoil, the kinetic energy  $E_0$  available to the electron and antineutrino in the final state is given by

$$E_0 = E_\beta + E_{\bar{\nu}} = M(A, Z - 1) - M(A, Z) = Q, \quad (3)$$

where  $M$  indicates the mass of the *atoms* in the initial and final state.

In practice, this method exploits only momentum and energy conservation: it measures the minimum energy carried away by the neutrino—that is, its rest mass—by observing the highest energy electrons emitted in this three-body decay. To balance the energy required to create the emitted neutrinos, the highest possible kinetic energy  $E_\beta$  of the electrons is slightly reduced. This energy deficit may be

noticeable when measuring with high precision the higher energy end (the so-called *end-point*) of the emitted electron kinetic energy distribution  $N_\beta(E_\beta, m_{\nu_e})$ . If one neglects the nucleus recoil energy,  $N_\beta(E_\beta, m_{\nu_e})$  is described in the most general form by

$$N_\beta(E_\beta, m_{\nu_e}) = p_\beta E_\beta (E_0 - E_\beta) \cdot \sqrt{(E_0 - E_\beta)^2 - m_{\nu_e}^2} F(Z, E_\beta) S(E_\beta) \cdot [1 + \delta_R(Z, E_\beta)] \theta(E_0 - E_\beta - m_{\nu_e}), \quad (4)$$

where  $F(Z, E_\beta)$  is the Coulomb correction (or Fermi function) which accounts for the effect of the nuclear charge on the wave function of the emitted electron,  $S(E_\beta)$  is the *form factor* which contains the nuclear matrix element  $\mathcal{M}(\mathcal{E}_\beta)$  of the electroweak interaction and can be calculated using the V-A theory, and  $\delta_R(Z, E_\beta)$  is the radiative electromagnetic correction, usually neglected due to its exiguity.  $\theta$  is the Heaviside step function, which confines the spectrum in the physical region  $(E_0 - E_\beta - m_{\nu_e}) > 0$ . The term  $p_\beta E_\beta (E_0 - E_\beta) \sqrt{(E_0 - E_\beta)^2 - m_{\nu_e}^2}$  is the phase space term in a three-body decay, for which the nuclear recoil has been neglected;  $p_\beta$  is the electron momentum. For the sake of completeness, it is worth noting that the particle emitted in the experiments considered here is the electron antineutrino  $\bar{\nu}_e$ . Since the CPT theorem assures that particle and antiparticle have the same rest mass, from now on, I will speak simply of “neutrino mass” both for  $\nu_e$  and for  $\bar{\nu}_e$ . Moreover, it must be stressed that since the effect of the neutrino mass on nuclear beta decay is purely due to kinematics, this measurement does not give any information on the Dirac or Majorana origin of the neutrino mass.

From oscillation experiments, we know that any neutrino flavor state is a superposition of mass states. Therefore, (4) can be generalized as [11, 12]

$$N_\beta(E_\beta, m_{\nu_e}) = R(E_\beta) \cdot \sum_{i=1}^3 |U_{ei}|^2 \sqrt{(E_0 - E_\beta)^2 - m_i^2} \theta(E_0 - E_\beta - m_i), \quad (5)$$

where  $R(E_\beta)$  is a term which groups all terms in (4) which do not depend on the neutrino mass,  $|U_{ei}|$  is the electron row of the neutrino mixing matrix, and  $m_i$  are the masses of the neutrino mass states. The square root term is the part of the phase space factor sensitive to the neutrino masses. An example of the resulting spectrum is shown in Figure 2.

Since the individual neutrino masses are too close to each other to be resolved experimentally, the measured spectra can still be analyzed with (4), but the quantity

$$m_{\nu_e} \equiv m_\beta = \sqrt{\sum_{i=1}^3 |U_{ei}|^2 m_i^2} \quad (6)$$

should now be interpreted as an effective electron neutrino mass, where the sum is over all mass values  $m_i$ . Therefore, a

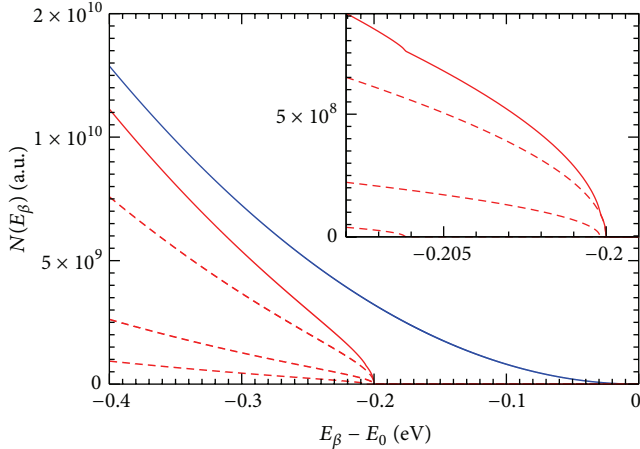


FIGURE 2: Expected electron spectrum following  $\beta$  decay. Blue curve: expected spectrum in the case  $m_{\nu_e} = 0$ . Red curve: expected spectrum in the case  $m_{\nu_e} = 200$  meV. The red dashed curves show the contributions to the total spectrum from the three mass states, with the mass differences driven by the present values of  $\sqrt{\Delta m_{21}^2}$  and  $\sqrt{\Delta m_{31}^2}$  [1].

limit on  $m_{\nu_e}$  implies trivially an upper limit on the minimum value  $m_{\min}$  of all  $m_i$ , independent of the mixing parameters  $U_{ei}$ :  $m_{\min} \leq m_{\nu_e}$ ; that is, the lightest neutrino cannot be heavier than  $m_{\nu_e}$ . By using the currently available information from oscillation data [1], it is possible to formulate the values of the neutrino masses (and the values of  $m_{\nu_e}$  as well) as a function of the lightest mass, that is,  $m_1$  in the Normal Hierarchy (NH) and  $m_3$  in the Inverted Hierarchy (IH). This is done in Figure 3, which shows that, in the case of NH, while the dominant component of  $\nu_e$  is  $\nu_1$ , the numerical value of  $m_{\nu_e}$  is equal to  $m_2$  over the whole range and also to  $m_1$  for  $m_1$  larger than few tenths of electronvolt. In the case of IH,  $m_{\nu_e}$  has practically the same value of  $m_1$  and  $m_2$ . Finally, in the case of QD spectrum,  $m_{\nu_e} \simeq m_1 \simeq m_2 \simeq m_3$  in both schemes. From the figure, it is also clear that the allowed values for  $m_{\nu_e}$  in the two mass schemes are quite different: in the case of IH, there is a lower limit for  $m_{\nu_e}$  of about 0.04 eV, while in the NH this limit is of about 0.01 eV. Therefore, if a future experiment will determine an upper bound for  $m_{\nu_e}$  smaller than 0.04 eV, this would be a clear indication in favor of the NH mass pattern. Finally, Figure 3 shows that the ultimate sensitivity needed for a direct neutrino mass measurement is set at about 0.01 eV, the lower bound in case of NH. However, if experiments on neutrino oscillations provide us with the values of all neutrino mass-squared differences  $\Delta m_{ij}^2$  (including their signs) and the mixing parameters  $|U_{ei}|^2$  and the value of  $m_{\nu_e}^2$  has been determined in a future search, then the individual neutrino mass squares can be determined:

$$m_j^2 = m_{\nu_e}^2 - \sum_{i=1}^3 |U_{ei}|^2 \Delta m_{ij}^2 \quad (\Delta m_{ij}^2 = m_i^2 - m_j^2). \quad (7)$$

On the other hand, if only the absolute values  $|\Delta m_{ij}^2|$  are known (but all of them), a limit on  $m_{\nu_e}^2$  from beta decay may

be used to define an upper limit on the maximum value  $m_{\max}$  of  $m_i$ :

$$m_{\max}^2 \leq m_{\nu_e}^2 + \sum_{i < j} |\Delta m_{ij}^2|. \quad (8)$$

In other words, knowing  $|\Delta m_{ij}^2|$ , one can use a limit on  $m_{\nu_e}$  to constrain the heaviest active neutrino.

At present, the most stringent experimental constraint on  $m_{\nu_e}$  is the one obtained by the Troitsk [13] and the Mainz [14] neutrino mass experiments,  $m_{\nu_e} < 2.05$  eV at 95% CL. This falls in the QD region for both mass schemes.

Another type of weak process sensitive to the neutrino mass scale is the neutrinoless double beta decay ( $\beta\beta-0\nu$ ), a second-order weak decay that violates the total lepton number conservation by two units, whose existence is predicted for many even-even nuclei:

$$(A, Z) \longrightarrow (A, Z + 2) + e_1^- + e_2^-. \quad (9)$$

The search for  $\beta\beta-0\nu$  is the only available experimental tool to demonstrate the Majorana character of the neutrino (i.e.,  $\nu \equiv \bar{\nu}$ ). In fact, the observation of  $\beta\beta-0\nu$  always requires and implies that neutrinos are massive Majorana particles [15]. However, there are many proposed mechanisms which could contribute to the  $\beta\beta-0\nu$  transition amplitude, and only when  $\beta\beta-0\nu$  is mediated by a light mass Majorana neutrino the observed decay is useful for determining the neutrino mass. In this case, the measured decay rate is given by

$$\frac{1}{\tau_{1/2}^{0\nu}} = \frac{m_{\beta\beta}^2}{m_e^2} F_N, \quad (10)$$

where  $\tau_{1/2}^{0\nu}$  is the  $\beta\beta-0\nu$  decay half-life,  $m_e$  is electron mass, and  $m_{\beta\beta}$  is the effective Majorana mass, defined below. The nuclear structure factor  $F_N$  is given by

$$F_N = G^{0\nu} (Q_{\beta\beta}, Z) |M^{0\nu}|^2, \quad (11)$$

where  $G^{0\nu}$  is the accurately calculable phase space integral and  $M^{0\nu}$  is the nuclear matrix element which is subject to uncertainty [16]. At present, the discrepancies among different nuclear model calculations of  $M^{0\nu}$  amount to a factor of about 2 to 3. These reflect on  $F_N$  and are an unavoidable source of systematic uncertainties in the determination of  $m_{\beta\beta}$  from the experimental data. Measuring the lifetime of different isotopes would allow one to disentangle the model dependency linked to the exact mechanism causing  $\beta\beta-0\nu$  and to reduce the systematic uncertainties on  $m_{\beta\beta}$ .

If  $\beta\beta-0\nu$  decay is observed and the nuclear matrix elements are known, one can deduce the corresponding  $m_{\beta\beta}$  value, which in turn is related to the oscillation parameters through

$$m_{\beta\beta} = \left| \sum_{i=1}^3 |U_{ei}|^2 m_i e^{i\alpha_i} \right|. \quad (12)$$

Due to the presence of the unknown Majorana phases  $\alpha_i$ , cancellation of terms in (12) is possible and  $m_{\beta\beta}$  could be

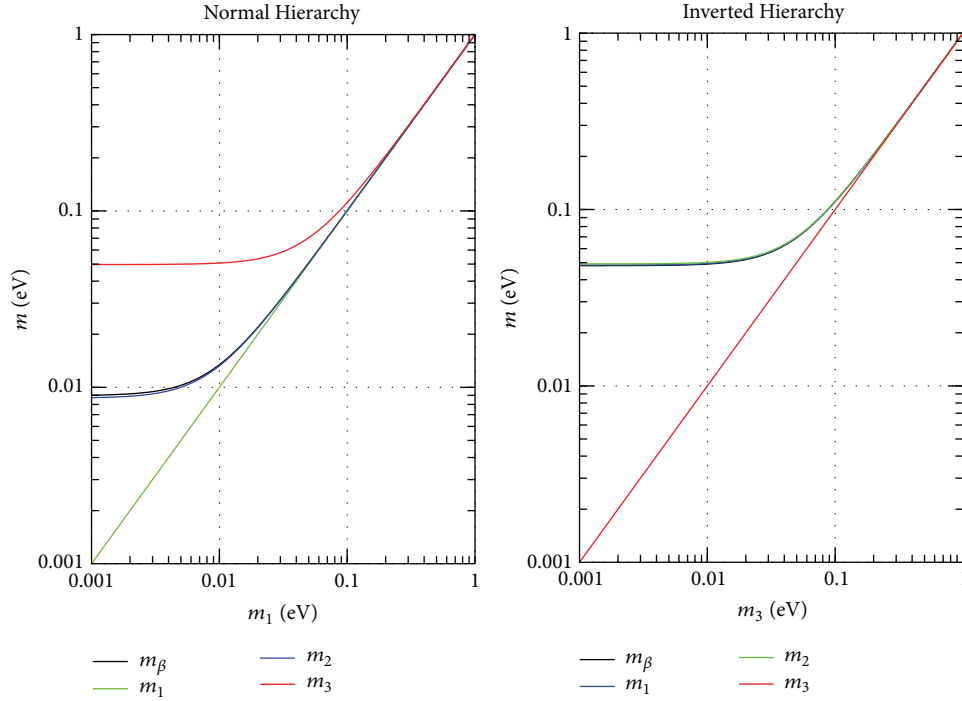


FIGURE 3: Effective electron neutrino mass  $m_\beta$  as a function of the lightest mass in both NH and IH mass schemes. The values of all three mass states are also plotted for comparison. The uncertainties on the oscillation parameters are reflected by uncertainties on the calculated masses which are not shown in the figure. The allowed  $3\sigma$  ranges in [1] give an uncertainty of about 30 (7)% on  $m_\beta$  for  $m_1$  ( $m_3$ ) = 0.001 eV in the NH (IH) scheme. The uncertainties progressively reduce going to larger masses and they are less than 1% for masses larger than 0.1 eV.

smaller than any of the masses  $m_i$ . Therefore, unlike the direct neutrino mass measurement, a limit on  $m_{\beta\beta}$  does not allow the constraint of the individual mass values  $m_i$  even when the mass differences  $\Delta m_{ij}^2$  are known. On the other hand, the observation of the  $\beta\beta-0\nu$  decay and the accurate determination of the  $m_{\beta\beta}$  value would not only establish that neutrinos are massive Majorana particles, but also contribute considerably to the determination of the absolute neutrino mass scale. Moreover, if the neutrino mass scale would be known from independent measurements, one could possibly obtain from the measured  $m_{\beta\beta}$  also some information about the CP violating Majorana phases [17].

Given the present knowledge of the neutrino oscillation parameters, it is possible to derive the relation between the effective Majorana mass and the lightest neutrino mass in the different neutrino mass schemes. This is done in a number of papers (see, e.g., [18]). Figure 4 shows the effective Majorana mass as a function of the effective electron neutrino mass in both NH and IH mass schemes, demonstrating the complementarity of the two methods.

As a final remark,  $\beta\beta-0\nu$  and  $\beta$  decays both depend on different combinations of the neutrino mass values and oscillation parameters.  $\beta\beta-0\nu$  decay rate is proportional to the square of a coherent sum of the Majorana neutrino masses because the process originates from the exchange of a *virtual* neutrino. On the other hand, in beta decay one can determine an incoherent sum because a *real* neutrino is emitted. That shows clearly that a complete neutrino physics

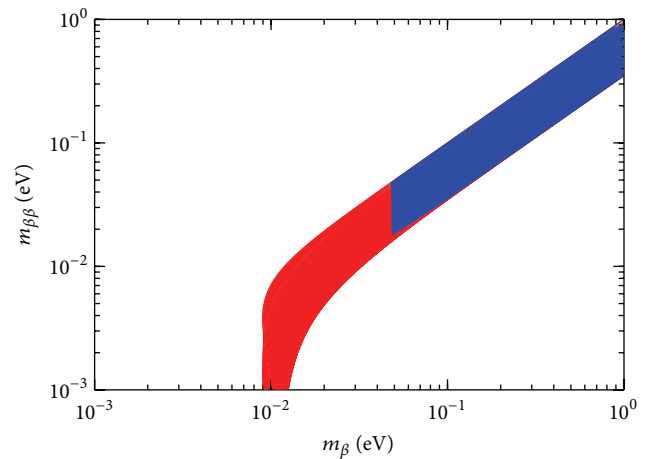


FIGURE 4: Relationship between the effective Majorana mass  $m_{\beta\beta}$  and the effective electron neutrino mass  $m_\beta$  for both IH (blue) and NH (red) mass schemes. The width of the bands is caused by the unknown Majorana phases.

program cannot renounce either of these two experimental approaches. The various methods that constrain the neutrino absolute mass scale are not redundant but rather complementary. If, ideally, a positive measurement is reached in all of them ( $\beta\beta-0\nu$  decay,  $\beta$  decay, and cosmology), one can test the results for consistency and with a bit of luck one can determine the Majorana phases.

#### 4. The Direct Neutrino Mass Measurement via Single Nuclear Beta Decay

As already pointed out, the most useful tool to constrain kinematically the neutrino mass is the study of the “visible” energy in single beta decay. The experimental beta spectra are normally analyzed by means of a transformation which produces a quantity generally linear with the kinetic energy  $E_\beta$  of the emitted electron:

$$K(E_\beta) \equiv \sqrt{\frac{N_\beta(E_\beta, m_{\nu_e})}{p_\beta E_\beta F(Z, E_\beta) S(E_\beta) [1 + \delta_R(Z, E_\beta)]}} \quad (13)$$

$$= (E_0 - E_\beta) \left( 1 - \frac{m_{\nu_e}^2}{(E_0 - E_\beta)^2} \right)^{1/4}.$$

The graph of this quantity as a function of  $E_\beta$  is named Kurie plot. In a Kurie plot, each bin has the same error bar and therefore the same statistical weight.

Assuming massless neutrinos and infinite energy resolution, the Kurie plot is a straight line intersecting the  $x$ -axis at the transition energy  $E_0$ . In case of massive neutrino, the Kurie plot is distorted close to the end-point and intersects the  $x$ -axis with vertical tangent at the energy  $E_0 - m_{\nu_e}$ . The two situations are depicted in Figure 5.

Most of the information on the neutrino mass is therefore contained in the final part of the Kurie plot, which is the region where the counting rate is lower. In particular, the relevant energy interval is  $\delta E \approx m_{\nu_e}$  and the fraction of events occurring here is

$$F(\delta E) = \int_{E_0 - \delta E}^{E_0} N_\beta(E, m_{\nu_e} = 0) dE \approx C \left( \frac{\delta E}{E_0} \right)^3, \quad (14)$$

where  $C$  is a constant of order unity which depends on the details of the beta transition. From this, it is apparent that kinematical mass measurements require beta decaying isotopes with the lowest end-point energy. Tritium is one of the best and most used isotopes thanks to its very low transition energy:  $E_0 = 18.6$  keV; nonetheless, the fraction of events falling in the last 5 eV of the tritium spectrum is only  $4 \times 10^{-11}$ .

Every instrumental effect such as energy resolution or background will tend to hinder or even wash out this tiny signal. In Figure 5, the effect on the spectral end-point of an energy resolution of 0.5 eV is shown. This distorts the Kurie plot in the opposite way with respect to the neutrino mass effect. It is therefore mandatory to evaluate and/or measure the detector response function, which includes the energy resolution but is not entirely determined by it. Finally, the analysis of the final part of the Kurie plot is complicated by the background due to cosmic rays and environmental radioactivity. Because of the low beta counting rate in the interesting region, spurious background counts may affect the neutrino mass determination.

The possibility to use beta decay to directly measure the neutrino mass was first suggested by Perrin [19] in 1933 and

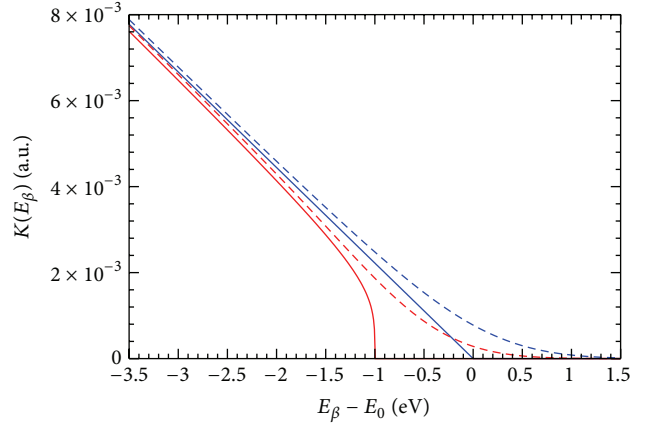


FIGURE 5:  ${}^3\text{H}$  Kurie plot close to the end-point, computed for neutrino masses equal to 0 (blue) and 1 eV (red) and an energy resolution  $\sigma_E$  of 0 (full line) and 0.5 eV (dashed line).

then by Fermi [20] in 1934, but the first sensitive experiments were performed only in the '70s. The first experiments were the one of Bergkvist [21, 22] and the one of the ITEP group [23], both of which used magnetic spectrometers to analyze the electrons emitted by tritium sources. This experimental approach has clear advantages such as (1) the high specific activity of tritium, (2) the high energy resolution and luminosity of spectrometers, and (3) the possibility to select and analyze only the electrons with kinetic energies close to  $E_0$ .

In the '80s and through the '90s, experiments with spectrometers using tritium were reporting largely negative  $m_{\nu_e}^2$  [24] (see Figure 6) or even an unlikely finite value of about 35 eV [23]. These were all signs of under- or overcorrected instrumental effects which were causing systematic shifts [25, 26]. In fact, despite the relative conceptual simplicity of the kinematic direct determination of the neutrino mass, it has been soon recognized that there are many subtle effects which threaten the accuracy of these measurements. Some are related to beta decay itself, since the atom or the molecule containing the decaying nucleus can be left in an excited state, leading even in this case to dangerous distortions of the Kurie plot (see Section 5.1). Other effects are due to the scattering and absorption of the electrons in the source itself. And last but not least, systematic effects are also caused by the imperfect characterization of the detector response. In the past 30 years, many experiments using tritium were performed. Starting from the '90s, magnetic spectrometers were gradually abandoned for electrostatic retarding spectrometers with adiabatic magnetic collimation [27, 28]. Many improvements in the detectors, in the tritium source, and in the data analysis and processing allowed the experiments to constantly improve the statistical sensitivity and to minimize the systematic uncertainties, as it is shown in Figure 6. Today, owing to a continuous and strenuous investigation of all experimental effects and systematic uncertainties,  $m_{\nu_e}^2$  measurements reported by the two most sensitive experiments [13, 14] are compatible with a zero mass, with the systematic errors reduced to the same level of statistical ones.

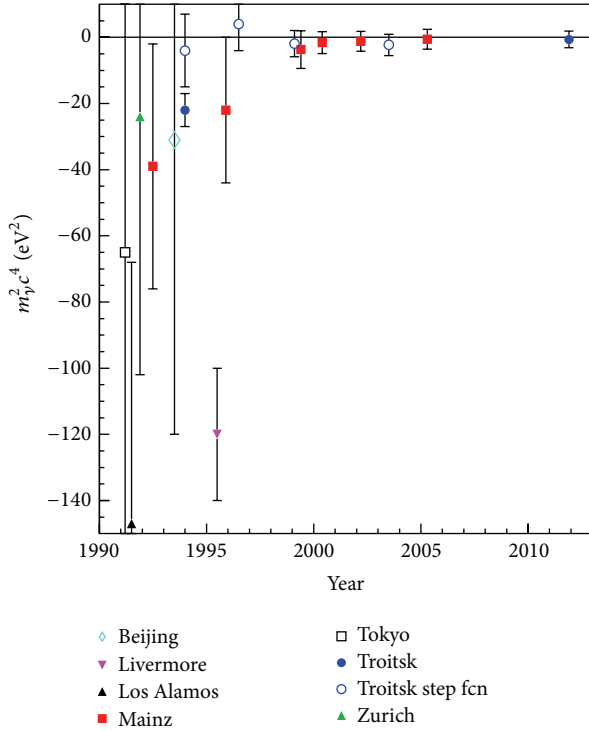


FIGURE 6: Historical trend of  $m_{\nu_e}^2$  measured with spectrometers using tritium (taken from [29]).

Nevertheless, today direct neutrino mass measurements remain affected by an intrinsic potential bias. As it already happened in the past, in a sensitive experiment small mis-corrections of instrumental effects may again either mimic or cancel the traces of a small positive neutrino mass. A weak unexpected effect not included in the data analysis may compensate and hide the signal of a small mass within the statistical sensitivity of an experiment, which would therefore report  $m_{\nu_e}^2$  values nicely compatible with the null hypothesis and thus quote just an upper limit. On the other hand, in a future experiment with a statistical sensitivity approaching the range predicted by oscillation parameters, a slightly excessive correction for an expected effect could mimic the signal for a tiny mass which would not contradict the community expectations. For these reasons, direct neutrino mass measurements call for a continuous crosscheck from different independent experiments to confirm both positive and negative findings.

Already in the '80s when the negative squared masses and the positive claim from ITEP were puzzling the neutrino community, De Rújula proposed the use of other beta decaying isotopes with low decay energy. In [30], it was noticed that  $^{187}\text{Re}$  has an end-point around 2 keV, much more favorable than the one of tritium. This isotope was at that time discarded because of its long half-life around  $10^9$  years. The focus of [30] was therefore on the isotope  $^{163}\text{Ho}$ , which decays by Electron Capture (EC) with a very low transition energy. In the EC process [31]

$$(A, Z) + e^- \longrightarrow (A, Z - 1) + \nu_e, \quad (15)$$

the available decay energy is

$$Q = M(A, Z) - M(A, Z - 1), \quad (16)$$

where  $M$  indicates the mass of the *atoms* in the initial and final states. Neglecting the nuclear recoil, the energy  $Q$  is shared between the neutrino and the radiation emitted in the deexcitation of the daughter atom

$$Q = E_\nu + E_X. \quad (17)$$

Here,  $E_X$  includes the energy of X-rays, Inner Bremsstrahlung photons, and Auger and Coster-Kronig electrons emitted in the atomic deexcitation of the daughter atom and adds up to the binding energy of the captured electron, allowing for a small indetermination due to the natural width of the atomic energy levels. Because of energy conservation, the end-points of the spectra of these electrons or photons—where the massive neutrino emitted in the EC is at rest—are sensitive to the neutrino mass. It is worth noting here that the kinematics of EC decay probes the mass of the neutrino  $\nu_e$ , whereas the one of regular beta decays probes the mass of the antineutrino  $\bar{\nu}_e$ : as already recalled above, the CPT invariance implies that the two measured masses are identical.

In particular, two measurements were discussed in 1981 for  $^{163}\text{Ho}$ : the end-point of the IBEC (Inner Bremsstrahlung in EC) spectrum [30]

$$^{163}\text{Ho} \longrightarrow \left( ^{163}\text{Dy}^{\text{H}^*} + \nu_e \right) \longrightarrow ^{163}\text{Dy}^{\text{H}'} + \gamma(k) + \nu_e \quad (18)$$

and the end-point of the SEEEC spectrum [32]

$$^{163}\text{Ho} \longrightarrow \left( ^{163}\text{Dy}^{\text{H}^*} + \nu_e \right) \longrightarrow ^{163}\text{Dy}^{\text{H}_1\text{H}_2} + e^- + \nu_e. \quad (19)$$

Even if at that time the  $Q$  value of  $^{163}\text{Ho}$  EC was largely unknown, this decay was already considered very promising for a sensitive neutrino mass measurement, since it was clear that its  $Q$  value is one of the lowest in nature. Both processes (18) and (19) start with a first intermediate atomic vacancy  $\text{H}^*$  caused by EC, where  $*$  denotes that the state is not necessarily on-shell. The energy of the vacant state has its own natural width. Because of the low  $Q$  value, this first vacancy  $\text{H}$  can be created only in one of the M1, M2, N1, N2, O1, O2, or P1 shells of the Dy daughter atom.

In the IBEC process (18) a photon is emitted during the virtual transition of an electron from  $\text{H}'$  to the intermediate state  $\text{H}^*$ , from which the electron was captured. For each possible final vacancy  $\text{H}'$  and for  $m_{\nu_e} = 0$ , the spectrum of the emitted photons is not made of monoenergetic lines at  $k = E(\text{H}') - E(\text{H}^*)$ , where  $E(\text{H})$  is the ionization energy of  $\text{H}$  shell in Dy, but it is a continuum with a kinematic limit  $k \leq k_{\text{max}}^{\text{H}'} = Q - E(\text{H}')$ , and the total photon spectrum is therefore a superposition of several spectra with different end-points. The spectral end-points follow the three-body statistical shape

$$N^{\text{H}'}(k) \propto k \left( k_{\text{max}}^{\text{H}'} - k \right) \sqrt{\left( k_{\text{max}}^{\text{H}'} - k \right) - m_{\nu_e}^2}. \quad (20)$$

In general, since IBEC is a second-order effect, its intensity is very low. However, the photon emission may experience large resonant enhancements for photons with energies  $k_{\text{res}}$  equal to the ones of the characteristic X-ray transitions of the daughter atom. In particular, De Rújula has shown for  $^{163}\text{Ho}$  that when  $H'$  is one of the N1, N2, O1, and O2 shells, then the dominant resonance close to the end-point is with the X-ray transitions  $H' \rightarrow M1$ , that is, when the intermediate vacancy of the virtual transition H corresponds to M1 shell. In this case, the distance between the resonance and the end-point is  $k_{\text{max}}^{H'} - k_{\text{res}} = Q - E(M1)$ , which for  $^{163}\text{Ho}$  is equal to a few hundred electronvolts. Unfortunately, calculations [33, 34] showed that, with  $Q$  around 2.8 keV, an IBEC measurement with  $^{163}\text{Ho}$  is not going to be statistically competitive with the tritium experiments, also because of complex destructive interference patterns.

The SEEEC process (19) is analogous to the IBEC with the role of the IB photon played by an Auger (or Coster-Kronig) electron. The spectrum of the ejected electron is a continuum with an end-point at  $E_{\text{max}}^{H1H2} = Q - E(H1) - E(H2)$ , for  $m_{\nu_e} = 0$ . Also, in this case, the kinematics of a 3-body decay process applies, and a phase space term  $p_{\nu_e} E_{\nu_e}$  appears in the spectral shape of ejected electrons. The continuous spectra show many resonances for different combinations of H, H1, and H2, but close to the end-point the dominant ones result from the M1 capture and are at  $E_{\text{res}} = E(M1) - E(H1) - E(H2)$ . These resonances provide an enhancement of the spectrum close to end-point, thereby increasing the statistical sensitivity to  $m_{\nu_e}$ . The inclusive spectrum of all the ejected electrons is quite complicated because of the many possible end-points  $E_{\text{max}}^{H1H2}$  and resonance peaks: nevertheless, the authors in [32] argue that the end-point region of this spectrum is unaffected by all the atomic details, since it is dominated by the upper tails of few resonances and maintains its usable sensitivity to  $m_{\nu_e}$ , although the estimated  $F(\Delta E)$ , depending on the  $Q$  value, may be substantially lower than for tritium.

One stressed advantage of IBEC and SEEEC measurements is that, unlike what happens in tritium beta decay, the probability of atomic excitations in the final state—such as shake-up or shake-off processes—is strongly suppressed and estimated to be  $<1/Z^2$  (see also Section 7.4).

More than 30 years later, none of the above suggestions has been successfully exploited to perform an experiment with a competitive sensitivity on  $m_{\nu_e}$ . Of the various attempts to perform an IB end-point measurements [34–38], only the one of Springer et al. [34] reported a limit on  $m_{\nu_e}$  of about 225 eV obtained by fitting the end-point of the X-ray spectrum.

Most of the measurements performed on  $^{163}\text{Ho}$  to directly measure the neutrino mass followed instead another proposal from Bennett et al. [39] in 1981. In [39], it is suggested that  $m_{\nu_e}$  and the transition energy  $Q$  can be determined or constrained by measuring the ratios of absolute capture rates (a better treatment includes  $C_i$  factors for the nuclear shape factor)

$$\frac{\lambda_i}{\lambda_j} = \frac{(n_i p_{\nu_i} E_{\nu_i} \beta_i^2 B_i)}{(n_j p_{\nu_j} E_{\nu_j} \beta_j^2 B_j)}, \quad (21)$$

where neutrino momentum  $p_{\nu_i}$  is given by

$$p_{\nu_i}^2 = (Q - E_i)^2 - m_{\nu_e}^2 = E_{\nu_i}^2 - m_{\nu_e}^2, \quad (22)$$

$n_i$  is the fraction of occupancy of the  $i$ th atomic shell,  $\beta_i$  is the Coulomb amplitude of the electron radial wave function (essentially, the modulus of the wave function at the origin), and  $B_i$  is an atomic correction for electron exchange and overlap. Following this idea, practically all the experimental researches on EC of  $^{163}\text{Ho}$  so far focused on the atomic emissions—photons and electrons contributing to  $E_X$  in (17)—following the EC and used the capture ratios to determine  $Q$  [34–38, 40–42]. Unfortunately, the accuracy achieved for  $m_{\nu_e}$  and  $Q$  with this method is adversely affected by the limited knowledge of the atomic parameters in (21).

As repeatedly underlined by De Rújula and Lusignoli [43], there is one experimental approach to the measurement of the neutrino mass from  $^{163}\text{Ho}$  EC which overcomes all the difficulties above: the calorimetric measurement of all the energy released in the EC ( $E_X$  in (17)) except for the energy of the neutrino. This will be discussed in Section 7.1.

Today all expectations for a new direct measurement of the neutrino mass with a substantially improved statistical sensitivity are directed to the KATRIN experiment [44]. KATRIN uses a large electrostatic spectrometer which will analyze the tritium beta decay end-point with an energy resolution of about 1 eV and with an expected statistical sensitivity of about 0.2 eV. KATRIN reaches the maximum size and complexity practically achievable for an experiment of its type and no further improved project can be presently envisaged. As an alternative for the study of tritium end-point, Project 8 proposes a new experimental approach based on the detection of the relativistic cyclotron radiation emitted by the beta electrons [45], which is presently under development [46].

## 5. Calorimetric Measurements

**5.1. General Considerations.** In the global effort to cure the weaknesses of direct neutrino mass measurements with spectrometers yielding negative  $m_{\nu_e}^2$  which started to show up since the '80s, Simpson first proposed the calorimetric approach [47]. In an ideal calorimetric experiment, the source is embedded in the detector and therefore only the neutrino energy escapes detection. The part of the energy spent for the excitation of atomic or molecular levels is measured through the deexcitation of these states, provided that their lifetime is negligible with respect to the detector time response. In other terms, the kinematical parameter which is effectively measured is the neutrino energy  $E_{\nu}$  (or  $E_0 - E_{\nu}$ ), in the form of a missing energy, a common situation in experimental particle physics. The advantages of a calorimetric measurement are (1) the measurement of all the energy temporarily stored in excited states, (2) the absence of source effects, such as self-absorption, and (3) the lack of backscattering from the detector. The effect of final states on the tritium beta spectrum was discussed thoroughly in many works [24, 26, 48]. In the following for simplicity we consider the so-called sudden approximation or first-order

perturbation of an atomic tritium beta decay, neglecting the sum over the mass eigenstates  $m_i$ . Due to the presence of atomic or molecular excited final states of the beta decay, the measured beta spectrum is a combination of different spectra characterized by different transition energies  $E_0 - V_i$ , where  $V_i$  is the energy of the  $i$ th final excited state of the decay

$$N_\beta(E_\beta, m_{\nu_e}) \approx \sum_i w_i p_\beta E_\beta (E_0 - E_\beta - V_i)^2 \cdot \left(1 - \frac{m_{\nu_e}^2}{(E_0 - E_\beta - V_i)^2}\right)^{1/2} F(Z, E_\beta) S(E_\beta), \quad (23)$$

with  $w_i$  describing the transition probability to the final  $i$ th excited state. The spectral shape induced by the presence of excited final states can be misleading when trying to extract the value of the neutrino mass. In fact, assuming that the neutrino mass is null and summing up over all the final states, from (23), one obtains

$$N_\beta(E_\beta, 0) \approx p_\beta E_\beta (E_0 - E_\beta - \langle V_i \rangle)^2 \cdot \left(1 + \frac{\langle V_i^2 \rangle - \langle V_i \rangle^2}{(E_0 - E_\beta - \langle V_i \rangle)^2}\right) F(Z, E_\beta) \cdot S(E_\beta), \quad (24)$$

which approximates the single beta spectrum (4) with a negative squared neutrino mass equal to  $-2\sigma^2 < 0$ , where  $\sigma$  is the variance of the final state spectrum given by  $\sigma^2 = \langle V_i^2 \rangle - \langle V_i \rangle^2$  (Figure 7), and with an end-point shifted by  $\langle V_i \rangle$ . In case of a tritium atom, the distribution of the electronic final states can be found by solving analytically the Schrödinger equation and one can calculate  $\sigma^2 = 740.5 \text{ eV}^2$ .

Indeed, tritium experiments use molecular tritium sources and in particular mostly  $T_2$  is adopted. To prevent systematic uncertainties which may give rise to a negative squared neutrino mass, the analysis of experimental spectra requires a complete and precise knowledge of the spectrum of the excitations—both atomic and molecular—of the daughter molecule. For molecular tritium, this spectrum can be calculated only numerically with an accuracy that has a direct impact on the experiment systematics.

The situation changes completely in the calorimetric approach. Even in this case the observed spectrum is a combination of different spectra. It can be obtained by operating the following replacements:

$$E_\beta \longrightarrow E'_\beta = E_\beta - V_i, \quad p_\beta = (E_\beta^2 - m_e^2)^{1/2} \longrightarrow p'_\beta = ((E_\beta - V_i)^2 - m_e^2)^{1/2} \quad (25)$$

motivated by the distinguishing feature of the calorimeters to measure simultaneously the beta electron energy and the deexcitation energy  $V_i$  of the final state.

By combining (23) and (25), one gets

$$N_\beta(E_\beta, m_{\nu_e}) \approx (E_0 - E_\beta)^2 \left(1 - \frac{m_{\nu_e}^2}{(E_0 - E_\beta)^2}\right)^{1/2} \cdot \sum_i w_i (E_\beta - V_i) ((E_\beta - V_i)^2 - m_e^2)^{1/2} \cdot F(Z, E_\beta - V_i) S(E_\beta - V_i). \quad (26)$$

Observing that  $F(Z, E_\beta - V_i) S(E_\beta - V_i) \approx F(Z, E_\beta) S(E_\beta)$  and expanding in a series of powers of  $V_i/E_\beta$ , one obtains

$$N_\beta(E_\beta, m_{\nu_e}) \approx p_\beta E_\beta (E_0 - E_\beta)^2 \cdot \left(1 - \frac{m_{\nu_e}^2}{(E_0 - E_\beta)^2}\right)^{1/2} F(Z, E_\beta) S(E_\beta) \cdot \sum_i w_i \left(1 - \frac{V_i}{E_\beta} - \frac{V_i E_\beta}{E_\beta^2 - m_e^2} + \frac{V_i^2}{2(E_\beta^2 - m_e^2)}\right). \quad (27)$$

Apart from the sum term, for a null neutrino mass, (27) describes a beta spectrum with a linear Kurie plot in the final region ( $E_\beta \gg V_i$ ); Figure 7 shows that the influence of the excited final states on the calorimetric beta spectrum is confined at low energy. Therefore, a calorimeter provides a faithful reconstruction of the beta spectral shape over a large energy range below the end-point. This is not true for spectrometers for which the measured spectrum at the end-point presents a deviation of the same size of that caused by a finite neutrino mass. Furthermore, it is apparent from Figure 7 that the presence of an excited state causes the spectrum of a spectrometer to mimic a lower  $E_0$  along with a negative  $m_{\nu_e}^2$ . The possibility to observe a substantial undistorted fraction of the spectrum is very useful to check systematic effects and to prove the general reliability of a calorimetric experiment.

As a general drawback, calorimeters present a major inconvenience which may be a serious limitation for the approach. In a calorimeter, the whole beta spectrum is acquired and the detector technology poses important restraints to the source strength. This in turn limits the statistics that can be accumulated. The consequences on the achievable statistical sensitivity are discussed in the next section. First of all the counting rate must be controlled to avoid distortions of the spectral shape due to pile-up pulses. Then, the concentration of the decaying isotope may not be freely adjustable. For example, at the time of Simpson experiments, the only way to make a sensitive calorimetric measurement was to ion-implant tritium in semiconductor ionization detectors such as Si(Li) or High Purity Ge (HPGe). There is however a trade-off between the required tritium implantation dose, that is, the tritium concentration, and the acceptable radiation damage. The tritium activity is then limited by the detector size in relation to its energy resolution.

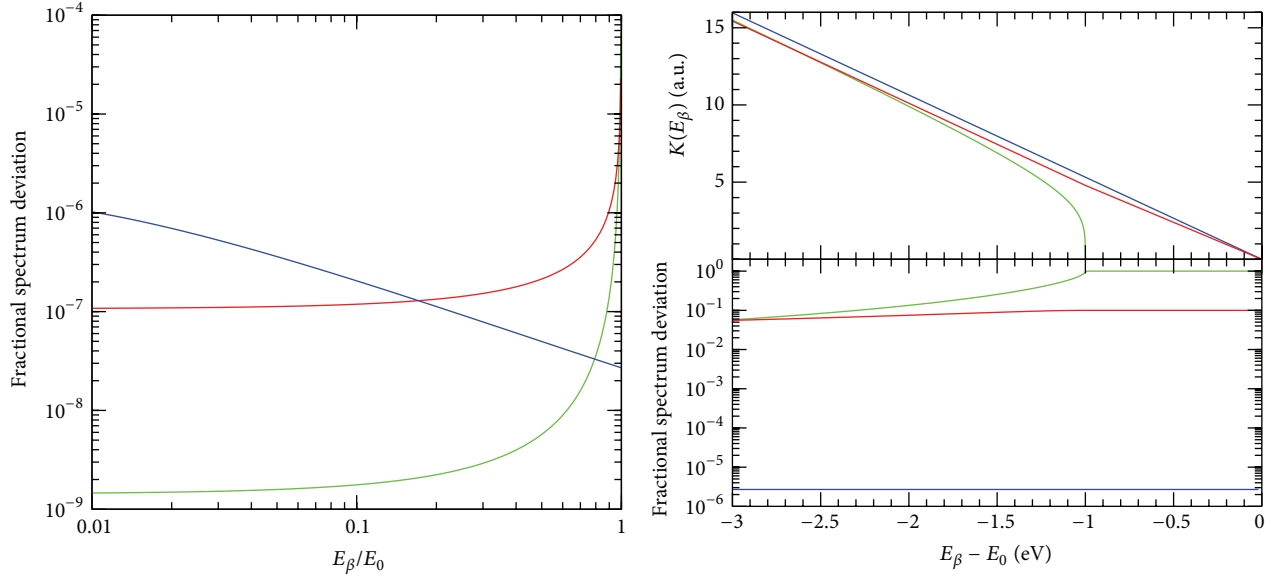


FIGURE 7: These plots compare the effect of a final excited state ( $V_1 = 1$  eV and  $\omega_1 = 0.1$  eV) on the beta spectrum as measured with a calorimeter (blue) and with a spectrometer (red) and the effect of  $m_{\nu_e}^2 = 1$  eV (green). The fractional spectrum deviation is the quantity  $1 - N^*(E_\beta)/N(E_\beta)$ , where  $N^*(E_\beta)$  and  $N(E_\beta)$  are, respectively, the observed beta spectra with and without excited final state.

This first generation of calorimetric experiments exploited Si(Li) or Ge detectors with implanted tritium but suffered for their intrinsic energy resolution which is limited to about 200 eV at 20 keV. With these experiments, a limit on  $m_{\nu_e}$  of about 65 eV was set [47]. At the same time, these experiments showed that the calorimetric approach does not cancel all the systematic uncertainties. As it was already recognized by Simpson in [47], one source of systematic uncertainty relates to the precise evaluation of the resolution function of these solid states detectors. The resolution function is obtained through X-ray irradiation from an external source. The response of the detector may be different for X-rays entering the detector from one direction and the betas emitted isotropically within the detector volume. Moreover, the beta emission is localized in the deep region of the detector where an incompletely recovered irradiation damage may lead to incomplete charge collection, while X-ray interactions are distributed in the whole detector volume.

Soon it became clear that calorimeters may also be affected by solid states effect. The “17 keV neutrino saga” [49, 50] started off from an unexpected feature observed first by Simpson in the low energy part of the tritium spectrum measured with the implanted Si(Li) detectors [51]. While a neutrino with a mass of 17 keV was finally deemed inexistent and the observed kink ascribed to a combination of various overlooked instrumental effects in spectrometric experiment [52], the evidence in calorimetric measurements remained unexplained. The invoked explanations include environmental effects in silicon and germanium and remain of interest for future calorimetric experiments. One of these solid state effects was first described by Koonin in 1991 [53]: it is a solid state effect known as Beta Environmental Fine

Structure (BEFS), which introduces oscillatory patterns in the energy distribution of the electrons emitted by a beta isotope in a lattice. It is an effect analogous to the Extended X-ray Absorption Fine Structure (EXAFS) and it will be addressed in more detail in Section 6.3.

So far, only tritium beta decay was considered, but all the arguments above apply to other isotopes undergoing nuclear beta decay. In particular, as it will be shown quantitatively in the next section, isotopes with a transition energy lower than that of tritium are better suited for a calorimetric experiment. The rest of the present work will focus on two such isotopes,  $^{187}\text{Re}$  and  $^{163}\text{Ho}$ , which have Q values around 2.5 keV. In fact, already in the ’80s many authors realized that low temperature detectors could offer a solution for making calorimetric measurements with high energy resolution and could be used either for tritium or, better, for the lower Q beta emitters  $^{187}\text{Re}$  and  $^{163}\text{Ho}$  (Section 5.3).

A final remark from the discussion above is that the spectrometer and the calorimeter methods have both complicated but totally different systematic effects. Therefore, once it is demonstrated that the achievable sensitivities are of the same order of magnitude in the two cases, it is scientifically very sound to develop complementary experiments exploiting these two techniques.

**5.2. Sensitivity of Calorimeters: Analytical Evaluation.** It is useful to derive an approximate analytic expression for the statistical sensitivity of a calorimetric neutrino mass experiment (see, e.g., [54]). The primary effect of a finite mass  $m_{\nu_e}$  on the beta spectrum is to cause the spectrum to turn more sharply down to zero at a distance  $m_{\nu_e}$  below the endpoint  $E_0$  (Figure 8(b)). To rule out such a mass, an experiment must be sensitive to the number of counts expected in this

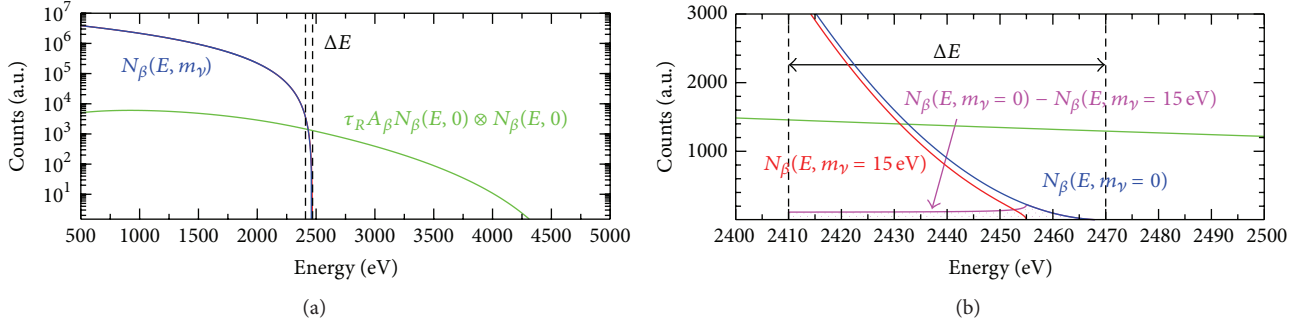


FIGURE 8: Effects of pile-up on the experimental energy spectrum of  $^{187}\text{Re}$  beta decay. (a) Beta spectrum compared with pile-up spectrum. (b) Zoom around the end-point, with a comparison between 0 and finite neutrino mass beta spectra.

interval. The fraction of the total spectrum within  $\Delta E$  of the end-point  $E_0$  is given by

$$F_{\Delta E}(m_{\nu_e}) = \int_{E_0 - \Delta E}^{E_0} N_{\beta}(E, m_{\nu}) dE. \quad (28)$$

For  $m_{\nu_e} = 0$ , this is approximately

$$F_{\Delta E}(0) \approx \left(\frac{\Delta E}{E_0}\right)^3. \quad (29)$$

For a finite mass, it is found also that

$$F_{\Delta E}(m_{\nu_e}) \approx F_{\Delta E}(0) \left(1 - \frac{3m_{\nu}^2}{2\Delta E^2}\right). \quad (30)$$

In addition to the counting statistics, the effect must be detected in the presence of an external background and of the background due to undetected pile-up of two events (Figure 8). Decays which occur within a definite time interval cannot be resolved by a calorimetric detector, giving rise to the phenomenon of pile-up. This implies that a certain fraction of the detected events is the sum of two or more single events. In particular, two low energy events can sum up and contribute to a count in the region close to the transition energy, contaminating the spectral shape in the most critical interval. In a first approximation the external background can be neglected. The pile-up spectrum can then be approximated by assuming a constant pulse-pair resolving time,  $\tau_R$ , such that events with greater separation are always detected as being doubles, while those at smaller separations are always interpreted as singles with an apparent energy equal to the sum of the two events. In reality, the resolving time will depend on the amplitude of both events, and the sum amplitude will depend on the separation time and the filter used, so a proper calculation would have to be done through a Monte Carlo applying the actual filters and pulse-pair detection algorithm being used in the experiment. However, this approximation is good enough to get the correct scaling and an approximate answer. In practice,  $\tau_R$  depends on the high frequency signal-to-noise ratio, but it is of the order of the detector rise time.

With these assumptions, for a pulse-pair resolving time of the detector  $\tau_R$ , the fraction of events which suffer from

not-identified pile-up of two events is, for a Poisson time distribution,

$$P(\Delta t < \tau_R) = 1 - e^{-A_{\beta}\tau_R} \approx A_{\beta}\tau_R, \quad (31)$$

where  $A_{\beta}$  is the source activity in the detector and  $\Delta t$  is the time separation between the two events. The beta spectrum of the unresolved pile-up events is given by the convolution product

$$\begin{aligned} N_{\text{pp}}(E) &= (1 - e^{-A_{\beta}\tau_R}) \int_0^{E_0} N_{\beta}(E', 0) N_{\beta}(E - E', 0) dE' \\ &= (1 - e^{-A_{\beta}\tau_R}) N_{\beta}(E, 0) \otimes N_{\beta}(E, 0). \end{aligned} \quad (32)$$

The coincidence probability, in the first approximation, is given by  $\tau_R A_{\beta}$ . As shown in Figure 8(b), a fraction  $F_{\Delta E}^{\text{pp}}$  of these events will fall in the region within  $\Delta E$  of the end-point  $E_0$  and can be approximated by

$$\begin{aligned} F_{\Delta E}^{\text{pp}} &= \int_{E_0 - \Delta E}^{E_0} N_{\text{pp}}(E) dE \\ &\approx \tau_R A_{\beta} \int_{E_0 - \Delta E}^{E_0} N_{\beta}(E, 0) \otimes N_{\beta}(E, 0) dE. \end{aligned} \quad (33)$$

Measuring a length of time  $t_M$ , the signal-to-background ratio in the region within  $\Delta E$  of the end-point  $E_0$  can be expressed as

$$\begin{aligned} \frac{\text{signal}}{\text{background}} &= \frac{A_{\beta} N_{\text{det}} t_M |F_{\Delta E}(m_{\nu_e}) - F_{\Delta E}(0)|}{\sqrt{A_{\beta} N_{\text{det}} t_M (F_{\Delta E}(0) + F_{\Delta E}^{\text{pp}})}} \\ &= \sqrt{A_{\beta} T} \frac{|F_{\Delta E}(m_{\nu_e}) - F_{\Delta E}(0)|}{\sqrt{(F_{\Delta E}(0) + F_{\Delta E}^{\text{pp}})}}, \end{aligned} \quad (34)$$

where  $N_{\text{det}}$  is the number of detectors and  $T = N_{\text{det}} t_M$  is the exposure. This ratio must be about 1.7 for a 90% confidence limit. Therefore, in absence of background, an approximated

expression for the 90% CL limit on  $m_{\nu_e} - \Sigma(m_{\nu_e})_{90}$ —can be written as [54]

$$\Sigma_{90}(m_{\nu_e}) = 1.13 \frac{E_0}{\sqrt[4]{t_M A_\beta N_{\text{det}}}} \left[ \frac{\Delta E}{E_0} + \frac{3}{10} \frac{E_0}{\Delta E} \tau_R A_\beta \right]^{1/4}. \quad (35)$$

The two terms in (35) arise from the statistical fluctuations of the beta and pile-up spectrum, respectively, in (34). Equation (35) shows the importance of improving the detector energy resolution and of minimizing the pile-up by reducing the detector rise time. On the other hand, it shows also that the largest reduction on the  $m_{\nu_e}$  limit can only come by substantially increasing the total statistics  $N_{\text{ev}} = t_M A_\beta N_{\text{det}}$ .

If the pile-up is negligible, that is, when the condition

$$\tau_R A_\beta \ll \frac{10}{3} \frac{\Delta E^2}{E_0^2} \quad (36)$$

is met, from (35), one can write the 90% confidence limit sensitivity as

$$\Sigma_{90}(m_{\nu_e}) \approx 1.13 \sqrt[4]{\frac{E_0^3 \Delta E}{N_{\text{ev}}}}, \quad (37)$$

where energy interval  $\Delta E$  in (37) cannot be taken smaller than about 2 times the detector energy resolution  $\Delta E_{\text{FWHM}}$ .

It is then apparent that to increase the sensitivity one has both to improve the energy resolution and to augment the statistics; however, there is a technological limit to the resolution improvements; thus, the statistics  $N_{\text{ev}} = t_M A_\beta N_{\text{det}}$  is in fact the most important factor in (37). For a more complete treatment, also in the presence of a not-negligible pile-up, refer to [54].

A similar approach for assessing the statistical sensitivity of  $^{163}\text{Ho}$  EC decay cannot be pursued with the same simplicity because of the more complex spectrum (see Section 7.1). Nevertheless, it is worth anticipating that with some approximations—discussed in Section 7.1—one can at least easily show that

$$\Sigma_{\text{EC}}(m_{\nu_e}) \propto E_0 - E_{i_{\text{max}}}, \quad (38)$$

where  $E_{i_{\text{max}}}$  is the energy of the Lorentzian peak whose high energy tail dominates the end-point region, that is, the M1 peak in (51). Equation (38) is to be compared to (37), which gives

$$\Sigma_\beta(m_{\nu_e}) \propto E_0^{3/4}. \quad (39)$$

From (38), it is apparent that for EC experiments in general—and for  $^{163}\text{Ho}$  in particular—not only is it winning to have the lowest possible  $Q$ , but also the end-point energy must be as close as possible to the binding energy of the deepest shell accessible to the EC.

*5.3. LTD for Calorimetric Neutrino Mass Measurements.* In 1981, De Rújula was already discussing with Fiorini the possibility of performing a calorimetric measurement of the Electron Capture process in  $^{163}\text{Ho}$ , apparently without any useful conclusion. It was only 3 years later—in 1984—that two independent seminal papers proposed for the first time the use of phonon-mediated detectors operated at low temperatures (simply called here low temperature detectors, LTDs) for single particle detection with high energy resolution. Fiorini and Niinikoski [55] proposed to apply these new detectors to various rare events searches in a calorimetric configuration, while McCammon et al. [56, 57] initiated the application to X-ray detection. It was immediately clear to McCammon et al. that this could be extended to the spectroscopy of an internal beta source by realizing high energy resolution calorimeters with implanted tritium [58].

In 1985, few years after De Rújula suggested the use of  $^{187}\text{Re}$  and  $^{163}\text{Ho}$  for a sensitive neutrino mass measurement in [30], Blasi et al. came up with the first operative proposal for an experiment using LTDs to measure  $^{187}\text{Re}$  spectrum calorimetrically [59]. In the same year, also Coron et al. started a research program aiming at exploiting LTDs to perform the calorimetry of  $^{163}\text{Ho}$  EC decay [60], which was soon discontinued for what concerns  $^{163}\text{Ho}$ . In the following years, the Genova group pioneered the development of LTDs that aimed at a direct neutrino mass measurement using the  $^{187}\text{Re}$  beta decay. The experiment was later called MANU and produced its first result in 1992. Some years later, in 1993, the Milano group, that mostly focused on carrying out a  $\beta\beta$ - $0\nu$  search with LTDs, also opened a research line to develop high energy resolution LTDs for a calorimetric measurement of  $^{187}\text{Re}$  beta decay. This project was named MIBETA and came to the first measurement in 1999. In 2005, the MANU and MIBETA experiments merged in the international project MARE. In parallel to the work on  $^{187}\text{Re}$ , starting from 1995, the Genova group was also carrying on a research for a calorimetric measurement of the  $^{163}\text{Ho}$  EC decay. This activity, later on, was first absorbed in MARE and then transferred into the HOLMES project. In 2012, the Heidelberg group, former member of the MARE collaboration, presented its own R&D program for a  $^{163}\text{Ho}$  calorimetric experiment, ECHO. Recently, also the Los Alamos group started a preliminary work for a  $^{163}\text{Ho}$  experiment, with a project named NuMECS. All these experiments and projects will be discussed in the next two sections.

Two other groups that participated in the efforts to develop LTDs for neutrino mass measurements in these three decades are worth mentioning. The Oxford group developed arrays of indium based Superconducting Tunnel Junctions (STJ) to search for the 17 keV neutrino in the  $^{63}\text{Ni}$  beta decay [61] and to measure precisely the exchange effect in the low energy part of the spectrum of the same decay [62]. The Duke University group developed transition edge sensors (TESs) based detectors for measuring calorimetrically the tritium decay [63, 64], but this project was abandoned before obtaining a statistically meaningful sample.

All these activities were triggered in the early '80s by the lucky coincidence to have the need for a tool to perform

calorimetric measurements of new low  $Q$  beta isotopes just at the time when a new promising particle detection technology was appearing on the scene. It took more than 20 years for the LTD technology to actually be mature enough to sustain the ambitions of calorimetric neutrino mass experiments; nowadays, LTDs can indeed deliver to this science case what they have been developed for. In particular, LTDs provide better energy resolution and wider material choice than conventional detectors. The energy resolution of few electronvolts is comparable to that of spectrometers and the restrictions caused by the full spectrum detection are lifted by the parallelization of the measurement with large arrays of detectors. Still, the detectors time constants of the order of microseconds and, correspondingly, the read-out bandwidth remain the most serious technical constraints to the full exploitation of LTDs in this field.

*5.3.1. LTD Basic Principles.* A complete overview of LTDs can be found in [65], while their state-of-the-art is well summarized in the proceedings of the biyearly international workshop on low temperature detectors [66].

LTDs were initially proposed as perfect calorimeters, that is, as devices able to thermalize thoroughly the energy released by the impinging particle. In this approach, the energy deposited by a single quantum of radiation into an energy absorber (weakly connected to a heat sink) determines an increase of its temperature  $T$ . This temperature variation corresponds simply to the ratio between the energy  $E$  released by the impinging particle and the heat capacity  $C$  of the absorber; that is,  $\Delta T = E/C$ . The only requirements are therefore to operate the device at low temperatures (usually  $<0.1\text{K}$ ) in order to make the heat capacity of the device low enough and to have a sensitive enough thermometer coupled to the energy absorber. Often LTDs with a total mass not exceeding 1 mg and few hundred micron linear dimensions are called low temperature (LT) microcalorimeters.

In the above linear approximation, using simple statistical mechanics arguments, it can be shown that the internal energy of an LTD weakly linked to a heat sink fluctuates according to

$$\Delta E_{\text{rms}}^2 = k_B T^2 C, \quad (40)$$

where  $T$  is the equilibrium operating temperature and  $k_B$  is the Boltzmann constant, independent of the weak link  $G$ . Equation (40) is often referred to as the *thermodynamical limit* to the LTD sensitivity and the internal energy fluctuations as Thermodynamic Fluctuation Noise (TFN). Although, strictly speaking, (40) is not the best energy resolution achievable by an LTD, it turns out that when a sensitive enough thermometer is considered and all sources of broadband noise are included in the calculation, the real *thermodynamical limit* of the energy resolution of an LTD can be expressed as [56]

$$\Delta E_{\text{rms}}^2 = \xi^2 k_B T_b^2 C_0, \quad (41)$$

where now  $T_b$  is the heat sink temperature,  $C_0$  is the heat capacity at  $T_b$ , and  $\xi$  is a numerical parameter of order one

which is derived from the LTD thermal details and for the optimal operating temperature. A detailed analysis of the optimal energy resolution for various thermometers can be found in [65].

From the above and (41), it is evident that the LTD absorber with its  $C$  and the thermometer with its sensitivity are the crucial ingredients for obtaining high energy resolution detectors. A sensitive thermometer is the one which allows the transduction of the fluctuations of the TFN to a signal larger than the other noise sources intrinsic to the thermometer itself and to the signal read-out chain. Today, this condition has been met—and (41) is achieved—for LT microcalorimeters using at least three types of optimized thermometers: semiconductor thermistors, transition edge sensors (TESs), and Au:Er metallic magnetic sensors. The thermal sensor of an LTD does not only affect the achievable energy resolution, but also determine the *speed* of the detector; that is, it determines the time scale of the signal formation with the details of the thermal mechanisms entering in the temperature transduction. Although the detector speed is a crucial parameter in calorimetric neutrino mass experiments, a complete technical treatment for the three sensor technologies is out of the scope of the present work. Here, it is enough to say that the three technologies above are sorted from the slowest to the fastest: the numerical values for the achievable speeds (from hundreds of nanoseconds to hundreds of microseconds) will be given in the following sections. Each sensor technology has its pros and cons which have driven the choice for the various neutrino mass experiments. The traded-off parameters, which include the achievable performances, the ease of fabrication, and the read-out technology, will be discussed in Section 5.3.3.

The next section is dedicated to the other critical component, that is, the absorber.

*5.3.2. Energy Absorber and Thermalization Process.* Under many respects, the absorber of LTDs plays the most crucial role in calorimetric experiments. First of all, (41) shows that the absorber heat capacity  $C$  sets the achievable energy resolution. When designing LTDs, usually the absorber is chosen to be made out of a dielectric and diamagnetic material, so that  $C$  is described only by the Debye term, which is proportional to  $(T/\Theta_D)^3$  at low temperatures, and can be extremely small for a good material with large Debye temperature  $\Theta_D$ . Insulators and semiconductors are often good examples of suitable dielectric and diamagnetic materials. Metals are instead discarded because of the electron heat capacity, which is proportional to  $T$  and remains large also at very low temperatures, thereby dominating the total  $C$  of the absorber. Superconductors are in principle also suitable, since the electronic contribution to the specific heat vanishes exponentially below the critical temperature  $T_c$ , and only the Debye term remains. For microcalorimeters, the situation is different because their reduced size allows tolerating also the heat capacity of a metal so that other considerations may be adopted to select the absorber material. Microcalorimeters for calorimetric measurements of the tritium,  $^{187}\text{Re}$ , or  $^{163}\text{Ho}$ , decay spectra must contain the unstable isotope in their

absorbers. As it will be discussed in more detail in the following, while tritium and  $^{163}\text{Ho}$  can be included by various means in materials with no special relation with hydrogen or holmium,  $^{187}\text{Re}$  is naturally found in physical and chemical forms suitable for making LTDs, that is, superconducting metal and dielectric compounds. In addition to the electronic and phononic heat capacities considered above, other contributions caused by nuclear heat capacity or by impurities may become important in certain conditions [67]. As it will be discussed later, this can be the case for metallic rhenium and embedded  $^{163}\text{Ho}$ .

The above leads to the conclusion that there is a large flexibility in the choice of the material for the absorber of microcalorimeters for calorimetric neutrino mass experiments: dielectrics and normal or superconducting metals have all indeed been used. In spite of this apparent flexibility, in such experiments, it turned out that the ideal energy resolution (41) is quite hard to achieve because of the details of the chain of physical processes which transform the energy deposited as ionization into the altered equilibrium thermal distribution of phonons—that is,  $\Delta T$  above—sensed by the thermometers (see [67–70] and references therein). This chain—also called the *thermalization process*—is responsible for the introduction of a fluctuation in the deposited energy  $E$  which is finally converted in the measured  $\Delta T$ : the so-called *thermalization noise*. The chain starts with the hot electron-hole pairs created by the primary ionizing interaction: on a time scale of  $10^{-10}$  s, this energy is degraded and partitioned between colder electronic and phononic excitations by means of electron-electron and electron-phonon scattering. The chain then proceeds with the conversion of the electronic excitations into phonons accompanied by a global cooling of all excitations, and it ends with the new thermal distribution of phonons which corresponds to a temperature increase  $\Delta T$  above the equilibrium operating temperature. The total time scale of this latter process and its details strongly depend on the material. Only when the time elapsed between the primary interaction and the signal formation is long enough to allow the phonon system to relax to the new quasi-equilibrium distribution, the detector works really as a calorimeter. In commonly used thermal sensors, the measured physical quantity is sensitive to the temperature of sensor electrons: therefore, at the end of the *thermalization*, there must be a last heat flow from the absorber phonons to the sensor electrons through a link which ultimately acts as a throttle for the signal rise. The extra noise shows up every time the deposited energy is not fully converted into heat [56], that is, into the new quasi-equilibrium thermal distribution, and gets trapped in long—compared to thermalization and signal formation time scales—living excitations. In a simplified picture, if  $\eta$  is the fraction of deposited energy  $E$  which actually goes into heat, the achievable energy resolution may be written as

$$\Delta E_{\text{rms}}^2 = \xi^2 k_B T_b^2 C_0 + (1 - \eta)^2 EF\omega, \quad (42)$$

where  $F$  is the Fano factor and  $\omega$  is the average excitation energy of the long living states. The second term is given by the statistical fluctuation of the number of long living states.

The parameters  $\eta$  and  $\omega$  are peculiar of each type of material. The parameter  $\eta$  may depend on the operating temperature and on the signal time scale: often, the *thermalization* slows down at low temperatures and the signal time scale must be adapted accordingly. Under all these respects, metals are the ideal material because they show fast and complete *thermalization* at every temperature—that is,  $\eta = 1$  is achieved on time scales of the order of nanoseconds or less—thanks to the strong interactions between electrons and phonons. Microcalorimeters with metallic absorbers in electrical contact with the sensor are often called *hot-electron microcalorimeters* [71, 72]. In *hot-electron microcalorimeters* the *thermalization* ultimately warms up the absorber electronic system and the hot absorber electrons can directly warm up the sensor electrons without throttling, therefore showing a very fast response time.

On the contrary, dielectrics often suffer from a large *thermalization noise* translating in a degraded energy resolution which increases with the deposited energy. In dielectrics, impurities and defects can act as traps which lie energetically inside the forbidden band-gap. Following the primary ionization created by the incident particle, electrons and holes can get trapped before their recombination to phonons. Experimentally, it is found that  $\omega$  can be as large as few tens of electronvolts, so that the second term (42) may easily dominate the energy resolution also for values  $\eta$  approaching unity. Semiconductors may be better than dielectrics, owing to their smaller band-gap. But only metals, semimetals (such as bismuth), and zero-gap semiconductors (such as HgTe) have been successfully employed in microcalorimeters showing energy resolutions close to the *thermodynamical limit* (41) [70].

In principle, superconductors should provide a further improvement thanks to their band-gap of few millielectronvolts: unfortunately, the *thermalization* in superconductors is a complex process in which  $\eta$  can be very small. In superconductors, the electronic excitations produced in the *thermalization* process described above are broken Cooper pairs, also called quasi-particles [73–75]. Microscopic calculations from the Bardeen-Cooper-Schrieffer theory predict that, indeed, a large part of the energy released inside the absorber can be trapped in quasi-particles states which can live for many seconds at temperatures below 0.1 K. The energy release inside a superconductor leads to a long living state far from equilibrium in which many Cooper pairs are continuously broken by phonons produced when quasi-particles recombine. A model describing this situation was proposed by Kaplan et al. [76], who found that the time the quasi-particles need to recombine ( $\tau_{\text{qp}}$ ) would be somewhere between 1 and 10 seconds. Analogous results were obtained by the analysis of Kozorezov et al. [75]. The global result of these models is that in superconductors  $\eta$  is expected to be very small on a time scale useful for an LTD. Despite these theoretical considerations, it is an experimental fact that some superconducting materials perform well as absorbers in cryogenic detectors. Indeed, deviations from the predicted temperature dependence of quasi-particle lifetime  $\tau_{\text{qp}}$  have been reported: for example, tin has been used for making LTDs with an energy resolution approaching the

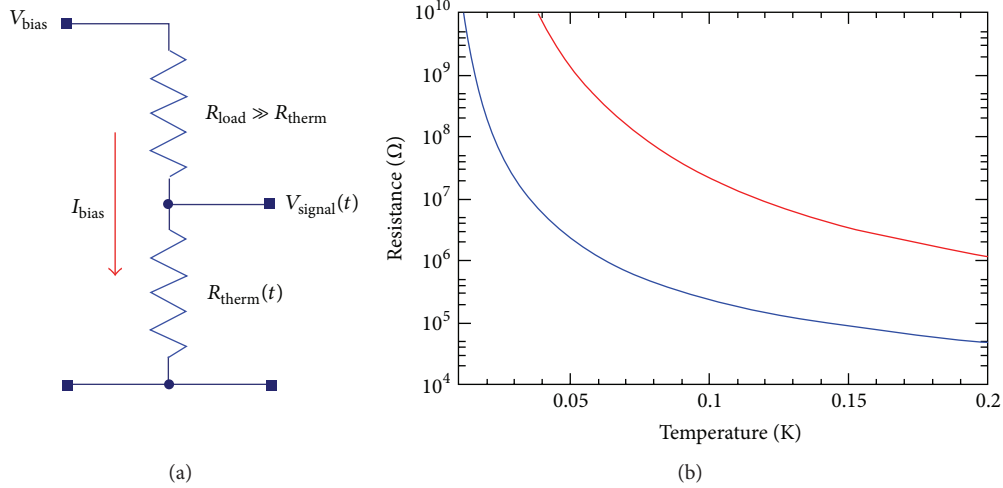


FIGURE 9: Constant current biasing of thermistors (a). Temperature dependence of the thermistor resistivity for  $T_0$  of 3 K (blue) and 10 K (red) (b).

*thermodynamical limit*, thanks to a fast and complete energy *thermalization*. This is apparently one characteristic shared also by other *soft* superconductors such as lead and indium. So far, no generally accepted explanation has been given for these apparent discrepancies between experimental results and theory, and the topic of quasi-particles recombination in LTDs remains an active field of research.

There are two other important sources of energy resolution degradation which are often observed in LTDs [56]. The first is the escape from the absorber of high energy phonons during the first stages of the *thermalization* process, which adds another fluctuation component to the finally thermalized energy. The second is the accidental direct detection of high energy phonons by the thermal sensors, which determines an excess systematic broadening of the energy resolution because its probability varies with the interaction position.

**5.3.3. Temperature Sensors, Read-Out, and Signal Processing.** The LTDs used for neutrino mass calorimetric measurements fall in the category of the low temperature microcalorimeters and are designed to provide energy resolutions better than about 10 eV, possibly approaching the *thermodynamical limit*. As shown in Section 5.2, the detector *speed*—that is, the detector signal bandwidth, or its rise time  $\tau_R$ —is another parameter guiding the design. Furthermore, neutrino mass experiments with LTDs need to use large arrays of detectors. This calls for ease of both fabrication and signal read-out. Along with the selection of the absorber material containing the source, the above points are the main guidelines for the design of an LTD based neutrino mass experiment. The choice of the sensor technology is one of the first steps in the design. To date, only three technologies have been exploited. These are the semiconductor thermistors, the transition edge sensors, and the magnetic metallic sensors, and they will be briefly discussed here (more details can be found in [65]). The possibility of employing other technologies, such as the one of superconducting microwave microresonators, is also

investigated, but its perspectives are not clear yet [77]. The application of LTDs to the spectroscopy of  $^{187}\text{Re}$  and  $^{163}\text{Ho}$  decays fully overlaps the range of use of microcalorimeters developed for soft X-ray spectroscopy; therefore, in the following, the discussion will be restricted to thermal sensors for X-ray detection.

**Semiconductor Thermistors.** These sensors are resistive elements with a heavy dependence of the resistance on the temperature. Usually, they consist of small crystals of germanium or silicon with a dopant concentration slightly below the metal-to-insulator transition [56]. The sensor low temperature resistivity is governed by variable range hopping (VRH) conduction and it is often well described by the expression  $\rho(T) = \rho_0 \exp(T_0/T)^{1/2}$ , where  $T_0$  and  $\rho_0$  are parameters controlled by the doping level [78] (Figure 9). Semiconductor thermistors are high impedance devices—1–100 M $\Omega$ —and are usually parameterized the sensitivity  $A$ , defined as  $-d \log R / d \log T$ , which typically ranges from 1 to 10. Semiconductor thermistors can be realized also in amorphous film form, like NbSi. Silicon thermistors are fabricated using multiple ion implantation in high purity silicon wafers to introduce the dopants in a thin box-like volume defined by photolithographic techniques. Germanium thermistors are fabricated starting from bulk high purity germanium crystals doped by means of neutron irradiation (nuclear transmutation doping, NTD) [79, 80]. Single NTD germanium sensors are obtained by dicing and further processing using a combination of craftsmanship and thin film techniques. In early times, the weak coupling to the heat sink was provided by the electrical leads used for the read-out; nowadays, microelectronic planar technologies and silicon micromachining are used to suspend the sensors on thin silicon nitride membranes or thin silicon beams. Thermistors are read-out in a constant current biasing configuration which allows converting the thermal signal  $\Delta T$  in a voltage signal  $\Delta V$  (Figure 9). Because of their high impedance, thermistors are best matched to JFETs.

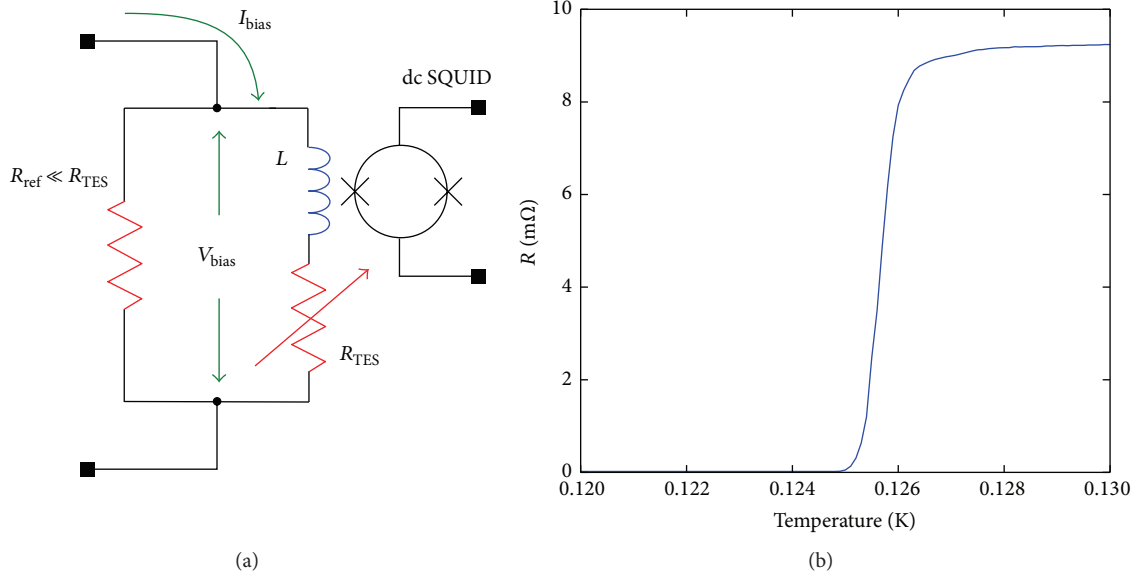


FIGURE 10: Read-out of a paramagnetic sensor (a). Temperature dependence of the sensor magnetization (b).

Semiconductor thermistor presents few drawbacks. First of all, their high impedance requires the JFET front end to be placed as close as possible—centimeters—to the devices to minimize microphonic noise and bandwidth limitations due to signal integration on parasitic electrical capacitance. Since commonly used silicon JFET must operate at temperatures not lower than about 110 K, this becomes quickly a technical challenge when increasing the number of detectors. Secondly, it has been experimentally observed that conductivity of semiconductor thermistors deviates from linearity at low temperatures [81, 82]. The deviation is understood in terms of a finite thermal coupling between electrons and phonons, whose side effect is to intrinsically limit the signal rise times to hundreds of microseconds for temperatures below 0.1 K. Semiconductors are now an established and robust technology, and arrays of microcalorimeters based on these devices have been widely used for X-ray spectroscopy [65] achieving energy resolutions lower than 5 eV with tin or HgTe absorbers.

*Superconducting Transition Edge Sensors (TESs).* TESs are also resistive devices made out of thin films of superconducting materials whose resistivity changes sharply from 0 to a finite value in a very narrow temperature interval around the critical temperature  $T_c$  (Figure 10). The superconducting material can be an elemental superconductor (such as tungsten or iridium), although it is more often a bilayer made of a normal metal and a superconductor. With bilayers,  $T_c$  of the superconductors is reduced by the proximity effect and can be controlled by adjusting the relative thicknesses of the two layers. Common material combinations used to fabricate TES bilayer with  $T_c$  between 0.05 and 0.1 K are Mo/Au, Mo/Cu, Ti/Au, or Ir/Au. TES fabrication exploits standard thin film deposition techniques, photolithographic patterning, and micromachining. Sensors can be designed to have, at the operating point, a sensitivity  $A$  as high as 1000

and a resistance usually less than  $1 \Omega$ . The most common ways to isolate TES microcalorimeters from the heat sink are the use of thin silicon nitride membranes or thin silicon beams. TESs are read-out at a constant voltage and their low impedance is ideal to use SQUIDs to amplify the current signal induced by a particle interaction (Figure 10). The constant voltage biasing provides the condition to achieve the extreme electrothermal feedback (ETF) regime [83] which leads to substantial improvements in resolution, linearity, response speed, and dynamic range. This regime also eases the operation of large pixel count arrays because ETF produces a self-biasing effect that causes the temperature of the film to remain in stationary equilibrium within its transition region. With respect to semiconductor thermistors, TESs offer many advantages: (1) large arrays can be fully fabricated with standard micro-fabrication processes, (2) the larger electron-phonon coupling allows signal rising as fast as few microseconds, and (3) the low impedance reduces the sensitivity to environmental mechanical noise. The main drawbacks of TESs are the limited dynamic range, the adverse sensitivity to magnetic fields of TES and SQUID, and the not fully understood physics of superconducting transitions and excess noise sources [66]. TES microcalorimeter arrays are being actively developed as X-ray spectrometers for many applications, which include material analysis and X-ray astrophysics [70]. TES sensors are particularly well suited to be coupled to metallic (gold) or semimetallic (bismuth) absorbers, providing fast response and energy resolutions lower than few electronvolts (Figure 12).

*Magnetic Metallic Sensors.* These sensors are quite different from the previous two, and their successful development is more recent [84]. They are paramagnetic sensors exposed to a small magnetic field. The temperature rise  $\Delta T$  causes a change in the sensor magnetization, which is sensed by a SQUID magnetometer (Figure 11). The nondissipative

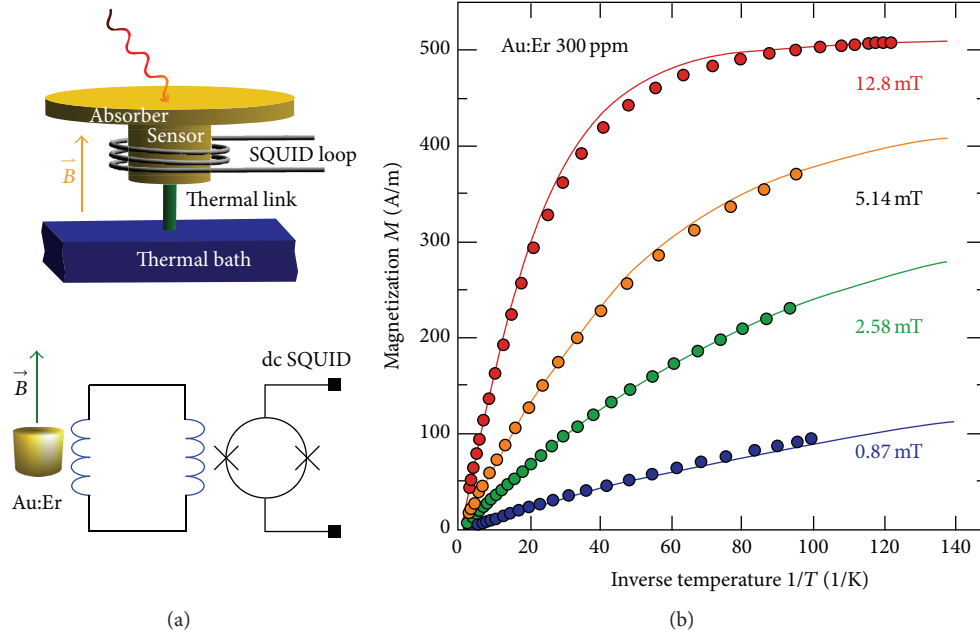


FIGURE 11: Constant voltage biasing of a TES (a). Temperature dependence of the TES resistivity at  $T_c$  (b).

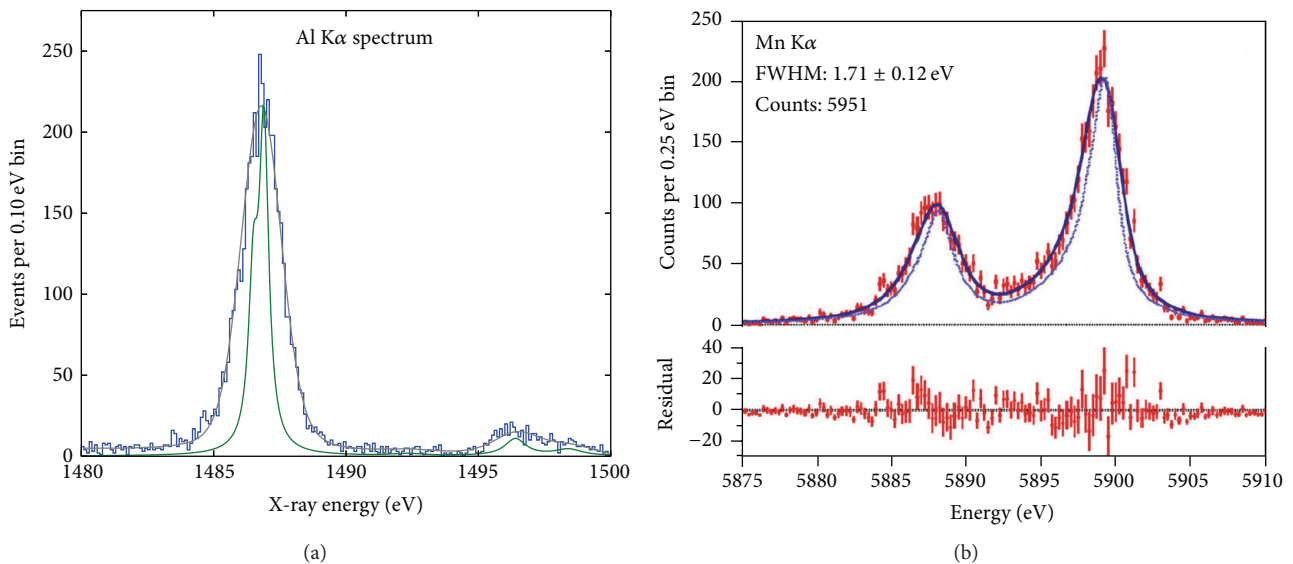


FIGURE 12: Energy resolutions achieved with a TES ( $\Delta E_{FWHM} = 1.5$  eV, courtesy of NIST) (a) and with an MMC [111] (b).

read-out scheme avoids the noise sources typical of dissipative systems, such as the Johnson noise of semiconductor thermistors and of TESs. State-of-the-art sensors use  $Er^+$  paramagnetic ions localized in an Au metallic host (Au:Er sensors). The use of a metallic host ensures a very fast sensor response time, since the spin-electron relaxation time for Au:Er is around  $0.1 \mu s$  at about 0.05 K. Microcalorimeters with magnetic metallic sensors (Magnetic Metallic Calorimeters, MMCs) are usually fully made out of gold to obtain both a fast and efficient energy thermalization to the absorber electronic system and a quick equilibration with the sensor electrons. Despite its high sensitivity, the paramagnetic

sensor has an intrinsically large heat capacity; therefore, the gold absorbers may be relatively large without adversely affecting the MMC performance. These microcalorimeters, in general, do not need special measures for thermally isolating the devices from the heat sink because the signal is predominantly developed in the electronic system and the electron-phonon coupling is rather weak and slow at low temperatures. An interesting feature of MMCs is the availability of a complete and successful modeling, allowing a precise design tailored to each specific application. The microfabrication of MMCs is somewhat more cumbersome than for TES microcalorimeters but, for the large part, can be

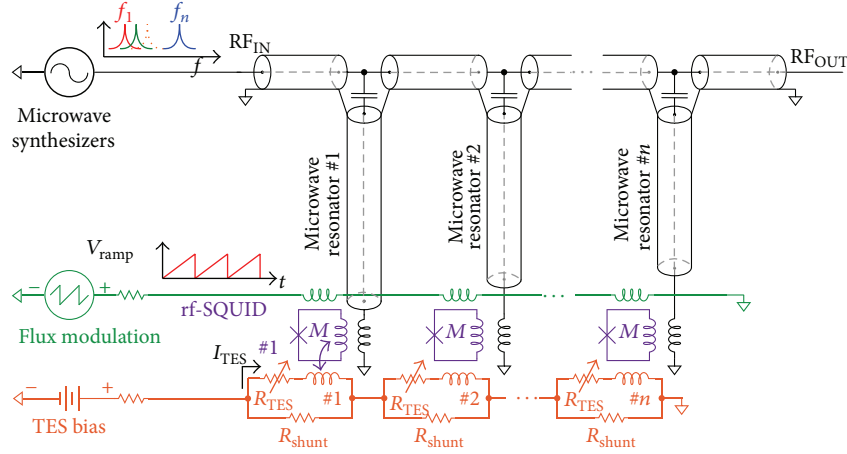


FIGURE 13: Circuit schematic for the microwave multiplexed read-out of TESs.

carried out with a standard microfabrication process [85, 86]. Presently, the most used design for arrays of MMCs has planar sensors on meander shaped pickup coils and achieves record energy resolutions of few electronvolts for soft X-rays (Figure 12) accompanied by large dynamic range and good linearity.

*Signal Read-Out.* Neutrino mass experiments are necessarily carried out using LTD arrays with a large pixel count, and this calls for the implementation of an efficient multiplexing system for reading out many sensors with the smallest possible number of amplifiers. This, in turn, reduces the number of read-out leads from room temperature to the array and the power dissipation at low temperature. Therefore, in order to be of some use for future experiments, a sensor technology must be compatible with some sort of multiplexed read-out, not causing restrictions on the available signal bandwidth and degradation of the resolving power. This makes the semiconductor thermistors not appealing for sensitive neutrino mass experiments since their inherent high impedance prevents the implementation of an effective multiplexed read-out. The opposite is true for the other two technologies owing to the use of a SQUID read-out.

TES arrays with SQUID read-out can be multiplexed according to three schemes [70]: Time Division Multiplexing (TDM) [87], Frequency Division Multiplexing (FDM) [88], and Code Division Multiplexing (CDM) [89]. The three schemes differ by the set of orthogonal modulation functions used to encode the signals. TDM and FDM (in the MHz band) are the most mature ones, and they have been already applied to the read-out of many multipixel scientific instruments. The more recently developed CDM combines the best features of TDM and FDM and is useful for applications demanding fast response and high resolution.

Recent advancements on Microwave Multiplexing ( $\mu$ MUX) suggest that this is the most suitable system for neutrino mass experiments, since it provides a larger bandwidth for the same multiplexing factor (number of multiplexed detector signals). It is based on the use of rf-SQUIDs as input devices, with flux ramp modulation [90] (Figure 13). The

modulated rf-SQUID signals can be read out by coupling the rf-SQUID to superconducting quarter-wave coplanar waveguide (CPW) resonators in the GHz range and using the homodyne detection technique. By tuning the CPW resonators at different frequencies, it is straightforward to multiplex many RF carriers. The feasibility of this approach has been demonstrated in [90] only with two channels, but it is making quick progress as shown with the multiplexed arrays of TES bolometers for millimeter astronomy of MUSTANG2 [91].

$\mu$ MUX is suitable for a fully digital approach based on the Software Defined Radio (SDR) technique [92, 93]. The comb of frequency carriers is generated by digital synthesis in the MHz range and upconverted to the GHz range by IQ-mixing. The GHz range comb is sent to the cold  $\mu$ MUX chips coupled to the TES array through one semirigid cryogenic coax cable, amplified by a cryogenic low noise High Electron Mobility Transistor (HEMT) amplifier, and sent back to room temperature through another coax cable. The output signal is downconverted by IQ-mixing, sampled with a fast analog-to-digital converter, and digital mixing techniques are used to recover the signals of each TES in the array (*channelization*).

Because of their excellent energy resolution combined with a very fast response time, the multiplexed read-out of MMCs is more demanding than that of TESs. To date, although some results have been obtained also with TDM,  $\mu$ MUX is the most promising approach for multiplexing MMCs [94], even if its development for these devices is still in progress.

*Signal Processing.* One of the conditions to obtain a thermodynamically limited energy resolution is to process the microcalorimeter signals with the Optimal Filter (OF) [56, 95]. For this purpose, the signal waveforms must be fully digitized and saved to disk for further offline processing. This approach allows one also to apply various specialized signal filters to the same waveform, with the aim of improving time resolution—thereby reducing  $f_{pp}$ —rejecting spurious events, and gating background induced events with a coincidence analysis. The storage of the raw data needed for offline

signal processing and for building the energy spectrum to be analyzed sets a practical limit to the lower energy limit of the final energy spectrum. While for rare event searches using LTD, such as dark matter or  $\beta\beta$ - $0\nu$  searches, there is no issue to save digitized waveforms for later offline analysis, this becomes quickly unpractical for sub-eV neutrino mass experiments: in fact the pulses collected over the whole spectrum would amount to about  $10^{14}$ , and their storage could fill up hundreds of petabytes—way more than LHC data! The only viable strategy is then to save just the relevant event parameters calculated by the pulse processing software, such as energy, arrival time, and few more useful shape parameters. In addition, it is likely that only a fraction of the spectrum of the order of 10% will be selected and saved for the neutrino mass analysis. For  $^{187}\text{Re}$  and  $^{163}\text{Ho}$ , this means that the analysis will be forcibly limited to an energy interval which extends, respectively, about 1200 eV and 750 eV—that is, just to the right of the M1 peak in the spectrum (Section 7.1)—below the spectrum end-point.

*5.4. Additional Direct Neutrino Measurements with LTDs.* LTD calorimeters can offer the opportunity to perform other interesting investigations on the data collected for the neutrino mass measurement: these include the searches for massive sterile neutrinos (Section 2), when the entire energy spectrum is available for analysis, and for the cosmic relic neutrinos (Cosmic Neutrino Background,  $C\nu\text{B}$ ). These by-products of the neutrino mass measurements are largely out of the scope of the present work and are discussed here briefly only for the sake of completeness.

The calorimetric spectra of  $^{187}\text{Re}$  or  $^{163}\text{Ho}$  are suitable to investigate the emission of heavy sterile neutrinos with a mixing angle  $\theta$ . Assuming the electron neutrino  $\nu_e$  is a mixture of two mass eigenstates  $\nu_H$  and  $\nu_L$ , with masses  $m_H \gg m_L$ , then  $\nu_e = \nu_L \cos\theta + \nu_H \sin\theta$  and the measured energy spectrum is  $N(E, m_L, m_H, \theta) = N(E, m_L)\cos^2\theta + N(E, m_H)\sin^2\theta$ . The emission of heavy neutrinos would manifest as a kink in the spectrum at an energy of  $Q - m_H$  for heavy neutrinos  $\nu_H$  with masses between about 0 and  $Q - E_{\text{th}} \leq 2.5$  keV, where  $E_{\text{th}}$  is the experimental low energy threshold. It is worth noting that the strategy is of course very analogous to the one adopted by Simpson [47, 51] which started off the already mentioned saga of the 17 keV neutrino. Moreover, such search may be affected by systematic uncertainties due to the background and due to the ripple observed in the  $^{187}\text{Re}$  spectrum and caused by the BEFS (Section 6.3). An alternative and possibly more robust approach to the search of sterile neutrino emission in  $^{163}\text{Ho}$  has been proposed in [96].

Cosmology predicts that there are about 55 neutrinos/cm<sup>3</sup> in the universe as leftovers of the Big Bang. Their average temperature today is about 1.95 K and therefore their observation is extremely difficult. It has been proposed that the  $C\nu\text{B}$  could be detected via the induced beta decay on beta decaying isotopes: for example,  $\nu_e + {}^3\text{H} \rightarrow {}^3\text{He} + e^-$ . This reaction could be detected as a peak at an energy of  $Q + m_{\nu_e}$  in beta decay spectra. The expected rate can be calculated starting from the beta decay lifetime, and for 100 g of tritium, it would be of about 10 counts/year [97]. Unfortunately, 100 g

is  $10^6$  times the amount of tritium contained in KATRIN, and the situation is not more favorable for other isotopes like  $^{187}\text{Re}$  or  $^{163}\text{Ho}$ . The reactions  $\nu_e + {}^{187}\text{Re} \rightarrow {}^{187}\text{Os} + e^-$  and  $\nu_e + e^- + {}^{163}\text{Ho} \rightarrow {}^{163}\text{Dy}^*$  are expected to give yearly about  $10^{-10}$  [98, 99] and  $10^{-5}$  events per gram of target isotope [100, 101], respectively. Recently, a dedicated experiment called PTOLEMY has been proposed [102]: it combines a large area surface-deposition tritium target, the KATRIN magnetic/electrostatic filtering, LTDs, RF tracking, and time-of-flight systems.

The possibility to detect heavy sterile neutrino Warm Dark Matter (WDM) via the above induced beta decays in  $^{187}\text{Re}$  and  $^{163}\text{Ho}$  has also been investigated, but, again, the expected rates are hopelessly low [103, 104].

## 6. Past Experiments

*6.1. Rhenium Experiments with LTDs.*  $^{187}\text{Re}$  was mentioned in [30] as an interesting alternative to tritium because its transition energy of about 2.5 keV is one of the lowest known. Thanks to this characteristic, the useful fraction of events close to the end-point is  $\sim 350$  times higher for  $^{187}\text{Re}$  than for tritium. In addition, the half lifetime of about  $4 \times 10^{10}$  years together with the large natural isotopic abundance (62.8%) of  $^{187}\text{Re}$  provides useful beta sources without any isotopic separation process. The beta decay rate in natural rhenium is of the order of  $\sim 1$  Bq/mg, almost ideally suited to calorimetric detection with LTDs.

As soon as the idea of developing LTDs for X-ray spectroscopy with energy resolutions caught on, metallic rhenium became one of the most appealing materials also for making X-ray absorbers. First of all metallic rhenium is a superconductor with a critical temperature  $T_c$  of about 1.69 K; therefore, ideally, it is a good candidate for photon detection free of thermalization noise. Then, the combination of high  $Z$ , high density ( $\rho = 21.02$  g/cm<sup>3</sup>), and high Debye temperature ( $\Theta_D \approx 417$  K) makes metallic rhenium a unique material for designing X-ray detectors with low heat capacity  $C$ —that is, high sensitivity—and high photon stopping power. Unfortunately, it soon became clear that metallic rhenium absorbers do not behave as expected and metallic rhenium was abandoned in favor of other more friendly materials as absorber for X-ray microcalorimeters. The results of early efforts on rhenium absorbers for X-ray microcalorimeters are reported in [105, 106]. The long time constants (up to 100 ms) and a significant deficit in the signal amplitude are the distinguishing features of microcalorimeters with metallic rhenium absorbers. In the same years, the Genova group was finding similar results, as discussed below.

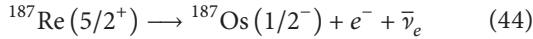
Although the explanation of the observed behavior most probably resides in the superconductivity of rhenium, also the heat capacity may contribute to poor and inconsistent performance. In fact, according to [107] the specific heat of rhenium in the normal state is given by

$$c(T) = 40.6 T^{-2} + 0.034 T^{-3} + 2290 T + 27 T^3 \mu\text{J}/(\text{mol K}), \quad (43)$$

where the last two terms are the contributions from normal conduction electrons and phonons, respectively. The first two terms are due to the nuclear heat capacity, which arises from the interaction between the large nuclear quadrupole moment of the two natural isotopes of rhenium—both with nuclear spin of  $5/2$ —and the electrical field gradient at the nucleus in the noncubic rhenium lattice. When rhenium is in the superconducting state, the nuclear heat capacity term should vanish since the slow spin-lattice relaxation thermally isolates the nuclear spin system. In the superconducting state, a irreproducible small fraction of the normal-state nuclear heat capacity may still be observed if trapped magnetic flux causes regions in the specimen to remain normal.

In spite of these difficulties, research on LTDs with metallic rhenium went on for the purpose of making detectors for calorimetric neutrino mass experiments, although other dielectric materials were also tested (see Section 6.5).

### 6.2. $^{187}\text{Re}$ Beta Decay Spectrum. $^{187}\text{Re}$ beta decay



is a unique first forbidden transition. Unlike nonunique transitions, the nuclear matrix element is computable, even if the calculation is not straightforward as in the case of tritium. In the literature, it is possible to find detailed calculations of both the matrix element and the Fermi function for this process [108, 109]. The electron and the neutrino are emitted in  $p_{3/2}$  and  $s_{1/2}$  states, respectively, or vice versa. Higher partial waves are strongly suppressed because of the low transition energy. The distribution of the kinetic energies  $E$  of the emitted electrons, calculated neglecting the neutrino mixing, is as follows (according to [108]):

$$\begin{aligned} N(E, m_{\nu_e}) &= N^{p_{3/2}}(E, m_{\nu_e}) + N^{s_{1/2}}(E, m_{\nu_e}) \\ &= CpE(E_0 - E)^2 \left[ F_1(Z, E) p^2 + F_0(Z, E) p_{\nu}^2 \right] \\ &\quad \cdot \sqrt{1 - \frac{m_{\nu_e}^2}{(E_0 - E)^2}}, \end{aligned} \quad (45)$$

where  $p$  is the electron momentum,  $p_{\nu}^2 = ((E_0 - E)^2 - m_{\nu_e}^2)$  is the neutrino momentum, and  $F_0(Z, E)$  and  $F_1(Z, E)$  are the relativistic Coulomb factors, which take into account the distortion of the electron wave function due to the electromagnetic interaction of the emitted electron in  $s_{1/2}$  and  $p_{3/2}$  states with the atomic nucleus. In general, the Coulomb factor takes the form

$$\begin{aligned} F_{k-1}(Z, E) &= \left( \frac{\Gamma(2k+1)}{\Gamma(k)\Gamma(1+2\gamma_k)} \right)^2 (2pR)^{2(\gamma_k-k)} \\ &\quad \cdot |\Gamma(\gamma_k + iz)|^2 e^{\pi z} \end{aligned} \quad (46)$$

with

$$\begin{aligned} \gamma_k &= \sqrt{k^2 - (\alpha Z)^2}, \\ z &= \alpha Z \frac{E}{p}, \end{aligned} \quad (47)$$

where  $\Gamma$  is the gamma function,  $\alpha$  is the fine structure constant, and  $R$  is the nuclear radius. It can be found numerically that  $p_{3/2}$  component of the spectrum is dominant; that is, [108]

$$\frac{I_{s_{1/2}}}{I_{p_{3/2}}} = \frac{\int_0^{E_0} N^{s_{1/2}}(E, m_{\nu_e}) dE}{\int_0^{E_0} N^{p_{3/2}}(E, m_{\nu_e}) dE} \approx 10^{-4}. \quad (48)$$

This has been confirmed experimentally in [110] (see Section 6.5). It can also be shown that (45) can be approximated by the expression

$$\begin{aligned} N(E, m_{\nu_e}) \\ = C' (1 + f_{187\text{Re}}(E)) (E_0 - E)^2 \sqrt{1 - \frac{m_{\nu_e}^2}{(E_0 - E)^2}}, \end{aligned} \quad (49)$$

where the correction factor  $f_{187\text{Re}}(E)$  is shown in Figure 14.

**6.3. Statistical Sensitivity and Systematics.** An accurate assessment of calorimetric neutrino mass experimental sensitivity requires the use of Monte Carlo frequentist approach [54]. The parameters describing the experimental configuration are the total number of  $^{187}\text{Re}$  decays  $N_{\text{ev}}$ , the FWHM of the Gaussian energy resolution  $\Delta E_{\text{FWHM}}$ , the fraction of unresolved pile-up events  $f_{\text{pp}}$ , and the radioactive background  $B(E)$ . The total number of events is given by  $N_{\text{ev}} = N_{\text{det}} A_{\beta} t_M$ , where  $N_{\text{det}}$ ,  $A_{\beta}$ , and  $t_M$  are the total number of detectors, the beta decay rate in each detector, and the measuring time, respectively. As discussed in Section 5.2,  $f_{\text{pp}} = \tau_R A_{\beta}$ , where  $\tau_R$  is the time resolution of the detectors.  $B(E)$  function is usually taken as a constant,  $B(E) = bT$ , where  $b$  is the average background count rate for unit energy and for a single detector, and  $T = N_{\text{det}} \times t_M$  is the experimental exposure. A set of experimental spectra are simulated and fitted with  $m_{\nu_e}^2$ ,  $E_0$ ,  $N_{\text{ev}}$ ,  $f_{\text{pp}}$ , and  $b$  as free parameters. The 90% CL  $m_{\nu_e}$  statistical sensitivity  $\Sigma_{90}(m_{\nu_e})$  of the simulated experimental configuration can be obtained from the distribution of  $m_{\nu_e}^2$  found by fitting the spectra. The statistical sensitivity is then given by  $\Sigma_{90}(m_{\nu_e}) = \sqrt{1.7\sigma_{m_{\nu_e}^2}}$ , where  $\sigma_{m_{\nu_e}^2}$  is the standard deviation of  $m_{\nu_e}^2$  distribution.

The symbols in Figure 15 are the results of Monte Carlo simulations for various experimental parameters and for  $b = 0$  compared to the analytic estimate.

As an example, Table 1 reports two experimental configurations which could allow one to achieve statistical sensitivities of about 0.2 and 0.1 eV, respectively. The two sensitivities could be attained measuring for 10 years, respectively,  $4 \times 10^4$  and  $3.2 \times 10^5$  detectors, while the total mass of natural metallic rhenium in the two cases would be about 400 g and 3.2 kg, respectively.

A flat background remains almost negligible as long as it is much lower than the pile-up contribution at the endpoint; that is,  $b \ll A_{\beta} f_{\text{pp}} / (2E_0)$ . For the two experiments in Table 1, this translates in a constant background, lower than about  $1 \times 10^{-2}$  and  $4 \times 10^{-3}$  counts/day/eV, respectively,

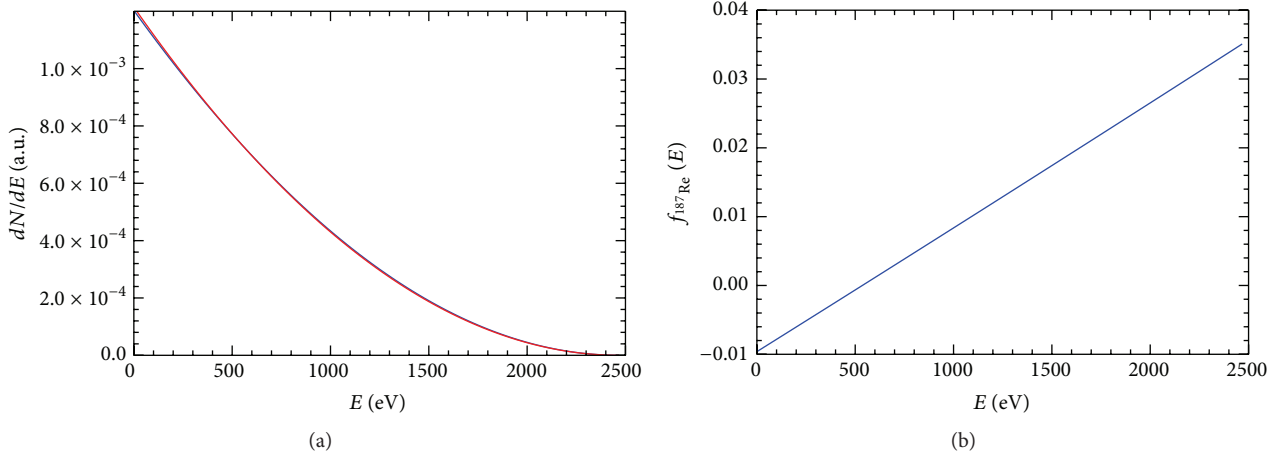


FIGURE 14: Theoretical shape of the  $^{187}\text{Re}$  beta decay spectrum (a). Deviation of the  $^{187}\text{Re}$  spectrum from a simple quadratic form (b).

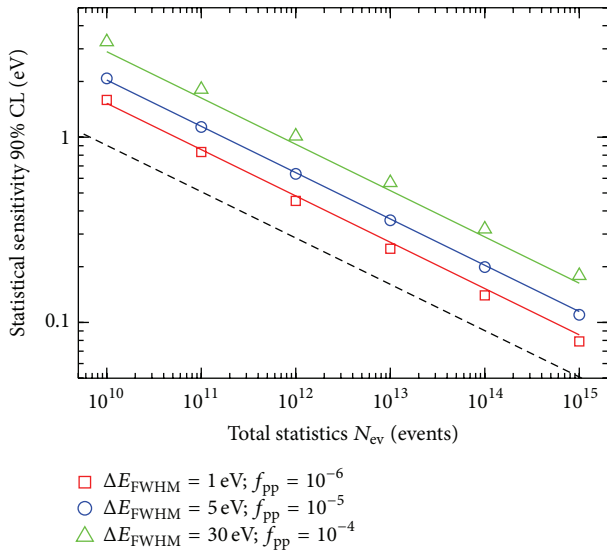


FIGURE 15: Statistical neutrino mass sensitivity for calorimetric measurements of the  $^{187}\text{Re}$  beta decay. Lines are obtained from (35) according to [54]. Symbols are obtained with Monte Carlo simulations (Section 6.3).

TABLE 1: Experimental exposure required for the target statistical sensitivity in the second column with  $b = 0$ .

Isotope	Sensitivity [eV]	$A_\beta$ [Hz]	$\tau$ [ $\mu\text{s}$ ]	$\Delta E$ [eV]	$N_{\text{ev}}$ [counts]	Exposure $T$ [detector $\times$ year]
$^{187}\text{Re}$	0.2	10	3	3	$1.3 \times 10^{14}$	$4.1 \times 10^5$
$^{187}\text{Re}$	0.1	10	1	1	$10.3 \times 10^{14}$	$3.3 \times 10^6$

which should be achievable without operating the arrays in the extreme low background conditions of an underground laboratory.

Given the strong dependence of the sensitivity on the total statistics, for a fixed experimental exposure  $T$ —that is, for a fixed measuring time and a fixed experiment size—and for

fixed detector performance  $\Delta E_{\text{FWHM}}$  and  $\tau_R$ , it always pays out to increase the single detector activity  $A_\beta$  as high as being technically feasible, even at the expenses of an increasing pile-up level. Of course, since the rhenium specific activity is practically fixed, the ultimate limit to  $A_\beta$  is set by the tolerable heat capacity of the absorber.

With the same Monte Carlo approach, it is also possible to investigate the source of systematic uncertainties peculiar to the calorimetric technique. As shown in [54], it appears that the most crucial and worrisome sources of systematics are the uncertainties related to the Beta Environmental Fine Structure (BEFS), the theoretical spectral shape of the  $^{187}\text{Re}$  beta decay, the energy response function, and the radioactive background. These sources are briefly discussed in the following.

The BEFS is a modulation of the beta emission probability due to the atomic and molecular surrounding of the decaying nuclei [53], which is explained by the electron wave structure in terms of reflection and interference. The BEFS oscillations depend on the interatomic distance, while their amplitude is tied to the electron-atom scattering cross section: although the phenomenon is completely understood, its description is quite complex and the parameters involved are not all known *a priori*. So far, it could be detected only in the low energy region— $E \lesssim 1.5 \text{ keV}$ —of the  $^{187}\text{Re}$  spectra, where both the beta rate and the BEFS are larger, but as far as the effect on the neutrino mass determination is concerned, the oscillation extends way up to the end-point (Figure 16). For a safe extrapolation up to the end-point and to minimize the systematic uncertainties, the BEFS must be characterized using much higher statistics beta spectra and independent EXAFS analysis of the material containing rhenium.

The theoretical description of the  $^{187}\text{Re}$  decay spectrum given in Section 6.2 is slightly contradicted by experimental observation, since available high statistics spectra are in fact better interpolated as  $N(E) \propto (E_0 - E)^2$ , that is, with  $f_{187\text{Re}}(E) \approx 1$ . This deviation from theory has not found a plausible explanation yet (Fedor Šimkovic, private communication) and it will become troublesome when larger statistics

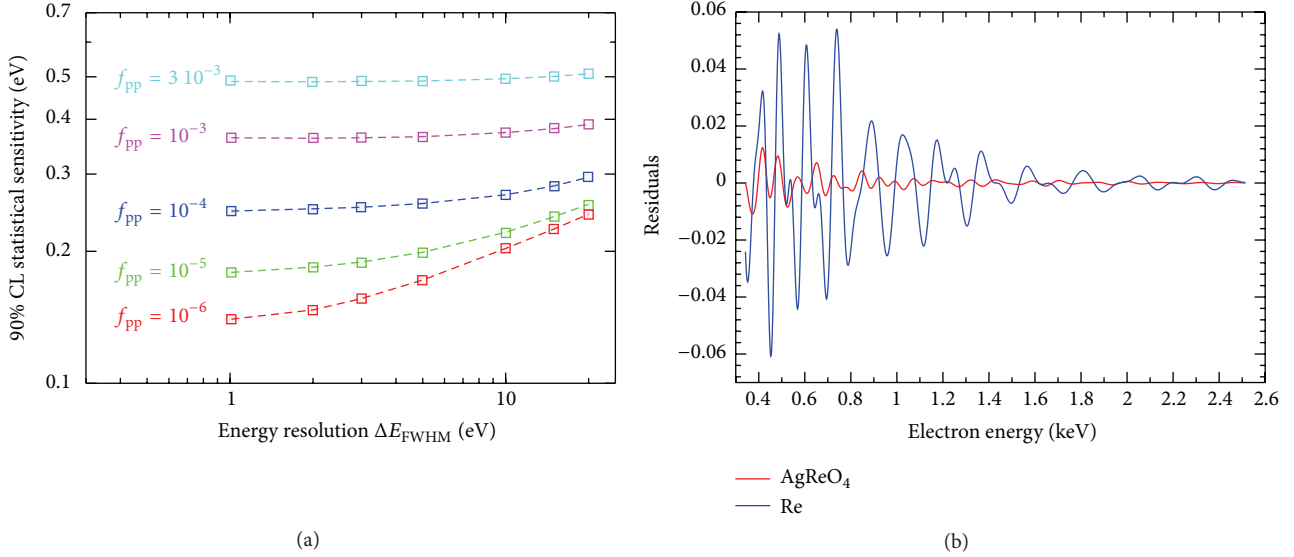


FIGURE 16: Monte Carlo computed statistical sensitivity of a  $^{187}\text{Re}$  decay calorimetric measurement for different experimental configurations and for  $N_{ev} = 10^{14}$  (a). BEFS ripple prediction for metallic rhenium and for  $\text{AgReO}_4$  for an infinite instrumental resolution (b).

experiments will call for more accurate description of the spectrum.

The detector response function is probed by means of X-ray sources which are not exactly monochromatic and which do not replicate the same type of interactions in the absorber as for beta decay. In fact, the X-ray interactions happen at a shallow depth, whereas the beta decays are uniformly distributed in the volume; moreover, in the case of X-rays, the energy is deposited by a primary photoelectron followed by a cascade of secondary X-rays and Auger electrons, whereas in beta decay all the energy is deposited along one single track. It is therefore extremely important—yet challenging—to fully understand the measured response function in order to disentangle the contributions to its shape caused by the external X-rays.

In calorimetric experiments, since the beta source cannot be switched off, the environmental and cosmic background in the energy range of the beta spectrum cannot be directly assessed. Therefore, a constant background is usually included in the fit model as the safest hypothesis. This hypothesis may happen to be not accurate enough for future high statistics measurements.

**6.4. MANU.** The research program in Genova which leads to the MANU experiment started in 1985 [59] with a focus on the use of metallic rhenium absorbers. At that time, there was absolutely no knowledge about the behavior of this material as absorber for LTDs. Therefore, the first years were devoted to study the heat capacity and the thermalization efficiency  $\eta$  of metallic rhenium.

The outcomes of the preliminary phase are summarized in [112]. The thermalization efficiency  $\eta$  was studied for many superconductors in form of small single crystals (cubic millimeters) of Al, Pb, In, Ti, Nb, Va, Zn, and Re, and a quasi-universal dependence on the ratio  $T/\Theta_D$  was found,

with  $\eta$  dropping sharply for  $T$  lower than about  $2 \times 10^{-4} \Theta_D$ . In particular, rhenium thermalization was investigated for single- and polycrystals between 50 mK and 200 mK. The rise time was limited to about 200  $\mu\text{s}$ , preventing the assessment of the thermalization efficiency at shorter time scales. Also, for rhenium, it was found that full thermalization is attained for an operating temperature above about 83 mK. The effect of magnetic fields was also investigated, and an unexpected and unexplained reduction of  $\eta$  for magnetic fields increasing up to 20 Gauss was found.

The first observation of  $^{187}\text{Re}$  spectrum was reported in [113]. After this, a period was spent to optimize the microcalorimeter performance, also exploiting the gained understanding of metallic rhenium absorbers: energy resolutions as good as about 30 eV were demonstrated with small—about 50  $\mu\text{g}$ —rhenium absorbers. In 2001, the results of the high statistics measurement of MANU were published [114]. The MANU experiment's microcalorimeter was a NTD germanium thermistor coupled with epoxy resin to a 1.572 mg rhenium single crystal. Two ultrasonically bonded aluminum wires provided both the path for the electrical signal and the thermal contact to the heat sink at 60 mK (Figure 17). The detector had a thin shield against environmental radiation made out of ancient Roman lead. A weak  $^{55}\text{Fe}$  source ( $10^{-3}$  counts/s) allowed the monitoring of the gain stability during the measurement, while the energy calibration was established through a removable fluorescence source emitting the K lines of Cl, Ca, and K. Signals were read out by a cold stage with unitary gain using a JFET at about 150 K, digitized at 12 bits in 1024 long records, and processed with an Optimal Filter. Further processing was used to detect pile-up events [115]. The high statistics measurement lasted for about 3 months and the detector performance is listed in Table 2 [114].  $^{55}\text{Fe}$   $\text{K}_\alpha$  line had a perfectly Gaussian shape with tails lower than 0.1%. The calibration with the fluorescence source

TABLE 2: Comparison of the MANU [116] and MIBETA [117] experiments.

	MANU	MIBETA
Source/absorber	Metallic Re	AgReO <sub>4</sub>
Sensor	Ge-NTD	Si implanted thermistor
Number of detectors	1	8
Total mass [ $\mu\text{g}$ ]	1572 (Re)	2174 (AgReO <sub>4</sub> )
Measuring time $t_M$ [h]	$\approx 2800$	$\approx 8700$
Total activity $A$ [Bq]	1.1 (above 350 eV)	1.17 (above 700 eV)
Energy resolution $\Delta E_{\text{FWHM}}$ [eV]	96 (at 5.9 keV)	28.5 (average at <sup>187</sup> Re end-point)
Rise time [ $\mu\text{s}$ ]	$\approx 1000$	492 (average 10–90%)
Statistics $N_{\text{ev}}$	$6 \times 10^6$ (above 420 eV)	$6.2 \times 10^6$ (above 700 eV)
Pile-up fraction $f_{\text{pp}}$	—	$2.3 \times 10^{-4}$
$E_0$ [eV]	$2470 \pm 1_{\text{stat}} \pm 4_{\text{sys}}$	$2465.3 \pm 0.5_{\text{stat}} \pm 1.6_{\text{sys}}$
$\tau_{1/2}$ [ $10^{10}$ y]	$4.12 \pm 0.02_{\text{stat}} \pm 0.11_{\text{sys}}$	$4.32 \pm 0.02_{\text{stat}} \pm 0.01_{\text{sys}}$
$m_{\nu_e}^2$ [eV <sup>2</sup> ]	$-462^{+579}_{-679}$	$-112 \pm 207_{\text{stat}} \pm 90_{\text{sys}}$
$m_{\nu_e}$ 90% [eV]	19	15
Background $b$ [c/eV/day]	$3 \times 10^{-4}$	$1.7 \times 10^{-4}$

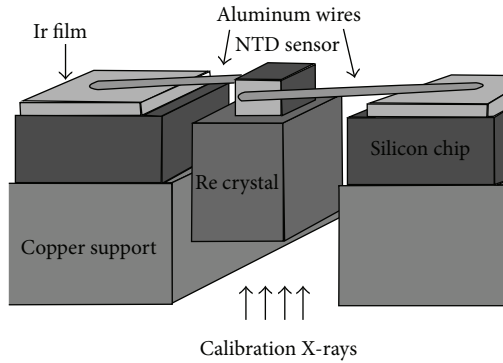


FIGURE 17: The MANU experiment detector (from [114]).

showed that the energy resolution is practically constant with energy, and the deviation from linearity of the energy response was of about 0.16% at <sup>187</sup>Re spectrum end-point.

The fit of the spectrum (Figure 18) gave a squared neutrino mass of  $m_{\nu_e}^2 = -462^{+579}_{-679}$  eV<sup>2</sup>, which translated in an upper limit  $m_{\nu_e} \leq 26$  eV at 95% CL or 19 eV at 90% CL [116].

The results reported in [114] were the most precise measurements of the transition energy  $E_0$  and of <sup>187</sup>Re half-life at the time of publishing; <sup>187</sup>Re half-life in particular is of great interest for geochronology for determining the age of minerals and meteorites.

This high statistics measurement allowed also the first time observation of the BEFS [118] and the setting of a limit for the emission of sterile neutrinos with masses below 1 keV [119] (Figure 19).

**6.5. MIBETA.** The Milano program for a neutrino mass measurement with <sup>187</sup>Re started in 1992 with an R&D to fabricate silicon implanted thermistors in collaboration with FBK [121]. The final objective was to make large arrays of high resolution microcalorimeters using micromachining [122].

NTD germanium based microcalorimeters were also tested. In light of the encouraging results obtained at Genova, at first, the program concentrated on metallic rhenium absorbers. Many single- and polycrystalline samples were tested with disappointing results: small signals, long time constants, and inconsistently varying pulse shapes. A possible correlation with the sample purity and with residual magnetic fields was individuated, but this was not enough to improve the results. Better detector responses were seen only at temperatures approaching 200 mK, too high for obtaining the necessary sensitivity as in (40). The research program therefore moved onto the systematic testing of dielectric rhenium compounds as microcalorimeter absorbers. From the beginning, the most suitable compounds looked like those based on the  $\text{ReO}_4^-$  (perrhenate) anion. A nonexhaustive list of tested compounds includes  $\text{Re}_2(\text{CO})_{10}$ ,  $\text{K}_2\text{ReCl}_6$ ,  $(\text{NH}_4)\text{ReO}_4$ ,  $\text{KReO}_4$ , and  $\text{AgReO}_4$ . The tests with  $\text{Re}_2(\text{CO})_{10}$  failed since this compound sublimates in vacuum at room temperature. The second-to-fourth materials, despite the good theoretical expectations and the large signal-to-noise ratio, showed a quite poor energy resolution—exceeding 100 eV at 6 keV—which could be explained to be due to a large thermalization noise.

Silver perrhenate ( $\text{AgReO}_4$ ), on the other hand, immediately exhibited good properties with limited thermalization noise. The calibration peaks were sufficiently symmetric, and energies resolutions as good as 18 eV FWHM at 6 keV were achieved.  $\text{AgReO}_4$  crystals are transparent, crumbly, and slightly hygroscopic, with a specific <sup>187</sup>Re activity of about  $5.4 \times 10^{-4}$  Hz/ $\mu\text{g}$  [123].

The MIBETA experiment ran between 2002 and 2003 an array of 10  $\text{AgReO}_4$  microcalorimeters for a high statistics measurement, which was preceded by a campaign of measurements dedicated to tuning the set-up and to reducing the background [124].

The array was made of  $\text{AgReO}_4$  crystals with masses ranging from 250 to 300  $\mu\text{g}$  to limit event pile-up, for a total mass

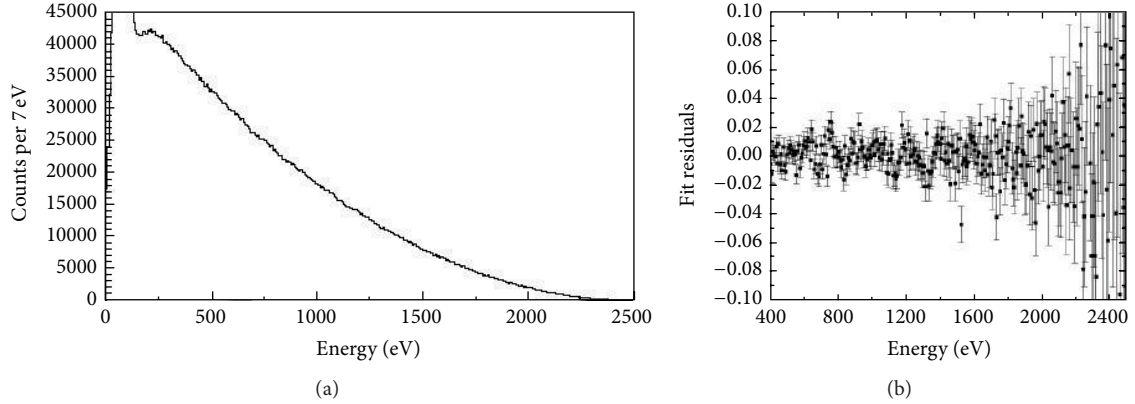


FIGURE 18: The MANU experiment final spectrum (a) and its fitting residuals showing the BEFS ripples (b) (from [114]).

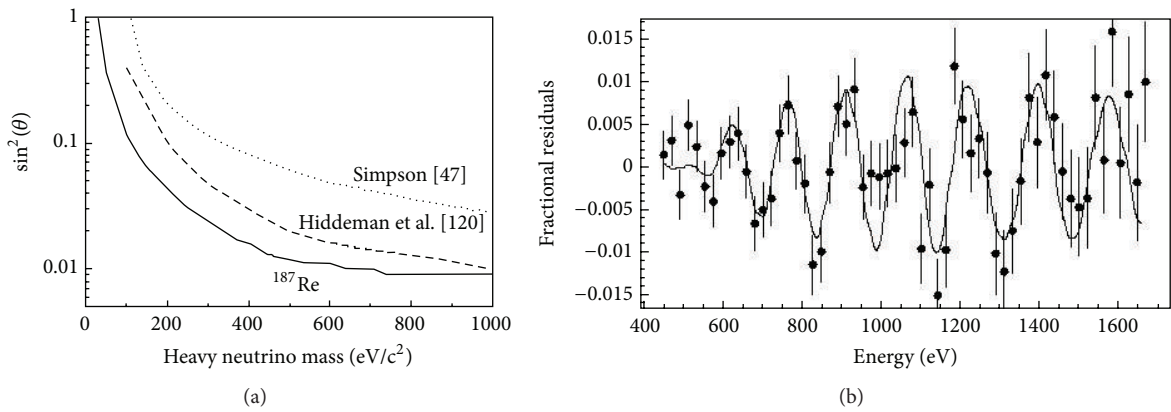


FIGURE 19: Heavy sterile neutrino mass exclusion plot obtained from MANU spectrum. A comparison with the previous limits from Simpson [47] and from Hiddeman et al. [120] is also shown (a). BEFS in the MANU spectrum [118] (b).

of 2.683 mg. The crystals were attached to silicon implanted thermistors with epoxy resin, and four ultrasonically bonded aluminum wires were used both as signal leads and heat links to the heat bath, stabilized at 25 mK (Figure 20). The 10 microcalorimeters were enclosed in two copper holders without lead shielding, to avoid the background caused by lead fluorescence at 88 keV, which in turn provokes escape peaks in  $\text{AgReO}_4$  very close to the beta end-point. The stability and performance of all detectors were monitored with a movable multiline fluorescence source at 2 K, which was activated for 25 min every 2 h to emit the K lines of Al, Cl, Ca, Ti, and Mn. When not used for the calibration, the primary  $^{55}\text{Fe}$  source was pulled inside a massive shield of ancient Roman lead [125], in order to minimize the contribution to the radioactive background caused by IB of  $^{55}\text{Fe}$ . The data acquisition program controlled the movements of the source and tagged the events collected during the calibrations. The first stage of the electronic chain used 10 JFETs cooled to about 120 K and placed few centimeters below the detectors. A 16-bit data acquisition system digitalized and saved to disk the signals for an Optimal Filter based offline analysis.

The high statistics measurement of MIBETA lasted for about 7 months. In the final analysis, the data from two

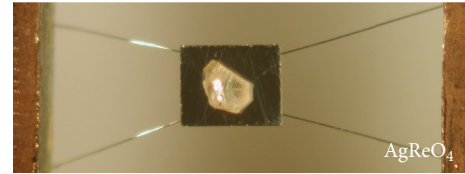


FIGURE 20: One of the MIBETA microcalorimeters with  $\text{AgReO}_4$ .

detectors, with poorer energy resolution, were not included. The total active mass was therefore 2.174 mg, for a  $^{187}\text{Re}$  activity of 1.17 Bq. The final beta spectrum obtained from the sum of the 8 working detectors corresponds to about 8745 hours $\times$ mg [117]. The performance of the detectors was quite stable during the run and is reported in Table 2.

All X-ray peaks in the calibration spectrum showed tails on the low energy side, and the thermalization noise of  $\text{AgReO}_4$  caused their width to increase with the energy (Figure 21). The fit of spectrum (Figure 21) gave a squared neutrino mass of  $m_{\nu_e}^2 = -112 \pm 207_{\text{stat}} \pm 90_{\text{sys}}$ , which translates in an upper limit  $m_{\nu_e} \leq 15$  eV at 90% CL [117]. The systematic error was dominated by the uncertainties on the

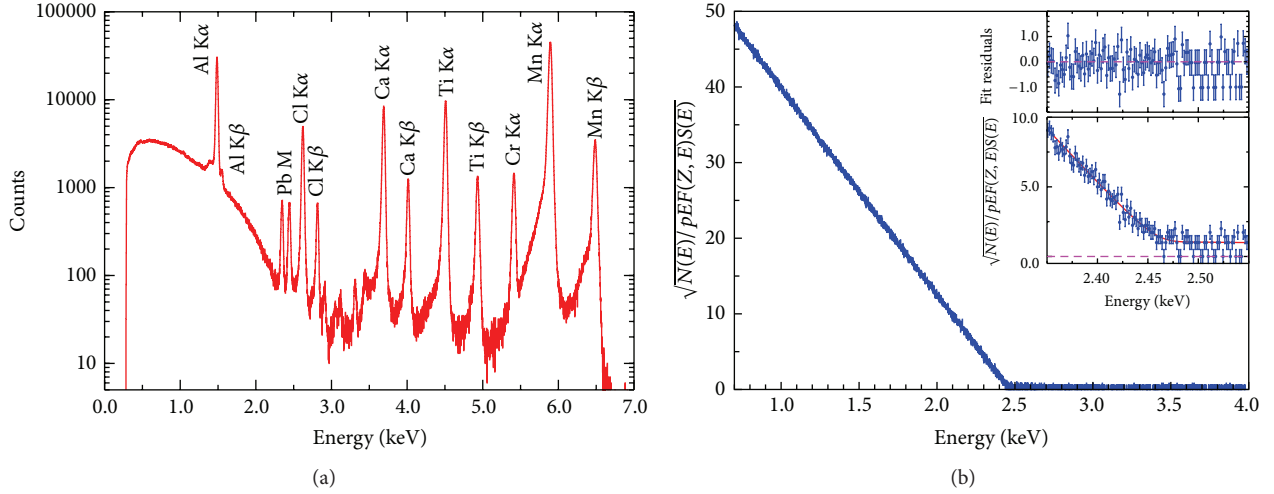
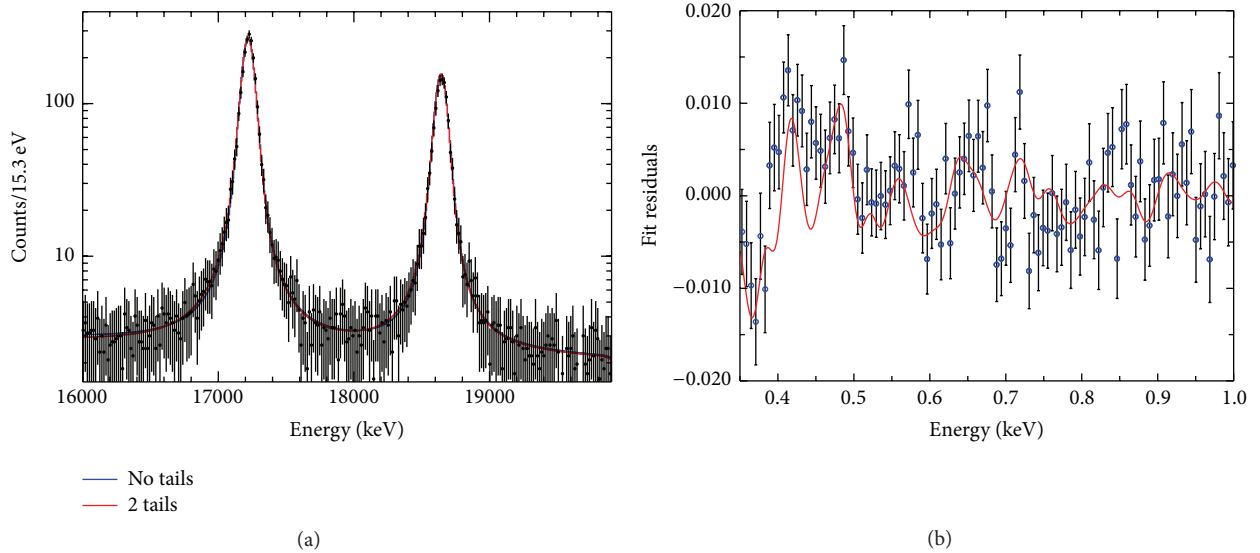


FIGURE 21: Final MIBETA calibration spectrum (a). Kurie plot of the final MIBETA data (b).


 FIGURE 22: Escape peaks due to the exposure of AgReO<sub>4</sub> microcalorimeters to a <sup>44</sup>Ti source [126] (a). BEFS in the MIBETA final spectrum [110] (b).

energy resolution function, on the background, and on the theoretical shape of the spectrum.

Additional lower statistics measurements with the same set-up were carried out to study and reduce the background and to investigate the energy response function. In particular, using the escape peaks caused at about 17 keV by the irradiation with a <sup>44</sup>Ti gamma source (see Figure 22) as comparison, it was possible to partly understand the complex shape of the X-ray calibration peaks and to establish that at least the longest of the observed tails were due to surface effects [126].

Although BEFS (see Section 6.3 and Figure 16) is almost one order of magnitude fainter in AgReO<sub>4</sub> compared to metallic rhenium, it was observed also in the high statistics spectra of MIBETA [110] (Figure 22). In particular, the BEFS ripple interpolation returns a  $p_{3/2}$  to  $s_{1/2}$  branching ratio in

<sup>187</sup>Re beta emission of about  $0.84 \pm 0.30$ , which is compatible with the expected prevalent  $p_{3/2}$  emission (see Section 6.2).

6.6. *MARE*. The MANU and MIBETA results, together with the constant advance in the LTD technology, made it reasonable to propose a larger scale project: the Microcalorimeter Arrays for a Rhenium Experiment (MARE). The ambition of MARE was to establish a sub-eV neutrino mass sensitivity through a gradual deployment approach. The project was started in 2005 by a large international collaboration [127, 128] and it was organized in two phases.

The final objective of a sub-eV statistical sensitivity on the electron neutrino mass was the goal of the second phase. To accomplish this, the program was to gradually deploy several large arrays—about 10<sup>4</sup> elements each—of detectors,

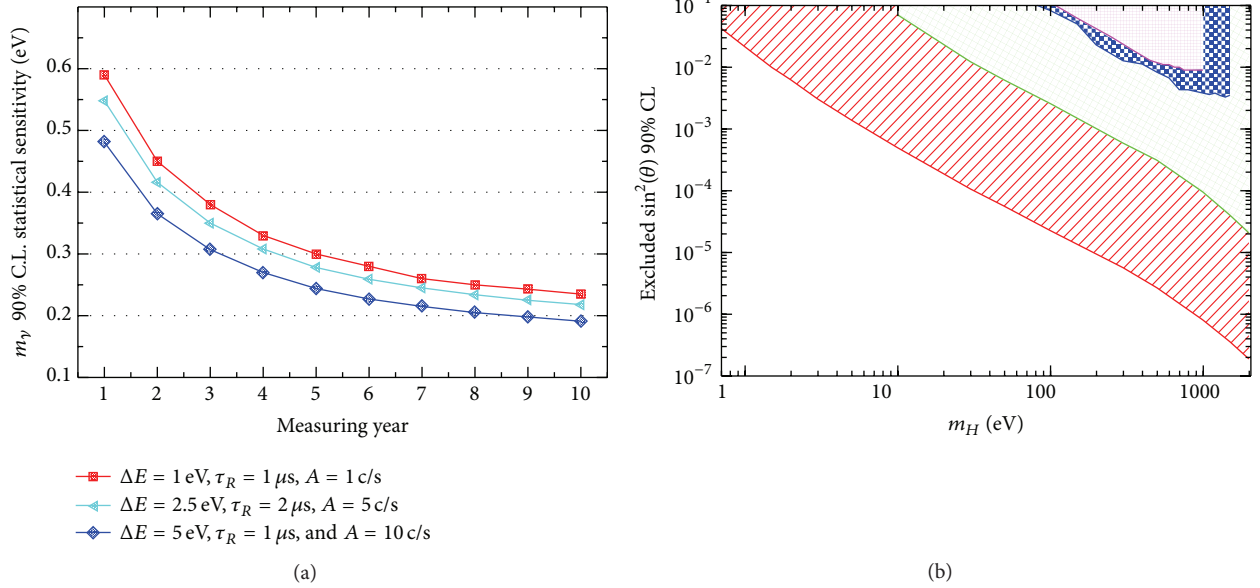


FIGURE 23: Statistical sensitivity of MARE final experiment. Curves are calculated for the deployment of 10000 pixels per year for the first 5 years (a). Statistical sensitivity to the emission of heavy neutrinos with mass  $m_H$ . From lower to upper curve: Monte Carlo simulation with  $N_{\text{ev}} = 10^{14}$ ,  $f_{\text{pp}} = 10^{-6}$ , and  $\Delta E = 1.5$  eV; Monte Carlo simulation with  $N_{\text{ev}} = 8 \times 10^9$ ,  $f_{\text{pp}} = 10^{-5}$ , and  $\Delta E = 15$  eV; MIBETA experiment (unpublished); MANU experiment [119] (b).

with energy and time resolutions of the order of 1 eV and 1  $\mu\text{s}$ , respectively. Each pixel was planned to have a source activity of about few counts per second in order to collect a total statistics of about  $10^{14}$  beta decays in up to ten years of measurement time (see Figure 23) [127]. Figure 23 shows also the MARE sensitivity to the emission of heavy sterile neutrinos with masses below 2 keV (Section 5.4).

Phase 1—also called MARE-1—had the task to ascertain the most suitable technical approach for the final experimental phase, also with the help of smaller scale experiments. An R&D program was started with the aim of improving the understanding of the superconducting rhenium absorbers and of their optimal coupling to sensors and developing the appropriate array technology and multiplexed read-out scheme [127]. At the same time, two intermediate size experiments carried out with the available technologies aimed to reach a neutrino mass sensitivity of the order of 1 eV and to improve the understanding of all the systematics peculiar of the calorimetric approach with  $^{187}\text{Re}$ . Furthermore, MARE-1 started to explore the alternative use of  $^{163}\text{Ho}$  for a calorimetric measurement of the neutrino mass. Given the unavoidable competition with the KATRIN experiment, the time schedule for MARE was quite tight.

The physics of metallic rhenium as absorber for the MARE detectors was the focus of the Genova and the Heidelberg groups. The best technologies available for the MARE-2 arrays were (1) the transition edge sensors (TESs) with Frequency Division Multiplexing, investigated by the Genova group and Physikalisches Technische Bundesanstalt (PTB, Berlin, Germany); (2) the Metallic Magnetic Calorimeters (MMCs) with Microwave SQUID Multiplexing, developed by

the Heidelberg group; and (3) Microwave Kinetic Inductance Detectors (MKID) with Microwave Multiplexing, explored by the Milano group. The Genova group, in collaboration with Miami and Lisbon, planned an experiment consisting of an array of 300 TES detectors with 1 mg rhenium single crystals [129]. With energy and time resolutions of about 10 eV and 10  $\mu\text{s}$ , respectively, the sensitivity attainable in 3 years of measuring time was estimated to be around 1.8 eV at 90% CL, for a statistics of about  $3 \times 10^{10}$  decays. The Milano group, together with the NASA/GSFC and Wisconsin groups, deployed an array of silicon implanted thermistors coupled to  $\text{AgReO}_4$  absorbers. The experiment used 8 of the 36 pixel arrays that NASA/GSFC had developed for the XRS2 instrument [130]. With 288 pixels attached to about 500  $\mu\text{g}$   $\text{AgReO}_4$  crystals, and with energy and time resolutions of about 25 eV and 250  $\mu\text{s}$ , respectively, a sensitivity around 3.3 eV at 90% CL was expected in 3 years of measuring time, with a statistics of about  $7 \times 10^9$  decays.

Unfortunately, the MARE-1 outcomes were quite disappointing, and MARE-2 ended up being cancelled before taking off. The lack of success of the MARE initiative was mostly the consequence of the final acknowledgment of the impossibility to fabricate rhenium microcalorimeters matching the specifications set by the aimed sub-eV sensitivity. The systematic investigations carried out at Heidelberg with rhenium absorbers coupled to MMC, despite some noteworthy progress, arrived to conclusions similar to those of past works: rhenium absorbers behave inconsistently, showing a large deficit in the energy thermalization accompanied by long time constants [131]. Therefore, the challenging idea of improving and scaling up the pioneer experiments using metallic rhenium absorbers turned out to be a dead-end road.

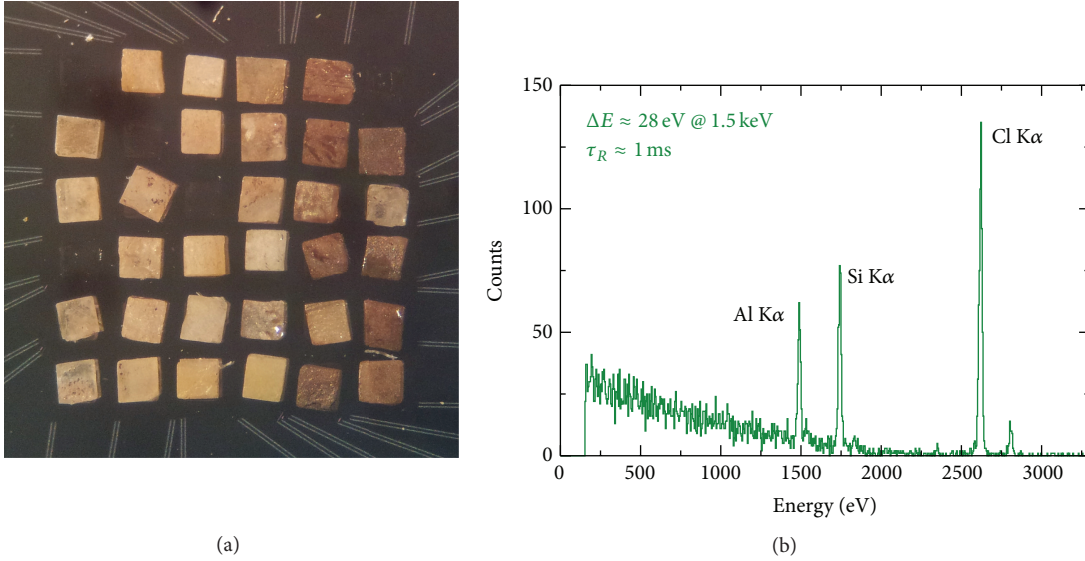


FIGURE 24: 31  $\text{AgReO}_4$  crystal glued on the first XRS2 array of MARE-1. The 16 usable pixels give  $\Delta E \approx 47$  eV at 2.6 keV,  $\tau_R \approx 1$  ms (a). Spectrum measured with the best pixel (b).

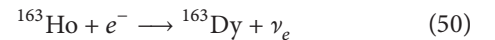
Indeed, also the other experimental efforts of MARE-1 encountered several difficulties [132]. For example, the setting up of arrays of  $\text{AgReO}_4$  crystals turned out to be more troublesome than expected (Figure 24). The freshly polished surfaces of  $\text{AgReO}_4$  crystals shaped to cuboids resulted to be incompatible with the sensor coupling methods used successfully in MIBETA with as-grown small crystals. Despite the use of a micromachined array of silicon implanted thermistors, the performance of the pixels was irreproducible and, while gradually populating and testing the XRS2 array with  $\text{AgReO}_4$  crystals, the performance of the instrumented pixels started to degrade. This made the array finally unusable. Given the sorts of the MARE project, also this branch of the MARE-1 program was thus dropped in 2013.

**6.7. Future of Rhenium Experiments.** From the MARE experience, it is clear that a large scale neutrino mass experiment based on  $^{187}\text{Re}$  beta decay is not foreseeable in the near future. It would require a major step forward in the understanding of the superconductivity of rhenium, but, after more than 20 years of efforts, this is not anymore in the priorities of the LTD scientific community. Besides the intrinsic problems of metallic rhenium, there are other considerations which make rhenium microcalorimeters not quite an appealing choice for high statistics measurements. Because of the large half-life of  $^{187}\text{Re}$ , the specific activity of metallic rhenium is too low to design pixels with both high performance and high intensity beta sources.  $^{187}\text{Re}$  activity required by a high statistics experiment must be therefore distributed over a large number of pixels—of the order of  $10^5$ —while the difficulties inherent with the production of high quality metallic rhenium absorbers contrast with the full microfabrication of the arrays. MARE-1 also demonstrated that  $\text{AgReO}_4$  is not a viable alternative to metallic rhenium. For these reasons, the

new hope for a calorimetric neutrino mass experiment with LTDs is  $^{163}\text{Ho}$ .

## 7. Current Experiments

**7.1. Calorimetric Absorption Spectrum of  $^{163}\text{Ho}$  EC.** De Rújula introduced the idea of a calorimetric measurement of  $^{163}\text{Ho}$  EC decay already in 1981 [30], but it was only one year later that this idea was fully exploited in the paper written by Lusignoli [43]. The EC decay



has the lowest known Q value, around 2.5 keV, and its half-life of about 4750 years is much shorter than  $^{187}\text{Re}$  one. In [43], the authors compute the calorimetric spectrum and give also an estimate of the statistical sensitivity to the neutrino mass at the spectrum end-point, including the presence of the pile-up background. Unfortunately, at that time, the experimental measurements of the Q value were scattered between 2 keV and 3 keV causing large uncertainties on the achievable statistical sensitivity.

A calorimetric EC experiment records all the deexcitation energy and therefore it measures the escaping neutrino energy  $E_\nu$ ; see (17). The deexcitation energy  $E_c$  is the energy released by all the atomic radiations emitted in the process of filling the vacancy left by the EC decay, mostly electrons with energies up to about 2 keV (the fluorescence yield is less than  $10^{-3}$ ) [32]. The calorimetric spectrum has lines at the ionization energies  $E_i$  of the captured electrons. These lines have a natural width  $\Gamma_i$  of a few eV; therefore, the actual spectrum is a continuum with marked peaks with Breit-Wigner shapes (Figure 25). The spectral end-point is shaped by the same neutrino phase space factor  $(Q - E)\sqrt{(Q - E)^2 - m_{\nu_e}^2}$  that appears in a beta decay spectrum,

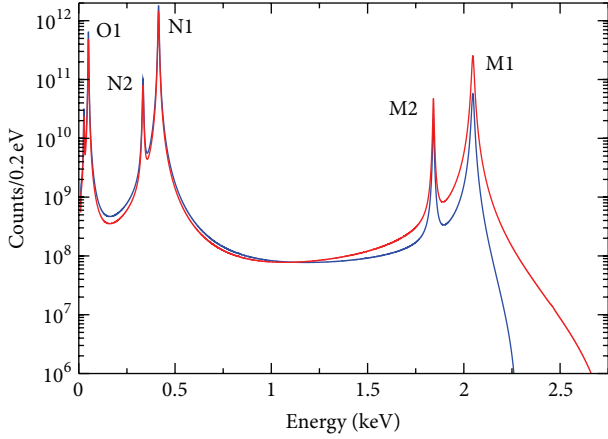


FIGURE 25: Calculated  $^{163}\text{Ho}$  EC calorimetric spectrum for  $Q = 2.3$  keV (blue) and  $Q = 2.8$  keV (red) and for  $\Delta E = 2$  eV and  $N_{\text{ev}} = 10^{14}$ .

with the total deexcitation energy  $E_c$  replacing the electron kinetic energy  $E$ . For a nonzero  $m_{\nu_e}$ , the deexcitation (calorimetric) energy  $E_c$  distribution is expected to be

$$N_{\text{EC}}(E_c, m_{\nu_e}) = \frac{G_\beta^2}{4\pi^2} (Q - E_c) \cdot \sqrt{(Q - E_c)^2 - m_{\nu_e}^2} \sum_i n_i C_i \beta_i^2 B_i \frac{\Gamma_i}{2\pi} \frac{1}{(E_c - E_i)^2 + \Gamma_i^2/4}, \quad (51)$$

where  $G_\beta = G_F \cos \theta_C$  (with the Fermi constant  $G_F$  and the Cabibbo angle  $\theta_C$ ),  $E_i$  is the binding energy of the  $i$ th atomic shell,  $\Gamma_i$  is the natural width,  $n_i$  is the fraction of occupancy,  $C_i$  is the nuclear shape factor,  $\beta_i$  is the Coulomb amplitude of the electron radial wave function (essentially, the modulus of the wave function at the origin), and  $B_i$  is an atomic correction for electron exchange and overlap. The sum in (51) runs over the Dy shells which are accessible to the EC with the available  $Q$  (M1, M2, N1, N2, O1, O2, and P1). The expression (51) is derived in [43], where numerical checks to test the validity of the approximations made are also presented.

Until about 2010, only three calorimetric absorption measurements were reported in the literature:

- (1) the ISOLDE collaboration used a Si(Li) detector with an implanted source [40, 133];
- (2) Hartmann and Naumann used a high temperature proportional counter with organometallic gas [42];
- (3) Gatti et al. used a cryogenic calorimeter with a sandwiched source [134].

However, none of these experiments had the sensitivity required for an end-point measurement; therefore, they all gave results in terms of capture rate ratios. The most evident limitations of these experiments were statistics and energy resolution. One further serious trouble for Si(Li) and cryogenic detectors was the incomplete energy detection caused by implant damage and weak thermal coupling of the source, respectively.

Recently, a new generation of calorimetric holmium experiments has been stimulated by the MARE project. In fact, despite the shortcomings of the previous calorimetric experiments and theoretical and experimental uncertainties, a  $^{163}\text{Ho}$  calorimetric absorption experiment seems the only way to achieve sub-eV sensitivity for the neutrino mass. Moreover, low temperature X-ray microcalorimeters have reached the necessary maturity to be used in a large scale experiment with good energy and time resolution; hence, they are the detectors of choice for a sub-eV holmium experiment.

Thanks to the short  $^{163}\text{Ho}$  lifetime, the limited number of nuclei needed for a neutrino mass experiment— $10^{11}$  nuclei for 1 decay/s—can be introduced in the energy absorber of a low temperature microcalorimeter. Therefore, holmium experiments can leverage the microcalorimeters development for high energy resolution soft X-ray spectroscopy, whereas rhenium experiments would need a dedicated development of detectors with metallic rhenium absorbers. Small footprint kilo-pixel arrays can be fully fabricated with well established microfabrication techniques.

Indeed, in microcalorimeters with metallic absorbers such as gold, the relatively high concentration of holmium ( $J = 7/2$ ) could cause an excess heat capacity due to hyperfine level splitting in the metallic host [67] and thereby degrade the microcalorimeter performance. Low temperature measurements have been already carried out in the framework of the MARE project to assess the gold absorber heat capacity (at temperatures  $< 150$  mK), both with holmium and with erbium implanted ions [135]. Those tests did not show any excess heat capacity, but more sensitive investigations need to be carried out.

The Genova group pioneered the application of LTDs to the measurement of the calorimetric spectrum of  $^{163}\text{Ho}$  [134] and continued this research until it converged in the MARE project [136]. For long, the focus has been on the production of  $^{163}\text{Ho}$  isotope, on the chemistry of metallic holmium, and on the techniques to embed the isotope in the detector absorbers.

The new experiments, now ready to start the production of high resolution detectors for the high statistics calorimetric measurement of  $^{163}\text{Ho}$  EC decay, will be the subject of the next sections.

**7.2. The  $Q$  Value of  $^{163}\text{Ho}$  Decay.** Until very recently, the question of the exact  $Q$  value of the  $^{163}\text{Ho}$  EC decay was not settled. Although the results showed a general tendency to accumulate around 2.8 keV, especially restricting to the calorimetric measurements [40, 131, 134], the reliability of the capture ratios as tool for determining  $Q$  remained questionable. Indeed,  $Q$  has never been measured directly from the end-point of  $^{163}\text{Ho}$  EC spectrum, but only from the capture ratios  $\lambda_i/\lambda_j$ , whose accuracy is limited (Section 4). The currently recommended value of  $Q$  is  $2.555 \pm 0.016$  keV [137], but it is deduced from a limited set of data. The statistical sensitivity of  $^{163}\text{Ho}$  experiments depends strongly on how close the end-point and the M1 capture peak are. To a good degree of approximation, the Lorentzian tail of the M1

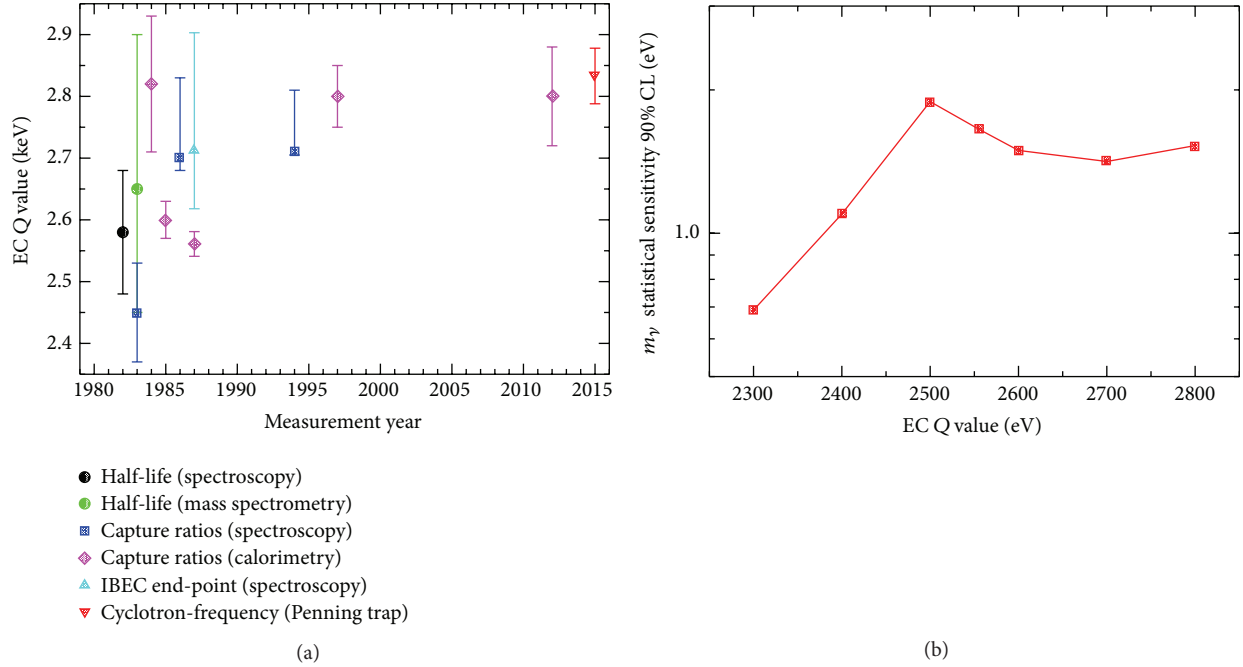


FIGURE 26: Summary of the Q values measured by several experiments since the early 1980s. The points are grouped by analysis and technique: decay half-life using X-ray spectroscopy [138] or mass spectrometry [139], capture ratios using X-ray spectroscopy [36–38] or calorimetry [40, 41, 131, 134], IBEC end-point [34], and the Penning trap mass spectrometer SHIPTRAP [140] (a). Monte Carlo computed statistical sensitivity as a function of Q for  $N_{ev} = 3 \times 10^{13}$  and with  $f_{pp} = 3 \times 10^{-4}$ ,  $\Delta E_{FWHM} = 1$  eV, and no background. The interval adopted for Q is the one which was considered as possible until the very recent measurement of the  $^{163}\text{Ho}$ - $^{163}\text{Dy}$  mass difference (b).

peak centered at  $E_{M1} = B(M1)$  dominates the end-point, and for  $m_{\nu_e}$  equal to zero one has

$$N_{EC}(E_c, m_{\nu_e} = 0) \propto \frac{(Q - E_c)^2}{(E_{M1} - E_c)^2} = \frac{(Q' - E')^2}{E'^2}, \quad (52)$$

where  $E' = E_c - E_{M1}$  and  $Q' = Q - E_{M1}$ . It can be shown that, in these conditions, the neutrino mass sensitivity is  $\Sigma_{EC}(m_{\nu_e}) \propto Q'$ . The uncertainty on Q, therefore, turns into the difficulty to design  $^{163}\text{Ho}$  experiments and to predict their sensitivity reach (Figure 26). Indeed, the shift of attention from  $^{187}\text{Re}$  to  $^{163}\text{Ho}$  has been eased by the reasonable hope that a very low Q could greatly enhance the achievable sensitivity of  $^{163}\text{Ho}$  experiments.

Very recently, Q value was determined from a measurement of the  $^{163}\text{Ho}$ - $^{163}\text{Dy}$  mass difference using the Penning trap mass spectrometer SHIPTRAP [140]. The measured value  $\Delta m = 2833 \pm 30_{\text{stat}} \pm 15_{\text{sys}}$  confirms the most recurrent Q measured in recent calorimetric experiments, although chemical shifts may still be expected for  $^{163}\text{Ho}$  embedded in the LTD absorbers. The knowledge of the Q value is indeed a crucial ingredient for the optimal design of an experiment, while its limited precision and accuracy prevent from using it as fixed parameter when the experimental data are interpolated to assess the neutrino mass [141]. Nevertheless, a comparison of Q from the interpolation with a value obtained with an independent measurement—such

as the  $^{163}\text{Ho}$ - $^{163}\text{Dy}$  mass difference—is a powerful tool to pinpoint systematic effects.

In any case, the direct assessment of Q from the end-point of the calorimetric spectrum remains the first important goal of the upcoming high statistics measurements.

**7.3. Statistical Sensitivity.** While the complexity of both the EC and the pile-up spectra makes an analytical estimate of the statistical sensitivity an impossible task, a Monte Carlo approach analogous to the one described in Section 6.3 can give useful results [142]. Most of the considerations made for  $^{187}\text{Re}$  are also valid in the case of  $^{163}\text{Ho}$ . The general conclusion about the importance of the total statistics is well exemplified by Figure 27 for the now established Q value of 2800 eV: indeed, the high Q value raises the stakes of the experimental challenge and the prospects for a sub-eV sensitivity are scaled down. Table 3 shows the exposures required for two possible experiments aiming at a  $m_{\nu_e}$  sensitivity of 0.2 and 0.1 eV, respectively (see also Figure 28). Although it may be possible to design microcalorimeters with a high  $^{163}\text{Ho}$  activity, sub-eV sensitivity will likely require arrays with total number of channels of the order of  $10^6$ . Indeed, there are several limitations to the possible activity  $A_{EC}$ , such as the effect of  $^{163}\text{Ho}$  nuclei on the detector performance or detector crosstalk and dead time considerations. As shown in Section 6.3, a high activity  $A_{EC}$  causes an increase of  $f_{pp}$  and thereby a reduced sensitivity to radioactive background. This, along with the relative thinner aspect ratio

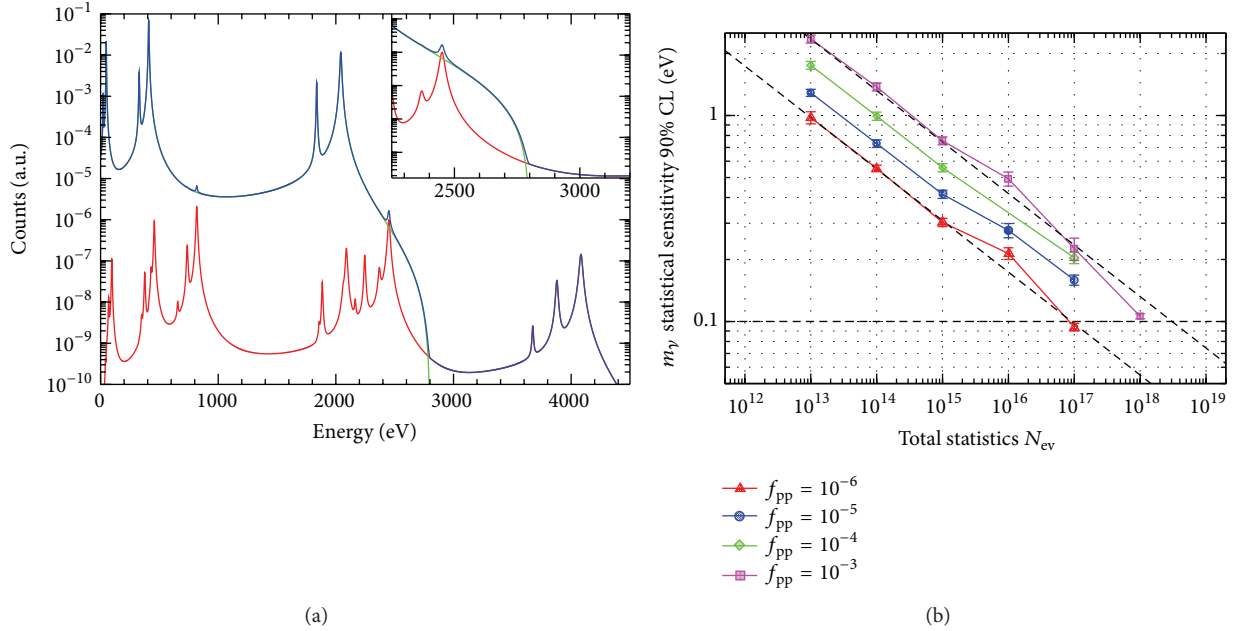


FIGURE 27: Calculated experimental  $^{163}\text{Ho}$  EC calorimetric spectrum for  $Q = 2.8$  keV,  $\Delta E = 2$  eV,  $f_{pp} = 10^{-4}$ , and  $N_{ev} = 10^{14}$  (blue). The pile-up spectrum is the red curve (a). Monte Carlo estimated statistical sensitivity for  $\Delta E = 1$  eV,  $\tau_R = 1$   $\mu\text{s}$ , and  $f_{pp} = 10^{-3}$ ,  $10^{-4}$ ,  $10^{-5}$ , and  $10^{-6}$  (from top to bottom). The dashed lines are the extrapolations of  $f_{pp} = 10^{-3}$  and  $f_{pp} = 10^{-6}$  curves using  $\Sigma \propto N_{ev}^{-1/4}$  scaling law. For  $f_{pp} = 10^{-6}$  ( $10^{-3}$ ), an extrapolated sensitivity of 0.1 eV can be obtained, for example, with an exposure of about  $N_{det} \times t_M = 10^8$  detector  $\times$  year and a single pixel activity of about  $A_{EC} = 10(1000)$  Bq (b).

TABLE 3: Experimental exposure required for various target statistical sensitivities, with no background and two different sets of detector parameters.

Q [eV]	Target sensitivity [eV]	$A_{EC}$ [counts/s]	$\Delta E$ [eV]	$\tau_R$ [ $\mu\text{s}$ ]	$N_{ev}$ counts	Exposure $T$ [detector $\times$ year]
2800	0.2	100	1	0.1	$9.8 \times 10^{15}$	$3.1 \times 10^6$
2800	0.1	100	0.3	0.1	$1.9 \times 10^{17}$	$5.9 \times 10^7$

of microcalorimeters with  $^{163}\text{Ho}$ , makes it likely that it is not strictly necessary to operate arrays in an underground laboratory [142].

No high statistics measurement faced so far the task of a careful estimation of systematic uncertainties. Nevertheless, it is fair to say that there are some substantial differences between the systematic uncertainties expected for  $^{187}\text{Re}$  and  $^{163}\text{Ho}$  experiments, which are worth mentioning. To avoid spectral distortions due to the escape of radiation, the absorbers must provide  $4\pi$  encapsulation with a minimum thickness of few microns. For gold absorbers, Monte Carlo simulations indicate a thickness of  $2 \mu\text{m}$  for a 99.99998% (99.927%) absorption of 2 keV electrons (photons).

Furthermore, M1 and M2 peaks in the calorimetric spectrum provide a useful tool to evaluate the detector response function overcoming the problems related to the use of an external X-ray source (Section 6.3). The same peaks can also be exploited for energy calibration, for tracking and correcting gain drifts, and for easing the summation of the spectra measured with the many pixels of the arrays.

The following section addresses the accuracy of the description of the calorimetric spectrum of  $^{163}\text{Ho}$  which is likely to be a relevant source of systematic uncertainties.

**7.4. A Better Description of the  $^{163}\text{Ho}$  EC Spectrum.** While the question of the actual  $Q$  value of the  $^{163}\text{Ho}$  EC transition is now settled, many authors are still debating about the precise shape of the calorimetric spectrum. Indeed, (51) is only an approximation. Already in the original work [43], the applicability of two approximations was demonstrated: the neglect of possible interference between the capture from different levels and the inclusion of transitions with off-shell intermediate states such as K and L.

Riisager in 1988 [143] discussed the distortions of the Lorentzian peak shape expected when considering that, in the atomic radiation cascade, the atomic phase space available at each step is altered by the natural width of previous transitions.

More recently, beginning with Robertson papers [144, 145], some authors started to recognize that the sum in (51)

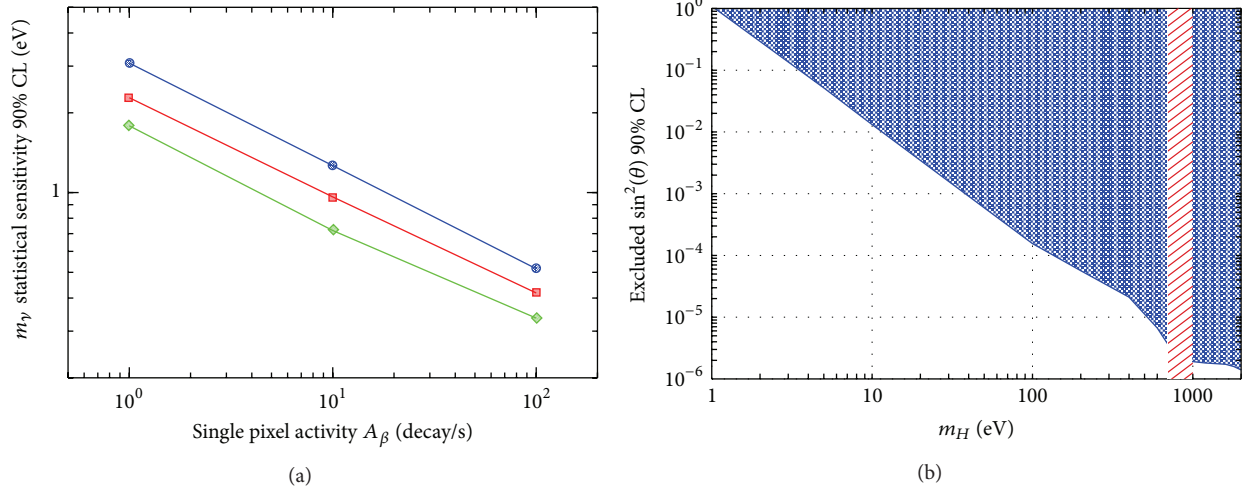


FIGURE 28: Calculated experimental  $^{163}\text{Ho}$  EC calorimetric spectrum for  $Q = 2.8$  keV,  $\Delta E = 1$  eV, for a constant exposure of  $10^5$  detector  $\times$  year and for (top to bottom)  $\tau_R = 10 \mu\text{s}$ ,  $1 \mu\text{s}$ , and  $0.1 \mu\text{s}$  (a). Sensitivity to heavy sterile neutrinos detected from kinks in a  $^{163}\text{Ho}$  calorimetric spectrum with  $Q = 2.8$  keV,  $N_{\text{ev}} = 3 \times 10^{13}$ ,  $\Delta E = 1$  eV, and  $f_{\text{pp}} = 3 \times 10^{-4}$  (b).

must be extended to more transitions which initially were deemed as negligible [146]. This is caused by the incomplete overlap between Ho and Dy atomic wave functions. Recalling that calorimeters measure the neutrino energy  $E_\nu$ , while writing (51), it was assumed that

$$E_\nu = Q - B(H), \quad (53)$$

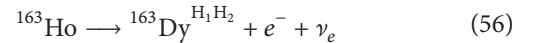
where  $B(H)$  is the binding energy of shell H in a Dy atom, that is, the energy to fill the hole H in  $\text{Dy}^+$  atom. But this is not correct. The hole H is in a neutral Dy atom with an extra (the eleventh) 4f electron, because the parent Ho atom has an electronic configuration which differs from the one of Dy in the number of 4f electrons (11 versus 10) (see also [147]). Following [31], this can be expressed as

$$E_\nu = Q - B(H) - E_R, \quad (54)$$

where  $E_R$  is a correction which accounts for the imperfect atomic wave functions overlap. So, the capture peaks in the calorimetric spectrum are expected to be shifted by a small amount which Robertson [145] calculated as  $E_R \approx B(4f)_{\text{Ho}}$ , where  $B(4f)_{\text{Ho}}$  is the binding energy of the 4f electron in the Ho atom. The atomic wave function mismatch goes along with the possibility of shake-up and shake-off processes, adding more final states to the  $^{163}\text{Ho}$  EC transition and, therefore, more terms in the sum in (51). These processes are the ones responsible for the presence in the final states of two (or more) vacancies created in the Dy atom, along with the extra 4f electron. The second vacancy is left by an atomic electron which has been shaken by the sudden change in the wave functions to a higher bound unoccupied state (shake-up) or to the continuum (shake-off). In the case of shake-up processes, the neutrino energy is given by [145]

$$E_\nu = Q - B(H1) - B(H2) - E_R \quad (55)$$

and the contribution to (51) is just another Lorentzian peak term with  $E_i = B(H1) + B(H2) + E_R$ . The case of the shake-off process is more complex because it is a three-body process



$$E_\nu + E_e = Q - B(H1) - B(H2) - E_R. \quad (57)$$

The corresponding contribution to (51) is not a narrow line since  $E_e$  adds up to the observable atomic deexcitation  $B(H1) - B(H2) - E_R$ . The actual shape of the energy spectrum of the shaken-off electrons can be calculated as shown in [148].

In general, the probability for the multihole processes is small and it can be estimated to be of the order  $10^{-5}$  [146]. The precise calculation of the 2- or 3-hole processes probability is treated in many recent papers [145, 149, 150], with the purpose to improve past results from [151], although, so far, all calculations apparently consider only shake-up processes. In Figure 29, the dashed line is the  $^{163}\text{Ho}$  EC calorimetric spectrum calculated including 2-hole excitations and using the parameters calculated in [149].

The very recent paper [152] extends the work presented in [148] and attempts also to assess the effect of the so far neglected shake-off processes on the end-point region of the spectrum. Although the authors state that their preliminary theoretical estimates should not be fully trusted, the intriguing result of their analysis is that the end-point count rate might be largely dominated by the shake-off processes, with a predicted enhancement of about a factor 40.

The awareness of all the above corrections to (51) triggered some skepticism about the actual feasibility of a neutrino mass measurement from the end-point of the calorimetric  $^{163}\text{Ho}$  EC spectrum. The main argument is that, since the neutrino mass is searched as the difference between the observed experimental spectrum and the theoretical one for  $m_\nu = 0$ , the *a priori* knowledge of the latter one is an absolute

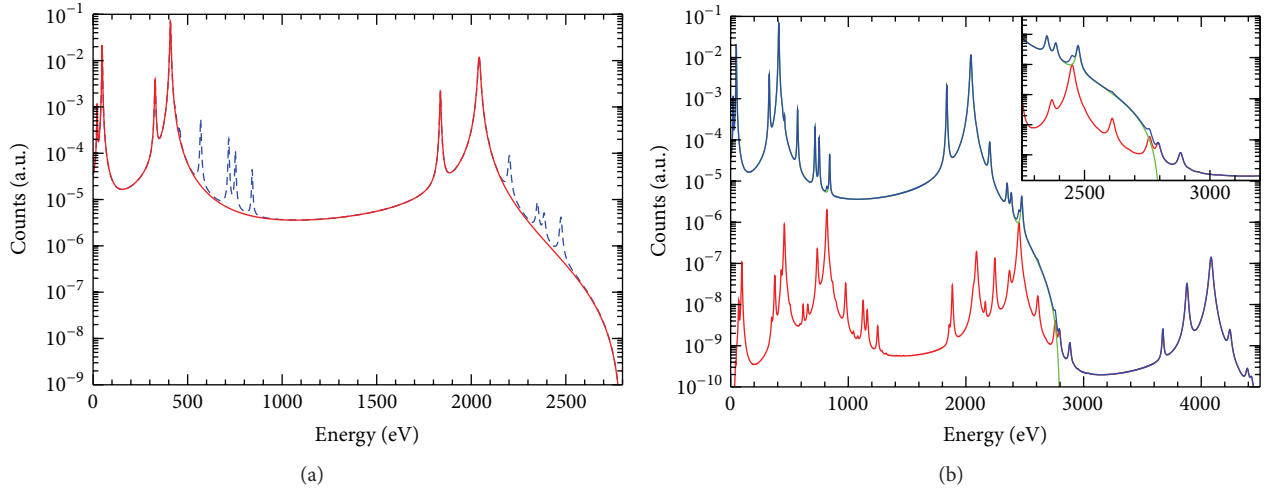


FIGURE 29: Predicted single and double holes calorimetric spectrum of the EC decay of  $^{163}\text{Ho}$  with  $Q = 2.8$  keV (a). The experimental spectrum analogous to the one in Figure 27 with double hole transitions included (b).

condition. Indeed an inaccurate and unreliable theoretical description of all these additional spectral components in the end-point region may induce systematic uncertainties in the neutrino mass determination. However, it can be argued that in the very last portion of the spectrum—where the phase space factor  $p_\nu E_\nu$  would be affected by  $m_\nu > 0$ —the various suggested spectral components are smooth and featureless and could be safely obtained by extrapolating the high statistics data collected on the right shoulder of M1 peak—where all the 2-hole processes leave their footprints.

The multihole processes bring also a more subtle threat to the  $^{163}\text{Ho}$  neutrino mass measurements with the underlying pile-up spectrum: as it can be seen in Figure 29, these higher order transitions cause additional peaks to appear in the end-point vicinity. Although the shape of the pile-up spectrum with its disturbing peaks can be accurately deduced from the high statistics measurement of the spectrum of  $^{163}\text{Ho}$  itself, it is worth noting that in [152] it is shown that the predicted count rate enhancement in the end-point region of the spectrum is accompanied by an increase of the signal-to-background ratio. Moreover, when considering the shake-off transition, most of the additional peak features in the pile-up spectrum are smoothed away.

In the near future, the experiments getting prepared for the neutrino mass measurement will explore the spectrum above the M peaks with increasing statistical precision thereby shedding a light on its actual shape. This will allow a more accurate prediction of the statistical sensitivity and a meaningful attempt to quantify the possible systematic uncertainties.

So far, the attention focused on the high order corrections to the spectrum due to the atomic processes following the EC, while the solid state effects such as the BEFS have been neglected. Although the relatively lower importance of these effects with respect to the multihole transitions presently justifies postponing their analysis, in order to properly analyze high statistics neutrino mass measurements, it will

be mandatory to fully assess how the BEFS manifests itself.  $^{163}\text{Ho}$  case is more complex than  $^{187}\text{Re}$  one (Section 6.3). One marked difference is that the calorimetric spectrum of  $^{163}\text{Ho}$  is a sum of few different spectra, each made up of few different sequences of atomic transitions filling one or more holes, while the spectrum of  $^{187}\text{Re}$  is just one beta transition. The energy spectrum of every atomic electron ejected to the continuum is modulated by the BEFS, but the largest contributions for  $E > E_{M1}$  are expected from the interference patterns in the spectra of the electrons shaken-off in the 2-hole processes with one M1 hole or M2 hole. However, it is likely that in the calorimetric spectrum of  $^{163}\text{Ho}$  the pattern resulting from the summation of the many independent contributions is going to be smoothed and diluted. Moreover, the BEFS depends on the matrix hosting  $^{163}\text{Ho}$  nuclei—which is gold for most of the planned experiments—and on the exact position occupied host lattice by the  $^{163}\text{Ho}$  nucleus. In particular, the BEFS amplitude depends on the lattice structure of the environment closely surrounding the  $^{163}\text{Ho}$  nuclei which is determined by the type of detector absorber and can be affected by the isotope embedding technique. For example, the local damage associated with  $^{163}\text{Ho}$  ion implantation may suppress the BEFS.

**7.5.  $^{163}\text{Ho}$  Production.**  $^{163}\text{Ho}$  is not a naturally occurring isotope: it was discovered at Princeton in a sample of  $^{162}\text{Er}$  that was neutron irradiated in a nuclear reactor [153]. To carry out neutrino mass experiments with  $^{163}\text{Ho}$ , the isotope must be produced in fairly large amounts. Upcoming medium size experiments will have to contain about  $10^{16}$  nuclei of  $^{163}\text{Ho}$ —that is, about  $3\ \mu\text{g}$ —for a total activity of the order of  $10^5$  Bq. The isotope production and separation are critical steps in every plan for an ambitious holmium neutrino mass experiment. There are many nuclear reactions which can be exploited to produce  $^{163}\text{Ho}$ . A comprehensive critical evaluation of all possible  $^{163}\text{Ho}$  production routes is presented

in [154] although, presently, not all the cross sections of the considered processes are experimentally known.

In general, the production process starts with a nuclear reaction, which can be either direct—such as  ${}^{\text{nat}}\text{Dy}(p, xn){}^{163}\text{Ho}$ —or indirect—such as  ${}^{163}\text{Er}(n, \gamma){}^{163}\text{Er} \rightarrow {}^{163}\text{Ho}$ . These reactions unavoidably coproduce other long living radioactive species—also owing to the presence of unnecessary isotopes in the target material—which need to be removed to prevent interferences to the neutrino mass measurement. Chemical separation of holmium can remove most of them, with the notable exception of the beta decaying isomer  ${}^{166m}\text{Ho}$  ( $\tau_{1/2} = 1200$  years,  $E_0 = 1854$  keV). Geant4 Monte Carlo simulations performed for gold absorbers show that each Bq of  ${}^{166m}\text{Ho}$  can contribute, by about 1 count/eV/day, to the background level in the end-point region of  ${}^{163}\text{Ho}$  spectrum [155]. Therefore,  ${}^{166m}\text{Ho}$  must be removed by means of a further isotope mass separation step. The key parameters of the entire process are the  ${}^{163}\text{Ho}$  isotope production rate, the  ${}^{166m}\text{Ho}/{}^{163}\text{Ho}$  ratio, and the efficiencies of chemical and mass separations. They determine the amount of starting material that is required to have the target number of  ${}^{163}\text{Ho}$  nuclei to be embedded in the detector absorbers. Of course, also the final embedding process causes further isotope losses which must be considered, although in some approaches the embedding is part of the production process—for example, when the embedding is achieved by means of the same accelerator used for mass separation. When all efficiencies entering in the process are considered, the  ${}^{163}\text{Ho}$  needed for the next high statistic measurements is likely to increment to tens or hundreds of MBq.

Early experiments used the same process with which the isotope was discovered, that is, neutron irradiation of  ${}^{162}\text{Er}$ . Another route used for past experiments is based on proton spallation with Ta targets. The experiments presented in the following use either neutron irradiation of enriched  ${}^{162}\text{Er}$  targets or proton irradiation of natural Dy targets.

Neutron irradiation of an enriched  ${}^{162}\text{Er}$  sample is a very efficient route. The starting material is usually enriched  $\text{Er}_2\text{O}_3$  which is available as by-product of the production of isotopes for medical applications. The large thermal neutron cross section  $\sigma(n, \gamma) \approx 20$  barns together with the availability of high thermal neutron flux nuclear reactors—as the one of the Institut Laue-Langevin (ILL, Grenoble, France) with a thermal neutron flux of about  $1.3 \times 10^{15}$  n/s/cm<sup>2</sup> [156]—gives an estimated  ${}^{163}\text{Ho}$  production rate of about 50 kBq( ${}^{163}\text{Ho}$ )/week/mg( $\text{Er}_2\text{O}_3$ ), for  $\text{Er}_2\text{O}_3$  enriched at 30% in  ${}^{162}\text{Er}$ . This rate may be reduced by the yet unknown cross section of the burn-up process  ${}^{163}\text{Ho}(n, \gamma){}^{164}\text{Ho}$ . Neutron irradiation causes also the production of  ${}^{166m}\text{Ho}$  owing to the presence of impurities such as  ${}^{164}\text{Er}$  and  ${}^{165}\text{Ho}$  in the enriched  $\text{Er}_2\text{O}_3$  target. If the  ${}^{164}\text{Er}$  route prevails, for a 10% isotopic abundance in the  $\text{Er}_2\text{O}_3$  target, a coproduction of about  $A({}^{166m}\text{Ho})/A({}^{163}\text{Ho}) \approx 0.001$  can be expected. One drawback of this route is the cost for the enriched  ${}^{162}\text{Er}$  procurement.

${}^{163}\text{Ho}$  production via proton irradiation of natural Dy target depends on the proton energy and has a production rate

which is not competitive with high-flux reactors, especially for large amounts. In [154], the production rate as a function of the total cumulative charge is estimated to be about few Bq( ${}^{163}\text{Ho}$ )/ $\mu\text{Ah/g}({}^{\text{nat}}\text{Dy})$  for 24 MeV protons.  ${}^{166m}\text{Ho}$  is produced by the neutrons from the reaction  ${}^{164}\text{Dy}(p, n)$  in  $(n, \gamma)$  captures on  ${}^{164}\text{Dy}$  or on  ${}^{165}\text{Ho}$  contaminations. Monte Carlo simulations give a coproduction lower than  $A({}^{166m}\text{Ho})/A({}^{163}\text{Ho}) \approx 10^{-6}$ . In spite of its low efficiency, the use of a natural target and the limited  ${}^{166m}\text{Ho}$  coproduction make this route appealing for small scale experiments.

**7.6. ECHo.** ECHo is a project carried out by the Heidelberg group in collaboration with many other European and Indian groups [157]. The midterm goal of this project—ECHo-1k—is a medium scale experiment with an array of 1000 MMCs, each implanted with 1 Bq of  ${}^{163}\text{Ho}$  [158]. With energy and time resolutions of at least 5 eV and 1  $\mu\text{s}$ , respectively, a statistical sensitivity of about 20 eV at 90% CL is expected after one year of measurement (Table 4). The microcalorimeters are derived from the gold detectors with Au:Er sensors designed and fabricated by the Heidelberg group for soft X-rays spectroscopy.

So far, the results of two prototypes with  ${}^{163}\text{Ho}$  in the absorbers have been presented. For the first prototype,  ${}^{163}\text{Ho}$  isotope was implanted at the isotope separation online facility ISOLDE (CERN). Here,  ${}^{163}\text{Ho}$  produced by spallation with protons on Ta was accelerated, mass separated, and implanted in the absorbers of four detectors. A total  ${}^{163}\text{Ho}$  activity of  $10^{-2}$  Bq was enclosed between two gold films with dimensions  $190 \times 190 \times 5 \mu\text{m}^3$ . The results of the characterization of these detectors are reported in [131, 159] and include an energy resolution of about 8 eV and a remarkable rise time of about 130 ns. In the high statistics spectrum, the peaks due to a contamination of coproduced  ${}^{144}\text{Pm}$  are visible, although decaying with time. In addition, there are structures on the high energy side of the NI peak which are tentatively interpreted to be due to higher order EC transitions. From this measurement, the intensities of NI and M1 lines give  $Q = 2.800 \pm 0.080_{\text{stat}}$  keV [131].

For the second prototype,  ${}^{163}\text{Ho}$  isotope is produced at the ILL high-flux nuclear reactor by neutron irradiating an enriched  $\text{Er}_2\text{O}_3$  target. The  $\text{Er}_2\text{O}_3$  sample is purified at Mainz both before and after irradiation. The  ${}^{163}\text{Ho}$  in the target is then mass separated and implanted offline at ISOLDE in the absorbers of two maXs-20 chips. The maXs-20 chips are arrays of 16 MMCs designed and optimized for soft X-ray spectroscopy [160]. About 0.2 Bq is encapsulated between two gold layers with dimensions  $250 \times 240 \times 5 \mu\text{m}^3$ . Preliminary measurements (see Figure 30) show an energy resolution of about 12 eV and a strong reduction of the background and confirm the structures on the right side of NI [161]. The persistence of these structures, in spite of the improvements in the background and in the instrumental line shape, supports their interpretation as being due to processes related to the  ${}^{163}\text{Ho}$  EC decay. Another preliminary analysis discussed in [148] interprets these as the broad structures expected for shake-off transitions.

TABLE 4: Comparison of the ECHO, HOLMES, and NuMECS projects.

	ECHO	HOLMES	NUMECS
$^{163}\text{Ho}$ production	$^{162}\text{Er} (n, \gamma)$	$^{162}\text{Er} (n, \gamma)$	Dy ( $p, nx$ )
Absorber	Gold	Gold	Nanoporous gold
Sensor	Au:Er magnetic	TES Mo/Cu	TES Mo/Cu
Present status			
$\Delta E$ at M1 peak [eV]	12	—	43 (incl. $\Gamma_{M1}$ )
$\tau_{\text{rise}}$ [ $\mu\text{s}$ ]	0.13	—	—
$A_{\text{EC}}$ [Bq]	0.2	—	0.1
Projected ( $E_0 = 2800$ eV)			
$N_{\text{det}}$	100	1000	4096
$\Delta E$ [eV]	<5	1	—
$\tau_{\text{rise}}$ [ $\mu\text{s}$ ]	<1	1	—
$A_{\text{EC}}$ [Bq/detector]	10	300	100
$f_{\text{PP}}$	$10^{-6}$	$3 \times 10^{-4}$	—
$t_M$ [y]	1	3	1
$\Sigma_{90}(m_{\nu_e})$ [eV]	10	1.5	1

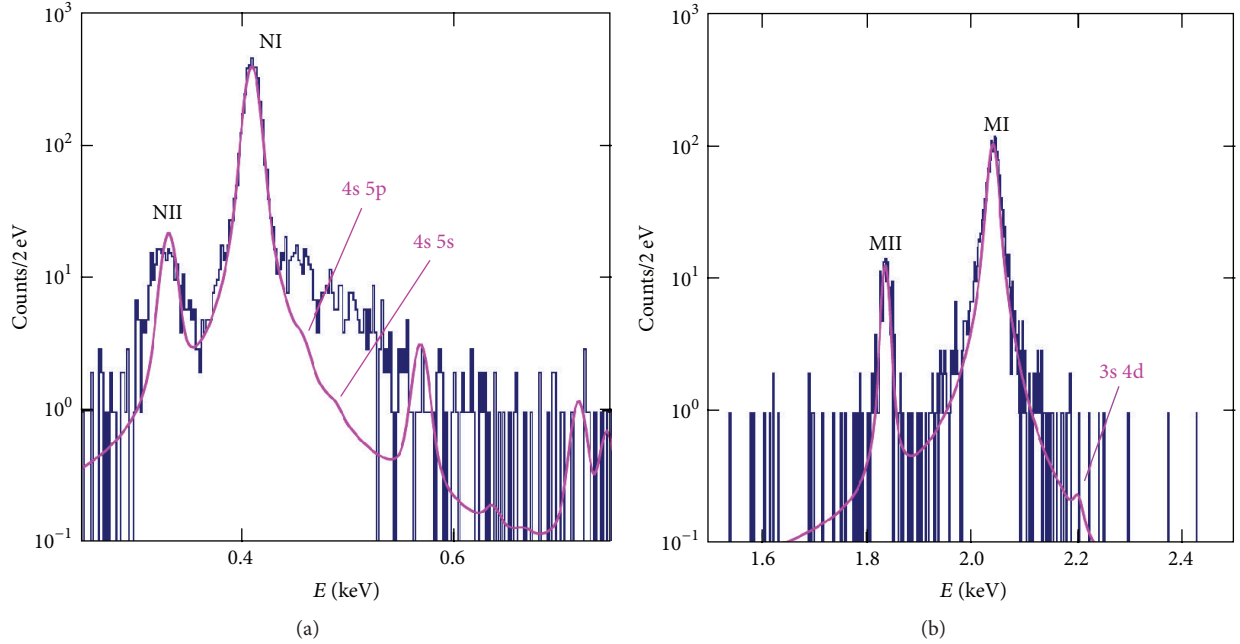


FIGURE 30: Latest measured spectrum from ECHO; see text (from [161]).

Present ECHO activities are aimed at running ECHO-1k in the next years (2016–2018) and include the development of the microwave multiplexed read-out of the MMCs [94], the optimization of MMCs design, and the production of 10 MBq of high purity  $^{163}\text{Ho}$ .

**7.7. HOLMES.** HOLMES is an experiment carried out by the Genoa and Milano groups in collaboration with NIST, ILL, PSI, and Lisbon [155, 162]. The baseline program is to deploy an array of about 1000 TES based microcalorimeters each with about 300 Bq of  $^{163}\text{Ho}$  fully embedded in the absorber, with the goal of energy and time resolutions as close as possible to 1 eV and 1  $\mu\text{s}$ , respectively (Table 4).

In this configuration, HOLMES can collect about  $3 \times 10^{13}$  decays in 3 years of measuring time and the expected  $m_{\nu_e}$  statistical sensitivity is about 1.5 eV at 90% CL. The choice of this configuration is driven by the aim of collecting the highest possible statistics with a reasonable exposure. Despite the high pile-up level and the technical challenge that derives from it, this provides a net improvement on the achievable  $m_{\nu_e}$  sensitivity and a lower impact of the radioactive background.

The amount of  $^{163}\text{Ho}$  needed for the experiment is estimated to be about 100 MBq and it is being produced at ILL by neutron irradiation of an enriched  $\text{Er}_2\text{O}_3$  target, subjected to chemical purification and postseparation at

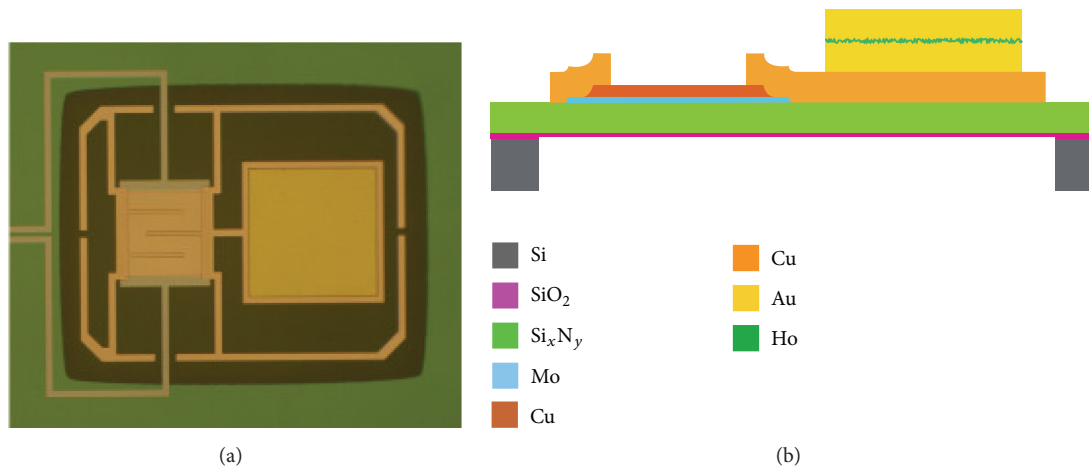


FIGURE 31: Prototype of the TES pixel for HOLMES: picture (a) and layout of the fabrication processes with the  $^{163}\text{Ho}$  implantation (b).

PSI (Villigen, Switzerland). A custom ion implanter is being set up in Genova to embed the isotope in the detector absorbers. It consists of a Penning sputter ion source, a magnetic/electrostatic mass analyzer, an acceleration section, and an electrostatic scanning stage. The full system is being designed to achieve an optimal mass separation of  $^{163}\text{Ho}$  versus  $^{166m}\text{Ho}$ . The implanter will be integrated with a vacuum chamber for the simultaneous evaporation of gold, first to control the  $^{163}\text{Ho}$  concentration and then to deposit a final Au layer to prevent  $^{163}\text{Ho}$  from oxidizing. The cathode of the ion source will be made of high purity metallic holmium to avoid end-point deformations due to the different  $Q$  shifts in diverse chemical species. The metallic holmium will be obtained by thermal reduction at about 2000 K, using the reaction  $\text{Ho}_2\text{O}_3 + 2\text{Y}(\text{met}) \rightarrow 2\text{Ho}(\text{met}) + \text{Y}_2\text{O}_3$  [132].

HOLMES uses TES microcalorimeter arrays with  $\mu\text{MUX}$  read-out, both fabricated at NIST (Boulder, USA). The DAQ exploits the Reconfigurable Open Architecture Computing Hardware (ROACH2) board equipped with a Xilinx Virtex 6 field programmable gate array (FPGA) [92], which has been developed in the framework of CASPER (Collaboration for Astronomy Signal Processing and Electronic Research).

Presently, the collaboration is working on the optimization of the isotope production processes. Two  $\text{Er}_2\text{O}_3$  samples have been irradiated at ILL and processed at PSI. ICP-MS is used to assess the amount of  $^{163}\text{Ho}$  produced and the efficiency of the chemical separation. From preliminary assessments, the total available  $^{163}\text{Ho}$  activity is about 50–100 MBq.

The optimization of the pixel design is also in progress [163] and Figure 31 shows the design that best matches HOLMES specifications. The absorber is made of gold and to avoid interference to the superconducting transition, it is placed side-by-side with the Mo/Cu sensor on a silicon nitride membrane. The design also includes features to control the microcalorimeter speed. Energy and time resolutions are within factors 2-3 of the target ones, owing also to new algorithms for pixel-identification [164, 165].

HOLMES is expected to start data taking in 2018, but a smaller scale experiment with a limited number of pixels will run in 2017, with the aim of collecting a statistics of about  $10^{10}$  decays in a few months.

**7.8. NuMECS.** NuMECS is a collaboration of several US institutions (LANL, NIST, NSCL, and CMU) with the goal to critically assess the potential of holmium calorimetric neutrino mass measurements [166]. The NuMECS program includes the validation of the isotope production, purification, and sensor incorporation techniques, the scalability to high resolution LTD arrays, and the understanding of underlying nuclear and atomic physics.

Recent work has successfully tested  $^{163}\text{Ho}$  production via proton irradiation of a natural dysprosium target. About 3 MBq of  $^{163}\text{Ho}$  has been produced by irradiating about 13 g of high purity natural dysprosium with  $3.4 \times 10^4 \mu\text{Ah}$  of 25 MeV protons at the Los Alamos National Laboratory Isotope Production Facility (IPF). At the same time, a cation-exchange high performance liquid chromatography (HPLC) procedure for the chemical separation of holmium has been developed and a separation efficiency of about 70% has been measured.

For the present testing phase, NuMECS uses TES microcalorimeters fabricated by NIST and specially designed to be mechanically robust. The TES sensor is at the end of a silicon beam, close to a pad used for testing the attachment of a wide range of absorbers (Figure 32).

To incorporate the isotope in the microcalorimeter absorber, NuMECS exploits the drying of solutions containing  $^{163}\text{Ho}$  isotope onto thin gold foils. After testing many procedures, the best results were recently obtained by deposition of an aqueous solution on nanoporous gold on a regular gold foil, followed by annealing in dilute  $\text{H}_2$  atmosphere at  $800^\circ\text{C}$ . The microcalorimeter absorber is made by folding and pressing a small piece of the gold foil.

Figure 32 shows a spectrum collected in 40 hours [167].  $^{163}\text{Ho}$  activity is about 0.1 Bq. Peaks have a low energy tail

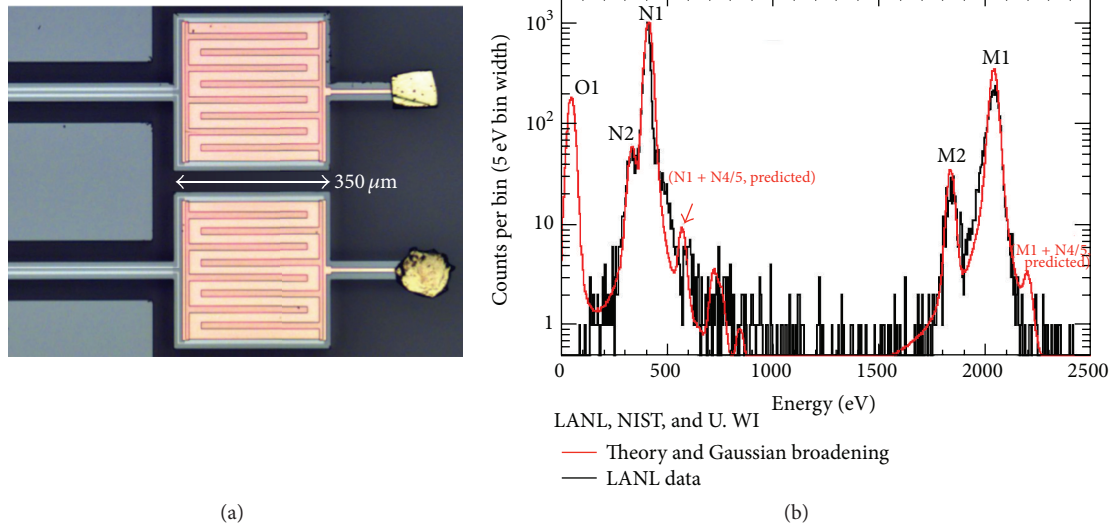


FIGURE 32: NuMECS TES detectors (a) and the latest spectrum measured from NuMECS (b); see text (from [167]).

and show an excess broadening, explained as caused by thermalization noise. A fit of the M1 peak gives  $\Delta E_{\text{FWHM}}$  of about 43 eV, inclusive of the peak natural width. All peaks are found within 1% of the tabulated positions. Remarkably, the spectrum does not show any of the satellite peaks predicted in [168], although the statistics is still limited. There is instead an unexplained shoulder on the high energy side of the N1 peak, which resembles the structure observed by ECHO and interpreted as shake-off transition in [148].

NuMECS future plans include the deployment of four 1024 pixel arrays, aiming at a  $m_{\nu_e}$  statistical sensitivity of about 1 eV.

## 8. Summary and Outlook

The use of  $^{187}\text{Re}$  and  $^{163}\text{Ho}$  as an alternative to tritium for the direct measurement of the neutrino mass was proposed in the same years when the low temperature detector technology was moving the first steps. The idea of making low temperature detectors with rhenium absorbers immediately caught on, both because it appeared to be of almost immediate realization and because it could have an appealing impact on X-ray spectroscopy. Unfortunately, in the long run, the technological difficulties inherent to the use of superconducting rhenium caused the interest of the low temperature detector community to fade away and the neutrino mass projects to have the same fate as the X-ray applications of rhenium detectors.

$^{163}\text{Ho}$  measurements took more time to take off, as if they were awaiting the readiness of the technology of microcalorimeter arrays applied to high resolution spectroscopy of soft X-rays. Now,  $^{163}\text{Ho}$  neutrino mass experiments are ready to leverage this mature technology, and the interest of the low temperature detector community is high, as demonstrated by the number of parallel efforts. Despite the unluckily high Q value, the good prospects to perform high statistics neutrino mass measurements in the next couple of years are also

attracting the attention of the neutrino physics community as a valid complementary alternative to KATRIN.

## Competing Interests

The author declares that there are no competing interests.

## Acknowledgments

The author would like to thank Andrea Giachero, Marco Faverezani, Elena Ferri, Andrei Puiu, and Monica Sisti, who in various ways supported him with the writing of this paper; Maurizio Lusignoli and Alvaro De Rújula, for the many useful discussions; Adriano Filipponi, for the unvaluable discussions on the BEFS; and Loredana Gastaldo, Michael Rabin, and Mark Philip Croce, for providing him with updated information on their experiments.

## References

- [1] K. Olive and P. D. Group, “Review of particle physics,” *Chinese Physics C*, vol. 38, no. 9, Article ID 090001, 2014.
- [2] D. Boyanovsky, H. J. De Vega, and N. G. Sanchez, “Constraints on dark matter particles from theory, galaxy observations, and N-body simulations,” *Physical Review D*, vol. 77, no. 4, Article ID 043518, 2008.
- [3] S. Hannestad, “Neutrino physics from precision cosmology,” *Progress in Particle and Nuclear Physics*, vol. 65, no. 2, pp. 185–208, 2010.
- [4] K. N. Abazajian, E. Calabrese, A. Cooray et al., “Cosmological and astrophysical neutrino mass measurements,” *Astroparticle Physics*, vol. 35, no. 4, pp. 177–184, 2011.
- [5] P. A. R. Ade, N. Aghanim, C. Armitage-Caplan et al., “Planck 2013 results. XVI. Cosmological parameters,” *Astronomy & Astrophysics*, vol. 571, article A16, 66 pages, 2014.
- [6] C. Giunti and C. W. Kim, *Fundamentals of Neutrino Physics and Astrophysics*, Oxford University Press, Oxford, UK, 2007.

- [7] G. Mention, M. Fechner, T. Lasserre et al., “Reactor antineutrino anomaly,” *Physical Review D—Particles, Fields, Gravitation and Cosmology*, vol. 83, no. 7, Article ID 073006, 2011.
- [8] X. Qian and P. Vogel, “Neutrino mass hierarchy,” *Progress in Particle and Nuclear Physics*, vol. 83, pp. 1–30, 2015.
- [9] K. N. Abazajian, M. Acero, S. Agarwalla et al., “Light sterile neutrinos: a white paper,” <http://arxiv.org/abs/1204.5379>.
- [10] C. Destri, H. J. De Vega, and N. G. Sanchez, “Fermionic warm dark matter produces galaxy cores in the observed scales because of quantum mechanics,” *New Astronomy*, vol. 22, pp. 39–50, 2013.
- [11] M. Nakagawa, H. Okonogi, S. Sakata, and A. Toyoda, “Possible existence of a neutrino with mass and partial conservation of muon charge,” *Progress of Theoretical Physics*, vol. 30, no. 5, pp. 727–729, 1963.
- [12] R. Shrock, “New tests for and bounds on neutrino masses and lepton mixing,” *Physics Letters B*, vol. 96, no. 1-2, pp. 159–164, 1980.
- [13] V. N. Aseev, A. I. Belesev, A. I. Berlev et al., “Upper limit on the electron antineutrino mass from the Troitsk experiment,” *Physical Review D*, vol. 84, Article ID 112003, 2011.
- [14] C. Kraus, B. Bornschein, L. Bornschein et al., “Final results from phase II of the Mainz neutrino mass search in tritium  $\beta$  decay,” *The European Physical Journal C: Particles and Fields*, vol. 40, no. 4, pp. 447–468, 2005.
- [15] J. Schechter and J. W. F. Valle, “Neutrinoless double- $\beta$  decay in  $su(2) \times u(1)$  theories,” *Physical Review D*, vol. 25, no. 11, article 2951, 1982.
- [16] S. R. Elliott and P. Vogel, “Double beta decay,” *Annual Review of Nuclear and Particle Science*, vol. 52, pp. 115–151, 2002.
- [17] S. Pascoli, S. T. Petcov, and W. Rodejohann, “On the CP violation associated with Majorana neutrinos and neutrinoless double-beta decay,” *Physics Letters B*, vol. 549, no. 1-2, pp. 177–193, 2002.
- [18] S. Dell’Oro, S. Marcocci, and F. Vissani, “New expectations and uncertainties on neutrinoless double beta decay,” *Physical Review D*, vol. 90, no. 3, Article ID 033005, 2014.
- [19] F. Perrin, “Possibilité d’émission de particules neutres de masse intrinsèque nulle dans les radioactivités  $\beta$ ,” *Comptes Rendues*, vol. 197, pp. 1625–1627, 1933.
- [20] E. Fermi, “An attempt of a theory of beta radiation. 1,” *Zeitschrift für Physik*, vol. 88, no. 3, pp. 161–177, 1934.
- [21] K.-E. Bergkvist, “A high-luminosity, high-resolution study of the end-point behaviour of the tritium  $\beta$ -spectrum (I). basic experimental procedure and analysis with regard to neutrino mass and neutrino degeneracy,” *Nuclear Physics B*, vol. 39, pp. 317–370, 1972.
- [22] K.-E. Bergkvist, “A high-luminosity, high-resolution study of the end-point behaviour of the tritium  $\beta$ -spectrum (II). The end-point energy of the spectrum. Comparison of the experimental axial-vector matrix element with predictions based on PCAC,” *Nuclear Physics B*, vol. 39, pp. 371–406, 1972.
- [23] V. Lubimov, E. Novikov, V. Nozik, E. Tretyakov, and V. Kosik, “An estimate of the  $\nu e$  mass from the  $\beta$ -spectrum of tritium in the valine molecule,” *Physics Letters B*, vol. 94, no. 2, pp. 266–268, 1980.
- [24] R. G. H. Robertson and D. A. Knapp, “Direct measurements of neutrino mass,” *Annual Review of Nuclear and Particle Science*, vol. 38, no. 1, pp. 185–215, 1988.
- [25] K. E. Bergkvist, “A questioning of a claim of evidence of finite neutrino mass,” *Physics Letters B*, vol. 154, no. 2-3, pp. 224–230, 1985.
- [26] K.-E. Bergkvist, “On some atomic effects in the tritium  $\beta$ -spectrum,” *Physica Scripta*, vol. 4, no. 1-2, p. 23, 1971.
- [27] C. Weinheimer, M. Przyrembel, H. Backe et al., “Improved limit on the electron-antineutrino rest mass from tritium  $\beta$ -decay,” *Physics Letters B*, vol. 300, no. 3, pp. 210–216, 1993.
- [28] A. I. Belesev, A. I. Bleule, E. V. Geraskin et al., “Results of the troitsk experiment on the search for the electron antineutrino rest mass in tritium beta-decay,” *Physics Letters B*, vol. 350, no. 2, pp. 263–272, 1995.
- [29] G. Drexlin, V. Hannen, S. Mertens, and C. Weinheimer, “Current direct neutrino mass experiments,” *Advances in High Energy Physics*, vol. 2013, Article ID 293986, 39 pages, 2013.
- [30] A. De Rújula, “A new way to measure neutrino masses,” *Nuclear Physics B*, vol. 188, no. 3, pp. 414–458, 1981.
- [31] W. Bambynek, H. Behrens, M. H. Chen et al., “Orbital electron capture by the nucleus,” *Reviews of Modern Physics*, vol. 49, no. 1, pp. 77–221, 1977.
- [32] A. De Rújula and M. Lusignoli, “Single electron ejection in electron capture as a tool to measure the electron neutrino mass,” *Nuclear Physics B*, vol. 219, no. 2, pp. 277–301, 1983.
- [33] K. Riisager, A. de Rújula, P. Hansen, B. Jonson, and H. Ravn, “The internal bremsstrahlung spectra from the EC  $\beta$  decay of  $^{193}\text{Pt}$  and  $^{163}\text{Ho}$ ,” *Physica Scripta*, vol. 31, no. 5, article 321, 1985.
- [34] P. T. Springer, C. L. Bennett, and P. A. Baisden, “Measurement of the neutrino mass using the inner bremsstrahlung emitted in the electron-capture decay of  $^{163}\text{Ho}$ ,” *Physical Review A*, vol. 35, no. 2, pp. 679–689, 1987.
- [35] B. Jonson, J. U. Andersen, G. J. Beyer et al., “Determination of the electron-neutrino mass from experiments on electron-capture beta decay,” *Nuclear Physics A*, vol. 396, pp. 479–493, 1983.
- [36] S. Yasumi, G. Rajasekaran, M. Ando et al., “The mass of the electron neutrino and electron capture in  $^{163}\text{Ho}$ ,” *Physics Letters B*, vol. 122, no. 5-6, pp. 461–464, 1983.
- [37] S. Yasumi, M. Ando, H. Maezawa et al., “The mass of the electron neutrino using electron capture in  $^{163}\text{Ho}$ ,” *Physics Letters B*, vol. 181, no. 1-2, pp. 169–172, 1986.
- [38] S. Yasumi, H. Maezawa, K. Shima et al., “The mass of the electron neutrino from electron capture in  $^{163}\text{Ho}$ ,” *Physics Letters B*, vol. 334, no. 1-2, pp. 229–233, 1994.
- [39] C. L. Bennett, A. L. Hallin, R. A. Naumann et al., “The X-ray spectrum following  $^{163}\text{Ho}$  M electron capture,” *Physics Letters B*, vol. 107, no. 1-2, pp. 19–22, 1981.
- [40] E. Laegsgaard, J. U. Andersen, G.-J. Beyer et al., “The capture ratio N/M in the EC beta decay of  $^{163}\text{Ho}$ ,” in *Proceedings of the 7th International Conference on Atomic Masses and Fundamental Constants*, pp. 652–658, Darmstadt, Germany, September 1984.
- [41] F. X. Hartmann and R. A. Naumann, “Observation of N and M orbital-electron capture in the decay of  $^{163}\text{Ho}$ ,” *Physical Review C*, vol. 31, no. 4, pp. 1594–1596, 1985.
- [42] F. X. Hartmann and R. A. Naumann, “High temperature gas proportional detector techniques and application to the neutrino mass limit using  $^{163}\text{Ho}$ ,” *Nuclear Instruments and Methods in Physics Research, Section A: Accelerators, Spectrometers, Detectors and Associated Equipment*, vol. 313, no. 1-2, pp. 237–260, 1992.
- [43] A. De Rújula and M. Lusignoli, “Calorimetric measurements of  $^{163}\text{holmium}$  decay as tools to determine the electron neutrino mass,” *Physics Letters B*, vol. 118, no. 4–6, pp. 429–434, 1982.

- [44] J. Angrik, T. Armbrust, A. Beglarian et al., *KATRIN Design Report 2004*, 2005.
- [45] B. Monreal and J. A. Formaggio, "Relativistic cyclotron radiation detection of tritium decay electrons as a new technique for measuring the neutrino mass," *Physical Review D*, vol. 80, no. 5, Article ID 051301, 2009.
- [46] D. M. Asner, R. F. Bradley, L. de Viveiros et al., "Single-electron detection and spectroscopy via relativistic cyclotron radiation," *Physical Review Letters*, vol. 114, no. 16, Article ID 162501, 2015.
- [47] J. J. Simpson, "Limits on the emission of heavy neutrinos in  $^3\text{H}$  decay," *Physical Review D*, vol. 24, no. 11, pp. 2971–2972, 1981.
- [48] C. Cheng-Rui and H. Tso-Hsiu, "On the determination of neutrino mass—a critical status report," *Physics Reports*, vol. 112, no. 1, pp. 1–51, 1984.
- [49] A. Franklin, "The appearance and disappearance of the 17-keV neutrino," *Reviews of Modern Physics*, vol. 67, no. 2, pp. 457–490, 1995.
- [50] F. E. Wietfeldt and E. B. Norman, "The 17 keV neutrino," *Physics Report*, vol. 273, no. 3, pp. 149–197, 1996.
- [51] J. J. Simpson, "Evidence of heavy-neutrino emission in beta decay," *Physical Review Letters*, vol. 54, no. 17, pp. 1891–1893, 1985.
- [52] H. Abele, G. Helm, U. Kania, C. Schmidt, J. Last, and D. Dubbers, "On the origin of the 17 keV neutrino signals, and a loss-free measurement of the  $^{35}\text{S}$   $\beta$ -spectrum," *Physics Letters B*, vol. 316, no. 1, pp. 26–31, 1993.
- [53] S. E. Koonin, "Environmental fine structure in low-energy  $\beta$ -particle spectra," *Nature*, vol. 354, pp. 468–470, 1991.
- [54] A. Nucciotti, E. Ferri, and O. Cremonesi, "Expectations for a new calorimetric neutrino mass experiment," *Astroparticle Physics*, vol. 34, no. 2, pp. 80–89, 2010.
- [55] E. Fiorini and T. O. Niinikoski, "Low-temperature calorimetry for rare decays," *Nuclear Instruments and Methods In Physics Research*, vol. 224, no. 1-2, pp. 83–88, 1984.
- [56] S. H. Moseley, J. C. Mather, and D. McCammon, "Thermal detectors as x-ray spectrometers," *Journal of Applied Physics*, vol. 56, no. 5, pp. 1257–1262, 1984.
- [57] D. McCammon, S. H. Moseley, J. C. Mather, and R. F. Mushotzky, "Experimental tests of a single-photon calorimeter for X-ray spectroscopy," *Journal of Applied Physics*, vol. 56, no. 5, pp. 1263–1266, 1984.
- [58] V. Barger and D. Cline, *Neutrino Mass and Low Energy Weak Interactions, Telemark, 1984*, World Scientific, River Edge, NJ, USA, 1985.
- [59] A. Blasi et al., I.N.F.N./BE-85/2, internalreport, 1985.
- [60] N. Coron, G. Dambier, G. J. Focker et al., "A composite bolometer as a charged-particle spectrometer," *Nature*, vol. 314, no. 6006, pp. 75–76, 1985.
- [61] R. J. Gaitskell, L. C. Angrave, N. B. Booth, A. D. Hahn, G. L. Salmon, and A. M. Swift, "A measurement of the beta spectrum of  $^{63}\text{Ni}$  using a new type of calorimetric cryogenic detector," *Nuclear Instruments and Methods in Physics Research, Section A: Accelerators, Spectrometers, Detectors and Associated Equipment*, vol. 370, no. 1, pp. 250–252, 1996.
- [62] L. C. Angrave, N. E. Booth, R. J. Gaitskell, G. L. Salmon, and M. R. Harston, "Measurement of the atomic exchange effect in nuclear  $\beta$  decay," *Physical Review Letters*, vol. 80, no. 8, p. 1610, 1998.
- [63] D. Deptuck, L. S. Erhardt, and J. P. Harrison, "Achievable neutrino mass limits from calorimetric beta spectroscopy," *Nuclear Instruments and Methods in Physics Research Section A: Accelerators, Spectrometers, Detectors and Associated Equipment*, vol. 444, no. 1-2, pp. 80–83, 2000.
- [64] L. S. Erhardt, D. Deptuck, and J. P. Harrison, "Transition-edge microcalorimeter for tritium beta decay," *Nuclear Instruments and Methods in Physics Research, Section A: Accelerators, Spectrometers, Detectors and Associated Equipment*, vol. 444, no. 1-2, pp. 92–95, 2000.
- [65] C. Enss, *Cryogenic Particle Detection*, vol. 99 of *Topics in Applied Physics*, Springer, Berlin, Germany, 2005.
- [66] E. Skirokoff, "Proceedings, 15th International Workshop on Low Temperature Detectors (LTD-15): Pasadena, California, June 24–28, 2013," *Journal of Low Temperature Physics*, vol. 176, no. 3–6, pp. 131–1108, 2014.
- [67] C. Enss and S. Hunklinger, *Low-Temperature Physics*, Springer, Berlin, Germany, 2005.
- [68] D. Twerenbold, "Cryogenic particle detectors," *Reports on Progress in Physics*, vol. 59, no. 3, pp. 349–426, 1996.
- [69] M. Chapellier, "Physics of electrons and phonons in low-temperature detectors," *Nuclear Instruments and Methods in Physics Research Section A: Accelerators, Spectrometers, Detectors and Associated Equipment*, vol. 520, no. 1–3, pp. 21–26, 2004, Proceedings of the 10th International Workshop on Low Temperature Detectors.
- [70] J. N. Ullom and D. A. Bennett, "Review of superconducting transition-edge sensors for X-ray and gamma-ray spectroscopy," *Superconductor Science and Technology*, vol. 28, no. 8, Article ID 084003, 2015.
- [71] M. Nahum, J. M. Martinis, and S. Castles, "Hot-electron microcalorimeters for X-ray and phonon detection," *Journal of Low Temperature Physics*, vol. 93, no. 3-4, pp. 733–738, 1993.
- [72] K. Irwin, G. Hilton, J. Martinis, and B. Cabrera, "A hot-electron microcalorimeter for X-ray detection using a superconducting transition edge sensor with electrothermal feedback," *Nuclear Instruments and Methods in Physics Research Section A: Accelerators, Spectrometers, Detectors and Associated Equipment*, vol. 370, no. 1, pp. 177–179, 1996.
- [73] D. Van Vechten and K. S. Wood, "Probability of quasiparticle self-trapping due to localized energy deposition in nonequilibrium tunnel-junction detectors," *Physical Review B*, vol. 43, no. 16, pp. 12852–12860, 1991.
- [74] A. Zehnder, "Response of superconductive films to localized energy deposition," *Physical Review B*, vol. 52, no. 17, p. 12858, 1995.
- [75] A. G. Kozorezov, A. F. Volkov, J. K. Wigmore, A. Peacock, A. Poelaert, and R. Den Hartog, "Quasiparticle-phonon downconversion in nonequilibrium superconductors," *Physical Review B—Condensed Matter and Materials Physics*, vol. 61, no. 17, pp. 11807–11819, 2000.
- [76] S. B. Kaplan, C. C. Chi, D. N. Langenberg, J. J. Chang, S. Jafarey, and D. J. Scalapino, "Quasiparticle and phonon lifetimes in superconductors," *Physical Review B*, vol. 14, no. 11, pp. 4854–4873, 1976.
- [77] M. Faverzani, P. Day, A. Nucciotti, and E. Ferri, "Developments of microresonators detectors for neutrino physics in Milan," *Journal of Low Temperature Physics*, vol. 167, no. 5-6, pp. 1041–1047, 2012.
- [78] J. Zhang, W. Cui, M. Juda et al., "Hopping conduction in partially compensated doped silicon," *Physical Review B*, vol. 48, no. 4, p. 2312, 1993.

- [79] E. E. Haller, N. P. Palaio, M. Rodder, W. L. Hansen, and E. Kreysa, "NTD germanium: a novel material for low temperature bolometers," in *Neutron Transmutation Doping of Semiconductor Materials*, pp. 21–36, Springer, New York, NY, USA, 1984.
- [80] E. E. Haller, "Advanced far-infrared detectors," *Infrared Physics and Technology*, vol. 35, no. 2-3, pp. 127–146, 1994.
- [81] J. Zhang, W. Cui, M. Juda et al., "Non-Ohmic effects in hopping conduction in doped silicon and germanium between 0.05 and 1 K," *Physical Review B*, vol. 57, no. 8, pp. 4472–4481, 1998.
- [82] É. Aubourg, A. Cummings, T. Shutt et al., "Measurement of electron-phonon decoupling time in neutron-transmutation doped germanium at 20 mK," *Journal of Low Temperature Physics*, vol. 93, no. 3-4, pp. 289–294, 1993.
- [83] K. D. Irwin, "An application of electrothermal feedback for high resolution cryogenic particle detection," *Applied Physics Letters*, vol. 66, no. 15, pp. 1998–2000, 1995.
- [84] A. Fleischmann, L. Gastaldo, S. Kempf et al., "Metallic magnetic calorimeters," *AIP Conference Proceedings*, vol. 1185, pp. 571–578, 2009.
- [85] W.-T. Hsieh, J. A. Adams, S. R. Bandler et al., "Fabrication of metallic magnetic calorimeter X-ray detector arrays," *Journal of Low Temperature Physics*, vol. 151, no. 1-2, pp. 357–362, 2008.
- [86] A. Burck, S. Kempf, S. Schäfer et al., "Microstructured magnetic calorimeter with Meander-shaped pickup coil," *Journal of Low Temperature Physics*, vol. 151, no. 1-2, pp. 337–344, 2008.
- [87] C. D. Reintsema, J. Beyer, S. W. Nam et al., "Prototype system for superconducting quantum interference device multiplexing of large-format transition-edge sensor arrays," *Review of Scientific Instruments*, vol. 74, no. 10, pp. 4500–4508, 2003.
- [88] M. A. Dobbs, M. Lueker, K. A. Aird et al., "Frequency multiplexed superconducting quantum interference device readout of large bolometer arrays for cosmic microwave background measurements," *Review of Scientific Instruments*, vol. 83, no. 7, Article ID 073113, 2012.
- [89] G. M. Stiehl, W. B. Doriese, J. W. Fowler et al., "Code-division multiplexing for X-ray microcalorimeters," *Applied Physics Letters*, vol. 100, no. 7, Article ID 072601, 2012.
- [90] O. Noroozian, J. A. B. Mates, D. A. Bennett et al., "High-resolution gamma-ray spectroscopy with a microwave-multiplexed transition-edge sensor array," *Applied Physics Letters*, vol. 103, no. 20, Article ID 202602, 2013.
- [91] S. R. Dicker, P. A. R. Ade, J. Aguirre et al., "MUSTANG2: a large focal plan array for the 100 meter Green Bank Telescope," in *Millimeter, Submillimeter, and Far-Infrared Detectors and Instrumentation for Astronomy VII*, vol. 9153 of *Proceedings of SPIE*, Montreal, Canada, July 2014.
- [92] S. McHugh, B. A. Mazin, B. Serfass et al., "A readout for large arrays of microwave kinetic inductance detectors," *Review of Scientific Instruments*, vol. 83, no. 4, Article ID 044702, 2012.
- [93] O. Bourrion, C. Vescovi, A. Catalano et al., "High speed readout electronics development for frequency-multiplexed kinetic inductance detector design optimization," *Journal of Instrumentation*, vol. 8, no. 12, Article ID C12006, 2013.
- [94] S. Kempf, M. Wegner, L. Gastaldo, A. Fleischmann, and C. Enss, "Multiplexed readout of MMC detector arrays using non-hysteretic rf-SQUIDS," *Journal of Low Temperature Physics*, vol. 176, no. 3-4, pp. 426–432, 2014.
- [95] E. Gatti and P. F. Manfredi, "Processing the signals from solid-state detectors in elementary-particle physics," *La Rivista del Nuovo Cimento*, vol. 9, no. 1, pp. 1–146, 1986.
- [96] P. E. Filianin, K. Blaum, S. A. Eliseev et al., "On the keV sterile neutrino search in electron capture," *Journal of Physics G: Nuclear and Particle Physics*, vol. 41, no. 9, Article ID 095004, 2014.
- [97] R. Lazauskas, P. Vogel, and C. Volpe, "Charged current cross section for massive cosmological neutrinos impinging on radioactive nuclei," *Journal of Physics G: Nuclear and Particle Physics*, vol. 35, no. 2, Article ID 025001, 2008.
- [98] A. G. Cocco, G. Mangano, and M. Messina, "Probing low energy neutrino backgrounds with neutrino capture on beta decaying nuclei," *Journal of Cosmology and Astroparticle Physics*, no. 6, article 015, 2007.
- [99] R. Hodák, F. Šimkovic, S. Kovalenko, and A. Faessler, "Towards the detection of light and heavy relic neutrinos," *Progress in Particle and Nuclear Physics*, vol. 66, no. 2, pp. 452–456, 2011.
- [100] M. Lusignoli and M. Vignati, "Relic antineutrino capture on  $^{163}\text{Ho}$  decaying nuclei," *Physics Letters B*, vol. 697, no. 1, pp. 11–14, 2011.
- [101] M. Vignati and M. Lusignoli, " $^{163}\text{Ho}$  as a target for cosmic antineutrinos," *Journal of Physics: Conference Series*, vol. 375, no. 4, Article ID 042006, 2012.
- [102] S. Betts, W. R. Blanchard, R. H. Carnevale et al., "Development of a relic neutrino detection experiment at PTOLEMY: princeton tritium observatory for light, early-universe, massive-neutrino yield," <http://arxiv.org/abs/1307.4738>.
- [103] Y. F. Li and Z.-Z. Xing, "A possible detection of the cosmic antineutrino background in the presence of flavor effects," *Physics Letters B*, vol. 698, no. 5, pp. 430–437, 2011.
- [104] Y. F. Li and Z.-Z. Xing, "Captures of hot and warm sterile antineutrino dark matter on EC-decaying  $^{63}\text{Ho}$  nuclei," *Journal of Cosmology and Astroparticle Physics*, vol. 2011, no. 8, article 006, 2011.
- [105] C. K. Stahle, *The development of high-resolution calorimetric X-ray detectors for Compton scattering experiments [Ph.D. thesis]*, Stanford University, 1992.
- [106] C. K. Stahle, D. Osheroff, R. L. Kelley, S. H. Moseley, and A. E. Szymkowiak, "Adapting calorimetric X-ray detectors for Compton scattering experiments performed at high energies," *Nuclear Instruments and Methods in Physics Research Section A: Accelerators, Spectrometers, Detectors and Associated Equipment*, vol. 319, no. 1-3, pp. 393–399, 1992.
- [107] P. E. Gregers-Hansen, M. Krusius, and G. R. Pickett, "Sign of the nuclear quadrupole interaction in rhenium metal," *Physical Review Letters*, vol. 27, no. 1, pp. 38–41, 1971.
- [108] R. Dvornický, K. Muto, F. Šimkovic, and A. Faessler, "Absolute mass of neutrinos and the first unique forbidden  $\beta$  decay of  $^{187}\text{Re}$ ," *Physical Review C*, vol. 83, no. 4, Article ID 045502, 2011.
- [109] H. J. De Vega, O. Moreno, E. M. De Guerra, M. Ramón Medrano, and N. G. Sánchez, "Role of sterile neutrino warm dark matter in rhenium and tritium beta decays," *Nuclear Physics B*, vol. 866, no. 2, pp. 177–195, 2013.
- [110] C. Arnaboldi, G. Benedek, C. Brofferio et al., "Measurement of the  $p$  to  $s$  wave branching ratio of  $^{187}\text{Re}$   $\beta$  decay from beta environmental fine structure," *Physical Review Letters*, vol. 96, no. 4, Article ID 042503, 2006.
- [111] J.-P. Porst, S. R. Bandler, J. S. Adams et al., "Characterization and performance of magnetic calorimeters for applications in X-ray spectroscopy," *Journal of Low Temperature Physics*, vol. 176, no. 5-6, pp. 617–623, 2014.
- [112] E. Cosulich, F. Gatti, and S. Vitale, "Further results on  $\mu$ -calorimeters with superconducting absorber," *Journal of Low Temperature Physics*, vol. 93, no. 3-4, pp. 263–268, 1993.

- [113] E. Cosulich, G. Gallinaro, F. Gatti, and S. Vitale, "Detection of  $^{187}\text{Re}$  beta decay with a cryogenic microcalorimeter. Preliminary results," *Physics Letters B*, vol. 295, no. 1, pp. 143–147, 1992.
- [114] M. Galeazzi, F. Fontanelli, F. Gatti, and S. Vitale, "End-point energy and half-life of the  $^{187}\text{Re}$   $\beta$  decay," *Physical Review C*, vol. 63, no. 1, Article ID 014302, 2000.
- [115] F. Fontanelli, M. Galeazzi, F. Gatti, A. M. Swift, and S. Vitale, "Data analysis in  $\beta$ -spectroscopy with cryogenic detectors," *Nuclear Instruments and Methods in Physics Research Section A: Accelerators, Spectrometers, Detectors and Associated Equipment*, vol. 421, no. 3, pp. 464–470, 1999.
- [116] F. Gatti, "Microcalorimeter measurements," *Nuclear Physics B—Proceedings Supplements*, vol. 91, no. 1, pp. 293–296, 2001.
- [117] M. Sisti, C. Arnaboldi, C. Brofferio et al., "New limits from the Milano neutrino mass experiment with thermal microcalorimeters," *Nuclear Instruments and Methods in Physics Research, Section A: Accelerators, Spectrometers, Detectors and Associated Equipment*, vol. 520, no. 1–3, pp. 125–131, 2004.
- [118] F. Gatti, F. Fontanelli, M. Galeazzi, A. M. Swift, and S. Vitale, "Detection of environmental fine structure in the low-energy  $\beta$ -decay spectrum of  $^{187}\text{Re}$ ," *Nature*, vol. 397, no. 6715, pp. 137–139, 1999.
- [119] M. Galeazzi, F. Fontanelli, F. Gatti, and S. Vitale, "Limits on the existence of heavy neutrinos in the range 50–1000 eV from the study of the  $^{187}\text{Re}$  beta decay," *Physical Review Letters*, vol. 86, no. 10, pp. 1978–1981, 2001.
- [120] K.-H. Hiddeman, H. Daniel, and O. Schwentker, "Limits on neutrino masses from the tritium beta spectrum," *Journal of Physics G: Nuclear and Particle Physics*, vol. 21, no. 5, p. 639, 1995.
- [121] A. Alessandrello, C. Brofferio, C. Cattadori et al., "Fabrication and low-temperature characterization of Si-implanted thermistors," *Journal of Physics D: Applied Physics*, vol. 32, no. 24, pp. 3099–3110, 1999.
- [122] A. Faes, F. Giacomozzi, B. Margesin, and A. Nucciotti, "Fabrication of silicon bolometers with bulk micromachining technology," *Nuclear Instruments and Methods in Physics Research, Section A: Accelerators, Spectrometers, Detectors and Associated Equipment*, vol. 520, no. 1–3, pp. 493–495, 2004.
- [123] A. Alessandrello, J. W. Beeman, C. Brofferio et al., "Bolometric measurements of beta decay spectra of  $^{187}\text{Re}$  with crystals of silver perrhenate," *Physics Letters, Section B*, vol. 457, no. 1–3, pp. 253–260, 1999.
- [124] C. Arnaboldi, C. Brofferio, O. Cremonesi et al., "Bolometric bounds on the antineutrino mass," *Physical Review Letters*, vol. 91, no. 16, Article ID 161802, 2003.
- [125] A. Alessandrello, C. Arpesella, C. Brofferio et al., "Measurements of internal radioactive contamination in samples of Roman lead to be used in experiments on rare events," *Nuclear Instruments and Methods in Physics Research Section B: Beam Interactions with Materials and Atoms*, vol. 142, no. 1–2, pp. 163–172, 1998.
- [126] E. Ferri, S. Kraft-Bermuth, A. Monfardini, A. Nucciotti, D. Schaeffer, and M. Sisti, "Investigation of peak shapes in the MIBETA experiment calibrations," *The European Physical Journal A*, vol. 48, no. 10, pp. 1–13, 2012.
- [127] Mare proposal, 2015, [http://crio.mib.infn.it/wig/silicini/proposal/proposal\\_MARE.v2.6.pdf](http://crio.mib.infn.it/wig/silicini/proposal/proposal_MARE.v2.6.pdf).
- [128] A. Nucciotti, "Neutrino mass calorimetric searches in the MARE experiment," *Nuclear Physics B—Proceedings Supplements*, vol. 229–232, pp. 155–159, 2012.
- [129] D. Pergolesi, L. Gastaldo, F. Gatti et al., "MANU-2: a second generation experiment for calorimetric neutrino mass determination with superconducting Re," *Nuclear Instruments and Methods in Physics Research Section A: Accelerators, Spectrometers, Detectors and Associated Equipment*, vol. 559, no. 2, pp. 349–351, 2006.
- [130] A. Nucciotti, C. Arnaboldi, J. W. Beeman et al., "Comparison between implanted Si and NTD-Ge thermistors performance in  $\text{AgReO}_4$  microcalorimeters for a new neutrino mass experiment," *Nuclear Instruments and Methods in Physics Research Section A: Accelerators, Spectrometers, Detectors and Associated Equipment*, vol. 559, no. 2, pp. 367–369, 2006.
- [131] P. C.-O. Ranitzsch, J.-P. Porst, S. Kempf et al., "Development of metallic magnetic calorimeters for high precision measurements of calorimetric  $^{187}\text{Re}$  and  $^{163}\text{Ho}$  spectra," *Journal of Low Temperature Physics*, vol. 167, no. 5–6, pp. 1004–1014, 2012.
- [132] E. Ferri, D. Bagliani, M. Biassotti et al., "Preliminary results of the MARE experiment," *Journal of Low Temperature Physics*, vol. 176, no. 5–6, pp. 885–890, 2014.
- [133] H. L. Ravn, G. J. Beyer, A. De Rujula et al., "The N/M electron capture ratio of the neutrino mass probe  $^{163}\text{Ho}$ ," in *Proceedings of the 4th Moriond Workshop Massive Neutrinos in Astrophysics and in Particle Physics*, pp. 287–294, La Plagne, France, January 1984.
- [134] F. Gatti, P. Meunier, C. Salvo, and S. Vitale, "Calorimetric measurement of the  $^{163}\text{Ho}$  spectrum by means of a cryogenic detector," *Physics Letters B*, vol. 398, no. 3–4, pp. 415–419, 1997.
- [135] K. Prasai, E. Alves, D. Bagliani et al., "Thermal properties of holmium-implanted gold films for a neutrino mass experiment with cryogenic microcalorimeters," *Review of Scientific Instruments*, vol. 84, no. 8, Article ID 083905, 2013.
- [136] L. Gastaldo, P. Manfrinetti, F. Gatti et al., "Superconducting absorber for  $^{163}\text{Ho}$  electron capture decay measurement," *Nuclear Instruments and Methods in Physics Research Section A: Accelerators, Spectrometers, Detectors and Associated Equipment*, vol. 520, no. 1–3, pp. 224–226, 2004.
- [137] C. W. Reich and B. Singh, "Nuclear Data Sheets for A = 163," *Nuclear Data Sheets*, vol. 111, no. 5, pp. 1211–1469, 2010.
- [138] J. U. Andersen, G. Beyer, G. Charpak et al., "A limit on the mass of the electron neutrino: the case of  $^{163}\text{Ho}$ ," *Physics Letters B*, vol. 113, no. 1, pp. 72–76, 1982.
- [139] P. A. Baisden, D. H. Sisson, S. Niemyer, B. Hudson, C. L. Bennett, and R. A. Naumann, "Measurement of the half-life of  $^{163}\text{Ho}$ ," *Physical Review C*, vol. 28, no. 1, pp. 337–341, 1983.
- [140] S. Eliseev, K. Blaum, M. Block et al., "Direct measurement of the mass difference of  $^{163}\text{Ho}$  and  $^{163}\text{Dy}$  solves the Q-value puzzle for the neutrino mass determination," *Physical Review Letters*, vol. 115, no. 6, Article ID 062501, 2015.
- [141] E. W. Otten, J. Bonn, and C. Weinheimer, "The Q-value of tritium  $\beta$ -decay and the neutrino mass," *International Journal of Mass Spectrometry*, vol. 251, no. 2–3, pp. 173–178, 2006.
- [142] A. Nucciotti, "Statistical sensitivity of  $^{163}\text{Ho}$  electron capture neutrino mass experiments," *The European Physical Journal C*, vol. 74, article 3161, 6 pages, 2014.
- [143] K. Riisager, "On low-energy nuclear electron capture," *Journal of Physics G: Nuclear Physics*, vol. 14, no. 10, p. 1301, 1988.
- [144] R. G. H. Robertson, "Can neutrino mass be measured in low-energy electron capture decay?" <http://arxiv.org/abs/1411.2906v1>.
- [145] R. G. Robertson, "Examination of the calorimetric spectrum to determine the neutrino mass in low-energy electron capture decay," *Physical Review C*, vol. 91, no. 3, Article ID 035504, 2015.

- [146] A. De Rújula, “Two old ways to measure the electron-neutrino mass,” <http://arxiv.org/abs/1305.4857>.
- [147] P. T. Springer, C. L. Bennett, and P. A. Baisden, “Enhanced interaction energy shifts in the X-ray spectrum of  $^{163}\text{Ho}$ ,” *Physical Review A*, vol. 31, no. 3, pp. 1965–1967, 1985.
- [148] A. De Rújula and M. Lusignoli, “The calorimetric spectrum of the electron-capture decay of  $^{163}\text{Ho}$ . A preliminary analysis of the preliminary data,” <http://arxiv.org/abs/1510.05462>.
- [149] A. Faessler, C. Enss, L. Gastaldo, and F. Šimkovic, “Determination of the neutrino mass by electron capture in  $^{163}\text{Ho}$  and the role of the three-hole states in  $^{163}\text{Dy}$ ,” *Physical Review C*, vol. 91, no. 6, Article ID 064302, 2015.
- [150] A. Faessler and F. Šimkovic, “Improved description of one- and two-hole excitations after electron capture in  $^{163}\text{Ho}$  and the determination of the neutrino mass,” *Physical Review C*, vol. 91, no. 4, Article ID 045505, 2015.
- [151] T. A. Carlson and C. W. Nestor Jr., “Calculation of electron shake-off probabilities as the result of X-ray photoionization of the rare gases,” *Physical Review A*, vol. 8, no. 6, pp. 2887–2894, 1973.
- [152] A. De Rújula and M. Lusignoli, “The calorimetric spectrum of the electron-capture decay of  $^{163}\text{Ho}$ . The spectral endpoint region,” <http://arxiv.org/abs/1601.04990>.
- [153] R. A. Naumann, M. C. Michel, and J. L. Power, “Preparation of long-lived holmium-163,” *Journal of Inorganic & Nuclear Chemistry*, vol. 15, no. 1-2, pp. 195–196, 1960.
- [154] J. W. Engle, E. R. Birnbaum, H. R. Trellue, K. D. John, M. W. Rabin, and F. M. Nortier, “Evaluation of  $^{163}\text{Ho}$  production options for neutrino mass measurements with microcalorimeter detectors,” *Nuclear Instruments and Methods in Physics Research, Section B: Beam Interactions with Materials and Atoms*, vol. 311, pp. 131–138, 2013.
- [155] B. Alpert, M. Balata, D. Bennett et al., “HOLMES,” *The European Physical Journal C*, vol. 75, article 112, 2015.
- [156] U. Köster, Y. Calzavara, S. Fuard et al., “ $^{319}\text{At}$  Radioisotope production at the high flux reactor of Institut Laue Langevin,” *Radiotherapy and Oncology*, vol. 102, supplement 1, p. S170, 2012.
- [157] ECHO web page, 2015, <https://www.kip.uni-heidelberg.de/echo/>.
- [158] L. Gastaldo, K. Blaum, A. Doerr et al., “The electron capture  $^{163}\text{Ho}$  experiment ECHO,” *Journal of Low Temperature Physics*, vol. 176, no. 5-6, pp. 876–884, 2014.
- [159] L. Gastaldo, P. C.-O. Ranitzsch, F. von Seggern et al., “Characterization of low temperature metallic magnetic calorimeters having gold absorbers with implanted  $^{163}\text{Ho}$  ions,” *Nuclear Instruments and Methods in Physics Research Section A: Accelerators, Spectrometers, Detectors and Associated Equipment*, vol. 711, pp. 150–159, 2013.
- [160] C. Pies, S. Schäfer, S. Heuser et al., “MaXs: microcalorimeter arrays for high-resolution x-ray spectroscopy at GSI/FAIR,” *Journal of Low Temperature Physics*, vol. 167, no. 3-4, pp. 269–279, 2012.
- [161] C. Hassel, K. Blaum, T. Day Goodacre et al., “Recent results for the ECHO experiment,” *Journal of Low Temperature Physics*, 2016.
- [162] “HOLMES webpage,” 2015, <https://artico.mib.infn.it/holmes>.
- [163] J. P. Hays-Wehle, D. R. Schmidt, J. N. Ullom, and D. S. Swetz, “Thermal conductance engineering for high-speed TES microcalorimeters,” *Journal of Low Temperature Physics*, 2016, Proceedings of the 16th International Workshop on Low Temperature Detectors (LTD’15), Grenoble, France, 20–24 July 2015.
- [164] E. Ferri, B. Alpert, D. Bennett et al., “Pile-up discrimination algorithms for the holmes experiment,” *Journal of Low Temperature Physics*, 2016.
- [165] B. Alpert, E. Ferri, D. Bennett et al., “Algorithms for identification of nearly-coincident events in calorimetric sensors,” *Journal of Low Temperature Physics*, 2015.
- [166] NuMECS, November 2015, <http://p25ext.lanl.gov/~kunde/NuMECS/>.
- [167] M. P. Croce, M. W. Rabin, V. Mocko et al., “Development of holmium-163 electron-capture spectroscopy with transition-edge sensors,” *Journal of Low Temperature Physics*, 2016.
- [168] A. Faessler, L. Gastaldo, and F. Šimkovic, “Electron capture in  $^{163}\text{Ho}$ , overlap plus exchange corrections and neutrino mass,” *Journal of Physics G: Nuclear and Particle Physics*, vol. 42, no. 1, Article ID 015108, 2015.

## Review Article

# Neutrinoless Double Beta Decay: 2015 Review

Stefano Dell’Oro,<sup>1</sup> Simone Marcocci,<sup>1</sup> Matteo Viel,<sup>2,3</sup> and Francesco Vissani<sup>1,4</sup>

<sup>1</sup>INFN, Gran Sasso Science Institute, Viale F. Crispi 7, 67100 L’Aquila, Italy

<sup>2</sup>INAF, Osservatorio Astronomico di Trieste, Via G. B. Tiepolo 11, 34131 Trieste, Italy

<sup>3</sup>INFN, Sezione di Trieste, Via Valerio 2, 34127 Trieste, Italy

<sup>4</sup>INFN, Laboratori Nazionali del Gran Sasso, Via G. Acitelli 22, 67100 Assergi, Italy

Correspondence should be addressed to Francesco Vissani; francesco.vissani@lngs.infn.it

Received 31 October 2015; Revised 13 January 2016; Accepted 27 January 2016

Academic Editor: Srubabati Goswami

Copyright © 2016 Stefano Dell’Oro et al. This is an open access article distributed under the Creative Commons Attribution License, which permits unrestricted use, distribution, and reproduction in any medium, provided the original work is properly cited. The publication of this article was funded by SCOAP<sup>3</sup>.

The discovery of neutrino masses through the observation of oscillations boosted the importance of neutrinoless double beta decay ( $0\nu\beta\beta$ ). In this paper, we review the main features of this process, underlining its key role from both the experimental and theoretical point of view. In particular, we contextualize the  $0\nu\beta\beta$  in the panorama of lepton number violating processes, also assessing some possible particle physics mechanisms mediating the process. Since the  $0\nu\beta\beta$  existence is correlated with neutrino masses, we also review the state of the art of the theoretical understanding of neutrino masses. In the final part, the status of current  $0\nu\beta\beta$  experiments is presented and the prospects for the future hunt for  $0\nu\beta\beta$  are discussed. Also, experimental data coming from cosmological surveys are considered and their impact on  $0\nu\beta\beta$  expectations is examined.

## 1. Introduction

In 1937, almost ten years after Paul Dirac’s “The quantum theory of electron” [1, 2], Majorana proposed a new way to represent fermions in a relativistic quantum field theory [3] and remarked that this could be especially useful for neutral particles. A single Majorana quantum field characterizes the situation in which particles and antiparticles coincide, as it happens for the photon. Racah stressed that such a field could fully describe massive neutrinos, noting that the theory by Majorana leads to physical predictions essentially different from those coming from Dirac theory [4]. Two years later, Furry [5] studied within this scenario a new process similar to the “double beta disintegration,” introduced by Goepfert-Mayer in 1935 [6]. It is the double beta decay without neutrino emission, or *neutrinoless double beta decay* ( $0\nu\beta\beta$ ). This process assumes a simple form; namely,

$$(A, Z) \longrightarrow (A, Z + 2) + 2e^{-}. \quad (1)$$

The Feynman diagram of the  $0\nu\beta\beta$  process, written in terms of the particles we know today and of massive Majorana neutrinos, is given Figure 1.

The main and evident feature of the  $0\nu\beta\beta$  transition is the explicit violation of the number of leptons and, more precisely, the creation of a pair of electrons. The discovery of  $0\nu\beta\beta$  would therefore demonstrate that lepton number is not a symmetry of nature. This, in turn, would support the exciting theoretical picture that leptons played a part in the creation of the matter-antimatter asymmetry in the Universe.

In the attempt to investigate the nature of the  $0\nu\beta\beta$  process, various other theoretical possibilities were considered, beginning by postulating new superweak interactions [7, 8]. However, the general interest has always remained focused on the neutrino mass mechanism. In fact, this scenario is supported by two important facts:

- (1) On the theoretical side, the triumph of the Standard Model (SM) of electroweak interactions in the 1970s [9–11] led to formulating the discussion of new physics signals using the language of effective operators, suppressed by powers of the new physics mass scale. There is only one operator that is suppressed only by one power of the new mass scale and violates the global symmetries of the SM or, more precisely,

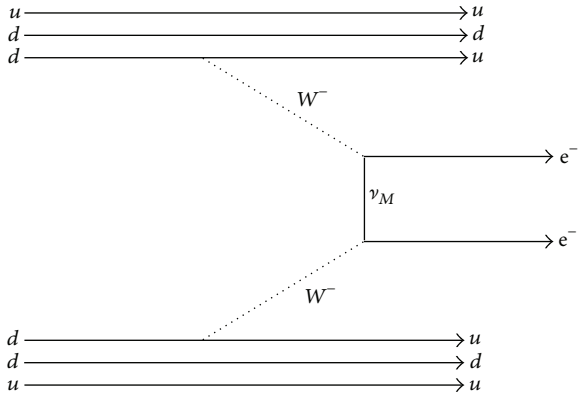


FIGURE 1: Diagram of the  $0\nu\beta\beta$  process due to the exchange of massive Majorana neutrinos, here denoted generically by  $\nu_M$ .

the lepton number: it is the one that gives rise to Majorana neutrino masses [12] (see also [13–16]).

- (2) On the experimental side, some anomalies in neutrino physics, which emerged throughout 30 years, found their natural explanation in terms of oscillations of massive neutrinos [17]. This explanation was confirmed by several experiments (see [18, 19] for reviews). Thus, although oscillation phenomena are not sensitive to the Majorana nature of neutrinos [20], the concept of neutrino mass has changed its status in physics, from the one of hypothesis to the one of fact. This, of course, strengthened the case for light massive neutrinos to play a major role for the  $0\nu\beta\beta$  transition.

For these reasons, besides being an interesting nuclear process,  $0\nu\beta\beta$  is also a key tool for studying neutrinos, probing whether their nature is the one of Majorana particles and providing us with precious information on the neutrino mass scale and ordering. Even though the predictions of the  $0\nu\beta\beta$  lifetime still suffer from numerous uncertainties, great progresses in assessing the expectations for this process have been and are being made. These will be discussed later in this review.

*About the Present Review.* In recent years, several review papers concerning neutrinoless double beta decay have been written. They certainly witness the vivid interest of the scientific community in this topic. Each work emphasizes one or more relevant aspects such as the experimental part [21–25], the nuclear physics [26, 27], the connection with neutrino masses [28, 29], and other particle physics mechanisms [30–33]. The present work is not an exception. We mostly focus on the first three aspects. This choice is motivated by our intention to follow the theoretical ideas that describe the most plausible expectations for the experiments. In particular, after a general theoretical introduction (Sections 2 and 3), we examine the present knowledge on neutrino masses in Section 4 and the status of expectations from nuclear physics in Section 5. Then we review the experimental situation (Section 6) and emphasize the link between neutrinoless double beta decay and cosmology (Section 7).

A more peculiar aspect of this review is the effort to follow the historical arguments, without worrying too much about covering once more well-known material or about presenting an exhaustive coverage of the huge recent literature on the subject. Another specific characteristic is the way the information on the neutrino Majorana mass is dealt with. In order to pass from this quantity to the (potentially measurable) decay rate, we have to dispose of quantitative information on the neutrino masses and on the matrix elements of the transition, which in turn requires the description of the nuclear wave functions and of the operators that are implied. Therefore, our approach is to consider the entire available information on neutrino masses and, in particular, the one coming from cosmology. We argue that the recent progresses (especially those coming from the Planck satellite data [34]) play a very central role for the present discussion. On the other side, the matrix elements have to be calculated (rather than measured) and are thus subject to uncertainties which are difficult to assess reliably. Moreover, the adopted methods of calculation do not precisely reproduce other measurable quantities (single beta decay, two-neutrino double beta decay, etc.). We thus prefer to adopt a cautious/conservative assessment of the theoretical ranges of these matrix elements.

We would like to warn the reader that other attitudes in the discussion are surely possible, and it is indeed the case for some of the mentioned review works. Using less stringent limits from cosmology and disregarding the uncertainties from nuclear physics are equivalent to assuming the most favorable situation for the experiments. This could be considered beneficial for the people involved in experimental search for the neutrinoless double beta decay. However, we prefer to adhere to a more problematic view in the present work, simply because we think that it more closely reflects the present status of facts. Considering the numerous experiments involved in the field, we deem that an updated discussion on these two issues has now become quite urgent. This will help us to assess and appreciate better the progresses expected in the close future, concerning the cosmological measurements of neutrino masses and perhaps also the theoretical calculations of the relevant nuclear matrix elements.

## 2. The Total Lepton Number

No elementary process where the number of leptons or the number of hadrons varies has been observed yet. This suggests the hypothesis that the lepton number  $L$  and the baryon  $B$  are subject to conservation laws. However, we do not have any deep justification for which these laws should be exact. In fact, it is possible to suspect that their validity is just approximate or circumstantial, since it is related to the range of energies that we can explore in laboratories. (Notice also that the fact that neutral leptons (i.e., neutrinos or antineutrinos) are very difficult to observe restricts the experimental possibilities to test the total lepton number.)

In this section, we discuss the status of the investigations on the total lepton number in the SM and in a number of minimal extensions, focusing on theoretical considerations. In particular, we introduce the possibility that neutrinos are endowed with Majorana mass and consider a few possible

manifestations of lepton number violating phenomena. The case of the  $0\nu\beta\beta$  will instead be addressed in the rest of this work.

**2.1.  $B$  and  $L$  Symmetries in the SM.** The SM in its minimal formulation has various global symmetries, including  $B$  and  $L$ , which are called “accidental.” This is due to the specific particle content of the model and to the hypothesis of renormalizability. Some combinations of these symmetries, like, for example, “ $B-L$ ,” are conserved also nonperturbatively. This is sufficient to forbid the  $0\nu\beta\beta$  transition completely in the SM. In other words, a hypothetical evidence for such a transition would directly point out to physics beyond the SM. At the same time, the minimal formulation of the SM implies that neutrinos are massless, and this contradicts the experimental findings. Therefore, the question of how to modify the SM arises, and this in turn poses the related burning question concerning the nature of neutrino masses.

**2.2. Majorana Neutrinos.** In 1937, Majorana proposed a theory of massive and “real” fermions [3]. This theory contains less fields than the one used by Dirac for the description of the electron [1, 2] and, in this sense, it is simpler. Following the formalism introduced in 1933 by Fermi when describing the  $\beta$  decay [36], the condition of reality for a quantized fermionic field can be written as

$$\chi = C\bar{\chi}^t, \quad (2)$$

where  $C$  is the charge conjugation matrix, while  $\bar{\chi} \equiv \chi^\dagger \gamma_0$  is the Dirac conjugate of the field. In particular, Majorana advocated a specific choice of the Dirac  $\gamma$ -matrices, such that  $C\gamma_0^t = 1$ , which simplifies various equations. The free particle Lagrangian density formally coincides with the usual one:

$$\mathcal{L}_{\text{Majorana}} = \frac{1}{2}\bar{\chi}(i\cancel{\partial} - m)\chi. \quad (3)$$

Following Majorana’s notations, the decomposition of the quantized fields into oscillators is

$$\chi(x) = \sum_{\mathbf{p}, \lambda} [a(\mathbf{p}, \lambda)\psi(x; \mathbf{p}, \lambda) + a^*(\mathbf{p}, \lambda)\psi^*(x; \mathbf{p}, \lambda)], \quad (4)$$

where  $\lambda = \pm 1$  is the relative orientation between the spin and the momentum (helicity). We adopt the normalization for the wave functions:  $\int d\mathbf{x}|\psi(t, \mathbf{x})|^2 = 1$ , and for the oscillators:  $a(\mathbf{p}, \lambda)a^*(\mathbf{p}', \lambda') + a^*(\mathbf{p}', \lambda')a(\mathbf{p}, \lambda) = \delta_{\mathbf{p}\mathbf{p}'}\delta_{\lambda\lambda'}$ . For any value of the momentum, there are 2 spin (or helicity) states:

$$\begin{aligned} a^*(\mathbf{p}+) |vac.\rangle &= |\mathbf{p} \uparrow\rangle, \\ a^*(\mathbf{p}-) |vac.\rangle &= |\mathbf{p} \downarrow\rangle. \end{aligned} \quad (5)$$

Figure 2 illustrates the comparison between the particle content of both a Dirac and a Majorana field in the case  $\mathbf{p} = 0$  (rest frame).

Evidently, a Majorana neutrino is incompatible with any  $U(1)$  transformation, for example,  $L$  or the weak hypercharge (i.e., however broken in the vacuum). In general,  $L$  will be violated by the presence of Majorana mass.

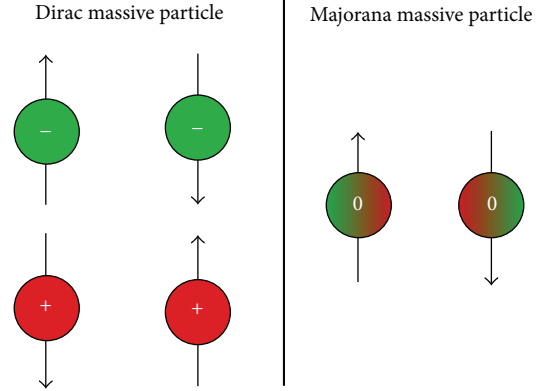


FIGURE 2: Massive fields in their rest frames. The arrows show the possible directions of the spin. (Left) the 4 states of Dirac massive field. The signs indicate the charge that distinguishes particles and antiparticles, for example, the electric charge of an electron. (Right) the 2 states of Majorana massive field. The symbol “zero” indicates the absence of any  $U(1)$  charge: particles and antiparticles coincide.

In the SM, the neutrino field appears only in the combination

$$\psi_L = P_L\psi, \quad (6)$$

where  $P_L \equiv (1 - \gamma_5)/2$  is the so-called chiral projector (Table 1). It is then possible to implement the hypothesis of Majorana in the most direct way by defining the real field:

$$\chi \equiv \psi_L + C\bar{\psi}_L^t. \quad (7)$$

In fact, we can conversely obtain the SM field by a projection:

$$\psi_L \equiv P_L\chi. \quad (8)$$

**2.3. Ultrarelativistic Limit and Massive Neutrinos.** The discovery that parity is a violated symmetry in weak interactions [37, 38] was soon followed by the understanding that the charged current (which contains the neutrino field) always includes the left chiral projector [39–41] (see Sections 2.2 and 3.1).

It is interesting to note the following implication. Within the hypothesis that neutrinos are massless, the Dirac equation becomes equivalent to two Weyl equations [42] corresponding to the Hamiltonian functions:

$$H_{\nu/\bar{\nu}} = \mp c\mathbf{p}\sigma, \quad (9)$$

where  $\sigma$  are the three Pauli matrices and the two signs apply to the neutral leptons that, thanks to the interaction, produce charged leptons of charge  $\mp 1$ , respectively. In other words, we can define these states as neutrinos and antineutrinos, respectively. Moreover, by looking at (9), one can see that the energy eigenstates are also helicity eigenstates. More precisely, the spin of the neutrino (antineutrino) is antiparallel (parallel) to its momentum. See Figure 3 for illustration.

The one-to-one connection between chirality and helicity holds only in the ultrarelativistic limit, when the mass of the

TABLE 1: List of the matter particles in the SM. The label “singlet” is often replaced with “right” and likewise for “doublet” it can become “left.” Hypercharge is assigned according to  $Q = T_{3L} + Y$ . The chirality of a field (and all its  $U(1)$  numbers) can be exchanged by considering the charge conjugate field; for example,  $e_L^c \equiv C\bar{e}_R^t$  has electric charge +1 and leptonic charge -1.

Name	Field symbol	$SU(3)_c$ multiplicity	$SU(2)_L$ multiplicity	$U(1)_Y$ charge	Lepton number $L$	Baryon number $B$
Quark doublet	$q_L$	3	2	+1/6	0	1/3
Singlet up quark	$u_R$	3	1	+2/3	0	1/3
Singlet down quark	$d_R$	3	1	-1/3	0	1/3
Lepton doublet	$l_L$	1	2	-1/2	1	0
Singlet charged lepton	$e_R$	1	1	-1	1	0

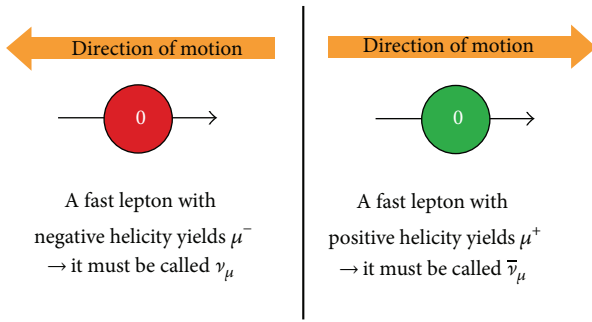


FIGURE 3: The chiral nature of weak interactions allows us to define what is a neutrino and what is an antineutrino *in the ultrarelativistic limit*, when chirality coincides with helicity and the value of the mass plays only a minor role.

neutrinos is negligible. This is typically the case that applies for detectable neutrinos, since the weak interaction cross sections are bigger at larger energies. However, these remarks do not imply in any way that neutrinos are massless. On the contrary, we know that neutrinos are massive.

A consequence of the chiral nature of weak interactions is that if we assume that neutrinos have the type of mass introduced by Dirac, we have a couple of states that are sterile under weak interactions in the ultrarelativistic limit. Conversely, the fact that the left chiral state exists can be considered a motivation in favor of the hypothesis of Majorana. In fact, this does not require the introduction of the right chiral state, as instead required by the Dirac hypothesis. Most importantly, it should be noticed that in the case of Majorana mass *it is not possible to define the difference between a neutrino and an antineutrino in a Lorentz invariant way*.

**2.4. Right-Handed Neutrinos and Unified Groups.** The similarity between  $L$  and  $B$  is perceivable already within the SM. The connection is even deeper within the so-called Grand Unified Theories (GUTs), that is, gauge theories with a single gauge coupling at a certain high energy scale. The standard prototypes are  $SU(5)$  [47] and  $SO(10)$  [48, 49]. GUTs undergo a series of symmetry-breaking stages at lower energies, eventually reproducing the SM. They lead to predictions on the couplings of the model and suggest the existence of new particles, even if theoretical uncertainties make it difficult to obtain reliable predictions. The possibilities to test

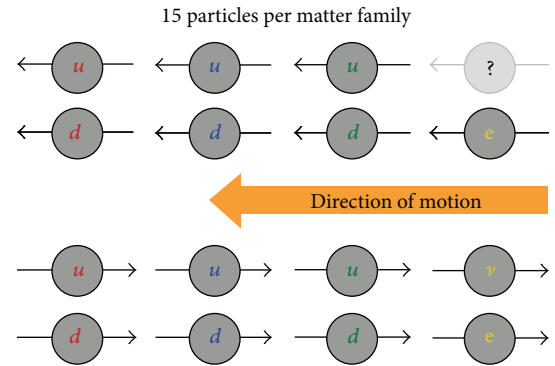


FIGURE 4: Helicity of the 15 massless matter particles contained in each family of the SM (see Table 1). The arrow gives the direction of the momentum.

these theories are limited, and major manifestations could be violations of  $L$  and  $B$ .

The matter content of GUTs is particularly relevant to the discussion. In fact, the organization of each family of the SM suggests the question whether right-handed neutrinos (RH) exist along with the other 7 RH particles (Figure 4). This question is answered affirmatively in some extensions of the SM. For example, this is true for gauge groups that also include a  $SU(2)_R$  factor, on top of the usual  $SU(2)_L$  factor. In the  $SO(10)$  gauge group, which belongs to this class of models, each family of matter includes the 15 SM particles plus 1 RH neutrino.

It should be noted that RH neutrinos do not participate in SM interactions and can therefore be endowed with a Majorana mass  $M$ , still respecting the SM gauge symmetries. However, they do participate in the new interactions, and, more importantly for the discussion, they can mix with the ordinary neutrinos via the Dirac mass terms,  $m^{\text{Dirac}}$ . Therefore, in presence of RH neutrinos, the SM Lagrangian (after spontaneous symmetry breaking) will include the terms

$$\mathcal{L}_{\text{mass}} = -\bar{\nu}_{Ri} m_{\ell i}^{\text{Dirac}} \nu_{L\ell} + \frac{1}{2} \bar{\nu}_{Ri} M_i C \bar{\nu}_{Ri}^t + h.c., \quad (10)$$

where  $\ell = e, \mu, \tau$  and  $i = 1, 2, 3$ . It is easy to understand that, at least generically, this framework implies that the lepton number is broken.

Let us assume the existence of RH neutrinos, either embedded in a unified group or not, and let us suppose that they are heavy (this happens, e.g., if the scale of the new gauge bosons is large and the couplings of the RH neutrinos to the scalar bosons implementing spontaneous symmetry breaking of the new gauge group are not small). In this case, upon integrating away the heavy neutrinos from the theory, the light neutrinos will receive Majorana mass, with size inversely proportional to the mass of the RH ones [13–16]. This is the celebrated Type I Seesaw Model. In other words, the hypothesis of heavy RH neutrinos allows us to account for the observed small mass of the neutrinos. Unfortunately, we cannot predict the size of the light neutrino mass precisely, unless we know both  $M$  and  $m^{\text{Dirac}}$ .

In principle, RH neutrinos could also be quite light. An extreme possibility is that some of them have masses of the order of eV or less and give rise to new flavor oscillations observable in terrestrial laboratories [50–52]. This could help to address some experimental anomalies [53, 54]. However, it has been known for long [55, 56] that the presence of eV neutrinos would also imply large effects in cosmology, both in the number of relativistic species and in the value of the neutrino mass. These effects are not in agreement with the existing information from cosmology (see Section 4.3) and, for this reason, we will not investigate this hypothesis further (we refer the interested reader to the various discussions on the impact of eV neutrinos on the  $0\nu\beta\beta$ ; see, e.g., [57–59]).

In view of the evidences of neutrinos masses, theories like SO(10) are particularly appealing, since they offer a natural explanation of light Majorana neutrino masses. However, a complete theory able to link in a convincing way fermion masses (including those of neutrinos) and to provide us with reliable predictions of new phenomena, such as  $0\nu\beta\beta$ , does not exist yet. Despite the fact that many attempts were made in the past, it seems that this enterprise is still in its initial stages.

**2.5. Leptogenesis.** Although particles and antiparticles have the same importance in our understanding of particle physics, we know that the Universe contains mostly baryons rather than antibaryons (the lepton number in the Universe is probed much less precisely; while we know that cosmic neutrinos and antineutrinos are abundant, it is not easy to measure their asymmetry which, according to standard cosmology, should be very small; however, we expect to have the same number of electrons and protons to guarantee the overall charge neutrality). In 1967, Sakharov proposed a set of necessary conditions to generate the cosmic baryon asymmetry [60]. This has been the beginning of many theoretical attempts to “explain” these observations in terms of new physics.

In the SM, although  $L$  and  $B$  are not conserved separately at the nonperturbative level [61–63], the observed value of the Higgs mass is not big enough to account for the observed baryon asymmetry [64, 65]. New violations of the global  $B$  or  $L$  are needed.

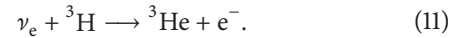
An attractive theoretical possibility is that RH neutrinos not only enhance the SM endowing neutrinos with Majorana mass, but also produce a certain amount of leptonic

asymmetry in the Universe. This is subsequently converted into a baryonic asymmetry thanks to  $B + L$  violating effects, which are built-in in the SM. It is the so-called Leptogenesis mechanism, and it can be wittingly described by asking the following question: *do we all descend from neutrinos?* The initial proposal of Leptogenesis dates back to 1980s [66], and there is a large consensus that this type of idea is viable and attractive. Subsequent investigators showed that the number of alternative theoretical possibilities is very large and, in particular, that there are other possible sources of  $L$  violations besides RH neutrinos. Conversely, the number of testable possibilities is quite limited [67].

We believe that it is important to stay aware of the possibility of explaining the baryon number excess through Leptogenesis theories. However, at the same time, one should not overestimate the heuristic power of this theoretical scheme, at least within the presently available information.

**2.6. Neutrino Nature and Cosmic Neutrino Background.** The Big Bang theory predicts that the present Universe is left with a residual population of  $\sim 56$  nonrelativistic neutrinos and antineutrinos per  $\text{cm}^3$  and per species. It constitutes a Cosmic Neutrino Background (C $\nu$ B). Due to their very low energy, (9) does not hold for these neutrinos. This happens because at least two species of neutrinos are nonrelativistic. The detection of this C $\nu$ B could therefore allow understanding which hypothesis (Majorana or Dirac) applies for the neutrino description.

Let us assume having a target of 100 g of  $^3\text{H}$ . Electron neutrinos can be detected through the reaction [69, 70]



In the standard assumption of a homogeneous Fermi-Dirac distribution of the C $\nu$ B, we expect  $\sim 8$  events per year if neutrinos are Majorana particles and about half if the Dirac hypothesis applies [71]. Indeed, in the former case, the states with positive helicity (by definition, antineutrinos) will act just as neutrinos, since they are almost at rest. Instead, in the latter case, they will remain antineutrinos and thus they will not react.

It can be noticed that the signal rate is not prohibitively small, but the major difficulty consists in attaining a sufficient energy resolution to keep at a manageable level the background from beta decay. We will not discuss further the feasibility of such an experiment, and refer to [70, 71] for more details.

### 3. Particle Physics Mechanisms for $0\nu\beta\beta$

In this section, we focus on one of the most appealing lepton number violating process, the  $0\nu\beta\beta$ . The exchange of light Majorana neutrinos is up to now the most appealing mechanism to eventually explain the  $0\nu\beta\beta$ . Some reasons justifying this statement were already mentioned, but here a more elaborate discussion is proposed. In particular, we review the basic aspects of the light neutrino exchange mechanism for  $0\nu\beta\beta$  and compare it to other ones. Moreover, the possibilities of inferring the size of neutrino masses from a hypothetical

observation of  $0\nu\beta\beta$  and of constraining (or proving the correctness) some alternative mechanisms with searches at the accelerators are also discussed.

**3.1. The Neutrino Exchange Mechanism.** The definition of a key quantity for the description of the neutrino exchange mechanism needs to be introduced. It is the propagator of virtual Majorana neutrinos. Due to the reality condition, (3) can lead to new types of propagators that do not exist within the Dirac theory. In fact, in this case, we can use the antisymmetry of the charge conjugation matrix and get

$$\langle 0 | T [\chi(x) \chi(y)] | 0 \rangle = -\Delta(x-y), \quad (12)$$

where  $\Delta$  denotes the usual propagator, and

$$\Delta(x) \equiv \int \frac{d^4 q}{(2\pi)^4} \frac{i(\hat{q} + m)}{q^2 - m^2 + i0} e^{-iqx}. \quad (13)$$

In the low energy limit (relevant to  $\beta$  decay processes) the interaction of neutrinos is well described by the current-current four-fermion interactions, corresponding to the Hamiltonian density

$$\mathcal{H}_{\text{Fermi}} = \frac{G_F}{\sqrt{2}} J^{a\dagger} J_a, \quad (14)$$

where  $G_F$  is the Fermi coupling, and we introduced the current  $J^a = J_{\text{lept}}^a + J_{\text{hadr}}^a$  for  $a = 0, 1, 2, 3$ , that decreases the charge of the system (its conjugate,  $J_a^\dagger$ , does the contrary). In particular, the leptonic current

$$J_{\text{lept}}^a = \sum_{\ell=e,\mu,\tau} \bar{\psi}_\ell \gamma^a (1 - \gamma_5) \psi_{\nu_\ell} \quad (15)$$

defines the ordinary neutrino with ‘‘flavor’’  $\ell$ . In order to implement the Majorana hypothesis, one can use (7) and introduce the field  $\chi = \psi_L + C\bar{\psi}_L^\dagger$ . Nothing changes in the interactions if one substitutes the field  $\psi_{\nu_\ell}$  with the corresponding field  $\chi_{\nu_\ell}$ , since the chiral projector selects only the first piece,  $\psi_{\nu_\ell}$ .

Let us assume that the field  $\chi$  is a mass eigenstate. A contribution to the  $0\nu\beta\beta$  transition arises at the second order of the Fermi interaction. Let us begin from the operator

$$\begin{aligned} & -G_F^2 \int d^4 x J_{\text{hadr}}^{a\dagger}(x) \bar{\psi}_e(x) \gamma_a P_L \chi_{\nu_e}(x) \\ & \cdot \int d^4 y J_{\text{hadr}}^{b\dagger}(y) \bar{\psi}_e(y) \gamma_b P_L \chi_{\nu_e}(y). \end{aligned} \quad (16)$$

By contracting the neutrino fields, the leptonic part of this operator becomes

$$\bar{\psi}_e(x) \gamma^a P_L \Delta(x-y) P_L \gamma^b C \bar{\psi}_e^\dagger(y) \quad (17)$$

while the ordinary propagator, sandwiched between two chiral projectors, reduces to

$$P_L \Delta(x) P_L = P_L \int \frac{d^4 q}{(2\pi)^4} \frac{im}{q^2 - m^2 + i0} e^{-iqx}. \quad (18)$$

The momentum  $q$  represents the virtuality of the neutrino, whose value is connected to the momenta of the final state electrons and to those of the intermediate virtual nucleons. In particular, since the latter are confined in the nucleus, the typical 3 momenta are of the order of the inverse of the nucleonic size, namely,

$$|\vec{q}| \sim \hbar c / \text{fm} \sim \text{few } 100 \text{ MeV}, \quad (19)$$

whereas the energy ( $q_0$ ) is small. The comparison of this scale with the one of neutrino mass identifies and separates ‘‘light’’ from ‘‘heavy’’ neutrinos for what concerns  $0\nu\beta\beta$ .

The most interesting mechanism for  $0\nu\beta\beta$  is the one that sees light neutrinos as mediators. It is the one originally considered in [5] and it will be discussed in great detail in the subsequent sections. In the rest of this section, instead, we examine various alternative possibilities.

We have some hints, mostly of theoretical nature, that the light neutrinos might have Majorana mass. However, the main reason for the hypothesis that the  $0\nu\beta\beta$  receives its main contribution from light Majorana neutrinos is the fact that experiments point out the existence of 3 light massive neutrinos.

### 3.2. Alternative Mechanisms to the Light Neutrino Exchange

**3.2.1. Historical Proposals.** A few years after the understanding of the  $K^0 - \bar{K}^0$  oscillation [97–99], which led Pontecorvo to conjecture that also neutrino oscillations could exist [17], alternative theoretical mechanisms for the  $0\nu\beta\beta$  other than the neutrino exchange were firstly advocated. In 1959, Feinberg and Goldhaber [7] proposed the addition of the following term in the effective Lagrangian density:

$$\mathcal{H}_{\text{pion}} = \frac{g}{m_e} \pi^+ \pi^+ e^\dagger C^{-1} e, \quad (20)$$

where  $m_e$  is the electron mass and  $g$  an unspecified dimensionless coupling. Similarly, after the hypothesis of superweak interactions in weak decays [100, 101], the importance for  $0\nu\beta\beta$  of operators like the one of (20) was stressed by Pontecorvo [8]. He also emphasized that the size and the origin of these operators could be quite independent from the neutrino masses.

**3.2.2. Higher Dimensional Operators.** The SM offers a very convenient language to order the interesting operators leading to violation of  $L$  and  $B$ . It is possible to consider effective (nonrenormalizable) operators that respect the gauge symmetry  $SU(3)_c \times SU(2)_L \times U(1)_Y$  but that violate  $L$  and/or  $B$  [12, 102]. Here, we consider a few representative cases (a more complete list can be found in [103, 104]), corresponding to the following terms of the Lagrangian and Hamiltonian densities:

$$\mathcal{H}_{\text{Weinberg}} = \frac{(l_L H)^2}{M} + \frac{l_L q_L q_L q_L}{M^2} + \frac{(l_L q_L d_R^c)^2}{M^2}. \quad (21)$$

The matter fields (fermions) in the equation are written in the standard notation of Table 1;  $H$  is the Higgs field, while

the constrains on the masses are  $M < 10^{11}$  TeV,  $M' > 10^{12}$  TeV, and  $M'' > 5$  TeV. In particular

- (i) the first (dimension-5) operator generates Majorana neutrino masses, and the bound on  $M$  derives from neutrino masses  $m_\nu < 0.1$  eV;
- (ii) the dimension-6 operator leads to proton decay and this implies the tight bound on the mass  $M'$ ;
- (iii) the dimension-9 operator contributes to the  $0\nu\beta\beta$ ; its role in the transition can be relevant if the scale of lepton number violation is low.

Summarizing, if one assumes that the scale of new physics is much higher than the electroweak scale, it is natural to expect that the leading mechanism behind the  $0\nu\beta\beta$  is the exchange of light neutrinos endowed with Majorana masses. It is also worthy to note that if light sterile neutrinos, dark matter, or, generally, other light states are added, more operators may be required. A large effective mass could also come from small adimensional couplings  $y$ , for example,  $1/M = y^2/\mu$ .

The number of possible mechanisms that eventually can lead to the above effective operators is also very large. One possible (plausible) origin of the dimension-5 operator is discussed in Section 2.4. However, other cases are possible and the same is true for the other operators.

**3.2.3. Heavy Neutrino Exchange.** Let us now consider the case of heavy RH neutrino exchange mechanism. The corresponding operator gives rise to the effective Hamiltonian density (for heavy neutrinos, the propagator of (18) is proportional to  $\delta(x - y)$ ):

$$\mathcal{H}_{\nu_{\text{heavy}}} = -\frac{G_F^2}{M_H} J_{\text{hadr}}^{a\dagger} \bar{\psi}_{e_L} \gamma^a \gamma^b C \bar{\psi}_{e_L}^{\dagger} J_{\text{hadr}}^{b\dagger}. \quad (22)$$

It is evident that this is a dimension-9 operator and it has in front a constant with mass dimension  $m^{-5}$ , since  $M_H$  indicates the relevant heavy neutrino mass. It has to be noted that such a definition can be used in an effective formula, but a gauge model requires expressing  $M_H$  in terms of the single RH neutrino masses  $M_I$  and of the mixing between left-handed neutrinos  $\nu_{e_L}$  and heavy neutrinos:

$$\frac{1}{M_H} = \frac{U_{ei}^2}{M_I}. \quad (23)$$

In particular, the mixings are small if  $M_I$  is large since  $U_{ei} = m_{ei}^{\text{Dirac}}/M_I$ . This suggests a suppression of the above effective operator with the cube of  $M_I$ , whereas the light neutrino exchange mechanism leads to a milder suppression, linear in  $M_I$  (if the mixing matrices have specific flavor structures, deviations from this generic expectation are possible). However, it is still possible that RH neutrinos are heavy, but not “very” heavy. Actually, this was the first case to be considered [13], and it could be of interest both for direct searches at accelerators (see Section 3.4) and for the  $0\nu\beta\beta$ . In fact, in this case, the mixing  $U_{ei}$  is not strongly suppressed and RH neutrinos can give an important contribution to the

transition [105]. However, two remarks on this case are in order. As it was argued in [106], in order to avoid fine tunings on the light neutrinos, the masses of RH neutrinos should not be much larger than about 10 GeV. Moreover, in the extreme limit in which the mass becomes light (i.e., it is below the value in (19)) and Type I Seesaw applies, the contribution of RH neutrinos cancels the one of ordinary neutrinos [107, 108].

**3.2.4. Models with RH Currents.** Another class of models of great interest are those that include RH currents and intermediate bosons. In the language of SM, the neutrino exchange leads to a core operator

$$\mathcal{H}_{W_{\text{bosons}}} = \frac{1}{M} W^+ W^+ e^t C^{-1} e, \quad (24)$$

where  $M$  is a mass scale and  $W$  identify the fields of the usual  $W$  bosons. When we consider virtual  $W$  bosons, this may eventually lead to the usual case. In principle, it is possible to replace the usual  $W$  bosons with the corresponding  $W_R$  bosons of a new  $SU(2)_R$  gauge group. In this hypothesis, the RH neutrinos play a more important role and are no longer subject to restrictions of the mixing matrix, as those of (23). However, the resulting dimension-9 operator is suppressed by 4 powers of the masses of the new gauge bosons.

Evidently, new RH gauge bosons with masses accessible to direct experimental investigation are of special interest (see Section 3.4). Since to date we do not have any experimental evidence, this possibility will not be emphasized in the following discussion. Anyway, investigations at the LHC are currently in progress and the interpretation of some anomalous events (among the collected data) as a hint in favor of relatively light  $W_R$  bosons has already been proposed [109–111].

**3.3. From  $0\nu\beta\beta$  to Majorana Mass: A Remark on “Natural” Gauge Theories.** In a well-known work, Schechter and Valle [112] employ the basic concepts of gauge theories to derive some important considerations on the  $0\nu\beta\beta$ . In particular, their argument proceeds as follows:

- (1) If the  $0\nu\beta\beta$  is observed, there will be some process (among elementary particles) where the electron-, up-, and downfields are taken twice. This “black box” process in [112] (Figure 5) effectively resembles the one caused by the dimension-9 operator in (21).
- (2) Using  $W$  bosons, it is possible to contract the two quark pairs and obtain something like the operator in (24).
- (3) Finally, the electron- and the  $W$ -fields can be converted into neutrino fields. A contribution to the Majorana neutrino mass is therefore obtained.
- (4) The possibility that this contribution could be canceled by others is barred out as “unnatural.”

This argument works in the “opposite direction” with respect to ones presented so far. Instead of starting from the Majorana mass to derive a contribution for the  $0\nu\beta\beta$ , it shows that from the observation of the  $0\nu\beta\beta$ , it is possible

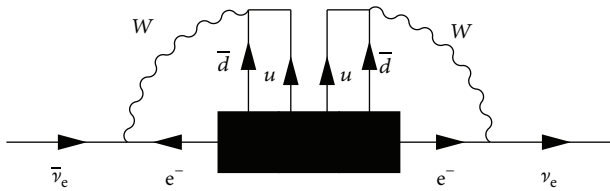


FIGURE 5: Diagram representing the contribution of the “black box” operator to the Majorana mass. Figure from [114].

to conclude the existence of the Majorana mass. The result could be seen as an application (or a generalization) of Symanzik’s rule as given by Coleman [113]: if a theory predicts  $L$ -violation, it will not be possible to screen it to forbid *only* a Majorana neutrino mass.

The size of the neutrino masses is not indicated in the original work, but a straightforward estimation of the diagram of Figure 5 shows that they are so small that they have no physical interest, being of the order of  $10^{-24}$  eV [114]. However, what can be seen as a weak point of the argumentation is the concept of “natural theory,” whose definition is not discussed in [112] but simply proclaimed. In fact, it is possible to find examples of models where the  $0\nu\beta\beta$  exists but the Majorana neutrino mass contribution is zero [106], in accordance with the claim of Pontecorvo [8] but clashing with the expectations deriving from that of [112].

We think that the (important) point made in [112] is valid not quite as a theorem (a word that, anyway, the authors never use to indicate their work). We rather believe it acts mostly as a reminder that any specific theory that includes Majorana neutrino masses will have various specific links between these masses,  $0\nu\beta\beta$ , and possibly other manifestations of  $L$ -violation. We see as a risk the fact that, due to the impossibility of avoiding the issue of model dependence, we will end up with the idea that we can accept “petition of principles.”

**3.4. Role of the Search at Accelerators.** There is the hope that the search for new particles at the accelerators might reveal new physics relevant to the interpretation or in some way connected to the  $0\nu\beta\beta$ . This is a statement of wide validity. For example, the minimal supersymmetric extension of the SM is compatible with new  $L$ -violating phenomena taking place already at the level of renormalizable operators [115]. Also the hypothesized extradimensions at the TeV scale might be connected to new  $L$ -violating operators [116]. Or even, models where the smallness of the neutrino mass is explained through loop effects imply typically new particles that are not ultraheavy [117]. Notice that these are just a few among the many theoretical possibilities to select which, unfortunately, lack clear principles.

The recent scientific literature tried at least to exploit some minimality criteria, and the theoretical models that received the largest attention are indeed those discussed above. A specific subclass, named  $\nu$ SM [118], is found interesting enough to propose a dedicated search at the CERN SPS [118, 119], aiming to find rare decays of the ordinary mesons

into heavy neutrinos. Other models that foresee a new layer of gauge symmetry at accessible energies and, more specifically, those connected to left-right gauge symmetry [120] might instead lead to impressive  $L$ -violation at accelerators [121–123]. This should be quite analogous to the  $0\nu\beta\beta$  process itself and that could be seen as manifestations of operators similar to those in (24).

We would like just to point out that, in both cases, in order to explain the smallness of neutrino masses, very small adimensional couplings are required. Although this position is completely legitimate, in front of the present understanding of particle physics, it seems fair to say that this leaves us with some theoretical question to ponder.

## 4. Present Knowledge of Neutrino Masses

In this section we discuss the crucial parameter describing the  $0\nu\beta\beta$  if the process is mediated by light Majorana neutrinos (as defined in Section 3.1). We take into account the present information coming from the oscillation parameters, cosmology, and other data. On the theoretical side, we motivate the interest for a minimal interpretation of the results.

**4.1. The Parameter  $m_{\beta\beta}$ .** We know three light neutrinos. They are identified by their charged current interactions; that is, they have “flavor”  $\ell = e, \mu, \tau$ . The Majorana mass terms in the Lagrangian density are described by a symmetric matrix:

$$\mathcal{L}_{\text{mass}} = \frac{1}{2} \sum_{\ell, \ell' = e, \mu, \tau} \nu_{\ell}^{\dagger} C^{-1} M_{\ell\ell'} \nu_{\ell'} + h.c.. \quad (25)$$

The only term that violates the electronic number by two units is  $M_{ee}$ , and this simple consideration motivates the fact that the amplitude of the  $0\nu\beta\beta$  decay has to be proportional to these parameters, while the width has to be proportional to its squared modulus. We can diagonalize the neutrino mass matrix by mean of a unitary matrix

$$M = U^t \text{diag}(m_1, m_2, m_3) U^{\dagger}, \quad (26)$$

where the neutrino masses  $m_i$  are real and nonnegative. Thus, we can define

$$m_{\beta\beta} \equiv \left| \sum_{i=1,2,3} U_{ei}^2 m_i \right|, \quad (27)$$

where the index  $i$  runs on the 3 light neutrinos with given mass. This parameter is often called “effective Majorana mass” (it can be thought of as the “electron neutrino mass” that rules the  $0\nu\beta\beta$  transition, but keeping in mind that it is different from the “electron neutrino mass” that rules the  $\beta$  decay transition).

The previous intuitive argument in favor of this definition is corroborated by calculating the Feynman diagram of Figure 1. Firstly, it has to be noted that the electronic neutrino  $\nu_e$  is not a mass eigenstate in general. Then, substituting (26) into (25), we see that we go from the flavor basis to the mass basis by setting

$$\nu_{\ell} = \sum_{i=1,2,3} U_{\ell i} \nu_i. \quad (28)$$

Therefore, in the neutrino propagators of Figure 1, we will refer to the masses  $m_i$  (that in our case are “light”) while, in the two leptonic vertices, we will have  $U_{ei}$ . Taking the product of these factors, we get the expression given in (27).

It should be noted that the leptonic mixing matrix  $U$  as introduced above differs from the ordinary one used in neutrino oscillation analyses. Indeed, the latter is given after rotating away the phases of the neutrino fields and observing that oscillations depend only upon the combination  $MM^\dagger/(2E)$ . This matrix contains only one complex phase which plays a role in oscillations (the “CP-violating phase”). Instead, in the case of  $0\nu\beta\beta$ , the observable is different. It is just  $|M_{ee}|$ . Here, there are new phases that cannot be rotated away and that play a physical role. These are sometimes called “Majorana phases.” Their contribution can be made explicit by rewriting (27) as follows:

$$m_{\beta\beta} = \left| \sum_{i=1,2,3} e^{i\tilde{\xi}_i} |U_{ei}^2| m_i \right|. \quad (29)$$

We can now identify  $U_{ei}$  of (29) with the mixing matrix used in neutrino oscillation analyses (note that the specific choice and the symbols for these phases may differ among authors).

Before proceeding in the discussion, some remarks are in order:

- (i) It is possible to adopt a convention for the neutrino mixing matrix such that the 3 mixing elements  $U_{ei}$  are real and positive. However, in the most common convention,  $U_{e3}$  is defined to be complex.
- (ii) Only two Majorana phases play a physical role, the third one just being matter of convention.
- (iii) It is not possible even in principle to reconstruct the Majorana mass matrix simply on experimental bases, unless we find another observable which depends on Majorana phases.

Furthermore, a specific observation on the Type I Seesaw Model is useful. Let us consider the simplest case with only  $\nu_e$  and one heavy neutrino  $\nu_H$  that mix with this state. The Majorana mass matrix is of the form

$$\begin{pmatrix} 0 & m^{\text{Dirac}} \\ m^{\text{Dirac}} & M_H \end{pmatrix}. \quad (30)$$

One should not be misled, concluding that in this case (and, generally, in the Type I Seesaw)  $m_{\beta\beta}$  is zero. In fact, as it is well known, the masses of the light neutrinos (in this case, of  $\nu_e$ ) arise when one integrates away the heavy neutrino state, getting

$$m_{\nu_e} = -\frac{(m^{\text{Dirac}})^2}{M_H}. \quad (31)$$

As discussed in [106], we obtain in this one-flavor case the nonzero contribution

$$m_{\beta\beta} = |m_{\nu_e}| \left( 1 + \frac{\langle q^2 \rangle}{M_H^2} \right). \quad (32)$$

The second factor is the direct contribution of the heavy neutrino (this formula agrees with the naive scaling expected from the heavy neutrino contribution; but in specific three-flavor models it is possible, at least in principle, that heavy neutrinos give a large and even dominating contribution to the  $0\nu\beta\beta$  decay rate [106]). The quantity  $\langle q^2 \rangle$  depends on the nuclear structure and it is of the order of  $(100 \text{ MeV})^2$  and thus (32) is valid if we assume  $|m_{\nu_e}| \ll 100 \text{ MeV} \ll M_H$ .

In the above discussion, we have emphasized the three-flavor case. The main reason for this is evidently that we know about the existence of only 3 light neutrinos. It is possible to test this hypothesis by searching for new oscillation phenomena, by testing the universality of the weak leptonic couplings and/or the unitarity of the matrix in (28), by searching directly at accelerators new and (not too) light neutrino states, and so forth. However, we believe that it is fair to state that, to date, we have no conclusive experimental evidence or strong theoretical reason to deviate from this minimal theoretical scheme. We will adopt it in the proceeding of the discussion. In this way, we can take advantage of the precious information that was collected on the neutrino masses to constrain the parameter  $m_{\beta\beta}$  and to clarify the various expectations.

**4.2. Oscillations.** In [35], a complete analysis of the current knowledge of the oscillation parameters and of neutrino masses can be found. Although the absolute neutrino mass scale is still unknown, it has been possible to measure, through oscillation experiments, the squared mass splittings between the three active neutrinos. In Table 2, the parameters relevant to our analysis are reported. The mass splittings are labeled by  $\delta m^2$  and  $\Delta m^2$ . The former is measured through the observation of solar neutrino oscillations, while the latter comes from atmospheric neutrino data. The definitions of these two parameters are the following:

$$\delta m^2 \equiv m_2^2 - m_1^2, \quad (33)$$

$$\Delta m^2 \equiv m_3^2 - \frac{m_1^2 + m_2^2}{2}.$$

Practically,  $\delta m^2$  regards the splitting between  $\nu_1$  and  $\nu_2$ , while  $\Delta m^2$  refers to the distance between the  $\nu_3$  mass and the midpoint of  $\nu_1$  and  $\nu_2$  masses.

The sign of  $\delta m^2$  can be determined by observing matter enhanced oscillations as explained within the MSW theory [125, 126]. It turns out, after comparing with experimental data, that  $\delta m^2 > 0$  [127]. Unfortunately, determining the sign of  $\Delta m^2$  is still unknown and it is not simple to measure it. However, it has been argued (see, e.g., [128]) that, by carefully measuring the oscillation pattern, it could be possible to distinguish between the two possibilities,  $\Delta m^2 > 0$  and  $\Delta m^2 < 0$ . This is a very promising perspective in order to solve this ambiguity, which is sometimes called the “mass hierarchy problem.” In fact, standard names for the two mentioned possibilities for the neutrino mass spectra are “Normal Hierarchy” ( $\mathcal{NH}$ ) for  $\Delta m^2 > 0$  and “Inverted Hierarchy” ( $\mathcal{IH}$ ) for  $\Delta m^2 < 0$ .

TABLE 2: Results of the global  $3\nu$  oscillation analysis, in terms of best fit values and allowed  $1\sigma$  range for the  $3\nu$  mass-mixing parameters relevant for our analysis as reported in [35]. The last column is our estimate of the  $\sigma$  while assuming symmetric uncertainties.

Parameter	Best fit	$1\sigma$ range	$\sigma_{\text{symmetric}}$
$\mathcal{NH}$			
$\sin^2(\theta_{12})$	$3.08 \cdot 10^{-1}$	$(2.91\text{--}3.25) \cdot 10^{-1}$	$0.17 \cdot 10^{-1}$
$\sin^2(\theta_{13})$	$2.34 \cdot 10^{-2}$	$(2.16\text{--}2.56) \cdot 10^{-2}$	$0.22 \cdot 10^{-2}$
$\sin^2(\theta_{23})$	$4.37 \cdot 10^{-1}$	$(4.14\text{--}4.70) \cdot 10^{-1}$	$0.33 \cdot 10^{-1}$
$\delta m^2$ [eV $^2$ ]	$7.54 \cdot 10^{-5}$	$(7.32\text{--}7.80) \cdot 10^{-5}$	$0.26 \cdot 10^{-5}$
$\Delta m^2$ [eV $^2$ ]	$2.44 \cdot 10^{-3}$	$(2.38\text{--}2.52) \cdot 10^{-3}$	$0.08 \cdot 10^{-3}$
$\mathcal{IH}$			
$\sin^2(\theta_{12})$	$3.08 \cdot 10^{-1}$	$(2.91\text{--}3.25) \cdot 10^{-1}$	$0.17 \cdot 10^{-1}$
$\sin^2(\theta_{13})$	$2.39 \cdot 10^{-2}$	$(2.18\text{--}2.60) \cdot 10^{-2}$	$0.21 \cdot 10^{-2}$
$\sin^2(\theta_{23})$	$4.55 \cdot 10^{-1}$	$(4.24\text{--}5.94) \cdot 10^{-1}$	$1.39 \cdot 10^{-1}$
$\delta m^2$ [eV $^2$ ]	$7.54 \cdot 10^{-5}$	$(7.32\text{--}7.80) \cdot 10^{-5}$	$0.26 \cdot 10^{-5}$
$\Delta m^2$ [eV $^2$ ]	$2.40 \cdot 10^{-3}$	$(2.33\text{--}2.47) \cdot 10^{-3}$	$0.07 \cdot 10^{-3}$

The oscillation data are analyzed in [35] by writing the leptonic (PMNS) mixing matrix  $U|_{\text{osc}}$  in terms of the mixing angles  $\theta_{12}$ ,  $\theta_{13}$ , and  $\theta_{23}$  and of the CP-violating phase  $\phi$  according to the (usual) representation

$$U|_{\text{osc}} = \begin{pmatrix} c_{12}c_{13} & s_{12}c_{13} & s_{13}e^{-i\phi} \\ -s_{12}c_{23} - c_{12}s_{13}s_{23}e^{i\phi} & c_{12}c_{23} - s_{12}s_{13}s_{23}e^{i\phi} & c_{13}s_{23} \\ s_{12}s_{23} - c_{12}s_{13}c_{23}e^{i\phi} & -c_{12}s_{23} - s_{12}s_{13}c_{23}e^{i\phi} & c_{13}c_{23} \end{pmatrix}, \quad (34)$$

where  $s_{ij}, c_{ij} \equiv \sin \theta_{ij}, \cos \theta_{ij}$ . Note the usage of the same phase convention and parameterization of the quark (CKM) mixing matrix even if, of course, the values of the parameters are different. With this convention, it is possible to obtain (29) by defining

$$U \equiv U|_{\text{osc}} \cdot \text{diag} \left( e^{-i\xi_1/2}, e^{-i\xi_2/2}, e^{i\phi - i\xi_3/2} \right). \quad (35)$$

Table 2 shows the result of the best fit and of the  $1\sigma$  range for the different oscillation parameters. It can be noted that the values are slightly different depending on the mass hierarchy. This comes from the different analysis procedures used during the evaluation, as explained in [35]. Therefore, throughout this work, the two neutrino mass spectra are treated differently from one another, since we used these hierarchy-dependent parameters. The uncertainties are not completely symmetric around the best fit point, but the deviations are quite small, as claimed by the authors themselves in the reference. In particular, the plots in the paper show Gaussian likelihoods for the parameters determining  $m_{\beta\beta}$ . In order to later propagate the errors, we decided to neglect the asymmetry, which has no relevant effects on the presented results. We computed the maximum between the distances of the best fit values and the borders of the  $1\sigma$  range (fourth column of Table 2) and we assumed that the parameters fluctuate according to a Gaussian distribution around the best fit value, with a standard deviation given by that maximum.

TABLE 3: Flavor composition of the neutrino mass eigenstates. The two cases refer to the values for the CP-violating phase  $\phi = 0$  and  $\phi = 1.39\pi$  ( $1.31\pi$ ), best fit value in case of  $\mathcal{NH}$  ( $\mathcal{IH}$ ) according to [35].

Eigenstate	$\mathcal{NH}$		$\mathcal{IH}$	
	$(\phi = 0)$	$(\phi = 1.39\pi)$	$(\phi = 0)$	$(\phi = 1.31\pi)$
$\nu_1$				
$\nu_e$	.676	.676	.675	.675
$\nu_\mu$	.254	.160	.252	.141
$\nu_\tau$	.070	.164	.073	.184
$\nu_2$				
$\nu_e$	.301	.301	.301	.301
$\nu_\mu$	.331	.425	.322	.432
$\nu_\tau$	.368	.274	.378	.267
$\nu_3$				
$\nu_e$	.023	.023	.024	.024
$\nu_\mu$	.415	.415	.426	.426
$\nu_\tau$	.562	.562	.550	.550

Thanks to the knowledge of the oscillation parameters, it is possible to put a first series of constraints on  $m_{\beta\beta}$ . However, as already recalled, since the complex phases of the mixing parameters in (29) cannot be probed by oscillations, the allowed region for  $m_{\beta\beta}$  is obtained letting them vary freely. The expressions for the resulting extremes (i.e., the  $m_{\beta\beta}$  maximum and minimum values due to the phase variation) can be found in Appendix A. We adopt the graphical representation of  $m_{\beta\beta}$  introduced in [129] and refined in [18, 130]. It consists in plotting  $m_{\beta\beta}$  in bilogarithmic scale as a function of the mass of the lightest neutrino, for both the cases of  $\mathcal{NH}$  and  $\mathcal{IH}$ . The resulting plot is shown in Figure 6(a). The uncertainties on the various parameters are propagated using the procedures described in Appendix B. This results in a wider allowed region, which corresponds to the shaded parts in the picture.

**4.2.1. Mass Eigenstates Composition.** The standard three-flavor oscillations involve three massive states that, consistently with (28), are given by the following (note that in this case we are in the ultrarelativistic limit; see Section 2.3):

$$|\nu_i\rangle = \sum_{\ell=e,\mu,\tau} U_{\ell i} |\nu_\ell\rangle. \quad (36)$$

Thus, it is possible to estimate the probability of finding the component  $\nu_\ell$  of each mass eigenstate  $\nu_i$ . This probability is just the squared module of the matrix element  $U_{\ell i}$ , since the matrix is unitary. The result is graphically shown in Figure 7. As already mentioned, since hierarchy-dependent parameters were used, the flavor composition of the various eigenstates slightly depends on the mass hierarchy. It is worth noting that the results also depend on the possible choices of  $\phi$ , while they do not depend on the eventual Majorana phases. Table 3 reports the calculation for the cases  $\phi = 0$  and  $\phi = 1.39\pi$  ( $1.31\pi$ ) and best fit value for the  $\mathcal{NH}$  ( $\mathcal{IH}$ ) according to [35].

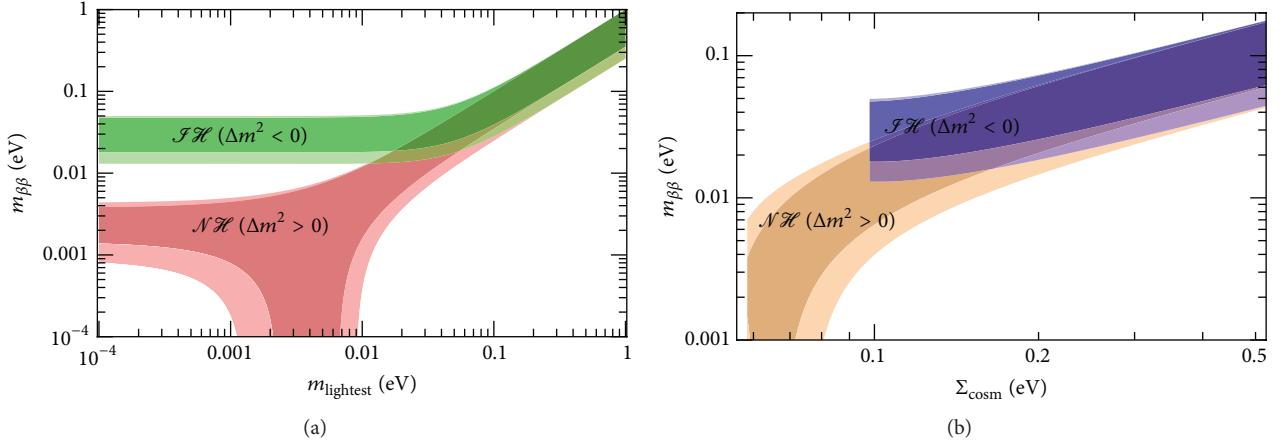


FIGURE 6: Updated predictions on  $m_{\beta\beta}$  from oscillations as a function of the lightest neutrino mass (a) and of the cosmological mass (b) in the two cases of  $\mathcal{NH}$  and  $\mathcal{IH}$ . The shaded areas correspond to the  $3\sigma$  regions due to error propagation of the uncertainties on the oscillation parameters. Figure from [124].

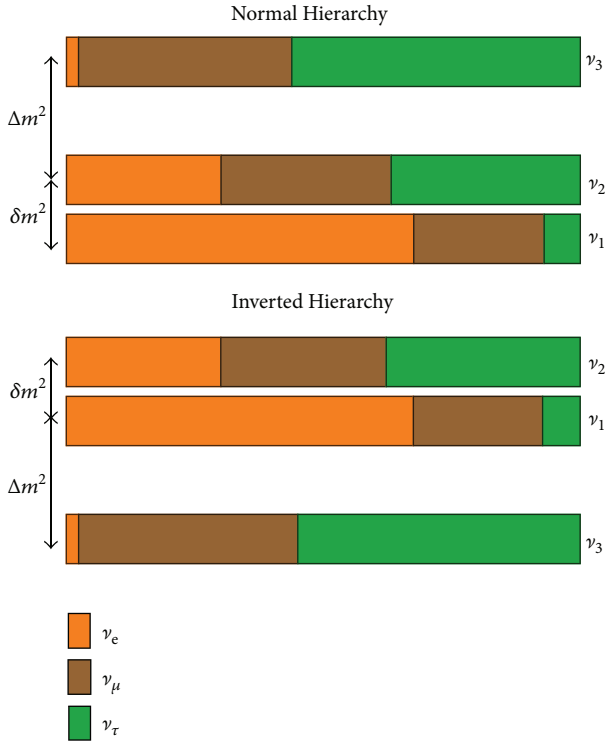


FIGURE 7: Graphic view of the probability of finding one of the flavor eigenstates if the neutrino is in a certain mass eigenstate. The value  $\phi = 0$  for the CP-violating phase is assumed.

### 4.3. Cosmology and Neutrino Masses

4.3.1. *The Parameter  $\Sigma$ .* The three-light neutrino scenario is consistent with all known facts in particle physics including the new measurements by Planck [34]. In this assumption, the physical quantity probed by cosmological surveys,  $\Sigma$ , is the sum of the masses of the three light neutrinos:

$$\Sigma \equiv m_1 + m_2 + m_3. \quad (37)$$

Depending on the mass hierarchy, is it possible to express  $\Sigma$  as a function of the lightest neutrino mass  $m$  and of the oscillation mass splittings. In particular, in the case of  $\mathcal{NH}$ , one gets

$$\begin{aligned} m_1 &= m, \\ m_2 &= \sqrt{m^2 + \delta m^2}, \end{aligned} \quad (38)$$

$$m_3 = \sqrt{m^2 + \Delta m^2 + \frac{\delta m^2}{2}},$$

while, in the case of  $\mathcal{IH}$ ,

$$\begin{aligned} m_1 &= \sqrt{m^2 + \Delta m^2 - \frac{\delta m^2}{2}}, \\ m_2 &= \sqrt{m^2 + \Delta m^2 + \frac{\delta m^2}{2}}, \end{aligned} \quad (39)$$

$$m_3 = m.$$

It can be useful to compute the mass of the lightest neutrino, given a value of  $\Sigma$ . This can be convenient in order to compute  $m_{\beta\beta}$  as a function of  $\Sigma$  instead of  $m$  (in Appendix C, an approximate (but accurate) alternative method for the numerical calculation needed to make this conversion is given). In this way,  $m_{\beta\beta}$  is expressed as a function of a directly observable parameter.

The close connection between the neutrino mass measurements obtained in the laboratory and those probed by cosmological observations was outlined long ago [131]. Furthermore, the measurements of  $\Sigma$  have recently reached important sensitivities, as discussed in Section 7.

In Figure 6(b), an updated version of the plot ( $m_{\beta\beta}$  versus  $\Sigma$ ) originally introduced in [132] is shown. Concerning the treatment of the uncertainties, we use again the assumption of Gaussian fluctuations and the prescription reported in Appendix B.

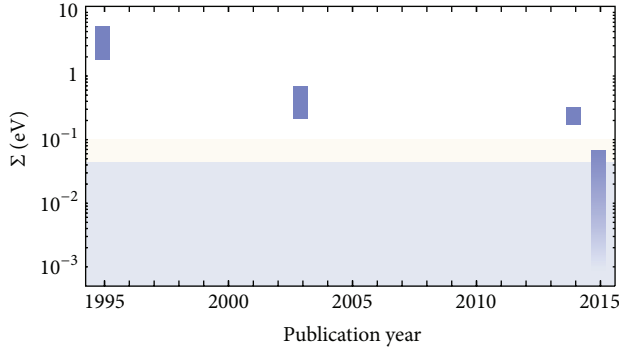


FIGURE 8: Evolution of some significant values for  $\Sigma$  as indicated by cosmology, based on well-known works [133–136]. Since the error for the first value is not reported in the reference, we assumed an error of 50% for the purpose of illustration. The yellow region includes values of  $\Sigma$  compatible with the  $\mathcal{N}\mathcal{H}$  spectrum, but not with the  $\mathcal{F}\mathcal{H}$  one. The gray band includes values of  $\Sigma$  incompatible with the standard cosmology and with oscillation experiments.

**4.3.2. Constraints from Cosmological Surveys.** The indications for neutrino masses from cosmology have kept changing for the last 20 years. A comprehensive review on the topic can be found in [137]. In Figure 8 the values for  $\Sigma$  given in [133–136] are shown. The scientific literature contains several authoritative claims for a nonzero value for  $\Sigma$  but, being different among each other, these values cannot be all correct (at least) and this calls us for a cautious attitude in the interpretation. Referring to the most recent years, two different positions emerge: on one side, we find claims that cosmology provides us with a hint for nonzero neutrino masses; on the other, we have very tight limits on  $\Sigma$ .

In the former case, it has been suggested [135, 138] that a total nonzero neutrino mass around 0.3 eV could alleviate some tensions present between cluster number counts (selected both in X-ray and by Sunyaev-Zeldovich effect) and weak lensing data. A sterile neutrino particle with mass in a similar range is sometimes also advocated [139, 140]. However, evidence for nonzero neutrino masses in either the active or sterile sectors seems to be claimed in order to fix the significant tensions between different data sets (cosmic microwave background (CMB) and baryonic acoustic oscillations (BAOs) on one side and weak lensing, cluster number counts, and high values of the Hubble parameter on the other).

In the latter case, the limit on  $\Sigma$  is so stringent that it better agrees with the  $\mathcal{N}\mathcal{H}$  spectrum, rather than with  $\mathcal{F}\mathcal{H}$  one (see the discussion in Section 7.1) (actually, it has been shown in [141] that the presence in the nuclear medium of  $L$ -violating four-fermion interactions of neutrinos with quarks from a decaying nucleus could account for an apparent incompatibility between the  $0\nu\beta\beta$  searches in the laboratory and the cosmological data; in fact, the net effect of these interactions (not present in the latter case) would be the generation of an effective “in-medium” Majorana neutrino mass matrix with a corresponding enhancement of the  $0\nu\beta\beta$  rate). The tightest experimental limits on  $\Sigma$  are usually obtained by combining

TABLE 4: Tight constraints on  $\Sigma$  obtained in 2015, by analyzing the data on the CMB by Planck Collaboration [34], polarization included, along with other relevant cosmological data probing smaller scales.

Upper bound on $\Sigma$ ( $2\sigma$ CL)	Included dataset
153 meV [34] <sup>a</sup>	SNe, BAO, $H_0$ prior
120 meV [43]	Lyman- $\alpha$
126 meV [44]	BAO, $H_0$ , $\tau$ priors, Planck SZ clusters
177 meV [45]	BAO
110 meV [46]	BAO, galaxy clustering, lensing

<sup>a</sup>Results as reported in <http://wiki.cosmos.esa.int/planckpla2015>, page 311.

CMB data with the ones probing smaller scales. In this way, their combination allows a more effective investigation of the neutrino induced suppression in terms of matter power spectrum, both in scale and redshift. Quite recently, a very stringent limit,  $\Sigma < 146$  meV ( $2\sigma$  CL), was set by Palanque-Desabrouille and collaborators [136]. New tight limits were presented after the data release by the Planck Collaboration in 2015 [34]. Some of the most significant results are reported in Table 4. The bounds on  $\Sigma$  indicated by these post-Planck studies are quite small, but they are still larger than the final sensitivities expected, especially thanks to the inclusion of other cosmological data sets probing smaller scales (see, e.g., [142, 143] for review works). Therefore, these small values cannot be considered surprising and, conversely, margins of further progress are present.

In our view, this situation should be considered as favorable since more proponents are forced to carefully examine and discuss all the available hypotheses. In view of this discussion, in Section 7, we consider two possible scenarios and discuss the implications from the cosmological investigations for the  $0\nu\beta\beta$  in both cases.

**4.4. Other Nonoscillations Data.** For the sake of completeness, we mention other two potential sources of information on neutrinos masses. They are

- (i) the study of kinematic effects (in particular of supernova neutrinos),
- (ii) the investigation of the effect of mass in single beta decay processes.

The first type of investigations, applied to SN1987A, produced a limit of about 6 eV on the electron antineutrino mass [144, 145]. The perspectives for the future are connected to new detectors, or to the existence of antineutrino pulses in the first instants of a supernova emission. The second approach, instead, is presently limited to about 2 eV [146, 147], even having the advantage of being obtained in controlled conditions, that is, in laboratory. Its future is currently in the hands of new experiments based on a  ${}^3\text{H}$  source [148] and on the electron capture of  ${}^{163}\text{Ho}$  [149–151], which have the potential to go below the eV in sensitivity.

*4.5. Theoretical Understanding.* Theorists have not been very successful in anticipating the discoveries on neutrino masses obtained by means of oscillations. The discussion within gauge models clarified that it is possible or even likely to have neutrino masses in gauge models (compare with Section 2.4). However, a large part of the theoretical community focused for a long time on models such as “minimal SU(5)”, where the neutrino masses are zero, emphasizing the interest in proton decay search rather than in neutrino mass search. On top of that, we had many models that aimed to predict, for example, the correct solar neutrino solution or the size of  $\theta_{13}$  before the measurements, but none of them were particularly convincing. More specifically, a lot of attention was given to the “small mixing angle solution” and the “very small  $\theta_{13}$  scenario” that are now excluded from the data.

Moreover, it is not easy to justify the theoretical position where neutrino masses are not considered along the masses of other fermions. This remark alone explains the difficulty of the theoretical enterprise that theorists have to face. For the reasons mentioned in Section 2.4, the SO(10) models are quite attractive to address a discussion of neutrino masses. However, even considering this specific class of well-motivated Grand Unified groups, it remains difficult to claim that we have a complete and convincing formulation of the theory. In particular, this holds for the arbitrariness in the choice of the representations (especially that of the Higgs bosons), for the large number of unknown parameters (especially the scalar potential), for the possible role of nonrenormalizable operators, for the uncertainties in the assumption concerning low scale supersymmetry, for the lack of experimental tests, and so forth. Note that, incidentally, preliminary investigations on the size of  $m_{\beta\beta}$  in SO(10) did not provide a clear evidence for a significant lower bound [152]. Anyway, even the case of an exactly null effective Majorana mass does not increase the symmetry of the Lagrangian and thus does not forbid the  $0\nu\beta\beta$ , as remarked in [153].

Here, we just consider one specific theoretical scheme, for illustration purposes. This should not be considered a full fledged theory, but rather it attempts to account for the theoretical uncertainties in the predictions. The hierarchy of the masses and of the mixing angles has suggested the hypothesis that the elements of the Yukawa couplings and thus of the mass matrices are subject to some selection rule. The possibility of a  $U(1)$  selection rule has been proposed in [154] and, since then, it has become very popular.

Immediately after the first strong evidences of atmospheric neutrino oscillations (1998) specific realizations for neutrinos have been discussed in various works (see [155] for references). These correspond to the neutrino mass matrix

$$M_{\text{neutrino}} = m \times \text{diag}(\varepsilon, 1, 1) C \text{diag}(\varepsilon, 1, 1), \quad (40)$$

where the flavor structure is dictated by a diagonal matrix that acts only on the electronic flavor and suppresses the matrix elements  $M_{e\mu}$ ,  $M_{e\tau}$ , and  $M_{ee}$  (twice). The dimensionful parameter (the overall mass scale) is given by  $\Delta \equiv \sqrt{\Delta m_{\text{atm}}^2} \approx 50$  meV. We thus have a matrix of coefficients  $C$  with elements  $C_{\ell\ell'} = \mathcal{O}(1)$  that are usually treated as random numbers of

the order of 1 in the absence of a theory. A choice of  $\varepsilon$  that suggested values of  $\theta_{12}$  and  $\theta_{13}$  in the correct region (before their measurement) is  $\varepsilon = \theta_C$  or  $\sqrt{m_\mu/m_\tau}$  [155]. Within these assumptions, the matrix element in which we are interested is

$$m_{\beta\beta} = |m\varepsilon^2 \mathcal{O}(1)| \approx (2-4) \text{ meV}. \quad (41)$$

Finally, we note that the SM renormalization of the elements of the neutrino mass matrix is multiplicative. The effect of renormalization is therefore particularly small for  $m_{\beta\beta}$  (see, e.g., equation (17) of [156] and the discussion therein). In other words, the value  $m_{\beta\beta} = 0$  (or values close to this one) should be regarded as a stable point of the renormalization flow.

Let us conclude repeating that, anyway, there are many reasons to consider the theoretical expectations with detachment, and the above theoretical scheme is not an exception to this rule. It is very important to keep in mind this fact in order to properly assess the value of the search for the  $0\nu\beta\beta$  and to proceed accordingly in the investigations.

## 5. The Role of Nuclear Physics

$0\nu\beta\beta$  is first of all a nuclear process. Therefore, the transition has to be described properly, taking into account the relevant aspects that concern nuclear structure and dynamics. In particular, it is a second-order nuclear weak process and it corresponds to the transition from a nucleus  $(A, Z)$  to its isobar  $(A, Z + 2)$  with the emission of two electrons. In principle, a nucleus  $(A, Z)$  can decay via double beta decay as long as the nucleus  $(A, Z+2)$  is lighter. However, if the nucleus can also decay by single beta decay,  $(A, Z + 1)$ , the branching ratio for the  $0\nu\beta\beta$  will be too difficult to be observed due to the overwhelming background rate from the single beta decay. Therefore, candidate isotopes for detecting the  $0\nu\beta\beta$  are even-even nuclei that, due to the nuclear pairing force, are lighter than the odd-odd  $(A, Z + 1)$  nucleus, making single beta decay kinematically forbidden (Figure 9). It is worth noting that, since the  $0\nu\beta\beta$  candidates are even-even nuclei, it follows immediately that their spin is always zero.

The theoretical expression of the half-life of the process in a certain nuclear species can be factorized as

$$[t^{1/2}]^{-1} = G_{0\nu} |\mathcal{M}|^2 |f(m_i, U_{ei})|^2, \quad (42)$$

where  $G_{0\nu}$  is the phase space factor (PSF),  $\mathcal{M}$  is the nuclear matrix element (NME), and  $f(m_i, U_{ei})$  is an adimensional function containing the particle physics beyond the SM that could explain the decay through the neutrino masses  $m_i$  and the mixing matrix elements  $U_{ei}$ .

In this section, we review the crucial role of nuclear physics in the expectations, predictions, and eventual understanding of the  $0\nu\beta\beta$ , also assessing the present knowledge and uncertainties. We are mainly restricted to the discussion of the light neutrino exchange as the candidate process for mediating the  $0\nu\beta\beta$  transition, but the mechanism of heavy neutrino exchange is also considered.

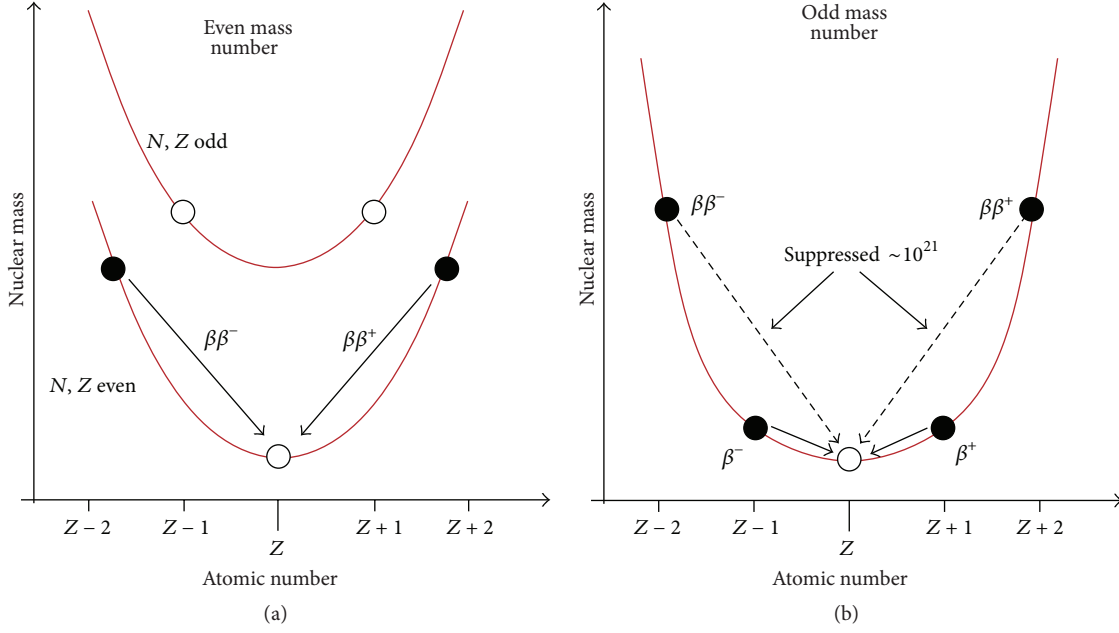


FIGURE 9: Nuclear mass as a function of the atomic number  $Z$  in the case of an isobar candidate with  $A$  even (a) and  $A$  odd (b).

In the former case ( $m \lesssim 100$  MeV, see (19)), the factor  $f$  is proportional to  $m_{\beta\beta}$ :

$$f(m_i, U_{ei}) \equiv \frac{m_{\beta\beta}}{m_e} = \frac{1}{m_e} \left| \sum_{k=1,2,3} U_{ek}^2 m_k \right|, \quad (43)$$

where the electron mass  $m_e$  is taken as a reference value. In the scheme of the heavy neutrino exchange ( $m \gtrsim 100$  MeV), the effective parameter is instead

$$f(m_i, U_{ei}) \equiv m_p \langle M_H^{-1} \rangle = m_p \left| \sum_{I=\text{heavy}} U_{eI}^2 \frac{1}{M_I} \right|, \quad (44)$$

where the proton mass  $m_p$  is now used, according to the tradition, as the reference value.

**5.1. Recent Developments on the Phase Space Factor Calculations.** The first calculations of PSFs date back to the late 1950s [157] and used a simplified description of the wave functions. The improvements in the evaluation of the PSFs are due to always more accurate descriptions and less approximations [158–160].

Recent developments in the numerical evaluation of Dirac wave functions and in the solution of the Thomas-Fermi equation allowed calculating accurately the PSFs for both single and double beta decay. The key ingredients are the scattering electron wave functions. The new calculations take into account relativistic corrections, the finite nuclear size, and the effect of the atomic screening on the emitted electrons. The main difference between these calculations and the older ones is of the order of a small percent for light nuclei ( $Z = 20$ ), about 30% for Nd ( $Z = 60$ ), and a rather large one, 90%, for U ( $Z = 92$ ).

In [95, 161, 162], the most up to date calculations of the PSFs for  $0\nu\beta\beta$  can be found. The results obtained in these works are quite similar. Throughout this paper, we use the values from the first reference.

**5.2. Models for the NMEs.** Let us suppose that the decay proceeds through an  $s$ -wave. Since we have just two electrons in the final state, we cannot form an angular momentum greater than one. Therefore, usually only  $0\nu\beta\beta$  matrix elements to final  $0^+$  states are considered. These can be the ground state,  $0_1^+$ , or the first excited state,  $0_2^+$ . Of course, we consider as a starting state just  $0^+$  state, since the double beta decay is possible only for  $(Z, A)$  even-even isobar nuclei.

The calculation of the NMEs for the  $0\nu\beta\beta$  is a difficult task because the ground and many excited states of open-shell nuclei with complicated nuclear structure have to be considered. The problem is faced by using different approaches and, especially in the last few years, the reliability of the calculations improved a lot. Here, a list of the main theoretical models is presented. The most relevant features for each of them are highlighted.

(i) *Interacting Shell Model (ISM)* [164, 165]. In the ISM only a limited number of orbits around the Fermi level is considered, but all the possible correlations within the space are included and the pairing correlations in the valence space are treated exactly. Proton and neutron numbers are conserved and angular momentum conservation is preserved. A good spectroscopy for parent and daughter nuclei is achieved.

(ii) *Quasiparticle Random Phase Approximation (QRPA)* [163, 166]. The QRPA uses a large valence space and thus it cannot comprise all the possible configurations. Typically, single

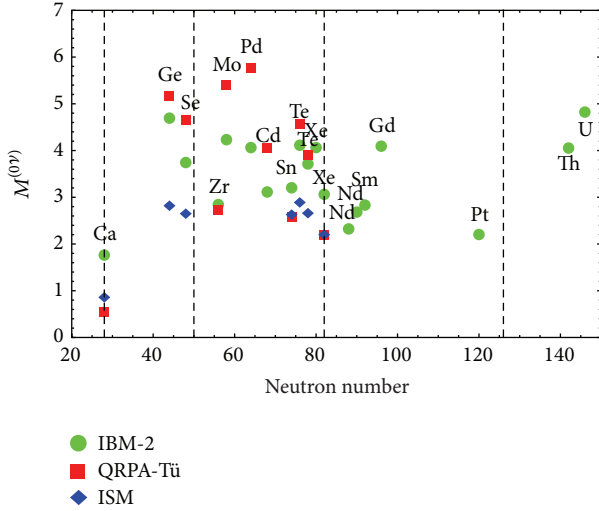


FIGURE 10: Most updated NMEs calculations for the  $0\nu\beta\beta$  with the IBM-2 [96], QRPA-Tü [163], and ISM [164] models. The results somehow differ among the models but are not too far away. Figure from [96].

particle states in a Woods-Saxon potential are considered. The proton-proton and neutron-neutron pairings are taken into account and treated in the BCS approximation (proton and neutron numbers are not exactly conserved).

(iii) *Interacting Boson Model (IBM-2)* [96]. In the IBM, the low-lying states of the nucleus are modeled in terms of bosons. The bosons are in either  $s$  boson ( $L = 0$ ) or  $d$  boson ( $L = 2$ ) states. Therefore, one is restricted to  $0^+$  and  $2^+$  neutron pairs transferring into two protons. The bosons interact through one- and two-body forces giving rise to bosonic wave functions.

(iv) *Projected Hartree-Fock Bogoliubov Method (PHFB)* [167]. In the PHFB, the NME are calculated using the projected-Hartree-Fock-Bogoliubov wave functions, which are eigenvectors of four different parameterizations of a Hamiltonian with pairing plus multipolar effective two-body interaction. In real applications, the nuclear Hamiltonian is restricted only to quadrupole interactions.

(v) *Energy Density Functional Method (EDF)* [168]. The EDF is considered to be an improvement with respect to the PHFB. The state-of-the-art density functional methods based on the well-established Gogny D1S functional and a large single particle basis are used.

The most common methods are ISM, QRPA, and IBM-2. In Figure 10, a comparison among the most recent NME calculations computed with these three models is shown. It can be seen that the disagreement can be generally quantified in some tens of percents, instead of the factors 2–4 of the past. This can be quite satisfactory. As it will be discussed in Section 5.3, the main source of uncertainty in the inference does not rely on the NME calculations anymore, but on the determination of the quenching of the axial vector coupling

constant. For this reason, in the subsequent discussion, we will be restricted to one of the considered models, namely, the IBM-2 [96], without significant loss of generality.

### 5.3. Theoretical Uncertainties

5.3.1. *Generality.* Following (42), an experimental limit on the  $0\nu\beta\beta$  half-life translates into a limit on the effective Majorana mass:

$$m_{\beta\beta} \leq \frac{m_e}{\mathcal{M} \sqrt{G_{0\nu} t^{1/2}}}. \quad (45)$$

From the theoretical point of view, in order to constrain  $m_{\beta\beta}$ , the estimation of the uncertainties both on  $G_{0\nu}$  and  $\mathcal{M}$  is crucial. Actually, the PSFs can be assumed to be quite well known, the error in their most recent calculations being around 7% [95].

A convenient parametrization for the NMEs is the following [169]:

$$\begin{aligned} \mathcal{M} &\equiv g_A^2 \mathcal{M}_{0\nu} \\ &= g_A^2 \left( M_{\text{GT}}^{(0\nu)} - \left( \frac{g_V}{g_A} \right)^2 M_F^{(0\nu)} + M_T^{(0\nu)} \right), \end{aligned} \quad (46)$$

where  $g_V$  and  $g_A$  are the axial and vector coupling constants of the nucleon,  $M_{\text{GT}}^{(0\nu)}$  is the Gamow-Teller (GT) operator matrix element between initial and final states (spin-spin interaction),  $M_F^{(0\nu)}$  is the Fermi contribution (spin independent interaction), and  $M_T^{(0\nu)}$  is the tensor operator matrix element. The form of (46) emphasizes the role of  $g_A$ . Indeed,  $\mathcal{M}_{0\nu}$  mildly depends on  $g_A$  and can be evaluated by modeling theoretically the nucleus. Actually, it is independent of  $g_A$  if the same quenching is assumed both for the vector and axial coupling constants, as we do here for definiteness, following [170].

5.3.2. *Is the Uncertainty Large or Small?* The main sources of uncertainties in the inference on  $m_{\beta\beta}$  are the NMEs. A comparison of the calculations from 1984 to 1998 revealed an uncertainty of more than a factor 4 [130]. A similar point of view comes out from the investigation of [171], where the results of the various calculations were used to attempt a statistical inference.

An important step forward was made with the first calculations of  $\mathcal{M}_{0\nu}$  that estimated also the errors; see [172, 173]. These works, based on the QRPA model, assessed a relatively small intrinsic error of  $\sim 20\%$ . The validity of these conclusions have been recently supported by the (independent) calculation based on the IBM-2 description of the nuclei [95, 96], which assesses an intrinsic error of 15% on  $\mathcal{M}_{0\nu}$ . However, the problem in assessing the uncertainties in the NMEs is far from being solved. Each scheme of calculation can estimate its own uncertainty, but it is still hard to understand the differences in the results among the models (Figure 10) and thus give an overall error. Notice also that when a process “similar” to the  $0\nu\beta\beta$  is considered (single beta decay, electron capture, and  $2\nu\beta\beta$ ) and the calculations

are compared with the measured rates, the actual differences are much larger than 20% [170]. This suggests that it is not cautious to assume that the uncertainties on the  $0\nu\beta\beta$  are instead subject to such a level of theoretical control.

Recently, there has been a lively interest in a specific and important reason of uncertainty, namely, the value of the axial coupling constant  $g_A$ . This has a direct implication on the issue that we are discussing, since any uncertainty on the value of  $g_A$  reflects itself into a (larger) uncertainty factor on the value of the matrix element  $\mathcal{M}$ . We will examine these arguments in greater detail in the rest of this section.

It is important to appreciate the relevance of these considerations for the experimental searches. If the value of the axial coupling in the nuclear medium is decreased by a factor  $\delta$ , namely,  $g_A \rightarrow g_A \cdot (1 - \delta)$ , the expected decay rate and therefore the number of signal events  $S$  will also decrease, approximatively as  $S \cdot (1 - \delta)^4$ . This change can be compensated by increasing the time of data taking or the mass of the experiment. However, the figure of merit, namely,  $S/\sqrt{B}$ , which quantifies the statistical significance of the measurement, changes only with the square root of the time or of the mass, in the typical case in which there are also background events  $B$ . For instance, if we have a decrease by  $\delta = 10$  (20)% of the axial coupling, we will obtain the same measurement after a time that is larger by a factor of  $1/(1 - \delta)^8 = 2.3$  (6). In other words, an effect that could be naively considered small has instead a big impact for the experimental search for the  $0\nu\beta\beta$ .

**5.3.3. The Size of the Axial Coupling.** It is commonly expected that the value  $g_A \approx 1.269$  measured in the weak interactions and decays of nucleons is “renormalized” in the nuclear medium towards the value appropriate for quarks [172, 173, 175]. It was argued in [170] that a further modification (reduction) is rather plausible. This is in agreement with what was stated some years before in [176], where the possibility of a “strong quenching” of  $g_A$  (i.e.,  $g_A < 1$ ) is actually favored. The same was also confirmed by recent study on single beta decay and  $2\nu\beta\beta$  [177]. It has to be noticed that, within the QRPA framework, the dependence of  $\mathcal{M}$  upon  $g_A$  is actually milder than quadratic, because the model is calibrated through the experimental  $2\nu\beta\beta$  decay rates using also another parameter, the particle-particle strength  $g_{pp}$  [178].

There could be different causes for the quenching of  $g_A$ . It was found that it can be attributed mainly to the following issues [170, 179]:

- (i) The limited model space (i.e., the size of the basis of the eigenstates) in which the calculation is done. This problem is by definition model dependent and it was extensively investigated in light nuclei in the 1970s [180–183], when it was argued that  $g_A \sim 1$ . In heavy nuclei, the question of quenching was first discussed in [180]. In this case,  $g_A$  was found to be even lower than 1, thus stimulating the statement that massive renormalization of  $g_A$  occurs.

- (ii) The contribution of nonnucleonic degrees of freedom. This effect does not depend much on the nuclear model adopted, but rather on the mechanism of coupling to nonnucleonic degrees of freedom. It was extensively investigated theoretically in the 1970s [184–186]. Recently, it has been investigated again within the framework of the chiral Effective Field Theory (EFT) [187]. It turns out that it may depend on momentum transfer and that it may lead in some cases to an enhancement rather than a quenching.
- (iii) The renormalization of the GT operator due to two-body currents. The first calculations for GT transitions for the  $0\nu\beta\beta$  operator based on the chiral EFT [187] showed the importance of two-body currents for the effective quenching of  $g_A$ . This was later confirmed in independent works [188, 189] and, more recently, by the use of a no-core-configuration-interaction formalism within the density functional theory [179].

It is still not clear if the quenching in both the transitions ( $0\nu\beta\beta$  and  $2\nu\beta\beta$ ) is the same. One argument which suggests that this is not unreasonable consists in noting that the  $2\nu\beta\beta$  can occur only through a GT ( $1^+$ ) transition. Instead, the  $0\nu\beta\beta$  could happen through all the possible intermediate states, so it is possible to argue that the transitions through states with spin parity different from  $1^+$  can be unquenched or even enhanced. Incidentally, it turns out that the dominant multipole in the  $0\nu\beta\beta$  transition is the GT one, thus making the hypothesis that the quenching in  $2\nu\beta\beta$  and  $0\nu\beta\beta$  is the same quite solid. Following [96], we adopt this as a working hypothesis in our discussion, however keeping in mind that some indications that the quenching might be different in the  $0\nu\beta\beta$  and  $2\nu\beta\beta$  transitions are present in other models [164, 189].

It would be extremely precious if these theoretical questions could be answered by some experimental data. It has been argued that the experimental study of nuclear transitions where the nuclear charge is changed by two units leaving the mass number unvaried, in analogy to the  $0\nu\beta\beta$  decay, could give important information. Despite the fact that the Double Charge Exchange reactions and  $0\nu\beta\beta$  processes are mediated by different interactions, some similarities between the two cases are present. These could be exploited to assess effectively the NME for the  $0\nu\beta\beta$  (and, more specifically, the entity of the quenching of  $g_A$ ). In the near future, a new project will be started at the Laboratori Nazionali del Sud (Italy) [190] with the aim of getting some inputs to deepen our theoretical understanding of this nuclear process.

**5.3.4. Quenching as a Major Cause of Uncertainty.** In view of the above considerations, we think that currently the value of  $g_A$  in the nuclear medium cannot be regarded as a quantity that is known reliably. It is rather an *important reason of uncertainty in the predictions*. In a conservative treatment, we should consider at least the following three cases:

$$g_A = \begin{cases} g_{\text{nucleon}} = 1.269 \\ g_{\text{quark}} = 1 \\ g_{\text{phen.}} = g_{\text{nucleon}} \cdot A^{-0.18}, \end{cases} \quad (47)$$

where the last formula includes phenomenologically the effect of the atomic number  $A$ . It represents the worst possible scenario for the  $0\nu\beta\beta$  search. The  $g_{\text{phen.}}$  parametrization as a function of  $A$  comes directly from the comparison between the theoretical half-life for  $2\nu\beta\beta$  and its observation in different nuclei, as reported in [170]. From the comparison between the theoretical half-life for the process and the experimental value it was possible to extract an effective value for  $g_A$ , thus determining its quenching. The assumption that  $g_A$  depends only upon the atomic number  $A$  is rather convenient for a cursory exploration of the potential impact of unaccounted nuclear physics effects on  $0\nu\beta\beta$ , but most likely it is also an oversimplification of the truth, as suggested by the residual difference between the calculated  $2\nu\beta\beta$  rates. Surely, it cannot replace an adequate theoretical modeling, that in the light of the following discussion has become rather urgent. Anyway, we stress that this is just a phenomenological description of the quenching, since the specific behavior is different in each nucleus and it somewhat differs from this parametrization [170].

The question of which is the “true value” of  $g_A$  is still open and introduces a considerable uncertainty in the inferences concerning massive neutrinos. The implications are discussed in Sections 6.6 and 6.7.

**5.4. The Case of Heavy Neutrino Exchange.** As already discussed in Section 3, it is possible to attribute the  $0\nu\beta\beta$  decay rate to the same particles that are added to the SM spectrum to explain oscillations, for example, heavy neutrinos. In this context one can assume that the exchange of  $M_H > 100$  MeV saturates the  $0\nu\beta\beta$  decay rate, also reproducing the ordinary neutrino masses. Heavy neutrino masses and mixing angles, compatible with the rate of  $0\nu\beta\beta$ , depend on the NMEs of the transition (compare, e.g., [105, 106]). Thus, nuclear physics has an impact also on the limits that are relevant to a direct search for heavy neutrinos with accelerators. Each scheme of nuclear physics calculation can estimate its intrinsic uncertainty. This is usually found to be small in modern computations (about 28% for heavy neutrino exchange [96]). In a conservative treatment, this uncertainty plus the already discussed unknown value of  $g_A$  should be taken into account. It has to be noticed that if the  $0\nu\beta\beta$  is due to a point-like (dimension-9) operator, as for heavy neutrino exchange, two nucleons are in the same point. Therefore, the effect of a hard core repulsion, estimated for modeling the “short-range correlations,” plays an important role in the determination of the uncertainties. A significant step forward has been recently made, pushing down this source of theoretical error of about an order of magnitude [96].

The most updated NMEs for the  $0\nu\beta\beta$  via heavy neutrino exchange are evaluated within the frames of the IBM-2 [96] and QRPA [174] models. A comparison between these results is shown in Figure 11. It can be seen that the values obtained within the QRPA model are always larger than those obtained with the IBM-2. The difference is quite big for many of the nuclei and might be due to the different treatment of the intermediate states. Also, in this case, we use the NMEs evaluated with the IBM-2 model. This allows us to keep

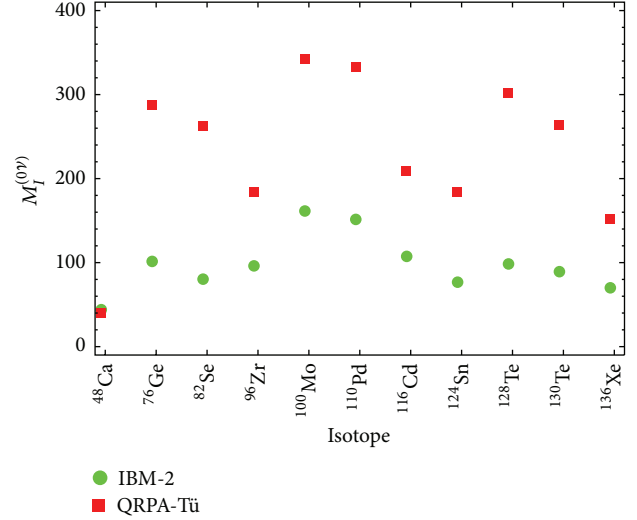


FIGURE 11: Most updated NMEs calculations for the  $0\nu\beta\beta$  via heavy neutrino exchange with the IBM-2 [96] and QRPA-Tü [174] models. In both cases, the value  $g_A = g_{\text{nucleon}}$  for the axial coupling constant and the Argonne parametrization for the short-range correlations are assumed. The results show a continuous overestimation of the QRPA estimations over the IBM-2 ones.

a more conservative approach by getting less stringent limits. Considering, for example, the case of  $^{76}\text{Ge}$ , we have

$$\mathcal{M}_{0\nu}(\text{Ge}) = \begin{cases} 104 \pm 29 & g_A = g_{\text{nucleon}} \\ 22 \pm 6 & g_A = g_{\text{phen.}} \end{cases} \quad (48)$$

From the experimental point of view, the limits on  $0\nu\beta\beta$  indicate that the mixings of heavy neutrinos  $|U_{eI}|^2$  are small. Using the current values for the PSF, NME, and sensitivity for the isotope [84], we get

$$\left| \sum_I \frac{U_{eI}^2}{M_I} \right| < \frac{7.8 \cdot 10^{-8}}{m_p} \cdot \left[ \frac{104}{\mathcal{M}_{0\nu}(\text{Ge})} \right] \cdot \left[ \frac{3 \cdot 10^{25} \text{ yr}}{\tau_{1/2}^{0\nu}} \right]^{1/2}, \quad (49)$$

where  $m_p$  is the proton mass and the heavy neutrino masses  $M_I$  are assumed to be  $\geq \text{GeV}$ .

Figure 12 illustrates the case of a single heavy neutrino mixing with the light ones and mediating the  $0\nu\beta\beta$  transition. In particular, the plot shows the case of the mixing for  $^{76}\text{Ge}$  assuming that a single heavy neutrino dominates the amplitude. The two regimes of heavy and light neutrino exchange are matched as proposed in [191]. The colored bands reflect the different sources of theoretical uncertainty.

As it is clear from Figure 12, the bound coming from  $0\nu\beta\beta$  searches is still uncertain. It weakens *by one order of magnitude* if the axial vector coupling constant is strongly quenched in the nuclear medium.

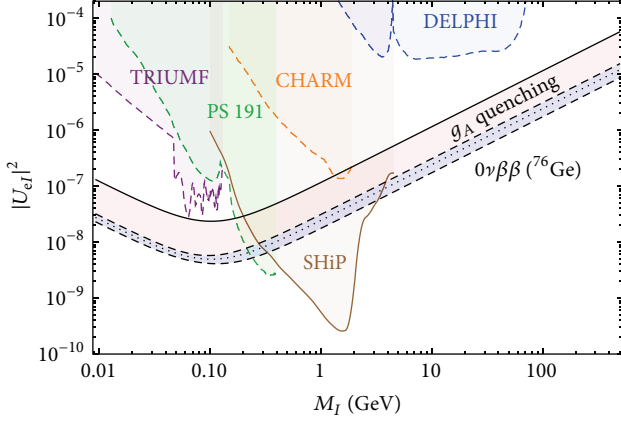


FIGURE 12: Bounds on the mixing between the electron neutrino and a single heavy neutrino from the combination of bounds obtained with Ge  $0\nu\beta\beta$  experiments [77] using the representation introduced in [191]. The bands correspond to the uncertainties discussed in the text. The dashed contours indicate the mass regions excluded by some of the accelerator experiments considered in [105]: CHARM (90% CL, [192]), DELPHI (95% CL, [193]), PS 191 (90% CL, [194]), and TRIUMF (90% CL, [195, 196]). The continuous contour indicates the expected probed region by the new proposed SHiP experiment at the CERN SPS [118]. Figure from [118].

The potential of the  $0\nu\beta\beta$  sensitivity to heavy neutrinos is therefore weakened and very sensitive to theoretical nuclear physics uncertainties. For some regions of the parameter space, even the limits obtained more than 15 years ago with accelerators are more restrictive than the current limits coming from  $0\nu\beta\beta$  search.

## 6. Experimental Search for the $0\nu\beta\beta$

The process described by (1) is actually just one of the forms that  $0\nu\beta\beta$  can assume. In fact, depending on the relative numbers of the nucleus protons and neutrons, four different mechanisms are possible:

$$\begin{aligned}
 (A, Z) &\longrightarrow (A, Z + 2) + 2e^- \quad (\beta^- \beta^-), \\
 (A, Z) &\longrightarrow (A, Z + 2) + 2e^+ \quad (\beta^+ \beta^+), \\
 (A, Z) + 2e^- &\longrightarrow (A, Z - 2) \quad (\text{EC EC}), \\
 (A, Z) + e^- &\longrightarrow (A, Z - 2) + e^+ \quad (\text{EC } \beta^+).
 \end{aligned} \tag{50}$$

Here,  $\beta^-$  ( $\beta^+$ ) indicate the emission of an electron (positron) and EC stands for electron capture (usually a K-shell electron is captured).

The explicit violation of the number of electronic leptons  $e$ ,  $\bar{e}$ ,  $\nu_e$ , or  $\bar{\nu}_e$  appears evident in each process in (50). A large number of experiments has been and is presently involved in the search for these processes, especially of the first one.

In this section, we introduce the experimental aspects relevant to the  $0\nu\beta\beta$  searches and we present an overview of the various techniques. We review the status of the past and present experiments, highlighting the main features and the

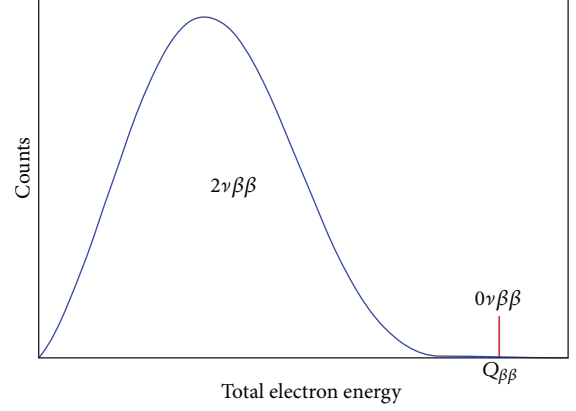


FIGURE 13: Schematic view of the  $2\nu\beta\beta$  and the  $0\nu\beta\beta$  spectra.

sensitivities. The expectations take into account the uncertainties coming from the theoretical side and, in particular, those from nuclear physics. The requirements for future experiments are estimated and finally the new constraints from cosmology are used as complementary information to that coming from the  $0\nu\beta\beta$  experiments.

**6.1. The  $0\nu\beta\beta$  Signature.** From the experimental point of view, the searches for a  $0\nu\beta\beta$  signal rely on the detection of the two emitted electrons. In fact, the energy of the recoiling nucleus being negligible, the sum of kinetic energy of the two electrons is equal to the  $Q$ -value of the transition. Therefore, if we consider these as a single body, we expect to observe a monochromatic peak at the  $Q$ -value (Figure 13).

Despite this very clear signature, because of the rarity of the process, the detection of the two electrons is complicated by the presence of background events in the same energy region, which can mask the  $0\nu\beta\beta$  signal. The main contributions to the background come from the environmental radioactivity, the cosmic rays, and the  $2\nu\beta\beta$  itself. In particular, the last contribution has the problematic feature of being unavoidable in presence of finite energy resolution, since it is originated by the same isotope which is expected to undergo  $0\nu\beta\beta$ .

In principle, any event producing an energy deposition similar to that of the  $0\nu\beta\beta$  decay increases the background level and hence spoils the experiment sensitivity. The capability of discriminating the background events is thus of great importance for this kind of search.

**6.2. The Choice of the Isotope.** The choice for the best isotope to look for  $0\nu\beta\beta$  is the first issue to deal with. From one side, the background level and the energy resolution need to be optimized. From the other, since the live-time of the experiment cannot exceed some years, the scalability of the technique, that is, the possibility to build a similar experiment with enlarged mass and higher exposure, is also fundamental. This translates in a series of criteria for the choice of the isotope.

(i) *High  $Q$ -Value ( $Q_{\beta\beta}$ ).* This requirement is probably the most important, since it directly influences the background.

TABLE 5: Isotopic abundance and  $Q$ -value for the known  $2\nu\beta\beta$  emitters [68].

Isotope	Isotopic abundance (%)	$Q_{\beta\beta}$ [MeV]
$^{48}\text{Ca}$	0.187	4.263
$^{76}\text{Ge}$	7.8	2.039
$^{82}\text{Se}$	9.2	2.998
$^{96}\text{Zr}$	2.8	3.348
$^{100}\text{Mo}$	9.6	3.035
$^{116}\text{Cd}$	7.6	2.813
$^{130}\text{Te}$	34.08	2.527
$^{136}\text{Xe}$	8.9	2.459
$^{150}\text{Nd}$	5.6	3.371

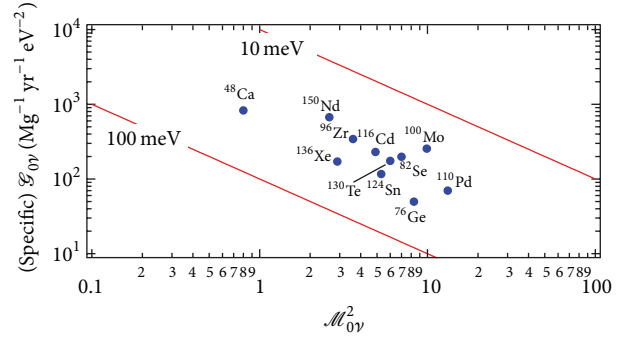
The 2615 keV line of  $^{208}\text{Tl}$ , which represents the end-point of the natural gamma radioactivity, constitutes an important limit in terms of background level.  $Q_{\beta\beta}$  should not be lower than  $\sim 2.4$  MeV (the only exception is  $^{76}\text{Ge}$ , due to the extremely powerful detection technique (see Section 6.4)). The ideal condition would be to have it even larger than 3270 keV, the highest energy beta among the  $^{222}\text{Rn}$  daughters ( $^{238}\text{U}$  chain), coming from  $^{214}\text{Bi}$ .

(ii) *High Isotopic Abundance.* This is a fundamental requirement to have experiments with sufficiently large mass. With the only exception of the  $^{130}\text{Te}$ , all the relevant isotopes have a natural isotopic abundance  $< 10\%$ . This practically means that the condition translates into *ease of enrichment* for the material.

(iii) *Compatibility with a Suitable Detection Technique.* It has to be possible to integrate the isotope of interest in a working detector. The source can either be separated from the detector or coincide with it. Furthermore, the detector has to be competitive in providing results and has to guarantee the potential for the mass scalability.

This results in a group of “commonly” studied isotopes among all the possible candidate  $0\nu\beta\beta$  emitters. It includes  $^{48}\text{Ca}$ ,  $^{76}\text{Ge}$ ,  $^{82}\text{Se}$ ,  $^{96}\text{Zr}$ ,  $^{100}\text{Mo}$ ,  $^{116}\text{Cd}$ ,  $^{130}\text{Te}$ ,  $^{136}\text{Xe}$ , and  $^{150}\text{Nd}$ . Table 5 reports the  $Q$ -value and the isotopic abundance for the mentioned isotopes.

From the theoretical side, referring to (42), one should also try to maximize both the PSF and the NME in order to get more strict bounds on  $m_{\beta\beta}$  with the same sensitivity in terms of half-life time. However, as recently discussed in [197], a uniform inverse correlation between the PSF and the square of the NME emerges in all nuclei (Figure 14). This happens to be more a coincidence than something physically motivated and, as a consequence, no isotope is either favored or disfavored for the search for the  $0\nu\beta\beta$ . It turns out that all isotopes have qualitatively the same decay rate per unit mass for any given value of  $m_{\beta\beta}$ .


 FIGURE 14: Geometric mean of the squared  $\mathcal{M}_{0\nu}$ , considered in [197] versus the specific  $G_{0\nu}$ . The case  $g_A = g_{\text{quark}}$  is assumed. Adapted from [197].

In recent time, also another criterion is becoming more and more relevant. This is simply the availability of the isotope itself in view of the next generations of  $0\nu\beta\beta$  experiments, which will have a very large mass. In fact, once the  $0\nu\beta\beta$  isotope mass for an experiment will be of the order of some tons, a nonnegligible fraction of the annual world production of the isotope of interest could be needed. This is, for example, the case of  $^{136}\text{Xe}$ , where the requests from the  $0\nu\beta\beta$  experiments also “compete” with those from the new proposed dark matter ones. The consequences are a probable price increase and a long storage for the isotope that needs to be taken into account.

6.3. *Sensitivity.* In the fortunate event of a  $0\nu\beta\beta$  peak showing up in the energy spectrum, starting from the law of radioactive decay, the decay half-life can be evaluated as

$$t^{1/2} = \ln 2 \cdot T \cdot \varepsilon \cdot \frac{N_{\beta\beta}}{N_{\text{peak}}}, \quad (51)$$

where  $T$  is the measuring time,  $\varepsilon$  is the detection efficiency,  $N_{\beta\beta}$  is the number of  $\beta\beta$  decaying nuclei under observation, and  $N_{\text{peak}}$  is the number of observed decays in the region of interest. If we assume to know exactly the detector features (i.e., the number of decaying nuclei, the efficiency, and the time of measurement), the uncertainty on  $t^{1/2}$  is only due to the statistical fluctuations of the counts:

$$\frac{\delta t^{1/2}}{t^{1/2}} = \frac{\delta N_{\text{peak}}}{N_{\text{peak}}}. \quad (52)$$

It seems reasonable to suppose Poisson fluctuations on  $N_{\text{peak}}$ . Since the expected number of events is “small,” the Poisson distribution differs in a nonnegligible way from the Gaussian. In order to quantify this discrepancy, we consider two values for  $N_{\text{peak}}$ , namely,  $N_{\text{peak}} = 5$  and  $N_{\text{peak}} = 20$ . In Table 6 we show the confidence intervals at  $1\sigma$  for the counts both considering a purely Poisson distribution (with mean equal to  $N_{\text{peak}}$ ) and a Gaussian one (with mean  $N_{\text{peak}}$  and standard deviation  $\sqrt{N_{\text{peak}}}$ ). Notice that, even if the number of counts is just 5, the Poisson and Gaussian distributions give almost the same relative uncertainties.

TABLE 6:  $1\sigma$  ranges for both Gaussian and Poisson distributions for two different values of  $N_{\text{peak}}$ . In the former case, we assumed a standard deviation equal to  $\sqrt{N_{\text{peak}}}$ . To compute the error columns, we halved the total width of the range and divided it by  $N_{\text{peak}}$ .

Distribution	$N_{\text{peak}}$	Range	Relative error (%)
Gauss	5	2.8–7.2	44.7
	20	15.5–24.5	22.4
Poisson	5	3.1–7.6	45.0
	20	15.8–24.8	22.5

If no peak is detected, the sensitivity of a given  $0\nu\beta\beta$  experiment is usually expressed in terms of “detector factor of merit,”  $S^{0\nu}$  [25]. This can be defined as the process half-life corresponding to the maximum signal that could be hidden by the background fluctuations  $n_B$  (at a given statistical CL). To obtain an estimation for  $S^{0\nu}$  as a function of the experiment parameters, it is sufficient to require that the  $0\nu\beta\beta$  signal exceeds the standard deviation of the total detected counts in the interesting energy window. At the confidence level  $n_\sigma$ , this means that we can write

$$n_{\beta\beta} \geq n_\sigma \sqrt{n_{\beta\beta} + n_B}, \quad (53)$$

where  $n_{\beta\beta}$  is the number of  $0\nu\beta\beta$  events and Poisson statistics for counts is assumed. If one now states that the background counts scale linearly with the mass of the detector (this is reasonable since, a priori, impurities are uniform inside the detector but, of course, this might not be always the case; e.g., if the main source of background is removed with volume fiducialization), from (51) it is easy to find an expression for  $S^{0\nu}$ :

$$\begin{aligned} S^{0\nu} &= \ln 2 \cdot T \cdot \varepsilon \cdot \frac{n_{\beta\beta}}{n_\sigma \cdot n_B} \\ &= \ln 2 \cdot \varepsilon \cdot \frac{1}{n_\sigma} \cdot \frac{x\eta N_A}{\mathcal{M}_A} \cdot \sqrt{\frac{M \cdot T}{B \cdot \Delta}}, \end{aligned} \quad (54)$$

where  $B$  is the background level per unit mass, energy, and time,  $M$  is the detector mass,  $\Delta$  is the FWHM energy resolution,  $x$  is the stoichiometric multiplicity of the element containing the  $\beta\beta$  candidate,  $\eta$  is the  $\beta\beta$  candidate isotopic abundance,  $N_A$  is the Avogadro number and, finally,  $\mathcal{M}_A$  is the compound molecular mass. Despite its simplicity, (54) has the advantage of emphasizing the role of the essential experimental parameters.

Of particular interest is the case in which the background level  $B$  is so low that the expected number of background events in the region of interest along the experiment life is of order of unity:

$$M \cdot T \cdot B \cdot \Delta \lesssim 1. \quad (55)$$

This is called the “zero background” experimental condition and it is likely the experimental condition that next generation experiments will face. Practically, it means that the goal is a great mass and a long time of data taking, keeping

the background level and the energy resolution as little as possible.

In this case,  $n_B$  is a constant, (54) is no more valid, and the sensitivity is given by

$$S_{0B}^{0\nu} = \ln 2 \cdot T \cdot \varepsilon \cdot \frac{N_{\beta\beta}}{n_\sigma \cdot n_B} = \ln 2 \cdot \varepsilon \cdot \frac{x\eta N_A}{\mathcal{M}_A} \cdot \frac{MT}{N_S}. \quad (56)$$

The constant  $N_S$  is now the number of observed events in the region of interest.

**6.4. Experimental Techniques.** The experimental approach to search for the  $0\nu\beta\beta$  consists in the development of a proper detector, able to reveal the two emitted electrons and to collect their sum energy spectrum (see Section 6.1) (additional information (e.g., the single electron energy or the initial momentum) can also be provided sometimes). The desirable features for such a detector are thus as follows.

(i) *Good Energy Resolution.* This is a fundamental requirement to identify the sharp  $0\nu\beta\beta$  peak over an almost flat background, as shown in Figure 15, and it is also the only protection against the (intrinsic) background induced by the tail of the  $2\nu\beta\beta$  spectrum. Indeed, it can be shown that the ratio  $R_{0\nu/2\nu}$  of counts due to  $0\nu\beta\beta$  and those due to  $2\nu\beta\beta$  in the peak region can be approximated by [199]

$$R_{0\nu/2\nu} \propto \left( \frac{Q_{\beta\beta}}{\Delta} \right)^6 \frac{t_{2\nu}^{1/2}}{t_{0\nu}^{1/2}}. \quad (57)$$

This expression clearly indicates that a good energy resolution is critical. But it also shows that the minimum required value actually depends on the chosen isotope, considered a strong dependence of (57) upon the  $2\nu\beta\beta$  half-life  $t_{2\nu}^{1/2}$ .

(ii) *Very Low Background.* Of course  $0\nu\beta\beta$  experiments have to be located underground in order to be protected from cosmic rays. Moreover, radio-pure materials for the detector and the surrounding parts, as well as proper passive and/or active shielding are mandatory to protect against environmental radioactivity. The longest natural radioactivity decay competing with  $0\nu\beta\beta$  is of the order of ( $10^9$ - $10^{10}$ ) yr versus lifetimes  $\geq 10^{25}$  yr.

(iii) *Large Isotope Mass.* Present experiments have masses of the order of some tens of kg up to a few hundred kg. Tons will be required for experiments aiming to cover the  $\mathcal{FH}$  region (see Section 6.7).

It has to be noted that it is impossible to optimize the listed features simultaneously in a single detector. Therefore, it is up to the experimentalists to choose which one to privilege in order to get the best sensitivity.

The experiments searching for the  $0\nu\beta\beta$  of a certain isotope can be classified into two main categories: detectors based on a calorimetric technique, in which the source is embedded in the detector itself, and detector using an external source approach, in which source and detector are two separate systems (Figure 16).

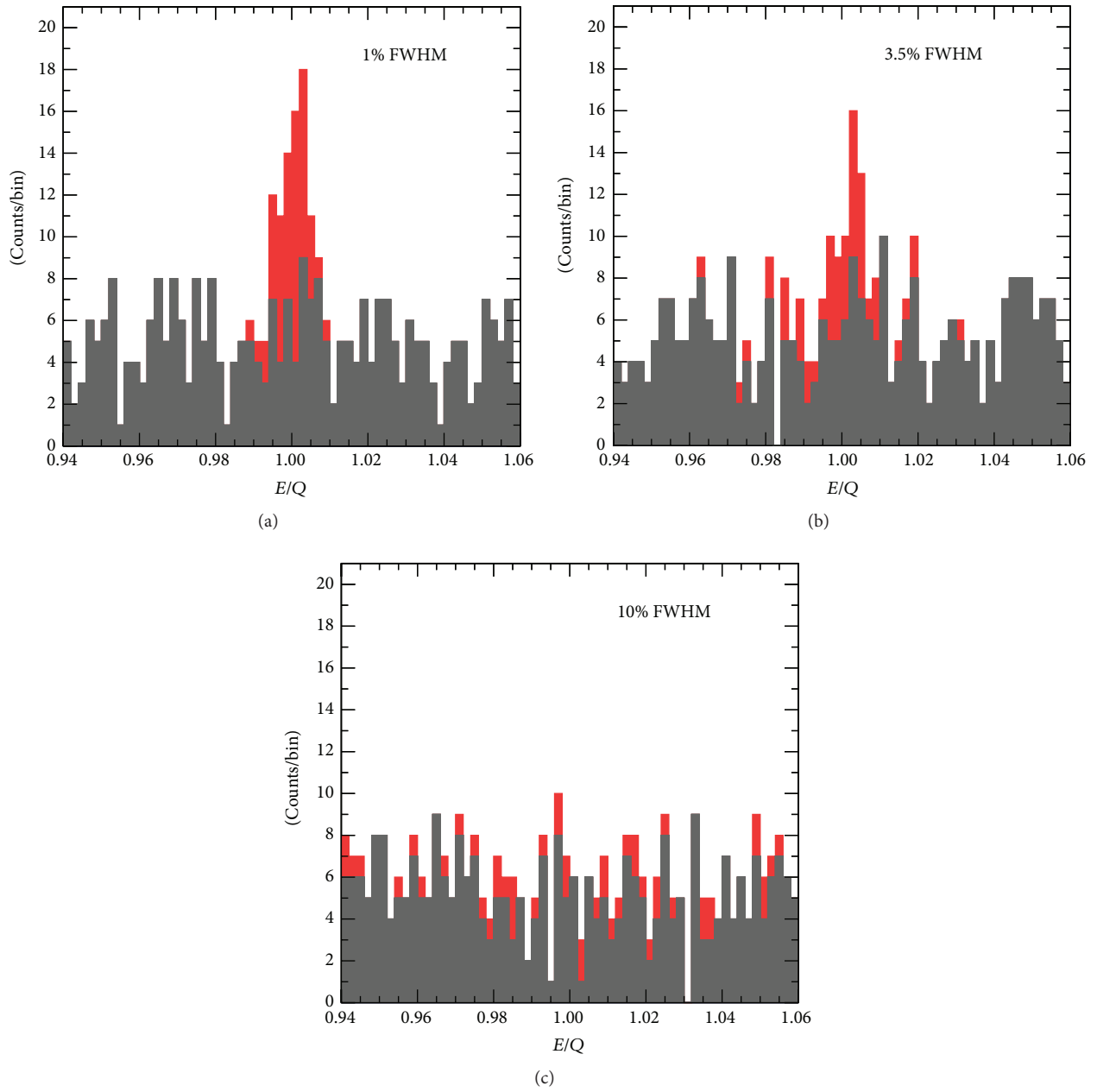


FIGURE 15: Signal and background (red and gray stacked histograms, resp.) in the region of interest around  $Q_{\beta\beta}$  for 3 Monte Carlo experiments with the same signal strength (50 counts) and background rate (1 count  $\text{keV}^{-1}$ ), but different energy resolution: (a) 1% FWHM; (b) 3.5% FWHM; (c) 10% FWHM. The signal is distributed normally around  $Q_{\beta\beta}$ , while the background is assumed flat. Figure from [198].

6.4.1. *Calorimetric Technique.* The calorimetric technique has already been implemented in various types of detectors. The main advantages and limitations for this technique can be summarized as follows [25]:

(+) large source masses are achievable thanks to the intrinsically high efficiency of the method. Experiments with masses up to  $\sim 200$  kg have already proved to work and ton-scale detectors seem possible.

(+) very high resolution is achievable with the proper type of detector ( $\sim 0.1\%$  FWHM with Ge diodes and bolometers).

(-) severe constraints on detector material (and thus on the isotope that can be investigated) arise from the request that the source material has to be embedded in the structure of the detector. However, this is not the case for some techniques (e.g., for bolometers and loaded liquid scintillators).

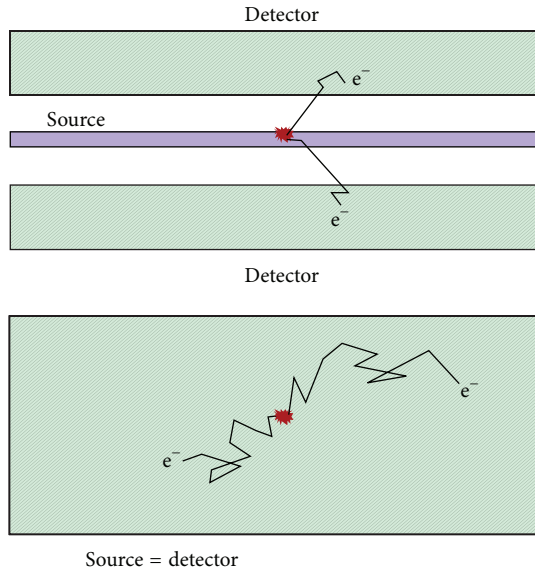


FIGURE 16: Schematic representation of the two main experimental categories for the  $0\nu\beta\beta$  search: calorimetric technique (source  $\equiv$  detector) and external source approach (source  $\neq$  detector).

- (–) the event topology reconstruction is usually difficult, with the exception of liquid or gaseous Xe TPC. However, the cost is paid in terms of a lower energy resolution.

Among the most successful examples of detectors using the calorimetric technique, we find the following:

- (i) *Ge Diodes*. The large volume, high-purity, and high energy resolution achievable make this kind of detector suitable for the  $0\nu\beta\beta$  search, despite the low  $Q_{\beta\beta}$  of  $^{76}\text{Ge}$ .
- (ii) *Bolometers*. Macrocalorimeters with masses close to 1 kg, very good energy resolution (close to that of Ge diodes), are now available for many compounds including  $0\nu\beta\beta$  emitters. The most significant case is the search for the  $0\nu\beta\beta$  of  $^{130}\text{Te}$  with  $\text{TeO}_2$  bolometers.
- (iii) *Xe Liquid and Gaseous TPC*. The lower energy resolution is “compensated” by the capability of reconstructing the event topology.
- (iv) *Liquid Scintillators Loaded with the  $0\nu\beta\beta$  Isotope*. These detectors have a poor energy resolution. However, a huge amount of material can be dissolved and, thanks to the purification processes, very low backgrounds are achievable. They are ideal detectors to set very stringent limits on the decay half-life.

**6.4.2. External Source Approach.** Also in the case of the external source approach, different detection techniques have been adopted, namely, scintillators, solid state detectors, and gas chambers. The main advantages and limitations for this technique can be summarized as follows:

- (+) the reconstruction of the event topology is possible, thus making in principle the achievement of the zero background condition easier. However,

the poor energy resolution does not allow distinguishing between  $0\nu\beta\beta$  events and  $2\nu\beta\beta$  events with total electron energy around  $Q_{\beta\beta}$ . Therefore  $2\nu\beta\beta$  represent an important background source.

- (–) the energy resolutions are low (of the order of 10%). The limit is intrinsic and it is mainly due to the electron energy deposition in the source itself.
- (–) large isotope masses are hardly achievable due to self-absorption in the source. Up to now, only masses of the order of some tens of kg have been possible, but an increase to about 100 kg target seems feasible.
- (–) the detection efficiencies are low (of the order of 30%).

So far, the most stringent bounds come from the calorimetric approach which, anyway, remains the one promising the best sensitivities and it is therefore the chosen technique for most of the future projects. However, the external source detector type has provided excellent results on the studies of the  $2\nu\beta\beta$ . Moreover, in case of discovery of a  $0\nu\beta\beta$  signal, the event topology reconstruction could represent a fundamental tool for the understanding of the mechanism behind the  $0\nu\beta\beta$ .

**6.5. Experiments: A Brief Review.** The first attempt to observe the  $0\nu\beta\beta$  process dates back to 1948 [200, 201]. Actually, the old experiments aiming to set a limit on the double beta decay half-lives did not distinguish between  $2\nu\beta\beta$  and  $0\nu\beta\beta$ . In the case of indirect investigations through geochemical observation, this was not possible even in principle.

However, the importance that the  $0\nu\beta\beta$  was acquiring in particle physics provided a valid motivation to continuously enhance the efforts in the search for this decay. On the experimental side, the considerable technological improvements allowed increasing the half-life sensitivity of several orders of magnitude ( $2\nu\beta\beta$  was first observed in the laboratory in  $^{82}\text{Se}$  in 1987 [202] and in many other isotopes in the subsequent years; see [68] for a review on  $2\nu\beta\beta$ ). The long history of  $0\nu\beta\beta$  measurements up to about the year 2000 can be found in [203–205]. Here, we concentrate only on a few experiments starting from the late 1990s.

Table 7 summarizes the main characteristics and performances of the selected experiments. It has to be noticed that, due to their different specific features, the actual comparison among all the values is not always possible. We tried to overcome this problem by choosing a common set of units of measurement.

**6.5.1. The Claimed Observation.** In 2001, after the publication of the experiment final results [74], a fraction of the Heidelberg-Moscow Collaboration claimed to observe a peak in the spectrum, whose energy corresponded to the  $^{76}\text{Ge}$   $0\nu\beta\beta$  transition  $Q$ -value [206]. After successive reanalysis (by fewer and fewer people), the final value for the half-life was found to be  $t^{1/2} = (2.23_{-0.31}^{+0.44}) \cdot 10^{25}$  yr [207]. This claim and the subsequent papers by the same authors aroused a number of critical replies (see, e.g., [24, 130, 208, 209]). Many of the questions and doubts still remain unanswered. To summarize, caution suggests that we disregard the claim, made in [74, 206, 207], that the transition was observed.

TABLE 7: In this table, the main features and performances of some past, present, and future  $0\nu\beta\beta$  experiments are listed.

Experiment	Isotope	Technique	Total mass [kg]	Exposure [kg yr]	FWHM @ $Q_{\beta\beta}$ [keV]	Background [counts/keV/kg/yr]	$S_{(90\% \text{ C.L.})}^{0\nu}$ [ $10^{25}$ yr]
<b>Past</b>							
Cuoricino [72]	$^{130}\text{Te}$	Bolometers	40.7 ( $\text{TeO}_2$ )	19.75	$5.8 \pm 2.1$	$0.153 \pm 0.006$	0.24
CUORE-0 [73]	$^{130}\text{Te}$	Bolometers	39 ( $\text{TeO}_2$ )	9.8	$5.1 \pm 0.3$	$0.058 \pm 0.006$	0.29
Heidelberg-Moscow [74]	$^{76}\text{Ge}$	Ge diodes	11 ( $^{\text{enr}}\text{Ge}$ )	35.5	$4.23 \pm 0.14$	$0.06 \pm 0.01$	1.9
IGEX [75, 76]	$^{76}\text{Ge}$	Ge diodes	8.1 ( $^{\text{enr}}\text{Ge}$ )	8.9	$\sim 4$	$\leq 0.06$	1.57
GERDA-I [77, 78]	$^{76}\text{Ge}$	Ge diodes	17.7 ( $^{\text{enr}}\text{Ge}$ )	21.64	$3.2 \pm 0.2$	$\sim 0.01$	2.1
NEMO-3 [79]	$^{100}\text{Mo}$	Tracker + calorimeter	6.9 ( $^{100}\text{Mo}$ )	34.7	350	0.013	0.11
<b>Present</b>							
EXO-200 [80]	$^{136}\text{Xe}$	LXe TPC	175 ( $^{\text{enr}}\text{Xe}$ )	100	$89 \pm 3$	$(1.7 \pm 0.2) \cdot 10^{-3}$	1.1
KamLAND-Zen [81, 82]	$^{136}\text{Xe}$	Loaded liquid scintillator	348 ( $^{\text{enr}}\text{Xe}$ )	89.5	$244 \pm 11$	$\sim 0.01$	1.9
<b>Future</b>							
CUORE [83]	$^{130}\text{Te}$	Bolometers	741 ( $\text{TeO}_2$ )	1030	5	0.01	9.5
GERDA-II [84]	$^{76}\text{Ge}$	Ge diodes	37.8 ( $^{\text{enr}}\text{Ge}$ )	100	3	0.001	15
LUCIFER [85]	$^{82}\text{Se}$	Bolometers	17 ( $\text{Zn}^{82}\text{Se}$ )	18	10	0.001	1.8
MAJORANA D. [86]	$^{76}\text{Ge}$	Ge diodes	44.8 ( $^{\text{enr}/\text{nat}}\text{Ge}$ )	100 <sup>a</sup>	4	0.003	12
NEXT [87, 88]	$^{136}\text{Xe}$	Xe TPC	100 ( $^{\text{enr}}\text{Xe}$ )	300	12.3–17.2	$5 \cdot 10^{-4}$	5
AMoRE [89]	$^{100}\text{Mo}$	Bolometers	200 ( $\text{Ca}^{\text{enr}}\text{MoO}_4$ )	295	9	$1 \cdot 10^{-4}$	5
nEXO [90]	$^{136}\text{Xe}$	LXe TPC	4780 ( $^{\text{enr}}\text{Xe}$ )	12150 <sup>b</sup>	58	$1.7 \cdot 10^{-5\text{b}}$	66
PandaX-III [91]	$^{136}\text{Xe}$	Xe TPC	1000 ( $^{\text{enr}}\text{Xe}$ )	3000 <sup>c</sup>	12–76	0.001	11 <sup>c</sup>
SNO+ [92]	$^{130}\text{Te}$	Loaded liquid scintillator	2340 ( $^{\text{nat}}\text{Te}$ )	3980	270	$2 \cdot 10^{-4}$	9
SuperNEMO [93, 94]	$^{82}\text{Se}$	Tracker + calorimeter	100 ( $^{82}\text{Se}$ )	500	120	0.01	10

<sup>a</sup>Our assumption (corresponding sensitivity from Figure 14 of [86]).<sup>b</sup>We assume 3 tons of fiducial volume.<sup>c</sup>Our assumption by rescaling NEXT.

TABLE 8: Lower bounds for  $m_{\beta\beta}$  for  $^{76}\text{Ge}$ ,  $^{130}\text{Te}$ , and  $^{136}\text{Xe}$ . The sensitivities were obtained by combining the most stringent limits from the experiments studying the isotopes. References [95] and [96] were used for the PSFs and for the NME, respectively. The different results correspond to different values of  $g_A$  according to (47).

Experiment	Isotope	$S^{0\nu}_{(90\% \text{ CL})}$ [ $10^{25}$ yr]	Lower bound for $m_{\beta\beta}$ [eV]		
			$g_{\text{nucleon}}$	$g_{\text{quark}}$	$g_{\text{phen.}}$
IGEX + HdM + GERDA-I [84]	$^{76}\text{Ge}$	3.0	$0.25 \pm 0.02$	$0.40 \pm 0.04$	$1.21 \pm 0.11$
Cuoricino + CUORE-0 [73]	$^{130}\text{Te}$	0.4	$0.36 \pm 0.03$	$0.58 \pm 0.05$	$2.07 \pm 1.05$
EXO-200 + KamLAND-ZEN [81]	$^{136}\text{Xe}$	3.4	$0.15 \pm 0.02$	$0.24 \pm 0.03$	$0.87 \pm 0.10$

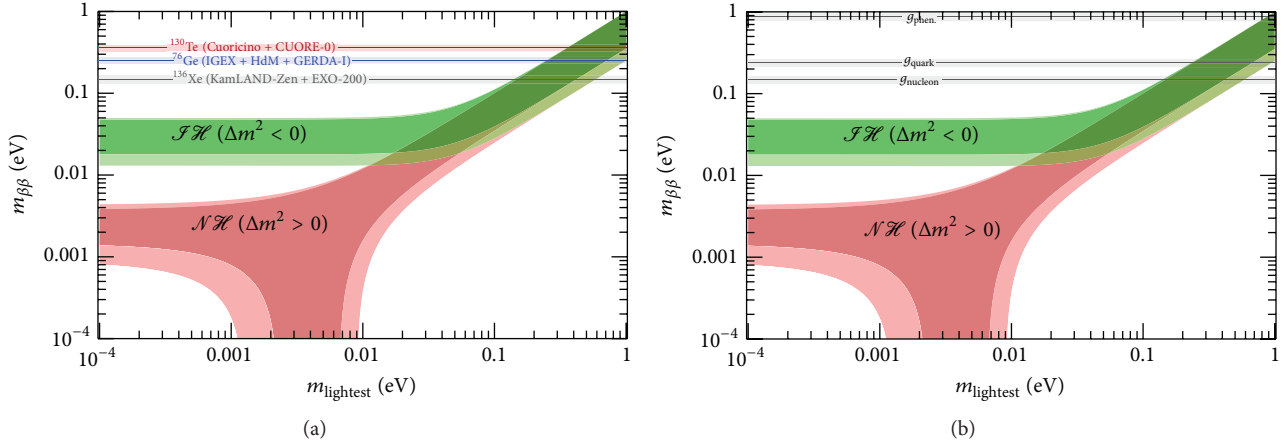


FIGURE 17: The colored regions show the predictions on  $m_{\beta\beta}$  from oscillations as a function of the lightest neutrino mass with the relative  $3\sigma$  regions. The horizontal bands show the experimental limits with the spread due to the theoretical uncertainties on the NME [96] and PSF [81, 95]. (a) Combined experimental limits for the three isotopes:  $^{76}\text{Ge}$  [84],  $^{130}\text{Te}$  [73], and  $^{136}\text{Xe}$ . The case  $g_A = g_{\text{nucleon}}$ . (b) Combined experimental limit on  $^{136}\text{Xe}$  for the three different values for  $g_A$ , according to (47).

Anyway, to date, the limit on the  $^{76}\text{Ge}$   $0\nu\beta\beta$  half-life is more stringent than the reported value [84].

**6.6. Present Sensitivity on  $m_{\beta\beta}$ .** Once the experimental sensitivities are known in terms of  $S^{0\nu}$ , by using (45), it is possible to correspondingly find the lower bounds on  $m_{\beta\beta}$ .

Figure 17 shows the most stringent limits up to date. They come from  $^{76}\text{Ge}$  [84],  $^{130}\text{Te}$  [73], and  $^{136}\text{Xe}$  [81]. In particular, the combined sensitivity from the single experimental limits is taken from the corresponding references.

In Figure 17(a), the case  $g_A = g_{\text{nucleon}}$  (unquenched value) is assumed. The uncertainties on NME and PSF are taken into account according to the procedure shown in Appendix B, and they result in the broadening of the lines describing the limits. As the plot shows, the current generation of experiments is probing the quasi degenerate part of the neutrino mass spectrum.

The effect of the quenching of  $g_A$  appears evident in Figure 17(b): the sensitivity for the same combined  $^{136}\text{Xe}$  experiment in the two cases of  $g_{\text{nucleon}}$  and  $g_{\text{phen.}}$  differs by a factor  $\geq 5$ . It is clear from the figure that this is the biggest uncertainty, with respect to all the other theoretical ones.

The single values for the examined cases are reported in Table 8.

**6.7. Near and Far Future Experiments.** It is also possible to extract the bounds on  $m_{\beta\beta}$  coming from the near future experiments starting from the expected sensitivities and using (45). The results are shown in Table 9. It can be seen that the mass region below 100 meV will begin to be probed in case of unquenched value for  $g_A$ . But still we will not enter the  $\mathcal{FH}$  region. In case  $g_A$  is maximally quenched, instead, the situation is much worse. Indeed, the expected sensitivity would correspond to values of  $m_{\beta\beta}$  which we already consider probed by the past experiments.

Let us now consider a next generation experiment (call it a “mega” experiment) and a next-to-next generation one (an “ultimate” experiment) with enhanced sensitivity. To define the physics goal we want to achieve, we refer to [124].

The most honest way to talk of the sensitivity is in terms of exposure or of half-life time that can be probed. From the point of view of the physical interest, however, besides the hope of discovering the  $0\nu\beta\beta$ , the most exciting investigation that can be imagined at present is the exclusion of the  $\mathcal{FH}$  case. This is the goal that most of the experimentalists are trying to reach with future  $0\nu\beta\beta$  experiments (see, e.g., [210]). For this reason, we require a sensitivity  $m_{\beta\beta} = 8$  meV. The mega experiment is the one that satisfies this requirement in the most favorable case, namely, when the quenching of  $g_A$

TABLE 9: Lower bounds for  $m_{\beta\beta}$  for the more (upper group) and less (lower group) near future  $0\nu\beta\beta$  experiments. References [95] and [96] were used for the PSFs and for the NME, respectively. The different results correspond to different values of  $g_A$  according to (47).

Experiment	Isotope	$S^{0\nu}_{(90\% \text{ CL})} [10^{25} \text{ yr}]$	Lower bound for $m_{\beta\beta}$ [eV]		
			$g_{\text{nucleon}}$	$g_{\text{quark}}$	$g_{\text{phen.}}$
CUORE [83]	$^{130}\text{Te}$	9.5	$0.073 \pm 0.008$	$0.14 \pm 0.01$	$0.44 \pm 0.04$
GERDA-II [84]	$^{76}\text{Ge}$	15	$0.11 \pm 0.01$	$0.18 \pm 0.02$	$0.54 \pm 0.05$
LUCIFER [85]	$^{82}\text{Se}$	1.8	$0.20 \pm 0.02$	$0.32 \pm 0.03$	$0.97 \pm 0.09$
MAJORANA D. [86]	$^{76}\text{Ge}$	12	$0.13 \pm 0.01$	$0.20 \pm 0.02$	$0.61 \pm 0.06$
NEXT [88]	$^{136}\text{Xe}$	5	$0.12 \pm 0.01$	$0.20 \pm 0.02$	$0.71 \pm 0.08$
AMoRE [89]	$^{100}\text{Mo}$	5	$0.084 \pm 0.008$	$0.14 \pm 0.01$	$0.44 \pm 0.04$
nEXO [90]	$^{136}\text{Xe}$	660	$0.011 \pm 0.001$	$0.017 \pm 0.002$	$0.062 \pm 0.007$
PandaX-III [91]	$^{136}\text{Xe}$	11	$0.082 \pm 0.009$	$0.13 \pm 0.01$	$0.48 \pm 0.05$
SNO+ [92]	$^{130}\text{Te}$	9	$0.076 \pm 0.007$	$0.12 \pm 0.01$	$0.44 \pm 0.04$
SuperNEMO [93]	$^{82}\text{Se}$	10	$0.084 \pm 0.008$	$0.14 \pm 0.01$	$0.41 \pm 0.04$

TABLE 10: Sensitivity and exposure necessary to discriminate between  $\mathcal{NH}$  and  $\mathcal{IH}$ : the goal is  $m_{\beta\beta} = 8 \text{ meV}$ . The two cases refer to the unquenched value of  $g_A = g_{\text{nucleon}}$  (mega) and  $g_A = g_{\text{phen.}}$  (ultimate). The calculations are performed assuming *zero background* experiments with 100% detection efficiency and no fiducial volume cuts. The last column shows the maximum value of the product  $B \cdot \Delta$  in order to actually comply with the zero background condition.

Experiment	Isotope	$S^{0\nu}_{0B} [\text{yr}]$	Exposure (estimate)	
			$M \cdot T [\text{ton}\cdot\text{yr}]$	$B \cdot \Delta_{(\text{zero bkg})} [\text{counts kg}^{-1} \text{ yr}^{-1}]$
mega Ge	$^{76}\text{Ge}$	$3.0 \cdot 10^{28}$	5.5	$1.8 \cdot 10^{-4}$
mega Te	$^{130}\text{Te}$	$8.1 \cdot 10^{27}$	2.5	$4.0 \cdot 10^{-4}$
mega Xe	$^{136}\text{Xe}$	$1.2 \cdot 10^{28}$	3.8	$2.7 \cdot 10^{-4}$
ultimate Ge	$^{76}\text{Ge}$	$6.9 \cdot 10^{29}$	125	$8.0 \cdot 10^{-6}$
ultimate Te	$^{130}\text{Te}$	$2.7 \cdot 10^{29}$	84	$1.2 \cdot 10^{-5}$
ultimate Xe	$^{136}\text{Xe}$	$4.0 \cdot 10^{29}$	130	$7.7 \cdot 10^{-6}$

is absent. Instead, the ultimate experiment assumes that  $g_A$  is maximally quenched. We chose the 8 meV value because, even taking into account the residual uncertainties on the NME and on the PSF, the overlap with the allowed band for  $m_{\beta\beta}$  in the  $\mathcal{IH}$  is excluded at more than  $3\sigma$ . Notice that we are assuming that at some point the issue of the quenching will be sorted out. Through (45), we obtain the corresponding value of  $t^{1/2}$  and thus we calculate the needed exposure to accomplish the task.

Referring to (56), if we suppose  $\varepsilon \simeq 1$  (detector efficiency of 100% and no fiducial volume cuts) and  $x \simeq \eta \simeq 1$  (all the mass is given by the candidate nuclei) and we assume one observed event (i.e.,  $N_S = 1$ ) in the region of interest, we get the simplified equation:

$$M \cdot T = \frac{\mathcal{M}_A \cdot S^{0\nu}}{\ln 2 \cdot N_A}. \quad (58)$$

This is the equation we used to estimate the product  $M \cdot T$  (exposure), and thus to assess the sensitivity of the mega and ultimate scenarios. The key input is, of course, the theoretical expression of  $t^{1/2}$ . The calculated values of the exposure are shown in Table 10 for the three considered nuclei:  $^{76}\text{Ge}$ ,  $^{130}\text{Te}$ , and  $^{136}\text{Xe}$ . The last column of the table gives the maximum allowed value of the product  $B \cdot \Delta$  that satisfies (55).

Figure 18 compares (in a schematic view) the masses of  $^{76}\text{Ge}$  and  $^{136}\text{Xe}$  corresponding to the present sensitivity [81, 84] to those of the “mega” and “ultimate” experiments assuming, for all three cases, the zero background condition and 5 years of data acquisition.

## 7. Interplay with Cosmology

Here, we want to assess the possibility of taking advantage of the knowledge about the neutrino cosmological mass to make

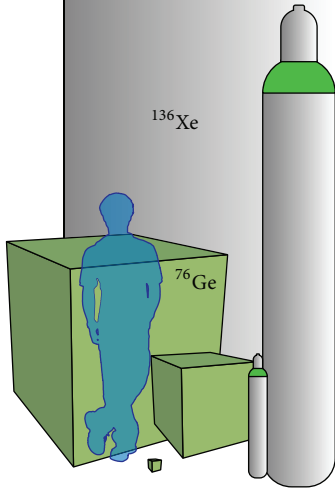


FIGURE 18: Masses corresponding to present, mega, and ultimate exposures, assuming zero background condition and 5 years of data acquisition. The cubes represent the amount of  $^{76}\text{Ge}$ , the (150 bar = 15 MPa) bottles, and the one of  $^{136}\text{Xe}$ . The smallest masses depict the present exposure, while the biggest bottle is out of scale.

inferences on some  $0\nu\beta\beta$  experiment results (or expected ones). In particular, we follow [211]. As already discussed in Section 4.3.2, we consider two possible scenarios. Firstly, we assume only upper limits on both  $\Sigma$  and  $m_{\beta\beta}$ , without any observation of  $0\nu\beta\beta$ . Later, we imagine an observation of  $0\nu\beta\beta$  together with a nonzero measurement of  $\Sigma$  (in both cases, we consider the unquenched value  $g_A = g_{\text{phen}}$  for the axial vector coupling constant).

**7.1. Upper Bounds Scenario.** The tight limit on  $\Sigma$  in [136] was obtained by combining Planck 2013 results [140] with the one-dimensional flux power spectrum measurement of the Lyman- $\alpha$  forest extracted from the BAO Spectroscopic Survey of the Sloan Digital Sky Survey [212]. In particular, the data from a new sample of quasar spectra were analyzed and a novel theoretical framework which incorporates neutrino nonlinearities self-consistently was employed.

The authors of [136] computed a probability for  $\Sigma$  that can be summarized to a very good approximation by

$$\Delta\chi^2(\Sigma) = \frac{(\Sigma - 22 \text{ meV})^2}{(62 \text{ meV})^2}. \quad (59)$$

Starting from the likelihood function  $\mathcal{L} \propto \exp(-\Delta\chi^2/2)$  with  $\Delta\chi^2$  as derived from Figure 7 in the reference, one can obtain the following limits:

$$\begin{aligned} \Sigma &< 184 \text{ meV} & (1\sigma \text{ CL}) \\ \Sigma &< 146 \text{ meV} & (2\sigma \text{ CL}) \\ \Sigma &< 208 \text{ meV} & (3\sigma \text{ CL}) \end{aligned} \quad (60)$$

which are very close to those predicted by the Gaussian  $\Delta\chi^2$  of (59). In particular, it is worth noting that, even if this measurement is compatible with zero at less than  $1\sigma$ , the best fit value is different from zero, as expected from the oscillation data and as evidenced by (59). We want to remark that, despite the impact, relative impact of systematic versus statistical errors on the estimated flux power is considered and discussed [212]; it is anyway advisable to take these results from cosmology with the due caution.

The plot showing  $m_{\beta\beta}$  as a function of  $\Sigma$ , which was already shown in Figure 6(b), is again useful for the discussion. A zoomed version of that plot (with linear instead of logarithmic scales for the axis) is presented in Figure 19(a). As already mentioned, the extreme values for  $m_{\beta\beta}$  after variation of the Majorana phases can be easily calculated (see Appendix A). This variation, together with the uncertainties on the oscillation parameters, results in a widening of the allowed regions. It is also worth noting that the error on  $\Sigma$  contributes to the total uncertainty. Its effect is a broadening of the light shaded area on the left side of the minimum allowed value  $\Sigma$  ( $m = 0$ ) for each hierarchy. In order to compute this uncertainty, we considered Gaussian errors on the oscillation parameters; namely,

$$\delta\Sigma = \sqrt{\left(\frac{\partial\Sigma}{\partial\delta m^2}\sigma(\delta m^2)\right)^2 + \left(\frac{\partial\Sigma}{\partial\Delta m^2}\sigma(\Delta m^2)\right)^2}. \quad (61)$$

It is possible to include the new cosmological constraints on  $\Sigma$  from [136] considering the following inequality:

$$\frac{(y - m_{\beta\beta}(\Sigma))^2}{(n\sigma[m_{\beta\beta}(\Sigma)])^2} + \frac{(\Sigma - \Sigma(0))^2}{(\Sigma_n - \Sigma(0))^2} < 1, \quad (62)$$

where  $m_{\beta\beta}(\Sigma)$  is the Majorana effective mass as a function of  $\Sigma$  and  $\sigma[m_{\beta\beta}(\Sigma)]$  is the  $1\sigma$  associated error, computed as discussed in [124].  $\Sigma_n$  is the limit on  $\Sigma$  derived from (59) for the CL  $n = 1, 2, 3, \dots$ . By solving (62) for  $y$ , it is thus possible to get the allowed contour for  $m_{\beta\beta}$  considering both the constraints from oscillations and from cosmology. In particular, the Majorana phases are taken into account by computing  $y$  along the two extremes of  $m_{\beta\beta}(\Sigma)$ , namely,  $m_{\beta\beta}^{\text{max}}(\Sigma)$  and  $m_{\beta\beta}^{\text{min}}(\Sigma)$ , and then connecting the two contours. The resulting plot is shown in Figure 19(b).

The most evident feature of Figure 19 is the clear difference in terms of expectations for both  $m_{\beta\beta}$  and  $\Sigma$  in the two hierarchy cases. The relevant oscillation parameters (mixing angles and mass splittings) are well known and they induce only minor uncertainties on the expected value of  $m_{\beta\beta}$ . These uncertainties widen the allowed contours in the upper, lower, and left sides of the picture. The boundaries in the rightmost regions are due to the new information from cosmology and are cut at various confidence levels. It is notable that, at  $1\sigma$ , due to the exclusion of  $\mathcal{FH}$ , the set of plausible values of  $m_{\beta\beta}$  is highly restricted.

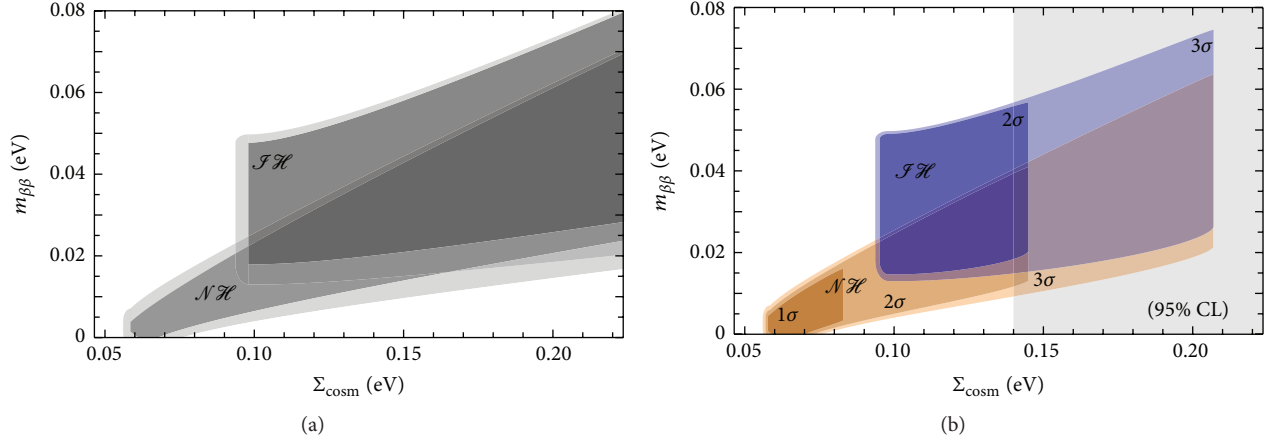


FIGURE 19: (a) Allowed regions for  $m_{\beta\beta}$  as a function of  $\Sigma$  with constraints given by the oscillation parameters. The darker regions show the spread induced by Majorana phase variations, while the light shaded areas correspond to the  $3\sigma$  regions due to error propagation of the uncertainties on the oscillation parameters. (b) Constraints from cosmological surveys are added to those from oscillations. Different CL contours are shown for both hierarchies. Notice that the  $1\sigma$  region for the  $\mathcal{IH}$  case is not present, being the scenario disfavored at this confidence level. The dashed band signifies the 95% CL excluded region coming from [136]. Figure from [211].

The impact of the new constraints on  $\Sigma$  appears to be even more evident by plotting  $m_{\beta\beta}$  as a function of the mass of the lightest neutrino. In this case, (62) becomes

$$\frac{(y - m_{\beta\beta}(m))^2}{(n\sigma [m_{\beta\beta}(m)])^2} + \frac{m^2}{m(\Sigma_n)^2} < 1. \quad (63)$$

The plot in Figure 20 globally shows that the next generation of experiments will have small possibilities of detecting a signal of  $0\nu\beta\beta$  due to light Majorana neutrino exchange. Therefore, if the new results from cosmology are confirmed or improved, ton or even multi-ton-scale detectors will be needed [124].

On the other hand, a  $0\nu\beta\beta$  signal in the near future could either disprove some assumptions of the present cosmological models or suggest that a different mechanism other than the light neutrino exchange mediates the transition. New experiments are interested in testing the latter possibility by probing scenarios beyond the SM [118, 122, 213].

**7.2. Measurements Scenario.** Here we consider the implications of the following nonzero value of  $\Sigma$  [135]:

$$\Sigma = (0.320 \pm 0.081) \text{ eV}. \quad (64)$$

We focus on the light neutrino exchange scenario and assume that  $0\nu\beta\beta$  is observed with a rate compatible with

- (1) the present sensitivity on  $m_{\beta\beta}$ ; in particular, we use the limit coming from the combined  $^{136}\text{Xe}$ -based experiments [81]; we refer to this as to the “present” case;
- (2) a value of  $m_{\beta\beta}$  that will be likely probed in the next few years; in particular, we use the CUORE experiment sensitivity [83], as an example of next generation of

$0\nu\beta\beta$  experiments; we refer to this as to the “near future” case.

For the sake of completeness, it is useful to recall a few definitions and relations. The likelihood of a simultaneous observation of some values for  $\Sigma$  and  $m_{\beta\beta}$  (resp., with uncertainties  $\sigma(\Sigma^{\text{meas}})$  and  $\sigma(m_{\beta\beta}^{\text{meas}})$  and distributed according to Gaussian distributions) can be written as follows:

$$\mathcal{L} \propto \exp\left[-\frac{(\Sigma - \Sigma^{\text{meas}})^2}{2\sigma(\Sigma^{\text{meas}})^2}\right] \exp\left[-\frac{(m_{\beta\beta} - m_{\beta\beta}^{\text{meas}})^2}{2\sigma(m_{\beta\beta}^{\text{meas}})^2}\right]. \quad (65)$$

Recalling the relation between  $\chi^2$  and the likelihood, namely,  $\mathcal{L} \propto e^{-\chi^2/2}$ , we obtain

$$\chi^2 = \frac{(\Sigma - \Sigma^{\text{meas}})^2}{\sigma(\Sigma^{\text{meas}})^2} + \frac{(m_{\beta\beta} - m_{\beta\beta}^{\text{meas}})^2}{\sigma(m_{\beta\beta}^{\text{meas}})^2} \quad (66)$$

which represents an elliptic paraboloid. Since we are dealing with a two-parameter  $\chi^2$ , we need to find the appropriate prescription to define the confidence intervals. At the desired confidence level, we get

$$\text{CL} = \iint_{\chi^2 < \chi_0^2} dx dy \frac{1}{2\pi\sigma_x\sigma_y} e^{-x^2/2\sigma_x^2 - y^2/2\sigma_y^2}, \quad (67)$$

and thus

$$\chi_0^2 = -2 \ln(1 - \text{CL}). \quad (68)$$

This defines the value for  $\chi^2$  correspondent to the confidence level CL.

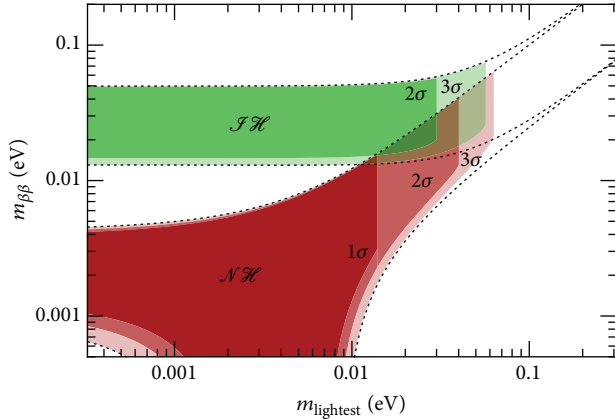


FIGURE 20: Constraints from cosmological surveys are added to those from oscillations in the representation of  $m_{\beta\beta}$  as a function of the lightest neutrino mass. The dotted contours represent the  $3\sigma$  regions allowed considering oscillations only. The shaded areas show the effect of the inclusion of cosmological constraints at different CL. The horizontal bands correspond to the expected sensitivity for future experiments. Figure from [211].

In order to write down the likelihood we need to evaluate the standard deviations both on  $\Sigma$  and on  $m_{\beta\beta}$ . While the error on  $\Sigma$  comes directly from the cosmological measurement, the one on  $m_{\beta\beta}$  has to be determined. It has two different contributions: one is statistical and comes from the Poisson fluctuations on the observed number of events (see Section 6.3), while the other comes from the uncertainties on the nuclear physics (see Section 5.3). Actually, a greater effect would rise if we took into account the error on  $g_A$ , but here we assume the quenching is absent.

For a few observed events, let us say less than 10 events, the global error is dominated by the statistical fluctuations. The error on the nuclear physics becomes the main contribution only if many events (more than a few tens) are detected. Using the described procedure and for the present case, we find an uncertainty on  $m_{\beta\beta}$  of about 31 meV for 5 observed events, which reduces to 24 meV for 10 events. If we neglect the statistical uncertainty, for example, we put  $N_{\text{events}}$ , the uncertainty becomes 14 meV. This means that the Poisson fluctuations effect is not negligible at all. Similarly, repeating the same work for the near future case, we obtain an uncertainty of 17 meV for 5 events, 13 meV for 10 events, and 8 meV for  $N_{\text{events}}$ .

Let us now concentrate on the case of 5  $0\nu\beta\beta$  observed events. If we cut the  $\chi^2$  at the 90% CL and we consider the data previously mentioned, we obtain the bigger, solid ellipses drawn in Figure 21. This shows that, in the near future case, a detection of  $0\nu\beta\beta$  would allow saying nothing about the mass hierarchy or about the Majorana phases. Interestingly, if  $0\nu\beta\beta$  were actually discovered with a  $m_{\beta\beta}$  a little bit lower than the one probed in the present case, some conclusions about the Majorana phases could be carried out. In any case, in order to state anything precise about  $m_{\beta\beta}$  and the Majorana phases, even assuming the discovery of  $0\nu\beta\beta$ , the uncertainty on the quenching of

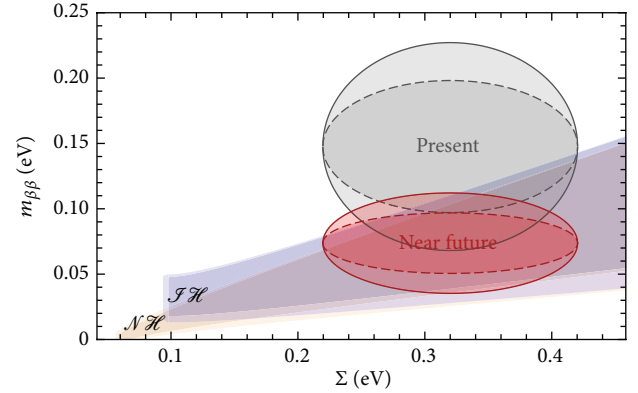


FIGURE 21: The plots show the allowed regions for  $m_{\beta\beta}$  as a function of the neutrino cosmological mass  $\Sigma$ . The ellipses show the 90% CL regions in which a positive observation of  $0\nu\beta\beta$  could be contained, according to the experimental uncertainties and 5 (solid) and 20 (dashed) actually observed events. In particular, the upper ellipse assumes the present limit from the combined  $^{136}\text{Xe}$  experiments [81]. The lower one assumes the sensitivity of CUORE [83].

the axial vector coupling constant has to be dramatically decreased.

If we repeat the same exercise assuming an observed number of events of 20, we obtain the smaller, dashed ellipses of Figure 21. In this case, an hypothetical observation coming from the present case is highly disfavored while, in the future case, even if nothing can be said about the hierarchy, some conclusions could be carried out regarding the Majorana phases.

This simple analysis shows that, thanks to the great efforts done in the NME and PSF calculations, it is most likely that the biggest contribution to the error will come from the statistical fluctuations of the counts. However, the theoretical uncertainty from the nuclear physics could make the picture really hard to understand because, up to now, it is a source of uncertainty of a factor 4–8 on  $m_{\beta\beta}$ .

**7.3. Considerations on the Information from Cosmological Surveys.** The newest results reported in Table 4 confirm and strengthen the cosmological indications of upper limits on  $\Sigma$ , and it is likely that we will have soon other substantial progress. Moreover, the present theoretical understanding of neutrino masses does not contradict these cosmological indications. These considerations emphasize the importance of exploring the issue of mass hierarchy in laboratory experiments and with cosmological surveys. However, as already stated, a cautious approach in dealing with the results from cosmological surveys is highly advisable.

From the point of view of  $0\nu\beta\beta$ , these results show that ton- or multi-ton-scale detectors will be needed in order to probe the range of  $m_{\beta\beta}$  now allowed by cosmology. Nevertheless, if next generation experiments see a signal, it will likely be a  $0\nu\beta\beta$  signal of new physics different from the light Majorana neutrino exchange.

## 8. Summary

In this review, we analyzed the  $0\nu\beta\beta$  process under many different aspects. We assessed its importance to test lepton number, to determine the nature of neutrino mass, and to probe its values. Various particle physics mechanisms that could contribute to the  $0\nu\beta\beta$  were examined, although with the conclusion that from the theoretical point of view the most interesting and promising remains the light Majorana neutrino exchange. We studied the current experimental sensitivity, focusing on the critical point of determining the uncertainties in the theoretical calculations and predictions. In view of all these considerations, the prospects for the near future experimental sensitivity were presented and the main features of present, past, and future  $0\nu\beta\beta$  experiments were discussed. Finally, we stressed the huge power of cosmological surveys in constraining neutrino masses and consequently the  $0\nu\beta\beta$  process.

## Appendix

### A. Extremal Values of $m_{\beta\beta}$

Recalling the definition of (27) for the Majorana effective mass:

$$m_{\beta\beta} = \left| \sum_{i=1}^3 U_{ei}^2 m_i \right|, \quad (\text{A.1})$$

it is possible to demonstrate that the extreme values assumed by this parameter due to free variations of the phases are (the proof shown here is based on the work reported in [129]) as follows:

$$m_{\beta\beta}^{\max} = \sum_{i=1}^3 |U_{ei}^2| m_i \quad (\text{A.2})$$

$$m_{\beta\beta}^{\min} = \max \left\{ 2 |U_{ei}^2| m_i - m_{\beta\beta}^{\max}, 0 \right\} \quad i = 1, 2, 3. \quad (\text{A.3})$$

*A.1. Formal Proof.* Regarding the first assertion, it is obvious that the sum of  $n$  complex numbers has the biggest allowed module when those numbers have aligned phases. Since the physical quantities depend on  $m_{\beta\beta}^2$ , without any loss of generality, it is possible to choose the first term ( $U_{e1}^2 m_1$ ) to be real. It thus follows that also the other two terms must be real: this is equivalent to considering the sum of the modules of the single terms.

To prove the second statement, let us consider the general case  $m_{\beta\beta} \sim |z_1 + z_2 + z_3| \equiv r$ , where  $z_i$  are complex numbers. We want to minimize  $r$ , by keeping  $|z_i|$  fixed. Let us define

$$\begin{aligned} r_1 &= |z_1| - |z_2| - |z_3|, \\ r_2 &= |z_2| - |z_1| - |z_3|, \\ r_3 &= |z_3| - |z_1| - |z_2|, \\ q_1 &= |z_1| - |z_2 + z_3|, \\ q_2 &= |z_2| - |z_1 + z_3|, \\ q_3 &= |z_3| - |z_1 + z_2|. \end{aligned} \quad (\text{A.4})$$

It is worth noting that only one of the  $r_i$  can be positive, at most. Therefore, it is possible to distinguish 4 cases:

- (i)  $r_1 > 0$ ;
- (ii)  $r_2 > 0$ ;
- (iii)  $r_3 > 0$ ;
- (iv)  $r_i \leq 0$  for  $i = 1, 2, 3$ .

In the first one, it is possible to show that  $r^{\min} = r_1$ . In fact, we can write

$$\begin{aligned} r &= |z_1 + z_2 + z_3| = |z_1 - (-z_2 - z_3)| \\ &\geq ||z_1| - |-z_2 - z_3|| = ||z_1| - |z_2 + z_3|| = |q_1|, \end{aligned} \quad (\text{A.5})$$

and, since

$$q_1 = |z_1| - |z_2 + z_3| \geq |z_1| - |z_2| - |z_3| = r_1 > 0, \quad (\text{A.6})$$

we obtain

$$r \geq |q_1| \geq q_1 \geq r_1. \quad (\text{A.7})$$

Similarly,  $r_2 > 0 \Rightarrow r^{\min} = r_2$  and  $r_3 > 0 \Rightarrow r^{\min} = r_3$  in the second and in the third cases, respectively. In the last case, it is necessary to observe that, if one of the  $r_i = 0$ , then  $r^{\min} = 0$ . Therefore, only the case in which  $r_i < 0 \forall i$  must be considered. In this case,  $q_1$  goes from negative when  $\arg(z_2) = \arg(z_3)$  to positive when  $\arg(z_2) = -\arg(z_3)$ . By continuity, this implies that a proper phase choice such that  $q_1 = 0$  must exist. Thus, one can conclude also in this case that  $r^{\min} = 0$  (by choosing  $r = |q_1|$ ).

In synthesis, the single case analysis leads to

$$r^{\min} = \max \{r_i, 0\}. \quad (\text{A.8})$$

This proves the original statement; since  $r_i = |z_i| - |z_j| - |z_k| + |z_i| - |z_i| = 2|z_i| - \sum_{l=1}^3 |z_l|$ , for  $i \neq j \neq k$ ,  $\{i, j, k\} = \{1, 2, 3\}$ .

*A.2. Remarks on the Case  $m_{\beta\beta}^{\min} = 0$ .* The three mixing elements  $|U_{ei}^2|$  are constrained by the unitarity:  $\sum_i |U_{ei}^2| = 1$ . This condition can be graphically pictured by using the inner region of an equilateral triangle with unitary height, where the distance from the  $i$ th side corresponds to the value of  $|U_{ei}^2|$  (see [129] for details). The result is displayed in Figure 22.

The experimental constraints on the oscillation parameters make it possible to evaluate the elements  $|U_{ei}^2|$  and, therefore, to identify a point inside the triangle, which is placed at the center of the colored bar in Figure 22. The different colors of the bar correspond to the  $1\sigma$ ,  $2\sigma$ , and  $3\sigma$  regions.

At each vertex, the value of  $m_{\beta\beta}$  coincides with  $m_{\beta\beta}^{\min}$  and with one of the mass eigenstates ( $\nu_e \equiv \nu_i$ ). Then, the value of  $m_{\beta\beta}^{\min}$  decreases moving from one vertex towards the inner part of the triangle, until it becomes zero inside the region delimited by the vertices defined by the conditions:

$$|U_{e1}^2| m_1 = |U_{e2}^2| m_2 \quad \text{when} \quad |U_{e3}^2| = 0, \quad (\text{A.9})$$

$$|U_{e1}^2| m_1 = |U_{e3}^2| m_3 \quad \text{when} \quad |U_{e2}^2| = 0, \quad (\text{A.10})$$

$$|U_{e2}^2| m_2 = |U_{e3}^2| m_3 \quad \text{when} \quad |U_{e1}^2| = 0. \quad (\text{A.11})$$

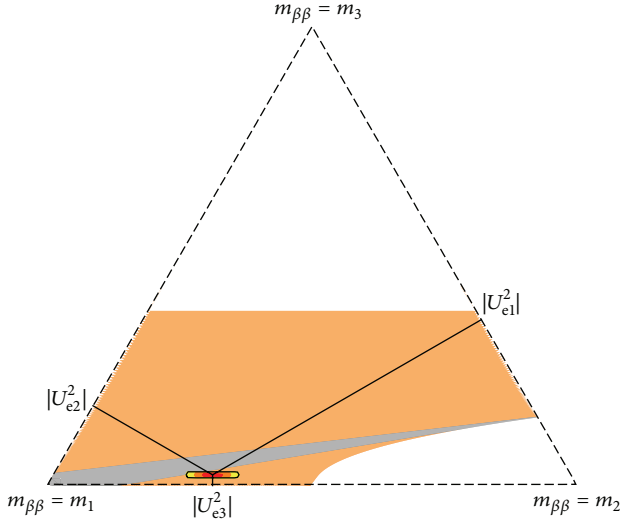


FIGURE 22: Representation of  $m_{\beta\beta}^{\min}$  in the unitarity triangle. The internal point in the middle of the small colored bar is identified by the constraints from the oscillation parameters. The colored regions correspond to  $1\sigma$  (red),  $2\sigma$  (orange), and  $3\sigma$  (yellow). The distance from a side represents the size of the corresponding mixing element  $|U_{ei}^2|$ . The inner shaded regions of the triangle enclose the areas where  $m_{\beta\beta}^{\min} = 0$  for a lightest neutrino mass that can vary from  $10^{-5}$  eV to the value which corresponds to a cosmological mass  $\Sigma = 0.14$  eV (orange, 90% CL current bound) and  $\Sigma = 0.06$  eV (gray, for purpose of illustration).

In fact, if we consider, for example, the first condition, from (A.9) we have

$$\begin{aligned} 2|U_{ei}^2|m_i - m_{\beta\beta}^{\max} &= 2|U_{ei}^2|m_i - |U_{e1}^2|m_1 - |U_{e2}^2|m_2 \\ &\quad - |U_{e3}^2|m_3 \\ &= 2|U_{ei}^2|m_i - 2|U_{e1}^2|m_1. \end{aligned} \quad (\text{A.12})$$

Substituting the possible values  $i = 1, 2, 3$ , and recalling that the condition to get  $m_{\beta\beta}^{\min}$  is expressed by (A.3), we obtain

$$m_{\beta\beta}^{\min} = \max\{-2|U_{e1}^2|m_1, 0\} = 0. \quad (\text{A.13})$$

The same argument can be applied also for the other two conditions. It is therefore possible to identify a region inside the triangle where  $m_{\beta\beta}^{\min}$  is zero. The experimental constraints on the oscillation parameters limit the possibility of  $m_{\beta\beta}^{\min} = 0$ , only to the case of  $\mathcal{NH}$ . Of course, the position and the extension of this region depend on the lightest neutrino mass.

Instead of choosing one particular value for the lightest neutrino mass, it is more convenient to plot the superposition of the regions obtained for increasing values of this parameter. In Figure 22, in orange we show the region obtained varying  $m_1$  from  $10^{-5}$  eV, up to the 90% CL maximum value it can have considering the limit on  $\Sigma$  from [136], according to (59). The gray region shows the superposition obtained when  $m_1 \sim 0$ ; namely, we show what happens if it turns out that the cosmological mass is close to its lower limit ( $\leq 0.06$  eV for the  $\mathcal{NH}$  case).

The existence of a  $m_{\beta\beta}^{\min} = 0$  region implies that, in principle,  $0\nu\beta\beta$  could be forbidden just by particular combinations of the phases, even if the neutrino is a Majorana particle.

## B. Error Propagation

It is convenient and usually appropriate to adopt statistical procedures that are as direct and as practical as possible. We are interested in the following situation. For any choice of the Majorana phases, the massive parameter that regulates  $0\nu\beta\beta$  can be thought of as  $M(m, \mathbf{x})$ . It is a function of the parameters that are determined by oscillation experiments up to their experimental error,  $x_i \pm \Delta x_i$ , and of another massive parameter  $m$ . Here a remark is necessary. When in the literature we found maximal or systematic uncertainties, in order to propagate their effects in our calculations, we decided to interpret them as the semiwidths of flat distributions and thus, dividing these numbers by  $\sqrt{3}$ , we could get the standard deviations of those distributions. Then, we considered those values as standard deviations for Gaussian fluctuations of the parameters around the given values.

For any fixed value of  $m$ , and for the other parameters set to their best fit values  $x_i$ , we can attach the following error to  $M$ :

$$\Delta M|_m = \sqrt{\sum_i \left(\frac{\partial M}{\partial x_i}\right)^2 \Delta x_i^2}. \quad (\text{B.1})$$

When we want to consider the prediction and the error for a fixed value of another massive parameter  $\Sigma(m, \mathbf{x})$ , we have to vary also  $m$ , keeping  $\delta\Sigma = \partial\Sigma/\partial m \delta m + \partial\Sigma/\partial x_i \delta x_i = 0$ . Therefore, in this case, we find

$$\Delta M|_\Sigma = \sqrt{\sum_i \left(\frac{\partial M}{\partial x_i} - \frac{\partial\Sigma/\partial x_i}{\partial\Sigma/\partial m} \frac{\partial M}{\partial m}\right)^2 \Delta x_i^2}. \quad (\text{B.2})$$

Of course, we will calculate  $m$  by inverting  $\Sigma(m, \mathbf{x}) = \Sigma$  (here, the symbol  $\Sigma$  denotes the function and also its value; however, this abuse of notation is harmless in practice).

## C. $\Sigma = f(m_{\text{lightest}})$ , Analytical Solution

Let us write in full generality the three-flavor relation for the mass probed in cosmology as

$$\Sigma = m + \sqrt{m^2 + a^2} + \sqrt{m^2 + b^2}, \quad (\text{C.1})$$

where  $m$ ,  $\Sigma$ ,  $a$ , and  $b$  are masses, that is, nonnegative parameters. It is possible to obtain  $m$  as a function of  $\Sigma$  in the physical range

$$\Sigma \geq a + b \quad (\text{C.2})$$

simply by solving a quartic equation. Since we are interested in certain specific cases ( $\mathcal{NH}$  or  $\mathcal{IH}$ ) we specify the discussion further.

When  $a \ll b$ , corresponding to the  $\mathcal{NH}$  case, it is convenient to write the quartic equation as

$$(3m^2 - 4m\Sigma + \lambda^2)(m^2 - \lambda^2) + 4a^2b^2 = 0, \quad (\text{C.3})$$

where

$$\lambda^2 \equiv \Sigma^2 - (a^2 + b^2). \quad (\text{C.4})$$

Indeed, we see that this quartic equation has spurious solutions in this limit, for example, those for  $m \approx \pm\lambda$ . Instead, we are interested in the one that (for  $a = 0$ ) reads

$$m = m_{\mathcal{NH}}(\Sigma, b) \equiv \frac{2\Sigma - \sqrt{\Sigma^2 + 3b^2}}{3} \quad (\text{C.5})$$

with  $\Sigma \geq b$ . In the case when  $a \approx b$ , instead, which corresponds to the  $\mathcal{FH}$  case, it is convenient to write the quartic equation as

$$(3m^2 + 2m\Sigma - \lambda^2)(m - \Sigma)^2 - (a^2 - b^2)^2 = 0, \quad (\text{C.6})$$

where

$$\lambda^2 \equiv \Sigma^2 - 2(a^2 + b^2). \quad (\text{C.7})$$

Again, we see that this quartic equation has spurious solutions in the limit  $a \approx b$ , for example,  $m \approx \Sigma$ . We are interested in the one that in the case  $a = b$  reads

$$m = m_{\mathcal{FH}}(\Sigma, b) \equiv \frac{-\Sigma + 2\sqrt{\Sigma^2 - 3b^2}}{3} \quad (\text{C.8})$$

with  $\Sigma \geq 2b$ .

Finally, we discuss useful approximate formulae for the specific parameterization suggested in [35]; namely,

$$\begin{aligned} a &= \delta m^2, \\ b &= \Delta m^2 + \frac{\delta m^2}{2} \end{aligned} \quad (\text{C.9})$$

for the  $\mathcal{NH}$  case and

$$\begin{aligned} a &= \Delta m^2 - \frac{\delta m^2}{2}, \\ b &= \Delta m^2 + \frac{\delta m^2}{2} \end{aligned} \quad (\text{C.10})$$

for the  $\mathcal{FH}$  one.

In the latter case, the approximation obtained by (C.8), namely,

$$m = m_{\mathcal{FH}}(\Sigma, \Delta m^2), \quad (\text{C.11})$$

is already excellent, being better than  $3\mu\text{eV}$  in the whole range of masses. Instead, (C.5) implies a maximum error that can reach  $5\text{ meV}$  for  $\mathcal{NH}$ . Although this is quite adequate for the present and near future sensitivity, it is possible to improve the approximation also in the case of  $\mathcal{NH}$  by using

$$m = m_{\mathcal{NH}}(\Sigma, \Delta m^2) - \frac{\delta m^2}{4m_{\mathcal{NH}}(\Sigma, \Delta m^2)}. \quad (\text{C.12})$$

This formula is obtained by linearly expanding in  $\delta m^2$  the relation that links  $\Sigma$  and  $m$ , (C.1), around the point  $m = m_{\mathcal{NH}}(\Sigma, \Delta m^2)$ . The error is remarkably small error and more than adequate for the present sensitivity: less than  $0.2\text{ meV}$ .

## Competing Interests

The authors declare that they have no competing interests.

## Acknowledgments

The authors wish to acknowledge extensive discussions with Professor F. Iachello and thank him for stimulating this study. Francesco Vissani also thanks E. Lisi.

## References

- [1] P. A. M. Dirac, "The quantum theory of electron," *Proceedings of the Royal Society of London A*, vol. 117, no. 778, pp. 610–624, 1928.
- [2] P. A. M. Dirac, "The quantum theory of the electron. Part II," *Proceedings of the Royal Society of London Series A: Mathematical and Physical Sciences*, vol. 118, no. 779, pp. 351–361, 1928.
- [3] E. Majorana, "Theory of the symmetry of electrons and positrons," *Il Nuovo Cimento*, vol. 14, pp. 171–184, 1937.
- [4] G. Racah, "On the symmetry of particle and antiparticle," *Il Nuovo Cimento*, vol. 14, pp. 322–328, 1937.
- [5] W. H. Furry, "On transition probabilities in double beta-disintegration," *Physical Review*, vol. 56, no. 12, pp. 1184–1193, 1939.
- [6] M. Goeppert-Mayer, "Double beta-disintegration," *Physical Review*, vol. 48, no. 6, pp. 512–516, 1935.
- [7] G. Feinberg and M. Goldhaber, "Microscopic tests of symmetry principles," *Proceedings of the National Academy of Sciences of the United States of America*, vol. 45, no. 8, pp. 1301–1312, 1959.
- [8] B. Pontecorvo, "Superweak interactions and double beta decay," *Physics Letters B*, vol. 26, no. 10, pp. 630–632, 1968.
- [9] S. L. Glashow, "Partial-symmetries of weak interactions," *Nuclear Physics*, vol. 22, no. 4, pp. 579–588, 1961.
- [10] S. Weinberg, "A model of leptons," *Physical Review Letters*, vol. 19, no. 21, pp. 1264–1266, 1967.
- [11] A. Salam, "Weak and electromagnetic interactions," in *Proceedings of the C68-05-19*, pp. 367–377, Lerum, Sweden, May 1968.
- [12] S. Weinberg, "Baryon- and lepton-nonconserving processes," *Physical Review Letters*, vol. 43, no. 21, pp. 1566–1570, 1979.
- [13] P. Minkowski, " $\mu \rightarrow e\gamma$  at a rate of one out of 109 muon decays?" *Physics Letters B*, vol. 67, no. 4, pp. 421–428, 1977.
- [14] T. Yanagida, "Horizontal symmetry and masses of neutrinos," in *Proceedings of the Workshop on the Baryon Number of the Universe and Unified Theories*, C79-02-13.1, pp. 95–99, Tsukuba, Japan, February 1979.
- [15] M. Gell-Mann, P. Ramond, and R. Slansky, "Complex spinors and unified theories," *Conference Proceedings C79-09-27*, pp. 315–321, 1979, <https://arxiv.org/abs/1306.4669>.
- [16] R. N. Mohapatra and G. Senjanović, "Neutrino mass and spontaneous parity nonconservation," *Physical Review Letters*, vol. 44, no. 14, pp. 912–915, 1980.
- [17] B. Pontecorvo, "Mesonium and anti-mesonium," *Soviet Physics—JETP*, vol. 6, p. 429, 1957, *Zhurnal Eksperimental'noi i Teoreticheskoi Fizik*, vol. 33, pp. 549–551, 1957.
- [18] A. Strumia and F. Vissani, "Neutrino masses and mixings and..." <http://arxiv.org/abs/hep-ph/0606054>.
- [19] M. C. Gonzalez-Garcia and Y. Nir, "Neutrino masses and mixing: evidence and implications," *Reviews of Modern Physics*, vol. 75, no. 2, pp. 345–402, 2003.
- [20] S. M. Bilenky, J. Hošek, and S. Petcov, "On oscillations of neutrinos with Dirac and Majorana masses," *Physics Letters B*, vol. 94, no. 4, pp. 495–498, 1980.

- [21] S. R. Elliott, "Recent progress in double beta decay," *Modern Physics Letters A*, vol. 27, no. 07, Article ID 1230009, 2012.
- [22] A. Giuliani and A. Poves, "Neutrinoless double-beta decay," *Advances in High Energy Physics*, vol. 2012, Article ID 857016, 38 pages, 2012.
- [23] J. J. Gómez-Cadenas, J. Martín-Albo, M. Mezzetto, F. Monrabal, and M. Sorel, "The search for neutrinoless double beta decay," *Rivista del Nuovo Cimento*, vol. 35, no. 2, pp. 29–98, 2012.
- [24] B. Schwingerheuer, "Status and prospects of searches for neutrinoless double beta decay," *Annalen der Physik*, vol. 525, no. 4, pp. 269–280, 2013.
- [25] O. Cremonesi and M. Pavan, "Challenges in double beta decay," *Advances in High Energy Physics*, vol. 2014, Article ID 951432, 40 pages, 2014.
- [26] J. D. Vergados, H. Ejiri, and F. Šimkovic, "Theory of neutrinoless double-beta decay," *Reports on Progress in Physics*, vol. 75, no. 10, Article ID 106301, 2012.
- [27] P. Vogel, "Nuclear structure and double beta decay," *Journal of Physics G: Nuclear and Particle Physics*, vol. 39, no. 12, Article ID 124002, 2012.
- [28] S. T. Petcov, "The nature of massive neutrinos," *Advances in High Energy Physics*, vol. 2013, Article ID 852987, 20 pages, 2013.
- [29] S. M. Bilenky and C. Giunti, "Neutrinoless double-beta decay: a probe of physics beyond the standard model," *International Journal of Modern Physics A*, vol. 30, Article ID 1530001, 2015.
- [30] W. Rodejohann, "Neutrino-less double beta decay and particle physics," *International Journal of Modern Physics E*, vol. 20, no. 9, pp. 1833–1930, 2011.
- [31] W. Rodejohann, "Neutrinoless double-beta decay and neutrino physics," *Journal of Physics G: Nuclear and Particle Physics*, vol. 39, no. 12, Article ID 124008, 2012.
- [32] F. F. Deppisch, M. Hirsch, and H. Päs, "Neutrinoless double-beta decay and physics beyond the standard model," *Journal of Physics G: Nuclear and Particle Physics*, vol. 39, no. 12, Article ID 124007, 2012.
- [33] H. Päs and W. Rodejohann, "Neutrinoless double beta decay," *New Journal of Physics*, vol. 17, no. 11, Article ID 115010, 2015.
- [34] P. A. R. Ade, N. Aghanim, M. Arnaud et al., "Planck 2015 results. XIII. Cosmological parameters," <http://arxiv.org/abs/1502.01589>.
- [35] F. Capozzi, G. L. Fogli, E. Lisi, A. Marrone, D. Montanino, and A. Palazzo, "Status of three-neutrino oscillation parameters, circa 2013," *Physical Review D*, vol. 89, no. 9, Article ID 093018, 2014.
- [36] E. Fermi, "Attempt at a theory of the emission of beta rays," *Rice Science*, vol. 4, pp. 491–495, 1933 (Italian).
- [37] T. D. Lee and C. N. Yang, "Question of parity conservation in weak interactions," *Physical Review*, vol. 104, no. 1, pp. 254–258, 1956.
- [38] C. S. Wu, E. Ambler, R. W. Hayward, D. D. Hoppes, and R. P. Hudson, "Experimental test of parity conservation in beta decay," *Physical Review*, vol. 105, no. 4, pp. 1413–1415, 1957.
- [39] L. D. Landau, "On the conservation laws for weak interactions," *Nuclear Physics*, vol. 3, pp. 127–131, 1957.
- [40] T. D. Lee and C. N. Yang, "Parity nonconservation and a two-component theory of the neutrino," *Physical Review*, vol. 105, pp. 1671–1675, 1957.
- [41] A. Salam, "On parity conservation and neutrino mass," *Il Nuovo Cimento*, vol. 5, no. 1, pp. 299–301, 1957.
- [42] H. Weyl, "Elektron und Gravitation. I," *Zeitschrift für Physik*, vol. 56, no. 5–6, pp. 330–352, 1929 (German).
- [43] N. Palanque-Delabrouille, C. Yèche, J. Baur et al., "Neutrino masses and cosmology with Lyman-alpha forest power spectrum," *Journal of Cosmology and Astroparticle Physics*, vol. 2015, no. 11, article 011, 2015.
- [44] E. Di Valentino, E. Giusarma, O. Mena, A. Melchiorri, and J. Silk, "Cosmological limits on neutrino unknowns versus low redshift priors," <http://arxiv.org/abs/1511.00975>.
- [45] X. Zhang, "Impacts of dark energy on weighing neutrinos after Planck 2015," <http://arxiv.org/abs/1511.02651>.
- [46] A. J. Cuesta, V. Niro, and L. Verde, "Neutrino mass limits: robust information from the power spectrum of galaxy surveys," <http://arxiv.org/abs/1511.05983>.
- [47] H. Georgi and S. L. Glashow, "Unity of all elementary-particle forces," *Physical Review Letters*, vol. 32, no. 8, pp. 438–441, 1974.
- [48] H. Georgi, "Unified gauge theories," in *Proceedings of the Theories and Experiments in High-Energy Physics*, pp. 329–339, Gables, Fla, USA, January 1975.
- [49] H. Fritzsch and P. Minkowski, "Unified interactions of leptons and hadrons," *Annals of Physics*, vol. 93, no. 1-2, pp. 193–266, 1975.
- [50] G. Bellini, D. Bick, G. Bonfini et al., "SOX: short distance neutrino oscillations with BoreXino," *Journal of High Energy Physics*, vol. 2013, no. 8, article 038, 2013.
- [51] F. P. An, A. B. Balantekin, H. R. Band et al., "Search for a light sterile neutrino at Daya Bay," *Physical Review Letters*, vol. 113, no. 14, Article ID 141802, 2014.
- [52] J. Ashenfelter, B. Balantekin, H. R. Band et al., "The PROSPECT physics program," <http://arxiv.org/abs/1512.02202>.
- [53] K. N. Abazajian, M. A. Acero, S. K. Agarwalla et al., "Light sterile neutrinos: a white paper," <http://arxiv.org/abs/1204.5379>.
- [54] S. Gariazzo, C. Giunti, and M. Laveder, "Light sterile neutrinos in cosmology and short-baseline oscillation experiments," *Journal of High Energy Physics*, vol. 2013, article 211, 2013.
- [55] A. D. Dolgov and F. L. Villante, "BBN bounds on active–sterile neutrino mixing," *Nuclear Physics B*, vol. 679, no. 1-2, pp. 261–298, 2004.
- [56] M. Cirelli, G. Marandella, A. Strumia, and F. Vissani, "Probing oscillations into sterile neutrinos with cosmology, astrophysics and experiments," *Nuclear Physics B*, vol. 708, no. 1–3, pp. 215–267, 2005.
- [57] J. Barry, W. Rodejohann, and H. Zhang, "Light sterile neutrinos: models and phenomenology," *Journal of High Energy Physics*, vol. 2011, no. 7, article 091, 2011.
- [58] I. Girardi, A. Meroni, and S. T. Petcov, "Neutrinoless double beta decay in the presence of light sterile neutrinos," *Journal of High Energy Physics*, vol. 2013, article 146, 2013.
- [59] S. Gariazzo, C. Giunti, M. Laveder, Y. F. Li, and E. M. Zavanin, "Light sterile neutrinos," *Journal of Physics G: Nuclear and Particle Physics*, vol. 43, no. 3, Article ID 033001, 2016.
- [60] A. D. Sakharov, "Violation of CP invariance, c asymmetry, and baryon asymmetry of the universe," *Pisma v Zhurnal Eksperimentalnoi i Teoreticheskoi Fiziki*, vol. 5, pp. 32–35, 1967.
- [61] G. 't Hooft, "Symmetry breaking through Bell-Jackiw anomalies," *Physical Review Letters*, vol. 37, no. 1, pp. 8–11, 1976.
- [62] V. A. Kuzmin, V. A. Rubakov, and M. E. Shaposhnikov, "On anomalous electroweak baryon-number non-conservation in the early universe," *Physics Letters B*, vol. 155, no. 1-2, pp. 36–42, 1985.

- [63] J. A. Harvey and M. S. Turner, “Cosmological baryon and lepton number in the presence of electroweak fermion-number violation,” *Physical Review D*, vol. 42, no. 10, pp. 3344–3349, 1990.
- [64] A. I. Bochkarev and M. E. Shaposhnikov, “Electroweak production of baryon asymmetry and upper bounds on the higgs and top masses,” *Modern Physics Letters A*, vol. 2, no. 6, pp. 417–427, 1987.
- [65] K. Kajantie, M. Laine, K. Rummukainen, and M. Shaposhnikov, “The electroweak phase transition: a non-perturbative analysis,” *Nuclear Physics B*, vol. 466, no. 1-2, pp. 189–258, 1996.
- [66] M. Fukugita and T. Yanagida, “Baryogenesis without grand unification,” *Physics Letters B*, vol. 174, no. 1, pp. 45–47, 1986.
- [67] M. Shaposhnikov, “Baryo/leptogenesis,” in *Proceedings of the 16th Annual International Conference on Particle Physics and Cosmology (COSMO '12)*, Beijing, China, September 2012.
- [68] R. Saakyan, “Two-neutrino double-beta decay,” *Annual Review of Nuclear and Particle Science*, vol. 63, pp. 503–529, 2013.
- [69] S. Weinberg, “Universal neutrino degeneracy,” *Physical Review*, vol. 128, no. 3, pp. 1457–1473, 1962.
- [70] A. G. Cocco, G. Mangano, and M. Messina, “Probing low energy neutrino backgrounds with neutrino capture on beta decaying nuclei,” *Journal of Cosmology and Astroparticle Physics*, vol. 2007, no. 6, article 015, 2007.
- [71] A. J. Long, C. Lunardini, and E. Sabancilar, “Detecting non-relativistic cosmic neutrinos by capture on tritium: phenomenology and physics potential,” *Journal of Cosmology and Astroparticle Physics*, vol. 2014, article 38, 2014.
- [72] E. Andreotti, C. Arnaboldi, F. T. Avignone et al., “ $^{130}\text{Te}$  neutrinoless double- $\beta$  decay with CUORICINO,” *Astroparticle Physics*, vol. 34, no. 11, pp. 822–831, 2011.
- [73] K. Alfonso, D. R. Artusa, F. T. Avignone III et al., “Search for neutrinoless double-beta decay of  $^{130}\text{Te}$  with CUORE-0,” *Physical Review Letters*, vol. 115, Article ID 102502, 2015.
- [74] H. V. Klapdor-Kleingrothaus, A. Dietz, L. Baudis et al., “Latest results from the Heidelberg-Moscow double beta decay experiment,” *European Physical Journal A*, vol. 12, no. 2, pp. 147–154, 2001.
- [75] C. E. Aalseth, F. T. Avignone, R. L. Brodzinski et al., “Neutrinoless double- $\beta$  decay of  $^{76}\text{Ge}$ : first results from the International Germanium Experiment (IGEX) with six isotopically enriched detectors,” *Physical Review C*, vol. 59, no. 4, article 2108, 1999.
- [76] C. E. Aalseth, F. T. Avignone III, R. L. Brodzinski et al., “IGEX  $^{76}\text{Ge}$  neutrinoless double-beta decay experiment: prospects for next generation experiments,” *Physical Review D*, vol. 65, Article ID 092007, 2002.
- [77] M. Agostini, M. Allardt, E. Andreotti et al., “Results on neutrinoless double- $\beta$  decay of  $^{76}\text{Ge}$  from Phase I of the GERDA experiment,” *Physical Review Letters*, vol. 111, no. 12, Article ID 122503, 2013.
- [78] K.-H. Ackermann, M. Agostini, M. Allardt et al., “The GERDA experiment for the search of  $0\nu\beta\beta$  decay in  $^{76}\text{Ge}$ ,” *The European Physical Journal C*, vol. 73, article 2330, 2013.
- [79] R. Arnold, C. Augier, J. D. Baker et al., “Search for neutrinoless double-beta decay of  $^{100}\text{Mo}$  with the NEMO-3 detector,” *Physical Review D*, vol. 89, no. 11, Article ID 111101, 2014.
- [80] J. B. Albert, D. J. Auty, P. S. Barbeau et al., “Search for Majorana neutrinos with the first two years of EXO-200 data,” *Nature*, vol. 510, pp. 229–234, 2014.
- [81] A. Gando, Y. Gando, H. Hanakago et al., “Limit on neutrinoless  $\beta\beta$  decay of  $^{136}\text{Xe}$  from the first phase of KamLAND-Zen and comparison with the positive claim in  $^{76}\text{Ge}$ ,” *Physical Review Letters*, vol. 110, no. 6, Article ID 062502, 2013.
- [82] K. Asakura, A. Gando, Y. Gando et al., “Results from KamLAND-Zen,” *AIP Conference Proceedings*, vol. 1666, Article ID 170003, 2015.
- [83] D. R. Artusa, F. T. Avignone III, O. Azzolini et al., “Searching for neutrinoless double-beta decay of  $^{130}\text{Te}$  with CUORE,” *Advances in High Energy Physics*, vol. 2015, Article ID 879871, 13 pages, 2015.
- [84] R. Brugnera and A. Garfagnini, “Status of the GERDA experiment at the laboratori nazionali del gran sasso,” *Advances in High Energy Physics*, vol. 2013, Article ID 506186, 15 pages, 2013.
- [85] L. Pattavina, “Scintillating bolometers for the LUCIFER project,” in *Proceedings of the XIV International Conference on Topics in Astroparticle and Underground Physics (TAUP '15)*, Torino, Italy, September 2015.
- [86] N. Abgrall, E. Aguayo, F. T. Avignone III et al., “The MAJORANA DEMONSTRATOR neutrinoless double- $\beta$  decay experiment,” *Advances in High Energy Physics*, vol. 2014, Article ID 365432, 18 pages, 2014.
- [87] J. J. Gómez-Cadenas, V. Álvarez, F. I. G. Borges et al., “Present status and future perspectives of the NEXT experiment,” *Advances in High Energy Physics*, vol. 2014, Article ID 907067, 22 pages, 2014.
- [88] A. Laing, “The NEXT double beta decay experiment,” in *Proceedings of the XIV International Conference on Topics in Astroparticle and Underground Physics (TAUP '15)*, Torino, Italy, September 2015.
- [89] Y. H. Kim, “The AMoRE project,” in *Proceedings of the 14th International Conference on Topics in Astroparticle and Underground Physics (TAUP '15)*, Torino, Italy, September 2015.
- [90] I. Ostrovskiy, “nEXO: the next generation  $^{136}\text{Xe}$  neutrinoless double beta decay search,” in *Proceedings of the XIV International Conference on Topics in Astroparticle and Underground Physics (TAUP '15)*, Torino, Italy, September 2015.
- [91] X. Ji, “PandaX and OnuDBD,” in *Proceedings of the International Workshop on Baryon and Lepton Number Violation (BLV '5)*, Amherst, Mass, USA, April 2015.
- [92] S. Andringa, E. Arushanova, S. Asahi et al., “Current status and future prospects of the SNO+ experiment,” *Advances in High Energy Physics*, vol. 2016, Article ID 6194250, 21 pages, 2016.
- [93] R. Arnold, C. Augier, J. D. Baker et al., “Results of the search for neutrinoless double- $\beta$  decay in  $^{100}\text{Mo}$  with the NEMO-3 experiment,” *Physical Review D*, vol. 92, no. 7, Article ID 072011, 2015.
- [94] S. Blot, “Recent results from the NEMO-3 experiment and the status of SuperNEMO,” in *Proceedings of the 14th International Conference on Topics in Astroparticle and Underground Physics (TAUP '15)*, Torino, Italy, September 2015.
- [95] J. Kotila and F. Iachello, “Phase-space factors for double- $\beta$  decay,” *Physical Review C*, vol. 85, Article ID 034316, 2012.
- [96] J. Barea, J. Kotila, and F. Iachello, “ $0\nu\beta\beta$  and  $2\nu\beta\beta$  nuclear matrix elements in the interacting boson model with isospin restoration,” *Physical Review C*, vol. 91, no. 3, Article ID 034304, 2015.
- [97] M. Gell-Mann and A. Pais, “Behavior of neutral particles under charge conjugation,” *Physical Review*, vol. 97, pp. 1387–1389, 1955.
- [98] K. Lande, E. T. Booth, J. Impeduglia, L. M. Lederman, and W. Chinowsky, “Observation of long-lived neutral  $\nu$  particles,” *Physical Review*, vol. 103, no. 6, pp. 1901–1904, 1956.

- [99] K. Lande, L. M. Lederman, and W. Chinowsky, "Report on long-lived  $K^0$  mesons," *Physical Review*, vol. 105, no. 6, pp. 1925–1927, 1957.
- [100] J. Prentki and M. J. G. Veltman, "Possibility of  $CP$  violation in semistrong interactions," *Physics Letters*, vol. 15, pp. 88–90, 1965.
- [101] T. D. Lee and L. Wolfenstein, "Analysis of  $CP$ -noninvariant interactions and the  $K_{10}$ ,  $K_{20}$  system," *Physical Review*, vol. 138, no. 6B, pp. B1490–B1496, 1965.
- [102] F. Wilczek and A. Zee, "Operator analysis of nucleon decay," *Physical Review Letters*, vol. 43, no. 21, pp. 1571–1573, 1979.
- [103] K. Choi, K. S. Jeong, and W. Y. Song, "Operator analysis of neutrinoless double beta decay," *Physical Review D*, vol. 66, no. 9, Article ID 093007, 2002.
- [104] F. Bonnet, M. Hirsch, T. Ota, and W. Winter, "Systematic decomposition of the neutrinoless double beta decay operator," *Journal of High Energy Physics*, vol. 2013, article 55, 2013, Erratum in *Journal of High Energy Physics*, vol. 2014, article 90, 2014.
- [105] A. Atre, T. Han, S. Pascoli, and B. Zhang, "The search for heavy Majorana neutrinos," *Journal of High Energy Physics*, vol. 2009, no. 5, article 030, 2009.
- [106] M. Mitra, G. Senjanović, and F. Vissani, "Neutrinoless double beta decay and heavy sterile neutrinos," *Nuclear Physics B*, vol. 856, no. 1, pp. 26–73, 2012.
- [107] M. Blennow, E. Fernandez-Martinez, J. Lopez-Pavon, and J. Menéndez, "Neutrinoless double beta decay in seesaw models," *Journal of High Energy Physics*, vol. 2010, article 96, 2010.
- [108] J. Lopez-Pavon, S. Pascoli, and C.-F. Wong, "Can heavy neutrinos dominate neutrinoless double beta decay?" *Physical Review D*, vol. 87, no. 9, Article ID 093007, 2013.
- [109] P. S. B. Dev and R. N. Mohapatra, "Unified explanation of the  $eejj$ , diboson, and dijet resonances at the LHC," *Physical Review Letters*, vol. 115, no. 18, Article ID 181803, 2015.
- [110] F. F. Deppisch, L. Graf, S. Kulkarni et al., "Reconciling the 2 TeV excesses at the LHC in a linear seesaw left-right model," *Physical Review D*, vol. 93, no. 1, Article ID 013011, 2016.
- [111] F. F. Deppisch, S. Kulkarni, H. Päs, and E. Schumacher, "Leptoquark patterns unifying neutrino masses, flavor anomalies and the diphoton excess," <http://arxiv.org/abs/1603.07672>.
- [112] J. Schechter and J. W. F. Valle, "Neutrinoless double- decay in  $SU(2) \times U(1)$  theories," *Physical Review D*, vol. 25, no. 11, pp. 2951–2954, 1982.
- [113] S. Coleman, *Aspects of Symmetry*, chapter 4, Cambridge University Press, Cambridge, UK, 1988.
- [114] M. Duerr, M. Lindner, and A. Merle, "On the quantitative impact of the Schechter-Valle theorem," *Journal of High Energy Physics*, vol. 2011, no. 6, article 091, 2011.
- [115] S. Weinberg, "Supersymmetry at ordinary energies. Masses and conservation laws," *Physical Review D*, vol. 26, no. 1, article 287, 1982.
- [116] R. N. Mohapatra and A. Y. Smirnov, "Neutrino mass and new physics," *Annual Review of Nuclear and Particle Science*, vol. 56, pp. 569–628, 2006.
- [117] R. N. Mohapatra and P. B. Pal, *Massive Neutrinos in Physics and Astrophysics*, vol. 60 of *World Scientific Lecture Notes in Physics*, 2nd edition, 1998.
- [118] S. Alekhin, W. Altmannshofer, T. Asaka et al., "A facility to search for hidden particles at the CERN SPS: the SHiP physics case," *Reports on Progress in Physics*, In press.
- [119] M. Anelli, S. Aoki, G. Arduini et al., "A facility to search for hidden particles (SHiP) at the CERN SPS," <http://arxiv.org/abs/1504.04956>.
- [120] J. C. Pati and A. Salam, "Lepton number as the fourth 'color,'" *Physical Review D*, vol. 10, no. 1, pp. 275–289, 1974.
- [121] W.-Y. Keung and G. Senjanović, "Majorana neutrinos and the production of the right-handed charged gauge boson," *Physical Review Letters*, vol. 50, no. 19, pp. 1427–1430, 1983.
- [122] V. Tello, M. Nemeveš, F. Nesti, G. Senjanović, and F. Vissani, "Left-right symmetry: from the LHC to neutrinoless double beta decay," *Physical Review Letters*, vol. 106, no. 15, Article ID 151801, 2011.
- [123] M. Nemevešek, F. Nesti, G. Senjanović, and Y. Zhang, "Limits on the left-right symmetry scale and heavy neutrinos from early LHC data," *Physical Review D*, vol. 83, no. 11, Article ID 115014, 2011.
- [124] S. Dell’Oro, S. Marocco, and F. Vissani, "New expectations and uncertainties on neutrinoless double beta decay," *Physical Review D*, vol. 90, no. 3, Article ID 033005, 2014.
- [125] L. Wolfenstein, "Neutrino oscillations in matter," *Physical Review D*, vol. 17, no. 9, pp. 2369–2374, 1978.
- [126] S. P. Mikheev and A. Y. Smirnov, "Resonance amplification of oscillations in matter and spectroscopy of solar neutrinos," *Soviet Journal of Nuclear Physics*, vol. 42, pp. 913–917, 1985.
- [127] S. Abe, K. Furuno, A. Gando et al., "Precision measurement of neutrino oscillation parameters with KamLAND," *Physical Review Letters*, vol. 100, no. 22, Article ID 221803, 2008.
- [128] P. Ghoshal and S. T. Petcov, "Neutrino mass hierarchy determination using reactor antineutrinos," *Journal of High Energy Physics*, vol. 2011, article 58, 2011.
- [129] F. Vissani, "Signal of neutrinoless double beta decay, neutrino spectrum and oscillation scenarios," *Journal of High Energy Physics*, vol. 3, no. 6, 1999.
- [130] F. Feruglio, A. Strumia, and F. Vissani, "Neutrino oscillations and signals in  $\beta$  and  $0\nu 2\beta$  experiments," *Nuclear Physics B*, vol. 637, no. 1–3, pp. 345–377, 2002.
- [131] Y. B. Zel’dovich and M. Y. Khlopov, "The neutrino mass in elementary particle physics and in big bang cosmology," *Soviet Physics Uspekhi*, vol. 24, no. 9, pp. 755–774, 1981.
- [132] G. L. Fogli, E. Lisi, A. Marrone et al., "Observables sensitive to absolute neutrino masses: constraints and correlations from world neutrino data," *Physical Review D*, vol. 70, Article ID 113003, 2004.
- [133] J. R. Primack, J. Holtzman, A. Klypin, and D. O. Caldwell, "Cold + hot dark matter cosmology with  $m(\nu_\mu) \approx m(\nu_\tau) \approx 2.4$  eV," *Physical Review Letters*, vol. 74, no. 12, pp. 2160–2163, 1995.
- [134] S. W. Allen, R. W. Schmidt, and S. L. Bridle, "A preference for a non-zero neutrino mass from cosmological data," *Monthly Notices of the Royal Astronomical Society*, vol. 346, no. 2, pp. 593–600, 2003.
- [135] R. A. Battye and A. Moss, "Evidence for massive neutrinos from cosmic microwave background and lensing observations," *Physical Review Letters*, vol. 112, no. 5, Article ID 051303, 2014.
- [136] N. Palanque-Delabrouille, C. Yèche, J. Lesgourgues et al., "Constraint on neutrino masses from SDSS-III/BOSS  $Ly\alpha$  forest and other cosmological probes," *Journal of Cosmology and Astroparticle Physics*, vol. 2015, no. 2, p. 45, 2015.
- [137] J. Lesgourgues, G. Mangano, G. Miele, and S. Pastor, *Neutrino Cosmology*, Cambridge University Press, 2013.

- [138] M. Wyman, D. H. Rudd, R. A. Vanderveld, and W. Hu, “Neutrinos help reconcile planck measurements with the local universe,” *Physical Review Letters*, vol. 112, no. 5, Article ID 051302, 2014.
- [139] J. Hamann and J. Hasenkamp, “A new life for sterile neutrinos: resolving inconsistencies using hot dark matter,” *Journal of Cosmology and Astroparticle Physics*, vol. 2013, article 044, 2013.
- [140] P. A. R. Ade, N. Aghanim, C. Armitage-Caplan et al., “Planck 2013 results. XVI. Cosmological parameters,” *Astronomy & Astrophysics*, vol. 571, article A16, 2014.
- [141] S. Kovalenko, M. I. Krivoruchenko, and F. Šimkovic, “Neutrino propagation in nuclear medium and neutrinoless double-beta decay,” *Physical Review Letters*, vol. 112, no. 14, Article ID 142503, 2014.
- [142] Y. Y. Y. Wong, “Neutrino mass in cosmology: status and prospects,” *Annual Review of Nuclear and Particle Science*, vol. 61, pp. 69–98, 2011.
- [143] J. Lesgourgues and S. Pastor, “Neutrino cosmology and Planck,” *New Journal of Physics*, vol. 16, Article ID 065002, 2014.
- [144] T. J. Loredo and D. Q. Lamb, “Bayesian analysis of neutrinos observed from supernova SN 1987A,” *Physical Review D*, vol. 65, no. 6, Article ID 063002, 2002.
- [145] G. Pagliaroli, F. Rossi-Torres, and F. Vissani, “Neutrino mass bound in the standard scenario for supernova electronic antineutrino emission,” *Astroparticle Physics*, vol. 33, no. 5-6, pp. 287–291, 2010.
- [146] C. Kraus, B. Bornschein, L. Bornschein et al., “Final results from phase II of the Mainz neutrino mass search in tritium  $\beta$  decay,” *European Physical Journal C*, vol. 40, no. 4, pp. 447–468, 2005.
- [147] V. N. Aseev, A. I. Beleshev, A. I. Berlev et al., “Upper limit on the electron antineutrino mass from the Troitsk experiment,” *Physical Review D*, vol. 84, no. 11, Article ID 112003, 2011.
- [148] A. Osipowicz, H. Blumer, G. Drexlin et al., “KATRIN: a next generation tritium beta decay experiment with sub-eV sensitivity for the electron neutrino mass. Letter of intent,” <http://arxiv.org/abs/hep-ex/0109033>.
- [149] B. Alpert, M. Balata, D. Bennett et al., “HOLMES—the electron capture decay of  $^{163}\text{Ho}$  to measure the electron neutrino mass with sub-eV sensitivity,” *The European Physical Journal C*, vol. 75, article 112, 2015.
- [150] P. J. Doe, J. Kofron, E. L. McBride et al., “Project 8: determining neutrino mass from tritium beta decay using a frequency-based method,” in *Proceedings of the Snowmass Conference*, September 2013, Conference: C13-07-29.2, <https://arxiv.org/abs/1309.7093>.
- [151] P. C.-O. Ranitzsch, J.-P. Porst, S. Kempf et al., “Development of metallic magnetic calorimeters for high precision measurements of calorimetric  $^{187}\text{Re}$  and  $^{163}\text{Ho}$  spectra,” *Journal of Low Temperature Physics*, vol. 167, no. 5-6, pp. 1004–1014, 2012.
- [152] F. Buccella and D. Falcone, “Bounds for neutrinoless double  $\beta$  decay in SO(10) inspired seesaw models,” *Modern Physics Letters A*, vol. 19, no. 40, article 2993, 2004.
- [153] S. Pascoli and S. T. Petcov, “Majorana neutrinos, neutrino mass spectrum and the  $|\langle m \rangle| \sim 10^{-3}$  eV frontier in neutrinoless double beta decay,” *Physical Review D*, vol. 77, Article ID 113003, 2008.
- [154] C. D. Froggatt and H. B. Nielsen, “Hierarchy of quark masses, cabibbo angles and CP violation,” *Nuclear Physics B*, vol. 147, no. 3-4, pp. 277–298, 1979.
- [155] F. Vissani, “Expected properties of massive neutrinos for mass matrices with a dominant block and random coefficients order unity,” *Physics Letters B*, vol. 508, no. 1-2, pp. 79–84, 2001.
- [156] F. Vissani, M. Narayan, and V. Berezinsky, “ $U_{e3}$  from physics above the GUT scale,” *Physics Letters B*, vol. 571, no. 3-4, pp. 209–216, 2003.
- [157] H. Primakoff and S. P. Rosen, “Double  $\beta$  decay,” *Reports on Progress in Physics*, vol. 22, no. 1, p. 121, 1959.
- [158] M. Doi, T. Kotani, H. Nishiura, K. Okuda, and E. Takasugi, “Neutrino mass, the right-handed interaction and the double beta decay. 2. General properties and data analysis,” *Progress of Theoretical Physics*, vol. 66, no. 5, pp. 1765–1788, 1981, Erratum in: *Progress of Theoretical Physics*, vol. 68, p. 348, 1982.
- [159] M. Doi, T. Kotani, H. Nishiura, and E. Takasugi, “Double  $\beta$  decay,” *Progress of Theoretical Physics*, vol. 69, no. 2, pp. 602–635, 1983.
- [160] T. Tomoda, “Double beta decay,” *Reports on Progress in Physics*, vol. 54, no. 1, pp. 53–126, 1991.
- [161] S. Stoica and M. Mirea, “New calculations for phase space factors involved in double- $\beta$  decay,” *Physical Review C*, vol. 88, no. 3, Article ID 037303, 2013.
- [162] D. Štefánik, R. Dvornický, F. Šimkovic, and P. Vogel, “Reexamining the light neutrino exchange mechanism of the  $0\nu\beta\beta$  decay with left- and right-handed leptonic and hadronic currents,” *Physical Review C*, vol. 92, Article ID 055502, 2015.
- [163] F. Šimkovic, V. Rodin, A. Faessler, and P. Vogel, “ $0\nu\beta\beta$  and  $2\nu\beta\beta$  nuclear matrix elements, quasiparticle random-phase approximation, and isospin symmetry restoration,” *Physical Review C*, vol. 87, no. 4, Article ID 045501, 2013.
- [164] J. Menéndez, A. Poves, E. Caurier, and F. Nowacki, “Disassembling the nuclear matrix elements of the neutrinoless  $\beta\beta$  decay,” *Nuclear Physics A*, vol. 818, no. 3-4, pp. 139–151, 2009.
- [165] E. Caurier, G. Martínez-Pinedo, F. Nowacki, A. Poves, and P. A. Zuker, “The shell model as a unified view of nuclear structure,” *Reviews of Modern Physics*, vol. 77, no. 2, pp. 427–488, 2005.
- [166] J. Hyvärinen and J. Suhonen, “Nuclear matrix elements for  $0\nu\beta\beta$  decays with light or heavy Majorana-neutrino exchange,” *Physical Review C*, vol. 91, no. 2, Article ID 024613, 2015.
- [167] P. K. Rath, R. Chandra, K. Chaturvedi, P. Lohani, P. K. Raina, and J. G. Hirsch, “Neutrinoless  $\beta\beta$  decay transition matrix elements within mechanisms involving light majorana neutrinos, classical majorons, and sterile neutrinos,” *Physical Review C*, vol. 88, Article ID 064322, 2013.
- [168] T. R. Rodríguez and G. Martínez-Pinedo, “Energy density functional study of nuclear matrix elements for neutrinoless  $\beta\beta$  decay,” *Physical Review Letters*, vol. 105, no. 25, Article ID 252503, 2010.
- [169] F. Šimkovic, G. Pantis, J. D. Vergados, and A. Faessler, “Additional nucleon current contributions to neutrinoless double  $\beta$  decay,” *Physical Review C*, vol. 60, no. 5, Article ID 055502, 1999.
- [170] J. Barea, J. Kotila, and F. Iachello, “Nuclear matrix elements for double- $\beta$  decay,” *Physical Review C*, vol. 87, no. 1, Article ID 014315, 2013.
- [171] J. N. Bahcall, H. Murayama, and C. Peña-Garay, “What can we learn from neutrinoless double beta decay experiments?” *Physical Review D*, vol. 70, no. 3, Article ID 033012, 2004.
- [172] V. A. Rodin, A. Faessler, F. Šimkovic, and P. Vogel, “On the uncertainty in the  $0\nu\beta\beta$  decay nuclear matrix elements,” *Physical Review C*, vol. 68, Article ID 044302, 2003.
- [173] V. A. Rodin, A. Faessler, F. Šimkovic, and P. Vogel, “Assessment of uncertainties in QRPA  $0\nu\beta\beta$ -decay nuclear matrix elements,” *Nuclear Physics A*, vol. 766, pp. 107–131, 2006.

- [174] A. Faessler, M. González, S. Kovalenko, and F. Šimkovic, “Arbitrary mass Majorana neutrinos in neutrinoless double beta decay,” *Physical Review D*, vol. 90, no. 9, Article ID 096010, 2014.
- [175] F. Šimkovic, S. M. Bilenky, A. Faessler, and T. Gutsche, “Possibility of measuring the  $CP$  Majorana phases in  $0\nu\beta\beta$  decay,” *Physical Review D*, vol. 87, no. 7, Article ID 073002, 2013.
- [176] A. Faessler, G. L. Fogli, E. Lisi, V. Rodin, A. M. Rotunno, and F. Šimkovic, “Overconstrained estimates of neutrinoless double beta decay within the QRPA,” *Journal of Physics G: Nuclear and Particle Physics*, vol. 35, no. 7, Article ID 075104, 2008.
- [177] J. Suhonen and O. Civitarese, “Probing the quenching of  $g_A$  by single and double beta decays,” *Physics Letters B*, vol. 725, no. 1–3, pp. 153–157, 2013.
- [178] E. Lisi, A. Rotunno, and F. Šimkovic, “Degeneracies of particle and nuclear physics uncertainties in neutrinoless  $\beta\beta$  decay,” *Physical Review D*, vol. 92, no. 9, Article ID 093004, 2015.
- [179] M. Konieczka, P. Baczyk, and W. Satula, “Beta-decay study within multi-reference density functional theory and beyond,” <http://arxiv.org/abs/1509.04480>.
- [180] J.-I. Fujita and K. Ikeda, “Existence of isobaric states and beta decay of heavier nuclei,” *Nuclear Physics*, vol. 67, no. 1, pp. 145–177, 1965.
- [181] D. H. Wilkinson, “Renormalization of the axial-vector coupling constant in nuclear  $\beta$  decay,” *Physical Review C*, vol. 7, no. 3, pp. 930–936, 1973.
- [182] D. H. Wilkinson, “Renormalization of the axial-vector coupling constant in nuclear  $\beta$ -decay (II),” *Nuclear Physics A*, vol. 209, no. 3, pp. 470–484, 1973.
- [183] D. H. Wilkinson, “Renormalization of the axial-vector coupling constant in nuclear  $\beta$ -decay (II),” *Nuclear Physics A*, vol. 209, pp. 365–381, 1974.
- [184] M. Ericson, “Axial vector nuclear sum rules and exchange effects,” *Annals of Physics*, vol. 63, no. 2, pp. 562–576, 1971.
- [185] S. Barshay, G. E. Brown, and M. Rho, “A new interpretation of the pion-nucleus optical potential for pionic atoms,” *Physical Review Letters*, vol. 32, pp. 787–790, 1974, Erratum in: *Physical Review Letters*, vol. 32, p. 1149, 1974.
- [186] K. Shimizu, M. Ichimura, and A. Arima, “Magnetic moments and GT-type  $\beta$ -decay matrix elements in nuclei with a LS doubly closed shell plus or minus one nucleon,” *Nuclear Physics A*, vol. 226, no. 2, pp. 282–318, 1974.
- [187] J. Menéndez, D. Gazit, and A. Schwenk, “Chiral two-body currents in nuclei: gamow-teller transitions and neutrinoless double-beta decay,” *Physical Review Letters*, vol. 107, Article ID 062501, 2011.
- [188] A. Ekström, G. Jansen, K. Wendt et al., “Effects of three-nucleon forces and two-body currents on Gamow-Teller strengths,” *Physical Review Letters*, vol. 113, Article ID 262504, 2014.
- [189] J. Engel, F. Šimkovic, and P. Vogel, “Chiral two-body currents and neutrinoless double- $\beta$  decay in the quasiparticle random-phase approximation,” *Physical Review C*, vol. 89, no. 6, Article ID 064308, 2014.
- [190] F. Cappuzzello, C. Agodi, M. Bondi, D. Carbone, M. Cavallaro, and A. Foti, “The role of nuclear reactions in the problem of  $0\nu\beta\beta$  decay and the NUMEN project at INFN-LNS,” *Journal of Physics: Conference Series*, vol. 630, no. 1, Article ID 012018, 2015.
- [191] S. Kovalenko, Z. Lu, and I. Schmidt, “Lepton number violating processes mediated by Majorana neutrinos at hadron colliders,” *Physical Review D*, vol. 80, Article ID 073014, 2009.
- [192] F. Bergsma, J. Dorenbosch, J. V. Allaby et al., “A search for decays of heavy neutrinos in the mass range 0.5–2.8 GeV,” *Physics Letters B*, vol. 166, no. 4, pp. 473–478, 1986.
- [193] P. Abreu, W. Adam, T. Adye et al., “Search for neutral heavy leptons produced in Z decays,” *Zeitschrift für Physik C Particles and Fields*, vol. 74, no. 1, pp. 57–71, 1997, Erratum to *Zeitschrift für Physik C Particles and Fields*, vol. 75, p. 580, 1997.
- [194] G. Bernardi, G. Carugno, J. Chauveau et al., “Further limits on heavy neutrino couplings,” *Physics Letters B*, vol. 203, no. 3, pp. 332–334, 1988.
- [195] D. I. Britton, S. Ahmad, D. A. Bryman et al., “Measurement of the  $\pi^+ \rightarrow e^+ \nu$  branching ratio,” *Physical Review Letters*, vol. 68, no. 20, pp. 3000–3003, 1992.
- [196] D. I. Britton, S. Ahmad, D. A. Bryman et al., “Improved search for massive neutrinos in  $\pi^+ \rightarrow e^+ \nu$  decay,” *Physical Review D*, vol. 46, no. 3, pp. R885–R887, 1992.
- [197] R. G. H. Robertson, “Empirical survey of neutrinoless double beta decay matrix elements,” *Modern Physics Letters A*, vol. 28, no. 8, Article ID 1350021, 2013.
- [198] J. J. Gómez-Cadenas and J. Martín-Albo, “Phenomenology of neutrinoless double beta decay,” <http://arxiv.org/abs/1502.00581>.
- [199] S. R. Elliott and P. Vogel, “Double beta decay,” *Annual Review of Nuclear and Particle Science*, vol. 52, pp. 115–151, 2002.
- [200] E. L. Fireman, “Artificial radioactive substances,” *Physical Review*, vol. 74, p. 1238, 1948.
- [201] E. L. Fireman, “A measurement of the half-life of double beta decay from  $_{50}\text{Sn}^{124}$ ,” *Physical Review*, vol. 75, no. 2, pp. 323–324, 1949.
- [202] S. R. Elliott, A. A. Hahn, and M. K. Moe, “Direct evidence for two neutrino double beta decay in  $^{82}\text{Se}$ ,” *Physical Review Letters*, vol. 59, pp. 2020–2023, 1987.
- [203] H. V. Klapdor-Kleingrothaus, *Seventy Years of Double Beta Decay: From Nuclear Physics to Beyond-Standard-Model Particle Physics*, World Scientific, River Edge, NJ, USA, 2010.
- [204] V. I. Tretyak and Y. G. Zdesenko, “Tables of double beta decay data: an update,” *Atomic Data and Nuclear Data Tables*, vol. 80, no. 1, pp. 83–116, 2002.
- [205] A. S. Barabash, “Experiment double beta decay: historical review of 75 years of research,” *Physics of Atomic Nuclei*, vol. 74, no. 4, pp. 603–613, 2011.
- [206] H. V. Klapdor-Kleingrothaus, A. Dietz, H. L. Harney, and I. V. Krivosheina, “Evidence for neutrinoless double beta decay,” *Modern Physics Letters A*, vol. 16, article 2409, 2001.
- [207] H. V. Klapdor-Kleingrothaus and I. V. Krivosheina, “The evidence for the observation of  $0\nu\beta\beta$  decay: the identification of  $0\nu\beta\beta$  events from the full spectra,” *Modern Physics Letters A*, vol. 21, no. 20, pp. 1547–1566, 2006.
- [208] C. E. Aalseth, F. T. Avignone, A. Barabash et al., “Comment on ‘evidence for neutrinoless double beta decay,’” *Modern Physics Letters A*, vol. 17, no. 22, pp. 1475–1478, 2002.
- [209] Y. G. Zdesenko, F. A. Danevich, and V. I. Tretyak, “Has neutrinoless double  $\beta$  decay of  $^{76}\text{Ge}$  been really observed?” *Physics Letters B*, vol. 546, no. 3–4, pp. 206–215, 2002.
- [210] D. R. Artusa, F. T. Avignone III, O. Azzolini et al., “Exploring the neutrinoless double beta decay in the inverted neutrino hierarchy with bolometric detectors,” *The European Physical Journal C*, vol. 74, article 3096, 2014.

- [211] S. Dell’Oro, S. Marcocci, M. Viel, and F. Vissani, “The contribution of light Majorana neutrinos to neutrinoless double beta decay and cosmology,” *Journal of Cosmology and Astroparticle Physics*, vol. 2015, no. 12, article 023, 2015.
- [212] N. Palanque-DeLabrouille, C. Yèche, A. Borde et al., “The one-dimensional Ly $\alpha$  forest power spectrum from BOSS,” *Astronomy & Astrophysics*, vol. 559, article A85, 19 pages, 2013.
- [213] V. Cirigliano, A. Kurylov, M. J. Ramsey-Musolf, and P. Vogel, “Neutrinoless double beta decay and lepton flavor violation,” *Physical Review Letters*, vol. 93, no. 23, Article ID 231802, 2004.

## Review Article

# The Results of MINOS and the Future with MINOS+

### A. Timmons

*Department of Physics and Astronomy, University of Manchester, Oxford Road, Manchester M13 9PL, UK*

Correspondence should be addressed to A. Timmons; [ashley.timmons@manchester.ac.uk](mailto:ashley.timmons@manchester.ac.uk)

Received 28 July 2015; Revised 21 October 2015; Accepted 19 November 2015

Academic Editor: Mauro Mezzetto

Copyright © 2016 A. Timmons. This is an open access article distributed under the Creative Commons Attribution License, which permits unrestricted use, distribution, and reproduction in any medium, provided the original work is properly cited. The publication of this article was funded by SCOAP<sup>3</sup>.

The MINOS experiment took data from 2005 up until 2012. The MINOS experiment took data from 2005 up until 2012, continuing beyond that as the MINOS+ experiment. The experiment is a two-detector, on-axis, long-baseline experiment, sending neutrinos from Fermilab to the Soudan Underground Laboratory in northern Minnesota. By searching for the deficit of muon neutrinos at the Far Detector, MINOS/MINOS+ is sensitive to the atmospheric neutrino oscillation parameters  $\Delta m_{32}^2$  and  $\theta_{23}$ . By using the full MINOS data set looking at both  $\nu_\mu$  disappearance and  $\nu_e$  appearance in both neutrino and antineutrino configurations at the NuMI beam along with atmospheric neutrino data recorded at the FD, MINOS has made the most precise measurement of  $\Delta m_{32}^2$ . Using a full three-flavour framework and searching for  $\nu_e$  appearance, MINOS/MINOS+ gains sensitivity to  $\theta_{13}$ , the mass hierarchy, and the octant of  $\theta_{23}$ . Exotic phenomenon is also explored with the MINOS detectors looking for nonstandard interactions and sterile neutrinos. The current MINOS+ era goals are to build on the previous MINOS results improving the precision on the three-flavour oscillation parameter measurements and strengthening the constraints placed on the sterile neutrino parameter space.

## 1. Introduction

Over the last couple of decades, physicists across the world have obtained model independent evidence for neutrino oscillations. It was in 1998 that Super-Kamiokade [1] observed muon neutrinos changing flavour as they transversed the atmosphere. Later in 2001, the Sudbury neutrino observatory experiment [2, 3] observed neutrinos oscillating between flavours which originated from the sun. Evidence for reactor antineutrinos was seen in 2002 with the KamLAND [4] experiment. There are now multiple generations of experiments designed to confirm and probe the nature of neutrino oscillations using a neutrino source from an accelerator [5, 6], solar neutrinos [7, 8], and nuclear reactor antineutrinos [9–12]. The implication of neutrino flavour change is indicative that the neutrino must have a nonzero mass and violate lepton number conservation, a clear observation of new physics beyond the standard model.

It was during this time of discovery that the MINOS [14] experiment was proposed. MINOS was designed with a long-baseline and two detectors 1.04 km and 735 km from the neutrino production target, respectively, with the goal

to measure the atmospheric neutrino oscillation parameters. A previously constructed long-baseline, two-detector experiment K2K [15] in Japan had the same goal. MINOS was unique in that its magnetised detectors allowed one to distinguish  $\nu_\mu$  and  $\bar{\nu}_\mu$  interactions on an event by event basis. The MINOS detectors encountered a higher flux of neutrinos than K2K and over the next few years MINOS contributed to the era of precision measurements of the fundamental parameters governing this quantum mechanical effect of neutrino oscillations. The MINOS experiment helped show how effectively a two-detector experiment can minimise the large systematic uncertainties associated with a neutrino interaction experiment. In 2012, the MINOS experiment ended and it is the continuation of the detectors taking data in the upgraded accelerator for the NO $\nu$ A [16] experiment that the MINOS+ [17] experiment was born. MINOS+ began taking data in September 2013, with a higher flux of neutrinos at high energies; MINOS+ becomes sensitive beyond the standard model neutrinos physics such as sterile neutrinos and large extra dimensions.

The theory of neutrino oscillation describes the change in neutrino flavour composition seen in data. These oscillations

arise due to a mixture between mass and flavour eigenstates; three active flavours of neutrino ( $\nu_e, \nu_\mu, \nu_\tau$ ) and three mass eigenstates ( $\nu_1, \nu_2, \nu_3$ ) are required to fully describe the neutrino oscillations observed in data. The energy dependence of these oscillations is governed by the difference of the square of the mass eigenstates,  $\Delta m_{32}^2$  and  $\Delta m_{21}^2$ , while the degree of mixing (the amplitude of the oscillations) is governed by three mixing angles  $\theta_{12}, \theta_{13}, \theta_{23}$  and a CP violating phase  $\delta_{13}$ . These parameters make up a  $3 \times 3$  rotation matrix known as the PMNS rotation matrix [18–20].

The difference between the two mass splittings is almost two orders of magnitude;  $\theta_{13}$  has been shown to be small by measurements of this parameter by reactors experiments [12, 21, 22] and so one can approximately decouple the two frequencies into two distinct regimes: the ‘‘solar’’ oscillation regime is driven by  $\Delta m_{21}^2$  and  $\theta_{12}$  and mostly determines the flavour composition of  $\nu_e$  particles propagating from within the sun towards Earth. The ‘‘atmospheric’’ oscillation regime is driven primarily by  $\Delta m_{32}^2$  and  $\theta_{23}$  and their values govern neutrino oscillation observed in  $\nu_\mu$  neutrinos decaying from secondary hadrons due to cosmic-rays interacting within Earth’s atmosphere. The MINOS experiment was designed to probe the atmospheric sector by using  $\nu_\mu$  neutrinos from a man made source. MINOS also has sensitivity to the parameter  $\theta_{13}$  through observing  $\nu_e$  and  $\bar{\nu}_e$  appearance, allowing for a full analysis combining both disappearance and appearance data.

*1.1. Oscillation Physics at MINOS.* The neutrino oscillation regime MINOS is most sensitive to and is driven by the larger of the two mass splitting differences  $\Delta m_{32}^2$ ; consequently, a two-flavour approximation can be used to describe the data using a single mass splitting  $\Delta m^2$  and effective mixing angle  $\theta$ . Using this approximation, one can express the muon neutrino survival probability as

$$P(\nu_\mu \rightarrow \nu_\mu) = 1 - \sin^2(2\theta) \sin^2\left(\frac{1.27\Delta m^2 [\text{eV}^2] L_\nu [\text{km}]}{E_\nu [\text{GeV}]}\right), \quad (1)$$

where  $L_\nu$  is the neutrino propagation distance and  $E_\nu$  is the neutrino energy. Previous analyses by MINOS rely on this two-favour approximation. However, the neutrino community is entering an era of precision measurement; the error on the atmospheric mass splitting is down to a few percent level and with the discovery of a nonzero  $\theta_{13}$  in 2012 by Daya bay [12],  $\theta_{13}$  has now become one of the most precisely measured angles, and so the need to move to a fuller treatment of neutrino oscillations is ever present.

Within a three-flavour framework, the oscillations are driven by the mass splittings  $\Delta m_{32}^2$  and  $\Delta m_{21}^2$ , where  $\Delta m_{31}^2 = \Delta m_{32}^2 + \Delta m_{21}^2$ . For exact calculations of the oscillation probabilities, one must consider all parameters due to interferences. One can modify the two-flavour oscillation probability parameters in (1) as follows:

$$\sin^2 2\theta = 4\sin^2\theta_{23}\cos^2\theta_{13}(1 - \sin^2\theta_{23}\cos^2\theta_{13}),$$

$$\begin{aligned} \Delta m^2 &= \Delta m_{32}^2 + \Delta m_{21}^2 \sin^2\theta_{12} \\ &+ \Delta m_{21}^2 \cos\delta_{\text{CP}} \sin\theta_{13} \tan\theta_{23} \sin 2\theta_{12}. \end{aligned} \quad (2)$$

Only by moving to a three-flavour framework can the degeneracies between the octant of  $\theta_{23}$  and determination of the mass hierarchy (sign of  $|\Delta m_{32}^2|$ ) be broken. These equations only account for neutrino oscillation within a vacuum; however, when neutrinos traverse through matter, the eigenstates become modified due to the MSW effect [23, 24]. To account for this, one can replace  $\theta_{13}$  with a modified mixing angle  $\theta_M$ , given by [25], such that

$$\sin^2 2\theta_M = \frac{\sin^2 2\theta_{13}}{\sin^2 2\theta_{13} + (A - \cos 2\theta_{13})^2}, \quad (3)$$

where the magnitude of  $A$  determines the size of the matter effect and can be expressed as  $A = \pm 2\sqrt{2}G_F n_e E_\nu / \Delta m_{31}^2$ , where  $G_F$  is the Fermi weak coupling constant and  $n_e$  is the density of electrons in the medium. The sign of  $A$  is positive (negative) for neutrinos (antineutrinos). The magnitude of  $\sin^2 2\theta_M$  in (3) influences the amount of mixing of  $\nu_\mu \leftrightarrow \nu_e$ . This MSW mechanism has an effect on a  $\nu_\mu$  disappearance analysis through  $\nu_\mu \leftrightarrow \nu_e$  mixing; therefore, in order to perform a precision measurement using  $\nu_\mu$  disappearance, one must also take into account  $\nu_e$  appearance.

MINOS is also sensitive to  $\nu_e$  interactions; the probability for  $\nu_e$  appearance to second order can be approximated to [26]

$$\begin{aligned} P(\nu_\mu \rightarrow \nu_e) &\approx \sin^2\theta_{23}\sin^2 2\theta_{13} \frac{\sin^2\Delta(1-A)}{(1-A)^2} \\ &+ \alpha \tilde{J} \cos(\Delta \pm \delta_{\text{CP}}) \frac{\sin\Delta A}{A} \frac{\sin\Delta(1-A)}{1-A} \\ &+ \alpha^2 \cos^2\theta_{23}\sin^2 2\theta_{12} \frac{\sin^2\Delta A}{A^2}, \end{aligned} \quad (4)$$

where  $\alpha \equiv \Delta m_{21}^2 / \Delta m_{31}^2$  ( $\sim 0.03$ ),  $\tilde{J} \equiv \cos\theta_{13}\sin 2\theta_{13}\sin 2\theta_{12}\sin 2\theta_{23}$ , and  $\Delta \equiv \Delta m_{31}^2 L_\nu / 4E_\nu$ . The second term in (4) will have a plus (minus) sign for neutrinos (antineutrinos). Being sensitive to  $\nu_e$  and  $\bar{\nu}_e$  appearance allows one to probe the mass hierarchy (as the sign of  $\Delta m_{31}^2$  will change) as well as the CP violating phase.

## 2. The MINOS Experiment

*2.1. The NuMI Beam.* The Neutrinos at the Main Injector (NuMI) neutrino beam [27] was built at Fermilab, to provide neutrinos for the MINOS experiment. The NuMI beam typically has a beam power of 350 kW with a design specification of up to 400 kW. A high-intensity beam is required to achieve a meaningful event rate at the MINOS Far Detector (FD) placed several hundred kilometres away. Such a distance significantly reduces the neutrino flux as it falls with the square of the distance from the decay point.

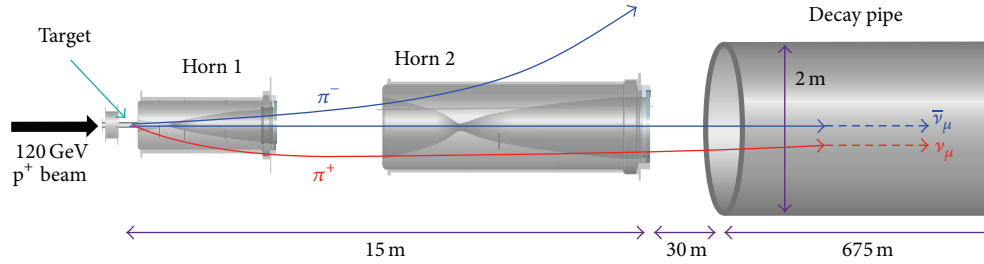


FIGURE 1: The NuMI beam.

To produce such a powerful neutrino beam, the first stage is to create protons from  $H^-$  ions. To achieve this, the ions are accelerated by a Radio Frequency (RF) quadrupole up to an energy of 750 keV. From there, a linear accelerator then accelerates the ions to an energy of 400 MeV which have subsequently passed through a thin carbon foil stripping the electrons off the ions to leave a beam of protons. The protons are fed into a rapid cycling synchrotron (Booster) and accelerated in batches up to energies of 8 GeV. Subsequently, they are fed into the Main Injector where they are accelerated to 120 GeV. The Main Injector has a circumference seven times larger than the Booster and so up to six batches can be inserted into the Main Injector at once. It is the interaction between these high energy protons upon a fixed graphite target which results in plethora of charged hadrons (predominantly pions, with a significant kaon component at higher energies). These charged hadrons pass through two parabolic, magnetic horns which focus either positive or negative hadrons depending on the direction of the electric current being pulsed through the horns. The focused hadrons travel along a 675 m decay pipe. It is the decay of these hadrons within the pipe that form the predominate muon flavour neutrino beam. By focusing the positive hadrons, a beam of predominate  $\nu_\mu$  is created ( $\nu_\mu$ -dominated beam mode); by focusing the negatively charged hadrons, the  $\bar{\nu}_\mu$  component can be increased ( $\bar{\nu}_\mu$ -enhanced beam mode). Figure 1 shows a diagram of the charged hadrons being focused by the two horns into the decay pipe.

Figure 2 shows the composition of the NuMI beam for charged current neutrino interactions observed in the MINOS Near Detector. The significant difference in composition and event rate between these beam modes arises mainly from the fact that the  $\bar{\nu}_\mu$  interaction cross section is a factor of approximately two lower than the  $\nu_\mu$  interaction cross section.

The neutrino energy spectrum provided by the NuMI beam is tunable, through changing the relative positions between the target and the focusing horns. Three of the possible configurations are shown in Figure 3. In Figure 4, the entire MINOS and MINOS+ running periods, from 2005 through to the present, are shown, illustrating when each different beam configuration was used. The main goal of MINOS was to measure the atmospheric oscillation parameters; this would require a large flux at the oscillation dip which would be located around the 2 GeV region. In the MINOS era, the configuration of the NuMI was set to the low

energy setting. For the MINOS+ era, the NO $\nu$ A experiment is 14 mrad off axis and requires the NuMI beam to be set at the medium energy configuration. MINOS/MINOS+ is an on-axis experiment (the detectors line up with the beam axis) and therefore MINOS+ observes a high flux of neutrinos at higher energies compared to the low energy configuration.

**2.2. The MINOS Detectors.** The MINOS experiment has two steel-scintillator calorimeters [29] designed with the same materials and to operate in an identical manner, known as being functionally identical. The calorimeters measure the energy deposition and event topologies of neutrino interaction events. The detectors are shown in Figure 6. Both detectors are made of alternating layers of 1.00 cm thick plastic scintillator and 2.54 cm thick steel planes. As neutrinos travel through the detector, they interact with the iron-nuclei, and the charged final-state particles travel through the scintillator depositing energy which is read out as light.

The light travels along wavelength shifting (WLS) fiber and is read out by a series of a photomultiplier tubes (PMTs). Figure 5 shows a strip of the scintillator used in the MINOS detectors; along the middle a groove is made so that a wavelength shifting fiber can be installed. It is from the light patterns that a neutrino candidate event can be reconstructed, so that information about the topology of the event can be extracted. The steel planes are magnetised by a coil aligned to the longitudinal axes of each detector giving a magnetic field of approximately 3 T. The trajectories of the charged particles are therefore curved (the direction depends on the polarity of the current in the coil) and thus  $\nu_\mu$  and  $\bar{\nu}_\mu$  CC interactions can be distinguished.

The Near Detector (ND) is situated 1.04 km downstream from the neutrino target at Fermilab. With a mass of 0.98 kton, the ND measures the reconstructed neutrino energy spectrum before oscillations have occurred. The ND has two distinct sections so that it can take advantage of the high neutrino flux at this location to define a relatively small target fiducial volume for selection of events for the near/far comparison. The section closest to the target is used to define the interaction vertex and measure the energy of the neutrino-induced hadronic shower; every plate is instrumented with plastic scintillator to act as a calorimeter. The second section is used as a muon spectrometer to measure the momenta of energetic muons where one in every five plates is instrumented with scintillator. The scintillator

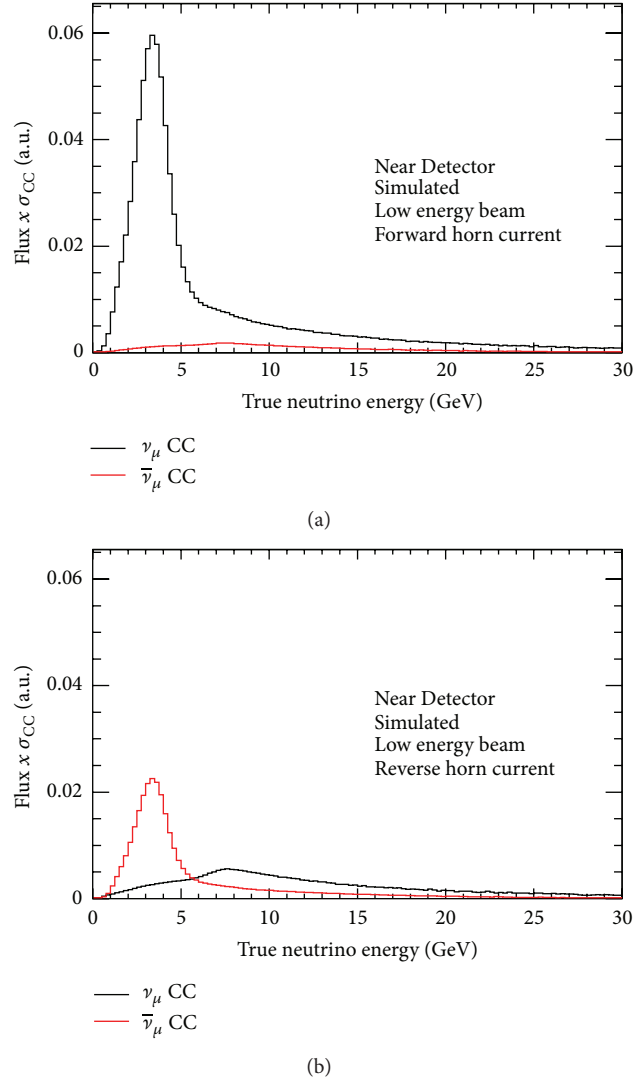


FIGURE 2: The reconstructed neutrino energy spectra at the MINOS Near Detector. (a) shows the energy spectrum for positively focused hadrons producing a predominately  $\nu_\mu$  beam. (b) is when negatively charged hadron is focused which increases the amount of  $\bar{\nu}_\mu$  events seen at the detectors. Note how in antineutrino mode the event rate is significantly less due to different cross sections between neutrinos and antineutrinos.

planes are made up of 4 cm wide strips. The strips on adjacent planes are oriented perpendicular to each other to allow three-dimensional reconstruction of events. The planes are oriented  $45^\circ$  to the vertical defining a coordinate system referred to as the  $u$  and  $v$  directions.

The Far Detector is 735 km downstream from the neutrino production target, 705 m underground in a mineshaft in northern Minnesota. The FD is significantly larger than the ND to compensate for the decrease in the neutrino flux. With a mass of 5.4 kton, the FD measures the reconstructed neutrino energy spectrum and will observe a different neutrino flavour composition of the beam due to neutrino oscillation. The geometry is similar to that of the ND in that it is split into two “super modules” of 239 and 247 planes; however, the FD does not have a vertex and spectrometer section due

to its distance away from the beam; it observes significantly less neutrino interactions. A veto shield composed of layers of scintillator covers the top and sides of the FD to better identify incoming cosmic-ray muons that may enter the fiducial volume of the detector helping to obtain a high pure sample of downward-going atmospheric  $\nu_\mu$  events.

The two-detector method is a very powerful experimental setup, since it allows the cancellation of large uncertainties that beset any neutrino oscillation experiment. The uncertainty in neutrino flux and cross sections are only known to tens of percent. Therefore, by looking at the disappearance and appearance in the FD relative to the ND, the uncertainties can be reduced significantly as only the relative uncertainty between the two detectors will affect the final measured result.

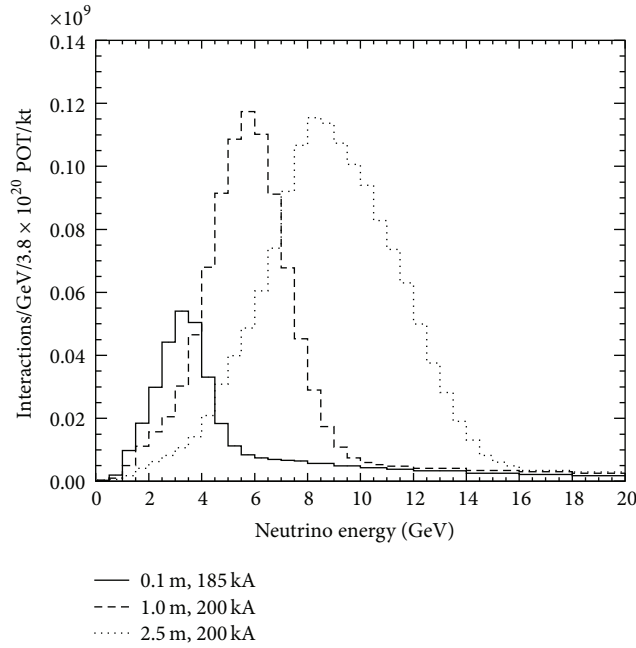


FIGURE 3: The true energy distribution of Near Detector events from the three different NuMI configurations. The target position (distance upstream of a nominal position) and horn current of each configuration are shown in the caption. “0.1 m, 185 kA” is the “low energy” configuration in which most of the MINOS data has been taken. “1.0 m, 200 kA” is the “medium energy” configuration which is the beam configuration in the NO $\nu$ A era and therefore is the beam setup in which MINOS+ is currently taking data in. The final configuration is the “pseudo high energy” configuration.

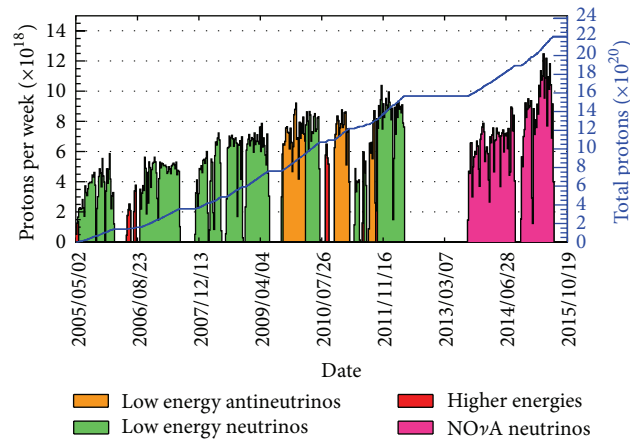


FIGURE 4: Showing the beam configuration for the MINOS and MINOS+ experiments. Most of the data for MINOS was taken in the low energy  $\nu_\mu$ -beam (in green) and  $\bar{\nu}_\mu$  (orange). Special runs where the beam was configured to higher energies or with the magnetic horns switched off are indicated by the red. The Magenta coloured runs are the beginning of the MINOS+ data taking in the  $\nu_\mu$ -beam during the NO $\nu$ A era.

### 3. Neutrino Interactions in the MINOS Detectors

There are three neutrino interactions that are of interest to MINOS as shown in Figure 7.

The main channel is the charged current (CC)  $\nu_\mu(\bar{\nu}_\mu)$  interaction:

$$\nu_\mu(\bar{\nu}_\mu) + X \longrightarrow \mu^{-(+)} + X'. \quad (5)$$

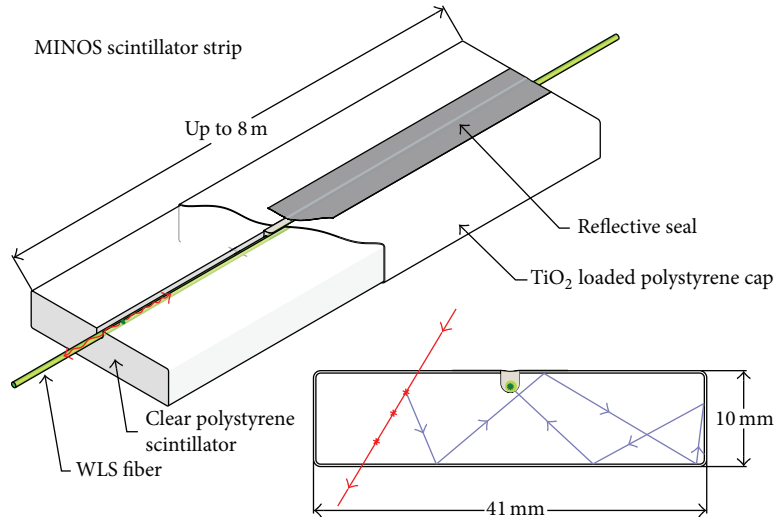


FIGURE 5: A strip of MINOS scintillator with the WLS fiber installed along the center. The image in the lower right corner depicts a charged particle (red line) depositing energy by producing light (blue line) as it passes through the strip. The light travels along the WLS fiber and is read out by a PMT.

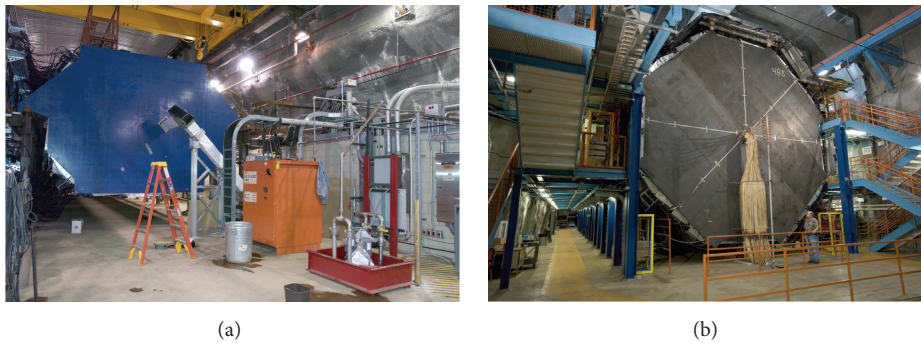


FIGURE 6: The MINOS detectors. (a) The Near Detector at Fermilab, (b) the Far Detector at the Soudan Underground Laboratory.

The cascade of hadrons,  $X'$ , produces a diffuse shower of energy deposits near the interaction vertex. MINOS was constructed with steel planes so that it can contain a significant proportion of the final-state muons. A muon produces a long track that curves due to the magnetic field. It is the direction of curvature that allows MINOS to identify the incoming neutrino as  $\nu_\mu$  or  $\bar{\nu}_\mu$ .

All active neutrino flavours undergo the neutral current (NC) interaction through the following process:

$$\nu + X \longrightarrow \nu + X'. \quad (6)$$

Only the hadronic shower is observed, producing a diffuse pattern of energy deposits within the detector. It is not possible to determine the flavour of neutrino.

Finally, electron neutrinos undergo CC interactions through the following process:

$$\nu_e (\bar{\nu}_e) + X \longrightarrow e^{-(+)} + X'. \quad (7)$$

The electron gives rise to an electromagnetic shower, which produces a much denser, more compact shower of energy deposits. This interaction is difficult to detect due to the steel

plate thickness, meaning only a few events leave any energy deposits in the plastic scintillator.

Above a few GeVs, the dominant process is deep inelastic scattering (DIS). Here, the neutrino has sufficient energy that it can resolve the individual quark constituents of the nucleon which manifests in the creation of a hadronic shower. However, at MINOS, the oscillation dip observed in muon neutrino disappearance at the Far Detector occurs just below 2 GeV; these neutrino interactions provide a large source of signal events for a neutrino oscillation analysis. At this energy, neutrinos can elastically scatter off an entire nucleon liberating a nucleon (or multiple nucleons) from the target. In the case of charged current scattering, this process is referred to as ‘‘quasi-elastic scattering’’ (CCQE). A detailed review on the current state of neutrino cross sections can be found here [30].

The energy of a neutrino event is calculated by summing the shower energy deposits and the muon track energy. The energy resolution of contained muon tracks is 4.6% [31]. If a muon track exits either one of MINOS detectors then the curvature of the track is used to calculate the energy. The curvature of a muon track is directly proportional to the ratio

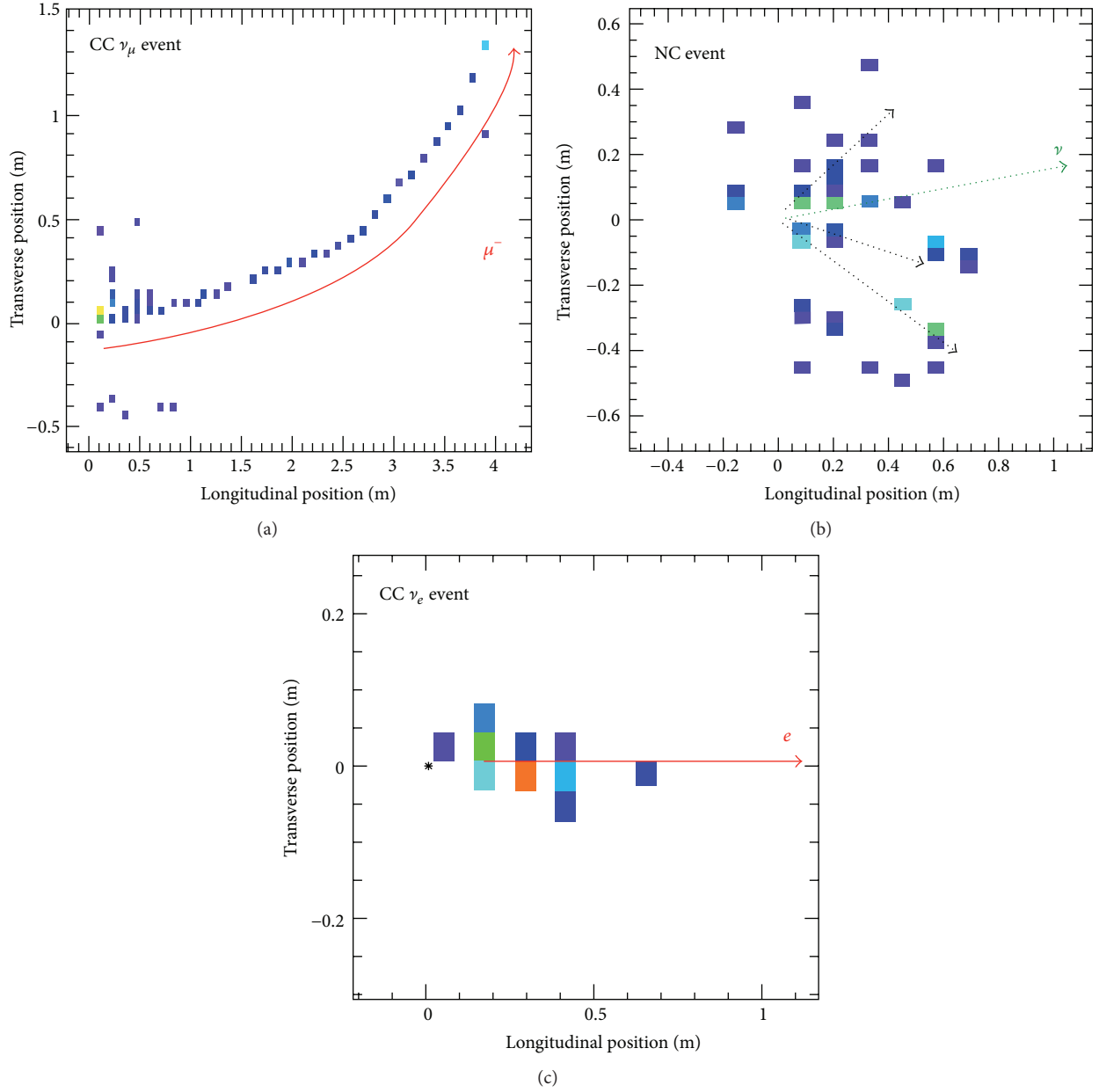


FIGURE 7: Neutrino interaction topologies observed in the MINOS detectors. (a) A charged current  $\nu_\mu$  interaction. (b) A neutral current interaction. (c) A charged current  $\nu_e$  interaction. Each coloured pixel represents a scintillator strip with energy deposited from a charged particle. The colour scale displays the amount of light: purple and blue are low light levels, through to orange and red for the highest light levels.

of its electric charge to its momentum; at the peak of the neutrino beam at around 3 GeV, the resolution is 11% [31].

All three interaction processes can result in a shower of energy deposited in the detectors. The MINOS detectors are too coarse to reliably use shower topology information and so the energy is reconstructed calorimetrically. The final calorimetric hadronic and electromagnetic shower resolutions are well modelled by simulation and the resolution is parameterised as  $56\%/\sqrt{E}$  for hadronic showers and  $21\%/\sqrt{E}$  for electromagnetic showers, where  $E$  is the particle energy in GeV [32, 33].

A calorimeter response is different for hadronic and electromagnetic showers. A fraction of the energy deposited by the showering particle is invisible; that is, it does not contribute to the calorimeter signal; this can cause some undesirable properties in a calorimeter causing nonlinearities. For CC  $\nu_\mu$  ( $\bar{\nu}_\mu$ ) interactions, a more sophisticated method is implemented to measure shower energies [13]. A  $k$ -nearest-neighbour algorithm [34] uses a multivariate analysis of a broader range of event-level information to provide an estimate of shower energy. The variables are by the algorithm as follows: the event length, the average energy deposited

per scintillator plane along the track, the transverse energy deposition, and the fluctuation of the energy deposition along the track. The  $k$ -nearest-neighbour algorithm uses the 400 nearest-neighbours and comparing them to a simulated library of events the total shower energy of an event can be estimated. Figure 8 shows the distribution of reconstructed overtrue shower energy for different ranges of true shower hadronic shower energy using calorimetric energy and  $k$ -nearest-neighbour algorithm estimator. It can be seen that the  $k$ -nearest-neighbour algorithm gives a better estimate of the shower energy at lower energies. This improves the hadronic energy resolution from 55% to 43% for showers between 1.0 and 1.5 GeV.

**3.1. Selection of Charged Current  $\nu_\mu$  and  $\bar{\nu}_\mu$  Interactions.** MINOS was designed to measure the neutrino oscillation parameters in the atmospheric region ( $\Delta m_{32}^2$  and  $\theta_{23}$ ). To achieve this, one needs a sample of  $\nu_\mu(\bar{\nu}_\mu)$  CC events. Figure 7 shows that this can be achieved by selecting neutrino candidate events with a muon track.

There are three main backgrounds that have an effect on signal purity. At low energies, NC interactions can result in a charged hadron producing a track, thus being mistaken for a  $\nu_\mu$ -CC event with a low energy muon track. Atmospheric  $\nu_\mu$  events represent a potential source of muon neutrinos distinct from those in the muon beam and hence are not useful when only considering a beam disappearance oscillation analysis. Wrong-sign events can become a background when the muon charge deduced from curvature is measured incorrectly if one wishes to separate  $\nu_\mu$  and  $\bar{\nu}_\mu$  samples to test if they oscillate with different probabilities.

To reduce the NC background, one needs to separate the NC and CC candidate events. MINOS uses a  $k$ -nearest-neighbour algorithm; a simulated high statistics data set is created with two known classes of events, one with a muon track and one without. Four variables are used to create a discriminating variable to be applied to all track-like events. The variables are the number of MINOS detector planes associated with a muon track (muon tracks tend to extend much further than NC showers), the average energy deposited per scintillator plane along the track, the transverse energy deposition profile, and the variation of the energy deposited along the muon track. Figure 9 shows the distribution of the  $k$ -nearest-neighbour algorithm as a single variable [35].

The event selection is identical for  $\bar{\nu}_\mu$  and  $\nu_\mu$  CC events due to their similar interaction topologies. The NuMI beam can be configured to produce an antineutrino-enhanced beam. From the curvature of the muon track reconstructed by a Kalman Filter [36] algorithm, the lepton number of the neutrino can be deduced. After track identification, all the remaining hits which are in proximity to one another are grouped into showers.

**3.2. Selection of Charged Current  $\nu_e$  Interactions.** The selection for  $\nu_e$  events relies on looking for events with a dense shower arising from electromagnetic interactions from an electron as it passes through the MINOS detectors. The dominant background comes from NC events generating a dense hadronic shower. Such behaviour can be caused by a

neutral pion decaying into a pair of photons. The majority of  $\nu_e$  appearance expected at the FD occurs in neutrino events with energy in the range 1–8 GeV and so only this range is considered.

The granularity of the MINOS detectors makes resolving any topology from electromagnetic showers almost impossible; therefore, all candidate events with a shower have their energy deposition patterns compared to a large library of order  $10^7$  simulated events containing signal (40%) and background events (60%). This technique is called Library Event Matching (LEM) [37–39]. The 50 simulated events that match the event with a similar pattern of energy deposited in each scintillator strip excited by the shower are chosen. Data and library events are not spatially translated to align them for the best matching. The matching procedure provides a quantitative means of determining the likelihood that two different charge topologies were created by the same primary deposition. For an arbitrary energy deposit, the mean expected charge on a photomultiplier tube will be some value  $\lambda$ . Consider strip  $i$  in the  $j$ th plane of the detector and events A and B, where the detector's response in event A was  $n_A$  photoelectrons and the response in event B was  $n_B$  photoelectrons. The likelihood  $L$ , of a data event corresponding to the same physical shower topology as a simulated library event, can therefore be calculated as

$$\log L = \sum_{i=1}^{N_{\text{strips}}} \log \left[ \int_0^\infty P(n_{\text{data}}^i | \lambda) P(n_{\text{lib}}^i | \lambda) d\lambda \right]. \quad (8)$$

An example of a good and bad match from LEM can be seen in Figure 10.

Three variables are constructed from the 50 best simulated events (signal or background); these are the fraction of the events that are true  $\nu_e$  CC events, the average inelasticity (this is the amount of energy that goes into the hadronic shower) of the true  $\nu_e$  CC events, and the average fraction of charge that overlaps between the data event and each  $\nu_e$  CC library event. These three variables along with the reconstructed energy of the data event are fed into a neural network which calculates a classification of how signal-like the data event is. A single variable,  $\alpha_{\text{LEM}}$ , is formed to quantify this, as shown in Figure 11. It is an output of an artificial neural network with several variables coming from the event comparisons. Events with  $\alpha_{\text{LEM}} > 0.6$  are selected for analysis; this number was optimised to maximise the sensitivity to  $\nu_e$  appearance [40]. Candidate  $\nu_e$ -CC and  $\bar{\nu}_e$ -CC events are required to fall within a fiducial volume and to be coincident in time (50  $\mu\text{s}$ ) and direction with the NuMI beam. Events are required to have shower-like topologies by rejecting events with tracks that are longer than 25 planes or extend more than 15 planes from a shower edge.

With the absence of a  $\nu_e$ -CC and  $\bar{\nu}_e$ -CC signal in the ND, the signal-selection efficiency cannot be extrapolated from the ND events in the same way as the background estimate. By using real data, well-identified  $\nu_\mu$ -CC events are selected. By removing the energy deposited by the muon track [41], these events can be used to calculate the signal-selection efficiency by inserting the energy deposition from an electron with identical momentum to that of the removed

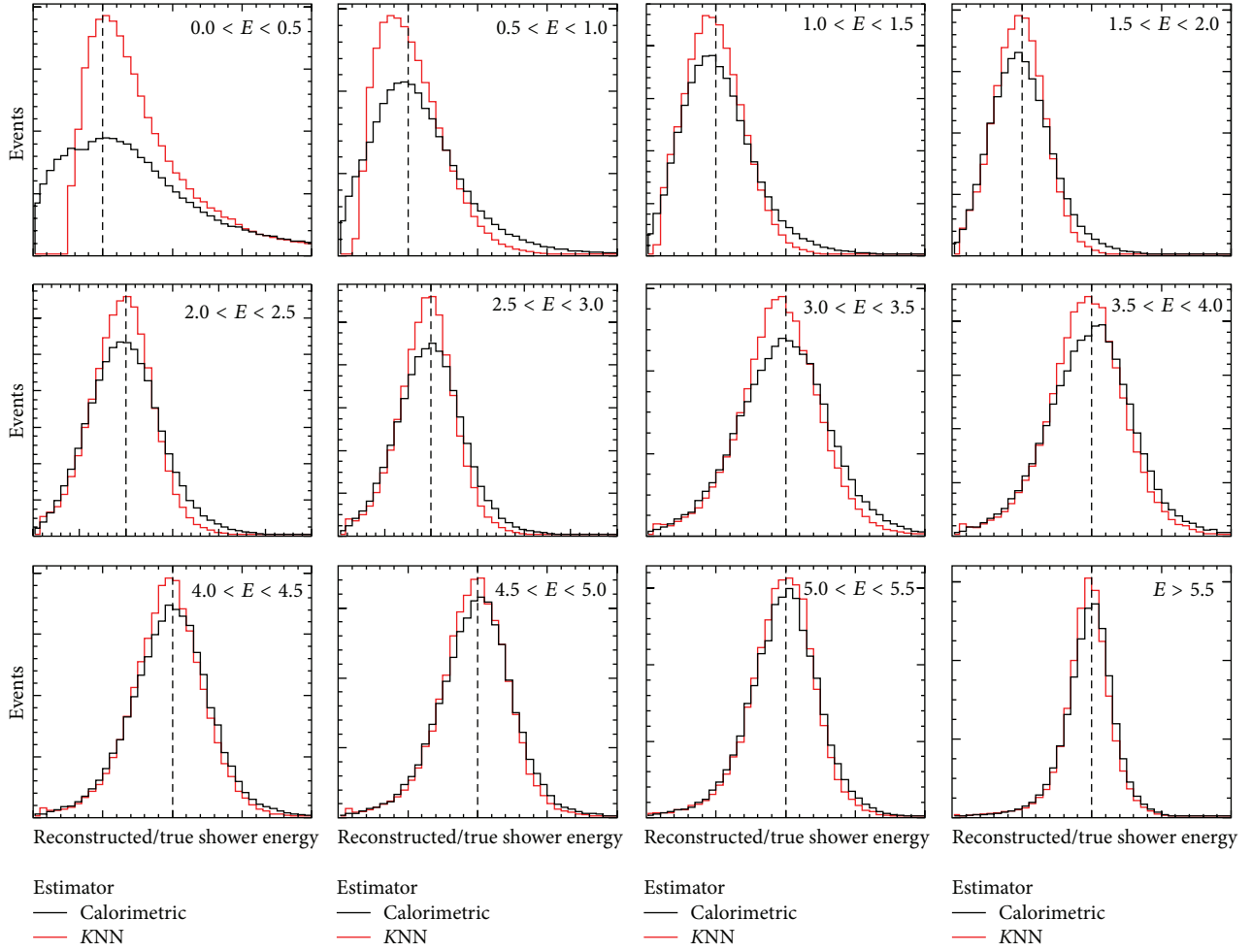


FIGURE 8: Distribution of reconstructed overtrue shower energy for different ranges of true shower energy (indicated in the corner of each panel). The calorimetric estimator is shown in black and the  $k$ -nearest-neighbour estimator in red. In each panel, the dashed line indicates the position of  $E_{\text{reco}}/E_{\text{true}} = 1$ . Figure taken from [13].

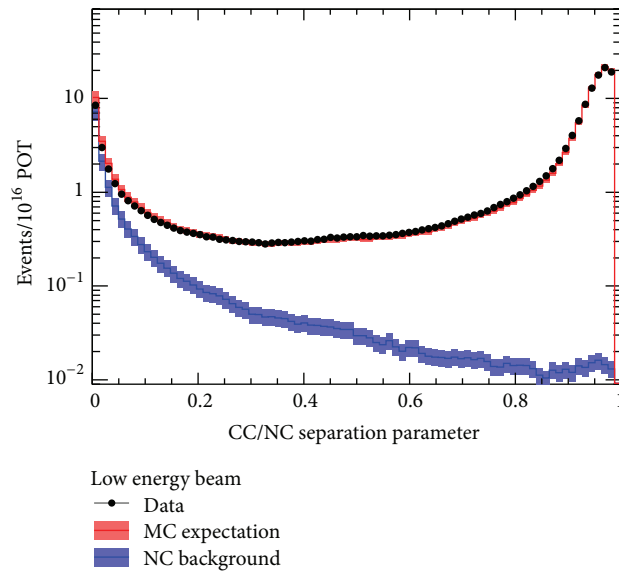


FIGURE 9: The  $k$ -nearest-neighbour discrimination variable used to separate  $\gamma_\mu$  CC interactions from track-like hadronic backgrounds. Events with a parameter value greater than 0.3 are selected as  $\gamma_\mu$  CC interactions for analysis.

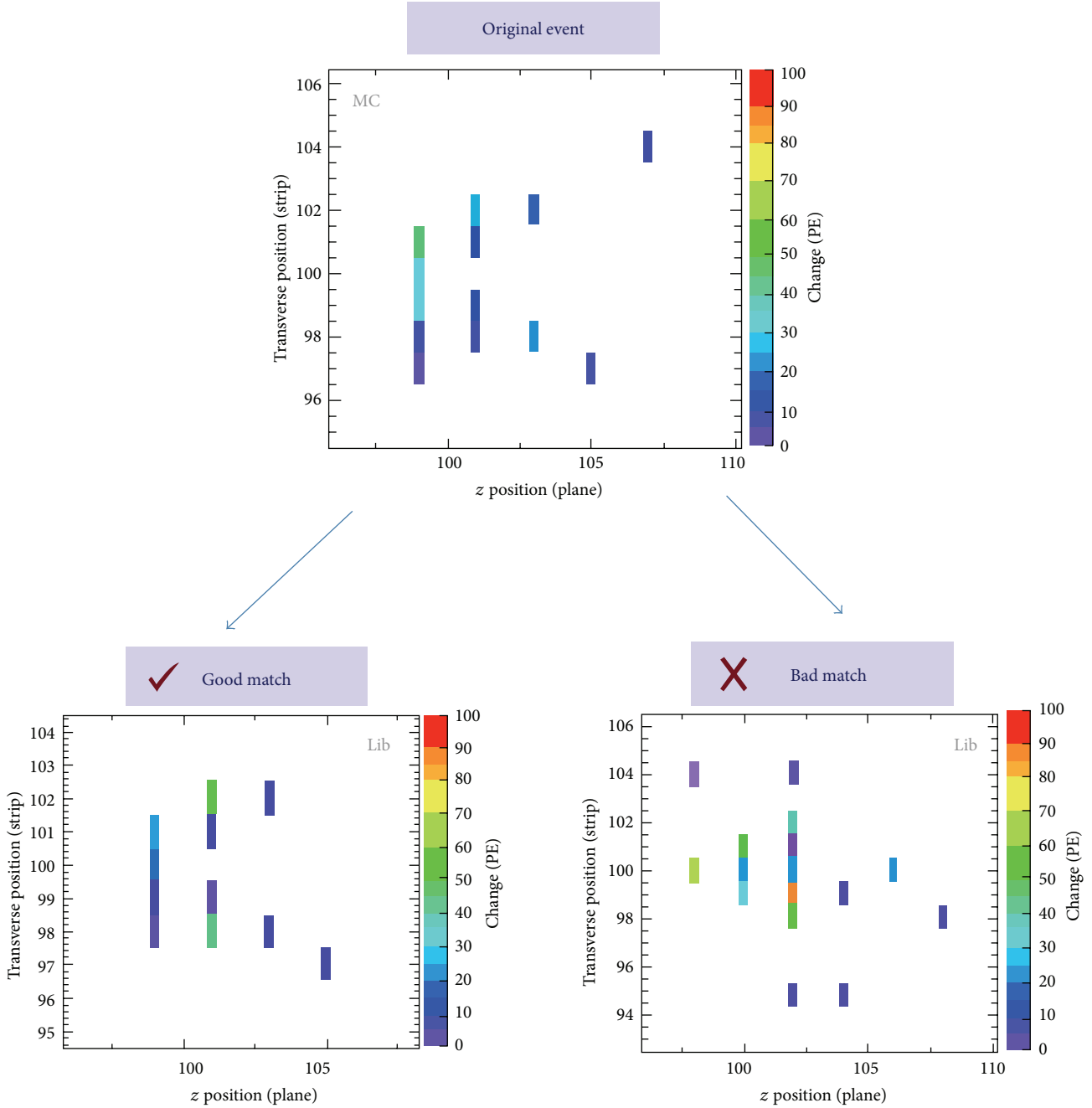


FIGURE 10: Showing an example of a simulated  $\nu_e$  event compared to a good and bad match from the LEM library.

muon. This allows one to effectively convert a well-identified sample of  $\nu_\mu$ -CC and  $\bar{\nu}_\mu$ -CC data events into a sample of  $\nu_e$ -CC and  $\bar{\nu}_e$ -CC data events. Using this method, the  $\nu_e$ -CC identification efficiency is found to be  $(57.4 \pm 2.8)\%$  in the neutrino-dominated beam and  $(63.3 \pm 3.1)\%$  in the antineutrino-enhanced beam.

**3.3. Selection of Neutral Current Interactions.** The signal for a NC event is a diffuse hadronic shower; however  $\nu_\mu$ -CC interactions can also have large hadronic showers, if the inelasticity of the event is high (most of the energy is given to

the shower). The muon track may then be difficult to detect if it does not significantly extend beyond the hadronic shower. To achieve a high purity of NC events, a number of selection cuts are used [42]. An event is classified as a NC event if it has no tracks or if a track does not extend more than six planes past the end of the shower. The NC identification efficiency is 89%, with 61% purity; this is determined by taking an average over the energy spectrum for simulated events. However, this selection will identify 97% of  $\nu_e$  CC interactions as NC events, which needs to be taken into account when searching for NC disappearance at the FD.

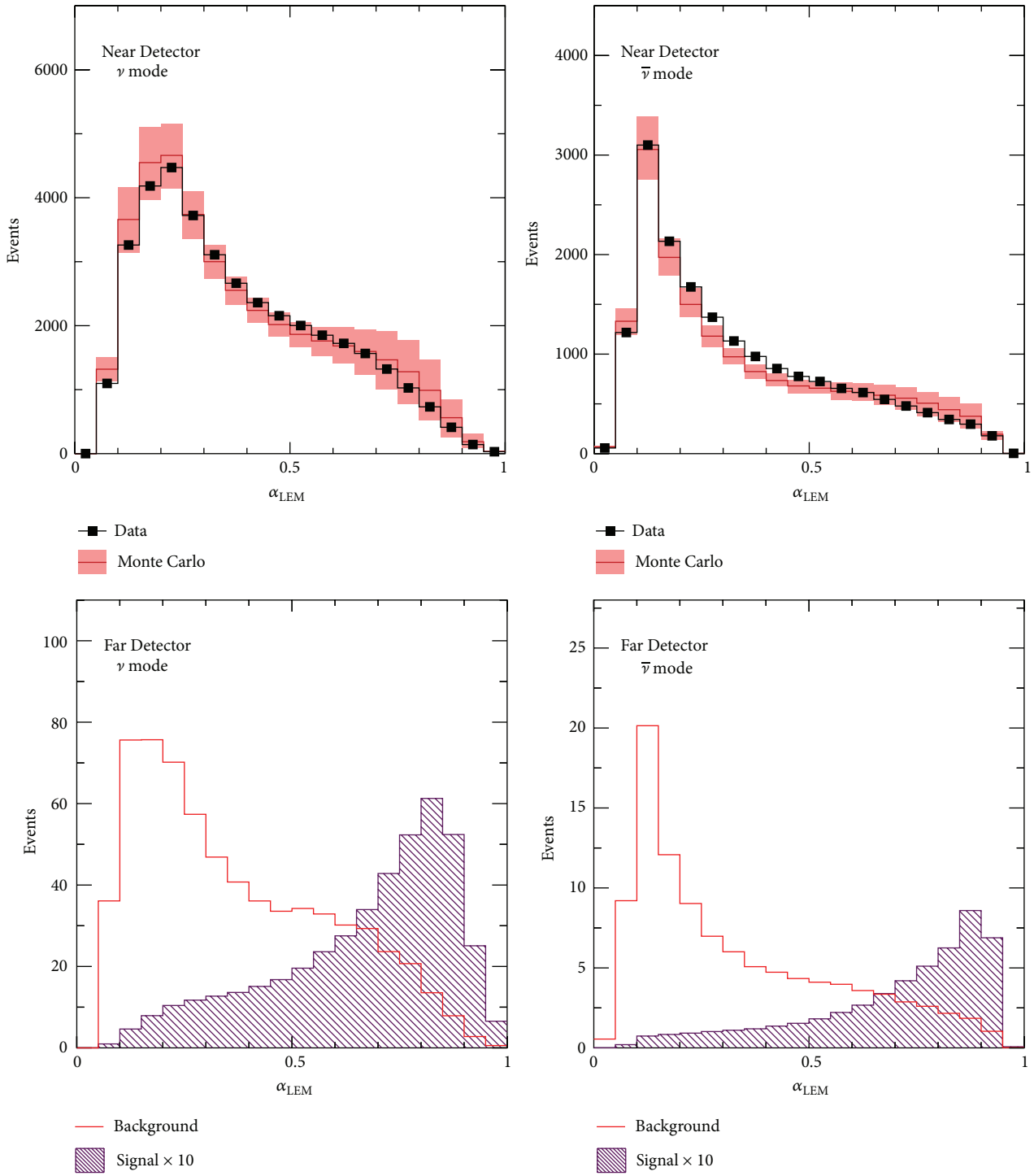


FIGURE 11: Distributions of  $\alpha_{LEM}$ . The plots in the left column correspond to the neutrino-dominated beam mode. The plots in the right column correspond to the antineutrino-enhanced beam mode. The top row shows the distributions for ND selected events with a band about the simulation representing the systematic uncertainty. The bottom row shows the distributions for the predicted FD background and signal multiplied by 10.

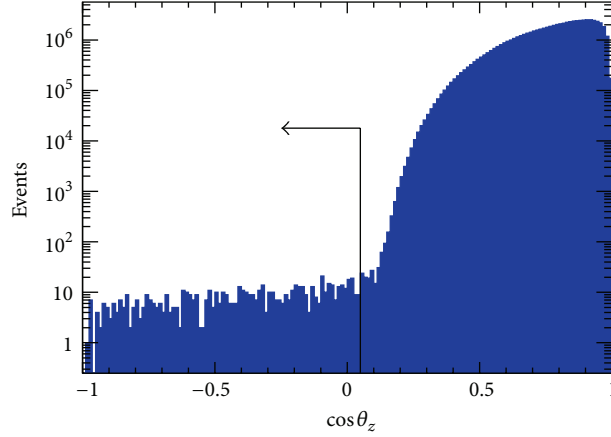


FIGURE 12: Distribution of reconstructed zenith angle for muons with good timings and topology. In the range  $\cos \theta_z > 0.10$ , the observed rate of muons is dominated by the cosmic-ray background and falls steeply as the mean rock overburden increases. To minimise the background from cosmic-ray muons, events for analysis are required to satisfy  $\cos \theta_z < 0.05$ .

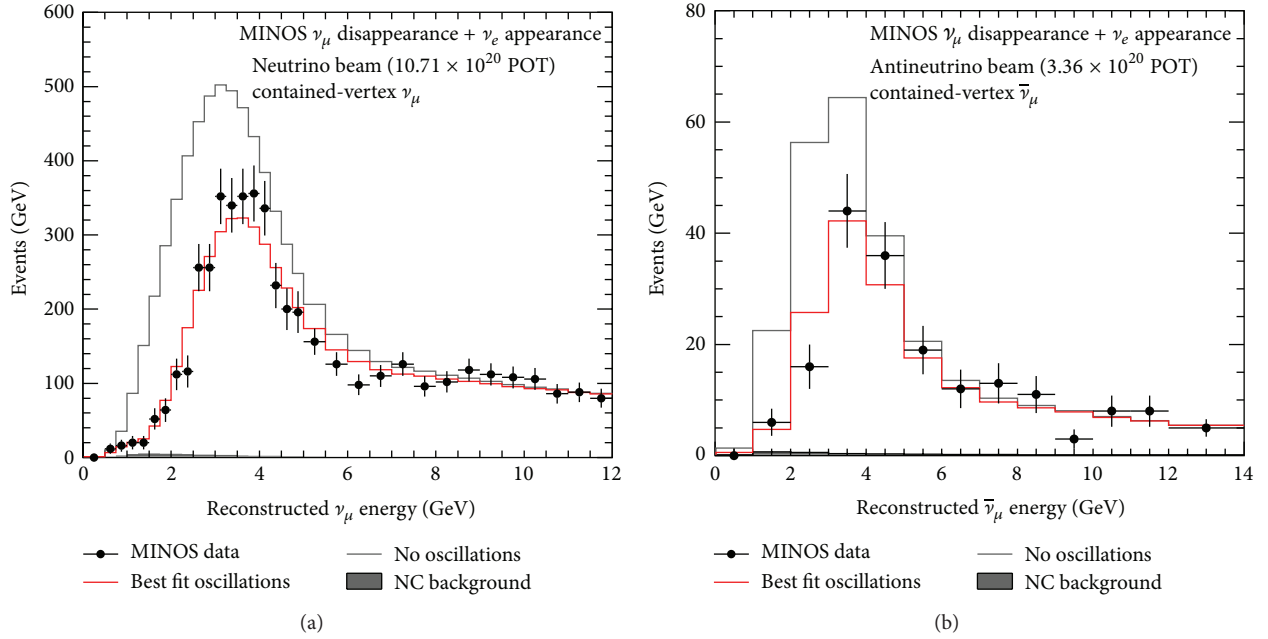


FIGURE 13: The FD reconstructed neutrino energy spectrum for  $\nu_\mu$  (a) and  $\bar{\nu}_\mu$  (b). The grey light shows the predicted FD energy spectrum if neutrinos did not oscillate. The red line indicates the best fit to the data. These energy spectra were fit along with the atmospheric and  $\nu_e$  samples discussed in the later subsections. For details on the fit and the result of the neutrino oscillation parameters obtained, see Section 6.

**3.4. Selection of Atmospheric Neutrinos.** Atmospheric neutrinos are selected as  $\nu_\mu$ -CC events in the MINOS FD outside of the  $10 \mu\text{s}$  window period when the NuMI beam is producing neutrinos [43]. The atmospheric neutrino signal is separated from the cosmic-ray background using two characteristic signatures of atmospheric neutrino interactions: either a reconstructed vertex inside the fiducial volume or a reconstructed upward-going or horizontal muon trajectory.

The FD timing resolution on a hit by hit basis is 2.5 ns, which is enough to calculate the direction of a muon track inside the FD. For upward and horizontal angles, where the rock overburden exceeds 14,000 m water-equivalent, the absorption of cosmic-ray muons by the Earth is sufficiently

high that the observed flux of muons is dominated by atmospheric muon neutrino interactions [44]. At the Soudan mine (the location of the FD), upward-going tracks with a zenith angle  $\cos \theta_z < 0.14$  are defined as being upward-going and horizontal [45]. Therefore, upward-going and horizontal tracks provide a signature for atmospheric neutrinos. To further reduce the background, the analysis requires  $\cos \theta_z < 0.05$  as shown in Figure 12.

For tracks where the end point lies inside the fiducial volume, the muon momentum is reconstructed from the measured track length; for exiting tracks, the momentum is obtained from the fitted track curvature. In both cases, the fitted curvature is used to determine the muon charge sign.

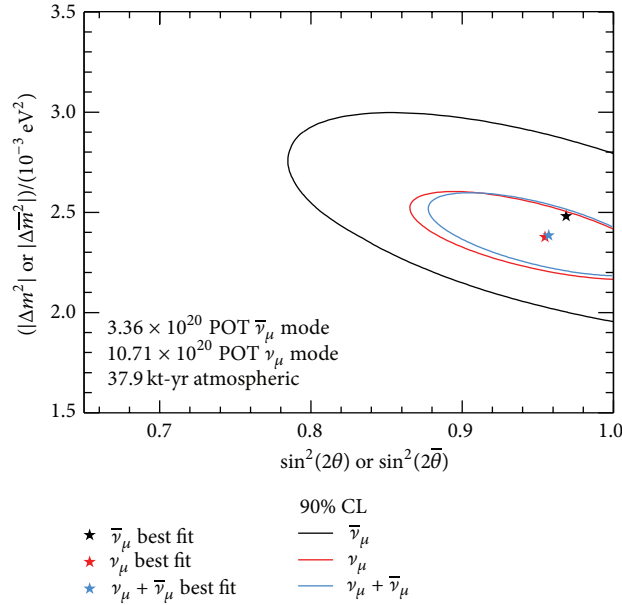


FIGURE 14: The allowed region for antineutrino oscillation parameters (black line), compared to the region measured with neutrinos alone (red line) and the region measured using both neutrinos and antineutrinos under the assumption that they have the same parameters (blue line).

#### 4. Muon Neutrino and Antineutrino Disappearance

MINOS can measure the atmospheric neutrino oscillation parameters  $\Delta m_{32}^2$  and  $\theta_{23}$  by fitting the energy dependence of  $\nu_\mu$ -CC and  $\bar{\nu}_\mu$ -CC disappearance. The FD sees the neutrino beam as a point source whereas the ND subtends a relatively large angle to the beam. Thus, once a neutrino parent decays, the ND would see a large spread in energies compared to the FD which preferentially selects higher energy neutrinos at a smaller angle from the direction of the parent hadron. MINOS pioneered the technique of resolving this kinematic issue by constructing a beam matrix that allows one to convert an energy spectrum observed in the ND to the corresponding spectrum observed at the FD [46]. This allows the measured ND energy spectrum to be used to predict what should be expected at the FD. Through this process, the effects of a large number of systematics, that affect both detectors in the same way, are mitigated. Only systematics affecting both detectors differently become a significant source of uncertainty, primarily reconstruction efficiencies and miscalibrations of the neutrino energy measurement in the detectors [47]. Figure 13 shows the reconstructed energy spectrum at the FD for  $\nu_\mu$  and  $\bar{\nu}_\mu$  neutrino events compared to two predictions, if there were no oscillations and a best fit to the FD data.

There is an uncertainty on the relative normalisation of the selected Near and Far Detector event samples which is dominated by differences in the reconstruction and selection efficiencies between the two detectors, as well as relative uncertainties on fiducial mass and live time; this uncertainty is found to be 1.6%. There are two different uncertainties on the measurement of hadronic shower energy [13]; these are

the relative mismodelling of the energy scale between the two detectors as well as the absolute mismodelling. It was found that the relative uncertainty for the ND is 1.9% and for the FD is 1.1%. The absolute mismodelling comes from the uncertainties on the modelling of hadronic showers which is fully correlated bin to bin in reconstructed energy and has an energy dependence of the form  $\sigma_{\text{shw}} = 6.6\% + (3.5\%) \times \exp(-E_{\text{reco}}/1.44 \text{ GeV})$  [48].

A previous two-flavour analysis [49] of  $\nu_\mu$  and  $\bar{\nu}_\mu$  disappearance using the combined accelerator and atmospheric data from MINOS yielded  $|\Delta m^2| = 2.41_{-0.10}^{+0.09} \times 10^{-3} \text{ eV}^2$  and  $\sin^2 2\theta = 0.950_{-0.036}^{+0.035}$ . A symmetry in CPT requires that neutrinos and antineutrinos oscillate in an identical way; thus, their oscillation parameters should be identical. With the ability to distinguish the lepton number of a neutrino, MINOS can measure the oscillation parameters for antineutrinos and neutrinos separately. Using both atmospheric and beam antineutrinos, MINOS measures the oscillation parameters to be  $|\Delta \bar{m}^2| = 2.50_{-0.35}^{+0.23} \times 10^{-3} \text{ eV}^2$  and  $\sin^2 2\bar{\theta} = 0.97_{-0.08}^{+0.03}$  [49] which is in good agreement with the parameters measured from  $\nu_\mu$  oscillations as shown in Figure 14.

**4.1. Atmospheric  $\nu_\mu$  and  $\bar{\nu}_\mu$  Disappearance.** MINOS is the first experiment to probe the resonance predicted to occur in multi-GeV, upward-going atmospheric neutrinos which travel through the Earth's mantle for both neutrino and antineutrino events on an event by event basis. The atmospheric events are separated into samples of contained-vertex and nonfiducial muons for neutrinos and antineutrinos. Figure 15 shows the atmospheric samples containing events with a contained-vertex. By measuring the  $\nu_\mu$ -CC and  $\bar{\nu}_\mu$ -CC interactions separately, this allows MINOS to gain sensitivity to the mass hierarchy and  $\theta_{23}$  octant. The difference between the

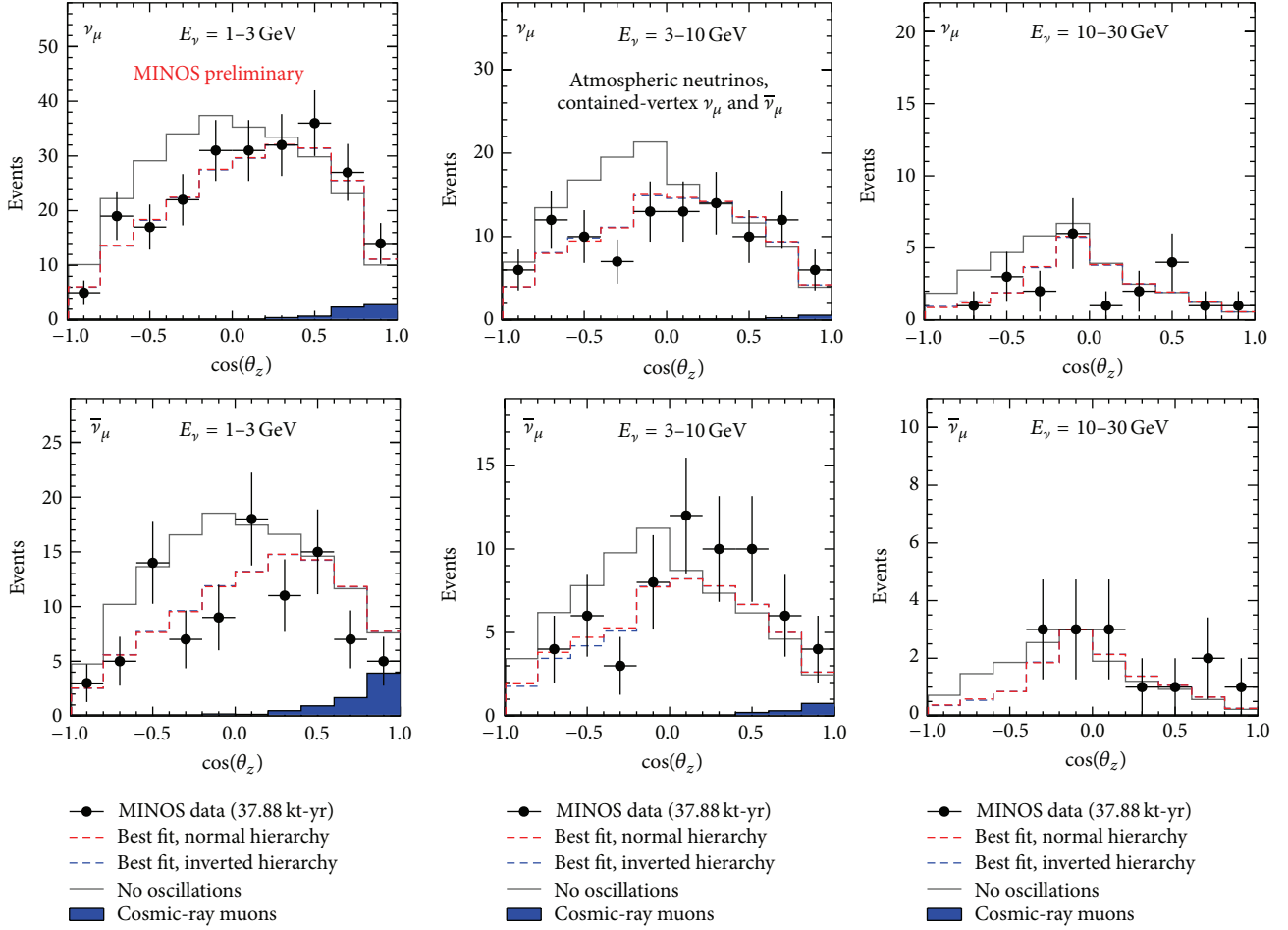


FIGURE 15: The distribution of reconstructed atmospheric  $\nu_\mu$  and  $\bar{\nu}_\mu$  CC interactions over various energy ranges observed at the FD, compared to the expectation with and without neutrino oscillation. Two different fits are performed for the normal and inverted hierarchy of  $\Delta m_{32}^2$ . The energy of the neutrino event is the sum of muon momentum (from range and/or curvature) and total shower energy.

inverted and normal mass hierarchy in Figure 15 is very marginal.

The neutrino events are binned as a function of  $\log_{10}(E)$  and  $\cos\theta_z$ , where  $E$  is the reconstructed energy of the event in GeV and  $\theta_z$  is the zenith angle of the muon track; this binning gives enhanced sensitivity to the MSW resonance. A sample of contained-vertex showers are also selected from the data, composed mainly of NC,  $\nu_e$ -CC, and  $\bar{\nu}_e$ -CC interactions. They are used to constrain the overall flux normalisation. For atmospheric neutrinos, the Earth is modelled by four layers of constant electron density using the PREM model [50]. Comparisons to a more detailed 52-layer model yielded very similar results and so the extra computational time was avoided by using the simple four-layer model.

## 5. $\nu_e$ and $\bar{\nu}_e$ Appearance

By searching for  $\nu_e$  and  $\bar{\nu}_e$  appearance at the FD, MINOS can perform a measurement of  $\theta_{13}$ . The POT exposure for this data set is  $10.6 \times 10^{20}$  protons-on-target (POT) using a  $\nu_\mu$ -dominated beam and  $3.3 \times 10^{20}$  POT using a  $\bar{\nu}_\mu$ -enhanced beam. Neutrino events with  $\alpha_{\text{LEM}} > 0.6$  are selected for

analysis in the  $\nu_\mu$ -dominated beam mode and in the  $\nu_\mu$ -enhanced beam. Neutrino events with  $\alpha_{\text{LEM}} < 0.6$  are considered background-like and therefore insensitive to  $\nu_e$  and  $\bar{\nu}_e$  appearance. The background consists of three components: NC interactions, CC- $\nu_\mu$  and  $\bar{\nu}_\mu$  interactions, and the intrinsic  $\nu_e$  component in the beam. The relative contribution between the ND and FD is different for all of these components, since they are affected differently by oscillation, and the kinematics of the production in the beam are different. Each background must be individually measured. By changing the configuration of the NuMI beam (low, medium, or pseudo-high), one can measure these backgrounds. The relative contributions of the background components change in a well understood way [51]. Neutrino events with  $\alpha_{\text{LEM}} < 0.6$  are used to provide validation to the analysis procedure; MINOS uses ND neutrino events with  $\alpha_{\text{LEM}} < 0.5$  to predict FD event yields. When these predicted FD yields are compared to those observed in the FD data, very good agreement is observed. The prediction and data agree to within  $0.3\sigma$  ( $0.6\sigma$ ) of the statistical uncertainty for the data in the  $\nu_\mu$  ( $\bar{\nu}_\mu$ ) beam modes.

For an appearance analysis, one has to consider a three-flavour neutrino oscillation probability that includes matter

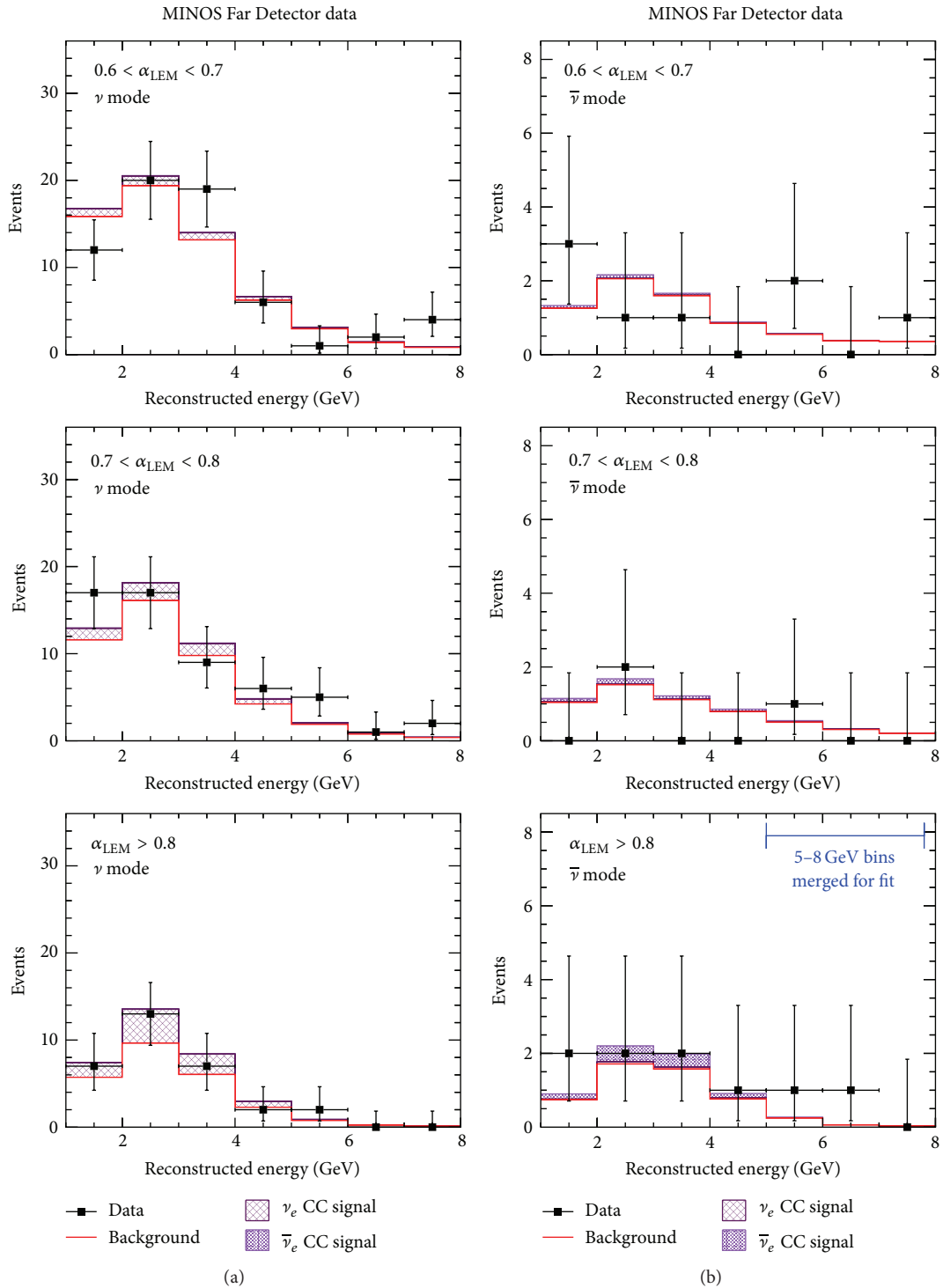


FIGURE 16: The reconstructed neutrino energy distributions for three  $\alpha_{\text{LEM}}$  ranges. The events with energy greater than 5 GeV are combined into a single bin for the fits. The vertical bars through the data points denote statistical uncertainties. The signal prediction assumes  $\sin^2(2\theta_{13}) = 0.051$ ,  $\Delta m_{32}^2 > 0$  (normal hierarchy),  $\delta_{\text{CP}} = 0$ , and  $\theta_{23} = \pi/4$  (maximal mixing). (a) corresponds to data taken in  $\nu_{\mu}$ -dominated beam mode samples and (b) is from  $\bar{\nu}_{\mu}$ -enhanced beam mode samples.

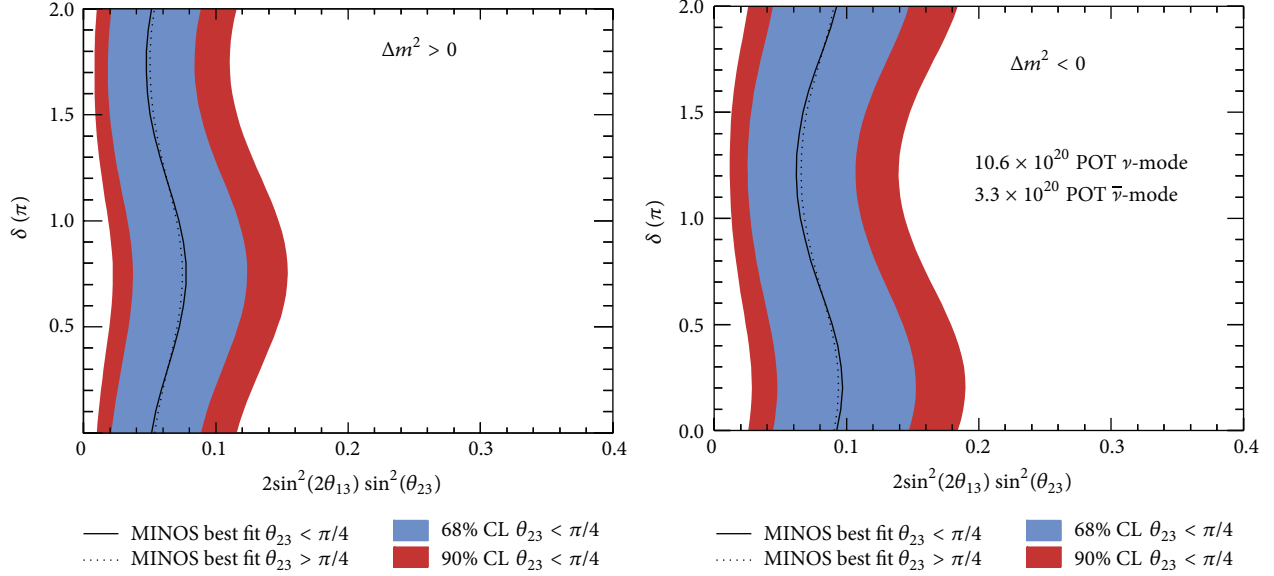


FIGURE 17: The allowed regions for  $2\sin^2(2\theta_{13})\sin^2(\theta_{23})$ .

effects. The fit is done simultaneously for data from both  $\nu_\mu$ -dominated beam mode and  $\bar{\nu}_\mu$ -enhanced beam mode samples. A total of 127.7 background events are expected at the FD in the neutrino-dominated beam and 17.5 events in the antineutrino-enhanced beam. In the data, 152 and 20 events are observed, respectively, and their energy distributions can be seen in Figure 16.

MINOS cannot distinguish  $\nu_e$  and  $\bar{\nu}_e$  events directly; however, the relative number of neutrino and antineutrino interactions in the neutrino-dominated and antineutrino-enhanced beams is well known. The parameter measured is  $2\sin^2(2\theta_{13})\sin^2(\theta_{23})$  while the values  $\Delta m_{32}^2$  and  $\delta_{CP}$  remain fixed. The fit is run over both hierarchies and all possible values of  $\delta_{CP}$ . For more details on this analysis, see [40]. The fit is performed using the 15 bins formed by three bins of  $\alpha_{LEM}$  and five bins of energy as seen in Figure 16; note that final three bins in energy from 5 to 8 GeV were merged for the fit.

MINOS finds that the data allow for a value of  $2\sin^2(2\theta_{13})\sin^2(\theta_{23}) = 0.051_{-0.030}^{+0.038}$  for the normal hierarchy with  $\delta_{CP} = 0$  and  $2\sin^2(2\theta_{13})\sin^2(\theta_{23}) = 0.093_{-0.049}^{+0.054}$  for the inverted hierarchy with  $\delta_{CP} = 0$ ; in both cases,  $\theta_{23} < \pi/4$ ; this can be seen in Figure 17. This is the first  $\bar{\nu}_e$  appearance search ever in a long-baseline  $\bar{\nu}_\mu$  beam.

## 6. A Combined Three-Flavour Analysis

To gain maximum sensitivity to the mass hierarchy and  $\delta_{CP}$ , one needs to perform a full three-flavour analysis combining  $\nu_\mu$  and  $\bar{\nu}_\mu$  disappearance with  $\nu_e$  and  $\bar{\nu}_e$  appearance. For this, one needs to account for both disappearance and appearance of neutrinos oscillations at both detectors.

For a full three-flavour fit, MINOS uses an accelerator neutrino data set comprising exposures of  $10.71 \times 10^{20}$  protons-on-target (POT) using a  $\nu_\mu$ -dominated beam and  $3.36 \times 10^{20}$  POT using a  $\bar{\nu}_\mu$ -enhanced beam. Both sets were acquired

in the low energy NuMI beam configuration. MINOS also collected 37.88 kt years of atmosphere neutrino data.

The oscillation parameters are determined by applying a maximum likelihood fit to the data. The parameters  $\Delta m_{32}^2$ ,  $\sin^2\theta_{23}$ ,  $\sin^2\theta_{13}$ , and  $\delta_{CP}$  are varied in the fit with an external constraint on the mixing angle  $\sin\theta_{13} = 0.0242 \pm 0.0025$  calculated from a weighted average of the latest published results from the reactor experiments Daya Bay [12], RENO [10], and Double Chooz [11]. The constraints are included by adding a Gaussian prior penalty term to the likelihood during the fit. The solar parameters are kept at the fixed values of  $\Delta m_{21}^2 = 7.54 \times 10^{-5} \text{ eV}^2$  and  $\sin^2\theta_{12} = 0.037$  [52]. To test the impact of the solar parameters on the fit, they were varied within their uncertainties and the effect was negligible on the final results.

Figure 18 shows the 2D confidence limits on  $\Delta m_{32}^2$  and  $\sin^2\theta_{23}$  as well as the 1D profiled confidence limits on  $\Delta m_{32}^2$  and  $\sin^2\theta_{23}$  separately. One can see the sensitivity to the octant of  $\theta_{23}$  through the inclusion of the atmospheric neutrino sample. The 68% (90%) confidence limits (CL) on these parameters are calculated by taking the range of negative log-likelihood values with  $-2\ln L < 1.00$  (2.71) relative to the overall best fit. This yields  $|\Delta m_{32}^2| = [2.28 - 2.46] \times 10^{-3} \text{ eV}^2$  at 68% CL and  $\sin\theta_{23} = 0.35 - 0.65$  at 90% CL in the normal hierarchy; consider  $|\Delta m_{32}^2| = [2.32 - 2.53] \times 10^{-3} \text{ eV}^2$  at 68% CL and  $\sin\theta_{23} = 0.34 - 0.67$  at 90% CL in the inverted hierarchy. The data disfavour maximal mixing  $\theta_{23} = \pi/4$  by  $-2\ln L < 1.54$ . These results give the most precise measurement made on  $\Delta m_{32}^2$  to date.

Figure 19 shows the 1D CL of the profiled likelihood surface for value of  $\delta_{CP}$  for each of the four possible combinations (hierarchy and octant of  $\theta_{23}$ ). The data disfavour 36% (11%) of the parameter space defined by  $\delta_{CP}$ , the  $\theta_{23}$  octant, and the mass hierarchy at 68% (90%) CL.

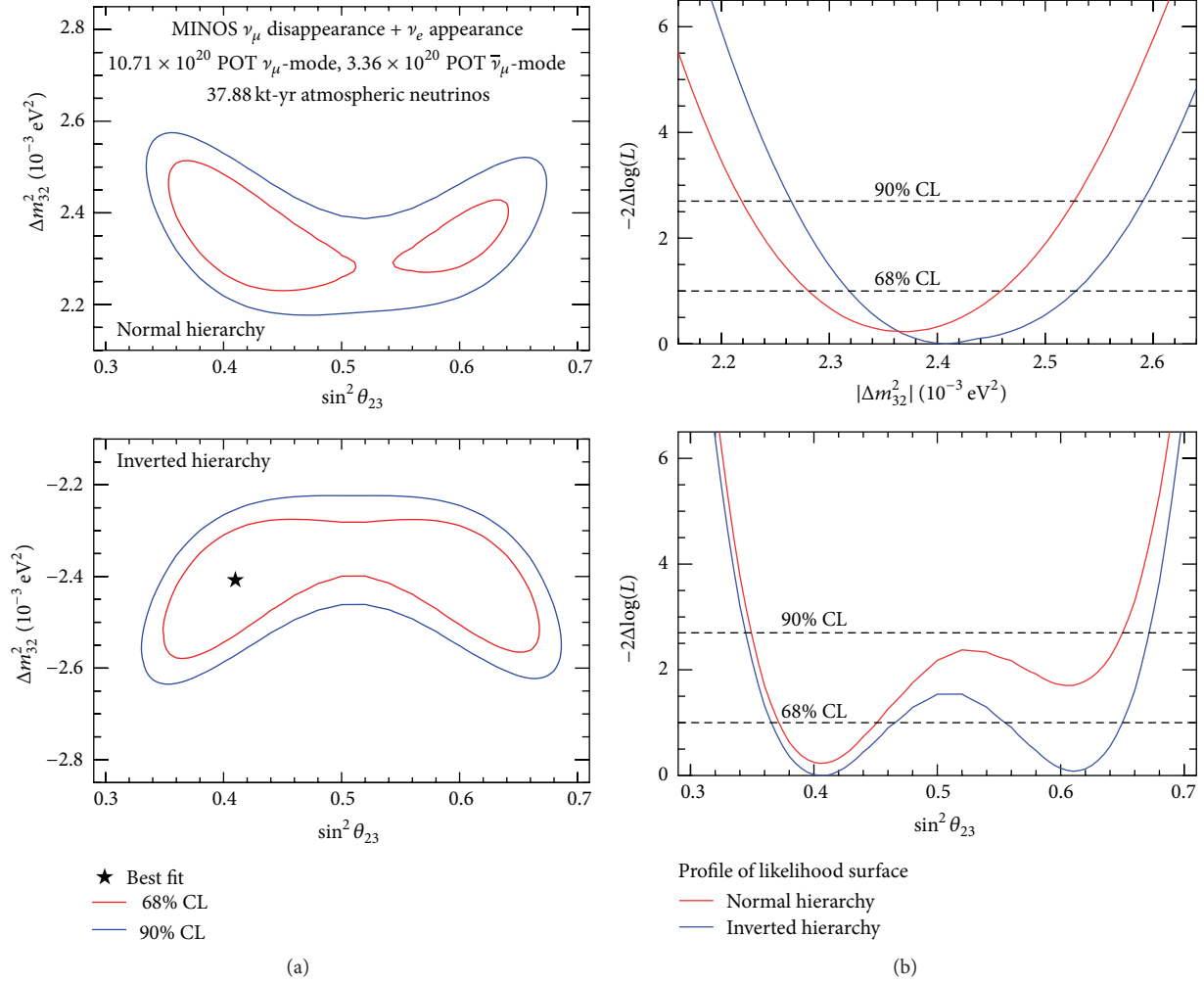


FIGURE 18: (a) show the 68% and 90% confidence limits on  $\Delta m_{32}^2$  and  $\sin^2 \theta_{23}$  for the normal hierarchy (top) and inverted hierarchy (bottom). At each point in this parameter space, the likelihood function is maximised with respect to  $\sin^2 \theta_{13}$ ,  $\delta_{\text{CP}}$ , and the systematic parameters constraints in the fit. The likelihood surface is calculated relative to the overall best fit, which is indicated by the star. (b) show the 1D likelihood profiles as a function of  $\Delta m_{32}^2$  and  $\sin^2 \theta_{23}$  for each hierarchy. The horizontal dotted lines indicate the 68% and 90% confidence limits.

## 7. NSI Interactions

Nonstandard interactions (NSI) [53–55] could occur between muon or tau neutrinos and matter and could alter the flavour composition of a neutrino beam as it propagates through the Earth's crust. Searches for NSI have already been performed with atmospheric neutrinos [56]. Using a two-flavour approach, one can write the probability for muon neutrino survival as

$$P(\nu_\mu \longrightarrow \nu_\mu) = 1 - \left[ 1 - \cos^2(2\theta) \frac{L_m^2}{L_0^2} \right] \sin^2\left(\frac{L}{L_m}\right), \quad (9)$$

where  $L$  is the neutrino path length and  $L_m$  is defined as the NSI matter oscillation length defined as

$$L_m \equiv \frac{L_0}{\left[ 1 \pm 2\sin(2\theta) L_0 \epsilon_{\mu\tau} |V| + (L_0 \epsilon_{\mu\tau} |V|^2) \right]^{1/2}}, \quad (10)$$

where  $L_0 \equiv 4E/\Delta m^2$ . The  $\pm$  signs in (10) arise from the matter potential,  $V$ , which is positive for neutrinos and negative for antineutrinos. The parameter  $\epsilon_{\mu\tau}$  is real-valued and carries its own sign. A positive value of  $\epsilon_{\mu\tau}$  implies that the neutrino disappearance probability is greater than the antineutrino disappearance probability, and vice versa.

The results presented here are based on an exposure of  $7.09 \times 10^{20}$  protons-on-target (POT) in neutrino mode, combined with a  $1.7 \times 10^{20}$  POT exposure in antineutrino mode. Due to the opposite sign of the matter potential in (10) for neutrinos and antineutrinos, NSI, if present, will alter the survival probability of neutrinos and antineutrinos in opposite directions. This analysis has identical event selection as for the  $\nu_\mu$  disappearance analysis, however, the fit takes into account perturbations from the standard three-flavour formalism brought about by NSI. The best fit parameters from this procedure are found to be  $\Delta m^2 = 2.39^{+0.14}_{-0.11} \times 10^{-3} \text{ eV}^2$ ,  $\sin^2 2\theta = 1.00^{+0.00}_{-0.06}$ , and  $\epsilon_{\mu\tau} = -0.07^{+0.08}_{-0.08}$  with

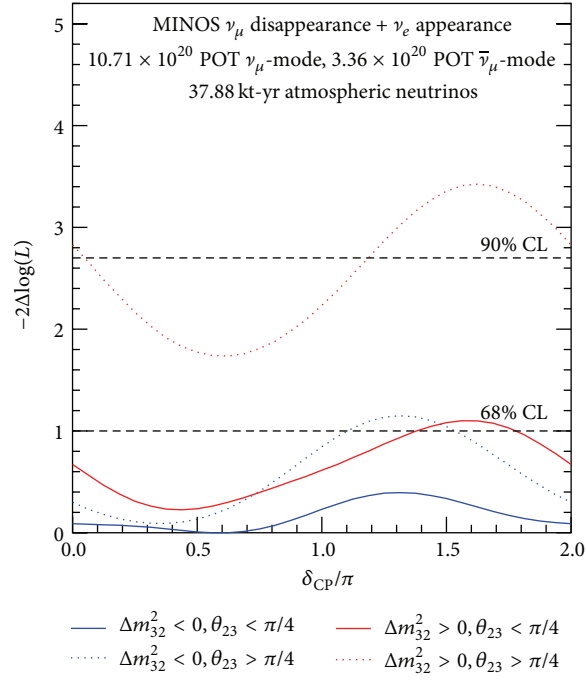


FIGURE 19: The 1D likelihood profile as a function of  $\delta_{\text{CP}}$  for each combination of mass hierarchy and  $\theta_{23}$  octant. For each value of  $\delta_{\text{CP}}$ , the likelihood was maximised with respect to  $\sin^2\theta_{13}$ ,  $\sin^2\theta_{23}$ , and  $\Delta m_{32}^2$ .

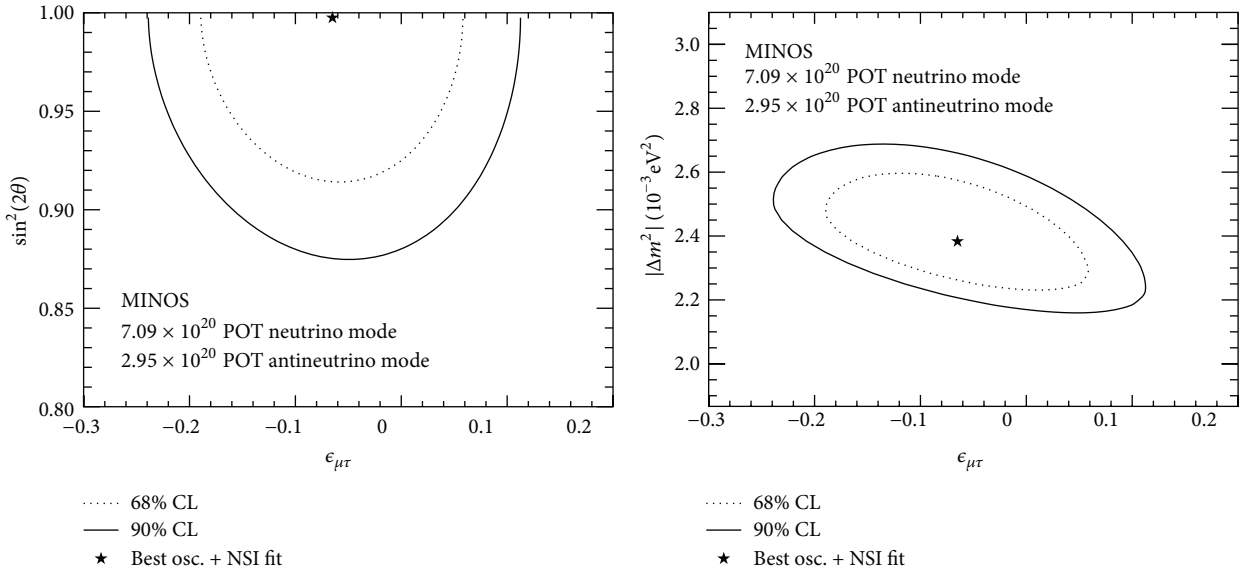


FIGURE 20: 2D contours for both 68% and 90%, showing the allowed regions of parameter space for  $\epsilon_{\nu\tau}$  from the fit to the data through muon disappearance.

the allowed region  $-0.20 < \epsilon_{\mu\tau} < 0.07$  (90% CL). The systematic uncertainties incorporated into the penalty terms when maximising the likelihood have a negligible effect on the fit. Figure 20 shows the allowed regions of the fit parameters; these are 2D CL contours, produced by profiling the likelihood with respect to the other parameters.

This is the first direct search for nonstandard interactions with high-purity samples of both neutrinos and antineutrinos conducting a simultaneous fit to neutrino and antineutrino

energy spectra of conventional  $\nu_{\mu} \rightarrow \nu_{\tau}$  oscillations with an additional NSI matter effect. This result is consistent with the null hypothesis of no NSI.

## 8. Sterile Neutrinos

There have been several anomalous results within the neutrino community that have questioned our understanding of neutrinos. The Liquid Scintillator Neutrino Detector (LSND)

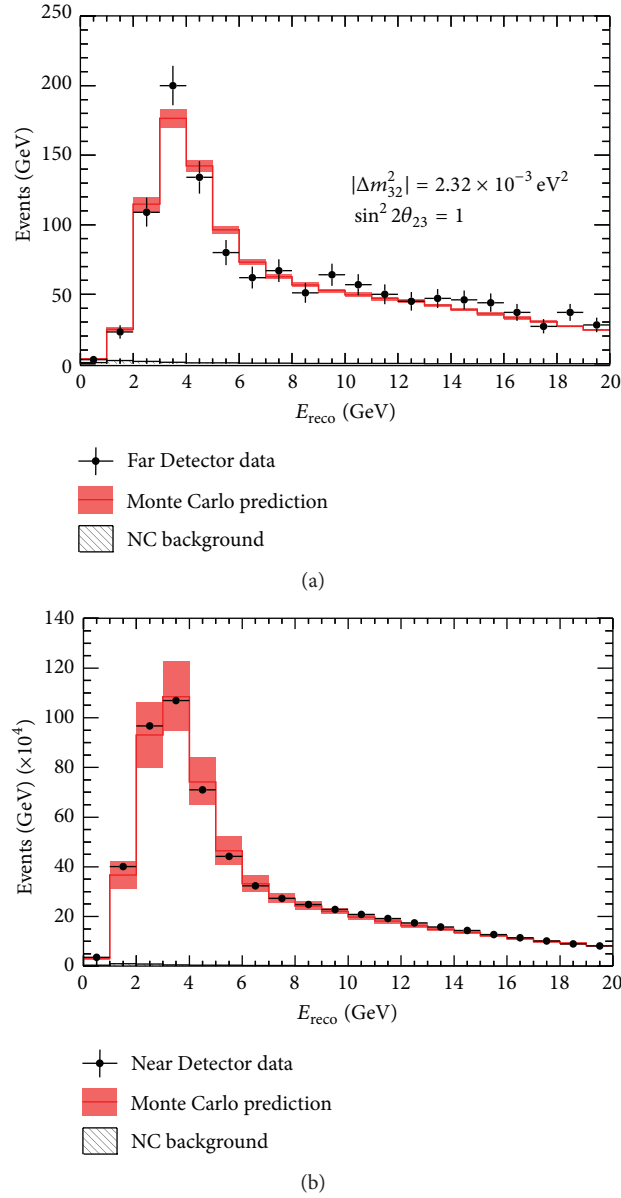


FIGURE 21: Showing the reconstructed energy spectrum for CC  $\nu_\mu$  interactions in the FD (a) and the ND (b). The grey hatched histogram is the NC background and the red line is the three-flavour prediction with systematic uncertainties included.

and MiniBooNE short-baseline experiments observed an excess in the data of electron antineutrinos that cannot be explained using the current three-flavour model [57–59]; a reinterpretation of reactor fluxes has also led to a discrepancy in neutrino-oscillation reactor experiments [60]. One explanation is the addition of one or more neutrino types which would oscillate with the three active neutrino flavours; a comprehensive overview of this explanation to account for the above discrepancies can be found in [61].

MINOS has sensitivity to sterile oscillation signatures by looking for perturbations from the three-flavour oscillation formalism in CC events and a deficit in NC events. This MINOS analysis [62] considers a 3 + 1 sterile neutrino model. By adding an additional neutrino, the PMNS is extended to a  $4 \times 4$  matrix which introduces three additional mixing

angles  $\theta_{24}$ ,  $\theta_{34}$ , and  $\theta_{14}$ . This extra mass state also introduces an extra mass splitting,  $\Delta m_{43}^2$ , where  $m_4 \gg m_3$  such that  $\Delta m_{43}^2 \sim \mathcal{O}(1 \text{ eV}^2)$ . An additional deficit of muon neutrinos at the FD aside from the expected loss due to three-flavour oscillations would be an indication of interference from these additional parameters.

Figures 21 and 22 show the NC and CC reconstructed neutrino energy spectrum for the FD and ND and are in good agreement with the expectation of a null sterile neutrino hypothesis. This agreement can be quantified by using the test statistic  $R$  for the number of NC events observed at the FD:

$$R = \frac{N_{\text{data}} - B_{\text{CC}}}{S_{\text{NC}}}, \quad (11)$$

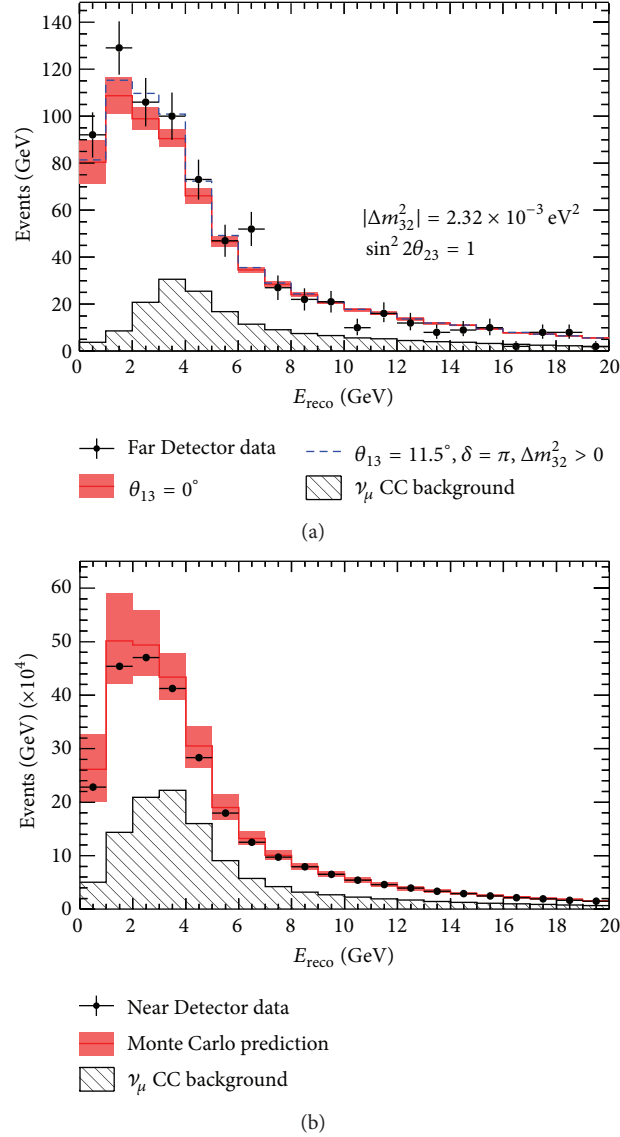


FIGURE 22: Showing the reconstructed energy spectrum for neutral current events at the FD (a) and the ND (b). The grey hatched histogram is the  $\nu_\mu$  CC background and the red line is the three-flavour prediction with systematic uncertainties included. The blue dashed line represents an additional three-flavour prediction with a different  $\theta_{13}$  with value  $11.5^\circ$ .

where  $N_{\text{data}}$  is the number of events observed,  $B_{\text{CC}}$  is the predicted number of CC background interactions, and  $S_{\text{NC}}$  is the predicted number of NC interactions in the detector. A value of  $R = 1$  would indicate no mixing in the data with sterile neutrinos. The test statistic  $R$  is simply based on the integrated number of events; over the full energy range, MINOS obtains  $R = 1.01 \pm 0.06$  (stat)  $\pm 0.05$  (syst) which is in good agreement with the null hypothesis [62].

MINOS is insensitive to the mixing angle  $\theta_{14}$  which is primarily involved in  $\nu_e$  appearance mixing; by looking at muon disappearance, MINOS has set 90% CLs limits on the other sterile mixing angles yielding  $\theta_{24} = (0.0^{+5}_{-0.0})^\circ$  and  $\theta_{34} = (0.0^{+25}_{-0.0})^\circ$  [62]. Figure 23 shows the contours for the mixing angles  $\theta_{23}$ ,  $\theta_{34}$ , and  $\theta_{24}$  at a particular value of  $\Delta m_{43}^2 = 0.5 \times 10^{-3} \text{ eV}^2$ .

MINOS sets a limit on the sterile-active neutrino coupling by constructing a quantity  $f_s$  and the fraction of  $\nu_\mu$  that have oscillated into  $\nu_s$ , expressed as

$$f_s = \frac{P_{\nu_\mu \rightarrow \nu_s}}{1 - P_{\nu_\mu \rightarrow \nu_\mu}}. \quad (12)$$

For neutrino events around the oscillation maximum with an energy of 1.4 GeV (the energy for the highest probability of muon neutrino disappearance) a large number of test values are randomly sampled from Gaussian distributions from the sterile 90% CLs quoted above and then selected for the mixing angles  $\theta_{24}$ ,  $\theta_{34}$ , and  $\theta_{23}$ . The value of  $f_s$  that is larger than 90% of the test cases is used as the limit, which yields  $f_s < 0.40$  at a 90% CL [62].

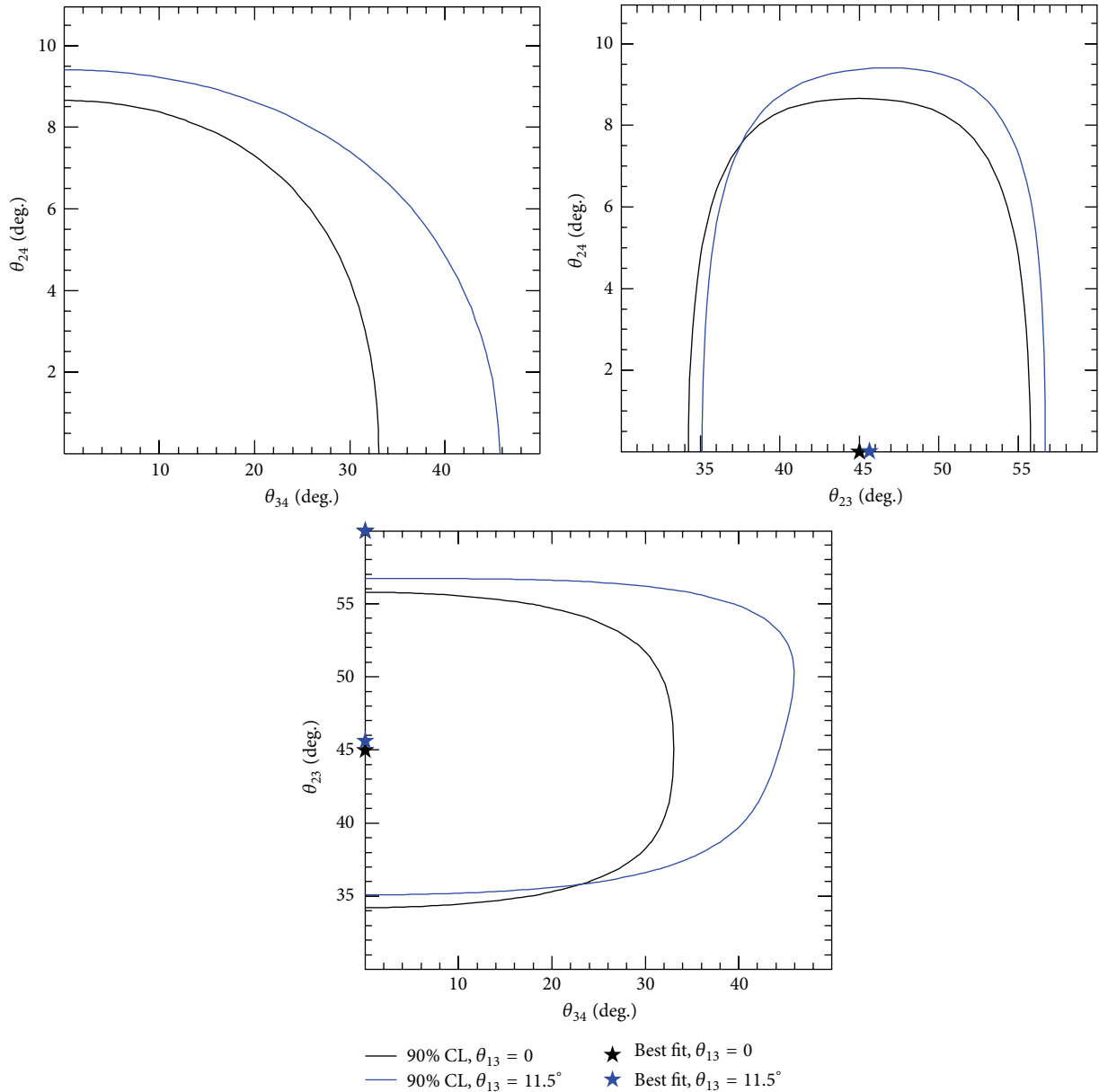


FIGURE 23: Showing the 90% CLs for the three mixing angles  $\theta_{23}$ ,  $\theta_{34}$ , and  $\theta_{24}$ . In the fit the sterile mass splitting was kept fixed at  $\Delta m_{43}^2 = 0.5 \times 10^{-3} \text{ eV}^2$ . The black and blue contours are for different fixed values of  $\theta_{13}$  of 0 and  $11.5^\circ$  respectively.

## 9. The Future with MINOS+

MINOS+ [17] is the continuation of the MINOS detectors taking data during the NuMI beam run in the medium energy configuration. Being on-axis, the neutrino flux at the detectors significantly increases at higher energies as shown in Figure 24. The beam peak in the medium configuration shifts from 3 GeV to 7 GeV allowing MINOS+ to observe around 4,000  $\nu_\mu$ -CC interactions in the FD each year. MINOS+ has been taking data since September 2013 and with the additional statistics will provide a useful contribution to the high-precision test of the three-flavour oscillation formalism and will improve on the world-leading measurements of muon neutrino disappearance made by MINOS.

With more statistics at high energies, MINOS+ is in the unique position to probe and significantly extend the reach of its searches for sterile neutrino signatures in the regions of parameter space favoured by LSND and MiniBooNE. Figure 25 shows a combination between the Bugey [28] reactor experiment combined with the sensitivity of data taken with MINOS+ assuming two years of MINOS+ running with a neutrino-dominated beam. A combination with an experiment sensitive to  $\theta_{14}$  (such as Bugey) is required with the MINOS+ data (sensitive primarily to  $\theta_{24}$ ) in order to set a limit in the LSND style parameter space. The combined 90% MINOS+-Bugey CL excludes a significant amount of the parameter space where sterile neutrinos in a 3+1 model could explain the anomalies seen in past experiments.

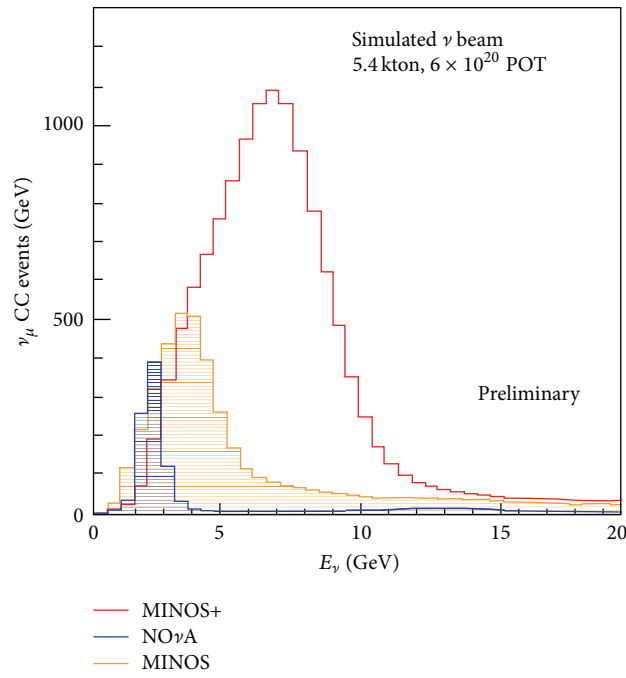


FIGURE 24: The  $\nu_{\mu}$  energy spectrum observed for the MINOS, MINOS+, and NO $\nu$ A experiments.

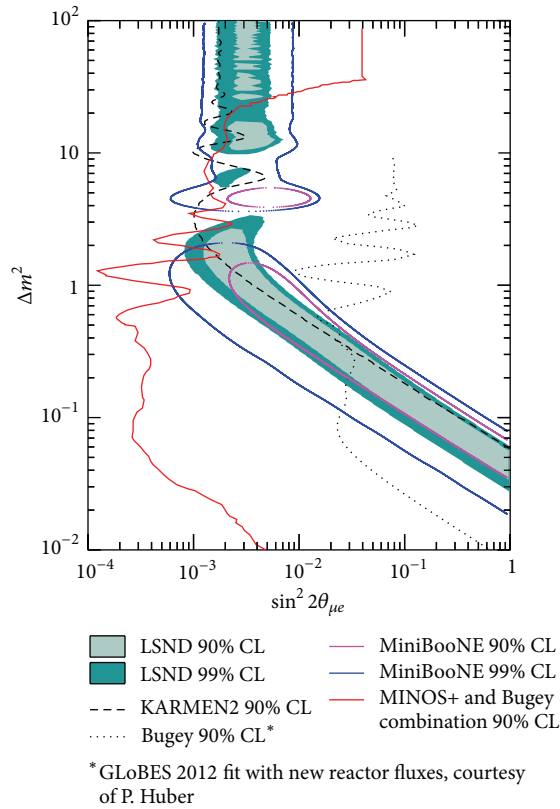


FIGURE 25: The sensitivity of MINOS+ to the existence of sterile neutrinos, when combined with data from the Bugey [28] reactor neutrino experiment. This figure assumes two years of MINOS+ running with a neutrino-dominated beam.

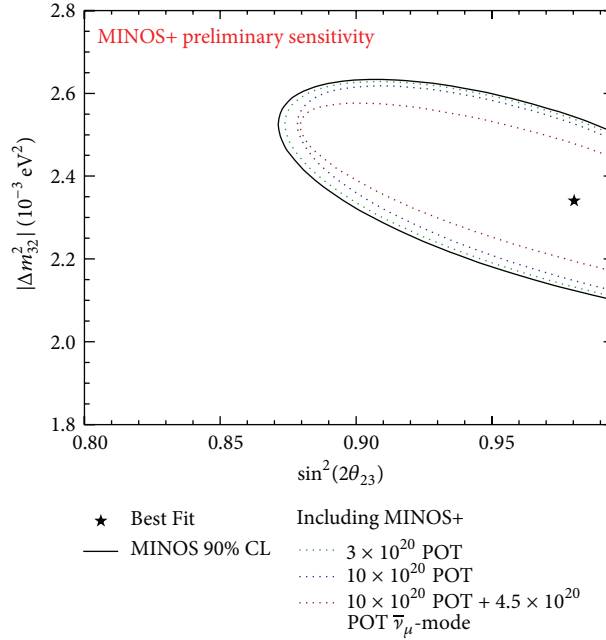


FIGURE 26: Showing the 90% CL contours, the MINOS+ experiment can achieve with three different projection running periods. The black contour is the current MINOS result, and the other ones are the MINOS+ sensitivity using simulation.

With the increased statistics and higher flux in neutrinos, MINOS+ can also probe nonstandard interaction neutrino physics. Figure 26 shows how various amounts of MINOS+ data will improve our ability to measure the standard neutrino oscillation parameters assuming NSI model.

## 10. Conclusion

The MINOS/MINOS+ experiment has been contributing to the neutrino oscillation community for over a decade. In this time, the most precise measurement of  $\Delta m_{32}^2$  has been made. Such a precise measurement is an example of how powerful and necessary a two-detector setup will be for future neutrino oscillation experiments to overcome the large systematics from flux and cross section uncertainties. With the ability to differentiate between neutrinos and antineutrinos, MINOS has measured oscillation parameters for both and showed that they lie in good agreement. Since the discovery of  $\theta_{13}$  to be nonzero, MINOS has been the first experiment to set constraints on the CP violating phase  $\delta_{CP}$  as well as incorporating both disappearance and appearance using a full three-flavour framework. MINOS+ will continue taking data and will improve the MINOS results as well as probing at higher energies to investigate the tension in the sterile neutrino debate.

## Disclosure

A. Timmons represents the MINOS Collaboration.

## Conflict of Interests

The author declares that there is no conflict of interests regarding the publication of this paper.

## Acknowledgments

The work of the MINOS and MINOS+ collaborations is supported by the US DoE, the UK STFC, the US NSF, the State and University of Minnesota, the University of Athens in Greece, and Brazil's FAPESP and CNPq. The author is grateful to the Minnesota Department of Natural Resources, the crew of the Soudan Underground Laboratory, and the personnel of Fermilab, for their vital contributions.

## References

- [1] Y. Fukuda, T. Hayakawa, E. Ichihara et al., "Evidence for oscillation of atmospheric neutrinos," *Physical Review Letters*, vol. 81, no. 8, pp. 1562–1567, 1998.
- [2] Q. R. Ahmad, R. C. Allen, T. C. Andersen et al., "Measurement of the rate of  $\nu_e + d \rightarrow p + p + e^-$  interactions produced by  $^8B$  solar neutrinos at the Sudbury neutrino observatory," *Physical Review Letters*, vol. 87, no. 7, Article ID 071301, 2001.
- [3] Q. R. Ahmad, R. C. Allen, T. C. Andersen et al., "Direct evidence for neutrino flavor transformation from neutral-current interactions in the sudbury neutrino observatory," *Physical Review Letters*, vol. 89, no. 1, Article ID 011301, 6 pages, 2002.
- [4] K. Eguchi, S. Enomoto, K. Furuno et al., "First results from KamLAND: evidence for reactor antineutrino disappearance," *Physical Review Letters*, vol. 90, no. 2, Article ID 021802, 6 pages, 2002.
- [5] R. Acquafredda, N. Agafonova, M. Ambrosio et al., "First events from the CNGS neutrino beam detected in the OPERA experiment," *New Journal of Physics*, vol. 8, p. 303, 2006.
- [6] K. Abe, N. Abgrall, H. Aihara et al., "The T2K experiment," *Nuclear Instruments and Methods in Physics Research Section A: Accelerators, Spectrometers, Detectors and Associated Equipment*, vol. 659, no. 1, pp. 106–135, 2011.

- [7] J. N. Abdurashitov, V. N. Gavrin, S. V. Girin et al., “Measurement of the solar neutrino capture rate with gallium metal,” *Physical Review C*, vol. 60, no. 5, Article ID 055801, 1999.
- [8] W. Hampel, J. Handt, G. Heusser et al., “GALLEX solar neutrino observations: results for GALLEX IV,” *Physics Letters B*, vol. 447, no. 1-2, pp. 127–133, 1999.
- [9] M. Apollonio, A. Baldini, C. Bemporad et al., “Initial results from the CHOOZ long baseline reactor neutrino oscillation experiment,” *Physics Letters B*, vol. 420, no. 3-4, pp. 397–404, 1998.
- [10] J. K. Ahn, S. Chebotaryov, J. H. Choi et al., “Observation of reactor electron antineutrinos disappearance in the RENO experiment,” *Physical Review Letters*, vol. 108, no. 19, Article ID 191802, 2012.
- [11] Y. Abe, C. Aberle, J. C. Anjos, J. C. Barriere, M. Bergevin, and A. Bernstein, “Reactor  $\bar{\nu}_e$  disappearance in the Double Chooz experiment,” *Physical Review D*, vol. 86, no. 5, Article ID 052008, 2012.
- [12] F. P. An, Q. An, J. Z. Bai et al., “Improved measurement of electron antineutrino disappearance at Daya Bay,” *Chinese Physics C*, vol. 37, no. 1, Article ID 011001, 2013.
- [13] C. Backhouse, *Measuring neutrino oscillation parameters using  $\nu_\mu$  disappearance in MINOS [DPhil thesis]*, University of Oxford, Oxford, UK, 2011.
- [14] D. S. Ayres, E. Ables, W. W. M. Alliso et al., “P-875: A Long-baseline Neutrino Oscillation Experiment at Fermilab,” MINOS Proposal, NuMI-L-63, February 1995.
- [15] M. H. Ahn, E. Aliu, S. Andringa et al., “Measurement of neutrino oscillation by the K2K experiment,” *Physical Review D*, vol. 74, no. 7, Article ID 072003, 2006.
- [16] D. S. Ayres, J. W. Dawson, G. Drake et al., “NOvA: Proposal to build a 30 kiloton off-axis detector to study  $\nu_\mu \rightarrow \nu_e$  oscillations in the NuMI beamline,” <http://arxiv.org/abs/hep-ex/0503053>.
- [17] G. Tzanakos, M. Bishai, M. Diwan, C. Escobar, R. A. Gomes, and P. Gouffon, “MINOS+: a proposal to FNAL to run MINOS with the medium energy NuMI beam,” Fermilab-Proposal 1016, 2011.
- [18] B. Pontecorvo, “Inverse beta processes and nonconservation of lepton charge,” *Soviet Physics—JETP*, vol. 7, pp. 172–173, 1958.
- [19] V. N. Gribov and B. Pontecorvo, “Neutrino astronomy and lepton charge,” *Physics Letters B*, vol. 28, no. 7, pp. 493–496, 1969.
- [20] Z. Maki, M. Nakagawa, and S. Sakata, “Remarks on the unified model of elementary particles,” *Progress of Theoretical Physics*, vol. 28, no. 5, pp. 870–880, 1962.
- [21] J. K. Ahn, S. Chebotaryov, J. H. Choi et al., “Observation of reactor electron antineutrinos disappearance in the RENO experiment,” *Physical Review Letters*, vol. 108, no. 19, Article ID 191802, 6 pages, 2012.
- [22] Y. Abe, C. Aberle, J. C. dos Anjos et al., “Reactor  $\bar{\nu}_e$  disappearance in the Double Chooz experiment,” *Physical Review D*, vol. 86, no. 5, Article ID 052008, 21 pages, 2012.
- [23] L. Wolfenstein, “Neutrino oscillations in matter,” *Physical Review D*, vol. 17, no. 9, pp. 2369–2374, 1978.
- [24] S. P. Mikheyev and A. Y. Smirnov, “Resonant amplification of  $\nu$  oscillations in matter and solar-neutrino spectroscopy,” *Il Nuovo Cimento C*, vol. 9, no. 1, pp. 17–26, 1986.
- [25] C. Giunti, C. W. Kim, and M. Monteno, “Atmospheric neutrino oscillations with three neutrinos and a mass hierarchy,” *Nuclear Physics B*, vol. 521, no. 1-2, pp. 3–36, 1998.
- [26] A. Cervera, A. Donini, M. B. Gavela et al., “Golden measurements at a neutrino factory,” *Nuclear Physics B*, vol. 579, no. 1-2, pp. 17–55, 2000.
- [27] K. Anderson, B. Bernstein, D. Boehnlein et al., “The NuMI facility technical design report,” Fermilab-Design 1998-01, 1998.
- [28] B. Achkar, R. Aleksan, M. Avenier et al., “Search for neutrino oscillations at 15, 40 and 95 meters from a nuclear power reactor at Bugey,” *Nuclear Physics B*, vol. 434, no. 3, pp. 503–532, 1995.
- [29] D. Michael, P. Adamson, T. Alexopoulos et al., “The magnetized steel and scintillator calorimeters of the MINOS experiment,” *Nuclear Instruments and Methods in Physics Research Section A: Accelerators, Spectrometers, Detectors and Associated Equipment*, vol. 596, no. 2, pp. 190–228, 2008.
- [30] J. A. Formaggio and G. P. Zeller, “From eV to EeV: neutrino cross sections across energy scales,” *Reviews of Modern Physics*, vol. 84, no. 3, article 1307, 2012.
- [31] P. Adamson, G. Cronea, L. Jenner et al., “The MINOS calibration detector,” *Nuclear Instruments and Methods in Physics Research A*, vol. 556, no. 1, pp. 119–133, 2006.
- [32] M. A. Kordosky, *Hadronic interactions in the MINOS detectors [Ph.D. thesis]*, University of Texas at Austin, Austin, Tex, USA, 2004, FERMILAB-THESIS-2004-34.
- [33] P. L. Vahle, *Electromagnetic interactions in the MINOS detectors [Ph.D. thesis]*, University of Texas at Austin, Austin, Tex, USA, 2004.
- [34] T. M. Cover and P. E. Hart, “Nearest neighbor pattern classification,” *IEEE Transactions on Information Theory*, vol. 13, no. 1, pp. 21–27, 1967.
- [35] R. Ospanov, *A measurement of muon neutrino disappearance with the MINOS detectors and the NuMI beam [Ph.D. thesis]*, University of Texas at Austin, 2008.
- [36] J. S. Marshall, *A study of muon neutrino disappearance with the MINOS detectors and the NuMI neutrino beam [Ph.D. thesis]*, University of Cambridge, 2008, ERMILAB-THESIS-2008-20.
- [37] J. P. Ochoa, *A search for muon neutrino to electron neutrino oscillations in the MINOS experiment [Ph.D. thesis]*, FERMILAB-THESIS-2009-44, 2009.
- [38] R. Toner, *Measuring  $\theta_{13}$  via muon neutrino to electron neutrino oscillations in the MINOS experiment [Ph.D. thesis]*, University of Cambridge, Cambridge, UK, 2011.
- [39] A. Schreckenberger, *Electron neutrino and antineutrino appearance in the MINOS detector [Ph.D. thesis]*, University of Minnesota, Minneapolis, Minn, USA, 2013.
- [40] P. Adamson, I. Anghel, C. Backhouse et al., “Electron neutrino and antineutrino appearance in the full MINOS data sample,” *Physical Review Letters*, vol. 110, no. 17, Article ID 171801, 2013.
- [41] A. Holin, *Electron neutrino appearance in the MINOS experiment [Ph.D. thesis]*, University College London, Fermilab-Thesis-2010-41, 2010.
- [42] G. Tinti, *Sterile neutrino oscillations in MINOS and hadron production in pC collisions [Ph.D. thesis]*, University of Oxford, Oxford, UK, 2010.
- [43] P. Adamson, C. Backhouse, G. Barr et al., “Measurements of atmospheric neutrinos and antineutrinos in the MINOS far detector,” *Physical Review D*, vol. 86, no. 5, Article ID 052007, 2012.
- [44] M. Crouch, “An improved world survey expression for cosmic ray vertical intensity vs. depth in standard rock,” in *Proceedings of the 20th International Cosmic Ray Conference*, vol. 6, pp. 165–168, USSR, Moscow, Russia, 1987.
- [45] D. DeMuth, G. J. Alner, D. Ayres et al., “Horizontal muons and a search for AGN neutrinos in Soudan 2,” *Astroparticle Physics*, vol. 20, no. 5, pp. 533–547, 2004.

- [46] J. J. Evans, *Measuring antineutrino oscillations with the MINOS experiment [Ph.D. thesis]*, University of Oxford, 2008, FERMILAB-THESIS-2009-14, 2008.
- [47] S. J. Coleman, *A measurement of neutrino oscillations with muon neutrinos in the MINOS experiment [Ph.D. thesis]*, College of William & Mary, Williamsburg, Va, USA, 2011.
- [48] S. Dytman, H. Gallagher, and M. Kordosky, “Hadronic shower energy scale uncertainty in the MINOS experiment,” <http://arxiv.org/abs/0806.2119>.
- [49] P. Adamson, I. Anghel, C. Backhouse et al., “Measurement of neutrino and antineutrino oscillations using beam and atmospheric data in MINOS,” *Physical Review Letters*, vol. 110, no. 25, Article ID 251801, 2013.
- [50] A. M. Dziewonski and D. L. Anderson, “Preliminary reference Earth model,” *Physics of the Earth and Planetary Interiors*, vol. 25, no. 4, pp. 297–356, 1981.
- [51] J. A. B. Coelho, *Investigacao de mecanismos alternativos a oscilacao de neutrinos no experimentos MINOS [Ph.D. thesis]*, Universidade Estadual de Campinas, São Paulo, Brazil, 2012.
- [52] G. L. Fogli, E. Lisi, A. Marrone, D. Montanino, A. Palazzo, and A. M. Rotunno, “Global analysis of neutrino masses, mixings, and phases: Entering the era of leptonic  $CP$  violation searches,” *Physical Review D*, vol. 86, no. 1, Article ID 013012, 2012.
- [53] J. W. F. Valle, “Resonant oscillations of massless neutrinos in matter,” *Physics Letters B*, vol. 199, no. 3, pp. 432–436, 1987.
- [54] M. C. Gonzalez-Garcia, M. M. Guzzo, P. I. Krastev et al., “Atmospheric neutrino observations and flavor changing interactions,” *Physical Review Letters*, vol. 82, no. 16, pp. 3202–3205, 1999.
- [55] A. Friedland, C. Lunardini, and M. Maltoni, “Atmospheric neutrinos as probes of neutrino-matter interactions,” *Physical Review D*, vol. 70, Article ID 111301, 2004.
- [56] G. Mitsuka, K. Abe, Y. Hayato et al., “Study of nonstandard neutrino interactions with atmospheric neutrino data in Super-Kamiokande I and II,” *Physical Review D*, vol. 84, no. 11, Article ID 113008, 15 pages, 2011.
- [57] A. Aguilar, L. B. Auerbach, R. L. Burman et al., “Evidence for neutrino oscillations from the observation of  $\bar{\nu}_e$  appearance in a  $\bar{\nu}_\mu$  beam,” *Physical Review D*, vol. 64, no. 11, Article ID 112007, 2001.
- [58] A. A. Aguilar-Arevalo, C. E. Anderson, S. J. Brice et al., “Search for electron antineutrino appearance at the  $\Delta m^2 \sim 1\text{eV}^2$  scale,” *Physical Review Letters*, vol. 103, no. 11, Article ID 111801, 2009.
- [59] A. A. Aguilar-Arevalo, B. C. Brown, L. Bugel et al., “Improved search for  $\bar{\nu}_\mu \rightarrow \bar{\nu}_e$  oscillations in the MiniBooNE experiment,” *Physical Review Letters*, vol. 110, no. 16, Article ID 161801, 2013.
- [60] G. Mention, M. Fechner, T. Lasserre et al., “Reactor antineutrino anomaly,” *Physical Review D*, vol. 83, no. 7, Article ID 073006, 2011.
- [61] K. N. Abazajian, M. A. Acero, S. K. Agarwalla et al., “Light sterile neutrinos: a white paper,” <http://arxiv.org/abs/1204.5379>.
- [62] P. Adamson, D. J. Auty, D. S. Ayres et al., “Active to sterile neutrino mixing limits from neutral-current interactions in MINOS,” *Physical Review Letters*, vol. 107, no. 1, Article ID 011802, 2011.

## Review Article

# Current Status and Future Prospects of the SNO+ Experiment

S. Andringa,<sup>1</sup> E. Arushanova,<sup>2</sup> S. Asahi,<sup>3</sup> M. Askins,<sup>4</sup> D. J. Auty,<sup>5</sup> A. R. Back,<sup>2,6</sup> Z. Barnard,<sup>7</sup> N. Barros,<sup>1,8</sup> E. W. Beier,<sup>8</sup> A. Bialek,<sup>5</sup> S. D. Biller,<sup>9</sup> E. Blucher,<sup>10</sup> R. Bonventre,<sup>8</sup> D. Braid,<sup>7</sup> E. Caden,<sup>7</sup> E. Callaghan,<sup>8</sup> J. Caravaca,<sup>11,12</sup> J. Carvalho,<sup>13</sup> L. Cavalli,<sup>9</sup> D. Chauhan,<sup>1,3,7</sup> M. Chen,<sup>3</sup> O. Chkvorets,<sup>7</sup> K. Clark,<sup>3,6,9</sup> B. Cleveland,<sup>7,14</sup> I. T. Coulter,<sup>8,9</sup> D. Cressy,<sup>7</sup> X. Dai,<sup>3</sup> C. Darrach,<sup>7</sup> B. Davis-Purcell,<sup>15</sup> R. Deen,<sup>8,9</sup> M. M. Depatie,<sup>7</sup> F. Descamps,<sup>11,12</sup> F. Di Lodovico,<sup>2</sup> N. Duhaime,<sup>7</sup> F. Duncan,<sup>7,14</sup> J. Dunger,<sup>9</sup> E. Falk,<sup>6</sup> N. Fatemighomi,<sup>3</sup> R. Ford,<sup>7,14</sup> P. Gorel,<sup>5</sup> C. Grant,<sup>4</sup> S. Grullon,<sup>8</sup> E. Guillian,<sup>3</sup> A. L. Hallin,<sup>5</sup> D. Hallman,<sup>7</sup> S. Hans,<sup>16</sup> J. Hartnell,<sup>6</sup> P. Harvey,<sup>3</sup> M. Hedayatipour,<sup>5</sup> W. J. Heintzelman,<sup>8</sup> R. L. Helmer,<sup>15</sup> B. Hreljac,<sup>7</sup> J. Hu,<sup>5</sup> T. Iida,<sup>3</sup> C. M. Jackson,<sup>11,12</sup> N. A. Jelley,<sup>9</sup> C. Jillings,<sup>7,14</sup> C. Jones,<sup>9</sup> P. G. Jones,<sup>2,9</sup> K. Kamdin,<sup>11,12</sup> T. Kaptanoglu,<sup>8</sup> J. Kaspar,<sup>17</sup> P. Keener,<sup>8</sup> P. Khaghani,<sup>7</sup> L. Kippenbrock,<sup>17</sup> J. R. Klein,<sup>8</sup> R. Knapik,<sup>8,18</sup> J. N. Kofron,<sup>17</sup> L. L. Kormos,<sup>19</sup> S. Korte,<sup>7</sup> C. Kraus,<sup>7</sup> C. B. Krauss,<sup>5</sup> K. Labe,<sup>10</sup> I. Lam,<sup>3</sup> C. Lan,<sup>3</sup> B. J. Land,<sup>11,12</sup> S. Langrock,<sup>2</sup> A. LaTorre,<sup>10</sup> I. Lawson,<sup>7,14</sup> G. M. Lefevre,<sup>6</sup> E. J. Leming,<sup>6</sup> J. Lidgard,<sup>9</sup> X. Liu,<sup>3</sup> Y. Liu,<sup>3</sup> V. Lozza,<sup>20</sup> S. Maguire,<sup>16</sup> A. Maio,<sup>1,21</sup> K. Majumdar,<sup>9</sup> S. Manecki,<sup>3</sup> J. Maneira,<sup>1,21</sup> E. Marzec,<sup>8</sup> A. Mastbaum,<sup>8</sup> N. McCauley,<sup>22</sup> A. B. McDonald,<sup>3</sup> J. E. McMillan,<sup>23</sup> P. Mekarski,<sup>5</sup> C. Miller,<sup>3</sup> Y. Mohan,<sup>8</sup> E. Mony,<sup>3</sup> M. J. Mottram,<sup>2,6</sup> V. Novikov,<sup>3</sup> H. M. O'Keeffe,<sup>3,19</sup> E. O'Sullivan,<sup>3</sup> G. D. Orebi Gann,<sup>8,11,12</sup> M. J. Parnell,<sup>19</sup> S. J. M. Peeters,<sup>6</sup> T. Pershing,<sup>4</sup> Z. Petriw,<sup>5</sup> G. Prior,<sup>1</sup> J. C. Prouty,<sup>11,12</sup> S. Quirk,<sup>3</sup> A. Reichold,<sup>9</sup> A. Robertson,<sup>22</sup> J. Rose,<sup>22</sup> R. Rosero,<sup>16</sup> P. M. Rost,<sup>7</sup> J. Rumleskie,<sup>7</sup> M. A. Schumaker,<sup>7</sup> M. H. Schwendener,<sup>7</sup> D. Scislawski,<sup>17</sup> J. Secret,<sup>24</sup> M. Seddighin,<sup>3</sup> L. Segui,<sup>9</sup> S. Seibert,<sup>8</sup> T. Shantz,<sup>7</sup> T. M. Shokair,<sup>8</sup> L. Sibley,<sup>5</sup> J. R. Sinclair,<sup>6</sup> K. Singh,<sup>5</sup> P. Skensved,<sup>3</sup> A. Sörensen,<sup>20</sup> T. Sonley,<sup>3</sup> R. Stainforth,<sup>22</sup> M. Strait,<sup>10</sup> M. I. Stringer,<sup>6</sup> R. Svoboda,<sup>4</sup> J. Tatar,<sup>17</sup> L. Tian,<sup>3</sup> N. Tolich,<sup>17</sup> J. Tseng,<sup>9</sup> H. W. C. Tseung,<sup>17</sup> R. Van Berg,<sup>8</sup> E. Vázquez-Jáuregui,<sup>14,25</sup> C. Virtue,<sup>7</sup> B. von Krosigk,<sup>20</sup> J. M. G. Walker,<sup>22</sup> M. Walker,<sup>3</sup> O. Wasalski,<sup>15</sup> J. Waterfield,<sup>6</sup> R. F. White,<sup>6</sup> J. R. Wilson,<sup>2</sup> T. J. Winchester,<sup>17</sup> A. Wright,<sup>3</sup> M. Yeh,<sup>16</sup> T. Zhao,<sup>3</sup> and K. Zuber<sup>20</sup>

<sup>1</sup> Laboratório de Instrumentação e Física Experimental de Partículas (LIP), Avenida Elias Garcia 14, 1°, 1000-149 Lisboa, Portugal

<sup>2</sup> School of Physics and Astronomy, Queen Mary University of London, 327 Mile End Road, London E1 4NS, UK

<sup>3</sup> Department of Physics, Engineering Physics & Astronomy, Queen's University, Kingston, ON, Canada K7L 3N6

<sup>4</sup> University of California, 1 Shields Avenue, Davis, CA 95616, USA

<sup>5</sup> Department of Physics, University of Alberta, 4-181 CCIS, Edmonton, AB, Canada T6G 2E1

<sup>6</sup> Physics & Astronomy, University of Sussex, Pevensey II, Falmer, Brighton BN1 9QH, UK

<sup>7</sup> Laurentian University, 935 Ramsey Lake Road, Sudbury, ON, Canada P3E 2C6

<sup>8</sup> Department of Physics & Astronomy, University of Pennsylvania, 209 South 33rd Street, Philadelphia, PA 19104-6396, USA

<sup>9</sup> University of Oxford, The Denys Wilkinson Building, Keble Road, Oxford OX1 3RH, UK

<sup>10</sup> The Enrico Fermi Institute and Department of Physics, The University of Chicago, Chicago, IL 60637, USA

<sup>11</sup> Department of Physics, University of California, Berkeley, CA 94720, USA

<sup>12</sup> Lawrence Berkeley National Laboratory, Nuclear Science Division, 1 Cyclotron Road, Berkeley, CA 94720-8153, USA

<sup>13</sup> Laboratório de Instrumentação e Física Experimental de Partículas and Departamento de Física, Universidade de Coimbra, 3004-516 Coimbra, Portugal

<sup>14</sup> SNOLAB, Creighton Mine No. 9, 1039 Regional Road 24, Sudbury, ON, Canada P3Y 1N2

<sup>15</sup> TRIUMF, 4004 Wesbrook Mall, Vancouver, BC, Canada V6T 2A3

<sup>16</sup> Brookhaven National Laboratory, Chemistry Department, Building 555, P.O. Box 5000, Upton, NY 11973-500, USA

<sup>17</sup> Center for Experimental Nuclear Physics and Astrophysics and Department of Physics, University of Washington, Seattle, WA 98195, USA

<sup>18</sup> Norwich University, 158 Harmon Drive, Northfield, VT 05663, USA

<sup>19</sup> Physics Department, Lancaster University, Lancaster LA1 4YB, UK

<sup>20</sup> Institut für Kern- und Teilchenphysik, Technische Universität Dresden, Zellescher Weg 19, 01069 Dresden, Germany

<sup>21</sup> Departamento de Física, Faculdade de Ciências, Universidade de Lisboa, Campo Grande, Edifício C8, 1749-016 Lisboa, Portugal

<sup>22</sup> Department of Physics, University of Liverpool, Liverpool L69 3BX, UK

<sup>23</sup> Department of Physics and Astronomy, University of Sheffield, Hicks Building, Hounsfield Road, Sheffield S3 7RH, UK

<sup>24</sup> Department of Chemistry & Physics, Armstrong Atlantic State University, 11935 Abercorn Street, Savannah, GA 31419, USA

<sup>25</sup> Instituto de Física, Universidad Nacional Autónoma de México (UNAM), Apartado Postal 20-364, 01000 México, DF, Mexico

Correspondence should be addressed to V. Lozza; valentina.lozza@tu-dresden.de

Received 22 July 2015; Accepted 22 November 2015

Academic Editor: Vincenzo Flaminio

Copyright © 2016 S. Andringa et al. This is an open access article distributed under the Creative Commons Attribution License, which permits unrestricted use, distribution, and reproduction in any medium, provided the original work is properly cited. The publication of this article was funded by SCOAP<sup>3</sup>.

SNO+ is a large liquid scintillator-based experiment located 2 km underground at SNOLAB, Sudbury, Canada. It reuses the Sudbury Neutrino Observatory detector, consisting of a 12 m diameter acrylic vessel which will be filled with about 780 tonnes of ultra-pure liquid scintillator. Designed as a multipurpose neutrino experiment, the primary goal of SNO+ is a search for the neutrinoless double-beta decay ( $0\nu\beta\beta$ ) of  $^{130}\text{Te}$ . In Phase I, the detector will be loaded with 0.3% natural tellurium, corresponding to nearly 800 kg of  $^{130}\text{Te}$ , with an expected effective Majorana neutrino mass sensitivity in the region of 55–133 meV, just above the inverted mass hierarchy. Recently, the possibility of deploying up to ten times more natural tellurium has been investigated, which would enable SNO+ to achieve sensitivity deep into the parameter space for the inverted neutrino mass hierarchy in the future. Additionally, SNO+ aims to measure reactor antineutrino oscillations, low energy solar neutrinos, and geoneutrinos, to be sensitive to supernova neutrinos, and to search for exotic physics. A first phase with the detector filled with water will begin soon, with the scintillator phase expected to start after a few months of water data taking. The  $0\nu\beta\beta$  Phase I is foreseen for 2017.

## 1. Introduction

SNO+ is a large-scale liquid scintillator experiment located at a depth of  $5890 \pm 94$  meter water equivalent (m.w.e.) in Vale's Creighton mine in Sudbury, Canada. The deep underground location, the high purity of materials used, and the large volume make SNO+ an ideally suited detector to study several aspects of neutrino physics.

The main goal of SNO+ is a search for the neutrinoless double-beta decay ( $0\nu\beta\beta$ ) of  $^{130}\text{Te}$ .  $0\nu\beta\beta$ -decay is a rare nuclear process that will happen if neutrinos are Majorana-type particles; that is, they are their own antiparticles. Understanding the Majorana nature of neutrinos is one of the most active areas of research in modern neutrino physics. The observation of the  $0\nu\beta\beta$ -decay would demonstrate lepton number violation, a key ingredient in the theory of leptogenesis. The process can be seen as two simultaneous  $\beta$ -decays, in which two neutrons are converted into two protons and two electrons, as the neutrinos from the two weak vertices mutually annihilate. The signature is a peak at the Q-value of the process in the summed energy spectrum of the two electrons. The measured quantity is the half-life of the decay. The effective Majorana neutrino mass,  $m_{\beta\beta}$ , which is highly dependent on the nuclear matrix elements, is derived from the half-life as described in [1]. A half-life of the order of  $10^{25}$

years corresponds to a neutrino mass range of about 200–400 meV. The large mass and low background of SNO+ allow the investigation of such a rare event.

The large volume and the high radio-purity are also the reason why SNO+ can explore several other physics topics. Observation of geoneutrinos will help in understanding the mechanisms for heat production in the Earth. Reactor antineutrino measurements constrain the neutrino oscillation parameters. Neutrinos and antineutrinos coming from supernova explosions would help to answer many unresolved questions in neutrino astronomy. Additionally, SNO+ has the potential to search for exotic physics like axion-like particles and invisible nucleon decay.

The depth of SNOLAB also provides the opportunity to measure low energy solar neutrinos, like pep and CNO neutrinos. The pep neutrinos are monoenergetic, with an energy of 1.44 MeV and a very well predicted flux, with an uncertainty of 1.2%, constrained by the solar luminosity [2]. A precise measurement of the flux can probe the Mikheyev, Smirnov, and Wolfenstein (MSW) effect of neutrino mixing as well as alternate models like Non Standard Interactions [3]. Another open question in the solar neutrino field is related to the solar metallicity. The Standard Solar Model was always in excellent agreement with helioseismology until recent analyses suggested a metallicity about 30% lower than the

previous model. This raised the question of the homogeneous distribution of elements heavier than helium in the Sun. The measurement of the CNO neutrino flux could be used to solve the problem [4].

This paper is structured as follows. In Sections 2 and 3 the SNO+ experiment is described, including the current status and detector upgrades. The expected background sources are presented in Section 4. In Sections 5 to 9 the broad physics program of SNO+ is described: the neutrinoless double-beta decay search (Section 5), the measurement of low energy solar neutrinos (Section 6), the measurements of geo and reactor antineutrinos (Section 7), the supernova neutrino watch (Section 8), and the exotic physics searches (Section 9). A brief conclusion follows at the end.

## 2. The SNO+ Experiment

The SNO+ experiment [5] is located in the underground laboratory of SNOLAB, Sudbury, Canada. A flat overburden of 2092 m of rock provides an efficient shield against cosmic muons corresponding to  $5890 \pm 94$  m.w.e. [6]. The resulting muon rate through a 8.3 m radius circular area is 63 muons per day. SNO+ will make use of the SNO detector structure [7, 8] consisting of a spherical acrylic vessel (AV) of 6 m radius and 5.5 cm thickness located within a cavity excavated in the rock. The vessel will be filled with about 780 tonnes of liquid scintillator and will be viewed by  $\sim 9300$  PMTs supported by a geodesic stainless steel structure (PSUP) of approximately 8.9 m radius. The volume between the AV and the PSUP, as well as the rest of the cavity, will be filled with about 7000 tonnes of ultra-pure water, which acts as a shield for the radioactivity coming from the rock (cavity walls) and the PMT array. A system of hold-up ropes suspends the acrylic vessel inside the PSUP. Additionally, in order to balance the buoyant force due to the lower density of the liquid scintillator compared to the external water, a new system of hold-down ropes has been installed on the top part of the AV and anchored at the cavity floor. A sketch of the detector is shown in Figure 1.

The major detector upgrades, including the liquid scintillator process systems, are described here.

**2.1. Liquid Scintillator.** The SNO+ liquid scintillator (LS) is composed of an aromatic hydrocarbon, linear alkylbenzene (LAB), as a solvent, and a concentration of 2 g/L 2,5-diphenyloxazole (PPO) as a fluor. LAB was selected as the liquid scintillator for SNO+ because of (1) its long time stability, (2) compatibility with the acrylic, (3) high purity levels directly from the manufacturer, (4) long attenuation and scattering length, (5) high light yield, and (6) linear response in energy. Additionally, it has a high flash point and is environmentally safe. LAB will be produced very close to the detector location (at the Cepsa plant in Becancour, Quebec, less than 900 km away), allowing short transport times which are important to reduce the possibility of cosmogenic activation.

**2.2. Te-Loading.** One of the main advantages of using LAB as liquid scintillator is the possibility of dissolving heavy

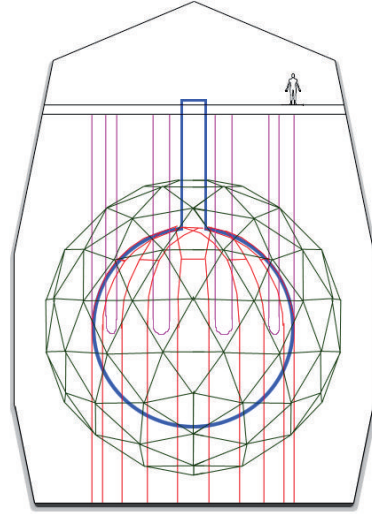


FIGURE 1: The SNO+ detector, figure from [9]. The 12 m diameter acrylic vessel (blue) is viewed by  $\sim 9300$  PMTs supported by a  $\sim 18$  m diameter geodesic structure (green) and is held by a system of high purity ropes (purple). The AV and the PSUP are within a volume of highly purified water. A rope net (red) will be used to offset the buoyancy of the liquid scintillator contained within the AV.

metals with long term stability and good optical properties. For the  $0\nu\beta\beta$ -decay phase of the experiment, SNO+ will load tellurium into the liquid scintillator. An innovative technique has been developed to load tellurium at concentration levels of several percent into LAB maintaining good optical properties and reasonably high light emission levels [10]. Telluric acid,  $\text{Te}(\text{OH})_6$ , is first dissolved in water and then, adding a surfactant, loaded into the scintillator. To better match the PMT quantum efficiency a secondary wavelength shifter will also be added to the mixture. Currently, we are investigating two different secondary wavelength shifters: perylene and bis-MSB. The former shifts the emission peak's range from 350–380 nm to  $\sim 450$ –480 nm with a predicted light yield in SNO+ of about 300 Nhits (detected photoelectron hits) per MeV of energy. The latter shifts the emission peak to  $\sim 390$ –430 nm with a light yield of 200 Nhits/MeV. The final choice will depend on the timing optical properties, the light yield, and the scattering length of the full scintillator mixture.

**2.3. Emission Timing Profiles and Optical Properties.** The emission timing profile and the optical properties of the LAB-PPO and the Te-loaded scintillator have been thoroughly investigated. The timing profile of scintillation pulses depends on the ionization density of the charged particles, with signals caused by electrons being faster than those from protons or alpha particles. This property allows the discrimination among particle types, which is very important for background rejection. The timing profile of electron and alpha particles in the unloaded scintillator has been measured in [11]. Results show that, for a LAB-PPO sample, a peak-to-total ratio analysis allows us to reject  $>99.9\%$  of the alpha particles while retaining  $>99.9\%$  of the electron signal.

The measurement of the timing profiles in the 0.3% Te-loaded scintillator is described in [12]. The presence of water and the surfactant in the cocktail reduces the long tail of the alpha decay (slow component) with respect to the unloaded scintillator, resulting in a poorer discrimination between  $\alpha$ -like and  $\beta$ -like signals. The light yield of the unloaded LAB-PPO scintillator has been measured in bench top tests and extrapolated for the full SNO+ volume using Monte Carlo (MC) simulations, leading to 520 Nhits/MeV.

The energy response to the electron energy deposition, the index of refraction, and the absorption length of the LAB-PPO liquid scintillator are investigated in [13, 14]. The energy response is linear in the region from 0.4 MeV to 3.0 MeV, while below 0.4 MeV the linearity is lost due to reemission effects and the loss of Cherenkov light (threshold of  $\sim 0.2$  MeV).

Finally, the quenching of proton and alpha particles for the unloaded scintillator and the Te-loaded cocktail has been measured in [15, 16]. The nonlinear energy-dependent proton/alpha light output is typically parametrized by Birks' parameter  $k_B$  [17]. Its measurement is extremely important for the development of background rejection techniques as described in Section 4. For protons in the unloaded SNO+ scintillator, the value measured in [15] is  $k_B = 0.0098 \pm 0.0003 \text{ cm}\cdot\text{MeV}^{-1}$ . The measured value for alpha particles is  $k_B = 0.0076 \pm 0.0003 \text{ cm}\cdot\text{MeV}^{-1}$ , corresponding, approximately, to a quenching factor of 10 for energies between 5 MeV and 9 MeV.

**2.4. Process Plant.** The scintillator purification plant of SNO+ is fully described in [18, 19]. It will use the same techniques and has the same cleanliness requirements as the Borexino experiment, by which we expect to reach a purity level of about  $10^{-17} \text{ g/g}_{\text{LAB}}$  for both the  $^{238}\text{U}$  and  $^{232}\text{Th}$  chain [20], corresponding to 9 counts per day (cpd) for the  $^{238}\text{U}$  chain and 3 cpd for the  $^{232}\text{Th}$  chain. Similar background levels have also been achieved by the KamLAND experiment [21]. A multistage distillation (to remove heavy metals and optical impurities) and a high temperature flash vacuum distillation are initially used to separately purify LAB and PPO. Then the PPO is combined with the LAB, and the scintillator is further purified by a  $\text{N}_2$ /steam gas stripping process to remove gases, such as Rn, Ar, Kr,  $\text{O}_2$ , and residual water.

After the detector fill, the entire scintillator volume can be recirculated in about 4 days to enable quasi-batch re-purification and *ex situ* radio-assaying. A rotating-stage liquid-liquid extraction column (water-LAB) and metal scavengers are used to effectively remove metals (K, Pb, Bi, Th, and Ra). Finally, microfiltration is used for removal of suspended fine particles.

During the neutrinoless double-beta decay phase, the tellurium, the water, and the surfactant will be purified prior to addition to the LAB-PPO scintillator. The purification technique for tellurium is described in [22]. It has been designed to remove both the U- and Th-chain impurities and the isotopes produced by cosmogenic neutron and proton spallation reactions while handling and storing tellurium on surface. It consists of a double-pass acid-recrystallization

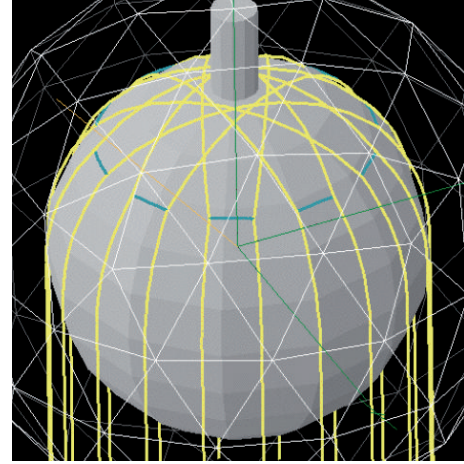


FIGURE 2: Sketch of the hold-down rope system on the top of the acrylic vessel to compensate for the buoyant force that the scintillator produces on the AV.

on the Earth's surface, for which the overall purification factor reached in U/Th and cosmogenic-induced isotopes is  $>10^4$ . Since the tellurium purification is expected to happen at the above ground facilities and some isotopes can be cosmogenically replenished even with short time exposures, a second purification stage is needed underground. In this stage telluric acid is dissolved in water at  $80^\circ\text{C}$  and left to cool to recrystallize without further rinsing. A further purification of about a factor 100 is obtained. Currently, we are investigating the possibility of moving the above ground purification underground, in order to reduce potential recontamination.

The water purification plant at the SNOLAB underground laboratory is based on the SNO light water purification plant, which has been upgraded to improve its performance.

Spike tests have shown that some of the isotopes produced by cosmogenic activation of the surfactant are harder to remove by purification than in the case of telluric acid. The procedure to obtain pure surfactant will therefore be based on its chemical synthesis in a dedicated underground plant.

**2.5. AV Rope System.** The SNO+ liquid scintillator has a lower density ( $\rho = 0.86 \text{ g/cm}^3$  for LAB-PPO at  $T = 12^\circ\text{C}$ ) compared to the surrounding light water, requiring a new hold-down rope system (see Figure 2) to compensate the buoyant force, anchoring the acrylic vessel to the cavity floor. The new hold-down rope system consists of very high purity, high-performance polyethylene fiber (Tensylon) ropes of 38 mm diameter. The original hold-up rope system has also been replaced with new Tensylon ropes of 19 mm diameter in order to reduce the radioactivity contamination.

**2.6. PMTs and Electronics.** SNO+ uses the original 8 inch SNO photomultiplier tubes (Hamamatsu R1408). Each PMT is equipped with a 27 cm diameter concentrator, increasing the effective photocathode coverage to about 54%. Faulty PMT bases have been repaired and replaced, and about 9400 PMTs (90 of which are facing outwards) are expected

TABLE 1: Calibration sources that are considered for use by the SNO+ experiment.

Source	AmBe	<sup>60</sup> Co	<sup>57</sup> Co	<sup>24</sup> Na	<sup>48</sup> Sc	<sup>16</sup> N	<sup>220</sup> Rn/ <sup>222</sup> Rn
Radiation	n, $\gamma$	$\gamma$	$\gamma$	$\gamma$	$\gamma$	$\gamma$	$\alpha, \beta, \gamma$
Energy [MeV]	2.2, 4.4 ( $\gamma$ )	2.5 (sum)	0.122	4.1 (sum)	3.3 (sum)	6.1	Various

to be in operation at the start of the SNO+ experiment data taking.

In SNO+ the use of liquid scintillator as target volume greatly increases the light yield in contrast to the SNO heavy water, allowing the measurement of very low energy signals, like pp solar neutrinos (0.4 MeV end-point energy). Moreover, some of the background event types have high rates of several hundred Hz. For these reasons, the SNO read-out boards and the data acquisition system were replaced with new ones capable of a higher bandwidth. New utilities have been added to the SNO+ trigger system which will allow for a more sophisticated use, a flexible calibration interface, and new background cuts to improve the physics sensitivity. The SNO+ trigger window is 400 ns long, during which time information and charge are collected from every PMT that fired. A dead-time of 30–50 ns separates two trigger windows [9].

In 2012 and 2014, the new electronics and trigger system were tested in runs with the detector empty and nearly half-filled with ultra-pure water (UPW).

**2.7. Cover Gas System.** As long-lived radon daughters are a potential background for the physics goals of SNO+ (see Section 4), the original SNO cover gas system has been upgraded to prevent radon ingress in the detector during operation. It consists of a sealed system filled with high purity nitrogen gas which acts as a physical barrier between the detector and the  $\sim 130 \text{ Bq/m}^3$  of radon in the laboratory air. A new system of radon tight buffer bags has been designed and installed to accommodate the mine air pressure changes, with the aim of reaching a factor  $10^5$  in radon reduction.

**2.8. Calibration Systems.** The SNO+ detector will be calibrated using both optical sources (LEDs and lasers coupled to optical fibers) and radioactive sources (beta, gamma, alpha, and neutron). The optical sources are used to verify the PMT response and to measure *in situ* the optical properties of the detector media, while the radioactive sources are used to check the energy scale, the energy resolution, the linearity of the response, and the detector asymmetries, and to determine the systematic uncertainties and the efficiency of all reconstructed quantities (i.e., energy, position, and direction). Additionally, a system of cameras in underwater enclosures will be used to monitor the position of the acrylic vessel and the hold-down rope system, and to triangulate the positions of the calibration sources inserted into the detector.

The SNO+ calibration hardware has been designed to match the purity requirements of SNO+ and the need to have materials compatible with LAB. The calibration sources will be attached to an umbilical and moved by a system of high purity ropes in order to scan the detector off the central axis in two orthogonal planes.

The set of radioactive sources that are considered for the SNO+ experiment is shown in Table 1, covering the energy range from 0.1 MeV to 6 MeV. In addition, the internal radioactivity can be used to calibrate the detector and check any energy shift or variation of the response during data taking. Typical calibration references are <sup>210</sup>Po-alpha, <sup>14</sup>C-beta, delayed <sup>214</sup>Bi-Po (<sup>238</sup>U chain), and <sup>212</sup>Bi-Po (<sup>232</sup>Th chain) coincidences and muon followers.

The optical calibration hardware consists of internally deployable sources—a laserball (light diffusing sphere) and a Cherenkov source for absolute efficiency measurements—and an external system consisting of sets of optical fibers attached to the PSUP in fixed positions, sending pulses from fast LEDs or lasers into the detector. This system allows frequent calibrations of the PMTs response, time, and gain [23], and measuring the scattering and attenuation length of the scintillator without the need for source insertion.

**2.9. Simulation and Analysis.** A Geant4-based software package RAT (RAT is an Analysis Tool) has been developed to simulate the physics events in the SNO+ detector in great detail, and to perform analyses such as vertex reconstruction. The RAT simulation includes full photon propagation, from generation via scintillation and Cherenkov processes, through to absorption and detection on the PMTs. The detailed data acquisition and trigger systems are also part of the simulation. Several particle generators have been developed to simulate  $0\nu\beta\beta$ -decay events, solar neutrinos, geoneutrinos, reactor antineutrinos, supernova neutrinos, and antineutrinos. The decay schemes of all relevant background isotopes are also part of the simulation tool. RAT communicates with a database that contains calibration constants and parameters describing the detector status during each run. This includes the optical properties of the various components of the scintillator cocktail, PMT calibration constants, and detector settings such as channel thresholds. Algorithms have been developed to reconstruct event information such as the vertex position, event direction (where relevant), and deposited energy. The SNO+ MC tool is continuously tuned to match newly available measurements.

For all SNO+ physics topics we have run a full Monte Carlo simulation to predict the fraction of background events in the corresponding region of interest (ROI), from which we have evaluated our sensitivities.

### 3. Physics Goals, Current Status, and Run Plan

The primary goal of SNO+ is to search for the neutrinoless double-beta decay of <sup>130</sup>Te. However, it has the potential to explore other physics including the following.

(i) *Low Energy pep and CNO Solar Neutrinos.* The pep neutrinos can be used to constrain new physics scenarios on how neutrinos couple to matter, while the CNO-neutrino flux can shed light on unresolved questions regarding solar metallicity.

(ii) *Geoneutrinos.* They are produced by the decay of U and Th chains in the Earth's crust and mantle. They can help to understand the heat production mechanisms of the Earth itself.

(iii) *Reactor Antineutrinos.* These can be used to better constrain the  $\Delta m_{21}^2$  neutrino oscillation parameter.

(iv) *Supernova Neutrinos and Antineutrinos.* The ability to detect a galactic supernova provides the potential for improving models of supernova explosions.

(v) *Exotic Physics.* The low background expected in SNO+ allows searches for processes predicted by physics beyond the standard model (other than  $0\nu\beta\beta$ -decay), like invisible nucleon decay, and solar axion or axion-like particle searches.

Currently, the SNO+ cavity is partially filled with ultra-pure water. The upgrades to the SNO+ detector are nearly completed with a few items to be finished before the start of data taking. The detector parts that need to be finalized are the installation of the calibration system, underwater cameras, and the calibration optical fibers in most of the positions above the SNO+ equator, and the replacement of the PMTs. The installation will proceed along with the rise of the water level in the cavity. The scintillator plant is nearly completed. The newly installed electronic and trigger system and part of the optical calibration system have been tested in air and with the partially water-filled detector.

The data taking period of SNO+ will be divided into three main phases.

*Water Phase.* In this phase, the acrylic vessel will be filled with about 905 tonnes of ultra-pure water and data taking will last for a few months. The main physics goals will be a search for exotic physics, including solar axion-like particles and invisible nucleon decay in  $^{16}\text{O}$ , the watch for supernova neutrinos, and the detection (potentially) of reactor antineutrinos. During this phase, the detector performance, the PMT response, and the data acquisition system characteristics will be tested. Optical calibrations to test the response of the PMT concentrators and the attenuation of the external water and the acrylic will be performed. The backgrounds coming from external sources, like external water, PMT array, hold-down ropes, and the acrylic vessel, will be characterized.

*Pure Scintillator Phase.* In this phase, the detector will be filled with about 780 tonnes of LAB-PPO liquid scintillator and data taking will last for a few months. The physics topics covered are the measurement of the low energy solar neutrinos, the measurement of geo and reactor antineutrinos, and the supernova neutrino watch. This phase will also be used to verify the optical model and the detector response and to characterize the backgrounds due to internal and external radioactive sources.

*Te-Loading Phase.* This phase is foreseen to start in 2017 and last for about 5 years. In this phase, also called Phase I, about 2.3 tonnes of natural tellurium (0.3% loading by weight) will be added to the detector for the search for the  $0\nu\beta\beta$ -decay of  $^{130}\text{Te}$ . Simultaneously, geo and reactor neutrinos can be observed, and the detector will be live to a potential supernova.

The physics program and capabilities of SNO+ will be discussed in Sections 5 to 9.

## 4. Backgrounds

The background sources of the SNO+ experiment can be divided into two main categories: internal and external. Internal backgrounds are all the non-signal interactions that occur inside the AV ( $R < 6$  m). External backgrounds are the interactions that are produced in the region outside the target volume but that can propagate or are reconstructed within it. Full Monte Carlo simulations, along with *ex situ* assays, are used to explore the different background sources and develop rejection techniques.

In the following subsections the various background sources are presented: internal  $^{238}\text{U}$  chain (Section 4.1),  $^{210}\text{Bi}$  and  $^{210}\text{Po}$  decays (Section 4.2), internal  $^{232}\text{Th}$  chain (Section 4.3), internal  $^{40}\text{K}$ ,  $^{39}\text{Ar}$ , and  $^{85}\text{Kr}$  decays (Section 4.4), cosmogenically induced isotopes (Section 4.5), ( $\alpha$ , n) reactions (Section 4.6), pile-up events (Section 4.7), and external backgrounds (Section 4.8).

*4.1. Internal  $^{238}\text{U}$  Chain.*  $^{238}\text{U}$  ( $T_{1/2} = 4.47 \times 10^9$  yr) is a naturally occurring radioisotope present in the liquid scintillator. The part of the decay chain relevant for SNO+ is shown in Figure 3. The  $^{238}\text{U}$  daughters of most concern are  $^{214}\text{Bi}$ ,  $^{210}\text{Tl}$ , and  $^{210}\text{Bi}$  (see Section 4.2). Secular equilibrium with the top part of the chain is assumed through the paper unless otherwise noted.

$^{214}\text{Bi}$  ( $T_{1/2} = 19.9$  min) beta-decays to  $^{214}\text{Po}$  with a Q-value of 3.27 MeV in 99.979% of the cases. This decay can be tagged using the  $^{214}\text{Po}$  alpha decay ( $T_{1/2} = 164.3$   $\mu\text{s}$ ,  $E_\alpha = 7.7$  MeV), during both the pure scintillator and the Te-loaded phase. In the pure scintillator phase, the  $\beta$ - $\alpha$  delayed coincidence will be used to measure the concentration of the  $^{238}\text{U}$ -chain contaminants.  $^{214}\text{Bi}$  is expected to be in secular equilibrium with the top part of the  $^{238}\text{U}$  chain for most of the data taking period. This equilibrium can be broken by radon ingress into the detector during calibration campaigns, or from emanation by the calibration hardware materials. However, for non-continuum sources of radon, due to the short half-life of  $^{214}\text{Bi}$ , equilibrium will be restored in a few weeks' time. In SNO+ the presence of the cover gas on the top of the detector provides an efficient barrier against laboratory air, highly reducing the radon ingress into the detector (see Section 2.7). Additionally, most of the radon short-lived daughters decay in the cover gas region or in the detector neck; thus they do not reach the fiducial volume.

During the Te phase, the delayed coincidence technique will be used to reject  $^{214}\text{Bi}$  events that fall into the region of interest (ROI) for the  $0\nu\beta\beta$ -decay search.

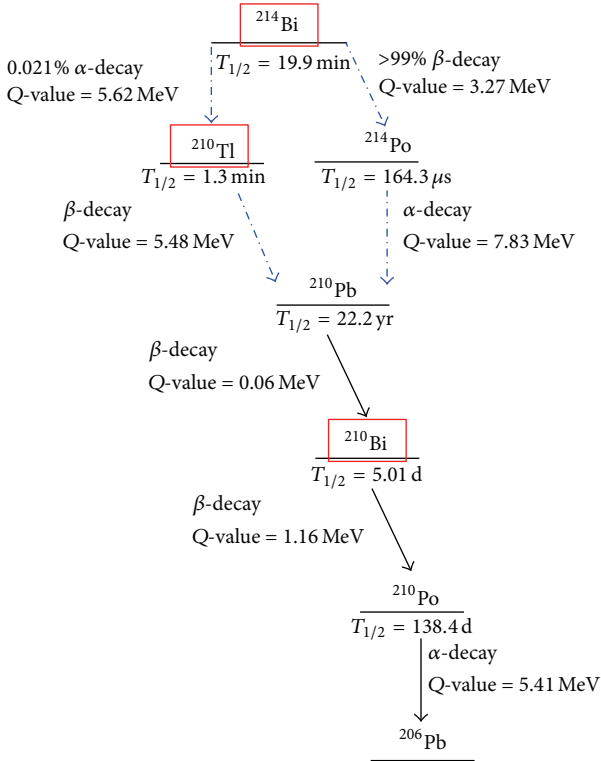


FIGURE 3: Part of  $^{238}\text{U}$ -decay chain relevant for SNO+ with  $Q$ -values (total kinetic energy released in the ground state-ground state transition), half-life, and decay modes [24]. The red squares highlight the nuclides of most concern:  $^{214}\text{Bi}$ ,  $^{210}\text{Tl}$ , and  $^{210}\text{Bi}$ . The decays used for  $\alpha$ - $\beta$  and  $\beta$ - $\alpha$  coincidence techniques are shown with a blue arrow (dash-dotted line).

Usually,  $\text{Bi-}\beta$  and  $\text{Po-}\alpha$  are separated by more than 250 ns and the SNO+ detector records them as two separate events. The secondary events (alpha candidates) are identified by applying an energy cut around the alpha energy, shifted due to quenching to  $\sim 0.8$  MeV electron equivalent energy, and by the short time separation from the preceding event. To reduce the misidentification of the events due to other decays occurring in the same energy region during the coincidence window, a position cut can also be applied. An  $\alpha$ - $\beta$  classification algorithm has been developed to further reduce the misidentification by classifying the events as  $\alpha$ -like or  $\beta$ -like based on the hit-time distribution.

Occasionally, the beta and the alpha decays are separated by less than 250 ns and they may be recorded as a single event by the SNO+ detector. These events are important for the  $0\nu\beta\beta$ -decay phase as they may fall into the ROI. In this case, the rejection technique is based on the distortion in the time distribution of the light detected by the PMTs compared to the case of a single interaction. This rejection technique is enhanced if a pulse shape analysis can be applied to distinguish beta from alpha events.

In 0.021% of the cases  $^{214}\text{Bi}$  alpha-decays to  $^{210}\text{Tl}$  ( $T_{1/2} = 1.3$  min), which beta-decays to  $^{210}\text{Pb}$  with a  $Q$ -value of 5.5 MeV. Due to the small branching ratio this route is less

TABLE 2: Target levels, in g/g, and corresponding decay rates for the internal  $^{238}\text{U}$ - and  $^{232}\text{Th}$ -chain contaminants in the various SNO+ phases. Secular equilibrium has been assumed for all the isotopes except  $^{210}\text{Pb}$ ,  $^{210}\text{Bi}$ , and  $^{210}\text{Po}$ . The levels of  $^{210}\text{Bi}$  and  $^{210}\text{Po}$  during the pure scintillator phase and the Te-loaded phase are expected to be out of secular equilibrium due to the intrinsic scintillator contamination and the leaching off of the AV surface. For the 0.3% Te-loaded scintillator the tellurium/polonium affinity component is also included in the  $^{210}\text{Po}$  decays/yr (see text).

Source	Target [g/g]	Decays/yr
Internal $\text{H}_2\text{O}$ , water phase		
$^{238}\text{U}$ chain	$3.5 \times 10^{-14}$	$1.2 \times 10^7$
$^{232}\text{Th}$ chain	$3.5 \times 10^{-15}$	$4.1 \times 10^5$
LAB-PPO, pure scintillator phase		
$^{238}\text{U}$ chain	$1.6 \times 10^{-17}$	4900
$^{232}\text{Th}$ chain	$6.8 \times 10^{-18}$	700
$^{210}\text{Bi}$	—	$7.6 \times 10^{8a}$
$^{210}\text{Po}$	—	$7.8 \times 10^{8a}$
0.3% Te-loaded scintillator, Te phase		
$^{238}\text{U}$ chain	$2.5 \times 10^{-15}$	$7.6 \times 10^5$
$^{232}\text{Th}$ chain	$2.8 \times 10^{-16}$	$2.8 \times 10^4$
$^{210}\text{Bi}$	—	$7.9 \times 10^{9b}$
$^{210}\text{Po}$	—	$9.5 \times 10^{9b}$

<sup>a</sup>Expected number of events in the first year after 9 months of water phase.

<sup>b</sup>Expected number of events in the first year after 9 months of water phase followed by 6 months of pure scintillator phase.

important than the previous one. An  $\alpha$ - $\beta$  delayed coincidence, similar to the  $\beta$ - $\alpha$  one, can be applied. However, due to the longer half-life of  $^{210}\text{Tl}$ , the mistagging probability is larger with respect to the  $^{214}\text{Bi}$ - $\text{Po}$  one which may result in a larger signal sacrifice.

Based on Borexino Phase-I achievements [20], the purity level aimed (target level) in the LAB-PPO scintillator for the  $^{238}\text{U}$  chain is  $1.6 \times 10^{-17}$  g/g (see Table 2). During the Te-loaded phase, the addition of the isotope, the water, and the surfactant to LAB will worsen the mixture purity, but we will maintain a strict target level of  $2.5 \times 10^{-15}$  g/g (see Table 2).

4.2.  $^{210}\text{Bi}$  and  $^{210}\text{Po}$  Backgrounds. The ingress of  $^{222}\text{Rn}$  into the SNO+ detector can break the secular equilibrium in the  $^{238}\text{U}$  chain at  $^{210}\text{Pb}$  ( $T_{1/2} = 22.2$  yr,  $Q$ -value = 0.06 MeV), resulting in a higher concentration of this isotope. Even if  $^{210}\text{Pb}$  is not a direct background for the SNO+ experiment, its daughters  $^{210}\text{Bi}$  ( $T_{1/2} = 5.0$  d,  $Q$ -value = 1.16 MeV) and  $^{210}\text{Po}$  ( $T_{1/2} = 138.4$  d,  $E_\alpha = 5.3$  MeV, shifted to  $\sim 0.5$  MeV electron equivalent energy) are potentially relevant for the various physics searches.  $^{210}\text{Bi}$ -beta decays are the main background for the CNO- $\nu$  measurement, as they have similar spectral shapes, while the  $^{210}\text{Po}$ -alpha decay is a background for the  $\beta$ - $\alpha$  and  $\alpha$ - $\beta$  delayed coincidences, resulting in mistagging and potential signal sacrifice. Additionally, the emitted alphas can interact with the atoms in the scintillator producing neutrons as described in Section 4.6. The cover gas system placed at the top of the acrylic vessel greatly

reduces the radon ingress into the detector. Furthermore, the majority of short-lived daughters decay before reaching the fiducial volume. However, due to its long half-life,  $^{210}\text{Pb}$  is not attenuated by the presence of the detector neck and reaches the target volume.

$^{210}\text{Pb}$  and its daughters may also leach from materials that are in contact with the liquid scintillator. Radon daughters deposited on the material's surface can implant by alpha recoil to a depth of a few hundred nm, where they eventually decay to  $^{210}\text{Pb}$ ,  $^{210}\text{Pb}$ ,  $^{210}\text{Bi}$ , and  $^{210}\text{Po}$  atoms might then leach off when the liquid scintillator mixture is in contact with the surface. This process can happen, for instance, during the handling and storing of the liquid scintillator, resulting in rates of  $^{210}\text{Pb}$ ,  $^{210}\text{Bi}$ , and  $^{210}\text{Po}$  out of equilibrium with the  $^{238}\text{U}$  chain. Concentrations of  $^{210}\text{Bi}$  and  $^{210}\text{Po}$  different from each other and the rest of the  $^{238}\text{U}$  chain have been seen by the Borexino experiment [25]. The levels initially measured by Borexino for these two isotopes are included in Table 2.

An additional source of  $^{210}\text{Pb}$ ,  $^{210}\text{Bi}$ , and  $^{210}\text{Po}$  is leaching from the internal surface of the AV, where radon daughters have implanted during the construction of SNO and when the detector was empty after draining the heavy water. This may create a continuous source of  $^{210}\text{Pb}$ ,  $^{210}\text{Bi}$ , and  $^{210}\text{Po}$  during the data taking period for all SNO+ phases. Leaching rates depend on several factors, like temperature, implantation depth, type of liquid in contact with the surface, and initial surface activity. The leaching rate of  $^{210}\text{Pb}$  and its daughters for all the scintillator mixtures and the ultra-pure water at different temperatures have been measured in bench top tests. With a measured activity of about 1 kBq on the inner AV surface, the activity of  $^{210}\text{Pb}$  daughters leached in the scintillator media might be as high as a few hundred Bq depending on the duration of the data taking period. The activity of the backgrounds leached in the scintillator is expected to increase with time, while that of inner surface events is expected to decrease.

In the Te-loaded phase, an additional source of  $^{210}\text{Po}$  is the tellurium itself. The CUORE collaboration has shown [26] that due to the chemical affinity between tellurium and polonium this element may still be present in tellurium after the crystal production process. In our background estimations we assume an additional  $^{210}\text{Po}$  activity of 0.06 Bq/kg<sub>Te</sub>, based on CUORE measurements. These decays, however, are not supported by  $^{210}\text{Pb}$  and are considerably reduced, to about 16% of the initial activity, in a year after tellurium production. This contribution is included in the purity levels of  $^{210}\text{Po}$  shown in Table 2.

**4.3. Internal  $^{232}\text{Th}$  Chain.**  $^{232}\text{Th}$  ( $T_{1/2} = 1.4 \times 10^{10}$  yr) is also a naturally occurring radioisotope present in the liquid scintillator. The daughters of most concern are  $^{212}\text{Bi}$  and  $^{208}\text{Tl}$  (see Figure 4).

$^{212}\text{Bi}$  ( $T_{1/2} = 60.6$  min) beta-decays to  $^{212}\text{Po}$  ( $T_{1/2} = 300$  ns) with a Q-value of 2.25 MeV in 64% of the cases. As for the  $^{214}\text{Bi} \rightarrow ^{214}\text{Po}$  decay, many events can be selected using a  $\beta$ - $\alpha$  delayed coincidence, which is used to extract the concentration of the  $^{232}\text{Th}$ -chain contaminants in equilibrium in the

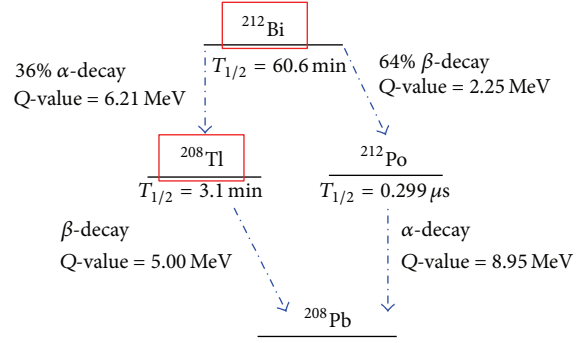


FIGURE 4: Part of  $^{232}\text{Th}$ -decay chain relevant for SNO+ with Q-values, half-life, and decay modes [24]. The red squares highlight the most important nuclides:  $^{212}\text{Bi}$  and  $^{208}\text{Tl}$ . The decays used for  $\alpha$ - $\beta$  and  $\beta$ - $\alpha$  coincidence techniques are shown with a blue arrow (dash-dotted line).

pure scintillator. Nearly 45% of the  $^{212}\text{Bi} \rightarrow ^{212}\text{Po}$  decays fall in the same trigger window and are a potential background for the  $0\nu\beta\beta$ -decay search. These can be rejected using the PMT timing distribution.

In the remaining 36% of the cases  $^{212}\text{Bi}$  alpha-decays to  $^{208}\text{Tl}$  ( $T_{1/2} = 3.0$  min), which beta-decays to  $^{208}\text{Pb}$  with a Q-value of 5.0 MeV. An  $\alpha$ - $\beta$  delayed coincidence can be applied to identify the  $^{208}\text{Tl}$  events as for the  $^{210}\text{Tl}$  case.

The LAB-PPO scintillator target level for the  $^{232}\text{Th}$  chain is  $6.8 \times 10^{-18}$  g/g (based on [20]), while the target level for the Te-loaded scintillator is  $2.8 \times 10^{-16}$  g/g (see Table 2).

**4.4. Internal  $^{40}\text{K}$ ,  $^{39}\text{Ar}$ , and  $^{85}\text{Kr}$  Backgrounds.** Other internal backgrounds are important for solar neutrino and other measurements.

$^{40}\text{K}$  ( $T_{1/2} = 1.248 \times 10^9$  yr) has a very distinctive energy spectrum, having both a beta component and a gamma peak at 1.46 MeV. Due to the long half-life, it is naturally present in the scintillator and detector materials.

$^{39}\text{Ar}$  ( $T_{1/2} = 269$  yr) and  $^{85}\text{Kr}$  ( $T_{1/2} = 10.8$  yr) decay with a Q-value of 0.565 MeV and of 0.687 MeV, respectively. The amount of these isotopes can be reduced by minimising the contact time of LAB with air and thoroughly degassing the scintillator.

**4.5. Cosmogenically Induced Backgrounds.** Besides the natural radioactivity present in the scintillator, LAB can be activated by cosmic ray neutrons and protons while it is above ground. The main expected background is  $^7\text{Be}$  ( $T_{1/2} = 53.2$  d, EC-decay with a 0.48 MeV gamma), with a maximum production rate at sea level (neutron and proton flux from [27, 28]) of about 1 kHz for 780 t of liquid scintillator. More than 99% of the produced  $^7\text{Be}$  can be efficiently removed by the scintillator purification plant.

$^{14}\text{C}$  ( $T_{1/2} = 5700$  yr, Q-value = 0.16 MeV) is naturally present in the liquid scintillator. It is a direct background for the very low energy pp neutrino measurements and may contribute to pile-up backgrounds (see Section 4.7). In SNO+, we expect a  $^{14}\text{C}/^{12}\text{C}$  ratio of the order of  $10^{-18}$ ,

similar to what was observed in the Borexino test facility [29], corresponding to a decay rate of a few hundred Hz. This is a reasonable assumption as in both cases the liquid scintillator is obtained from old oil fields, in which most of  $^{14}\text{C}$  has decayed away. The amount of  $^{14}\text{C}$  produced by cosmogenic activation of LAB during transport to site is negligible in comparison.

$^{11}\text{C}$  ( $T_{1/2} = 20$  min,  $Q$ -value = 1.98 MeV) is mainly produced by muon interactions with the carbon nuclei of the liquid scintillator. We expect a total of  $(1.14 \pm 0.21) \times 10^3$  decays/kt/yr during operation, extrapolated from KamLAND data in [30]. This is about a factor 100 less than what was observed in Borexino [31] due to the deeper underground location. A threefold coincidence tagging technique, like the one developed by Borexino [32], together with an electron-positron discrimination analysis [33], will further reduce these events.

Other muon induced backgrounds are generally very short lived (milliseconds to seconds half-life) and can be rejected by vetoing the detector for a few minutes after each muon event.

Important cosmogenic-induced backgrounds are isotopes produced by spallation reactions on tellurium while it is stored on surface [34], like  $^{124}\text{Sb}$  ( $T_{1/2} = 60.2$  d,  $Q$ -value = 2.90 MeV),  $^{22}\text{Na}$  ( $T_{1/2} = 950.6$  d,  $Q$ -value = 2.84 MeV),  $^{60}\text{Co}$  ( $T_{1/2} = 1925$  d,  $Q$ -value = 2.82 MeV),  $^{110\text{m}}\text{Ag}$  ( $T_{1/2} = 249.8$  d,  $Q$ -value = 2.89 MeV,  $E_{\text{parent}}(\text{level}) = 0.118$  MeV), and  $^{88}\text{Y}$  ( $T_{1/2} = 106.6$  d,  $Q$ -value = 3.62 MeV). We have developed a purification technique [22] (see Section 2.4) that, together with underground storage, reduces the cosmogenic-induced background on tellurium to a negligible level.

**4.6. ( $\alpha$ ,  $n$ ) Backgrounds.** Neutrons can be produced in the liquid scintillator by ( $\alpha$ ,  $n$ ) reactions on  $^{13}\text{C}$  or  $^{18}\text{O}$  atoms, muon interactions in the scintillator volume,  $^{238}\text{U}$  fission, and ( $\gamma$ ,  $n$ ) reactions for  $E_\gamma > 3$  MeV. Excluding the muon induced neutrons, the most prominent neutron source inside the scintillator volume is the  $\alpha + ^{13}\text{C} \rightarrow ^{16}\text{O} + n$  reaction ( $E_{\text{thr.}} = 0.0$  keV), which is a potential background for both the  $0\nu\beta\beta$ -decay search and the antineutrino measurement. The main source of alpha particles in the various scintillator mixtures is  $^{210}\text{Po}$ . Other U- and Th-chain's alpha emitters form a negligible contribution, as they are expected to be  $\sim 4$  orders of magnitude less abundant.

Neutrons produced in ( $\alpha$ ,  $n$ ) reactions will scatter from protons during the thermalization process, resulting in recoils emitting scintillation light. The visible proton energy together with the energy lost by the alphas before interaction is the prompt signal. If the isotope is in an excited state, the emitted deexcitation gammas are also part of the prompt signal. The thermalized neutrons in  $>99\%$  of the cases are eventually captured by hydrogen atoms with the emission of the characteristic 2.22 MeV- $\gamma$ . In the remaining  $\sim 1\%$  of the cases the thermal neutron is captured either on tellurium isotopes, producing mainly a 0.6 MeV gamma, or on  $^{12}\text{C}$ , producing a 4.95 MeV gamma. The prompt and the delayed signal can be used to reject the ( $\alpha$ ,  $n$ ) background using a delayed coincidence technique similar to that of  $\beta$ - $\alpha$  events.

**4.7. Pile-Up Backgrounds.** A pile-up event occurs when two or more decays (signal or background or a mixture) happen in the same trigger window and thus are potentially detected as a single event with energy equal to the sum of the single energies. Pile-up events become important when the event rate of one or all of the contributing decays is very high (hundreds of Hz), like  $^{14}\text{C}$  decays or  $^{210}\text{Bi}$  or  $^{210}\text{Po}$ . A rejection technique, using the distortion of the timing, is used to efficiently reduce these backgrounds [35, 36].

**4.8. External Backgrounds.** Sources of external background include the hold-down and hold-up ropes, the PMT array, the AV bulk, and the external water (see Table 3). Radioactive decays occur outside the scintillator volume, so the main concerns for the signal extraction analysis are the high energy gammas and betas emitted by  $^{214}\text{Bi}$ ,  $^{208}\text{Tl}$ , and  $^{40}\text{K}$  decays. External background events reconstructing inside the AV can be greatly reduced by applying a fiducial volume cut. Events can be further reduced using the PMT time distribution. *In situ* analysis during the water phase and the pure liquid scintillator phase will help to constrain the external backgrounds for the Te-loaded phase.

## 5. $^{130}\text{Te}$ Neutrinoless Double-Beta Decay

The main goal of the SNO+ experiment is the search for neutrinoless double-beta decay of  $^{130}\text{Te}$  ( $Q$ -value =  $2527.518 \pm 0.013$  keV [40]) by loading large quantities of the isotope into the liquid scintillator volume. This approach has several advantages: (1) external backgrounds can be removed by fiducialization, (2) internal and external background levels can be measured before and after the isotope deployment, allowing identification and removal of possible contamination, (3) internal backgrounds can be tagged by coincidences or particle identification, (4) the detector response can be tested with and without the isotope, (5) the spatial distribution of most background isotopes in a liquid is known to be uniform, (6) the loading can be easily and affordably scaled up or (7) changed to another isotope, and (8) tellurium and scintillator can be removed and repurified if high levels of backgrounds are found.

The choice of  $^{130}\text{Te}$  as the preferred  $0\nu\beta\beta$  candidate is the result of an extensive investigation by the SNO+ collaboration. The decision was based on several factors, including the following points:

- (1)  $^{130}\text{Te}$  has a large natural abundance of 34.08%, which allows loading of several tonnes of isotope without enrichment.
- (2) The measured half-life of the  $^{130}\text{Te}$   $2\nu\beta\beta$  decay is  $(7.0 \pm 0.9$  (stat)  $\pm 1.1$  (syst))  $\times 10^{20}$  yr [41], one of the longest of all the  $0\nu\beta\beta$  isotopes. This is particularly important for liquid scintillator-based experiments, as the energy resolution is usually some hundreds of keV.
- (3) An innovative loading technique has been developed, which enables deployment of up to 5% (by weight) of

TABLE 3:  $^{238}\text{U}$ - and  $^{232}\text{Th}$ -chain levels for external background sources. Shown are measured levels and expected decay rates.

Source	Measured levels	Decays/yr
Internal ropes	$^{214}\text{Bi}$ : $(2.8 \pm 5.4) \times 10^{-10} \text{ g}_\text{U}/\text{g}$ [37]	4966
	$^{208}\text{Tl}$ : $<2.0 \times 10^{-10} \text{ g}_\text{Th}/\text{g}$ [37]	<418
Hold-down ropes	$^{214}\text{Bi}$ : $(4.7 \pm 3.2) \times 10^{-11} \text{ g}_\text{U}/\text{g}$ [37]	$4.06 \times 10^6$
	$^{208}\text{Tl}$ : $(2.27 \pm 1.13) \times 10^{-10} \text{ g}_\text{Th}/\text{g}$ [37]	$2.32 \times 10^6$
Hold-up ropes	$^{214}\text{Bi}$ : $(4.7 \pm 3.2) \times 10^{-11} \text{ g}_\text{U}/\text{g}$ [37]	$8.34 \times 10^5$
	$^{208}\text{Tl}$ : $(2.27 \pm 1.13) \times 10^{-10} \text{ g}_\text{Th}/\text{g}$ [37]	$4.78 \times 10^5$
Water shielding	$^{214}\text{Bi}$ : $2.1 \times 10^{-13} \text{ g}_\text{U}/\text{g}$ [38]	$1.32 \times 10^8$
	$^{208}\text{Tl}$ : $5.2 \times 10^{-14} \text{ g}_\text{Th}/\text{g}$ [38]	$3.92 \times 10^6$
Acrylic vessel	$^{214}\text{Bi}$ : $<1.1 \times 10^{-12} \text{ g}_\text{U}/\text{g}^{\text{a}}$ [7]	$1.28 \times 10^7$
	$^{208}\text{Tl}$ : $<1.1 \times 10^{-12} \text{ g}_\text{Th}/\text{g}^{\text{a}}$ [7]	$1.50 \times 10^6$
Acrylic vessel external dust <sup>b</sup>	$^{214}\text{Bi}$ : $(1.1 \pm 0.1) \times 10^{-6} \text{ g}_\text{U}/\text{g}$ [39]	$7.8 \times 10^5$
	$^{208}\text{Tl}$ : $(5.6 \pm 0.5) \times 10^{-6} \text{ g}_\text{Th}/\text{g}$ [39]	$4.6 \times 10^5$
Acrylic vessel internal dust	$^{214}\text{Bi}$ : $(1.1 \pm 0.1) \times 10^{-6} \text{ g}_\text{U}/\text{g}$ [39]	$4.15 \times 10^4$
	$^{208}\text{Tl}$ : $(5.6 \pm 0.5) \times 10^{-6} \text{ g}_\text{Th}/\text{g}$ [39]	$2.48 \times 10^4$
PMTs	$^{214}\text{Bi}$ : $100 \times 10^{-6} \text{ g}_\text{U}/\text{PMT}$ [7]	$3.7 \times 10^{11}$
	$^{208}\text{Tl}$ : $100 \times 10^{-6} \text{ g}_\text{Th}/\text{PMT}$ [7]	$4.4 \times 10^{10}$

<sup>a</sup> Assumed  $1.0 \times 10^{-12} \text{ g/g}$ .

<sup>b</sup> It is assumed that the top hemisphere of the external AV surface is not cleaned, while the bottom hemisphere is at target level.

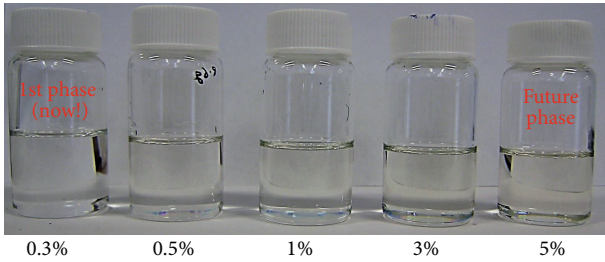


FIGURE 5: TeLS samples from the investigation of higher tellurium loading in LAB scintillator. The samples increase in loading from 0.3% (by weight) on the left to 5% on the right.

natural tellurium while maintaining good light transmission, minimal scattering, and an acceptable light yield (see Section 2.2). The 0.3% tellurium scintillator cocktail (TeLS) has been proven to be stable for a period of over two years. In Figure 5, various SNO+ loaded cocktails are shown. Cocktails with higher loading still maintain good optical transparency.

- (4) The TeLS does not present inherent optical absorption lines in the visible wavelength range, such that a secondary wavelength shifter may be added to the cocktail to better match the SNO+ PMT response.

**5.1. Backgrounds.** For the  $^{130}\text{Te}$   $0\nu\beta\beta$  search, an asymmetric region of interest (ROI) is defined, which extends from  $-0.5\sigma$  to  $1.5\sigma$  around the Gaussian signal peak. For the 0.3% Te-loaded cocktail with a light yield of 200 Nhits/MeV (see Section 2.2) the energy resolution at 2.5 MeV is  $\sim 270 \text{ keV}$  (FWHM), while the averaged position resolution at the same energy is  $\sim 15 \text{ cm}$  at the detector's center. An asymmetric ROI

retains most of the  $0\nu\beta\beta$  decays but considerably reduces the backgrounds from  $2\nu\beta\beta$  and low energy  $^{238}\text{U}$ - and  $^{232}\text{Th}$ -chain decays. Most external backgrounds are rejected by a 3.5 m fiducial radius cut, which preserves 20% of signal events. Inside the 3.5 m fiducial volume (FV) and 2.47 MeV to 2.70 MeV energy ROI, the main background sources are as follows.

**$^8\text{B}$  Solar Neutrinos.** Flat continuum background from the elastically scattered (ES) electrons normalized using the total  $^8\text{B}$  flux and published solar mixing parameters [42].

**$2\nu\beta\beta$ .** Irreducible background due to the  $2\nu\beta\beta$  decays of  $^{130}\text{Te}$ : these events appear in the ROI due to the energy resolution of SNO+.

**External Backgrounds.**  $^{208}\text{Tl}$  and  $^{214}\text{Bi}$  nuclides contained in the AV, hold-down rope system, water shielding, and PMT glass are the major contributors in the defined ROI. The FV cut of 20% reduces these background events by several orders of magnitude. The PMT hit-time distribution cut reduces the external background events falling in the FV by an additional factor of two.

**Internal  $^{238}\text{U}$ - and  $^{232}\text{Th}$ -Chain Backgrounds.** The dominant backgrounds in the signal ROI are due to  $^{214}\text{Bi}$ -Po and  $^{212}\text{Bi}$ -Po decays. Currently, we have achieved approximately 100% rejection of separately triggered  $^{214}\text{Bi}$ -Po and  $^{212}\text{Bi}$ -Po decays falling inside the ROI and FV using the  $\beta$ - $\alpha$  delayed coincidence. For  $^{212}\text{Bi}$ -Po and  $^{214}\text{Bi}$ -Po pile-up decays, cuts based on PMT hit timing achieve a rejection factor of  $\sim 50$  for events that fall in the ROI and FV. Other minor contributions in the ROI are due to  $^{234\text{m}}\text{Pa}$  ( $^{238}\text{U}$  chain),  $^{210}\text{Tl}$  ( $^{238}\text{U}$  chain), and  $^{208}\text{Tl}$  ( $^{232}\text{Th}$  chain).

TABLE 4: Expected background counts in the signal ROI and 3.5 m FV in SNO+ for the first year (year 1) and in 5 years of the 0.3% Te-loading phase. A light yield of 200 Nhits/MeV has been assumed. Cuts have been applied as described in the text.

Isotope	1 year	5 years
$2\nu\beta\beta$	6.3	31.6
${}^8\text{B } \gamma \text{ ES}$	7.3	36.3
Uranium chain	2.1	10.4
Thorium chain	1.7	8.7
External	3.6	18.1
$(\alpha, n)$	0.1	0.8
Cosmogenics	0.7	0.8
Total	21.8	106.8

*Cosmogenic Backgrounds.* The most relevant isotopes are  ${}^{60}\text{Co}$ ,  ${}^{110\text{m}}\text{Ag}$ ,  ${}^{88}\text{Y}$ , and  ${}^{22}\text{Na}$  (see Section 4.5). The developed purification techniques together with a long period of underground storage will reduce the cosmogenically induced background to less than one event per year in the FV and ROI.

*$(\alpha, n)$  Backgrounds.* Both the prompt signal and the delayed 2.22 MeV- $\gamma$  produced by  $(\alpha, n)$  reactions can leak into the  $0\nu\beta\beta$  ROI. Coincidence-based cuts have been developed that remove more than 99.6% of the prompt and  $\sim 90\%$  of delayed events that fall in the FV and ROI.

*Pile-Up Backgrounds.* The most important pile-up backgrounds for  $0\nu\beta\beta$  search are due to high-rate  ${}^{210}\text{Po} + 2\nu\beta\beta$  and  ${}^{210}\text{Bi} + 2\nu\beta\beta$ , with bismuth and polonium coming from both the TeLS and the vessel surface. Timing-based cuts have been developed that reduce the pile-up backgrounds to a negligible level.

We have estimated the fraction of each background that falls in the ROI and FV based on our Monte Carlo simulations. A summary of the various background sources in the ROI and FV is shown in Table 4. The main contributions are due to  ${}^8\text{B } \gamma \text{ ES}$  and to  $2\nu\beta\beta$ . A total of about 22 events/yr in the FV and ROI are expected. The scale of the external background events within the ROI can be checked by fitting events outside the fiducial volume. Internal U- and Th-chain residuals can be checked via the  ${}^{214}\text{Bi-Po}$  and the  ${}^{212}\text{Bi-Po}$  delayed coincidences, whose tagging efficiency can be tested during the pure LAB-PPO scintillator phase. In addition, some of the cosmogenic-induced backgrounds, like  ${}^{124}\text{Sb}$  and  ${}^{88}\text{Y}$ , can be constrained using their relatively short half-life, while  ${}^8\text{B-}\gamma$  and  $2\nu\beta\beta$  decays can be constrained by their known value. Furthermore, the detector response will be tested through a detailed calibration (see Section 2.8).

The expected signal and background spectrum for a five-year live-time is shown in Figure 6 for the 0.3% loading. A fiducial volume cut is applied at 3.5 m,  $>99.99\%$  rejection for  ${}^{214}\text{Bi-Po}$  and  $>98\%$  for  ${}^{212}\text{Bi-Po}$  are assumed, and the light yield is 200 Nhits/MeV. The  $0\nu\beta\beta$  signal shown is for  $m_{\beta\beta} = 200$  meV, which corresponds to  $T_{1/2}^{0\nu\beta\beta} \sim 1 \times 10^{25}$  yr using the IBM-2 nuclear matrix element [43].

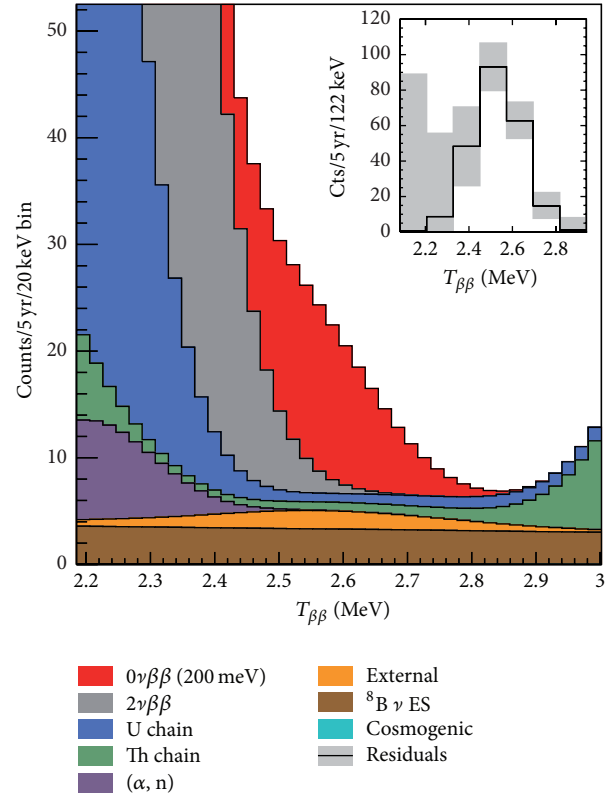


FIGURE 6: Summary stacked plot of all backgrounds and a hypothetical  $0\nu\beta\beta$  signal corresponding to a mass  $m_{\beta\beta} = 200$  meV for 5-year data taking. Events are shown in the FV of 3.5 m, for 0.3% natural tellurium loading and 200 Nhits/MeV light yield.  $T_{\beta\beta}$  is the effective kinetic energy.

5.2. *Sensitivity.* The expected number of  $0\nu\beta\beta$  events occurring in the SNO+ detector is given by

$$S = \epsilon \cdot N_{130} \cdot \ln 2 \cdot \frac{t}{T_{1/2}^{0\nu\beta\beta}}, \quad (1)$$

where  $\epsilon$  is the signal detection efficiency,  $N_{130}$  is the number of  ${}^{130}\text{Te}$  atoms in the detector,  $t$  is the live-time, and  $T_{1/2}^{0\nu\beta\beta}$  is the half-life of  ${}^{130}\text{Te } 0\nu\beta\beta$ . To compute the SNO+ sensitivity, we assume that the number of observed events in the FV and ROI is equal to the expected backgrounds. In this case the numerical value of the derived bound on the number of signal events is similar for either a Bayesian or a frequentist definition of 90% confidence level. With the natural tellurium concentration of 0.3% (by weight) in Phase I, corresponding to about 800 kg of  ${}^{130}\text{Te}$ , a 20% FV cut, and five years of data taking, SNO+ can set a lower limit on the half-life of  $T_{1/2}^{0\nu\beta\beta} > 9 \times 10^{25}$  yr at 90% CL ( $T_{1/2}^{0\nu\beta\beta} > 4.8 \times 10^{25}$  yr at 3 $\sigma$  level). This corresponds to a limit on the effective Majorana neutrino mass,  $m_{\beta\beta}$ , of 55–133 meV, using a phase space factor  $G = 3.69 \times 10^{-14} \text{ yr}^{-1}$  [44] and  $g_A = 1.269$ ; the range is due to differences in nuclear matrix element calculation methods [43, 45–48].

*5.3. Higher Tellurium Concentration in the Future.* One of the main advantages of the SNO+ technique is the possibility of moving toward higher sensitivities by increasing the loading. R&D efforts have demonstrated that, with 3% (by weight) tellurium loading, a light yield of 150 Nhits/MeV can be achieved using perylene as a secondary wavelength shifter. In SNO+ Phase II, this loss in light yield will be compensated by an upgrade to high quantum efficiency PMTs and improvements to PMT concentrators. These improvements will increase the light yield by a factor of  $\sim 3$ . A preliminary study shows that SNO+ Phase II can set a lower limit on the  $0\nu\beta\beta$  half-life of  $T_{1/2}^{0\nu\beta\beta} > 7 \times 10^{26}$  years (90% CL), for a  $m_{\beta\beta}$  range of 19–46 meV.

## 6. Solar Neutrino Physics

SNO+ has the opportunity to measure low energy solar neutrinos with unprecedented sensitivity. This is due to the reduced production rate of cosmogenic isotopes at the SNOLAB depth and requires that the intrinsic background sources are low enough.

At scintillator purity levels similar to that of Borexino Phase I [20, 25], the unloaded scintillator phase of SNO+ provides excellent sensitivity to CNO, pep, and low energy  $^8\text{B}$  neutrinos. With the scintillator sourced from a supply low in  $^{14}\text{C}$ , SNO+ could also measure pp neutrinos with a sensitivity of a few percent. Due to the relatively high end-point of the spectrum,  $^8\text{B}$   $\nu$ s with energy above the  $^{130}\text{Te}$  end-point can also be measured during the  $0\nu\beta\beta$ -decay phase.

The first measurement of the flux of neutrinos from the subdominant CNO fusion cycle would constrain the metallicity of the solar interior and thus provide critical input to the so-called solar metallicity problem: the current disagreement between helioseismological observations of the speed of sound and model predictions, due to uncertainties in the heavy element (metal) content of the Sun. Historically, model predictions for the speed of sound were in excellent agreement with observation, one of the primary reasons for confidence in the Standard Solar Model during the period of uncertainty surrounding the solar neutrino problem. However, recent improvements in solar atmospheric modeling, including transitioning from one-dimensional to fully three-dimensional models, and including effects such as stratification and inhomogeneities [49], produced a lower value for the heavy element abundance of the photosphere and, thus, changed the prediction for the speed of sound. The theoretical prediction for the CNO flux depends linearly on the core metallicity and can be further constrained by a precision measurement of the  $^8\text{B}$  flux, due to their similar dependence on environmental factors. A measurement of CNO neutrinos would thus resolve this uncertainty and also advance our understanding of heavier mass main-sequence stars, in which the CNO cycle dominates over the pp fusion chain.

Precision measurements of the pep flux and the low energy  $^8\text{B}$  spectrum offer a unique opportunity to probe the interaction of neutrinos with matter and to search for new physics. The shape of the  $\nu_e$  survival probability in

the transition region between vacuum oscillation ( $\leq 1$  MeV) and matter-enhanced oscillation ( $\geq 5$  MeV) is particularly sensitive to new physics effects, such as flavor changing neutral currents or mass-varying neutrinos, due to the resonant nature of the MSW interaction. The pep neutrinos are a line source at 1.44 MeV, thus offering the potential for a direct disappearance measurement partway into this vacuum-matter transition region. However, due to their production region closer to the core of the Sun, the effect of new physics on the  $^8\text{B}$  neutrino spectrum is significantly more pronounced. Thus, the most powerful search combines a precision measurement of the pep flux with a  $^8\text{B}$  spectral measurement.

Borexino has published the first evidence for pep neutrinos [33], with a significance of just over  $2\sigma$  from zero. In order to distinguish different models, a precision of at least 10% is required. A number of experiments have extracted the  $^8\text{B}$  spectrum [42, 50–53], and there is some weak evidence for nonstandard behaviour in the combined data set [54] but the significance is low (roughly  $2\sigma$ ). The theoretical uncertainty on pep neutrinos is very small, and well constrained by solar luminosity measurements. The  $^8\text{B}$  flux is well measured by the SNO experiment [42]. Precise oscillation measurements are therefore possible.

Should the SNO+ scintillator be sourced from a supply naturally low in  $^{14}\text{C}$ , similar to or within an order of magnitude or so of the level observed in Borexino, there also exists the potential for a precision measurement of pp neutrinos. Borexino has produced the first direct detection of these neutrinos, with a precision of a little over 10% [55]. A percent level measurement would allow a test of the so-called luminosity constraint, thus testing for additional energy loss or generation mechanisms in the Sun, and allowing us to monitor the Sun's output using neutrinos.

*6.1. Backgrounds.* The sensitivity of the SNO+ solar phase will depend critically on the leaching rate of  $^{210}\text{Bi}$ . As described in Section 4.2, radon daughters, implanted on the internal AV surface, are expected to leach off during the various SNO+ phases with a rate that depends both on the temperature and on the liquid in contact with the vessel. We will be able to evaluate the levels of these backgrounds both during the initial water fill and during the scintillator fill itself. We are also investigating mitigation techniques to be applied in case the background levels are initially too high to perform the solar measurement. These techniques include *in situ* recirculation, further purification, and the use of a balloon to shield from external backgrounds.

Other backgrounds for the measurements of pep and CNO neutrinos are the levels of  $^{214}\text{Bi}$  ( $^{238}\text{U}$  chain),  $^{212}\text{Bi}$  ( $^{232}\text{Th}$  chain), and  $^{11}\text{C}$  in the pure scintillator.  $^{238}\text{U}$  and  $^{232}\text{Th}$  levels in the scintillator can be effectively constrained using the  $\beta$ - $\alpha$  delayed coincidence, as described in Section 4.  $^{11}\text{C}$  decays, which were the main background for the measurement of pep neutrinos in Borexino [32], can be identified by a threefold coincidence algorithm (see Section 4.5).

Another muon induced isotope that is a potential background for low energy  $^8\text{B}$  neutrino searches is  $^{10}\text{C}$

( $T_{1/2} = 19.3$  s,  $Q$ -value = 3.65 MeV). However, due to the isotope's short half-life and the low cosmic muon rate at SNOLAB depth, it can be removed by cutting events that occur within a few minutes from each muon event.

**6.2. Sensitivity.** Sensitivity studies were performed assuming one year of unloaded scintillator data, which could be either prior to or following the Te-loaded phase. An extended maximum likelihood fit was performed in energy, with a conservative 50% fiducial volume, in order to reduce external background contributions to negligible levels. A two-dimensional fit would allow an increase in fiducial volume and thus improve sensitivity. Thirty-four signals were included in the fit: the four neutrino signals ( $^8\text{B}$ ,  $^7\text{Be}$ , CNO, and pep) as well as thirty background event types. Backgrounds expected to be in equilibrium were constrained to a single fit parameter;  $^{210}\text{Po}$ ,  $^{210}\text{Pb}$ , and  $^{210}\text{Bi}$  were treated independently, that is, not assumed to be in equilibrium with the parent decays. Background parameters included in the fit were the normalisations of  $^7\text{Be}$ ,  $^{39}\text{Ar}$ ,  $^{40}\text{K}$ ,  $^{85}\text{Kr}$ ,  $^{210}\text{Po}$ ,  $^{210}\text{Pb}$ ,  $^{14}\text{C}$ ,  $^{238}\text{U}$  chain, and  $^{232}\text{Th}$  chain.  $^{210}\text{Bi}$  was linked to CNO in the fit due to the similarity of the energy spectra; the separation is best achieved by imposing an *ex situ* constraint on the level of  $^{210}\text{Bi}$  decays, or by using observables other than energy.

The nominal background levels assumed were those achieved by Borexino during their initial running. It was assumed that purification techniques (in particular, distillation) can reduce  $^7\text{Be}$  contamination to negligible levels. Gaussian constraints were applied to backgrounds where an *ex situ* or independent *in situ* measurement of the rate is anticipated.  $\alpha$  tagging is expected to reduce the  $^{210}\text{Po}$  peak by 95%, with an uncertainty of 20% on the remaining 5% of the events. Coincidence decays provide a 50% constraint on  $^{85}\text{Kr}$ , 25% on the  $^{232}\text{Th}$ -chain backgrounds, and 7% on the portion of the  $^{238}\text{U}$  chain that is treated as being in equilibrium.

The fit range was between 0.2 MeV and 6.5 MeV, with 10 keV bins in visible energy. Extending the fit to higher energies would improve the accuracy on the  $^8\text{B}$  flux measurement. Bias and pull tests show that the fit is stable and accurate, and robust to changes in bin size or energy range (to within changes in statistics, e.g.,  $^8\text{B}$  flux accuracy is reduced if the energy range of the fit is reduced).

The simulations suggest that, with one year of data, the uncertainty on the pep flux will be less than 10%. The uncertainty on the linked CNO+  $^{210}\text{Bi}$  flux is 4.5%, into which we fold a conservative uncertainty for separating the two signals, resulting in a 15% predicted uncertainty on the CNO flux. The  $^7\text{Be}$  flux can be measured to 4%, and  $^8\text{B}$  to better than 8%. The uncertainty on the neutrino flux measurements is dominated by statistics, and by correlations between the neutrino signals themselves. A study of energy scale and resolution systematics shows that these parameters can be floated as nuisance parameters in the fit, and the data will constrain them to better than the required precision, with subpercent level impact on the neutrino flux uncertainties. Calibration sources will be deployed in order to measure effects such

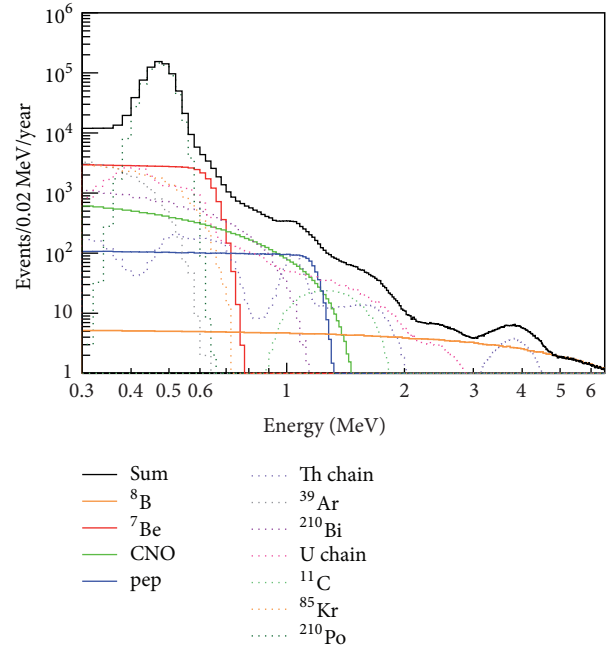


FIGURE 7: Expected solar neutrino fluxes as detected by SNO+ and the corresponding main backgrounds. Backgrounds levels are assumed to be equal to those initially achieved by Borexino [20, 25] (see text). Events are shown for the LAB-PPO scintillator, 400 Nhits/MeV light yield, and a fiducial volume cut of 5.5 m. A 95% reduction is applied to the  $^{214}\text{Bi}$ - $^{214}\text{Po}$  backgrounds via delayed coincidence tagging, and a 95% reduction on the  $^{210}\text{Po}$  and the remaining  $^{214}\text{Po}$  events via alpha tagging.

as any non-Gaussianity of the resolution function, and any potential nonlinearity in the energy scale. In Figure 7 the full solar neutrino signals as detected by SNO+ are shown together with the main background sources for the LAB-PPO scintillator. A fiducial volume cut is applied at 5.5 m.

$^{214}\text{Bi}$ - $^{214}\text{Po}$  events are reduced by 95% using the  $\beta$ - $\alpha$  delayed coincidence as described in Section 4.1. A 95% rejection is applied to the  $^{210}\text{Po}$  events and the remaining  $^{214}\text{Po}$  events via alpha tagging. There is no rejection applied to the  $^{212}\text{Bi}$  and  $^{212}\text{Po}$  events. This is a conservative approach as we expect to reject the majority of these events using a  $\beta$ - $\alpha$  delayed coincidence as for the  $0\nu\beta\beta$  search (see Section 5).

Studies show that the precision with which the pp neutrinos could be observed depends critically on the levels of backgrounds such as  $^{14}\text{C}$  and  $^{85}\text{Kr}$  in the scintillator. If these backgrounds are low, within 10–50 times that seen in Borexino, SNO+ could achieve a few-percent level measurement of the pp neutrino flux with just 6 months of solar neutrino data.

## 7. Antineutrino Studies

Antineutrino events in SNO+ will include geoneutrinos from the Earth's radioactive chains of uranium and thorium, antineutrinos from nuclear reactors, and the antineutrinos emitted by a supernova burst (which are considered in detail in Section 8). The measurement of geoneutrinos will

constrain the radiogenic heat flow of the Earth for geophysics studies, while the measurement of reactor antineutrinos, with a known energy spectrum and a precise propagation distance, can better constrain the neutrino oscillation parameters [56].

**7.1. Signal Detection.** Antineutrinos are detected in SNO+ via inverse beta decay (IBD):  $\bar{\nu}_e$ s with energy greater than 1.8 MeV interact with the protons in the liquid scintillator, producing a positron and a neutron. The antineutrino energy is measured by the scintillation light emitted by the positron as it slows down and annihilates:

$$\begin{aligned} E_{\bar{\nu}_e} &\simeq E_{\text{prompt}} + (M_n - M_p) - m_e \\ &\simeq E_{\text{prompt}} + 0.8 \text{ MeV}, \end{aligned} \quad (2)$$

where  $M_n$ ,  $M_p$ , and  $m_e$  are the neutron, proton, and electron masses. The neutron emitted in the reaction will first thermalize and then be captured by hydrogen, leading to the characteristic 2.22 MeV delayed gamma from the deuterium formation. The prompt + delayed signal allows the identification of the antineutrino event. The coincidence time interval is defined by the period elapsed from neutron emission to its capture, generally about 200  $\mu\text{s}$ , while the spatial separation between the prompt and the delayed event depends on the distance travelled by the delayed gamma before scintillation light is emitted. The exact values to use for the time and distance coincidence tag, to identify the  $\bar{\nu}_e$  events, depend crucially on the correct simulation of the neutron propagation in the scintillator mixture being used (unloaded or Te-loaded scintillator). Neutron propagation in each of the scintillator cocktails planned by SNO+ will be checked with a detailed calibration program using an AmBe source. This source, already extensively used by SNO, has a well-known neutron energy spectrum, extending to energies higher than those of the expected antineutrino signals. The calibration results will be cross-checked with a detailed Monte Carlo simulation.

**7.2. Backgrounds.** As the antineutrino signal is identified as a delayed coincidence in SNO+, the main backgrounds are true or random coincidences in the detector with the identified neutron capture. Most of the background neutrons are expected to come from external background sources and are therefore captured and reconstructed in the external regions of the detector. Events that reach the region inside the vessel can be mitigated by a fiducial volume cut, or by a radius-dependent analysis. The major source of neutrons inside the scintillator is the  $(\alpha, n)$  reactions, which are mainly caused by  $^{210}\text{Po}$ -alpha leached off the vessel surface and are expected to increase with time, as described in Section 4.6. The associated prompt signal, mainly due to the proton recoil, will be at energies lower than 3.5 MeV or, in case the product nucleus is in an excited state, in definite gamma peaks which will allow the study of the  $(\alpha, n)$  background's time evolution.

**7.3. Reactor Antineutrinos and Oscillations.** In SNO+ we expect around 90 reactor antineutrino events per year. The total flux is obtained summing 3 components: (1) 40% of it

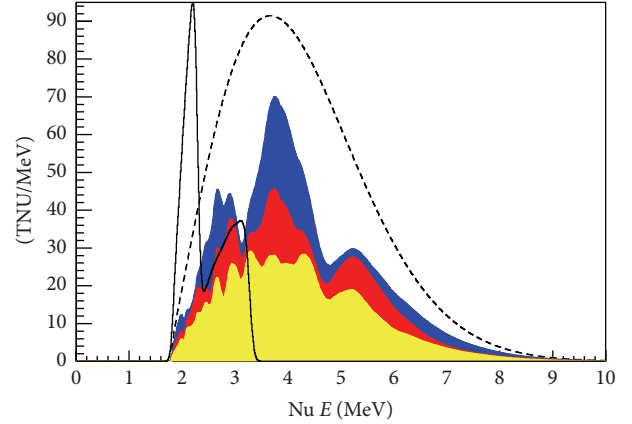


FIGURE 8: Expected visible antineutrino energy spectrum in SNO+, for  $10^{32}$  proton-years per MeV. The nonoscillated reactor spectrum (dashed line) is shown together with the geoneutrino spectrum (solid line, arbitrary normalisation). The stacked oscillated reactor spectrum is shown with different colors, each corresponding to a reactor complex: reactor at 240 km in blue (top), reactors at 350 km in red (middle), and other reactors in yellow (bottom). See text for details.

comes from one reactor complex in Canada at a baseline of 240 km, (2) 20% is from two other complexes at baselines of around 350 km, and (3) 40% is divided between reactors in the USA and elsewhere at longer baselines. The signals from the first two sources (1 and 2) induce a very clear oscillation pattern (see Figure 8), which lead to a high sensitivity to the  $\Delta m_{12}^2$  neutrino oscillation parameter. For  $E < 3.5$  MeV the geoneutrino signals and reactor signals overlap. Most of the backgrounds are concentrated in the energy region of the geoneutrinos. For a preliminary study of the reactor neutrino oscillation sensitivity, we conservatively exclude the region below 3.5 MeV. Assuming a light yield of 300 Nhits/MeV, expected for the Te-loaded phase with perylene as secondary wavelength shifter, and a 5.5 m FV cut, we expect to reach a sensitivity in  $\Delta m_{12}^2$  of  $0.2 \times 10^{-5} \text{ eV}^2$ , similar to the KamLAND result [56] in about 7 years of data taking. The full analysis will take the complete antineutrino spectrum into account, using constraints for the backgrounds, and measuring simultaneously the geoneutrino flux.

Generally, the  $\bar{\nu}_e$  flux from the Canadian reactors (CANDU-type) is expected to be stable in time due to the continuous refuelling process. However, in the next few years there are expected upgrades in which different reactor cores will be turned off, with only one reactor core switched off at a time in each of the complexes. This will cause changes in the reactor spectrum, with an expected total flux reduction below 10% at each moment. This time evolution can be used to identify the very clear oscillation pattern in the reactor spectrum for each of the two identified baselines (240 km and 350 km) and to distinguish them from other antineutrino sources.

The oscillation patterns from the more distant reactors are less evident after they are combined. There is still a visible feature at antineutrino energies of 4.5 MeV from

an accumulation of reactors at distances of the order of 550 km. A detailed description of the spectrum at this energy is still under discussion [57]. A preliminary study shows that the combined systematic uncertainties associated with the unoscillated spectrum description are below 5%. These uncertainties can be reduced using, for the distant reactors (source 3), direct measurements at close-by detectors, like those of Daya Bay [57].

**7.4. Geoneutrinos and Earth Studies.** Interest in geoneutrinos has increased in the last few years with significant collaborations between neutrino physicists and geo-physicists. Joint results may finally explain the radiogenic heat flow of the Earth.

In SNO+ the geoneutrinos from the uranium and thorium chains can be detected. These antineutrinos come mainly from thick continental crust, with increases due to variations in local crust components [58].

The energy spectra of geoneutrinos are well-known for each of the standard decay chains [59]. The effect of neutrino oscillations is largely averaged out due to the long range in production distances, leading to a total survival probability of

$$\langle P_{ee} \rangle = \cos^4 \theta_{13} \cdot \left( 1 - \frac{\sin^2(2\theta_{12})}{2} \right) + \sin^4 \theta_{13} \approx 0.547, \quad (3)$$

where  $\theta_{13} = 9.1^\circ$  and  $\theta_{12} = 33.6^\circ$  [42]. Detailed studies of the impact of the MSW effects on the energy spectrum are in progress.

As a first analysis step, we will fix the total U/Th ratio according to standard geological models [60] and fit for the total flux assuming a precise shape for the energy spectrum of geoneutrinos. The possible effect of local variations of this ratio is being quantified together with that from the low energy reactor spectrum. Systematic uncertainties in the energy scale and energy resolution and from the constraints on the alpha-n backgrounds will vary for each of the data taking phases. Overall, the SNO+ sensitivity to the total flux is expected to be dominated by statistical uncertainties. The accuracy will be close to that of Borexino for similar data-taking periods: the larger volume of the SNO+ detector compensates for the higher rate reactor background. We expect a similar rate of geoneutrinos and reactor antineutrinos in the 1.8 MeV–3.5 MeV energy region. However, the reactor spectrum extends up to much higher energies and contains features that can help in establishing the oscillation parameters. The time evolution analysis will also help to separate the reactor background (Section 7.3). In the Te-loaded phase the low energy backgrounds are expected to be about 50–150 times higher than in the pure scintillator phase, which can make the extraction of the geoneutrino signal more difficult.

We aim to additionally separate both the uranium and thorium contributions and the mantle and crust contributions in a global analysis of the geoneutrino spectrum including data from KamLAND [61] and Borexino [62].

## 8. Supernova Neutrino Observation

The era of neutrino astronomy commenced with the observation of 24 events, all associated with the inverse beta decay of  $\bar{\nu}_e$ , from the collapse of supernova SN 1987A at  $\sim 50$  kpc [63]. SNO+, with its large high purity liquid scintillator volume and the deep location underground, is one of the most promising experiments for the detection of neutrinos from core collapse supernovae (CCSNe), offering a rich sample of detection channels, low backgrounds, and a large number of target particles and nuclei. CCSNe are an exceptional source of neutrinos of all flavors and types, and a measurement is expected to shed light on the explosion mechanism. The shape of the individual supernova (SN)  $\nu_\alpha$  ( $\nu_\alpha = \nu_e, \bar{\nu}_e, \nu_x$ , where in this context  $\nu_x$  is the sum of  $\nu_\mu, \bar{\nu}_\mu, \nu_\tau$ , and  $\bar{\nu}_\tau$ ) energy spectra is expected to approximate a thermal spectrum [64] in the absence of neutrino flavor changing mechanisms. At postbounce times  $t < 1$  s, before shock revival, the flavor changes are expected to be reduced to those induced by the well-known MSW effect in a quasi-static environment [65, 66]. At later times, many further effects interfere, significantly modifying the spectral shape. These effects are nontrivial and still lack a full understanding and a consistent analytical treatment. At present, sensitivity studies to thermal spectral parameters are only meaningful for at most the first second of the burst. It is estimated that half of all neutrinos are emitted in this time span [67].

**8.1. Signal Detection in SNO+.** For the detection potential of SNO+ presented in this paper, we assume that the distance from the SN to Earth is  $d = 10$  kpc, known from, for example, the detection of the electromagnetic radiation released in the SN event, and that  $3 \times 10^{53}$  erg of binding energy ( $\epsilon_\nu$ ) are released in the form of neutrinos, equally partitioned amongst all six flavors and types. The mean energies used are 12 MeV for  $\nu_e$ , 15 MeV for  $\bar{\nu}_e$ , and 18 MeV for  $\nu_x$  [68], which are generic mean SN neutrino energies [69] consistent with the findings from SN 1987A.

The possible SN neutrino interaction channels during the SNO+ pure scintillator phase are listed in Table 5 together with the expected event rates. Several events due to  $\bar{\nu}_e$  are expected, because of the comparatively large cross section for the IBD reaction [70]. This process, seen during SN 1987A, is the only interaction of SN neutrinos observed to date. Additionally, SNO+ can measure the flux of  $\nu_x$  and  $\nu_e$ . As the mean neutrino energy is below about 30 MeV,  $\nu_e$ s and  $\bar{\nu}_e$ s will be detected mainly by the charged current (CC) interactions, while supernova  $\nu_x$ s can only be detected by the more challenging neutral current (NC) reactions. One NC reaction is neutrino-proton elastic scattering (ES),  $\nu + p \rightarrow \nu + p$  [71], which is the only channel that provides spectral information about  $\nu_x$ s. The total cross section of this process [72] is about a factor of three smaller than the cross section of IBD; however, the reaction is possible for all six neutrino types yielding a similar number of events for a detector threshold above  $\sim 0.2$  MeV.

**8.2. SNO+ Sensitivity to the  $\nu_x$  Spectral Shape.** In the preliminary estimations of the SNO+ sensitivity to  $\nu_x$  spectral

TABLE 5: Supernova neutrino interaction channels in LAB-PPO. The event rates, per 780 tonnes of material, assume the incoming neutrino time-integrated flux described in the text. No flavor changing mechanisms are considered. The uncertainties on the event rates only include the cross section uncertainties [16].

Reaction	Number of events
NC: $\nu + p \rightarrow \nu + p$	$429.1 \pm 12.0^a$
CC: $\bar{\nu}_e + p \rightarrow n + e^+$	$194.7 \pm 1.0$
CC: $\bar{\nu}_e + {}^{12}\text{C} \rightarrow {}^{12}\text{B}_{\text{g.s.}} + e^+$	$7.0 \pm 0.7$
CC: $\nu_e + {}^{12}\text{C} \rightarrow {}^{12}\text{N}_{\text{g.s.}} + e^-$	$2.7 \pm 0.3$
NC: $\nu + {}^{12}\text{C} \rightarrow {}^{12}\text{C}^*(15.1\text{ MeV}) + \nu'$	$43.8 \pm 8.7$
CC/NC: $\nu + {}^{12}\text{C} \rightarrow {}^{11}\text{C} \text{ or } {}^{11}\text{B} + X$	$2.4 \pm 0.5$
$\nu$ -electron elastic scattering	$13.1^b$

<sup>a</sup>  $118.9 \pm 3.4$  above a trigger threshold of 0.2 MeV visible energy.

<sup>b</sup> The Standard Model cross section uncertainty is <1%.

shape through  $\nu$ -p ES we conservatively assume a spatial radius cut of 5 m and a 0.2 MeV threshold, corresponding to a minimal neutrino energy of  $E_\nu^{\text{min}} \approx 21.9$  MeV. This is close to the threshold we expect to use for events that will be permanently stored. We are currently discussing other settings for the trigger thresholds to avoid any loss of potential low energy supernova events.

In Figure 9 the reconstructed energy spectrum of all neutrinos emitted in the first second of the SN ( $\nu_e$ ,  $\bar{\nu}_e$ , and  $\nu_x$ ) and detected in SNO+ via the  $\nu$ -p ES reaction is shown together with the true neutrino spectrum. The reconstructed energy spectrum is obtained from the detected proton energy unfolded using the TUnfold algorithm [73], on the basis of binned data. The strongly nonlinear quenching of the proton energy, which shifts most of the scattering events below  $\sim 0.5$  MeV electron equivalent energy, and the finite detector resolution are taken into account. The number of events in the lowest bin is slightly overestimated, due to bin-to-bin migrations caused by the finite energy resolution. The statistical and total systematic uncertainties are also shown. A fit to the  $\nu_x$  spectrum is only possible if the  $\nu_e$  and  $\bar{\nu}_e$  spectra are measured independently. SNO+ is sensitive to the spectral shape of  $\bar{\nu}_e$ s via the IBD reaction, while in the case of  $\nu_e$ s it has to be assumed that an independent detector, with, for example, a Pb target like HALO [74] or a LAr target [70], provides the necessary spectral information.

The resulting best fit  $E_\nu$  spectrum is also shown in Figure 9 and is in excellent agreement. The systematic uncertainties propagated within the fit are the  $\nu$ -p ES cross section, the number of target protons,  $N_p$ , the ionization quenching parameter, the spectral  $\nu_e$  and  $\bar{\nu}_e$  parameters, and the energy resolution of the detector. The corresponding best fit values are  $\langle E_{\nu_x} \rangle = 17.8_{-3.0}^{+3.5}$  (stat.) $_{-0.8}^{+0.2}$  (syst.) MeV and  $\varepsilon_{\nu_x} = (102.5_{-42.2}^{+82.3}$  (stat.) $_{-13.0}^{+16.2}$  (syst.))  $\times 10^{51}$  erg [16], while the respective expectation values are 18 MeV and  $100 \times 10^{51}$  erg.

8.3. SNEWS. SNO+ is preparing to participate in the inter-experiment Supernova Early Warning System (SNEWS) [75], which has the goal to provide a fast and reliable alert using the

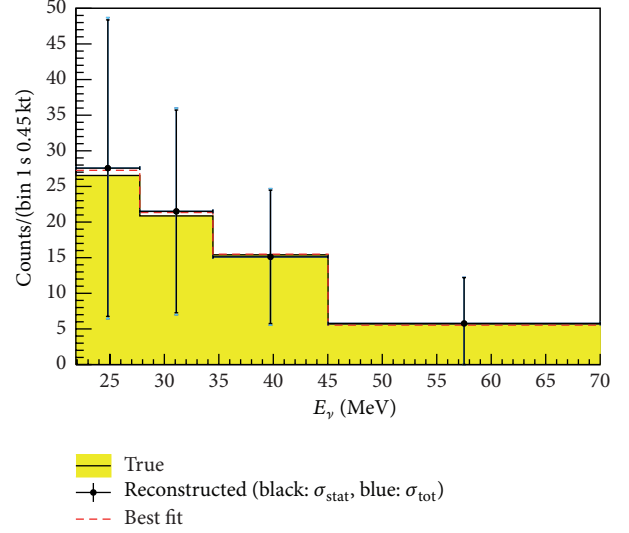


FIGURE 9: True, reconstructed, and best fit SN neutrino energy distribution of the  $\nu$ -p ES detection channel within the FV and above the detector threshold [16]. Shown is the sum of the  $\nu_e$ ,  $\bar{\nu}_e$ , and  $\nu_x$  spectra, considering their time-integrated flux in the first second of the reference SN. The statistical uncertainties are shown in black, while the total uncertainties are shown in blue. The contribution from systematic uncertainty is too small to be resolved.

coincident observation of burst signals in several operating detectors. As neutrinos escape from the SN tens of minutes up to several hours before the first photons, their detection offers the possibility of alerting the astronomical community to the appearance of the next SN light signal.

## 9. Exotic Physics Searches

Due to its location deep underground, which significantly reduces the cosmogenic background, and the high radio-purity of the materials used, SNO+ has a unique sensitivity to search for exotic physics, including certain modes of nucleon decay and axion or axion-like particle searches.

9.1. Invisible Nucleon Decay. Nucleon decay modes to a final state undetected by the experiment, for example,  $n \rightarrow 3\nu$ , can be searched for by detecting the decay products of the remaining unstable nucleus as it deexcites. This process has been previously investigated by some experiments such as SNO [76] by searching for the decay of  ${}^{16}\text{O}$  nuclei, and Borexino [77] and KamLAND [78] by looking for the decay of  ${}^{12}\text{C}$  nuclei. We plan to search for the invisible nucleon decay of  ${}^{16}\text{O}$  during the initial water phase of the experiment. In the case of a decaying neutron, the resulting  ${}^{15}\text{O}$  will deexcite emitting a 6.18 MeV gamma 44% of the time. For a decaying proton, the nucleus is left as  ${}^{15}\text{N}$  which in 41% of the decays deexcites emitting a 6.32 MeV gamma [79]. Both these signals will be in a favorable region of the SNO+ energy spectrum (5.4 MeV–9 MeV) in which few backgrounds are expected. These are (1) internal and external  ${}^{208}\text{Tl}$  and  ${}^{214}\text{Bi}$  decays, (2) solar neutrinos, and (3) reactor and atmospheric

TABLE 6: Expected backgrounds in the 5.4–9 MeV energy region during six months of water fill. A fiducial volume cut of 5.5 m is applied to all events. The events after the  $\cos\theta_{\text{sun}} > -0.8$  cut are also shown.  $\epsilon(n)$  and  $\epsilon(p)$  are the neutron and proton decay-mode detection efficiencies in the 5.5 m FV and energy window.

Decay source	Events in six months	
	$\cos\theta_{\text{sun}} > -0.8$ Cut	
$^{214}\text{Bi}$	0	0
$^{208}\text{Tl}$	0.6	0.6
Solar neutrinos	86.4	17.7
Reactor antineutrinos	1.5	1.3
External $^{214}\text{Bi}$ - $^{208}\text{Tl}$	9.2	8.9
Total	97.7	28.5
$\epsilon(n)$	0.1089	0.1017
$\epsilon(p)$	0.1264	0.1129

antineutrinos. The expected contribution of each background in the 5.4–9 MeV energy region, in six months of running, is shown in Table 6. The targeted purity for the SNO+ internal water is the average of the SNO collaboration’s  $\text{H}_2\text{O}$  and  $\text{D}_2\text{O}$  levels (see Table 2). The purity can be measured *in situ* using events below 5 MeV and cross checked using water assays. Solar neutrino events can be reduced by placing a cut on the direction of the event, which is reconstructed using the topology of the detected Cherenkov light. Reactor antineutrino events can be tagged using a delayed coincidence. The background due to atmospheric neutrinos is expected to be small based on SNO data [76].

The events in Table 6 are given for a fiducial volume cut of 5.5 m, which helps in reducing the external backgrounds. An additional cut at  $\cos\theta_{\text{sun}} > -0.8$  relative to the solar direction further reduces the dominant solar background, removing  $\sim 80\%$  of the events with a sacrifice of  $\sim 10\%$  on the signals and the isotropic backgrounds. Figure 10 shows the energy spectrum of the water phase backgrounds: solar neutrinos, reactor antineutrinos, and radioactive decays from the uranium and thorium chains, after the two cuts are applied. It also shows the shapes based on the current best limits of the signal gammas from invisible proton [76] and neutron [78] decay.

Using a Poisson method [80] we can set the lower limit, at 90% CL, on the invisible nucleon decay lifetime  $\tau$  by

$$\tau > \frac{N_{\text{nucleons}} \times \epsilon \times f_T}{S_{90\%}}, \quad (4)$$

where  $N_{\text{nucleons}} = 2.4 \times 10^{32}$ ,  $\epsilon$  is the efficiency of detecting the decay in the signal window from Table 6,  $S_{90\%}$  is the expected signal events at 90% CL, and  $f_T$  is the live-time of 0.5 years. Assuming we reach the expected background, a limit of  $\tau_n > 1.25 \times 10^{30}$  and  $\tau_p > 1.38 \times 10^{30}$  years for the decay of neutrons and protons, respectively, can be set. This is an improvement over the existing limit set by KamLAND,  $\tau > 5.8 \times 10^{29}$  years, by a factor of  $\sim 2$  with just six months of running time. A likelihood approach is in development which is expected to provide a further improvement on the limit.

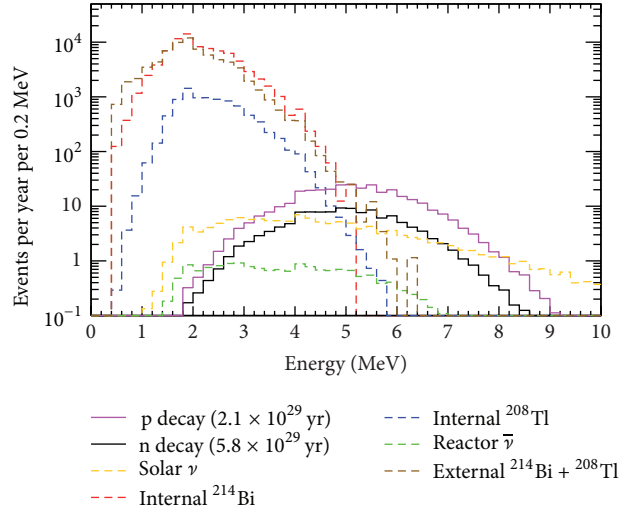


FIGURE 10: Expected energy spectrum for the water phase backgrounds. The signal from invisible proton [76] and neutron [78] decay is also shown. A fiducial radius cut of 5.5 m and a cut on  $\cos\theta_{\text{sun}} > -0.8$  are applied.

9.2. *Axion-Like Particle Search.* An axion-like particle (ALP) is defined as a neutral pseudoscalar particle that exists as an extension to the QCD Lagrangian [81].

A possible reaction channel for ALP production in the Sun is  $p + d \rightarrow {}^3\text{He} + A$ , where  $A$  is the ALP with an energy of 5.5 MeV [82]. In SNO+ the couplings of ALPs to electrons,  $g_{Ae}$ , photons,  $g_{A\gamma}$ , and nucleons,  $g_{AN}$ , can be observed mainly through Compton conversion ( $A + e^- \rightarrow e^- + \gamma$ ) and the axioelectric effect ( $A + e^- + Z_X \rightarrow e^- + Z_X$ , with  $Z_X$  the charge of the involved nucleus  $X$ ). In both cases, for low ALP masses the signature is monoenergetic at  $\sim 5$  MeV electromagnetic energy deposition.

Different strategies for different phases of SNO+ are used for the detection of ALPs. In the water phase, the most likely interaction is the Compton conversion, which produces a Cherenkov ring with topology similar to that of  ${}^8\text{B}$ -neutrinos. The main background events are very similar to those described for the invisible nucleon decay search (see Section 9.1) as the two signals have similar energies. However, since the Compton conversion has a strong directional bias, we expect to remove a significant amount of isotropic backgrounds, leaving  ${}^8\text{B}$ -neutrinos as the dominant one. With 6 months of water data, due to the deeper location and larger fiducial volume, we expect to approach the current limit set by Borexino [82].

The BGO collaboration proposed a separate limit on the ALP couplings without having to assume axions interact via Compton conversion [83]. In this case, the detection of solar ALPs via the axioelectric effect, which depends on the nucleus charge as  $Z_X^5$ , could be particularly interesting during the Te-loaded phase. Due to the significantly large tellurium mass, SNO+ has the possibility of improving the limit on the axion-electron coupling constant set by the BGO collaboration by several orders of magnitude.

## 10. Conclusions

In this paper the broad physics program of the SNO+ experiment is presented. Three main data taking phases are planned: one with the detector filled with ultra-pure water, one with unloaded liquid scintillator, and one with 2.34 tonnes of tellurium loaded into the detector.

The primary physics goal of SNO+ is a sensitive search for  $0\nu\beta\beta$ -decay of  $^{130}\text{Te}$ . We expect to set a lower limit on the half-life of this process of  $T_{1/2}^{0\nu\beta\beta} > 9 \times 10^{25}$  yr (90% CL) in 5 years of data taking. This limit corresponds to an effective Majorana mass ranging from 55 to 133 meV, at the top of the inverted neutrino mass hierarchy. The possibility of loading 10 times more tellurium in order to cover the majority of the inverted hierarchy region is under investigation.

Along with the  $0\nu\beta\beta$ -decay search, SNO+ also has the potential to measure the low energy solar neutrinos, like pep neutrinos. If the same purity levels as initially achieved by Borexino are reached, SNO+ can measure the pep neutrinos with an uncertainty less than 10% in one year of data taking with pure liquid scintillator. Additionally, if the background is low enough SNO+ can measure CNO neutrinos.

Another physics topic that can be explored by SNO+ is the measurement of geoneutrinos in a geologically interesting location, which will be complementary to the measurements done by Borexino and KamLAND. Furthermore, SNO+ can measure reactor antineutrinos, which will help in reducing the uncertainty on the oscillation parameters.

With its depth and low background, SNO+ has an extraordinary opportunity to measure the supernova  $\nu_x$  energy spectrum for the first time. This measurement provides valuable information in order to probe and constrain supernova dynamics. Participation in SNEWS will further support a reliable early warning to the astronomical community in the event of a nearby supernova.

During the water fill, SNO+ can search for exotic physics and set competitive limits in the invisible nucleon decay of  $^{16}\text{O}$ .

We expect to start operation with the water fill phase soon, followed by the liquid scintillator fill phase after a few months of data taking. The Te-loaded phase is foreseen in 2017.

## Conflict of Interests

The authors declare that there is no conflict of interests regarding the publication of this paper.

## Acknowledgments

Capital construction funds for the SNO+ experiment are provided by the Canada Foundation for Innovation (CFI). This work has been in part supported by the Science and Technology Facilities Council (STFC) of the United Kingdom (Grants nos. ST/J001007/1 and ST/K001329/1), the Natural Sciences and Engineering Research Council of Canada, the Canadian Institute for Advanced Research (CIFAR), the National Science Foundation, national funds from Portugal

and European Union FEDER funds through the COMPETE program, through FCT, Fundação para a Ciência e a Tecnologia (Grant no. EXPL/FIS-NUC/1557/2013), the Deutsche Forschungsgemeinschaft (Grant no. ZU123/5), the European Union's Seventh Framework Programme (FP7/2007-2013, under the European Research Council (ERC) Grant Agreement no. 278310 and the Marie Curie Grant Agreement no. PIEF-GA-2009-253701), the Director, Office of Science, of the U.S. Department of Energy (Contract no. DE-AC02-05CH11231), the U.S. Department of Energy, Office of Science, Office of Nuclear Physics (Award no. DE-SC0010407), the U.S. Department of Energy (Contract no. DE-AC02-98CH10886), the National Science Foundation (Grant no. NSF-PHY-1242509), and the University of California, Berkeley. The authors acknowledge the generous support of the Vale and SNOLAB staff.

## References

- [1] K. Zuber, "Double-beta decay," *Contemporary Physics*, vol. 45, no. 6, pp. 491–502, 2004.
- [2] A. M. Serenelli, W. C. Haxton, and C. Peña-Garay, "Solar models with accretion. I. Application to the solar abundance problem," *The Astrophysical Journal*, vol. 743, no. 1, article 24, 2011.
- [3] A. Friedland, C. Lunardini, and C. Peña-Garay, "Solar neutrinos as probes of neutrino-matter interactions," *Physics Letters B*, vol. 594, no. 3-4, pp. 347–354, 2004.
- [4] W. C. Haxton and A. M. Serenelli, "CN-cycle solar neutrinos and the Sun's primordial core metallicity," *The Astrophysical Journal*, vol. 687, no. 1, pp. 678–691, 2008.
- [5] M. C. Chen, "The SNO liquid scintillator project," *Nuclear Physics B—Proceedings Supplements*, vol. 145, no. 1–3, pp. 65–68, 2005.
- [6] B. Aharmim, S. N. Ahmed, T. C. Andersen et al., "Measurement of the cosmic ray and neutrino-induced muon flux at the Sudbury Neutrino Observatory," *Physical Review D*, vol. 80, no. 1, Article ID 012001, 2009.
- [7] J. Boger, R. L. Hahn, J. K. Rowley et al., "The Sudbury Neutrino Observatory," *Nuclear Instruments and Methods in Physics Research A*, vol. 449, no. 1-2, pp. 172–207, 2000.
- [8] N. Jelley, A. B. McDonald, and R. G. H. Robertson, "The Sudbury Neutrino Observatory," *Annual Review of Nuclear and Particle Science*, vol. 59, pp. 431–465, 2009.
- [9] P. G. Jones, *Background rejection for the neutrinoless double-beta decay experiment SNO+ [Ph.D. thesis]*, Lincoln College, Oxford, UK, 2011, <http://ethos.bl.uk/OrderDetails.do?uin=uk.bl.ethos.559770>.
- [10] M. Yeh, S. Hans, W. Beriguete et al., "A new water-based liquid scintillator and potential applications," *Nuclear Instruments and Methods in Physics Research, Section A: Accelerators, Spectrometers, Detectors and Associated Equipment*, vol. 660, no. 1, pp. 51–56, 2011.
- [11] H. M. O'Keefe, E. O'Sullivan, and M. C. Chen, "Scintillation decay time and pulse shape discrimination in oxygenated and deoxygenated solutions of linear alkylbenzene for the SNO+ experiment," *Nuclear Instruments and Methods in Physics Research A*, vol. 640, no. 1, pp. 119–122, 2011.
- [12] S. Grullon, "Light yield and scintillation decay time constants of Te-loaded liquid scintillator for the SNO+ experiment," in

- Proceedings of the 26th International Conference on Neutrino Physics and Astrophysics (Neutrino '14)*, Boston University, Boston, Mass, USA, June 2014.
- [13] H. Wan Chan Tseung, J. Kaspar, and N. Tolich, "Measurement of the dependence of the light yields of linear alkylbenzene-based and EJ-301 scintillators on electron energy," *Nuclear Instruments and Methods in Physics Research Section A: Accelerators, Spectrometers, Detectors and Associated Equipment*, vol. 654, no. 1, pp. 318–323, 2011.
- [14] H. Wan Chan Tseung and N. Tolich, "Ellipsometric measurements of the refractive indices of linear alkylbenzene and EJ-301 scintillators from 210 to 1000 nm," *Physica Scripta*, vol. 84, no. 3, Article ID 035701, 2011.
- [15] B. von Krosigk, L. Neumann, R. Nolte, S. Röttger, and K. Zuber, "Measurement of the proton light response of various LAB based scintillators and its implication for supernova neutrino detection via neutrino-proton scattering," *The European Physical Journal C*, vol. 73, article 2390, 2013.
- [16] B. von Krosigk, *Measurement of proton and  $\alpha$ -particle quenching in LAB based scintillators and determination of spectral sensitivities to supernova neutrinos in the SNO+ detector [Ph.D. thesis]*, Technische Universität Dresden, Dresden, Germany, 2015.
- [17] J. B. Birks, *The Theory and Practice of Scintillation Counting*, Pergamon Press, New York, NY, USA, 1964.
- [18] R. Ford, M. Chen, O. Chkvorets, D. Hallman, and E. Vázquez-Jáuregui, "SNO+ scintillator purification and assay," *AIP Conference Proceedings*, vol. 1338, pp. 183–194, 2011.
- [19] R. J. Ford, "A scintillator purification plant and fluid handling system for SNO+," *AIP Conference Proceedings*, vol. 1672, Article ID 080003, 2015.
- [20] C. Arpesella, H. O. Back, M. Balata et al., "Direct measurement of the  $^7\text{Be}$  solar neutrino flux with 192 days of borexino data," *Physical Review Letters*, vol. 101, no. 9, Article ID 091302, 2008.
- [21] K. Eguchi, S. Enomoto, K. Furuno et al., "First results from KamLAND: evidence for reactor antineutrino disappearance," *Physical Review Letters*, vol. 90, no. 2, Article ID 021802, 2003.
- [22] S. Hans, R. Rosero, L. Hu et al., "Purification of telluric acid for SNO+ neutrinoless double-beta decay search," *Nuclear Instruments and Methods in Physics Research Section A: Accelerators, Spectrometers, Detectors and Associated Equipment*, vol. 795, pp. 132–139, 2015.
- [23] R. Alves, S. Andringa, S. Bradbury et al., "The calibration system for the photomultiplier array of the SNO+ experiment," *Journal of Instrumentation*, vol. 10, no. 3, Article ID P03002, 2015.
- [24] National Nuclear Data Center, "Nuclear structure & decay data," <http://www.nndc.bnl.gov/nudat2/>.
- [25] G. Alimonti, C. Arpesella, M. B. Avanzini et al., "The liquid handling systems for the Borexino solar neutrino detector," *Nuclear Instruments and Methods in Physics Research Section A: Accelerators, Spectrometers, Detectors and Associated Equipment*, vol. 609, no. 1, pp. 58–78, 2009.
- [26] F. Alessandria, E. Andreotti, R. Ardito et al., "CUORE crystal validation runs: results on radioactive contamination and extrapolation to CUORE background," *Astroparticle Physics*, vol. 35, no. 12, pp. 839–849, 2012.
- [27] T. W. Armstrong, K. C. Chandler, and J. Barish, "Calculations of neutron flux spectra induced in the Earth's atmosphere by galactic cosmic rays," *Journal of Geophysical Research*, vol. 78, no. 16, pp. 2715–2726, 1973.
- [28] N. Gehrels, "Instrumental background in balloon-borne gamma-ray spectrometers and techniques for its reduction," *Nuclear Instruments and Methods in Physics Research Section A: Accelerators, Spectrometers, Detectors and Associated Equipment*, vol. 239, no. 2, pp. 324–349, 1985.
- [29] G. Alimonti, G. Angloher, C. Arpesella et al., "Measurement of the  $^{14}\text{C}$  abundance in a low-background liquid scintillator," *Physics Letters B*, vol. 422, no. 1–4, pp. 349–358, 1998.
- [30] S. Abe, S. Enomoto, K. Furuno et al., "Production of radioactive isotopes through cosmic muon spallation in KamLAND," *Physical Review C*, vol. 81, no. 2, Article ID 025807, 2010.
- [31] G. Bellini, J. Benziger, D. Bick et al., "Precision measurement of the  $^7\text{Be}$  solar neutrino interaction rate in Borexino," *Physical Review Letters*, vol. 107, no. 14, Article ID 141302, 2011.
- [32] C. Galbiati, A. Pocar, D. Franco, A. Ianni, L. Cadonati, and S. Schönert, "Cosmogenic  $^{11}\text{C}$  production and sensitivity of organic scintillator detectors to pep and CNO neutrinos," *Physical Review C*, vol. 71, no. 5, Article ID 055805, 2005.
- [33] G. Bellini, J. Benziger, D. Bick et al., "First evidence of pep solar neutrinos by direct detection in Borexino," *Physical Review Letters*, vol. 108, no. 5, Article ID 051302, 6 pages, 2012.
- [34] V. Lozza and J. Petzoldt, "Cosmogenic activation of a natural tellurium target," *Astroparticle Physics*, vol. 61, pp. 62–71, 2015.
- [35] E. Arushanova, "Pileup background rejection in SNO+ experiment," in *Proceedings of the Joint Particle, Astroparticle, and Nuclear Physics Groups Annual Meeting (IoP '15)*, Manchester, UK, April 2015.
- [36] E. Arushanova and A. R. Back, "Probing neutrinoless double beta decay with SNO+," <http://arxiv.org/abs/1505.00247>.
- [37] I. Lawson and B. Cleveland, "Low background counting at SNOLAB," in *Proceedings of the Topical Workshop on Low Radioactivity Techniques (LRT '10)*, vol. 1338 of *AIP Conference Proceedings*, pp. 68–77, Sudbury, Canada, August 2010.
- [38] B. Aharmim, S. N. Ahmed, A. E. Anthony et al., "Electron energy spectra, fluxes, and day-night asymmetries of  $^8\text{B}$  solar neutrinos from measurements with NaCl dissolved in the heavy-water detector at the Sudbury Neutrino Observatory," *Physical Review C*, vol. 72, no. 5, Article ID 055502, 47 pages, 2005.
- [39] N. J. T. Smith, "Facility and science developments at SNOLAB," in *Proceedings of the ASPERA Workshop: The Next Generation Projects in Deep Underground Laboratories*, Zaragoza, Spain, June 2011, <http://indico.cern.ch/event/130734/contribution/21/material/slides/0.pdf>.
- [40] M. Redshaw, B. J. Mount, E. G. Myers, and F. T. Avignone III, "Masses of  $^{130}\text{Te}$  and  $^{130}\text{Xe}$  and double- $\beta$ -decay Q value of  $^{130}\text{Te}$ ," *Physical Review Letters*, vol. 102, no. 21, Article ID 212502, 4 pages, 2009.
- [41] R. Arnold, C. Augier, J. Baker et al., "Measurement of the  $\beta\beta$  decay half-life of  $^{130}\text{Te}$  with the NEMO-3 Detector," *Physical Review Letters*, vol. 107, no. 6, Article ID 062504, 2011.
- [42] B. Aharmim, S. N. Ahmed, A. E. Anthony et al., "Combined analysis of all three phases of solar neutrino data from the Sudbury Neutrino Observatory," *Physical Review C*, vol. 88, no. 2, Article ID 025501, 2013.
- [43] J. Barea, J. Kotila, and F. Iachello, "Nuclear matrix elements for double- $\beta$  decay," *Physical Review C*, vol. 87, no. 1, Article ID 014315, 2013.
- [44] J. Kotila and F. Iachello, "Phase-space factors for double- $\beta$  decay," *Physical Review C—Nuclear Physics*, vol. 85, no. 3, Article ID 034316, 2012.

- [45] F. Šimkovic, V. Rodin, A. Faessler, and P. Vogel, “ $0\nu\beta\beta$  and  $2\nu\beta\beta$  nuclear matrix elements, quasiparticle random-phase approximation, and isospin symmetry restoration,” *Physical Review C*, vol. 87, no. 4, Article ID 045501, 2013.
- [46] J. Menéndez, A. Poves, E. Caurier, and F. Nowacki, “Disassembling the nuclear matrix elements of the neutrinoless  $\beta\beta$  decay,” *Nuclear Physics A*, vol. 818, no. 3-4, pp. 139–151, 2009.
- [47] J. Hyvärinen and J. Suhonen, “Nuclear matrix elements for  $0\nu\beta\beta$  decays with light or heavy Majorana-neutrino exchange,” *Physical Review C*, vol. 91, no. 2, Article ID 024613, 2015.
- [48] T. R. Rodríguez and G. Martínez-Pinedo, “Energy density functional study of nuclear matrix elements for neutrinoless  $\beta\beta$  decay,” *Physical Review Letters*, vol. 105, no. 25, Article ID 252503, 2010.
- [49] M. Asplund, N. Grevesse, A. J. Sauval, and P. Scott, “The chemical composition of the sun,” *Annual Review of Astronomy and Astrophysics*, vol. 47, pp. 481–522, 2009.
- [50] S. Abe, K. Furuno, A. Gando et al., “Measurement of the  $^8\text{B}$  solar neutrino flux with the KamLAND liquid scintillator detector,” *Physical Review C*, vol. 84, no. 3, Article ID 035804, 6 pages, 2011.
- [51] G. Bellini, J. Benziger, S. Bonetti et al., “Measurement of the solar  $^8\text{B}$  neutrino rate with a liquid scintillator target and 3 MeV energy threshold in the Borexino detector,” *Physical Review D*, vol. 82, no. 3, Article ID 033006, 2010.
- [52] M. Smy, “Results from Super-Kamiokande,” in *Proceedings of the 25th International Conference on Neutrino Physics and Astrophysics (Neutrino '12)*, Kyoto, Japan, June 2012.
- [53] A. Renshaw, “Solar neutrino results from Super-Kamiokande,” *Physics Procedia*, vol. 61, pp. 345–354, 2015.
- [54] R. Bonventre, A. LaTorre, J. R. Klein, G. D. Orebi Gann, S. Seibert, and O. Wasalski, “Nonstandard models, solar neutrinos, and large  $\theta_{13}$ ,” *Physical Review D*, vol. 88, no. 5, Article ID 053010, 2013.
- [55] G. Bellini, J. Benziger, D. Bick et al., “Neutrinos from the primary proton-proton fusion process in the Sun,” *Nature*, vol. 512, no. 7515, pp. 383–386, 2014.
- [56] A. Gando, Y. Gando, K. Ichimura et al., “Constraints on  $\theta_{13}$  from a three-flavor oscillation analysis of reactor antineutrinos at KamLAND,” *Physical Review D*, vol. 83, no. 5, Article ID 052002, 2011.
- [57] F. P. An, A. B. Balantekin, H. R. Band et al., “Spectral measurement of electron antineutrino oscillation amplitude and frequency at Daya Bay,” *Physical Review Letters*, vol. 112, no. 6, Article ID 061801, 2014.
- [58] H. K. C. Perry, J.-C. Mareschal, and C. Jaupart, “Enhanced crustal geo-neutrino production near the Sudbury Neutrino Observatory, Ontario, Canada,” *Earth and Planetary Science Letters*, vol. 288, no. 1-2, pp. 301–308, 2009.
- [59] S. Enomoto, “Using Neutrinos to study the earth: geo-neutrinos,” in *Proceedings of the 13th International Workshop on Neutrino Telescopes (NeuTel '09)*, Venice, Italy, March 2009.
- [60] A. M. Dziewonski and D. L. Anderson, “Preliminary reference Earth model,” *Physics of the Earth and Planetary Interiors*, vol. 25, no. 4, pp. 297–356, 1981.
- [61] A. Gando, Y. Gando, K. Ichimura et al., “Partial radiogenic heat model for Earth revealed by geoneutrino measurements,” *Nature Geoscience*, vol. 4, pp. 647–651, 2011.
- [62] G. Bellini, J. Benziger, D. Bick et al., “Measurement of geo-neutrinos from 1353 days of Borexino,” *Physics Letters B*, vol. 722, no. 4-5, pp. 295–300, 2013.
- [63] I. V. Krivosheina, “SN1987A—historical view about registration of the neutrino signal with BAKSAN, Kamiokande II and IMB detectors,” *International Journal of Modern Physics D*, vol. 13, no. 10, Article ID 2085, 2004.
- [64] M. T. Keil, G. G. Raffelt, and H.-T. Janka, “Monte Carlo study of supernova neutrino spectra formation,” *The Astrophysical Journal*, vol. 590, no. 2, pp. 971–991, 2003.
- [65] J. Xu, M.-Y. Huang, L.-J. Hu, X.-H. Guo, and B.-L. Young, “Detection of supernova neutrinos on the earth for large  $\theta_{13}$ ,” *Communications in Theoretical Physics*, vol. 61, no. 2, pp. 226–234, 2014.
- [66] S. Sarikas, G. G. Raffelt, L. Hüpdepohl, and H.-T. Janka, “Suppression of self-induced flavor conversion in the Supernova accretion phase,” *Physical Review Letters*, vol. 108, no. 6, Article ID 061101, 2012.
- [67] G. Pagliaroli, F. Vissani, M. L. Costantini, and A. Ianni, “Improved analysis of SN1987A antineutrino events,” *Astroparticle Physics*, vol. 31, no. 3, pp. 163–176, 2009.
- [68] B. Dasgupta and J. F. Beacom, “Reconstruction of supernova  $\nu_\mu$ ,  $\nu_\tau$ , anti- $\nu_\mu$ , and anti- $\nu_\tau$  neutrino spectra at scintillator detectors,” *Physical Review D*, vol. 86, no. 11, Article ID 113006, 2011.
- [69] T. Lund and J. P. Kneller, “Combining collective, MSW, and turbulence effects in supernova neutrino flavor evolution,” *Physical Review D*, vol. 88, no. 2, Article ID 023008, 2013.
- [70] K. Scholberg, “Supernova neutrino detection,” *Annual Review of Nuclear and Particle Science*, vol. 62, pp. 81–103, 2012.
- [71] J. F. Beacom, W. M. Farr, and P. Vogel, “Detection of supernova neutrinos by neutrino-proton elastic scattering,” *Physical Review D*, vol. 66, no. 3, Article ID 033001, 2002.
- [72] L. A. Ahrens, S. H. Aronson, P. L. Connolly et al., “Measurement of neutrino-proton and antineutrino-proton elastic scattering,” *Physical Review D*, vol. 35, no. 3, pp. 785–809, 1987.
- [73] S. Schmitt, “TUnfold: an algorithm for correcting migration effects in high energy physics,” *Journal of Instrumentation*, vol. 7, no. 10, Article ID T10003, 2012.
- [74] D. Väänänen and C. Volpe, “The neutrino signal at HALO: learning about the primary supernova neutrino fluxes and neutrino properties,” *Journal of Cosmology and Astroparticle Physics*, vol. 2011, article 019, 2011.
- [75] P. Antonioli, R. T. Fienberg, F. Fleuret et al., “SNEWS: the SuperNova Early Warning System,” *New Journal of Physics*, vol. 6, article 114, 2004.
- [76] S. N. Ahmed, A. E. Anthony, E. W. Beier et al., “Constraints on nucleon decay via invisible modes from the Sudbury Neutrino Observatory,” *Physical Review Letters*, vol. 92, no. 10, Article ID 102004, 4 pages, 2004.
- [77] H. O. Back, M. Balata, A. de Bari et al., “New limits on nucleon decays into invisible channels with the BOREXINO counting test facility,” *Physics Letters B*, vol. 563, no. 1-2, pp. 23–34, 2003.
- [78] T. Araki, S. Enomoto, K. Furuno et al., “Search for the invisible decay of neutrons with KamLAND,” *Physical Review Letters*, vol. 96, no. 10, Article ID 101802, 5 pages, 2006.
- [79] H. Ejiri, “Nuclear deexcitations of nucleon holes associated with nucleon decays in nuclei,” *Physical Review C*, vol. 48, no. 3, pp. 1442–1444, 1993.
- [80] O. Helene, “Upper limit of peak area,” *Nuclear Instruments and Methods In Physics Research*, vol. 212, no. 1-3, pp. 319–322, 1983.

- [81] P. W. Graham, I. G. Irastorza, S. K. Lamoreaux, A. Lindner, and K. A. van Bibber, "Experimental searches for the axion and axion-like particles," *Annual Review of Nuclear and Particle Science*, vol. 65, no. 1, pp. 485–514, 2015.
- [82] G. Bellini, J. Benziger, D. Bick et al., "Search for solar axions produced in the  $p(d, {}^3\text{He})\alpha$  reaction with Borexino detector," *Physical Review D*, vol. 85, no. 9, Article ID 092003, 2012.
- [83] A. V. Derbin, L. Gironi, S. S. Nagorny et al., "Search for axioelectric effect of solar axions using BGO scintillating bolometer," *The European Physical Journal C*, vol. 74, no. 9, article 3035, 2014.

## Review Article

# The Antineutrino Energy Structure in Reactor Experiments

**Pau Novella**

*Instituto de Física Corpuscular (IFIC), CSIC and Universitat de València, C/Catedrático José Beltrán 2, 46980 Paterna, Spain*

Correspondence should be addressed to Pau Novella; [pau.novella@ific.uv.es](mailto:pau.novella@ific.uv.es)

Received 26 July 2015; Revised 5 November 2015; Accepted 10 December 2015

Academic Editor: Seon-Hee Seo

Copyright © 2015 Pau Novella. This is an open access article distributed under the Creative Commons Attribution License, which permits unrestricted use, distribution, and reproduction in any medium, provided the original work is properly cited. The publication of this article was funded by SCOAP<sup>3</sup>.

The recent observation of an energy structure in the reactor antineutrino spectrum is reviewed. The reactor experiments Daya Bay, Double Chooz, and RENO have reported a consistent excess of antineutrinos deviating from the flux predictions, with a local significance of about  $4\sigma$  between 4 and 6 MeV of the positron energy spectrum. The possible causes of the structure are analyzed in this work, along with the different experimental approaches developed to identify its origin. Considering the available data and results from the three experiments, the most likely explanation concerns the reactor flux predictions and the associated uncertainties. Therefore, the different current models are described and compared. The possible sources of incompleteness or inaccuracy of such models are discussed, as well as the experimental data required to improve their precision.

## 1. Introduction

In the last two decades, several neutrino oscillation experiments [1] have demonstrated that neutrinos are massive particles. Thus, neutrinos have become a main probe to explore physics beyond the Standard Model. Within the three neutrino paradigms, the neutrino oscillation probability can be described by three mixing angles ( $\theta_{12}, \theta_{23}, \theta_{13}$ ), two independent mass square differences ( $\Delta m_{21}^2, \Delta m_{31}^2$ ), and one phase  $\delta_{CP}$  responsible for the CP-violation in the leptonic sector. While the dominant oscillations driven by  $\theta_{12}$  and  $\theta_{23}$  have been measured by different experiments in the so-called solar and atmospheric sectors, the third mixing angle  $\theta_{13}$  remained unrevealed until very recently. The first direct indication of a nonzero value of this angle has come from the accelerator-based experiments MINOS [2] and T2K [3]. However, the current accelerator neutrino experiments cannot measure  $\theta_{13}$  independently of other oscillation parameters. Complementing the role of accelerator-based facilities, reactor neutrino experiments stand as the direct way to provide an accurate value of  $\theta_{13}$ . In a two-flavor scheme and for short baselines ( $L \sim 2$  km), the survival probability of a reactor electron antineutrino  $\bar{\nu}_e$  with

energy  $E_\nu$  can be described as

$$P(\bar{\nu}_e \rightarrow \bar{\nu}_e) \cong 1 - \sin^2 2\theta_{13} \sin^2 \left( \frac{1.27 \Delta m_{31}^2 (\text{eV}^2) L (\text{m})}{E_\nu (\text{MeV})} \right). \quad (1)$$

The value of  $\theta_{13}$  can be measured directly from the oscillation amplitude, inferred from an energy-dependent deficit in the number of observed neutrinos.

After a series of short- and medium-baseline ( $\sim 100$ – $1000$  m) reactor neutrino experiments carried out in 80 s and 90 s, a new generation of experiments has been operating for the past few years. Three different collaborations (Daya Bay [4], Double Chooz [5], and RENO [6]) have reported very precise measurements of the mixing angle  $\theta_{13}$ . As these experiments rely partially on the comparison of the observed antineutrino flux with respect to the expected one, a revision of the relatively old reactor flux models was performed in [7, 8], becoming the new references and reducing the uncertainties at the 3% level. This reevaluation of the flux led to the so-called reactor antineutrino anomaly [9], pointing

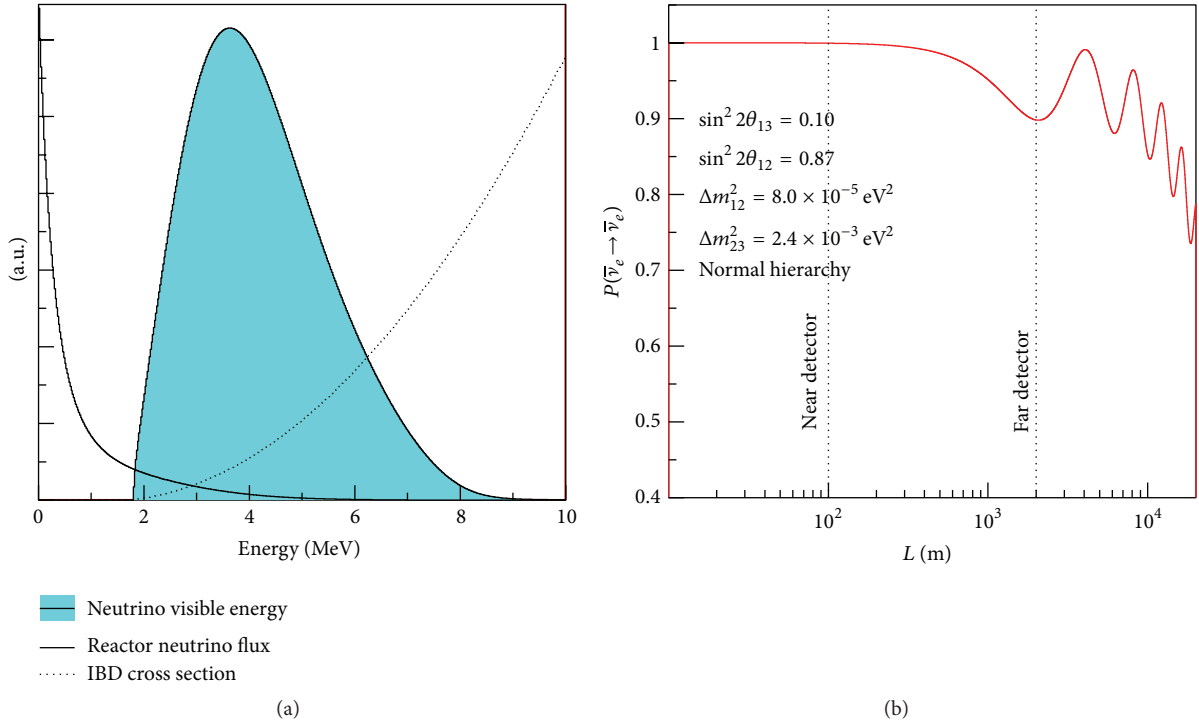


FIGURE 1: (a)  $\bar{\nu}_e$  visible spectrum as a result of the flux shape and IBD cross section. (b)  $\bar{\nu}_e$  survival probability for  $E_{\bar{\nu}} = 4$  MeV, as a function of the distance  $L$  for an arbitrary value of  $\sin^2 2\theta_{13} = 0.10$ . This probability assumes a three-flavor neutrino scenario and normal hierarchy of the neutrino masses.

at a possible short-baseline oscillation that would imply the existence of at least one sterile neutrino. While this suggests a possible underestimation of the reactor flux uncertainties, it does not impact the determination of  $\theta_{13}$ . Beyond this anomaly, Daya Bay, Double Chooz, and RENO have reported very recently [5, 10–12] an energy distortion around 5 MeV, which deviates from the expectation at about  $3\text{--}4\sigma$ . Apart from reinforcing the idea of an underestimation of the flux errors, this experimental result has induced a world-wide effort in trying to understand the origin of this discrepancy.

This work reviews the observation of such a 5 MeV energy structure by the three current reactor experiments. The possible causes are described as well as the different experimental approaches carried out to identify its origin. The incompleteness of the reactor flux predictions is presented as the most likely explanation, so the different models developed so far are reviewed. Within those models, a number of possible sources of biases or error underestimations are listed, thus pointing at possible experimental ways to improve our current knowledge. This review is organized as follows: Section 2 describes the current  $\bar{\nu}_e$  reactor experiments, relying on the flux predictions presented in Section 3; the observation of the energy distortion is reported in Section 4, followed by a critical analysis of its possible origin in Section 5; the reactor flux models are revisited in Section 6 as the most likely cause; finally, Section 7 summarizes the state of the art and discusses the experimental data required to gain further knowledge on the  $\bar{\nu}_e$  reactor flux and the origin of the energy structure.

## 2. A New Generation of Reactor Neutrino Experiments

The most common way of detecting reactor neutrinos is via the inverse beta decay (IBD):  $\bar{\nu}_e + p \rightarrow n + e^+$ . When this reaction takes place in liquid scintillator doped with  $\sim 1\%$  of gadolinium, it produces two signals separated by about  $\sim 30 \mu\text{s}$ : the first one due to  $e^+$  and its annihilation (prompt signal) and the second one due to the  $n$  capture in a Gd nucleus (delayed signal). This characteristic signature yields a very efficient background rejection. The prompt energy deposition ( $E_e$ ) relates directly to the interacting antineutrino energy ( $E_{\bar{\nu}}$ ):  $E_e \simeq E_{\bar{\nu}} + (M_p - M_n - M_e) + 2M_e$ , where  $M_p$ ,  $M_n$ , and  $M_e$  are the proton, neutron, and electron masses, respectively. The observed energy spectrum is the convolution of the reactor  $\bar{\nu}_e$  flux and the IBD cross section. As shown in Figure 1(a), the mean energy of the  $\bar{\nu}_e$  spectrum is around 4 MeV, which corresponds to a prompt energy  $E_e$  of  $\sim 3$  MeV. For this energy, the oscillation effect due to  $\theta_{13}$  starts arising at  $L \sim 0.5$  km and reaches the first maximum around 2 km, where the effect of  $\theta_{12}$  is still negligible as can be seen in Figure 1(b). Therefore, neutrino reactor experiments with short baselines offer a clean laboratory to search for  $\theta_{13}$ .

In spite of its characteristic signature, the IBD signal can be mimicked by the accidental and correlated backgrounds. The accidental background stands for the random coincidence of a positron-like signal coming from natural radioactivity and the capture in the detector of a neutron created by

cosmic muon spallation in the surrounding materials. The correlated background consists of events which may mimic both the prompt and the delayed signals of the IBD. Along with the stopping muons, the fast neutrons and cosmogenic isotopes, both generated in muon interactions, are the main sources of this background. Fast neutrons entering the detector lead to proton recoils, thus faking a prompt signal, before being captured. Muons crossing the detector can produce long-lived  $\beta$ - $n$  decay isotopes, like  ${}^9\text{Li}$  and  ${}^8\text{He}$ . As the half-life of such cosmogenic isotopes is  $\sim 100$  ms, their decay cannot be associated with the muon interaction.

The sensitivity to the  $\theta_{13}$ -driven oscillation is optimized by detecting a deficit in the expected neutrino events around 2 km away from the nuclear power plant (*far* detector), as shown in Figure 1(b). However, some of the largest systematic errors in reactor experiments arise from the uncertainties in the original  $\bar{\nu}_e$  fluxes. In order to reduce them, a relative comparison between two or more identical detectors located at different distances from the reactors becomes critical. As originally proposed in [13], a *near* detector placed a few hundred meters away can measure the fluxes before any oscillation takes place. The comparison between the far and near detectors leads to a breakthrough in the sensitivity to  $\theta_{13}$ , as all the fully correlated systematic uncertainties cancel out. Further steps in the sensitivity optimization rely on reducing the relative detection efficiency and energy scale uncertainties of the detectors, as well as on minimizing the backgrounds.

Following the above ideas, a new generation of reactor experiments is running since 2010. In China, the Daya Bay experiment [4] has built a far site and two near sites meant to measure the  $\bar{\nu}_e$  fluxes from the 6 cores (17.4 GW<sub>th</sub> in total) of the three power plants existing in the area. The Double Chooz experiment [5] operates two identical detectors located 400 m (since 2014) and 1050 m away from the two 4.25 GW<sub>th</sub> reactor cores of the CHOOZ nuclear plant in France. RENO [6] also consists of two identical detectors measuring the antineutrino fluxes generated at the 6 cores (17.3 GW<sub>th</sub> in total) of the Youngwang nuclear plant in South Korea. Although there are some differences in the detector designs of the three experiments, they all rely on the same principles and technology. The detectors are divided into three concentric volumes: the target (the inner-most volume filled with Gd-doped liquid scintillator), the  $\gamma$ -catcher (filled with undoped liquid scintillator), and the buffer (filled with mineral oil). The light produced by interactions in the liquid scintillator is read out by a number of photomultiplier tubes (PMTs) located in the buffer walls.

### 3. Antineutrino Flux Prediction

In a nuclear reactor, about 6 antineutrinos from  $\beta$ -decays are generated per fission, releasing an average energy of about 200 MeV. As the unstable fission products are rich in neutrons, they undergo  $\beta$  decays generating a nearly pure electron antineutrino flux. Only four isotopes, whose fission products can produce  $\bar{\nu}_e$  with energies above the IBD threshold (1.8 MeV), contribute to more than 99% of the flux:  ${}^{235}\text{U}$ ,  ${}^{239}\text{Pu}$ ,  ${}^{238}\text{U}$ , and  ${}^{241}\text{Pu}$ . However, such a flux consists of a superposition of thousands of  $\beta$ -decay branches. A fraction of

the neutrons produced in the  ${}^{235}\text{U}$  fissions is captured by  ${}^{238}\text{U}$ , giving place to mostly  ${}^{239}\text{Pu}$ . Thus, the core burns  ${}^{235}\text{U}$  while accumulating  ${}^{239}\text{Pu}$  as it is operated, in the so-called burn-up process. Apart from these two main isotopes which make up about 90% of the flux, the  ${}^{241}\text{Pu}$  and  ${}^{238}\text{U}$  fissions contribute to the remaining 10%. From a practical point of view, this implies that an accurate reactor flux prediction relies on two main aspects: (1) the simulation of the time evolution of the core fuel composition (i.e., the contributions of each one of the four main isotopes) and (2) the knowledge of the  $\beta$  spectra associated to the decay chains of the fission products.

In order to compute the expected neutrino flux in a reactor experiment like Daya Bay, Double Chooz, or RENO, three main ingredients need to be taken into account: (1) the detector-related normalization terms, (2) the reactor flux as a function of time, and (3) the IBD cross section. In absence of oscillations, the number of expected antineutrinos from a nuclear core can be described as

$$N^{\text{exp}} = \frac{\epsilon N_p}{4\pi} \frac{1}{L^2} \frac{P_{\text{th}}}{\langle E_f \rangle} \langle \sigma_f \rangle, \quad (2)$$

where  $\epsilon$  is the detection efficiency,  $N_p$  is the number of protons in the target,  $L$  is the distance to the center of the reactor, and  $P_{\text{th}}$  is the thermal power.  $\langle E_f \rangle$  is the mean energy released per fission:

$$\langle E_f \rangle = \sum_k \alpha_k \langle E_f \rangle_k, \quad (3)$$

where  $\alpha_k$  is the fractional fission rate of the  $k$ th isotope ( $k = {}^{235}\text{U}, {}^{239}\text{Pu}, {}^{238}\text{U}, {}^{241}\text{Pu}$ ). The mean cross section per fission  $\langle \sigma_f \rangle_k$  is defined as

$$\langle \sigma_f \rangle = \sum_k \alpha_k \langle \sigma_f \rangle_k = \sum_k \alpha_k \int_0^\infty dE S_k(E) \sigma_{\text{IBD}}(E), \quad (4)$$

where  $S_k(E)$  is the reference spectrum of the  $k$ th isotope and  $\sigma_{\text{IBD}}$  is the inverse beta decay cross section. The three variables  $P_{\text{th}}$ ,  $\langle E_f \rangle$ , and  $\langle \sigma_f \rangle$  are time dependent, with  $\langle E_f \rangle$  and  $\langle \sigma_f \rangle$  depending on the evolution of the fuel composition in the reactor and  $P_{\text{th}}$  depending on the operation of the reactor.

The current reactor experiments have used the reference spectra  $S_k(E)$  from [7, 8] as an input to their oscillation analyses. However, as far as the determination of these spectra is concerned,  $S_k(E)$  can be expressed as the sum of the contributions from all the fission products ( $N_f$ ):

$$S_k(E) = \sum_{f=1}^{N_f} \mathcal{A}_f S_f(E), \quad (5)$$

where  $\mathcal{A}_f$  is the activity of the fission product and the spectrum  $S_f(E)$  of each fission product is in turn a sum of  $N_b$   $\beta$ -branches connecting the ground state (or an isomeric state) of the parent nucleus to different excited levels of the daughter nucleus:

$$S_f(E) = \sum_{b=1}^{N_b} \text{BR}_f^b S_f^b(Z_f, A_f, E_{0f}^b, E), \quad (6)$$

$BR_f^b$  and  $E_{0f}^b$  being the branching ratio and the endpoint energy of the  $b$  branch of the  $f$  fission product, respectively, and  $Z_f$  and  $A_f$  being the charge and atomic number of the parent nucleus. It is worth noticing that (5) and (6) are valid for both electron and antineutrino spectra. The beta decay spectrum  $S_f^b$  for a single transition in a nucleus with endpoint energy  $E_{0f}^b = E_e - E_\nu$  is then

$$S_f^b(E_e, Z_f, A_f) = S_0(E_e) F(E_e, Z_f, A_f) C(E_e) \left(1 + \delta(E_e, Z_f, A_f)\right), \quad (7)$$

where  $S_0$  is a normalization constant taking into account the phase space [7, 14],  $F(E_e, Z_f, A_f)$  is the Fermi function accounting for the Coulomb interaction of the outgoing electron with the charge of the daughter nucleus, and  $C(E_e)$  is a shape factor [15] for forbidden transitions due to additional lepton momentum terms ( $C(E) = 1$  for allowed transitions). Beyond these terms, some additional effects need to be considered for precision studies: this is the role of the  $\delta(E_e, Z, A)$  factor. It accounts for the radiative (R), finite size (FS) and weak magnetism (WM) corrections:  $\delta(E_e, Z_f, A_f) = \delta_R + \delta_{FS} + \delta_{WM}$ . The R corrections are due to the emission of virtual and real photons by the charged particles present in the  $\beta$ -decay, and it is computed in [16, 17]. The FS correction accounts for the finite size of the nucleus, as the electric charge and hypercharge are not point-like [18, 19]. The WM term refers to the induced current yielding the largest contribution to the shape of the  $\beta$  spectrum [18, 20].

Finally, the simplified form from Vogel and Beacom [21] can be used to describe the IBD cross section:

$$\sigma_{\text{IBD}}(E_\nu^{\text{true}}) = E_{e^+} K \sqrt{E_{e^+}^2 - m_e^2}, \quad (8)$$

where

$$E_{e^+} = \frac{1}{2} \left( \sqrt{m_n^2 - 4m_p \left( -E_\nu + \Delta + \frac{\Delta^2 - m_e^2}{2m_p} \right)} - m_n \right) \quad (9)$$

and  $m_e$  and  $E_{e^+}$  are the positron mass and energy. The variables  $m_n$  and  $m_p$  are the masses of the neutron and proton with  $\Delta = m_n - m_p$ . The constant  $K$  is inversely proportional to the neutron lifetime. Using the MAMBO-II measurement of the neutron lifetime [22] leads to  $K = 0.961 \times 10^{-43} \text{ cm}^2 \text{ MeV}^{-2}$ .

**3.1. Reactor Flux Models.** In order to predict the reference spectra  $S_k(E)$ , two different approaches are developed. The *ab initio* or summation method takes advantage of the available information on the  $\beta$  decays of each fission fragment (nuclear databases), summing over each nuclide's individual spectrum to obtain aggregate spectra. On the other hand, the so-called conversion method exploits the aggregate  $\beta$  spectra measured in the Institut Laue-Langevin (ILL) [23–26], fitting the data to a set of virtual  $\beta$  branches and converting the result into the corresponding antineutrino spectra (e.g., [27]). While it is worth noticing that both methods rely on measured

$\beta$  spectra, the conversion approach yields the most precise results since the uncertainties are constrained by the ILL measurements. Although this is reviewed in this work, the errors associated with the conversion method have been claimed to be at the level of 2–3%. As the nuclear databases are known to suffer from a lack of relevant data (concerning both  $\beta$  decays and fission yields) and from the need of more precise measurements, the summation method provides typically an envelope error of about 10–20%. Recently, there have been improvements in both the conversion and summation techniques [7, 28], being one of the main goals to optimize the results from the current reactor experiments.

Given the limitations of the *ab initio* approach, the reactor antineutrino spectra have been estimated historically relying on the total electron spectra associated with the beta decays of all fission products of  $^{235}\text{U}$ ,  $^{239}\text{Pu}$ , and  $^{241}\text{Pu}$ . Such  $\beta$ -spectra were obtained at ILL by irradiating thin target foils of these isotopes with thermal neutrons. As  $^{238}\text{U}$  nuclei undergo fission with fast neutrons, the associated spectrum could not be measured at that time and therefore its prediction has been typically based on the summation method. The same applies to all spectra above 8 MeV, as the ILL measurements were performed only up to this energy. In [7], a mixed approach has been developed combining the precise reference of the electron spectra from ILL with the physical distribution of beta branches of all fission products provided by the nuclear databases. This new analysis has provided a better handle on the systematic errors of the conversion and a new set of reference spectra for  $^{235}\text{U}$ ,  $^{239}\text{Pu}$ ,  $^{241}\text{Pu}$ , and  $^{238}\text{U}$  (although the latter is still based on a purely summation technique). While the shapes of the spectra and their uncertainties are found to be comparable to those of the previous analysis of the ILL data, the normalization is shifted by about +3% on average, thus leading to the reactor neutrino anomaly. The reevaluation of short-baseline reactor data in the light of these new reference spectra reveals a deficit in the number of observed antineutrinos, which might be explained in terms of sterile neutrino oscillations. One of the main reasons for this normalization shift is the treatment of the corrections  $\delta(E_e, Z_p, A_p)$  in (7), and in particular the WM term. These corrections have been further investigated in [8], deriving a consistent set of reference spectra in both shape and normalization. To complete the picture of the state-of-the-art conversion method, it must be noticed that the cumulative  $\beta$  spectrum of the fission products of  $^{238}\text{U}$  has been finally measured in [29], in the range from 2.875 MeV to 7.625 MeV.

Despite the larger uncertainties, the summation method is still a powerful tool to predict reactor antineutrino fluxes. To start with, this approach provides estimations of the reference spectra which are independent from the measurements at ILL. As these measurements are unique, a cross-check based on nuclear databases is specially valuable. The summation method is also the only way to predict the antineutrino energy spectra beyond 8.0 MeV for  $^{235}\text{U}$ ,  $^{239}\text{Pu}$ , and  $^{241}\text{Pu}$ , and beyond 7.6 MeV for  $^{238}\text{U}$ . While it is true that some authors (e.g., [7, 8]) have provided polynomial parameterizations of the spectra that can be used to extrapolate the predictions above 8 MeV (as typically

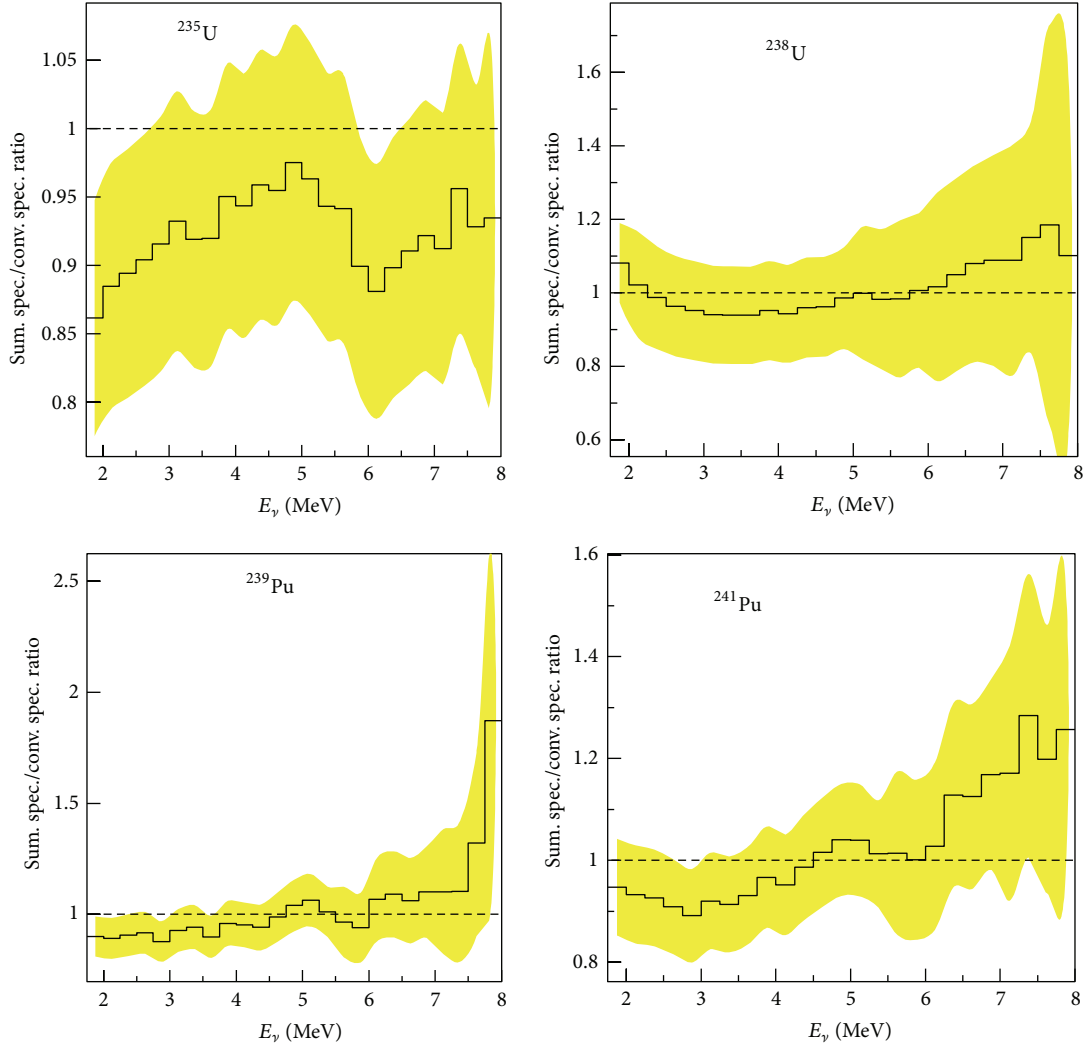


FIGURE 2: Ratio of summation-derived spectra (from [28]) to the start-of-the-art conversion-derived spectra (from [8, 29]), as a function of the  $\bar{\nu}_e$  energy. The shadowed band shows the  $1\sigma$  error.

done by reactor experiments), such an extrapolation is not physically motivated and the associated error cannot be estimated in a robust way. Furthermore, the binning of 250 keV in which the ILL spectra were originally published is large enough to hide possible structures coming from some contributions to the reactor fluxes. Taking into account all these considerations, the summation technique has become a main tool to shed light on the reactor antineutrino spectra and the nuclear databases have been recently improved by new  $\beta$ -decay measurements. In particular, a new set of reference energy spectra has been obtained in [28] taking into account the new measurements of the  $^{102;104;105;106;107}\text{Tc}$ ,  $^{105}\text{Mo}$ , and  $^{101}\text{Nb}$  nuclei. These measurements are taken with the Total Absorption Technique (TAS), insensitive to the Pandemonium effect [30] which typically affects the  $\gamma$  spectrometry with Ge detectors. Beyond the relevant improvement in the summation-based reference spectra, the work in [28] highlights the need of new TAS measurements.

In order to compare the state-of-the-art reference spectra, the ratio of the summation spectra derived in [28] to the conversion-based predictions ( $^{235}\text{U}$ ,  $^{239}\text{Pu}$ , and  $^{241}\text{Pu}$  from [8] and  $^{238}\text{U}$  from [29]) is shown in Figure 2. Both sets of predictions agree within  $1\sigma$ , although no strong conclusions can be settled given the large error bands.

#### 4. Observation of an Energy Structure around 5 MeV

In the Neutrino 2012 conference, the RENO collaboration mentioned the observation of an excess in the number of antineutrinos between 4 and 6 MeV of the positron energy spectrum [31], with respect to the flux prediction. In Neutrino 2014, both RENO and Double Chooz collaborations reported and quantified such an excess [11, 12, 32]. Daya Bay also presented a similar energy structure at the ICHEP 2014 and at NuTel 2015 [33] conferences.

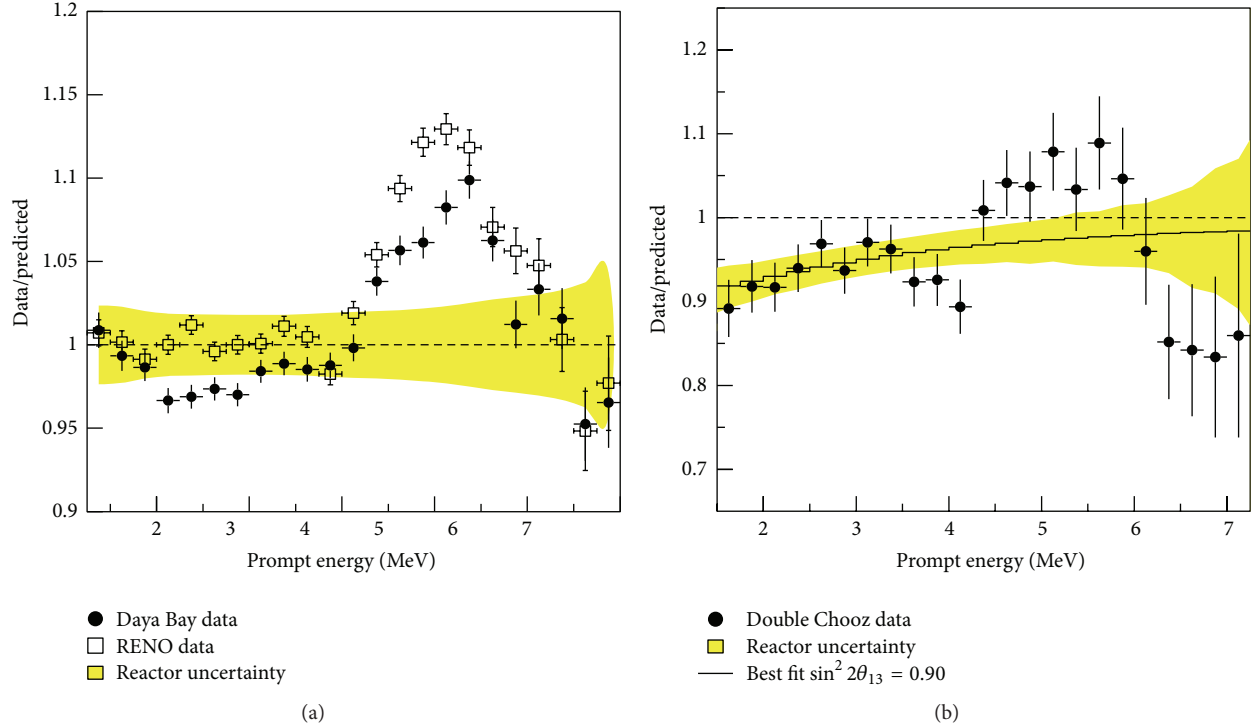


FIGURE 3: Ratio of background-subtracted  $\bar{\nu}_e$  candidates to nonoscillation prediction, as a function of the IBD prompt energy. (a) Daya Bay and RENO ratios for  $\bar{\nu}_e$  candidates observed at the near sites. (b) Double Chooz ratio for  $\bar{\nu}_e$  candidates measured at the far detector. The shadowed region represents the typical reactor error derived from the [8, 29] reference  $\bar{\nu}_e$  spectra, which is dominant for the considered energy region.

The first journal publication of this effect has been provided by Double Chooz in [5]. Using the data from the far detector, a best fit value of the flux normalization of  $9 \pm 2\%$  (with respect to the central value prediction) is quoted between 4.25 and 6 MeV. This translates into a significance of  $3\sigma$ . The energy distortion is consistent with the ones presented in previous Double Chooz publications [34–36], where a significant measurement of the data-prediction discrepancy was not possible due to the limited statistics and the nonoptimized detector energy response. Daya Bay has also released a paper [10] on the reactor neutrino flux measurement, concerning both the normalization and the energy spectrum. The measured prompt energy spectrum in the near detectors shows a deviation from the reactor models with a significance beyond  $2\sigma$  over the full energy range, and around  $4\sigma$  between 4 and 6 MeV. The excess in this energy range has been estimated to be about 1% of all events in both the near and far detectors. Once corrected by the  $\theta_{13}$  oscillation effect, the energy spectra measured in the near and far detectors are consistent. Two reactor predictions have been considered in Daya Bay, one based on the conventional ILL models and another one based on the reevaluations provided in [7, 8]. The disagreement between the data and the prediction arises in both cases, the significance being of the deviations very similar. The significance has also been computed adopting two different approaches, one relying on the contribution of  $\chi^2$  of each energy bin and another one on the  $p$  values within local energy windows, yielding consistent results. In addition,

the RENO collaboration has shown in the proceedings of Neutrino 2014 [11, 12] the energy structure in the 4–6 MeV energy range for both the near and far detectors. The observed excess of  $\bar{\nu}_e$  is consistent among the two, and the significance of the excess at the near detector is estimated to be  $3.5\sigma$ . The excess of  $\bar{\nu}_e$  with respect to the total expected flux is quoted as  $2.3 \pm 0.4$  (data)  $\pm 0.5$  (prediction)% for the near detector, and  $1.8 \pm 0.7$  (data)  $\pm 0.5$  (prediction)% for the far detector.

The ratio of the background-subtracted  $\bar{\nu}_e$  candidates spectrum to the nonoscillation prediction is shown in Figure 3 for the Daya Bay and RENO near detectors and for the Double Chooz far detector. The excess reported by the three collaborations amounts to about 10% over the expected number of  $\bar{\nu}_e$  in this energy range, and both RENO and Daya Bay have observed consistent structures in their near and far detectors. It might be argued that the excess observed in RENO is larger than in Daya Bay and Double Chooz. However, given the discrepancy between RENO and Daya Bay in the 2–4 MeV range (see Figure 3), such a difference in the amplitude of the distortion might be due to differences in the flux predictions beyond the 4–6 MeV window. In order to compare the observed distortions in a robust and quantitative way, the  $\bar{\nu}_e$  prediction of the three reactor experiments should be based on the same reactor model (which comprises not only the reference spectra  $S_k(E)$ , but also the simulation of the reactor core evolution, the treatment of the spent fuel, etc.). It is also worth noticing that the significance of the excess quoted by the three experiments cannot be directly

compared, as they are computed in different ways. Daya Bay normalizes the predicted spectrum to the observed number of events, thus evaluating the discrepancy in terms of the energy spectrum between 4 and 6 MeV, and not the total rate. On the other hand, Double Chooz performs an evaluation based on the total predicted and expected rates in the 4.25–6.00 MeV energy window. Independently of how the distortion significance is estimated, it is limited by the uncertainties in the flux prediction, which are at the level of 2-3% for both the rate and the spectral shape.

As the three experiments detect the reactor  $\bar{\nu}_e$  in the same way and with very similar detectors, the possible causes of this energy structure are common and might include, in principle, detector and/or background issues. An explanation in terms of the reactor flux prediction (incompleteness of the model or underestimation of the uncertainties) would be also correlated among the three experiments, as they all rely on the conversion method to obtain the  $^{235}\text{U}$ ,  $^{239}\text{Pu}$ , and  $^{241}\text{Pu}$  antineutrino spectra. There are however two differences. Firstly, Double Chooz uses in [5] the measurement in [29] to derive the  $^{238}\text{U}$   $\bar{\nu}_e$  spectrum, while Daya Bay and RENO take the summation-based spectrum from [7]. Secondly, Double Chooz constrains the flux normalization to the measurement in Bugey4 [37], taken 15 m away from the core. This is why Double Chooz quotes a flux normalization error of 1.7%, thus reducing the errors in Daya Bay and RENO (2.7% and 2.0%, resp.). Beyond this, Daya Bay has also explored some variations to the reference model but concluded that the structure still remains. In particular, the local distortion around 5 MeV cannot be described extending the reactor model with a single  $\beta$ -branch or a monoenergetic line.

While this disagreement between data and flux models needs to be investigated, it must be noticed that the impact on the  $\theta_{13}$  mixing angle is negligible. As demonstrated in [5] for Double Chooz, even with only the far detector being used for the oscillation analysis, the  $\theta_{13}$  measurement is not affected by the energy distortion. This can be easily understood since the amplitude of the  $\theta_{13}$ -driven oscillation is vanishing around 5 MeV. In the case of Daya Bay and RENO, whose analyses involve both near and far detectors, the impact of the energy structure is even smaller as the role of the flux prediction is not as relevant due to the interdetector comparison.

## 5. Possible Sources of the Energy Structure

The spectral shape of the energy structure at 5 MeV cannot be produced by any standard neutrino oscillations scenario, even considering sterile neutrinos. In particular, it has been observed by Daya Bay and RENO at two different baselines (the near and far detectors). Therefore, it can be assumed that the discrepancy between the data and the flux models might be due to one of these reasons: (1) the existence of nonstandard IBD interactions, (2) a detection issue distorting the energy scale, (3) an unaccounted background source, and (4) missing contributions to the reactor models. Being the reactor  $\bar{\nu}_e$  spectrum uncertainty of the order of 2-3% and the maximum deviation between data and prediction around 10%, the current reactor experiments cannot establish this discrepancy beyond a significance of  $\sim 4\sigma$ . However, the

available data allow for a dedicated analysis on the possible causes of the discrepancy. The current reactor experiments have been capable of reinforcing the case for a reactor-model explanation, while disfavoring other possible causes, namely, the misinterpretation of the detector response and the incompleteness of the background model. The dedicated studies addressing the possible sources of the prompt energy spectrum distortion are described below.

*5.1. Antineutrino Interactions.* An unaccounted or nonstandard neutrino interaction in the detectors of the reactor experiments might lead to an excess of observed neutrinos. In the energy range of reactor  $\bar{\nu}_e$  (below 10 MeV), the typical cross section of charged and neutral current neutrino interactions follow an increasing pattern with energy after a given threshold. This kind of trend can hardly explain a bump-like excess around 5 MeV in the positron energy spectrum. Within the target volume of the detectors, the antineutrinos can interact basically with H, C, and Gd and in the  $\gamma$ -catcher only with H and C. As Double Chooz has observed the energy structure using neutrons captures in Gd and in H [36], an unaccounted interaction with Gd can be excluded. The antineutrinos might interact with some C isotope with enough energy to separate one neutron, the final nuclei remaining in excited state. The combination of the deexcitation  $\gamma$  and the neutron might mimic the IBD signal. However, the rate of such process should be rather small (as there are not empirical evidences in the current experiments) and could not explain the  $\sim 10\%$  excess.

*5.2. Energy Scale.* A detector-related issue affecting the energy scale might also explain, in principle, the energy structure. However, some studies performed by Daya Bay and Double Chooz rule out this possibility. In [5], the accuracy of the energy scale around 5 MeV has been confirmed by spallation neutrons captured on carbon, which occur predominantly in the  $\gamma$ -catcher volume as the capture cross section is smaller than on Gd. The C captures result in an energy peak at 5 MeV, whose agreement between data and MC simulation has been found to be within 0.5%. Along the same lines, Daya Bay, Double Chooz, and RENO have also checked the energy reconstruction by means of the  $\beta$  decays of  $^{12}\text{B}$  collected in data, showing no energy distortion when compared to the corresponding simulation. This is consistent with the fact that any nonlinear effect, due to the scintillator properties or the electronics response, is observed for energies above 4 MeV. Furthermore, the energy resolution estimated with the collected data is also in good agreement with that of Monte Carlo.

*5.3. Background Model.* The events found in the 4–6 MeV range fulfill all the IBD characteristics, in particular concerning the neutron capture time and distance distribution, and the spatial distribution of the prompt signals. Thus, the three collaborations disfavor the hypothesis of an unaccounted background contribution. In addition, the reactor off data taken in Double Chooz allows for an independent and inclusive background measurement, thus accounting even for possible unknown sources [38]. The measured total

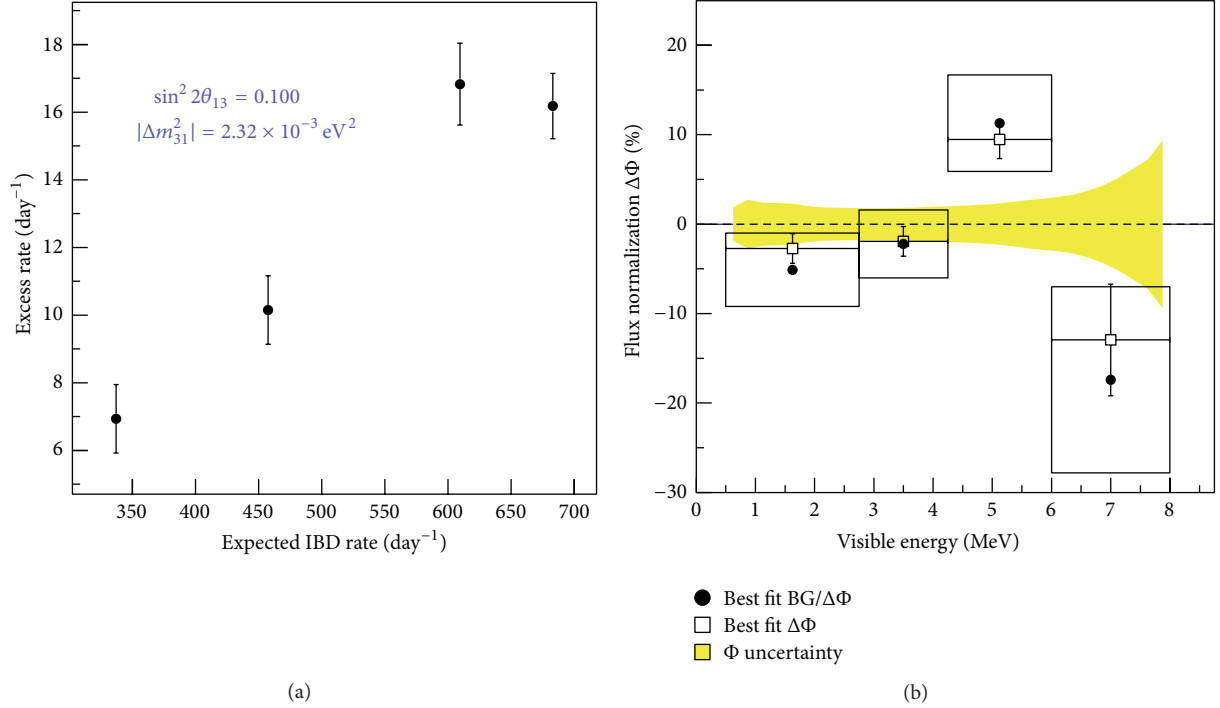


FIGURE 4: Correlation of the  $\bar{\nu}_e$  excess around 5 MeV with the reactor power. (a)  $\bar{\nu}_e$  excess in the RENO near detector as a function of the expected IBD (data from [11, 12]). (b) RRM best fit values of the reactor flux normalization (with respect to the central value prediction) in the far detector of Double Chooz (data from [5]). Results with and without the background (BG) model constraint are shown with empty squares and solid dots, respectively.

rate in [5] according to the candidates selection cuts is computed to be  $0.75 \pm 0.37$  events/day. While keeping the independence with the background model, this background measurement is slightly modified by means of a Reactor Rate Modulation (RRM) [39] fit:  $0.90 + 0.43$  and  $0.90 - 0.36$  events/day. These total background measurements are lower than the sum of the individual background sources accounted for in the background model (accidental coincidences, fast neutrons/stopping muons, and cosmogenic isotopes):  $1.6 + 0.41$  and  $1.6 - 0.17$  events/day ( $1.7\sigma$  discrepancy with respect to the reactor off measurement). Therefore, the existence of an unaccounted background source, leading to the excess around 5 MeV, is strongly disfavored. Beyond this comparison with the inclusive background measurement, dedicated studies with reactor on and reactor off data have been developed to look for direct indications of unknown background sources. No significant evidences have been found.

**5.4. Reactor Flux Model.** The remaining possible cause of the energy distortion is that one of an additional reactor  $\bar{\nu}_e$  component beyond the current model. In particular, if the excess around 5 MeV is due to an unaccounted reactor contribution, it must be correlated to the reactor power. On the other hand, if it is due to an unknown background, the rate of the excess should be independent of the power. Such a correlation has been demonstrated by Daya Bay, Double Chooz, and RENO, by estimating the excess for different reactor powers. Daya Bay has shown in ICHEP 2015 the time stability of the prompt energy spectrum and the time distribution of

events for two different energy windows (4.5–5.5 MeV and 3.0–4.0 MeV), proving that the structure remains the same over time, and thus for different conditions of the reactors operation. In [5], the Double Chooz collaboration shows the correlation of the excess with the reactor power in a flux model independent way, by parameterizing the spectrum and measuring an effective excess for different reactor conditions. Consistent results are found for  $\bar{\nu}_e$  candidates obtained with neutron captures in Gd and H. RENO has also reported in Neutrino 2015 and NuTel 2015 such a correlation by means of the measurement of the excess for different reactor powers, as shown in Figure 4(a).

As the Double Chooz RRM analysis utilizes the correlation between the observed rate and the thermal power to derive both the mixing angle  $\theta_{13}$  and the total background rate, it can be used to test the hypothesis of a bias in the flux prediction. In particular, it can confront the data to the background model and the flux model at the same time, thus providing indications about the most likely cause of the energy structure. In [5], five independent RRM fits have been carried out in different energy regions, constraining  $\sin^2 2\theta_{13}$  to the best fit value in [4] while leaving as free parameters both the total background rate and a flux normalization term (with respect to the central value of the flux model). The best fit values of the background rate are fully consistent with both the background model and the reactor off measurement, while the best fit values for the flux normalization deviates ( $2\sigma$ ) from the prediction in the 4.25–6.00 MeV window, as shown in Figure 4(b). This result is consistent with the reported

correlation between the excess and the thermal power, thus reinforcing the case for a flux model bias and disfavoring again the background model as the source of the energy distortion. If one constrains the total background rate to the background model, the discrepancy between the flux model and the RRM best fit value is increased to  $3.0\sigma$ .

## 6. Reviewing the Reactor Flux Predictions

As discussed above, the most likely explanation for the energy structure is that one of unaccounted contributions in the reactor flux models. Hereafter, this work assumes that this is the unique source of the data-prediction disagreement around 5 MeV. Under this well motivated assumption, the different approaches to the flux estimations need to be reviewed from a critical point of view. To start with, the errors of the conversion-based reference spectra must be reevaluated somehow, as the current quoted uncertainties do not cover the observed energy distortion. This is obviously related to the identification of the possible missing pieces in the reactor models. Such contributions in the conversion-based flux might be related to (1) the aggregate  $\beta$  measurements, (2) the conversion procedure itself, and (3) the nuclear corrections, mostly related to the forbidden decays. To shed light on all these possibilities, the summation-based predictions might play a major role, but the associated limitations need to be taken into account. All these aspects are discussed below.

**6.1. The Aggregate Spectra.** As the  $^{235}\text{U}$ ,  $^{239}\text{Pu}$ , and  $^{241}\text{Pu}$  reference spectra obtained by means of the conversion method rely on the ILL data, any issue affecting the ILL spectrometer would propagate to the reactor flux predictions. In principle, biases in both the overall normalization and the energy reconstruction (or the associated errors) might be possible, thus giving rise to the reactor  $\bar{\nu}_e$  anomaly and the energy structure around 5 MeV, respectively. As pointed out in [40] following a summation approach, the presence of a bump between 5 and 7 MeV in both the calculated electron and antineutrino spectra might be an indication of an artifact in the original ILL measurements rather than an effect of the conversion method.

Beyond the ILL data, the summation-derived  $\bar{\nu}_e$  spectra from  $^{238}\text{U}$  (used as reference in Daya Bay, RENO, and first publications by Double Chooz) might be considered a candidate to explain the energy distortion, given the large associated errors. Because of the different experimental setups, RENO reports that about 12% of the fissions are due to  $^{238}\text{U}$ , while Daya Bay quotes only 7.6%. As the energy structure in RENO is about 50% larger than in Daya Bay, this might indicate that the  $^{238}\text{U}$  fissions are contributing to it. This isotope is indeed responsible for about 20% of the  $\bar{\nu}_e$  flux between 4 and 6 MeV. In [41], it has been reported that two different databases predict, within the summation scheme, bumps in the region of interest. However, the amplitude is not large enough to cover the structure observed in reactor experiments. Furthermore, the analysis in [41] has not considered the work in [29], where the  $^{238}\text{U}$  aggregate spectrum has been measured. On the contrary, Double Chooz

has used [29] to predict the  $\bar{\nu}_e$  flux and has found that the energy bump remains, with roughly the same amplitude.

**6.2. The Conversion Procedure.** The conversion technique has been reviewed extensively in the literature since the first antineutrino predictions based on the ILL data [27]. As discussed previously, the method was recently improved in [7, 8]. While the different approximations have been performed to fit the data to a number of virtual  $\beta$  branches, the results have been consistent as far as energy shape and error budget are concerned (this is not the case of the overall normalization). This leaves small room for a possible issue in the technique itself. However, the ILL reactor is different to the ones currently used in the reactor experiments. The neutron flux spectra at typical pressurized water reactors (like the ones in Daya Bay, Double Chooz, and RENO) are harder in energy than the thermal spectrum of the ILL reactor. As highlighted in [41], this opens the possibility of epithermal neutron contributions to the  $^{235}\text{U}$ ,  $^{239}\text{Pu}$ ,  $^{241}\text{Pu}$ , and  $^{238}\text{U}$  fissions, resulting in a shoulder at 5 MeV in the  $\bar{\nu}_e$  spectrum. However, since there are not fission yield measurements for the nuclei that dominate that energy region, this hypothesis is hard to demonstrate or refute.

**6.3. Nuclear Corrections.** The uncertainties quoted in [7] have been revisited in [14], since they lead to a significance of the reactor neutrino anomaly of about  $3\sigma$ . As described in Section 3, an antineutrino spectrum can be estimated from a beta spectrum if the linear combination of operators involved in the decay, the endpoint energy, and the nuclear charge is known. However, the fission  $\beta$  spectra involve about 6000 decays, being forbidden about 30% of them. This implies that some assumptions are needed when deriving the reactor  $\bar{\nu}_e$  flux, given the limited knowledge on the structure of the forbidden transitions. Such assumptions affect eventually the error budget of the predictions in both the conversion and summation methods. In [14], it has been noticed that different treatments of the forbidden transitions (and the associated  $\delta$  corrections) can lead to antineutrino spectra that differ in both shape and magnitude at about 4%. In particular, if all forbidden decays are treated as allowed transitions, the antineutrino spectra are increased, thus leading to the reactor neutrino anomaly reported in [9]. However, this is not always the case if different approaches for the forbidden transitions are adopted. It is concluded that uncertainties in the  $\bar{\nu}_e$  predictions are about 4%, implying an increase of roughly a factor 2 with respect to the estimations in [7, 8]. Along the same lines, the effect of first forbidden transitions on the  $\beta$ -decay neutrino spectra is analyzed in [42] by performing microscopic nuclear structure calculations. The authors conclude that these decays may be responsible for a fraction of the deficit of neutrinos observed in the reactor experiments. Although the works in [14, 42] are addressing the issue of the reactor neutrino anomaly, the conclusions apply also to the energy structure observed around 5 MeV: the disagreement between the data and the flux prediction might be due to the forbidden transitions contributing to that energy region.

Concerning the nuclear corrections to be applied to the forbidden transitions, three relevant points have been

highlighted in [41]. First, it has been noticed that several of the  $\beta$  decays contributing to the bump region have a total angular momentum and parity which involve no WM correction. This increases the flux predictions with respect to [7, 8, 28], where this fact has not been taken into account. Second, the shape factor  $C(E_e)$  is not the same for all forbidden transitions: in [7], the  $C(E_e)$  corresponding to a unique forbidden transition has been assumed for all the cases. Finally, the FS corrections for these transitions applied in the literature are always approximated. Despite these considerations, a more accurate treatment of the forbidden decays performed in [41] cannot account for a significant fraction of the energy structure.

*6.4. The Limitations of the Summation Method.* In order to get insights on the above topics, the summation method is a powerful handle as it provides an ILL-independent set of reference spectra and a tool to estimate the effect of the different nuclear corrections and assumptions. However, it is worth remarking that the errors associated to this technique are too large to establish any conclusion. Furthermore, the use of different databases can lead to somehow different conclusions. As an example, the ENDF/B.VII.1 compiled nuclear data [43] has been used in [40] to derive the  $\bar{\nu}_e$  spectra, yielding an energy bump in the antineutrino energy in the 5–7 MeV region ( $E_e = 4\text{--}6$  MeV). However, the ENDF/B.VII.1 data used in the analysis is not taking into account the new TAS measurements described in [28]. By using the reference spectra from [28] or the ENDF/B.VII.1 database combined with the new TAS measurements (hereafter updated ENDF/B.VII.1) [44], the bump is significantly reduced. A detailed comparison of the updated ENDF/B.VII.1 and JEFF-3.11 [45] decay libraries has been presented in [41]: in the case of the JEFF-3.11-based results, the bump is totally removed. Finally, it must be noticed that the same kind of limitations of the available nuclear data arises when considering the reactor neutrino anomaly (i.e., the flux normalization). As an example, Daya Bay has measured an absolute  $\bar{\nu}_e$  rate in good agreement with the current world average and with the ENDF/B-VII.1 prediction (i.e., no indication of anomaly). However, comparing the Daya Bay data with the JEFF-3.1.1 estimations yields a deficit in the  $\bar{\nu}_e$  rate, thus suggesting the anomaly.

## 7. Summary and Discussion

The three current antineutrino disappearance reactor experiments (Daya Bay, Double Chooz, and RENO) have observed an energy distortion around 5 MeV in the prompt energy spectrum ( $\sim 6$  MeV in  $\bar{\nu}_e$  spectrum), deviating from the predictions at a  $\sim 4\sigma$  level as an excess in the number of  $\bar{\nu}_e$ . The structure is observed in the near detectors of Daya Bay and RENO (with baselines around 300 m) and in the far detectors of the three experiments (with baselines around 1-2 km), so it cannot be explained in terms of any standard neutrino oscillations. Given the correlation of the excess with the reactor power, the three collaborations conclude that the most likely explanation is an incompleteness or bias in the reactor flux models. Although the origin of the energy structure might not be related to the reactor antineutrino anomaly (that

might be described in terms of sterile neutrino oscillations), both features reinforce the case for a revision of the current reactor flux predictions. A possible underestimation of the error budget in the reactor models, due to unknown or not well described contributions, has to be considered.

There are two general methods to estimate the reactor fluxes as a composition of the  $\bar{\nu}_e$  spectra from the main fissile isotopes. The most precise one, and the state-of-the-art reference for reactor experiments, is the conversion method: it relies on the  $\beta$  aggregate spectra measured in the ILL, fitting the data to a set of virtual branches and converting the results into the corresponding  $\bar{\nu}_e$  spectra. Currently, this method quotes an uncertainty of 2-3%. The second approach is the so-called summation method: it builds the  $\bar{\nu}_e$  spectra as the sum of each nuclide's individual  $\beta$  spectrum, according to the available information in the nuclear databases. This technique typically yields an error envelope of 10–20%. While uncertainty associated with the summation-based spectra covers the  $\sim 10\%$  deviation observed in the experimental data around 5 MeV of the prompt energy spectrum, the error of the conversion-based spectra does not. The later method might be affected by (1) an issue in the ILL data, (2) intrinsic limitations of the technique, and (3) nuclear effects or uncertainties not accounted for. The forbidden transitions might play a major role in the later aspect.

The available reactor data can be used to shed some light on the puzzle of the flux predictions. In particular, one can perform fits to the observed  $\bar{\nu}_e$  spectrum for different sets of parameters and assumptions used in the predictions (like the number of  $\beta$  branches or the treatment of forbidden transitions). The fit results can help to identify or rule out possible contributions to the prompt energy shoulder at  $\sim 5$  MeV. It is also possible to take the  $\bar{\nu}_e$  spectra from Daya Bay, Double Chooz, and RENO and deconvolute them back to the corresponding  $\beta$  spectra, which in turn can be confronted to the ILL data. The observation of the same structure in the  $\beta$  spectra would be an indication of a bias in the ILL data. Finally, the summation method can be used to review the error on the predicted spectra by analyzing the effect of the different approximations concerning the nuclear corrections and the forbidden transitions. If it is concluded from this kind of studies that the error in the  $\bar{\nu}_e$  spectra is larger than currently assumed (as suggested by some authors), the discrepancy between the observed data and the models would need to be reevaluated.

Despite the above considerations, the available reactor data is not enough to find out the actual origin of the energy distortion. The same applies to the current nuclear data concerning  $\beta$  decays. However, the situation might improve once the near-future campaign of very short-baseline reactor experiments (meant to explore the possibility of sterile neutrino oscillations) starts delivering data. In order to rule out the possibility of an issue in the original ILL measurements, a new aggregate  $\beta$  spectrum is the most direct approach. While this new measurement would be valuable, it might not be the ultimate solution to the origin of the discrepancy between the data and the models. Beyond cross-checking the ILL measurement, it is also worth exploring the limitations of

the related conversion procedure, especially regarding the neutron spectra in different types of reactors. The comparison of aggregate  $\beta$  spectra measured in a very thermal reactor and in a reactor with a harder neutron spectrum, as proposed in [41], would suffice to quantify the impact on the predicted  $\bar{\nu}_e$  flux.

The available nuclear data is not capable of identifying the origin of the energy structure by means of the summation method. In order to improve the precision and accuracy of the summation-derived predictions, new  $\beta$  decay measurements are needed. In particular, improving the knowledge on the forbidden  $\beta$  transitions is crucial. The summation-method itself can be used to define the list of most relevant transitions to be measured, by tagging the nuclei that contribute the most to the energy region of interest. As a matter of fact, the main contributors have been identified in works like [40, 44]. As most of the relevant transitions are first forbidden, the  $\beta$  spectrum needs to be measured with high precision so the shape correction factor can be explored. As already demonstrated in the literature, the TAS technique has arose as the best option for several transitions. A new campaign of measurements will boost the capabilities of the summation method, thus becoming a major tool to resolve the nature of the reactor  $\bar{\nu}_e$  energy structure.

### Note Added in Proof

After the submission of this paper, the RENO collaboration has released a paper [46] where the observation of the energy structure is described. Although with 500 live days of data instead of 800, the paper accounts for the results presented in the Neutrino 2014 and NuTel 2015 conferences (cited in this review), including the figures of the prompt energy spectrum at both far and near detectors.

### Conflict of Interests

The author declares that there is no conflict of interests regarding the publication of this paper.

### References

- [1] K. A. Olive, K. Agashe, C. Amsler et al., "Review of particle physics," *Chinese Physics C*, vol. 38, Article ID 090001, 2014.
- [2] P. Adamson, D. J. Auty, D. S. Ayres et al., "Improved search for muon-neutrino to electron-neutrino oscillations in MINOS," *Physical Review Letters*, vol. 107, no. 18, Article ID 181802, 2011.
- [3] K. Abe, N. Abgrall, Y. Ajima et al., "Indication of electron neutrino appearance from an accelerator-produced off-axis muon neutrino beam," *Physical Review Letters*, vol. 107, no. 4, Article ID 041801, 8 pages, 2011.
- [4] F. P. An, A. B. Balantekin, H. R. Band et al., "Spectral measurement of electron antineutrino oscillation amplitude and frequency at Daya Bay," *Physical Review Letters*, vol. 112, no. 6, Article ID 061801, 2014.
- [5] Y. Abe, J. C. dos Anjos, J. C. Barriere et al., "Improved measurements of the neutrino mixing angle  $\theta_{13}$  with the Double Chooz detector," *Journal of High Energy Physics*, vol. 2014, no. 10, article 086, 2014.
- [6] J. K. Ahn, S. Chebotaryov, J. H. Choi et al., "Observation of reactor electron antineutrinos disappearance in the RENO experiment," *Physical Review Letters*, vol. 108, no. 19, Article ID 191802, 2012.
- [7] T. A. Mueller, D. Lhuillier, M. Fallot et al., "Improved predictions of reactor antineutrino spectra," *Physical Review C—Nuclear Physics*, vol. 83, no. 5, Article ID 054615, 2011.
- [8] P. Huber, "Determination of antineutrino spectra from nuclear reactors," *Physical Review C*, vol. 84, no. 2, Article ID 024617, 2011, Erratum in: *Physical Review C*, vol. 85, Article ID 029901, 2012.
- [9] G. Mention, M. Fechner, T. Lasserre et al., "Reactor antineutrino anomaly," *Physical Review D*, vol. 83, no. 7, Article ID 073006, 2011.
- [10] F. P. An, A. B. Balantekin, H. R. Band et al., "Measurement of the reactor antineutrino flux and spectrum at Daya Bay," <http://arxiv.org/abs/1508.04233>.
- [11] S.-B. Kim, "Observation of reactor electron antineutrino disappearance at RENO," *Nuclear Physics B—Proceedings Supplements*, vol. 235–236, pp. 24–29, 2013, Proceedings of the 25th International Conference on Neutrino Physics and Astrophysics.
- [12] S.-H. Seo, "New results from RENO and the 5 MeV excess," *AIP Conference Proceedings*, vol. 1666, Article ID 080002, 2015.
- [13] V. P. Martemyanov, L. A. Mikaelyan, V. V. Sinev, V. I. Kopeikin, and Y. V. Kozlov, "The Kr2Det project: search for mass-3 state contribution  $|U_{e3}|^2$  to the electron neutrino using a one-reactor-two-detector oscillation experiment at the krasnoyarsk underground site," *Physics of Atomic Nuclei*, vol. 66, no. 10, pp. 1934–1939, 2003, From: *Yadernaya Fizika*, vol. 66, p. 1982, 2003.
- [14] A. C. Hayes, J. L. Friar, G. T. Garvey, G. Jungman, and G. Jonkmans, "Systematic uncertainties in the analysis of the reactor neutrino anomaly," *Physical Review Letters*, vol. 112, no. 20, Article ID 202501, 2014.
- [15] H. F. Schopper, *Weak Interactions and Nuclear Beta Decay*, North-Holland, Amsterdam, The Netherlands, 1966.
- [16] A. Sirlin, "General properties of the electromagnetic corrections to the beta decay of a physical nucleon," *Physical Review*, vol. 164, no. 5, pp. 1767–1775, 1967.
- [17] A. Sirlin, "Radiative correction to the  $\bar{\nu}_e(\nu_e)$  spectrum in  $\beta$  decay," *Physical Review D*, vol. 84, no. 1, Article ID 014021, 4 pages, 2011.
- [18] P. Vogel, "Analysis of the antineutrino capture on protons," *Physical Review D*, vol. 29, no. 9, pp. 1918–1922, 1984.
- [19] D. H. Wilkinson, "Evaluation of beta-decay II. Finite mass and size effects," *Nuclear Instruments and Methods in Physics Research A*, vol. 290, no. 2-3, pp. 509–515, 1989.
- [20] B. R. Holstein, "Recoil effects in allowed beta decay: the elementary particle approach," *Reviews of Modern Physics*, vol. 46, no. 4, pp. 789–814, 1974.
- [21] P. Vogel and J. F. Beacom, "Angular distribution of neutron inverse beta decay,  $\bar{\nu}_e + \bar{p}e^+ + n$ ," *Physical Review D*, vol. 60, no. 5, Article ID 053003, 10 pages, 1999.
- [22] A. Pichlmaier, V. Varlamov, K. Schreckenbach, and P. Geltenbort, "Neutron lifetime measurement with the UCN trap-in-trap MAMBO II," *Physics Letters B*, vol. 693, no. 3, pp. 221–226, 2010.
- [23] K. Schreckenbach, H. R. Faust, F. von Feilitzsch, A. A. Hahn, K. Hawerkamp, and J. L. Vuilleumier, "Absolute measurement of the beta spectrum from  $^{235}\text{U}$  fission as a basis for reactor antineutrino experiments," *Physics Letters B*, vol. 99, no. 3, pp. 251–256, 1981.

- [24] K. Schreckenbach, G. Colvin, W. Gelletly, and F. Von Feilitzsch, "Determination of the antineutrino spectrum from  $^{235}\text{U}$  thermal neutron fission products up to 9.5 MeV," *Physics Letters B*, vol. 160, no. 4-5, pp. 325–330, 1985.
- [25] F. von Feilitzsch, A. A. Hahn, and K. Schreckenbach, "Experimental  $\beta$ -spectra from  $^{239}\text{Pu}$  and  $^{235}\text{U}$  thermal neutron fission products and their correlated antineutrino spectra," *Physics Letters B*, vol. 118, no. 1–3, pp. 162–166, 1982.
- [26] A. A. Hahn, K. Schreckenbach, W. Gelletly, F. von Feilitzsch, G. Colvin, and B. Krusche, "Antineutrino spectra from  $^{241}\text{Pu}$  and  $^{239}\text{Pu}$  thermal neutron fission products," *Physics Letters B*, vol. 218, no. 3, pp. 365–368, 1989.
- [27] K. Schreckenbach, G. Colvin, W. Gelletly, and F. Von Feilitzsch, "Determination of the antineutrino spectrum from  $^{235}\text{U}$  thermal neutron fission products up to 9.5 MeV," *Physics Letters B*, vol. 160, no. 4-5, pp. 325–330, 1985.
- [28] M. Fallot, S. Cormon, M. Estienne et al., "New antineutrino energy spectra predictions from the summation of beta decay branches of the fission products," *Physical Review Letters*, vol. 109, no. 20, Article ID 202504, 2012.
- [29] N. Haag, A. Gütlein, M. Hofmann et al., "Experimental determination of the antineutrino spectrum of the fission products of  $^{238}\text{U}$ ," *Physical Review Letters*, vol. 112, no. 12, Article ID 122501, 2014.
- [30] J. C. Hardy, L. C. Carraz, B. Jonson, and P. G. Hansen, "The essential decay of pandemonium: a demonstration of errors in complex beta-decay schemes," *Physics Letters B*, vol. 71, no. 2, pp. 307–310, 1977.
- [31] S. B. Kim, "New results from RENO," in *Proceedings of the 25th International Conference on Neutrino Physics and Astrophysics (Neutrino '12)*, Kyoto, Japan, 2012, <http://neu2012.kek.jp>.
- [32] H. de Kerret, "Results from Double Chooz," in *Proceedings of the 26th International Conference on Neutrino Physics and Astrophysics (Neutrino '14)*, Boston, Mass, USA, June 2014, <http://neutrino2014.bu.edu/>.
- [33] L. Zhan, "Recent results from daya bay," in *Proceedings of the 16 International Workshop on Neutrino Telescopes*, Venice, Italy, March 2015, <https://agenda.infn.it/conferenceDisplay.py?confId=8620>.
- [34] Y. Abe, C. Aberle, T. Akiri, J. C. Anjos, F. Ardellier, and A. F. Barbosa, "Indication of reactor  $\bar{\nu}_e$  disappearance in the double chooz experiment," *Physical Review Letters*, vol. 108, no. 13, Article ID 131801, 2012.
- [35] Y. Abe, C. Aberle, J. C. dos Anjos et al., "Reactor  $\bar{\nu}_e$  disappearance in the Double Chooz experiment," *Physical Review D*, vol. 86, no. 5, Article ID 052008, 2012.
- [36] Y. Abe, C. Aberle, J. C. dos Anjos et al., "First measurement of  $\theta_{13}$  from delayed neutron capture on hydrogen in the Double Chooz experiment," *Physics Letters B*, vol. 723, no. 1–3, pp. 66–70, 2013.
- [37] Y. Declais, H. de Kerret, B. Lefèvre et al., "Study of reactor antineutrino interaction with proton at Bugey nuclear power plant," *Physics Letters B*, vol. 338, no. 2-3, pp. 383–389, 1994.
- [38] Y. Abe, C. Aberle, J. C. dos Anjos et al., "Direct measurement of backgrounds using reactor-off data in Double Chooz," *Physical Review D*, vol. 87, no. 1, Article ID 011102, 7 pages, 2013.
- [39] Y. Abe, J. C. dos Anjos, J. C. Barriere et al., "Background-independent measurement of  $\theta_{13}$  in Double Chooz," *Physics Letters B*, vol. 735, pp. 51–56, 2014.
- [40] D. A. Dwyer and T. J. Langford, "Spectral structure of electron antineutrinos from nuclear reactors," *Physical Review Letters*, vol. 114, no. 1, Article ID 012502, 2015.
- [41] A. C. Hayes, J. L. Friar, G. T. Garvey et al., "Possible origins and implications of the shoulder in reactor neutrino spectra," *Physical Review D*, vol. 92, no. 3, Article ID 033015, 2015.
- [42] D. L. Fang and B. A. Brown, "Effect of first-forbidden decays on the shape of neutrino spectra," *Physical Review C*, vol. 91, no. 2, Article ID 025503, 2015.
- [43] M. B. Chadwick, M. Herman, P. Obložinský et al., "ENDF/B-VII.1 nuclear data for science and technology: cross sections, covariances, fission product yields and decay data," *Nuclear Data Sheets*, vol. 112, no. 12, pp. 2887–2996, 2011.
- [44] A. A. Sonzogni, T. D. Johnson, and E. A. McCutchan, "Nuclear structure insights into reactor antineutrino spectra," *Physical Review C*, vol. 91, no. 1, Article ID 011301, 2015.
- [45] M. A. Kellett, O. Bersillon, and R. W. Mills, "The JEFF3.1/-3.1.1 radioactive decay data and fission yields sub-libraries—2009," JEFF Report 20, NEA Report 6287, 2009.
- [46] J. H. Choi, W. Choi, Y. Choi et al., "Observation of energy and baseline dependent reactor antineutrino disappearance in the RENO experiment," <http://arxiv.org/abs/1511.05849>.

## Review Article

# Measurement of Atmospheric Neutrino Oscillations with Very Large Volume Neutrino Telescopes

J. P. Yáñez<sup>1</sup> and A. Kouchner<sup>2</sup>

<sup>1</sup>DESY, 15735 Zeuthen, Germany

<sup>2</sup>Laboratoire AstroParticule et Cosmologie (APC), Université Paris Diderot, CNRS/IN2P3, CEA/IRFU, Observatoire de Paris, Sorbonne Paris Cité, 75205 Paris, France

Correspondence should be addressed to J. P. Yáñez; [juan.pablo.yanez@desy.de](mailto:juan.pablo.yanez@desy.de)

Received 18 September 2015; Accepted 1 November 2015

Academic Editor: Vincenzo Flaminio

Copyright © 2015 J. P. Yáñez and A. Kouchner. This is an open access article distributed under the Creative Commons Attribution License, which permits unrestricted use, distribution, and reproduction in any medium, provided the original work is properly cited. The publication of this article was funded by SCOAP<sup>3</sup>.

Neutrino oscillations have been probed during the last few decades using multiple neutrino sources and experimental set-ups. In the recent years, very large volume neutrino telescopes have started contributing to the field. First ANTARES and then IceCube have relied on large and sparsely instrumented volumes to observe atmospheric neutrinos for combinations of baselines and energies inaccessible to other experiments. Using this advantage, the latest result from IceCube starts approaching the precision of other established technologies and is paving the way for future detectors, such as ORCA and PINGU. These new projects seek to provide better measurements of neutrino oscillation parameters and eventually determine the neutrino mass ordering. The results from running experiments and the potential from proposed projects are discussed in this review, emphasizing the experimental challenges involved in the measurements.

## 1. Introduction

Massive, mixed neutrinos, inferred from the phenomenon of oscillations, remain until this day, the only physics found beyond the original formulation of the Standard Model. While the Standard Model can be extended to account for these experimental facts, precise measurements of the parameters involved in the phenomenon are necessary to

constrain the different theories that attempt to explain it.

The current knowledge favors the existence of three active neutrinos (flavor eigenstates  $\nu_e$ ,  $\nu_\mu$ , and  $\nu_\tau$ ) whose mixing can be fully determined by the PMNS (Pontecorvo-Maki-Nakagawa-Sakata) matrix  $U$ . The matrix is often parameterized as the product of three rotation matrices, related to the mixing angles  $\theta_{12}$ ,  $\theta_{13}$ , and  $\theta_{23}$ , and a complex CP phase  $\delta$ :

$$U = \begin{pmatrix} 1 & 0 & 0 \\ 0 & c_{23} & s_{23} \\ 0 & -s_{23} & c_{23} \end{pmatrix} \begin{pmatrix} c_{13} & 0 & e^{-i\delta}s_{13} \\ 0 & 1 & 0 \\ -e^{i\delta}s_{13} & 0 & c_{13} \end{pmatrix} \begin{pmatrix} c_{12} & s_{12} & 0 \\ -s_{12} & c_{12} & 0 \\ 0 & 0 & 1 \end{pmatrix} \begin{pmatrix} e^{i\rho_1} & 0 & 0 \\ 0 & e^{i\rho_2} & 0 \\ 0 & 0 & 1 \end{pmatrix}, \quad (1)$$

where  $c_{ij} \equiv \cos\theta_{ij}$  and  $s_{ij} \equiv \sin\theta_{ij}$ . The last matrix in the multiplication does not affect neutrino oscillations and only exists if neutrinos are Majorana particles [1].

The three angles that determine the mixing matrix are known to a precision of 10% or better [2–4]. The absolute differences of the square of the masses (mass splittings

$\Delta m_{ij}^2 = m_i^2 - m_j^2$  with  $i, j = 1, 2, 3$ ), which play a role in oscillations, are known to a precision better than 5%. While the sign of the mass splitting between the states 1-2 ( $m_2 > m_1$ ) is known from matter effects in solar neutrino oscillations, the relative difference between  $m_3$  and  $m_1$  remains unknown. The relative values of the neutrino masses are commonly referred to as the neutrino mass ordering (NMO) (the determination of the mass ordering is sometimes confused with the determination of the neutrino “mass hierarchy,” which requires additional information on the absolute scale of the neutrino masses [5]), which has two possible options: the normal ordering (NO), with  $m_1 < m_2 < m_3$ , and the inverted ordering (IO), with  $m_3 < m_1 < m_2$ . The determination of the NMO is important as the parameter can discriminate between flavor symmetry models [6]. Also, the sensitivity of experiments attempting to determine the neutrino nature depends on the NMO [7, 8]. Finally, knowing the NMO would help to measure the value of the  $\delta$  phase, which in turn would be an important step forward towards solving the fundamental question of the prevalence of matter over antimatter in the Universe. Better measurements of all the parameters involved in neutrino oscillations are therefore necessary to understand if the current model is correct and how to incorporate it to the Standard Model.

In this view, atmospheric neutrinos remain a promising tool for studying oscillations: they cover a wide energy range, from MeV to TeV, and can reach a detector after traveling distances from a few to about 12700 km when they cross the Earth. No man-made beam covers a similar parameter space. However, the flux strongly decreases with energy. Detecting it implies building large detectors, such as very large volume neutrino telescopes (VLVNTs) to study atmospheric neutrino oscillations.

In the recent years first ANTARES and then IceCube/DeepCore have proven that these studies are feasible by analyzing interactions of neutrinos with energy as low as 15 GeV. The current result from IceCube on  $\sin^2\theta_{23}$  and  $\Delta m_{32}^2$  reaches a precision which is only a factor of three to four times less stringent than global fits which combine all available data [2, 3, 9]. Building upon the success of these studies, proposals of new, more densely instrumented telescopes, as extensions or part of new projects, have appeared. PINGU and ORCA aim to improve the precision of these measurements and reduce the energy threshold to a few GeV, where matter effects are strong, and use these effects to measure the NMO.

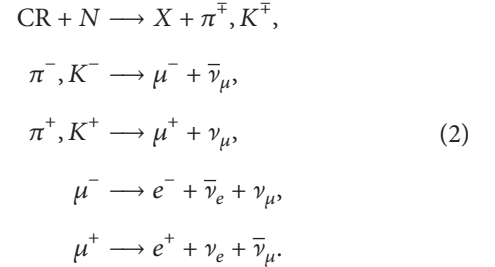
This review begins by covering, in Section 2, the current knowledge on atmospheric neutrinos and how oscillations affect their flux. Section 3 describes the design and operation of VLVNTs. Special attention is paid to relevant sources of uncertainty. The neutrino oscillation results produced by these experiments until this date are covered in Section 4. Section 5 discusses the possible studies with future detectors, and a short summary is given in Section 6.

## 2. Atmospheric Neutrino Oscillations

The flux of atmospheric neutrinos in the energies relevant for a VLVNT, together with how the flux is modified by neutrino

oscillations for those neutrinos that cross the Earth, is the topics covered in this section.

*2.1. A Neutrino Beam from Cosmic Rays.* Cosmic rays (CR) continuously arrive at the Earth from all directions and interact with nuclei in the atmosphere at altitudes of about 25 km above sea level and initiate showers of particles. During the shower development, charged mesons are produced that eventually decay in comparable numbers of muons and neutrinos:



The atmospheric muons produced in air showers can travel long distances before they decay. They are able to penetrate deep into the Earth, depending on their energy and the material that they are crossing [1], and constitute the dominant background in the measurement of atmospheric neutrinos.

Atmospheric neutrinos have been measured over a wide energy range [10–18] and multiple models predict their flux [19–21] (see Figure 1). The most noticeable difference between the models is the absolute flux, which changes by up to 20% both for electron and for muon (anti)neutrinos. Apart from that, the models agree that atmospheric neutrinos follow a power-law energy spectrum with a spectral index close to 3 in the energy range  $E_\nu = [3-100]$  GeV. Measurements from [11] estimate an uncertainty of  $\pm 0.04$  on the spectral index of atmospheric neutrinos. A similar uncertainty has been also derived from varying the underlying cosmic ray model in neutrino flux calculations [22].

Muon neutrinos dominate the flux and also have the hardest spectral index (see Figure 1). Since electron (anti)neutrinos mainly come from muons that lose energy before decaying (see (2)) their spectral index is softer, and their relative contribution to the total neutrino flux depends on energy and direction. The direction-averaged flux of  $\bar{\nu}_\mu$  is between 1.1 and 1.3 times smaller than that of  $\nu_\mu$ , depending on the energy. The electron (anti)neutrino direction-averaged flux at a few GeV is about 2.5 times smaller than its muon (anti)neutrino counterpart. Figure 2 shows isocontours of the neutrino flux flavor ratio as a function of energy and zenith angle for neutrinos that cross the Earth. The flux difference between  $\nu_\mu$  and  $\nu_e$  grows with both energy and  $|\cos\theta_z|$ . Already at 40 GeV the direction-averaged ratio is close to four.

Above 10 GeV the neutrino flux as a function of zenith angle is almost symmetric around  $\cos\theta_z = 0$ . The angular dependence of the flux at the detection site is influenced by hadronization processes, the local atmospheric density, and geomagnetic effects at the interaction point. The uncertainties associated with these processes result in energy-dependent

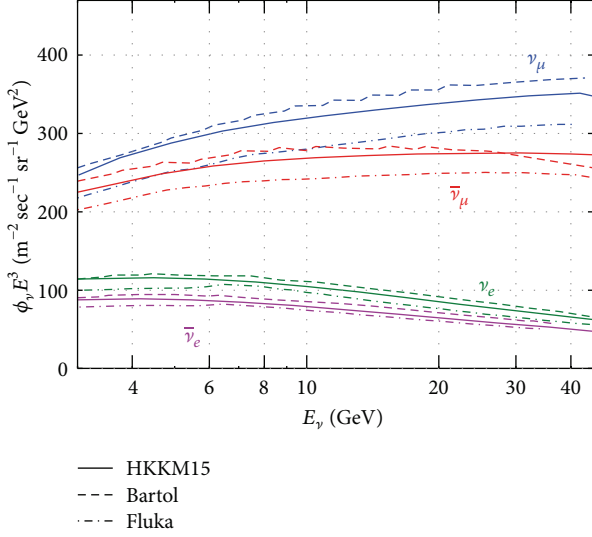


FIGURE 1: Comparison of predicted atmospheric neutrino fluxes per flavor for the energy range relevant for neutrino oscillation measurements with VLNT. Reproduced from [19, 23].

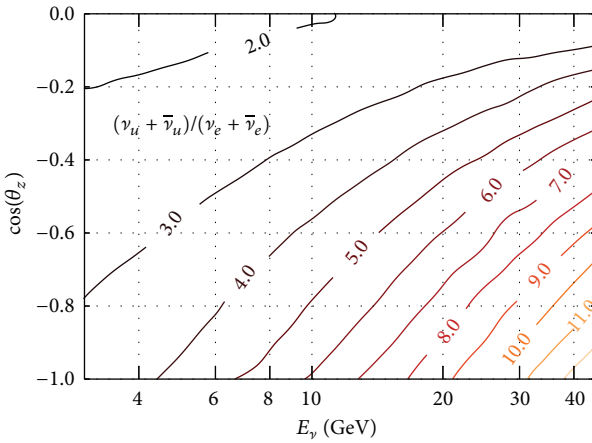


FIGURE 2: Isocontours of the ratio of  $(\nu_\mu + \bar{\nu}_\mu)/(\nu_e + \bar{\nu}_e)$  as a function of energy and neutrino arrival direction for neutrinos that cross the Earth, as predicted by the latest HKKM model [23]. The ratio is nearly up-down symmetric.

modeling errors of the arrival zenith angle by up to 20% on the ratio  $\nu/\bar{\nu}$  for muon neutrinos and 8% for electron neutrinos [22].

**2.2. Neutrino Oscillations at  $E_\nu \geq 5$  GeV.** The flux of atmospheric neutrinos at a detection site is modified by oscillations. The oscillations that act over the  $L/E$  parameter space accessible with atmospheric neutrinos that cross the Earth ( $L/E \sim 10^1 - 10^3$  km/GeV) are mainly driven by the large mass splitting,  $\Delta m_{32}^2 \approx \Delta m_{31}^2$ , and the mixing angles  $\theta_{13}, \theta_{23}$ . These are therefore parameters that VLNTs are sensitive to.

Neutrinos propagating in matter are subject to a potential due to coherent forward scattering with the particles in the medium [24]. For explanatory purposes, we consider the case of neutrinos traveling through matter with constant electron

density that results in a potential  $A = \pm 2\sqrt{2}G_F n_e(x)E_\nu$ , where  $G_F$  is the Fermi constant and the plus (minus) sign corresponds to neutrinos (antineutrinos). Computation of neutrino oscillation probabilities for the relevant energies has been done in [25], from where we take the approximations for the  $\nu_\mu$  to  $\nu_e$  transition, given by

$$P_{\mu e} \approx \sin^2 \theta_{23} \sin^2 2\theta_{13}^M \sin^2 \left[ \Delta^M \frac{L}{4E} \right], \quad (3)$$

while the survival probability of  $\nu_\mu$  is a somewhat more complicated expression,

$$P_{\mu\mu} \approx 1 - \sin^2 \theta_{13}^M \sin^2 2\theta_{23} \sin^2 \left[ (\Delta - \Delta^M + A) \frac{L}{8E} \right] - \cos^2 \theta_{13}^M \sin^2 2\theta_{23} \sin^2 \left[ (\Delta + \Delta^M + A) \frac{L}{8E} \right] - \sin^4 \theta_{23} \sin^2 2\theta_{13}^M \sin^2 \left[ \Delta^M \frac{L}{4E} \right], \quad (4)$$

and the transitions to  $\nu_\tau$  are simply

$$P_{\mu\tau} \approx 1 - P_{\mu e} - P_{\mu\mu}. \quad (5)$$

In these expressions  $\Delta \equiv \Delta m_{31}^2$  and  $\Delta^M$  is the effective mass splitting in matter, given by

$$\Delta^M \approx \sqrt{(\Delta m_{31}^2 \cos 2\theta_{13} - A)^2 + (\Delta m_{31}^2 \sin 2\theta_{13})^2}. \quad (6)$$

The superscript  $M$  also accompanies  $\theta_{13}$ , whose effective value in matter is

$$\sin 2\theta_{13}^M \approx \frac{\Delta m_{31}^2 \sin 2\theta_{13}}{\Delta^M}. \quad (7)$$

The mixing angle  $\theta_{23}$  is known to be close to maximal ( $\sim \pi/4$ ), and  $|\Delta m_{31}^2|$  is of the order of  $10^{-3}$  eV<sup>2</sup> [1]. The angle  $\theta_{13}$  has been recently measured and found to be small but nonzero [26–28]. It is then the case that  $\theta_{13}^M$  can acquire any value, depending on the neutrino energy and the electron density of the material being crossed, as shown in (7). For a low electron density or neutrino energy, the parameters (and equations) in vacuum are recovered. A particularly interesting case appears when  $A = \Delta m_{31}^2 \cos 2\theta_{13}$ , which gives  $\theta_{13}^M = \pi/4$ , maximizing the mixing between states 1–3; that is, a resonance appears [29]. The effective mass splitting acquires its minimum value under this condition and is reduced by a factor  $\sin 2\theta_{13}$ .

The resonance that leads to maximal 1–3 mixing can only happen if the potential  $A$  and the mass difference  $\Delta m_{31}^2$  have the same sign, and so for neutrinos in the case of NO and antineutrinos in the case of IO. Identifying whether the resonance takes place in neutrinos or antineutrinos is a way to identify the NMO.

For  $A \gg \Delta m_{31}^2 \cos 2\theta_{13}$  a saturation effect occurs, where the effective angle in matter goes to  $\pi/2$  and the effective mass splitting is then well approximated by  $A$ . In the saturated regime transitions of the type  $\nu_e \rightarrow \nu_\mu$ , given in (3),

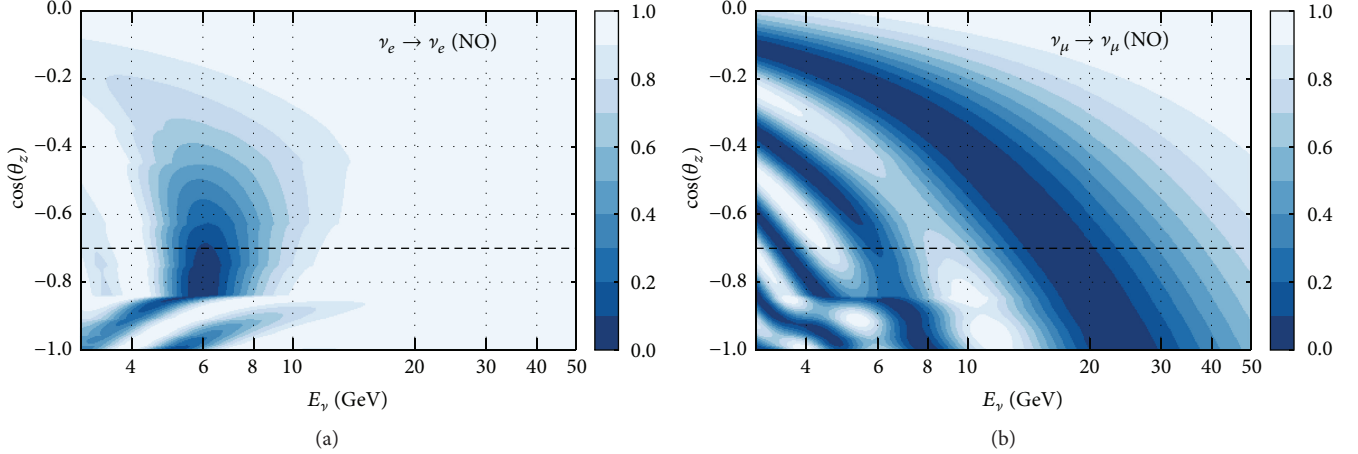


FIGURE 3: Survival probabilities for  $\nu_e$  (a) and  $\nu_\mu$  (b) as a function of neutrino energy and arrival direction for Earth crossing trajectories affected by oscillations ( $\cos(\theta_z) \leq 0$ ). Calculated using the values in [3] assuming a normal mass ordering. Resonant matter effects produce the large disappearance of  $\nu_e$  around 6 GeV and  $\cos\theta_z \sim -0.8$ , as well as the discontinuities on the survival pattern of  $\nu_\mu$  below 15 GeV. The abrupt changes observed at  $\cos\theta_z \sim -0.85, -0.45$  are due to sharp jumps in the electron density profile of the Earth. The dashed line indicates the connection between these figures and Figure 4.

are suppressed by the factor  $\sin^2 2\theta_{13}^M$ . The effective matter parameters also modify  $P_{\mu\mu}$  by making the last two terms in (4) go to zero, resulting in the simpler expression

$$P_{\mu\mu} = 1 - \sin^2 2\theta_{23} \sin^2 \left[ \Delta \frac{L}{4E} \right], \quad (8)$$

with all the oscillated  $\nu_\mu$  turning into  $\nu_\tau$ .

The CP-violating phase  $\delta$  is not present in the approximate formulas shown. The reason is that the parameter  $\delta$  always appears in oscillation probabilities accompanied by a factor  $\Delta m_{21}^2 / \Delta m_{31}^2$ , which suppresses its contribution [30]. Note, however, that the approximations presented here serve the purpose of explaining the main features of neutrino oscillations in matter. Figures contained in this review, as well as the latest data analyses discussed, use numerical calculations of oscillation probabilities that do not rely on simplified analytical expressions.

**2.3. An Oscillating Atmospheric Neutrino Flux.** The atmospheric neutrinos under consideration, of a few GeV, are mostly  $\nu_\mu + \bar{\nu}_\mu$  produced around a height of 25 km in the atmosphere, where the matter density is low enough to be approximated as vacuum. For most production angles the neutrinos proceed to cross the Earth, which has a nonnegligible matter density.

Earth's matter profile can be well explained as concentric shells, each one with a constant density [31]. To study the transitions that take place, consider the oscillation parameters from [3] and the electron number density of the mantle,  $n_e = 2.5 \text{ cm}^{-3} N_A$ , where  $N_A$  is Avogadro's number. Neutrinos crossing the mantle experience the resonance around  $E_\nu \simeq 6 \text{ GeV}$  (see (7)), while the saturation condition  $A \gg \Delta m_{31}^2 \cos 2\theta_{13}$  is fulfilled already at  $E_\nu \sim 12 \text{ GeV}$ . Neutrinos measured by VLNTs then experience oscillations in either the resonant or saturated regime, depending on the energy threshold of the detector.

Another interesting effect takes place on neutrinos that cross the Earth's core. These neutrinos experience a symmetric electron density profile that changes abruptly. For the right combination of neutrino energy and electron densities, a so-called *parametric resonance* can appear [32–35]. The effect, however, is not the dominant one at the energies to which future projects (Section 5) will be sensitive.

In the saturated regime atmospheric neutrino oscillations are independent of the mass ordering, dominated by  $\nu_\mu \rightarrow \nu_\tau$  transitions and well described by (8). Near the resonance condition transitions involving electron (anti)neutrinos also play a role, and patterns become complex. Figure 3 shows the survival probabilities of  $\nu_e$  and  $\nu_\mu$  for neutrinos and normal mass ordering. The original electron neutrino flux is expected to fully disappear due to matter effects over  $E_\nu = [5, 8] \text{ GeV}$  and  $\cos\theta_z = [-0.9, -0.5]$ . The suppression of these oscillations due to saturation can be observed at about 10 GeV. The survival probability of  $\nu_\mu$  shows abrupt changes that are due to the effects of matter. Muon neutrinos oscillate even if the resonance conditions are not fulfilled, which makes the effects of the resonance less obvious than for electron neutrinos. Resonant matter effects appear in the  $\nu_\mu$  survival probability as modifications on the otherwise smooth and periodic disappearance pattern, as shown in Figure 3. Saturation is reached above 15 GeV and the survival probability becomes smooth.

Figure 4 shows the transition probabilities of  $\nu_e$  and  $\nu_\mu$  into different flavors for the arrival direction  $\cos\theta_z = -0.7$  assuming a normal mass ordering. They correspond to a one-dimensional projection of Figure 3 along the dashed line. The bands demonstrate how the uncertainties on the oscillation parameters impact the expected probabilities. For  $\nu_e$  it is easy to observe the same disappearance as in Figure 3, with neutrinos oscillating equally into  $\nu_\mu$  and  $\nu_\tau$ . Transitions of  $\nu_\mu$  to other flavors are complicated by matter effects, which open the  $\nu_\mu \leftrightarrow \nu_e$  channel and thus modify the survival probability of  $\nu_\mu$ .

Measurements of neutrino fluxes above the saturation energy of about 15 GeV are largely independent of  $\theta_{13}$ , the neutrino/antineutrino admixture of the sample, and the ordering of neutrino masses. They provide excellent data for determining  $\sin^2\theta_{23}$  as well as  $|\Delta m_{31}^2|$ .

The NMO can only be accessed with neutrinos below 15 GeV, where matter induced resonances occur either for neutrinos or for antineutrinos. The survival probability of muon (anti)neutrinos, the main component of atmospheric neutrinos, is modified by matter effects by about 20%. As will be discussed in Section 3, VLNT cannot separate neutrinos from antineutrinos event-wise and instead rely on the  $\nu/\bar{\nu}$  flux ratio and the difference in cross sections to identify whether oscillation probabilities of neutrinos or antineutrinos are modified by matter effects.

An interesting feature introduced by matter effects is that, instead of oscillating fully into  $\nu_\tau$ , muon neutrinos also change into  $\nu_e$ . Transitions of these type are almost symmetric between the two flavors (see Figure 4), but since the flux of  $\nu_\mu$  is several times that of  $\nu_e$  at the energy and zenith angle of interest (see Figure 2), the net effect is a significant excess of electron neutrinos with respect to the original  $\nu_e$  flux. In the NO, the  $\nu_e$  flux is enhanced, while for an IO the enhancement is realized for  $\bar{\nu}_e$ . Because of the initial  $\nu_\mu/\bar{\nu}_\mu$  flux ratio and the differences in the  $\nu_e/\bar{\nu}_e$  cross sections, different orderings result in a different number of detected events. Figure 5 shows the ratio between expected interaction rates of  $\nu_e + \bar{\nu}_e$  for normal and inverted orderings, including all of the oscillation channels. A factor of 2.1 is applied to neutrinos to account for the difference in cross sections. The normal mass ordering predicts up to 30% more events in the region  $E_\nu = [5, 8]$  GeV and  $\cos\theta_z = [-0.9, -0.5]$ . Measurements of the flux of atmospheric electron neutrinos thus provide suitable data for determining the NMO.

The VLNTs currently in operation are presented in detail in the next section. With an energy threshold of about 15 GeV they operate in the saturated regime. They can measure muon neutrino disappearance as well as tau neutrino appearance, and thus  $\theta_{23}$  and  $|\Delta m_{31}^2|$ . Measuring the sign of  $\Delta m_{31}^2$ , on the other hand, requires measuring differences in oscillation probabilities below this threshold (see Figures 3 and 4). This is the main goal of the next-generation detectors discussed in Section 5.

### 3. Very Large Volume Neutrino Telescopes

A generic VLNT is a three-dimensional array of photo-sensors detecting the Cherenkov light of charged particles produced after a neutrino interaction. The secondaries of neutrino interactions above a few GeV produce enough light so that they can be observed by sensors several meters apart. The spacing between the optical sensors defines the energy threshold of VLNTs, which is approximately 15 GeV in currently operating detectors.

**3.1. VLNTs in Operation.** The optical sensors of VLNTs are deployed at depths of 1km or more, in an optically transparent, naturally occurring medium. Sensors are laid out in lines or strings that are operationally independent. The

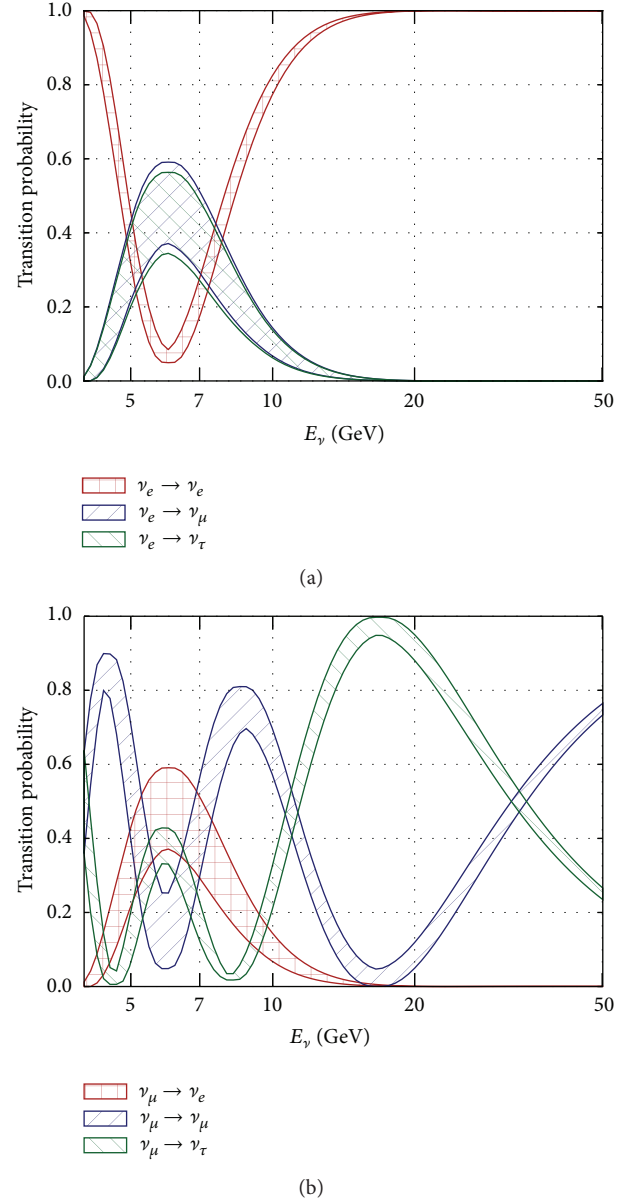


FIGURE 4: Transition probabilities for electron (a) and muon (b) neutrinos that arrive at a detector from  $\cos\theta_z = -0.7$  (mantle-crossing trajectory marked by a dashed line in Figure 3). The bands encompass the results of the calculation once the uncertainties on the oscillation parameters from [3] are included. Normal mass ordering is assumed. If the resonance was absent (inverted mass ordering or transitions for antineutrinos) (a) would show oscillations with amplitudes smaller than 0.1, while (b) would show transitions only between muon and tau neutrinos.

spacing between sensors is uneven, being considerably larger in the  $x$ - $y$  plane (in between lines/strings) than in the  $z$  plane. The sensors also have a preferred acceptance for light coming from below, although this might change for future detectors.

The neutrino telescopes currently in operation are IceCube in Antarctica [42], ANTARES in the Mediterranean Sea [43], and the prototype of the Gigaton Volume Detector in Lake Baikal [44]. Both ANTARES and IceCube have

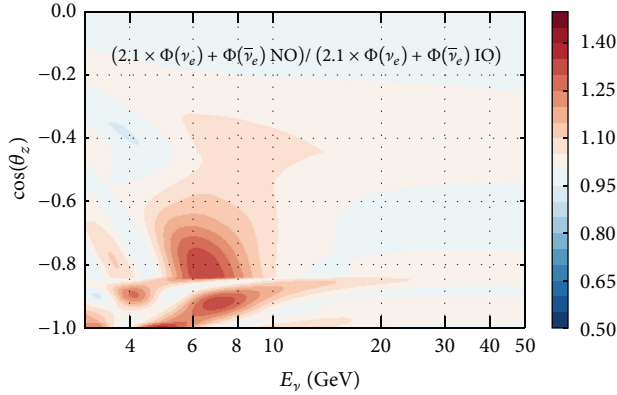


FIGURE 5: Expected interaction rate of electron neutrinos and antineutrinos predicted by a NO over the rate predicted assuming an IO. Using the oscillation parameters in [3]. Because of the flux ratio  $\nu_\mu/\bar{\nu}_\mu$  and the cross section difference, estimated to be 2.1 times larger for neutrinos than antineutrinos, more electron neutrino interactions are expected for a NO.

published studies of neutrino oscillations and are therefore the only ones discussed in this review.

**3.1.1. Detector Design and Layout.** ANTARES is located between depths of 2025–2475 m, 20 km away from Toulon (French Riviera), in the Mediterranean Sea [43]. It comprises 885 optical modules (OMs) [45], distributed along 12 flexible lines. OMs are grouped in triplets, with 25 triplets per line. The distance between triplets is 14.5 m, and the separation between lines ranges from 60 to 70 m, as sketched in Figure 6. Acoustic devices, tiltmeters, and compasses are used to monitor the shape of the detector, which is influenced by sea currents.

IceCube is located at depths between 1450 and 2450 m at the geographic South Pole [42]. The in-ice part of IceCube consists of 5160 downward-facing digital optical modules (DOMs) [46]. The detector has 86 strings, each holding 60 DOMs. Of these, 78 strings are arranged in a hexagonal grid with a typical distance of 125 m (horizontal spacing) and 17 m (vertical spacing) between DOMs. A sketch of the detector layout is shown in Figure 7.

The lower center region of IceCube, from 1760 m down to 2450 m, houses DeepCore [47], a region of denser instrumentation (7 m DOM vertical spacing), where eight strings are separated by 40–70 m. Some 50% of the PMTs in this region have 35% higher quantum efficiency than the standard IceCube PMTs. The DeepCore fiducial volume used for data analysis is defined by a cylinder with a height of 350 m and a radius of approximately 150 m that starts below a dust layer, where the light transparency is reduced, as shown in Figure 7. This volume, which corresponds to roughly 2.5 times that of ANTARES, encloses about 550 DOMs with reduced spacing and results in a threshold for detection and reconstruction of neutrinos of about 15 GeV.

The optical modules of both IceCube and ANTARES are glass spheres enclosing a ten-inch PMT, optical coupling gel, and a  $\mu$ -metal cage for magnetic shielding. The IceCube

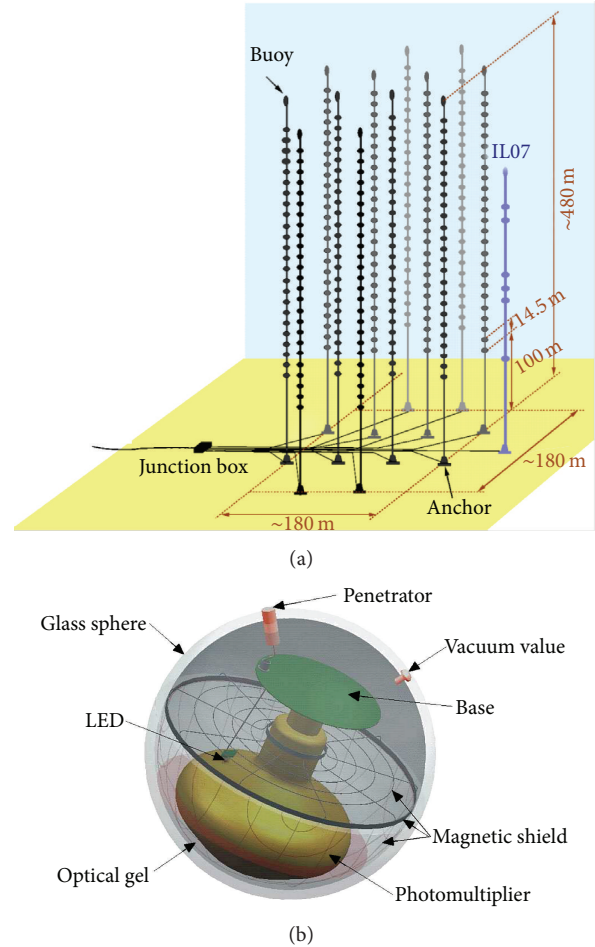


FIGURE 6: The ANTARES detector configuration (a). The 12 detection lines are connected to a single junction box providing power and transferring all data recorded by the OMs to the shore station through a main electrooptical cable. (b) shows the OM and the components it houses, including a 10" photomultiplier tube.

OM digitizes the waveforms detected by the PMT inside the module before transmission [46], while the ANTARES OM keeps the readout to a minimum and only transmits the time and amplitude of a signal above threshold [53]. ANTARES optical modules have a baseline noise rate of 70 kHz at single photon level [54], while for IceCube (DeepCore) OMs the noise is 0.45 kHz (0.65 kHz) [55].

**3.1.2. Optical Medium and Calibration.** The optical properties of the medium affect the time of arrival and the number of detected Cherenkov photons. At the ANTARES site (salt water) the absorption length, which is 60 m for blue light ( $\lambda \approx 470$  nm) and 26 m for UV light ( $\lambda \approx 375$  nm), reduces the number of photons observed. The effective scattering length, which is 256 m for blue light and 122 m for UV light, is considerably larger than the spacing between sensors [56]. In the clear ice in which DeepCore is located the absorption length of UV light ( $\lambda \approx 400$  nm) is of the order of 200 m, which is larger than the spacing between sensors. The effective scattering length in the deep Antarctic ice is

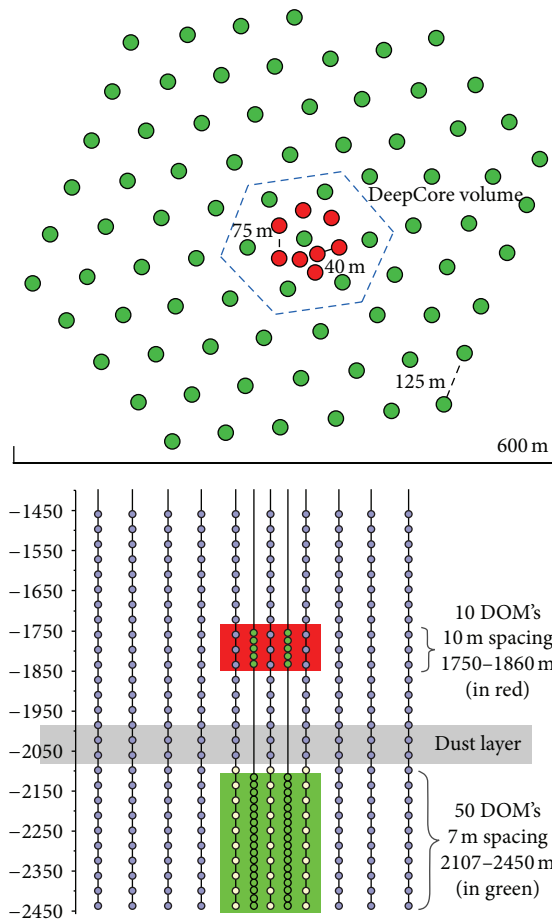


FIGURE 7: IceCube. Top and side schematic projections of the detector. The DeepCore volume used for analysis is highlighted in both figures.

approximately 50 m, comparable to the string distance of DeepCore, thus significantly modifying the expected time of arrival of photons [57, 58].

Water offers the advantage of being a homogeneous medium. Nonetheless, sea currents can deviate the detector lines so the position of the lines needs to be monitored constantly. This is achieved by combining acoustic triangulations with tilt and compass measurements yielding a precision better than 10 cm, which does not affect the angular resolution [59]. High sea currents can also trigger bioluminescence bursts that must be accounted for in the optical background simulation, in addition to the stable optical noise arising from  $^{40}\text{K}$  decays. The latter can be used for determining the absolute detection efficiency of the optical modules.

In ice, the positions of the optical modules are fixed and known to be within a few cm. Noise levels are constant and a hundred times lower than in salt water after the detector has stabilized. A disadvantage of using ice is that the medium is not homogeneous and its structure has to be modeled. This is particularly challenging in the immediate surroundings of the optical modules. Columns of the original glacier are melted to deploy the instrumentation. The refreezing process leaves behind clear ice near to the boundaries of the hole,

and a cylinder of ice of about 10 cm in diameter with a high concentration of bubbles towards the center of the column. These changes in ice properties modify the DOM angular acceptance measured in the laboratory. Future detectors in ice will consider the possibility of degassing the water to avoid trapping air bubbles inside the hole ice and with that reduce the impact of the medium.

The absolute optical efficiency of the optical modules as well as their angular acceptance must be determined in situ after deployment. ANTARES and IceCube use both controlled light sources and minimum ionizing muons to calibrate the efficiency and timing accuracy of their optical modules [60–62]. Relative arrival times are known with a precision better than 3 ns and 1.5 ns for IceCube [46] and ANTARES, respectively.

**3.2. Neutrino Interactions.** The dominant neutrino interaction for most of the energy range that VLNTs can access is neutrino-nucleon deep inelastic scattering (DIS), with other processes being only a subdominant contribution. Nonetheless, below 15 GeV, the region of interest to search for matter effects in neutrino oscillations and the NMO, quasi-elastic scattering, and production of resonances compete with DIS processes. Figure 8 shows a calculation of the competing  $\nu N$  cross sections around the GeV region, together with the data available.

Most of the knowledge of neutrino-nucleon cross sections between 1 and 15 GeV comes from bubble chambers or spark chamber detectors which collected comparatively small data samples. Thus, the constraints on the models that describe them are rather weak [36]. The uncertainty with the largest impact on the neutrino cross sections for quasi-elastic and resonant interactions, which changes them by up to 40%, is the value of the axial mass that effectively describes the nucleon form factor and has an estimated error of 15%–25% [36, 63]. DIS interactions in the crossover region have a small momentum transfer. Nonperturbative QCD calculations are required [64], and the estimated errors are as well of the order of 20% [65].

Deep inelastic scattering accounts for 90% or more of the total cross section of neutrinos and antineutrinos above an energy of roughly 12 GeV, as shown in Figure 8. DIS in the perturbative regime is comparatively better understood than the processes discussed so far, with uncertainties coming mainly from the determination of the parton distribution functions (PDFs) of the nucleons. The uncertainties on the PDFs change the total cross section by 5% or less [65].

At these energies the neutrino-nucleon DIS charged current (CC) cross section is quasi-independent of the inelasticity  $y$  ( $y = 1 - E_{\text{lepton}}/E_\nu$ ) of the interaction, while for antineutrinos the cross section is accompanied by a factor  $(1 - y^2)$ , which suppresses kinematic configurations where the hadronic part of the interaction takes most of the energy. The inelasticity dependence makes the total  $\bar{\nu}N$  cross section about one-half of that of  $\nu N$ .

While the neutrino-nucleon DIS CC cross sections for  $\nu_e$  and  $\nu_\mu$  are equal, the  $\nu_\tau N$  one is suppressed due to the mass of the tau lepton. It is only at  $E_\nu \sim 40$  GeV that the cross section reaches half of the value of the other neutrino flavors [66].

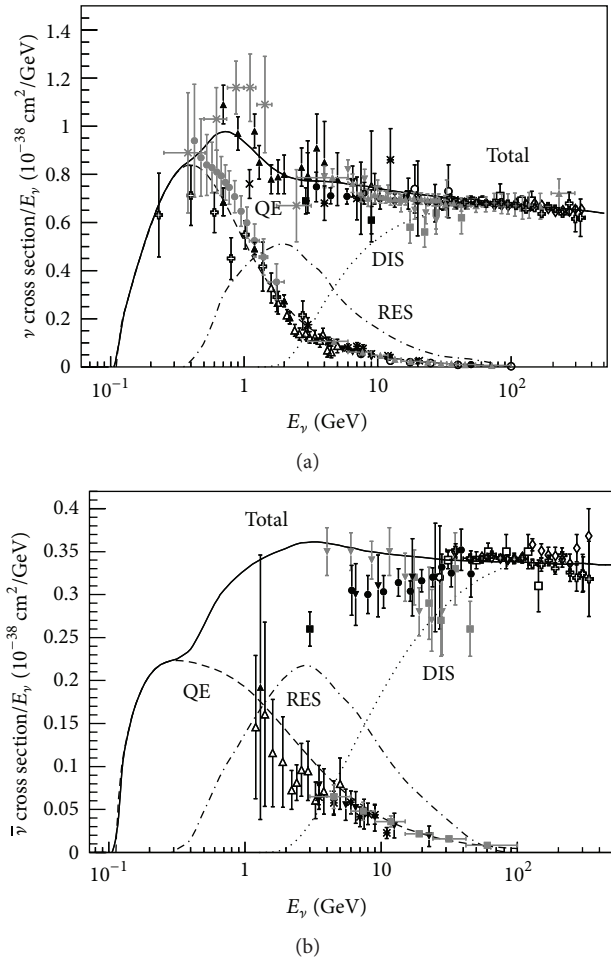


FIGURE 8: Collection of existing muon neutrino (a) and antineutrino (b) charged current cross section measurements and predictions as a function of neutrino energy (see [36] for details on the experiments contributing to the data points and [37] for a description of the model used). The contributing processes in this energy region include quasi-elastic (QE) scattering, resonance production (RES), and deep inelastic scattering (DIS). Taken from [36].

In neutral current interactions (NC) one or several hadrons are produced, initiating a hadronic shower. In charged current (CC) interactions a hadronic shower is also present, but now the neutrino transforms into a charged lepton. Electrons and taus also initiate a shower of particles after they are produced (the tau lepton has a 17% probability to decay into a muon. However, due to energy losses and other particles involved in the processes, muons from tau decays with a range larger than a few meters are uncommon). Muons, on the other hand, travel practically undisturbed and lose energy at a quasi-constant rate. For muons passing through water  $dE/dx \sim 0.25 \text{ GeV/m}$  up to a few hundred GeV [1]. Once they travel distances comparable to the detector spacing they can be identified, and charged current  $\nu_\mu$  interactions can be tagged.

**3.3. Event Reconstruction.** Neutrino interactions are reconstructed using the number of photons recorded by the optical

module (or time over threshold), as well as the time at which they arrive. For the energy range under consideration, the most general hypothesis is an interaction which produces a hadronic shower (all interaction types), an electromagnetic shower ( $\nu_e$  CC), or a long range muon ( $\nu_\mu$  CC). The direction in which these particles are produced is reconstructed from the arrival times of the emitted photons. The Cherenkov light of muons is produced almost perfectly in a cone. The light coming from the cascade is also beamed in the Cherenkov angle, but the smearing due to multiple particle contributions to it is larger, which degrades the achievable precision of directional reconstructions. This smearing effect is stronger for hadronic showers.

The energy reconstruction of showers is primarily given by the number of photons detected from a given interaction, and its accuracy depends mainly on the reconstructed position of the interaction vertex. To estimate the energy an assumption has to be made on whether the shower is hadronic or electromagnetic. The energy of muons can be estimated by the observed range in the detector.

In principle it is possible to fit the directions of both cascade and track components in an interaction. The sparse instrumentations of the detectors, however, make it challenging. In the simplest approach, tracks and cascades are assumed to be collinear.

**3.4. Simulation Tools.** The measurement of diffuse fluxes in VLVNTs, such as the one required to determine oscillation parameters, relies fully on the correct modeling of the experimental set-up. Atmospheric muons, the leading source of background, are simulated in IceCube using full showers and parameterizations obtained from CORSIKA [69]. ANTARES uses the MUPAGE program, which produces muons based on a parameterization tuned to MACRO data [70].

Neutrino interactions in IceCube are simulated using the GENIE package [71] ( $E_\nu \leq 200 \text{ GeV}$ ) and NuGen/ANIS [72] ( $E_\nu \geq 50 \text{ GeV}$ ). Besides GENIE, ANTARES uses an in-house neutrino generator based on LEPTO [73] for the full energy range, with the PYTHIA package [74] handling the hadronization processes. The neutrinos produced are then weighted to match the flux predictions of the Honda and/or Bartol groups [20, 75].

The propagation of short-ranged particles produced in the interaction is done, both in IceCube and ANTARES, using the Geant software [76] as basis. Parameterizations of the light yield of these particles are produced by both experiments and used to obtain the detector response to high-energy hadrons, electrons, and photons [77], while low-energy hadrons ( $E \leq 30 \text{ GeV}$ ) are propagated individually. Muons are propagated using code optimized for simulation of long ranged leptons, namely, MUSIC [78] and MUM [79] in ANTARES and MMC [80] in IceCube.

The Cherenkov photons produced during the propagation of charged particles are individually traced through the ice in IceCube/DeepCore, while ANTARES uses expectation from tables. Low-energy future projects (Section 5) plan to use individual photon tracing to assure that the optical properties of the medium are included in detail. After the photons are propagated, the response of the optical module is

recreated, and events from simulation and experimental data are treated equally.

*3.5. Large Statistics versus Precise Reconstruction.* The current knowledge on the oscillation parameters in the atmospheric sector comes from experiments which differ from VLVNTs substantially: they are Super-Kamiokande [81], T2K [82], MINOS [83], which is no longer in operation, and the recently commissioned NOvA [84]. Table 1 contains a qualitative comparison of the detectors and neutrino sources used by these experiments and VLVNTs.

Super-Kamiokande, which also measures atmospheric neutrinos, has about twenty (ten) times the number of optical sensors as DeepCore (ANTARES), separated by a few cm, placed on a cylindrical tank with a diameter similar to the interstring distance in ANTARES/DeepCore. Neutrinos are detected using the rings produced after the Cherenkov light of the charged products of the interaction hits the walls of the detector. Muons, electrons, and pions can be identified by the differences in the ring pattern they produce. Because of its considerable smaller size and the steepness of the spectrum of atmospheric neutrinos, its operating energy is lower than that of VLVNTs.

Long baseline experiments, such as T2K, MINOS, and NOvA, use neutrinos from particle accelerators and have near and far detectors. While T2K uses Super-Kamiokande as a far detector, MINOS and NOvA follow an experimental set-up where the far detector is smaller than Super-Kamiokande but is more densely instrumented, can be magnetized, and observes the path of individual particles coming from a neutrino interaction. These set-ups benefit from their controlled neutrino source and detailed event reconstruction. Unlike the case of atmospheric neutrino experiments, long baseline experiments have a unique baseline and cover a narrow energy range, allowing for better precision but also limiting the  $L/E$  region that they can access. It should also be noted that, as stated in Section 3.2, the poor knowledge of neutrino interactions at energies of a few GeV introduces significant uncertainties in the data analysis of long baseline oscillation experiments.

VLVNTs have become competitive with accelerator based experiments thanks to the possibility of observing multiple combinations of baseline and energy ( $L/E$ ) and with Super-Kamiokande because VLVNTs can collect large event samples and in an energy range where most events are DIS which can be modeled with high accuracy. The sparse instrumentation does not permit observation of small details of the interaction but in the same way reduces the impact from uncertainties in the hadronization processes, one of the leading systematic uncertainties for MINOS [87] and T2K [4]. Reconstruction accuracy and proper handling of systematic uncertainties are the most important points to consider for precision measurements with VLVNT.

## 4. Neutrino Oscillation Measurements from Running VLVNTs

The ANTARES and IceCube collaborations have published measurements of oscillations studying the muon neutrino

disappearance channel. Above 15 GeV, where these detectors operate, muon neutrinos oscillate into tau neutrinos, following (8). Signal neutrinos, that is,  $\nu_\mu$  interacting via CC with  $E_\nu \sim 25$  GeV, are typically recorded by a handful of optical modules both for ANTARES and for IceCube's DeepCore. The events develop over a distance of order of 100 m and thus can be fully contained in both detectors.

The measurement of neutrino oscillations in VLVNTs follows a general strategy which begins with the reduction of the dominant sources of background, that is, atmospheric muons and pure noise. Straight cuts are applied on variables of which the distribution for neutrinos differs from that of background sources. They generally aim for a neutrino purity higher than 95%.

For the currently published results of both experiments, the presence of a muon in a neutrino interaction is required for an event to be selected for analysis. The analyses are done by comparing the histograms of data and simulation as a function of the reconstructed variable(s) used. The simulation is modified by the physics parameters of interest,  $\theta_{23}$  and  $\Delta m_{32}^2$ , and by nuisance parameters which absorb the systematic uncertainties involved in the measurement. Errors are derived from a scan of the likelihood landscape, and/or directly using a  $\chi^2$  approximation.

The results of ANTARES and IceCube that have been made public until now use only events coming below the horizon. ANTARES removes the downgoing region because it is dominated by atmospheric muons. IceCube uses the instrumentation outside DeepCore to veto atmospheric muons; nevertheless the contribution of these muons in the downgoing region is still significant, so the region is also removed from analysis. This situation is different for Super-Kamiokande, where events from the entire zenith range are used in oscillation studies and top-down ratios are used to reduce uncertainties. Ongoing studies within IceCube are exploring the possibility of using neutrinos coming from above the horizon in future results [88].

*4.1. First Measurements of Oscillations from ANTARES.* The ANTARES collaboration presented the first results on the study of neutrino oscillations from VLVNTs [38]. The analysis relied on the muon track reconstruction described in [89], which fits the depth at which the Cherenkov cone of light arrives at the OMs as a function of time. This corresponds to a hyperbola of which the orientation of the asymptotes depends on the zenith angle. An algorithm that searches for these patterns, without assuming any knowledge on the arrival angle of the emitter, was implemented. The algorithm is capable of rejecting noise hits and keeping events down to energies of 20 GeV ( $R_\mu = 100$  m) with photons in a single line and 50 GeV ( $R_\mu = 250$  m) in multiple lines. Misreconstructed muons that appear upgoing are removed by selecting only events which have a good fit quality. This cut also effectively reduces the contribution of NC interactions from all flavors and  $\nu_e$  CC interactions.

The median zenith angle resolution with respect to the neutrino direction of single-line events is  $3.0^\circ$ , and it reduces to  $0.8^\circ$  for multiline events. The energy of the neutrino is

estimated solely by the muon range, resulting in a lower limit to the neutrino energy, where  $E_{\text{reco}} = (50\% \pm 22\%)E_\nu$ .

The analysis is done by comparing data and simulation as a function of  $E_{\text{reco}}/\cos\theta_{\text{reco}}$  by means of a  $\chi^2$ , combining single- and multiline selections. Only events below the horizon ( $\cos\theta_{\text{reco}} < -0.15$ ) are considered. Systematic uncertainties are implemented using two normalization coefficients, for single- and multiline events, as pull factors in the  $\chi^2$  following the method presented in [90]. These factors absorb the effects of changes in the average quantum efficiency ( $\pm 10\%$ ), optical properties of sea water ( $\pm 10\%$ ), the spectral index of atmospheric neutrinos ( $\pm 0.03$ ), and disagreements between data and simulation during the selection (varying cut values). The overall normalization of the  $\nu_\mu$  flux and detector efficiency are left unconstrained.

The data analyzed were taken between March 2007 and December 2010, corresponding to a detector live time of 863 days. A total of 2126 neutrino candidates were selected. The measured oscillation parameters, which were found to be compatible with the world's average, are indicated in Figure 13. Data and simulation were in good agreement, as it can be seen in Figure 9, which results in a  $\chi^2/\text{NDF} = 17.1/21$ . The case of no oscillations could be rejected at the  $3\sigma$  confidence level. The ANTARES collaboration will proceed to an updated analysis of this kind with the full data sample collected until the end of the data taking, circa 2017.

**4.2. First Measurements from IceCube DeepCore.** To this date, IceCube has reported results of four neutrino oscillation analyses of the low-energy DeepCore data. The selection, reconstruction, and analysis methods have been refined in each step. The low-energy data for all studies comes from the DeepCore filter and trigger [47]. The main source of background at this stage are triggers due to sensor self-noise and atmospheric muons. The instrumentation outside the fiducial volume of DeepCore (see Section 2.1 and Figure 7) is used to tag atmospheric muons. Low-energy neutrino interactions are required to start within the DeepCore fiducial volume, while no requirement is imposed for full containment.

Systematic uncertainties are accounted for using additional parameters which modify the expected number of events. An energy-dependent term ( $E^{-\gamma}$ ,  $\gamma \pm 0.05$ ) and a free overall normalization absorb total cross section uncertainties and the uncertainties on the spectral index of the neutrino flux. The electron neutrino flux is varied by  $\pm 20\%$  around the predicted value. The cosmic ray models which predict the cosmic muon contamination are varied to obtain a robust estimate. The effects of changing the optical description of the pristine ice, as well as the refrozen ice around the DOMs, are studied by producing multiple simulation sets.

The initial three oscillation studies from DeepCore, presented first herein, were restricted to a single year of detector live time. Two used a partial configuration (IC79, two DeepCore strings missing) and one used the full detector (IC86). The first analysis [39], from here on IC79-A, used a DeepCore low-energy sample where the effect of oscillations is expected ( $E_\nu < 100$  GeV, 719 events) and an IceCube high-energy sample, where oscillations play no role, to constrain

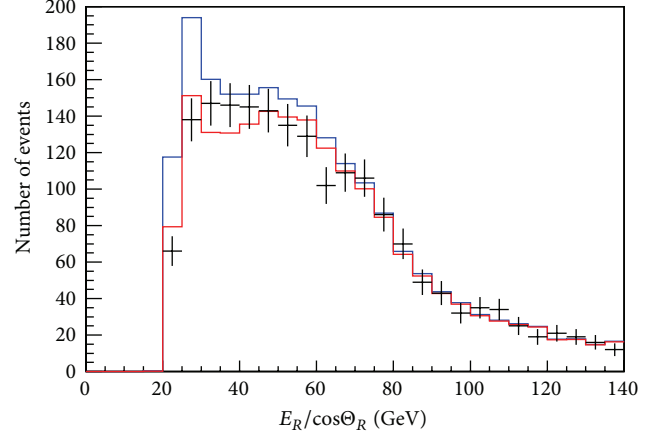


FIGURE 9: Distribution of  $E_{\text{reco}}/\cos\theta_{\text{reco}}$  for events selected in the oscillation analysis of ANTARES. Data are shown in black, simulation without oscillations is in blue, and simulation with the fit parameters is given in red. From [38].

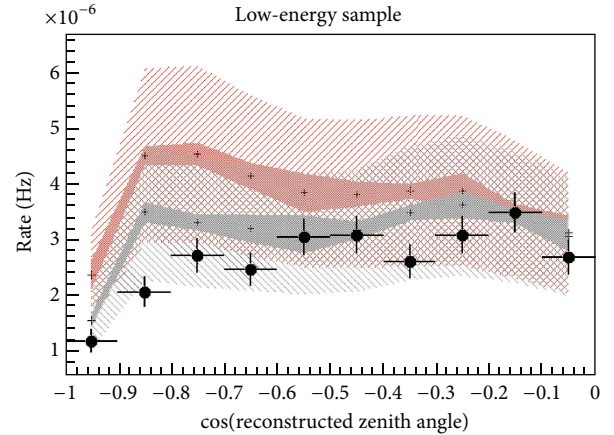


FIGURE 10: Data and simulation expectation at world average oscillation parameters (in black) and the case of no oscillations (in red) for the low-energy sample of IceCube's IC79-A analysis. Systematic uncertainties are split into a fully correlated part (hatched bands) and uncorrelated part (shaded bands). From [39].

flux and detection uncertainties ( $E_\nu \approx 1$  TeV, 39638 events). The measurement was done by analyzing the distribution of events as a function of zenith angle in the low-energy sample (see Figure 10). The zenith angle of both samples was estimated using the muon track reconstruction described in [92]. Atmospheric muons were mainly removed by reconstructing all events as upgoing, and making cuts on parameters related to the quality of the reconstruction (without muon tagging).

The data were analyzed using a  $\chi^2$  optimization with pulls, also following the method in [90]. The results obtained for the atmospheric oscillation parameters were compatible with contemporary global fits [93], although the errors were a factor 4 to 9 larger (see Figure 13).

Two subsequent analyses of the data, from here on IC79-B and IC86-A, created new event selections based on the rejection of atmospheric muons by using the veto, separating

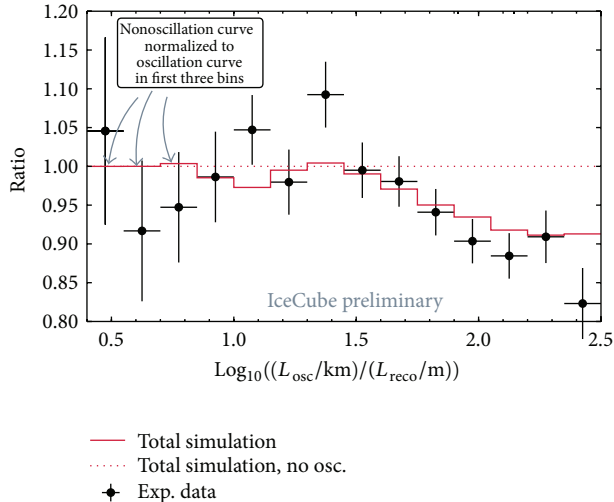


FIGURE 11: Ratio of the distribution of oscillation length over reconstructed track length to the no oscillation hypothesis from simulation in the IC79-B analysis. The best fit is also shown. From [40].

the background rejection from the reconstruction of events [40, 48]. In both cases only the low-energy DeepCore data were analyzed.

The data used for IC79-B were acquired during the same period of time as for IC79-A; however, due to the change in the selection of events the final sample studied was a factor 10 larger. The zenith angle of events was reconstructed with a similar method as in IC79-A [40]. A second observable, the reconstructed muon range  $L_{\text{muon}}$  [94], was used as an energy proxy and the data were analyzed as a function of both observables. The ratio of events with respect to the no oscillation scenario, together with the best fit, is shown as a function of reconstructed  $L_{\text{osc}}/L_{\text{reco}}$  in Figure 11, where  $L_{\text{osc}}$  is the distance the neutrino traveled and  $L_{\text{reco}}$  is the reconstructed length of the muon produced in the interaction. The best fit and estimated errors of this method were similar to those of IC79-A.

The first analysis of data from the full detector configuration [48], IC86-A, was performed using a selection of photons and event reconstruction based on the method published by ANTARES [89]. The selection of photons was modified to remove multiply scattered photons instead of noise. Unscattered, or *direct*, photons were identified by restricting their possible arrival times to those given by the hyperbolic pattern that Cherenkov light produces as a function of time as it crosses a string. About 70% of the neutrino interactions which trigger the detector do not have a clear core of direct photons and thus are removed.

The *direct* photons found are used to fit track and cascade hypotheses. The zenith angle from the track fit was used as an observable, and the ratio of the  $\chi^2$  of the track and cascade fits was used to separate track-like from cascade-like events. An estimator of the total energy of the neutrino was also implemented, which takes the muon range estimator from IC79-A and also fits a hadronic cascade at the vertex.

In IC79-B and IC86-A the data were analyzed using a likelihood optimization with nuisance parameters to account for systematic uncertainties. For IC86-A, uncertainties related to the detector were also included as nuisance parameters. Simulation sets with varied detector settings were produced and interpolated at the final level of the analysis, allowing the fitter to make arbitrary modifications to them.

In similar live time as IC79-A and IC79-B, IC86-A selected 1487 neutrino events for analysis. While the best fit obtained was in agreement with the other results, the error in  $\Delta m_{32}^2$  was reduced by about 20% with respect to IC79-A, while maintaining a similar precision on  $\sin^2 2\theta_{23}$ . Figure 12 shows a comparison of data and best fit simulation in projections in energy of the two-dimensional histogram used in the analysis. A comparison of the confidence regions in  $\sin^2 \theta_{23}$  and  $\Delta m_{32}^2$  of the single year analyses of IceCube DeepCore, together with the result from ANTARES, is shown in Figure 13.

**4.3. Precision Measurements with IceCube DeepCore.** The latest result from IceCube DeepCore [9] is an update to the IC86-A analysis introduced before, now with almost a thousand days of detector live time. The measurement demonstrates the potential for VLNTs to become relevant experiments in the field of neutrino oscillations.

While the analysis strategy is still to focus on the selection on clear tracks, for which a core of direct photons can be identified, three large improvements are introduced, namely,

- (i) an optimization of the event selection, which results in 40% more events;
- (ii) the cosmic muon background derived from data (tagged muons), avoiding the need of computationally expensive model-dependent simulation;
- (iii) an improved estimator of the energy deposited at the interaction point, which reduces the error on the total neutrino energy by more than 30% at 20 GeV.

A demonstration of how the data-derived background is used can be seen in Figure 14, where the distribution of events as a function of reconstructed zenith angle at the final level and two earlier stages of the event selection is shown. At each step the cosmic muon background is more strongly suppressed. The contribution of atmospheric muons in the downgoing region can be seen at all steps, including the final sample to be analyzed.

For their IC86-B result, the IceCube collaboration has expanded the list of possible sources of uncertainties considered. Non-DIS events are a nonnegligible fraction of the sample at  $E_{\text{reco}} \leq 20$  GeV, and additional cross sections uncertainties on these interactions (about 20%) were also included. A possible shift of 5% in the energy scale of hadronic showers was also taken into account.

In 950 days of live time, a total of 5174 events were observed, while 6830 were expected without oscillations. Note that the energy range of the search was reduced in comparison with IC86-A to  $E_{\text{reco}} = [7, 56]$  GeV. The data were analyzed in a full three-neutrino oscillation formalism,

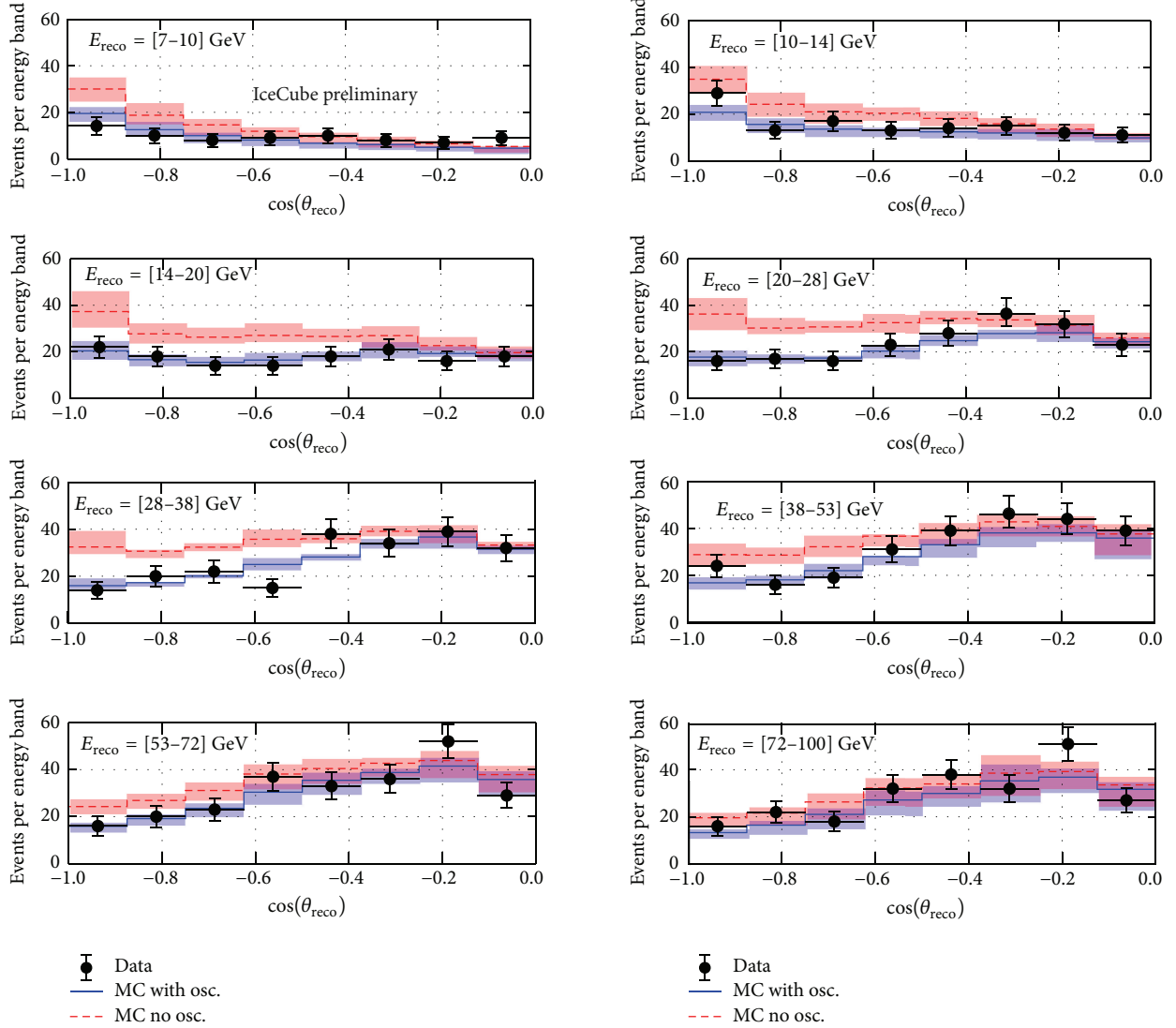


FIGURE 12: Comparison between data and simulation for the two-dimensional histogram used in the IC86-A analysis of IceCube. The data are shown as a function of the zenith angle for the energy bins studied. Bands indicate the impact of the estimated systematic uncertainties. Figure taken from [41].

including the effects induced by matter as neutrinos cross the Earth. The parameters that best describe the data, assuming a normal mass ordering, are  $\sin^2\theta_{23} = 0.53^{+0.09}_{-0.12}$  and  $\Delta m_{32}^2 = 2.72^{+0.19}_{-0.20} \times 10^{-3} \text{ eV}^2$ . No significant preference was found for either the normal or inverted mass orderings. Purely statistical uncertainties are  $^{+0.06}_{-0.08}$  for  $\sin^2\theta_{23}$ , and  $^{+0.14}_{-0.15} \times 10^{-3} \text{ eV}^2$  for  $\Delta m_{32}^2$ , from which it is deduced that statistical and systematic uncertainties have an almost equal impact on the result.

Data and simulation are in good agreement, with a  $\chi^2/\text{NDF} = 54.9/56$  for the energy-zenith angle histogram used in the fit. Figure 15 compares the  $L_{\text{reco}}/E_{\text{reco}}$  distributions of data and best fit simulation, where the agreement can be observed (note that the analysis is not done on this variable, but in a two-dimensional energy-zenith angle histogram instead). The 90% confidence contours on the atmospheric

oscillation parameters obtained are shown in Figure 16, together with the results from the other experiments leading the field.

The results from VLVNTs will be further improved by adding statistics to the analyzed data sample and refining the reconstruction methods. However, the most decisive improvements will come with the construction of the next-generation VLVNTs presented in the next section.

## 5. Neutrino Oscillations with the Next Generation of VLVNTs

After the measurements from ANTARES and IceCube/DeepCore in the atmospheric sector, the next goal of VLVNTs is to further decrease the energy threshold below the 15 GeV domain in order to improve the sensitivity to the PMNS

TABLE 1: Qualitative comparison of experiments measuring the atmospheric neutrino oscillation parameters. The table is divided into detector and flux characteristics. Note that the far detector of T2K is Super-Kamiokande but uses accelerator neutrinos. Detector performances taken from [4, 9, 38, 43, 49, 83, 95]. Expected neutrino events quoted from published results of  $\nu_\mu$  disappearance at analysis level (note that for VLVNTs this number can vary significantly depending on the studied range in energy, zenith angle, and topology). COH refers to coherent production. For details on the other interaction channels and energy ranges see Figure 8.

Parameter	VLVNT		SK	MINOS, T2K, and NOvA	
	ANTARES	DeepCore			
Instrumentation density ( $\text{m}^{-3}$ )	$9.1 \times 10^{-5}$ OMs	$2.3 \times 10^{-5}$ DOMs	0.2 OMs	15 channels	
Detection principle	Cherenkov light over tens of meters		Cherenkov rings	Trackers/calorimeters	
Detector (far)	$E_\nu$ resolution	50% $\pm$ 22%	25% at 20 GeV	3% at 1 GeV	10–15% at 10 GeV
	$\theta_\nu$ resolution	3° at 20 GeV	8° at 20 GeV	2–3°	—
Particle ID capabilities	Muon/no muon in interaction		$e, \mu, \pi$ (rings)	Individual particles, charge	
Source of neutrinos	Atmosphere: mix of $\nu_e, \bar{\nu}_e, \nu_\mu,$ and $\bar{\nu}_\mu$			Accelerator: $\nu_\mu/\bar{\nu}_\mu$ modes	
Baseline	10–12700 km			300–800 km	
Flux determination	Atm. $\nu$ models, self-fit		+top/down ratios	Near/far detector	
Neutrino flux	Energy range	10–100 GeV	Few MeV–few GeV	Few GeV	
Main interaction channel	DIS		QE	QE, RES, COH, and DIS	
$\nu$ events expected with osc.	530	1800	2000	30 (T2K), 900 (MINOS)	
and without osc. (per year)	660	2300	2300	120 (T2K), 1050 (MINOS)	

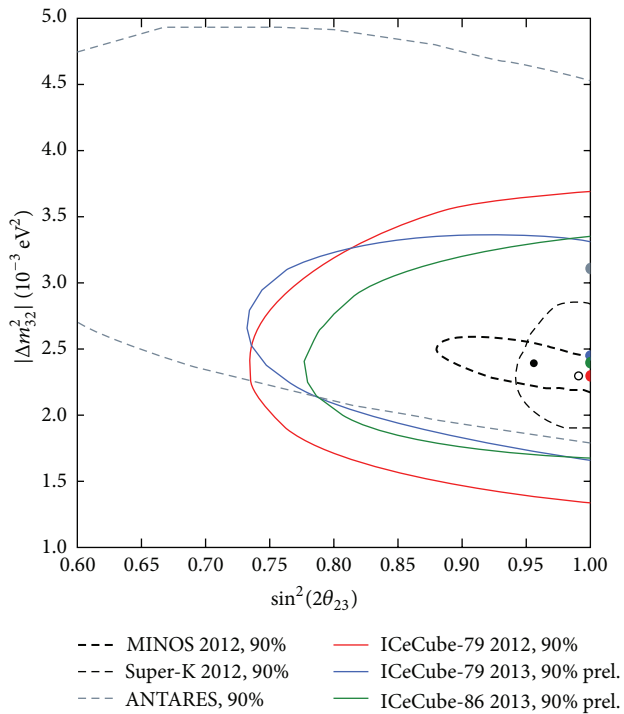


FIGURE 13: 90% CL contours from ANTARES [38] and IceCube’s single year measurements [39, 40, 48], compared to earlier measurements by MINOS [49], T2K [50], and Super-Kamiokande [51]. Taken from [52].

matrix elements and determine the NMO. Measuring the neutrino mass ordering is the main objective of the forthcoming ORCA (Oscillation Research with Cosmics in the Abyss) [85] and PINGU (Precision IceCube Next-Generation Upgrade) [86, 96] detectors as part of the KM3NeT [97] and IceCube Gen2 [98] infrastructures, respectively.

5.1. Design of Future Detectors. Both ORCA and PINGU will be more densely equipped than the currently operating detectors and should reach several megatons in instrumented volume. Their concepts are similar in many ways, with the most significant differences coming from the detection medium, the proposed detector layout, and the (default) optical module design.

5.1.1. Hardware and Detector Geometry. The PINGU optical module will most likely be a simplified and modernized version of that of IceCube, which has demonstrated its stability and reliability over almost ten years of operation. The PINGU DOM design removes components that are no longer required, such as the local coincidence logic and the multiple amplification modes, while providing a larger dynamic range than the original IceCube DOM and improved time resolution of 2 ns [86]. A schematic view of the IceCube and PINGU (Gen2) DOMs is shown in Figure 17. By maintaining the basic IceCube design, the PINGU DOM minimizes risk and cost. The ORCA optical module will follow the KM3NeT design [97] with each DOM housing 31 small (3”) PMTs arranged in a 17” glass sphere together with the associated electronics, as can be seen from Figure 18. This design offers the possibility of creating coincidences within the OM to suppress the large  $^{40}\text{K}$  decay background as well as the thermal noise of the PMTs. The orientation of the PMTs within the OM is also used in the reconstruction of events, although not yet at its full potential. A single sphere houses three to four times the photo cathode area of an ANTARES OM with an almost uniform angular coverage, improving the cost effectiveness by a factor four. Several prototypes of such a multi-PMT OM have been successfully tested in situ [99].

The final layouts of ORCA and PINGU are still under optimization (preliminary results tend to indicate that the best vertical spacing between OM is around 10 m for ORCA, while similar studies in the PINGU case favor a vertical

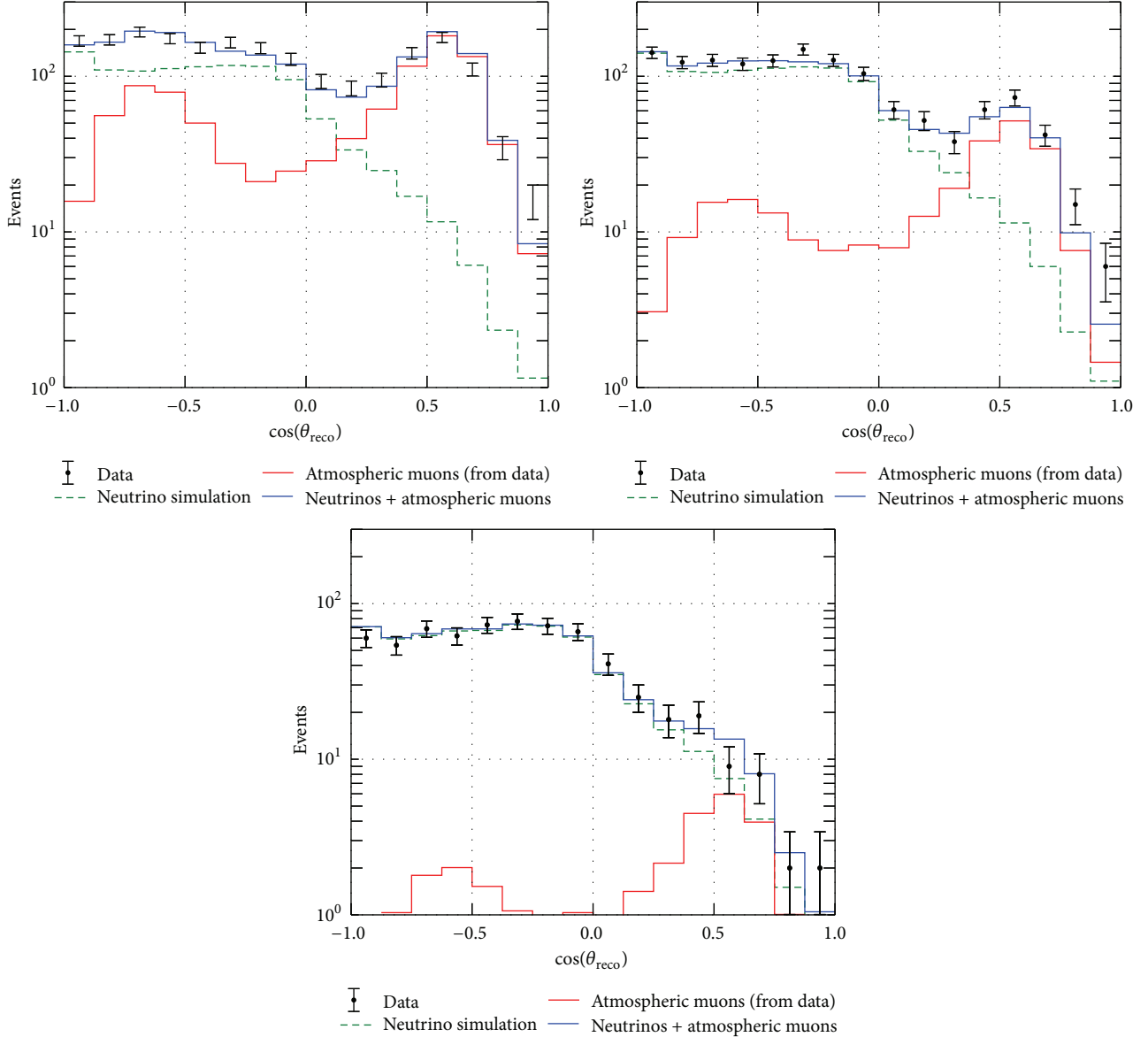


FIGURE 14: Zenith angle distributions of neutrino simulation and atmospheric muons derived from data for three subsequent steps in the event selection with increasing veto cuts in IceCube's IC86-B analysis. A comparison is also made to a 10% control sample of the data. Note that the region  $\cos \theta_z > 0$  is not used in the final analysis of the data. Taken from [9].

spacing of about 3 m, close to the adopted benchmark). The current benchmark geometries used for establishing the detector performances consist of 40 (115) strings with a horizontal spacing of  $\sim 20$  m for PINGU (ORCA). The vertical spacing is set to 6 m for ORCA and 3 m for PINGU. While a PINGU string will hold up to 96 DOMs, there are 18 DOMs in a default ORCA string. The maximum number of DOMs that a PINGU string can hold is given by the mechanical constraints of the downhole cable and the appearance of shadowing effects, while for ORCA the constraint comes from the launcher vehicle (a large spherical frame in which the DOMs slot into dedicated cavities) used for string deployments. The separation between the sensors of both detectors is smaller than the absorption and scattering lengths of their respective

media, making the optical properties of ice and salt water less relevant than for ANTARES and IceCube/DeepCore.

The footprints of the ORCA and PINGU detectors are shown in Figure 19. The instrumented mass of both detectors is of order 3.5 to 4 Mt, and their effective masses reach the same value for neutrinos of energy above 10 GeV. While the PINGU extension is foreseen to be embedded inside the current IceCube/DeepCore detector (which will be used for background vetoing), the ORCA detector will be located around 10 km west from the ANTARES site, at a depth of 2475 m.

**5.1.2. Costs and Timescale.** PINGU estimates a cost of 48 M\$ for hardware and 23 M\$ for logistics [100]. The estimated cost

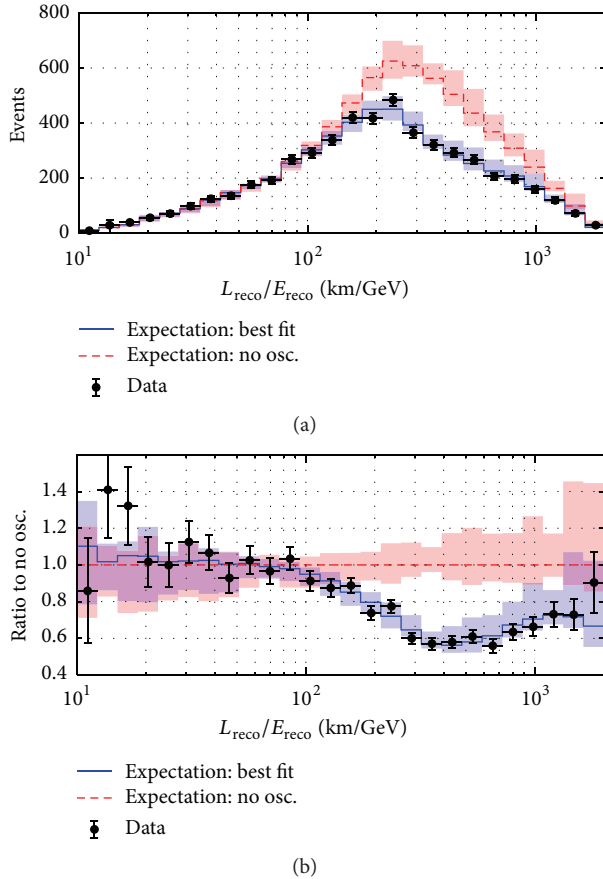


FIGURE 15: Distribution of events as a function of reconstructed  $L/E$  of IceCube's IC86-B analysis. Data are compared to the best fit and expectation with no oscillations (a) and the ratio of data and best fit to the expectation without oscillations is also shown (b). Bands indicate estimated systematic uncertainties. From [9].

of ORCA is 40 M€. Funding request processes are currently driving the possible time line of the projects.

PINGU will be built as part of the IceCube Gen2 project. From a technical point of view the installation of the detector at South Pole could start by the end of 2020 [101]. Based on the experience gained with the IceCube, the deployment is expected to take only three years. The first construction phase of ORCA, a demonstrator array of 6-7 strings (already funded), started in late 2014 with the deployment of the main electrooptical cable, followed by the deployment of a junction box in April 2015. The demonstrator is expected to be deployed by the end of 2016 and will be used to carry out studies of detector-related systematic effects and event reconstructions. In an optimistic case, the deployment of the full detector case could happen by 2020. Both PINGU and ORCA plan to take data during their construction phase.

**5.2. Projected Performance.** The determination of the NMO, the main physics goal of these projects, relies on a detailed analysis of deviations of the order of  $\sim 10\%$  and  $\sim 30\%$  in the rates of detected atmospheric muon and electron neutrinos (see Figures 3, 4, and 5) as a function of energy and arrival

zenith angle. Therefore, the key parameters that characterize the potential of a detector are its effective mass, the energy and zenith angle resolutions achievable, and its particle (mis)identification capabilities. In the following discussion the latest, preliminary, studies from ORCA [85, 102] and PINGU [86, 91] are presented.

These studies are based on full Monte Carlo simulations adapted from IceCube and ANTARES. All ORCA results account for an optical background induced by  $^{40}\text{K}$  decays of 5–10 kHz per PMT and a time-correlated hit rate of 500 Hz per OM (two coincident hits in different PMTs inside the same OM). Since PINGU DOMs will follow closely the design used for IceCube, the typical in situ behaviour of the IceCube/DeepCore DOMs, with a noise rate of 650 Hz, is used in the simulations.

The published results of ANTARES and IceCube have so far focused on  $\nu_\mu$  disappearance and therefore only selected events where a muon was observed. The sensitivity to the NMO, on the other hand, also comes from oscillations that involve  $\nu_e$ . It is therefore useful to detect all neutrino flavors, placing them in two categories depending on their topology: tracks and cascades (see Section 5.2.2).

**5.2.1. Reconstruction of Tracks and Cascades.** Track-like events are those where a muon is observed coming out of the interaction vertex. Track-like topologies are CC  $\nu_\mu$  interactions as well as the  $\nu_\tau$  CC interactions when the decay of the tau lepton produces a muon. The cascade-like topologies are CC  $\nu_e$  interactions, CC  $\nu_\tau$  interactions without a muon in the final state, and NC interactions from all flavors. Independent studies indicate that after accounting for reasonable detector resolution effects, the cascade channel provides more sensitivity to the effects of the NMO. Note, however, that the two channels are complementary as track-like events can provide better precision in  $\sin^2\theta_{23}$ . It is consequently important to be able to distinguish the two topologies with high efficiency and purity.

The event reconstruction in PINGU is a simultaneous global likelihood fit of the interaction vertex position and time, the zenithal and azimuthal angles, the energy of the cascade at the vertex, and the length of the daughter muon track. The event hypothesis assumes that tracks and cascades are collinear. The likelihood is calculated using the time of arrival of single photons and the expected noise in the time windows analyzed. The expectations for minimum ionizing muon tracks and electromagnetic cascades needed for the likelihood are stored in tables, obtained from direct simulation of particle and photon propagation, as it is already done for IceCube [62]. An event is reconstructed by comparing photon expectation for a given event hypothesis to the photons observed. All the DOMs in PINGU, as well as those in IceCube/DeepCore, are used in the reconstruction [86].

Fitting eight parameters at once while simultaneously looking up expectations from tables makes the reconstruction CPU intensive, but in return it provides robust results and similar resolutions for track-like and cascade-like topologies. While it would be possible to use the information provided by this reconstruction to obtain an estimate of the inelasticity of the event, this has not been explored so far.

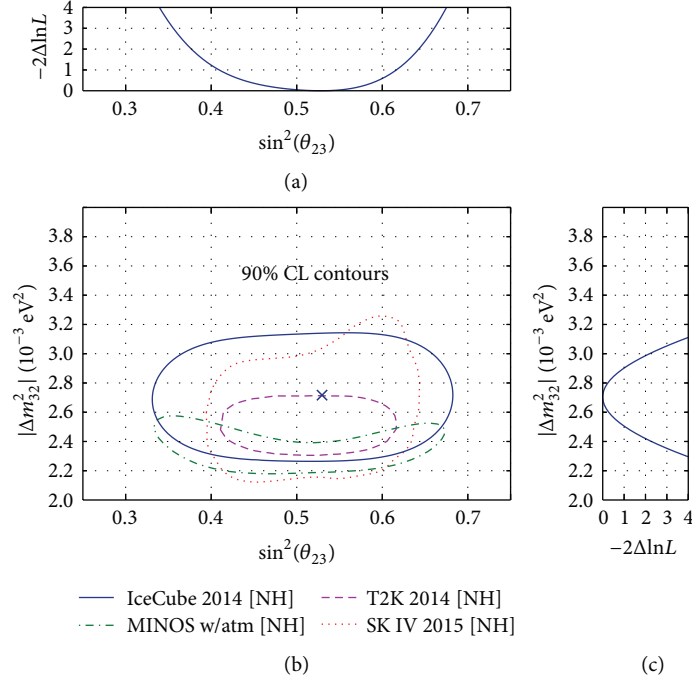


FIGURE 16: 90% confidence contours of the latest result from IceCube (IC86-B) in the  $\sin^2\theta_{23} - \Delta m_{32}^2$  plane in comparison with the ones of the most sensitive experiments [49, 67, 68]. The log-likelihood profiles for individual oscillation parameters are also shown (a, c). A normal mass ordering is assumed. Updated from [9].

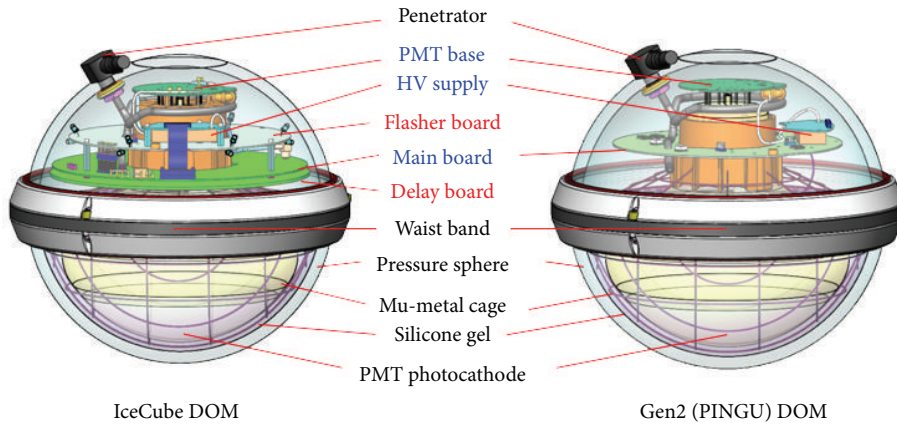


FIGURE 17: Comparison between the currently operating IceCube DOM and the updated PINGU/Gen2 DOM.

Energy and zenith angle resolutions for different interactions are shown in Figures 20 and 21, together with those obtained by ORCA with the methods explained hereunder.

ORCA uses two distinct algorithms for tracks and cascades. The track reconstruction is directly adapted from the main reconstruction of ANTARES [103] and focuses on the muon direction using the combined information of the PMT spatial positions and the Cherenkov photon arrival times. The neutrino energy estimation is mainly given by the reconstructed muon track length, which is complemented by the number of hits used in the track reconstruction algorithm. Muon tracks produced in neutrino interactions at  $E_\nu \geq 15 \text{ GeV}$  are not always fully contained, which turns

the estimate into a lower limit above these energies, as shown in Figure 20. The time residuals under a spherical emission profile (shower-like) or according to a Cherenkov cone (track-like) are used to obtain sensitivity to the inelasticity in the track channel.

The cascade reconstruction in ORCA takes advantage of the long scattering length in sea water, which preserves the structure of the Cherenkov light cone, and tries to identify the leading lepton in the cascade. An example of the distribution of the expected number of photons as a function of emission angle for different inelasticity intervals is shown in Figure 22. A peak is always visible at the Cherenkov angle ( $42^\circ$ ), whose height with respect to the off-peak region

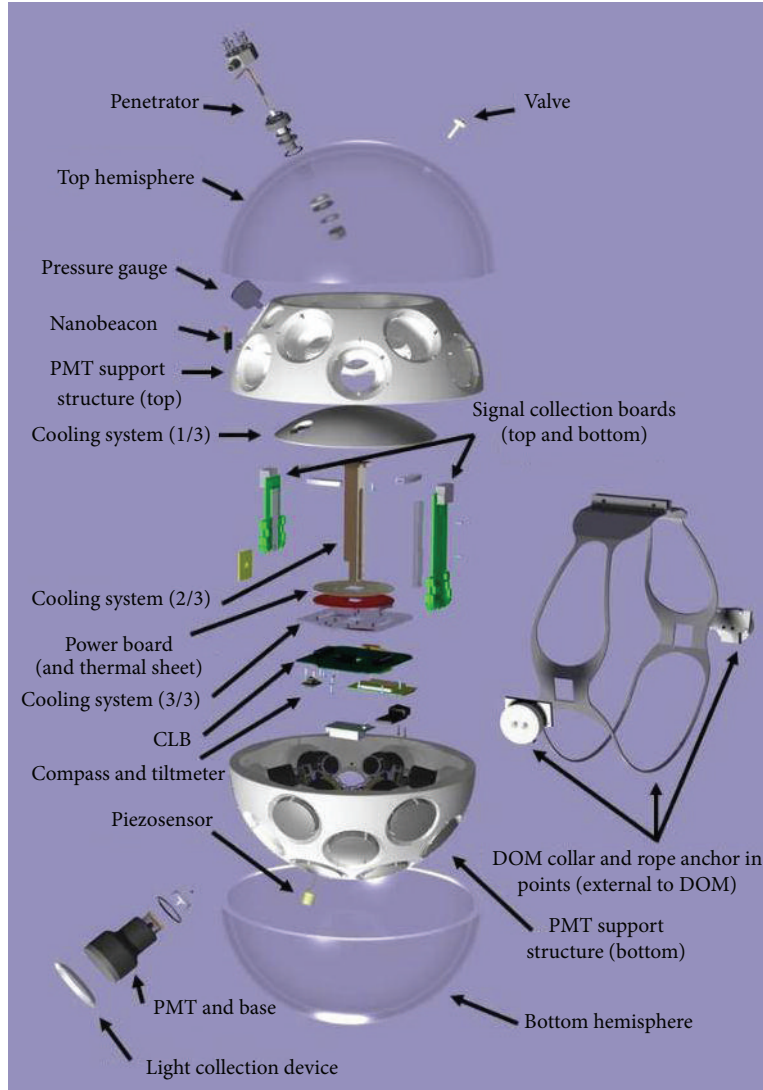
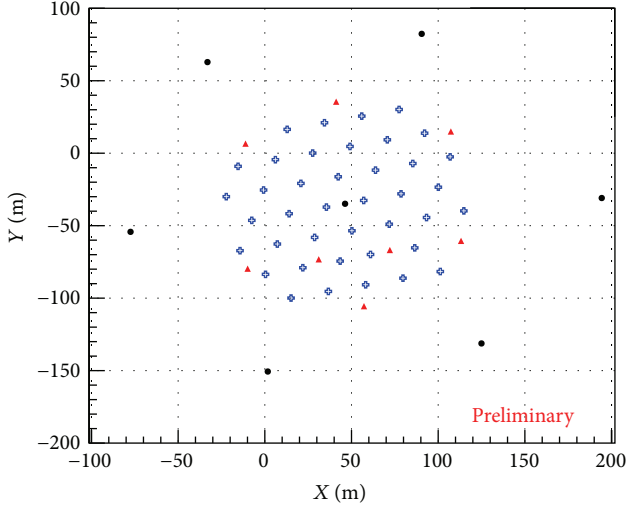


FIGURE 18: An exploded view of the multi-PMT optical module of KM3NeT/ORCA.

depends on  $y$ . Cascades are reconstructed in two separate steps using maximum likelihood fits. First the interaction vertex is obtained with a resolution of about 0.5–1 m by an algorithm based on hit time residuals. It is then followed by a fit of the direction, energy, and inelasticity of the event. The performances of the cascade reconstruction are summarized in Figures 20 and 21.

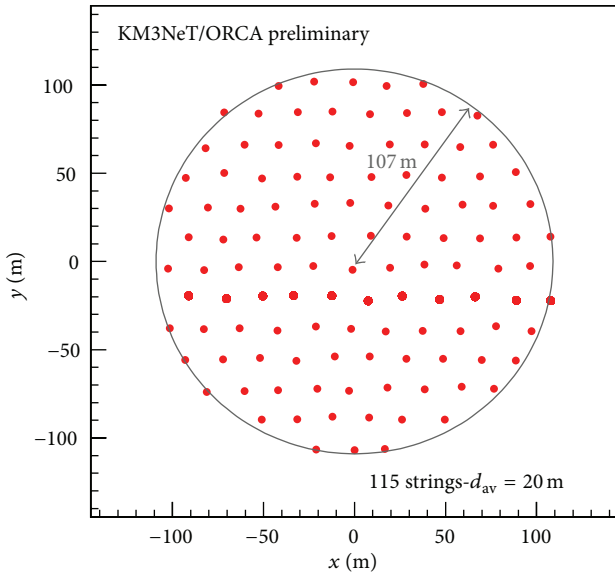
In ORCA the inelasticity of about 60% of the tracks with true  $y \leq 0.25$  or  $y \geq 0.75$  is reconstructed correctly; the accuracy of the inelasticity estimator of cascades is slightly worse. The inelasticity could be used for potential statistical separation between neutrinos and antineutrinos, which can be exploited for the mass ordering measurement [104]. It can also be tested to separate charged current interactions from neutral current interactions. While both PINGU and ORCA are studying this possibility, inelasticity estimates are not yet part of the current analyses that are discussed in the following sections.

**5.2.2. Particle Identification and Background Rejection.** VLVNTs measuring atmospheric neutrinos should be able to identify and reject atmospheric muons, the largest source of background, and differentiate between events with track-like and cascade-like topologies. PINGU plans to tag atmospheric muons following the strategy developed in DeepCore, that is, using the outer detector strings to identify particles that enter the fiducial volume, and restricting the analysis to starting and upgoing events (see [9] and Figure 14). The cosmic muon background is expected to be on the level of a few percent, similar to DeepCore. Event reconstruction and selection in PINGU do not rely on direct hits, the single largest impact on signal efficiency in the latest DeepCore results. Signal efficiency in PINGU, therefore, is expected to be minimally affected by background rejection and reconstruction methods and largely defined by the number of photons observed from an interaction.



- IceCube
- ▲ DeepCore
- ◆ PINGU

(a)



(b)

FIGURE 19: (a) An envisaged 40-string PINGU layout (blue strings). The black circles refer to the standard IceCube strings and the red triangles to the DeepCore strings. (b) ORCA benchmark detector footprint.

The ORCA detector does not rely on an outer detector to tag muons. Current analyses reduce the impact of these muons by selecting only upgoing events and rejecting the misreconstructed ones using variables such as their reconstruction quality and the position of their reconstructed interaction vertex. The topology of neutrino interactions, track-like or cascade-like, is identified using the distribution of hit time residuals, distances between reconstructed vertices at various reconstruction steps, the quality of the reconstructions, and topological variables, among others. A single

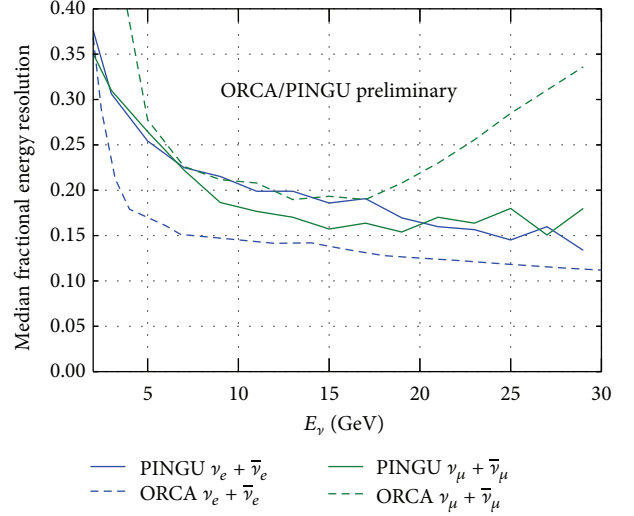


FIGURE 20: Expected median fractional energy resolution for electron and muon neutrinos in PINGU (solid) and ORCA (dashed). Reproduced from [85, 86].

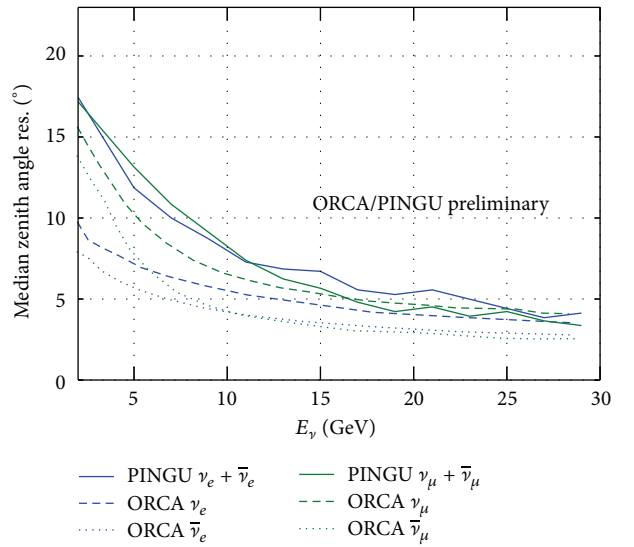


FIGURE 21: Expected median zenith angle resolution for electron and muon neutrinos in PINGU (solid) and ORCA (dashed). For ORCA individual resolutions for neutrinos and antineutrinos are shown, while a mixture of both is given for PINGU. Resolutions are better for antineutrinos than for neutrinos due to the smaller average inelasticity, leading to a smaller intrinsic scattering angle between the neutrino and the leading lepton. Values taken from [85, 86].

multivariate method which incorporates the parameters listed above is applied to the data and classifies events as tracks, showers, or atmospheric muons. The procedure achieves  $\sim 1\%$  muon contamination in the final sample without a severe signal loss.

The approach followed in PINGU to separate tracks from cascades also uses a multivariate method with variables describing the reconstruction quality of the event under the track versus cascade hypothesis, as well as the reconstructed

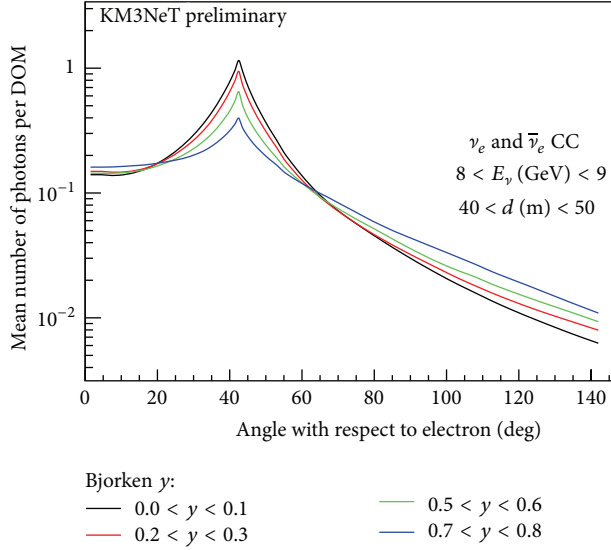


FIGURE 22: Number of expected photons as a function of the emission angle between the shower direction and the direction from the vertex to the DOM for different intervals of interaction inelasticity  $y$ .

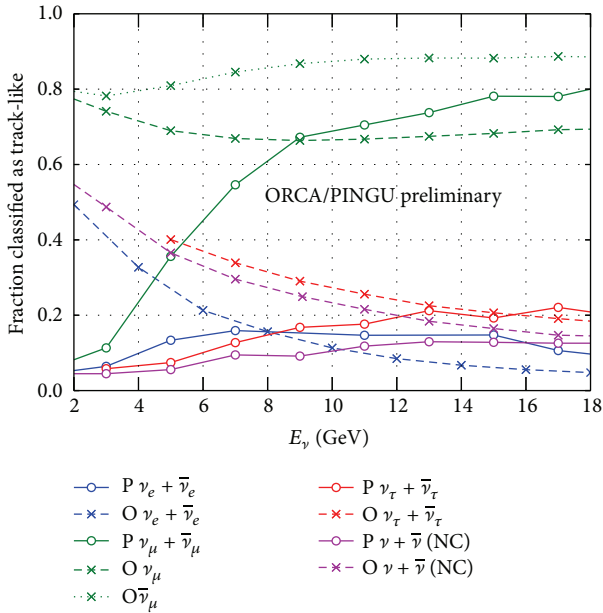


FIGURE 23: Fraction of events selected as tracks for different categories of simulated events for ORCA (dashed lines, labeled as O) and PINGU (solid lines, labeled as P). As expected,  $\bar{\nu}_\mu$  performs better because of their average lower inelasticity. From [88].

muon track length as input. Figure 23 shows a comparison of the performance of these classification methods for neutrino interactions around the energies relevant for mass ordering measurements for PINGU and ORCA. Current methods differ at low energies, with PINGU showing a bias towards classifying low-energy tracks as cascades and ORCA exhibiting the opposite behavior. Above 10 GeV both classification schemes result in a similar outcome. The results suggest

TABLE 2: List of the uncertainties studied by ORCA and PINGU which have the largest impact on their respective NMO analyses (more systematic uncertainties have been studied; see text). Sources of uncertainty are additional parameters in the fit. Studies are performed for a set of true oscillation parameters. The best known values for all other parameters are injected for creating the data templates. PINGU uses priors to penalize deviations while fitting these parameters. ORCA does not use priors and instead reports the standard deviation of the fit results.

Uncertainties	ORCA $\sigma$ (fit yield)	PINGU $\sigma$ (prior)
$\theta_{23}, \Delta m_{31}^2$	Unconstrained	
$\theta_{13}$	Integrated $\pm 1^\circ$	$0.2^\circ$
$\theta_{12}, \Delta m_{21}^2$	Fixed	
$\delta_{\text{CP}}$	Fixed at zero <sup>a</sup>	
Overall rate factor	2.0%	Unconstrained
$E^{-\gamma}$ (slope, spectral index)	0.5%	$\pm 0.05$
Energy scale	Not used	$\pm 10\%$
$\nu/\bar{\nu}$ ratio	4.0%	$\pm 10\%$
$\mu/e$ flavor ratio	1.2%	$\pm 3\%$
NC cross section scaling	11.0%	GENIE model

<sup>a</sup>Both projects have studied how  $\delta_{\text{CP}}$  impacts their sensitivity but the results are not yet reflected in the projections given in this review.

that the behavior of the particle identification algorithms at low energy can be tuned for optimizing sensitivity to the NMO measurement. In both cases, the final performances are subject to further optimization.

**5.3. Physics Potential and Systematics.** The preliminary performances described above are used by the PINGU and ORCA collaborations as inputs to estimate the confidence level with which the projected experiments will be able to reject a given NMO. This is done by drawing several thousands of pseudoexperiments generated under each mass ordering hypothesis, as outlined in [105]. The analysis is conducted by comparing the two-dimensional histograms of pseudodata and simulation as a function of the reconstructed energy and zenith. The pseudo-data sets are generated using different input parameters, such as the values of the mixing angles, in order to study the impact of degeneracies in the measurement.

A full log-likelihood ratio (LLR) method is used by both collaborations to report their expected sensitivity. In this method each pseudoexperiment is analyzed by performing a log-likelihood fit with the oscillation parameters as free parameters (mostly  $\theta_{23}$ ,  $\Delta m_{32}^2$ , and  $\theta_{13}$ ) and assuming both hierarchies in turn. Sources of systematic uncertainty are incorporated as additional parameters in the fit (see Table 2).

As such methods can be quite CPU expensive, in particular when studying various sources of systematics, the PINGU collaboration also implemented a simplified  $\Delta\chi^2$ -based approach. This method is a parametric analysis based on the Fisher information matrix, which relies on the partial derivatives of the event counts in each bin with respect to all parameters under study. Inverting the Fisher matrix yields the full covariance matrix between the parameters. The

covariance matrix of the mixing angle  $\theta_{23}$  is calculated at several values to overcome the limitations of the method. The results obtained with the Fisher matrix are in agreement with the LLR method and are also used to report the projected sensitivity of PINGU.

The parameters of the fits performed by ORCA and PINGU, presented in Table 2, are the oscillation parameters of interest plus a set of parameters related to uncertainties on the detection process, neutrino fluxes, cross sections, and the remaining oscillation parameters. The oscillation parameters, in particular  $\theta_{23}$ , have the largest impact on the achievable precision. The overall normalization has the second largest impact on the precision. This absorbs uncertainties on the efficiency of the detector, the absolute atmospheric neutrino flux, and interaction cross sections. PINGU has recently studied uncertainties on the neutrino flux by using a more refined description, which involves a set of 18 parameters [22]. The impact found was a reduction of the three-year sensitivity by  $0.2\sigma$  [106] (not yet included in Figure 24). Cross sections have been also studied in more detail by modifying the six most relevant parameters of the model implemented in GENIE. The reduction in sensitivity was found to be negligible. Studies within ORCA and PINGU have tested the impact of  $\delta_{CP}$  and found an additional reduction of up to  $0.5\sigma$  at the three-year benchmark [85, 88]. Note that all figures in this review do not include this effect.

The LLR (and  $\Delta\chi^2$  for PINGU) resulting from fits to the pseudoexperiments are used to calculate the separability of the two possible mass orderings. The median (i.e., with 50% statistical power) sensitivities to the NMO are shown in Figure 24(a) after 3 years of data taking. The results are obtained by fixing  $\delta_{CP}$  to zero and are shown as a function of  $\theta_{23}$ . Both collaborations observe that constraining  $\theta_{23}$  to either octant while doing a fit artificially increases the sensitivity to the NMO; thus the parameter is left unconstrained in these studies.

Though ORCA and PINGU sensitivities should be compared with caution, as the various inputs are slightly different, both studies find a better sensitivity to the NMO for a true value of  $\theta_{23}$  in the second octant in the case of normal mass ordering. For the case of inverted ordering, the sensitivity has a much weaker dependence on the value of  $\theta_{23}$ . The consistency of the two results is encouraging, as they have been obtained with completely independent analysis chains.

The expected improvement in sensitivities with running time, which does not yet include the effects of  $\delta_{CP}$  nor the reconstructed inelasticity, is shown in Figure 24(b). Once more, the discrimination power of both detectors is comparable.

The identification of the mass ordering devised by both collaborations also produces a measurement of  $\theta_{23}$  and the absolute value of the atmospheric mass splitting. Projections of the sensitivity to  $\sin^2\theta_{23}$  have a strong dependence on the assumed true values. For  $\sin^2\theta_{23} = 0.45$  both PINGU and ORCA expect to achieve errors of the order of 0.05 after three years of operation. The precision achievable on the absolute value of the mass splitting is roughly independent of the true value, and the expected error on the measurement for both projects is about  $0.05 \times 10^{-3}$ . Both experiments are

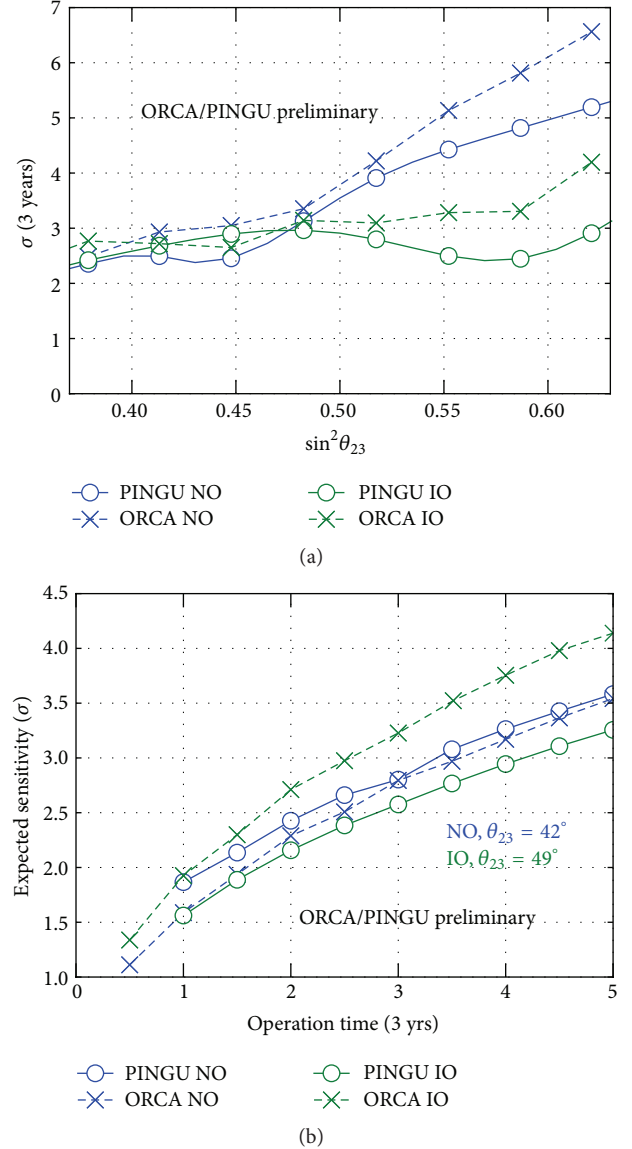


FIGURE 24: (a) Significance of ORCA and PINGU for rejecting a given hypothesis for the neutrino mass ordering plotted as a function of  $\theta_{23}$ , after 3 years of data taking. (b) Median significance as a function of time for the benchmark detectors described in the text. The oscillation parameters injected are close to those found in [3] ( $\theta_{23} = 42^\circ$  for a NMO,  $\theta_{23} = 49^\circ$  for an IMO). From [85, 91].

expected to produce measurements with better precision to those projected for NOvA and T2K by the year 2020.

The results shown in the present paper are a compilation of the most recent, publicly shown projections of both collaborations, and include most leading systematics effects [85, 88, 91, 107]. Recently a thorough study of the interplay between the oscillations parameters has been reported in [108], consistent with the recent results from ORCA and PINGU. The authors also introduced uncertainties in the estimated energy and zenith resolutions, as well as additional (conservative) uncorrelated uncertainties. Their results show that after 5 years of data taking, the loss in sensitivity ranges

from 24% to 40% under pessimistic assumptions (such as fully uncorrelated errors in each analysis bin), thus leaving room for a measurement of the NMO by ORCA and PINGU on a reasonable time scale.

## 6. Summary

Atmospheric neutrinos are a versatile tool to study neutrino oscillations. This naturally occurring beam covers baselines as large as Earth's diameter and has an energy range which spans over the regimes of oscillations in vacuum, and with resonant and saturated matter effects. Current VLVNTs, ANTARES and IceCube, can detect neutrinos in the latter regime and have already produced measurements of the atmospheric oscillation parameters,  $\theta_{23}$  and  $|\Delta m_{32}^2|$ . Constant improvements in the understanding and modeling of the detector and media, as well as more sophisticated data analysis techniques, have led to promising results, which have started to become comparable with those of other more mature experimental set-ups.

Proposed VLVNTs, ORCA and PINGU, aim to lower the energy threshold and access the resonant regime, with the goal of measuring the sign of  $\Delta m_{31}^2$  and completely determining the neutrino mass ordering. While both projects are on the way of optimizing their detector geometries and/or analysis techniques, current studies are nevertheless mature and indicate that they could provide a significant measurement ( $\geq 3\sigma$ , depending on the true value of  $\theta_{23}$ ) of the neutrino mass ordering after 3–4 years of operation.

## Conflict of Interests

The authors declare that there is no conflict of interests regarding the publication of this paper.

## Acknowledgments

The authors are grateful to J. Brunner, M. Jongen, J. Hofestädt, W. Winter, D. Cowen, S. Böser, and T. DeYoung for useful discussions and clarifications on both the theoretical and experimental aspects covered in this paper.

## References

- [1] K. Olive, "Particle Data Group," *Chin. Phys. C*, vol. 38, no. Particle, Article ID 090001, 2014.
- [2] D. V. Forero, M. Tórtola, and J. W. F. Valle, "Neutrino oscillations refitted," *Physical Review D*, vol. 90, no. 9, Article ID 093006, 2014.
- [3] M. Gonzalez-Garcia, M. Maltoni, and T. Schwetz, "Updated fit to three neutrino mixing: status of leptonic CP violation," *Journal of High Energy Physics*, vol. 2014, no. 11, article 052, 2014.
- [4] K. Abe, J. Adam, H. Aihara et al., "Measurements of neutrino oscillation in appearance and disappearance channels by the T2K experiment with  $6.6 \times 10^{20}$  protons on target," *Physical Review D*, vol. 91, no. 7, Article ID 072010, 2015.
- [5] W. Winter, "Neutrino mass hierarchy: theory and phenomenology," in *Proceedings of the 26th International Conference on Neutrino Physics and Astrophysics (Neutrino '14)*, vol. 1666, Boston, Mass, USA, June 2014.
- [6] C. H. Albright and M.-C. Chen, "Model predictions for neutrino oscillation parameters," *Physical Review D*, vol. 74, no. 11, Article ID 113006, 2006.
- [7] M. Lindner, A. Merle, and W. Rodejohann, "Improved limit on  $\theta_{13}$  and implications for neutrino masses in neutrinoless double beta decay and cosmology," *Physical Review D*, vol. 73, no. 5, Article ID 053005, 2006.
- [8] A. Garfagnini, "Neutrinoless double beta decay experiments," *International Journal of Modern Physics: Conference Series*, vol. 31, Article ID 1460286, 2014, (In: 12th Conference on Flavor Physics and CP Violation (FPCP '14), Marseille, France, May 2014).
- [9] M. G. Aartsen, M. Ackermann, J. Adams et al., "Determining neutrino oscillation parameters from atmospheric muon neutrino disappearance with three years of IceCube DeepCore data," *Physical Review D*, vol. 91, no. 7, Article ID 072004, 2015.
- [10] M. Aglietta, G. Battistoni, E. Bellotti et al., "Experimental study of atmospheric neutrino flux in the NUSEX experiment," *Europhysics Letters*, vol. 8, no. 7, pp. 611–614, 1989.
- [11] K. Daum, W. Rhode, P. Bareyre et al., "Determination of the atmospheric neutrino spectra with the Fréjus detector," *Zeitschrift für Physik C Particles and Fields*, vol. 66, no. 3, pp. 417–428, 1995.
- [12] W. W. M. Allison, G. J. Alner, D. S. Ayres et al., "Measurement of the atmospheric neutrino flavour composition in Soudan 2," *Physics Letters B*, vol. 391, no. 3–4, pp. 491–500, 1997.
- [13] R. Clark, R. Becker-Szendy, C. B. Bratton et al., "Atmospheric muon neutrino fraction above 1 GeV," *Physical Review Letters*, vol. 79, no. 3, pp. 345–348, 1997.
- [14] S. Hatakeyama, T. Hara, Y. Fukuda et al., "Measurement of the flux and zenith-angle distribution of upward through-going muons in Kamiokande II + III," *Physical Review Letters*, vol. 81, no. 10, pp. 2016–2019, 1998.
- [15] Y. Fukuda, T. Hayakawa, E. Ichihara et al., "Study of the atmospheric neutrino flux in the multi-GeV energy range," *Physics Letters B*, vol. 436, no. 1–2, pp. 33–41, 1998.
- [16] R. Abbasi, Y. Abdou, M. Ackermann et al., "Determination of the atmospheric neutrino flux and searches for new physics with AMANDA-II," *Physical Review D*, vol. 79, no. 10, Article ID 102005, 15 pages, 2009.
- [17] S. Adrian-Martinez, A. Albert, I. Al Samarai et al., "Measurement of the atmospheric  $\nu_\mu$  energy spectrum from 100 GeV to 200 TeV with the ANTARES telescope," *The European Physical Journal C*, vol. 73, article 2606, 2013.
- [18] M. G. Aartsen, M. Ackermann, J. Adams et al., "Development of a general analysis and unfolding scheme and its application to measure the energy spectrum of atmospheric neutrinos with IceCube," *The European Physical Journal C*, vol. 75, article 116, 2015.
- [19] M. Honda, T. Kajita, K. Kasahara, and S. Midorikawa, "Improvement of low energy atmospheric neutrino flux calculation using the JAM nuclear interaction model," *Physical Review D*, vol. 83, no. 12, Article ID 123001, 34 pages, 2011.
- [20] G. Barr, T. Gaisser, P. Lipari, S. Robbins, and T. Stanev, "Three-dimensional calculation of atmospheric neutrinos," *Physical Review D*, vol. 70, Article ID 023006, 2004.
- [21] G. Battistoni, A. Ferrari, T. Montaruli, and P. R. Sala, "The FLUKA atmospheric neutrino flux calculation," *Astroparticle Physics*, vol. 19, no. 2, pp. 269–290, 2003.
- [22] G. D. Barr, S. Robbins, T. K. Gaisser, and T. Stanev, "Uncertainties in atmospheric neutrino fluxes," *Physical Review D*, vol. 74, no. 9, Article ID 094009, 2006.

- [23] M. Honda, M. S. Athar, T. Kajita, K. Kasahara, and S. Midorikawa, "Atmospheric neutrino flux calculation using the NRLMSISE-00 atmospheric model," *Physical Review D*, vol. 92, Article ID 023004, 2015.
- [24] L. Wolfenstein, "Neutrino oscillations in matter," *Physical Review D*, vol. 17, no. 9, pp. 2369–2374, 1978.
- [25] S. Choubey and P. Roy, "Probing the deviation from maximal mixing of atmospheric neutrinos," *Physical Review D*, vol. 73, no. 1, Article ID 013006, 2006.
- [26] F. P. An, J. Z. Bai, A. B. Balantekin et al., "Observation of electron-antineutrino disappearance at daya bay," *Physical Review Letters*, vol. 108, no. 17, Article ID 171803, 7 pages, 2012.
- [27] J. K. Ahn, S. Chebotaryov, J. H. Choi et al., "Observation of reactor electron antineutrinos disappearance in the RENO experiment," *Physical Review Letters*, vol. 108, no. 19, Article ID 191802, 2012.
- [28] Y. Abe, J. C. dos Anjos, J. C. Barriere et al., "Improved measurements of the neutrino mixing angle  $\theta_{13}$  with the Double Chooz detector," *Journal of High Energy Physics*, vol. 2014, no. 10, article 086, 2014, Erratum in: *Journal of High Energy Physics*, vol. 2015, no. 2, article 074, 2015.
- [29] S. P. Mikheev and A. Y. Smirnov, "Resonance amplification of oscillations in matter and spectroscopy of solar neutrinos," *Soviet Journal of Nuclear Physics*, vol. 42, pp. 913–917, 1985, *Yadernaya Fizika*, vol. 42, p. 1441, 1985.
- [30] M. Freund, "Analytic approximations for three neutrino oscillation parameters and probabilities in matter," *Physical Review D*, vol. 64, no. 5, Article ID 053003, 12 pages, 2001.
- [31] A. M. Dziewonski and D. L. Anderson, "Preliminary reference Earth model," *Physics of the Earth and Planetary Interiors*, vol. 25, no. 4, pp. 297–356, 1981.
- [32] V. A. T. V. K. Ermilova, F. V. A. Chechin, and K. Soob, "Parametric enhancement of neutrino oscillations in matter," *Short Notices of the Lebedev Institute*, vol. 5, p. 26, 1986.
- [33] E. K. Akhmedov, "On neutrino oscillations in a nonhomogeneous medium," *Soviet Journal of Nuclear Physics*, vol. 47, no. 2, pp. 301–302, 1988.
- [34] P. I. Krastev and A. Y. Smirnov, "Parametric effects in neutrino oscillations," *Physics Letters B*, vol. 226, no. 3–4, pp. 341–346, 1989.
- [35] S. T. Petcov, "Diffractive-like (or parametric-resonance-like?) enhancement of the Earth (day-night) effect for solar neutrinos crossing the Earth core," *Physics Letters B*, vol. 434, no. 3–4, pp. 321–332, 1998.
- [36] J. A. Formaggio and G. P. Zeller, "From eV to EeV: neutrino cross sections across energy scales," *Reviews of Modern Physics*, vol. 84, no. 3, pp. 1307–1341, 2012.
- [37] D. Casper, "The nuance neutrino physics simulation, and the future," *Nuclear Physics B—Proceedings Supplements*, vol. 112, no. 1–3, pp. 161–170, 2002.
- [38] S. Adrian-Martinez, I. Al Samarai, A. Albert et al., "Measurement of atmospheric neutrino oscillations with the ANTARES neutrino telescope," *Physics Letters B*, vol. 714, no. 2–5, pp. 224–230, 2012.
- [39] M. G. Aartsen, R. Abbasi, Y. Abdou et al., "Measurement of atmospheric neutrino oscillations with IceCube," *Physical Review Letters*, vol. 111, no. 8, Article ID 081801, 2013.
- [40] M. G. Aartsen, R. Abbasi, Y. Abdou et al., "The IceCube neutrino observatory part V: neutrino oscillations and supernova searches," in *Proceedings of the 33rd International Cosmic Ray Conference*, Rio de Janeiro, Brazil, July 2013, <http://arxiv.org/abs/1309.7008>.
- [41] J. P. Yanez, *Proceedings, 26th International Conference on Neutrino Physics and Astrophysics (Neutrino 2014): Boston, Massachusetts, United States, June 2–7, 2014*, vol. 1666 of *AIP Conference Proceedings*, 2015.
- [42] A. Achterberg, M. Ackermann, J. Adams et al., "First year performance of the IceCube neutrino telescope," *Astroparticle Physics*, vol. 26, no. 3, pp. 155–173, 2006.
- [43] M. Ageron, J. A. Aguilar, I. Al Samarai et al., "ANTARES: the first undersea neutrino telescope," *Nuclear Instruments and Methods in Physics Research A*, vol. 656, no. 1, pp. 11–38, 2011.
- [44] A. D. Avrorin, A. V. Avrorin, V. M. Aynutdinov et al., "The prototyping/early construction phase of the BAIKAL-GVD project," *Nuclear Instruments and Methods in Physics Research Section A: Accelerators, Spectrometers, Detectors and Associated Equipment*, vol. 742, pp. 82–88, 2014, Proceedings of the 4th Roma International Conference on Astroparticle Physics (RICAP '13).
- [45] P. Amram, M. Anghinolfi, S. Anvar et al., "The ANTARES optical module," *Nuclear Instruments and Methods in Physics Research Section A: Accelerators, Spectrometers, Detectors and Associated Equipment*, vol. 484, no. 1–3, pp. 369–383, 2002.
- [46] R. Abbasi, M. Ackermann, J. Adams et al., "The IceCube data acquisition system: signal capture, digitization, and timestamping," *Nuclear Instruments and Methods in Physics Research Section A: Accelerators, Spectrometers, Detectors and Associated Equipment*, vol. 601, no. 3, pp. 294–316, 2009.
- [47] R. Abbasi, Y. Abdou, T. Abu-Zayyad et al., "The design and performance of IceCube DeepCore," *Astroparticle Physics*, vol. 35, no. 10, pp. 615–624, 2012.
- [48] J. P. Yáñez, G. Yodh, S. Yoshida et al., "The IceCube neutrino observatory part V: neutrino oscillations and supernova searches," in *Proceedings of the International Cosmic Ray Conference*, Rio de Janeiro, Brazil, 2013.
- [49] P. Adamson, I. Anghel, C. Backhouse et al., "Measurement of neutrino and antineutrino oscillations using beam and atmospheric data in MINOS," *Physical Review Letters*, vol. 110, no. 25, Article ID 251801, 2013.
- [50] K. Abe, N. Abgrall, Y. Ajima et al., "First muon-neutrino disappearance study with an off-axis beam," *Physical Review D*, vol. 85, no. 3, Article ID 031103, 8 pages, 2012.
- [51] Y. Itow, "Recent results in atmospheric neutrino oscillations in the light of large  $\theta_{13}$ ," *Nuclear Physics B—Proceedings Supplements*, vol. 235–236, pp. 79–86, 2013, the XXV International Conference on Neutrino Physics and Astrophysics (Neutrino 2012).
- [52] J. Brunner, "Measurement of neutrino oscillations with neutrino telescopes," *Advances in High Energy Physics*, vol. 2013, Article ID 782538, 16 pages, 2013.
- [53] J. A. Aguilar, I. Al Samarai, A. Albert et al., "Performance of the front-end electronics of the ANTARES neutrino telescope," *Nuclear Instruments and Methods in Physics Research Section A*, vol. 622, no. 1, pp. 59–73, 2010.
- [54] C. Tamburini, S. Martini, B. Al Ali et al., "Effects of hydrostatic pressure on growth and luminescence of a moderately-piezophilic luminous bacteria *Photobacterium phosphoreum* ANT-2200," *PLoS ONE*, vol. 8, no. 6, Article ID e66580, 2013.
- [55] R. Abbasi, Y. Abdou, T. Abu-Zayyad et al., "Calibration and characterization of the IceCube photomultiplier tube," *Nuclear Instruments and Methods in Physics Research Section A: Accelerators, Spectrometers, Detectors and Associated Equipment*, vol. 618, no. 1–3, pp. 139–152, 2010.

- [56] J. A. Aguilar, A. Albert, P. Amram et al., “Transmission of light in deep sea water at the site of the Antares neutrino telescope,” *Astroparticle Physics*, vol. 23, no. 1, pp. 131–155, 2005.
- [57] M. G. Aartsen, R. Abbasi, Y. Abdou et al., “Measurement of South Pole ice transparency with the IceCube LED calibration system,” *Nuclear Instruments and Methods in Physics Research Section A: Accelerators, Spectrometers, Detectors and Associated Equipment*, vol. 711, pp. 73–89, 2013.
- [58] D. Chirkin, R. Abbasi, Y. Abdou et al., “The IceCube neutrino observatory part VI: ice properties, reconstruction and future developments,” in *Proceedings of the the 33rd International Cosmic Ray Conference*, Rio de Janeiro, Brazil, 2013.
- [59] J. A. Aguilar, I. Al Samarai, A. Albert et al., “AMADEUS—the acoustic neutrino detection test system of the ANTARES deep-sea neutrino telescope,” *Nuclear Instruments and Methods in Physics Research Section A*, vol. 626–627, pp. 128–143, 2011.
- [60] J. A. Aguilar, I. Al Samarai, A. Albert et al., “Time calibration of the ANTARES neutrino telescope,” *Astroparticle Physics*, vol. 34, no. 7, pp. 539–549, 2011.
- [61] S. Adrián-Martínez, A. Albert, M. André et al., “Time calibration with atmospheric muon tracks in the ANTARES neutrino telescope,” <http://arxiv.org/abs/1507.04182>.
- [62] M. G. Aartsen, R. Abbasi, M. Ackermann et al., “Energy reconstruction methods in the IceCube neutrino telescope,” *Journal of Instrumentation*, vol. 9, Article ID P03009, 2014.
- [63] T. Kajita, Ed., *Proceedings of the International Workshop on Sub-Dominant Oscillation Effects in Atmospheric Neutrino Experiments held on December 9–11, 2004, in Kashiwa, Japan*, 2005.
- [64] A. Bodek and U. K. Yang, “Higher twist,  $\xi_w$  scaling, and effective LO PDFs for lepton scattering in the few GeV region,” *Journal of Physics G: Nuclear and Particle Physics*, vol. 29, no. 8, p. 1899, 2003, Neutrino factories. Proceedings, 4th International Workshop, NuFact’02, London, UK, July 1–6, 2002.
- [65] A. Cooper-Sarkar, P. Mertsch, and S. Sarkar, “The high energy neutrino cross-section in the Standard Model and its uncertainty,” *Journal of High Energy Physics*, vol. 2011, no. 8, article 42, 2011.
- [66] K. Kodama, N. Ushida, C. Andreopoulos et al., “Final tau-neutrino results from the DONuT experiment,” *Physical Review D*, vol. 78, no. 5, Article ID 052002, 20 pages, 2008.
- [67] K. Abe, J. Adam, H. Aihara et al., “Precise measurement of the neutrino mixing parameter  $\theta_{23}$  from muon neutrino disappearance in an off-axis beam,” *Physical Review Letters*, vol. 112, no. 18, Article ID 181801, 8 pages, 2014.
- [68] M. Nakahata, “Recent results from super-kamiokande,” in *Presented at 16th International Workshop on Neutrino Telescopes*, Venice, Italy, 2015.
- [69] D. Heck, J. Knapp, J. N. Capdevielle, G. Schatz, and T. Thouw, *CORSIKA: a Monte Carlo Code to Simulate Extensive Air Showers*, Forschungszentrum Karlsruhe GmbH, 1998, <http://inspirehep.net/record/469835/files/FZKA6019.pdf>.
- [70] G. Carminati, M. Bazzotti, S. Biagi et al., “MUPAGE: a fast atmospheric MUon generator for neutrino telescopes based on parametric formulas,” in *Proceedings of the International Cosmic Ray Conference*, Lodz, Poland, July 2009.
- [71] C. Andreopoulos, A. Bell, D. Bhattacharya et al., “The GENIE neutrino Monte Carlo generator,” *Nuclear Instruments and Methods in Physics Research Section A*, vol. 614, no. 1, pp. 87–104, 2010.
- [72] A. Gazizov and M. P. Kowalski, “ANIS: high energy neutrino generator for neutrino telescopes,” *Computer Physics Communications*, vol. 172, no. 3, pp. 203–213, 2005.
- [73] G. Ingelman, A. Edin, and J. Rathsmann, “LEPTO 6.5—a Monte Carlo generator for deep inelastic lepton-nucleon scattering,” *Computer Physics Communications*, vol. 101, no. 1-2, pp. 108–134, 1997.
- [74] T. Sjöstrand, P. Edén, C. Friberg et al., “High-energy-physics event generation with PYTHIA 6.1,” *Computer Physics Communications*, vol. 135, no. 2, pp. 238–259, 2001.
- [75] M. Sajjad Athar, M. Honda, T. Kajita, K. Kasahara, and S. Midorikawa, “Atmospheric neutrino flux at INO, South Pole and Pyhäsalmi,” *Physics Letters B*, vol. 718, no. 4-5, pp. 1375–1380, 2013.
- [76] S. Agostinelli, J. Allison, K. Amako et al., “Geant4—a simulation toolkit,” *Nuclear Instruments and Methods in Physics Research Section A: Accelerators, Spectrometers, Detectors and Associated Equipment*, vol. 506, no. 3, pp. 250–303, 2003.
- [77] J. Brunner, “Antares simulation tools,” in *Proceedings of the 1st VLvT Workshop*, Amsterdam, The Netherlands, October 2003.
- [78] P. Antonioli, C. Ghetti, E. V. Korolkova, V. A. Kudryavtsev, and G. Sartorelli, “A three-dimensional code for muon propagation through the rock: MUSIC,” *Astroparticle Physics*, vol. 7, no. 4, pp. 357–368, 1997.
- [79] I. A. Sokalski, E. V. Bugaev, and S. I. Klimushin, “MUM: flexible precise Monte Carlo algorithm for muon propagation through thick layers of matter,” *Physical Review D*, vol. 64, no. 7, Article ID 074015, 2001.
- [80] D. Chirkin and W. Rhode, “Propagating leptons through matter with Muon MonteCarlo (MMC),” <http://arxiv.org/abs/hep-ph/0407075>.
- [81] S. Fukuda, Y. Fukuda, T. Hayakawa et al., “The Super-Kamiokande detector,” *Nuclear Instruments and Methods in Physics Research Section A: Accelerators, Spectrometers, Detectors and Associated Equipment*, vol. 501, no. 2-3, pp. 418–462, 2003.
- [82] K. Abe, N. Abgrall, H. Aihara et al., “The T2K experiment,” *Nuclear Instruments and Methods in Physics Research Section A: Accelerators, Spectrometers, Detectors and Associated Equipment*, vol. 659, no. 1, pp. 106–135, 2011.
- [83] D. G. Michael, P. Adamson, T. Alexopoulos et al., “The magnetized steel and scintillator calorimeters of the MINOS experiment,” *Nuclear Instruments and Methods in Physics Research Section A: Accelerators, Spectrometers, Detectors and Associated Equipment*, vol. 596, no. 2, pp. 190–228, 2008.
- [84] “The NOvA technical design report,” Tech. Rep. FERMILAB-DESIGN-2007-01, 2007, <http://lss.fnal.gov/archive/design/fermilab-design-2007-01.pdf>.
- [85] J. Brunner, “Measuring neutrino oscillations and the neutrino mass hierarchy in the Mediterranean sea,” in *Proceedings of the 34th International Cosmic Ray Conference (ICRC ’15)*, The Hague, The Netherlands, July-August 2015.
- [86] M. Aartsen, K. Abraham, M. Ackermann et al., “Letter of intent: the precision IceCube next generation upgrade (PINGU),” <http://arxiv.org/abs/1401.2046>.
- [87] P. Adamson, C. Andreopoulos, K. E. Arms et al., “Measurement of neutrino oscillations with the MINOS detectors in the NuMI beam,” *Physical Review Letters*, vol. 101, Article ID 131802, 2008.
- [88] J. P. Yanez, “From DeepCore to PINGU: measuring atmospheric neutrino oscillations at the South Pole,” in *Proceedings of the Very Large Volume Neutrino Telescope Workshop (VLvT ’15)*, Rome, Italy, September 2015.
- [89] J. A. Aguilar, I. Al Samarai, A. Albert et al., “A fast algorithm for muon track reconstruction and its application to the ANTARES

- neutrino telescope,” *Astroparticle Physics*, vol. 34, no. 9, pp. 652–662, 2011.
- [90] G. L. Fogli, E. Lisi, A. Marrone, D. Montanino, and A. Palazzo, “Getting the most from the statistical analysis of solar neutrino oscillations,” *Physical Review D*, vol. 66, no. 5, Article ID 053010, 22 pages, 2002.
- [91] K. Clark, “Status of the PINGU detector,” in *Proceedings of the International Cosmic Ray Conference*, The Hague, The Netherlands, July 2015.
- [92] J. Ahrens, X. Bai, R. Bay et al., “Muon track reconstruction and data selection techniques in AMANDA,” *Nuclear Instruments and Methods in Physics Research Section A*, vol. 524, no. 1–3, pp. 169–194, 2004.
- [93] M. Gonzalez-Garcia, M. Maltoni, J. Salvado, and T. Schwetz, “Global fit to three neutrino mixing: critical look at present precision,” *Journal of High Energy Physics*, vol. 2012, no. 12, article 123, 2012.
- [94] S. Euler, “Atmospheric neutrino oscillations with DeepCore,” in *Proceedings of the International Cosmic Ray Conference*, vol. 4, p. 67, 2011.
- [95] R. Wendell, C. Ishihara, K. Abe et al., “Atmospheric neutrino oscillation analysis with subleading effects in Super-Kamiokande I, II, and III,” *Physical Review D*, vol. 81, no. 9, Article ID 092004, 16 pages, 2010.
- [96] D. J. Koskinen, “Icecube-DeepCore-PINGU: fundamental neutrino and dark matter physics at the South Pole,” *Modern Physics Letters A*, vol. 26, no. 39, p. 2899, 2011.
- [97] P. Bagley, J. Craig, A. Holford et al., “Technical Design Report,” Tech. Rep., 2010.
- [98] M. G. Aartsen, M. Ackermann, J. Adams et al., “IceCube-Gen2: a vision for the future of neutrino astronomy in Antarctica,” <http://arxiv.org/abs/1412.5106>.
- [99] S. Adrian-Martinez, M. Ageron, F. Aharonian et al., “Deep sea tests of a prototype of the KM3NeT digital optical module,” *The European Physical Journal C*, vol. 74, article 3056, 2014.
- [100] T. DeYoung, “Neutrino physics prospects with PINGU,” in *Presented at the Meeting of the APS Division of Particles and Fields (DPF ’15)*, Ann Arbor, Mich, USA, August 2015.
- [101] K. Hanson and IceCube-Gen2 Collaboration, “IceCube-Gen2: the science, the detector, drilling, and logistics,” in *Proceedings of the Very Large Volume Neutrino Telescopes (VLVnT ’15)*, Rome, Italy, September 2015.
- [102] M. Jongen, “Sensitivity to the neutrino mass hierarchy of KM3NeT/ORCA,” in *Proceedings of the 34th International Cosmic Ray Conference (ICRC ’15)*, The Hague, The Netherlands, July-August 2015.
- [103] S. Adrian-Martinez, I. Al Samarai, A. Albert et al., “Search for cosmic neutrino point sources with four years of data from the antares telescope,” *The Astrophysical Journal*, vol. 760, no. 1, article 53, 2012.
- [104] M. Ribordy and A. Y. Smirnov, “Improving the neutrino mass hierarchy identification with inelasticity measurement in PINGU and ORCA,” *Physical Review D*, vol. 87, no. 11, Article ID 113007, 20 pages, 2013.
- [105] D. Franco, C. Jollet, A. Kouchner et al., “Mass hierarchy discrimination with atmospheric neutrinos in large volume ice/water Cherenkov detectors,” *Journal of High Energy Physics*, vol. 2013, no. 4, article 008, 2013.
- [106] J. Sandroos, “Atmospheric flux uncertainties and the neutrino mass hierarchy,” in *Proceedings of the VLVnT Workshop*, Rome, Italy, September 2015.
- [107] J. P. A. M. de André, J. Pedro, and IceCube-PINGU Collaboration, “Atmospheric neutrino status and prospects,” in *Proceedings of the 17th International Workshop on Neutrino Factories and Future Neutrino Facilities (NuFact ’15)*, Rio de Janeiro, Brazil, August 2015.
- [108] F. Capozzi, E. Lisi, and A. Marrone, “PINGU and the neutrino mass hierarchy: statistical and systematic aspects,” *Physical Review D*, vol. 91, no. 7, Article ID 073011, 18 pages, 2015.

## Review Article

# The Deep Underground Neutrino Experiment

**Maury Goodman**

*Argonne National Lab for the DUNE Collaboration, Argonne, IL 60439, USA*

Correspondence should be addressed to Maury Goodman; [maury.goodman@anl.gov](mailto:maury.goodman@anl.gov)

Received 29 July 2015; Accepted 19 November 2015

Academic Editor: Mauro Mezzetto

Copyright © 2015 Maury Goodman. This is an open access article distributed under the Creative Commons Attribution License, which permits unrestricted use, distribution, and reproduction in any medium, provided the original work is properly cited. The publication of this article was funded by SCOAP<sup>3</sup>.

The Deep Underground Neutrino Experiment (DUNE) is a worldwide effort to construct a next-generation long-baseline neutrino experiment based at the Fermi National Accelerator Laboratory. It is a merger of previous efforts and other interested parties to build, operate, and exploit a staged 40 kt liquid argon detector at the Sanford Underground Research Facility 1300 km from Fermilab, and a high precision near detector, exposed to a 1.2 MW, tunable  $\nu$  beam produced by the PIP-II upgrade by 2024, evolving to a power of 2.3 MW by 2030. The neutrino oscillation physics goals and the status of the collaboration and project are summarized in this paper.

## 1. Introduction

The Deep Underground Neutrino Experiment (DUNE) has been established as an international partnership to fulfill the goals established by the Particle Physics Program Prioritization Panel in the United States [1]. The design, goals, and status of the collaboration, experiment, and project have been recently described in detail in a Conceptual Design Report (CDR) [2] written for a “CD-1 Refresh” review that took place in July 2015 for the U.S. Department of Energy.

Members of the international neutrino community broadly agree on the goals for study to remove gaps in our understanding of the neutrino sector in the current Standard Model of Particle Physics:

- (i) determination of the mass ordering between the normal mass ordering ( $m_3 > m_1$ ; NO) and the inverted ordering ( $m_1 > m_3$ ; IO) (a common notation is to call these the normal hierarchy (NH) and inverted hierarchy (IH), but for the case of nonhierarchical degenerate neutrino mass, there is still sensitivity to the ordering, so this paper uses the slightly more precise notation NO and IO),
- (ii) determination of the value of the CP (Charge Parity) violation phase  $\delta$ ,
- (iii) determination of the octant of  $\theta_{23}$ ,

- (iv) more precision in the determination of the values of the mixing angles and  $\Delta m^2$  values,
- (v) search for new physics beyond the three-neutrino paradigm,
- (vi) determination of the overall mass scale,
- (vii) determination of whether the neutrino is Dirac or Majorana.

The first five issues can be addressed with precise new accelerator experiments with detectors located near and far from the proton target. One requires a deep underground location to reduce backgrounds in the search for neutrinoless double beta decay. Through the first two decades of the 21st century, a large variety of experiments have been proposed to accomplish this program. Since the scale in size and cost is larger than previous neutrino experiments, a large variety of solutions in terms of baseline, location, overburden, detector size, detector design, and beam energy spectrum have been investigated to achieve an optimum program. Many of the advocates of these programs have coalesced into a new international collaboration based on two facilities: the Fermilab accelerator complex that will host the Long-Baseline Neutrino Facility (LBNF) and the Sanford Underground Research Facility (SURF) located 1300 km away in South Dakota. LBNF will be operated as a fully international facility hosted by Fermilab. The detectors, totaling 40 kt fiducial

mass of liquid argon, will be designed, built, commissioned, and operated by the international DUNE collaboration. The scope of LBNF includes an intense on-axis neutrino beam aimed at the far site, the conventional facilities at both the near and far sites, and the cryogenic infrastructure needed to support the DUNE detector at the far site. The DUNE detectors include a high-performance near neutrino detector, a beamline measurement system, and a massive liquid argon time projection chamber (LArTPC) for use as a neutrino detector deep underground at SURF.

DUNE and LBNF encompass an ambitious and long-term program to improve our knowledge of neutrino physics and particle astrophysics. They represent what will be a significant investment by the world's high energy physics community. The goals of the program will not be accomplished in a single phase. A partially applicable analogy is to look at the tremendous success of the LHC program as of 2015, even though it has not yet run at its design energy of 14 TeV. At the same time that the DUNE physics program is ambitious, the facility and detectors are also flexible in their ability to adapt to changing understanding of the neutrino sector or any new and unexpected physics beyond the three-neutrino paradigm that might be uncovered in the coming decade.

A previous look at potential future experiments and facilities, including the LBNE program in the United States and the Hyper-Kamiokande program in Japan, is provided in the last special issue on neutrino oscillations in [3]. A more detailed look at the science opportunities for LBNE was given in [4]. As this special issue focuses on neutrino mass and oscillations, in this paper I will cover only the oscillation physics of DUNE, and the status of the collaboration. In Section 2 I summarize DUNE's beam physics program. In Section 3 some complementary measurements using atmospheric neutrinos are discussed. Other physics capabilities, including nucleon decay, astrophysical neutrinos, and neutrino physics in the near detector are covered extensively in [2, 4]. I will not review the current design of the 1.2 MW beamline and the other facilities that are described in volume 3 of the CDR or describe in any detail the design for the 40 kt (fiducial volume) LArTPC that can be found in volume 4 [2]. In Section 4 I will summarize the current status and timeline for DUNE and LBNF.

## 2. Neutrino Oscillation Physics Capabilities Using the NuMI Beam

SURF is located 1300 km from Fermilab. A study of baseline optimization for the measurement of CP violation, mass ordering, and  $\theta_{23}$  octant in a long-baseline experiment concluded that a detector at a baseline of at least 1000 km in a wide-band  $\nu_\mu$  beam is the optimal configuration [5]. SURF well satisfies this requirement and as the site of the original Davis solar neutrino experiment was thoroughly investigated as a candidate site for a Deep Underground Science and Engineering Lab, it is well suited for a large scientific endeavor. Briefly the optimization comes from the fact that CP violation and matter effects, which are sensitive to the mass ordering, both cause a difference in the rate of neutrino and antineutrino oscillation events. But those

TABLE 1: Integrated rates of CC-like events. Signal  $\nu_e$  rates are shown for both NO and IO and  $\delta_{CP} = 0$ . Background rates assume NO.

(150 kt·MW·yr)	$\nu$ mode	$\bar{\nu}$ mode
$\nu_e$ signal NO (IO)	861 (495)	61 (37)
$\bar{\nu}_e$ signal NO (IO)	13 (26)	167 (378)
Total signal NO (IO)	874 (521)	228 (415)
Beam $\nu_e + \bar{\nu}_e$ CC Bkgd	159	89
NC Bkgd	22	12
Beam $\nu_\tau + \bar{\nu}_\tau$ Bkgd	42	23
Beam $\nu_\mu + \bar{\nu}_\mu$ Bkgd	3	2
Total Bkgd	226	126
$\nu_\mu$ ( $\bar{\nu}_\mu$ ) signal	10842	3754
$\bar{\nu}_\mu$ ( $\nu_\mu$ ) Bkgd	958	2598
NC Bkgd	88	50
Beam $\nu_\tau + \bar{\nu}_\tau$ Bkgd	63	39

differences are different. The size of the asymmetry from the matter effect grows with increasing baseline and dominates for a baseline over 1000 km.

The oscillation probabilities for  $\nu_e$  ( $\bar{\nu}_e$ ) appearance in a  $\nu_\mu$  ( $\bar{\nu}_\mu$ ) beam at the Fermilab/SURF distance are shown in Figure 1 as a function of neutrino energy for several possible values of the CP phase parameter  $\delta_{CP}$ . These curves illustrate the choice of a broadband beam that can not only measure the rate of  $\nu_e$  and  $\bar{\nu}_e$  appearance but also map out the spectrum down to energies of 500 MeV.

Figure 1 also shows the decision about beam optimization, such as the choice of proton momentum. That choice involves tradeoffs in secondary particle production, cycle time, and beam power, all of which affect the integrated flux. The reference design in Chapter 3 of the CDR [2] has chosen a proton beam energy of 80 GeV, a beam power (after the PIP-II upgrades) of 1.07 MW, a graphite target, a horn current of 230 kA, and a 4 m diameter decay pipe that is 204 m long. Further optimizations of these parameters are continuing and some improvements in sensitivity can be expected as reflected in the curves labeled “optimized design” in some of the sensitivity plots in this paper. A discussion of efforts to optimize the LBNF beam design can be found in Section 3.7 of volume 2 of the CDR [2].

Signal and background event rates assuming a 150 kt·MW·yr exposure in each of a neutrino and antineutrino beam are shown in Table 1. This and all subsequent figures assume an exposure of 300 kt·MW·yr which corresponds to 3.5 years each in neutrino and antineutrino mode, a 40 kt fiducial volume detector and a 1.07 MW 80 GeV beam. This includes the assumption of equal duration runs of neutrinos and antineutrinos, but that split can be adjusted depending on the early results of this and other neutrino experiments, such as NO $\nu$ A and T2K [6, 7], to maximize parameter sensitivity. The spectra of reconstructed  $\nu_\mu$  and  $\nu_e$  signal and background events are shown in Figures 2 and 3. These spectra are used in the accurate determination of neutrino oscillation parameters.

The 1300 km baseline allows the neutrino and antineutrinos in the NuMI beam to travel through enough matter to be affected by the MSW effect. This leads to a large asymmetry

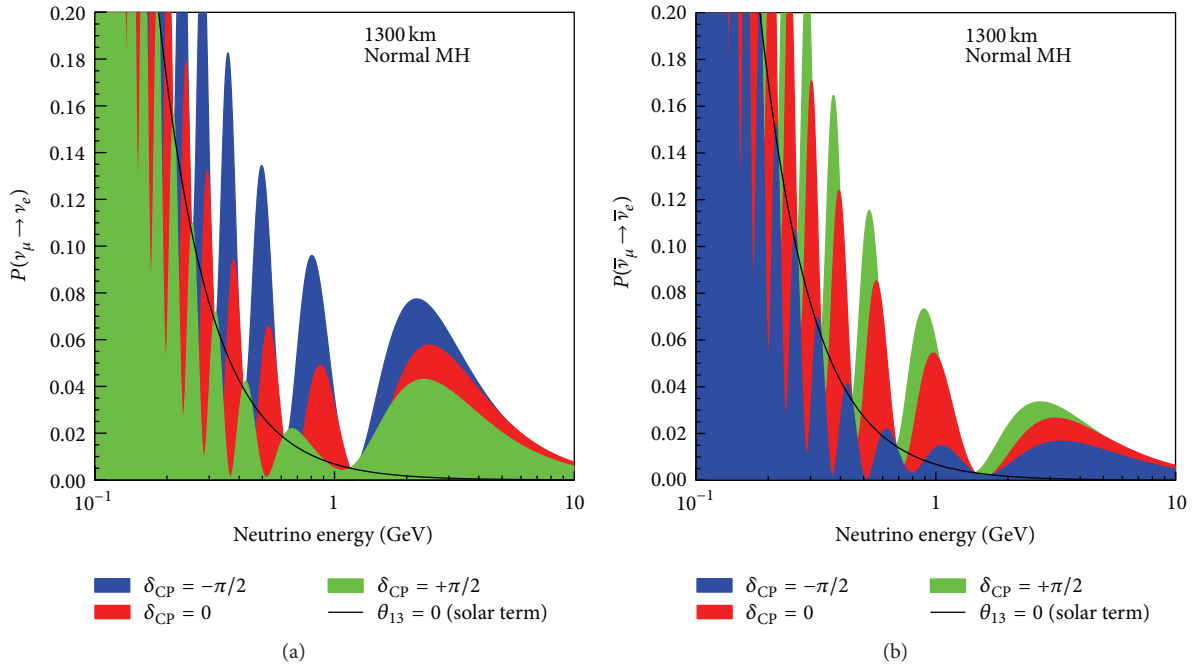


FIGURE 1: The appearance probability for  $\nu_e$  (a) and  $\bar{\nu}_e$  (b) as a function of neutrino energy in a  $\nu_\mu/\bar{\nu}_\mu$  beam. The curves are calculated for 1300 km baseline and NO, three values of  $\delta_{CP}$  for the Daya Bay best fit value of  $\theta_{13}$  and for  $\theta_{13} = 0$ .

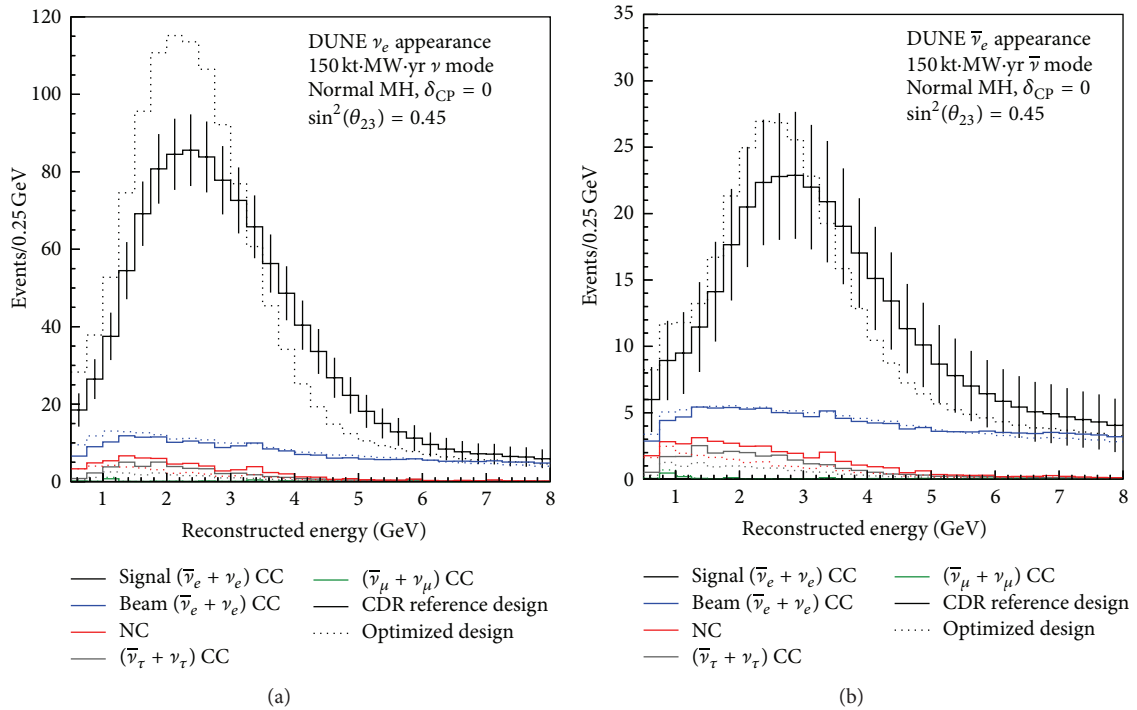


FIGURE 2: Reconstructed energy distributions of selected  $\nu_\mu \rightarrow \nu_e$  and  $\bar{\nu}_\mu \rightarrow \bar{\nu}_e$  appearance events for 150 kt·MW·yr exposure, assuming NO and  $\delta_{CP} = 0$ . Event rates and backgrounds are shown both for the reference design (solid) and for an optimized beam (dots) which has been designed but not fully costed.

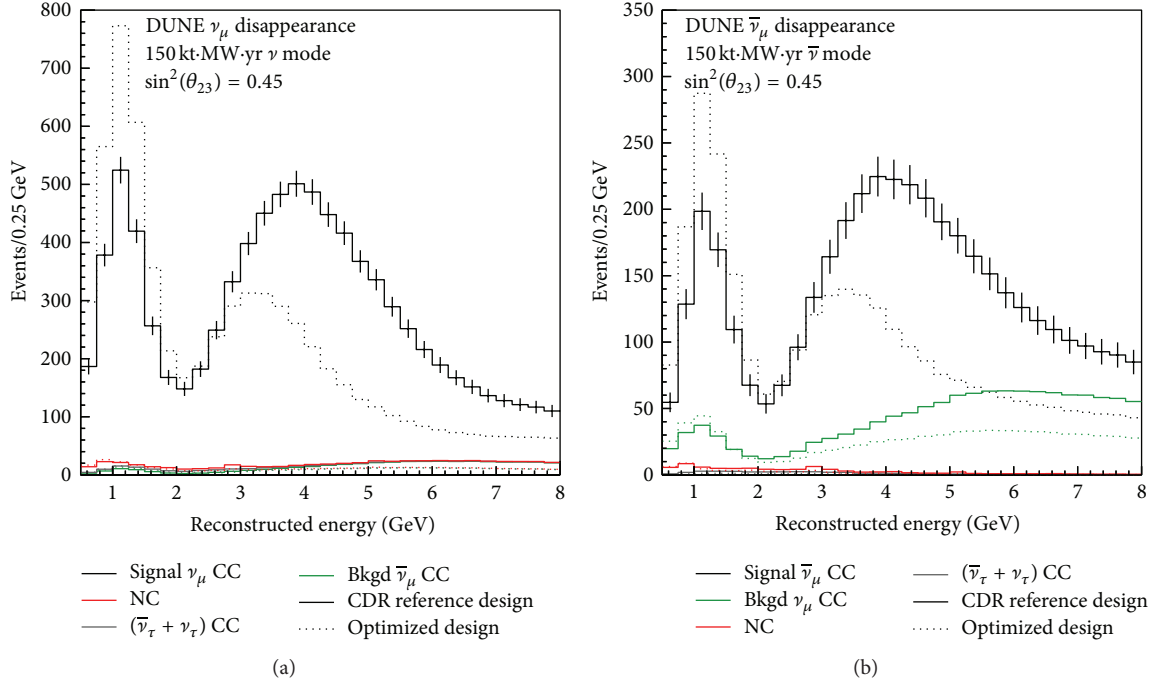


FIGURE 3: Reconstructed energy distributions of selected  $\nu_\mu$  and  $\bar{\nu}_\mu$  events for 150 kt-MW-yr exposure, assuming NO and  $\delta_{CP} = 0$ .

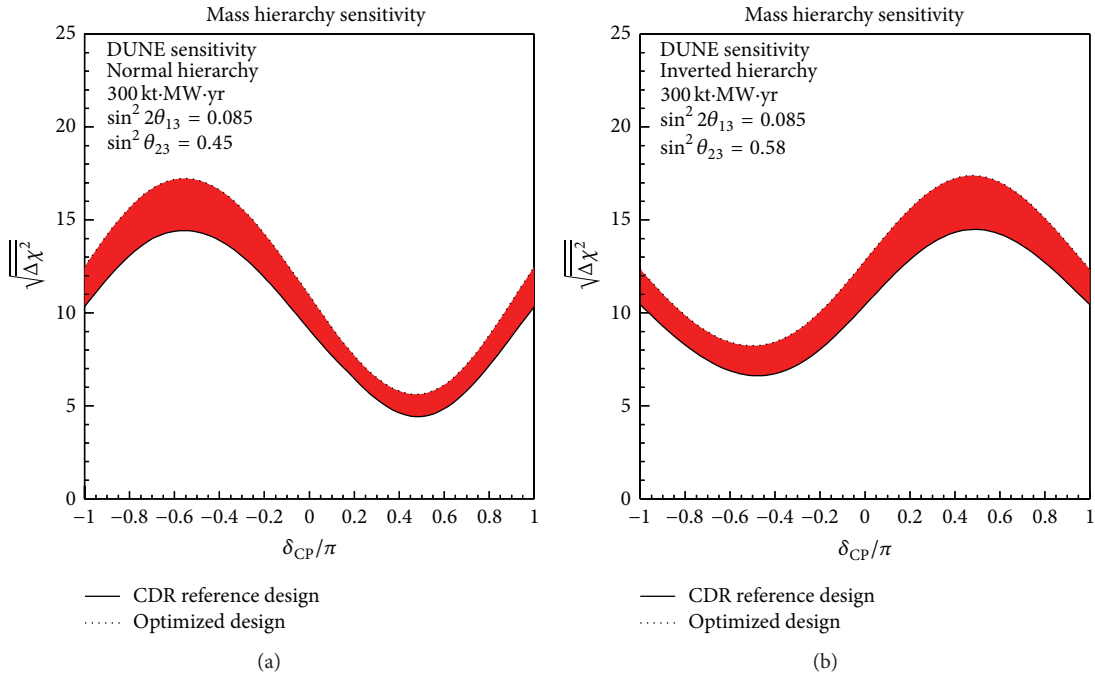


FIGURE 4: These figures show the sensitivity with which the mass ordering can be determined using the LBNF beam as a function of  $\delta_{CP}$  for the NO (a) and IO (b). The shaded region shows the range between the CDR reference design and a possible optimized design of the beam.

in the  $\nu_\mu \rightarrow \nu_e$  versus  $\bar{\nu}_\mu \rightarrow \bar{\nu}_e$  oscillation probabilities, the sign of which depends on the mass ordering. There are only two possible values of the ordering, and the asymmetry in the region of the peak flux for DUNE is  $\pm 40\%$ , larger than the maximal possible asymmetry due to CP violation.

Figure 4 shows how well the mass ordering (called the mass hierarchy in the figures) can be measured as a function of  $\delta_{CP}$  using beam neutrinos. The areas of lower sensitivity are for values of the ordering and  $\delta_{CP}$  where the total asymmetry is smaller, and the better sensitivity happens where the total

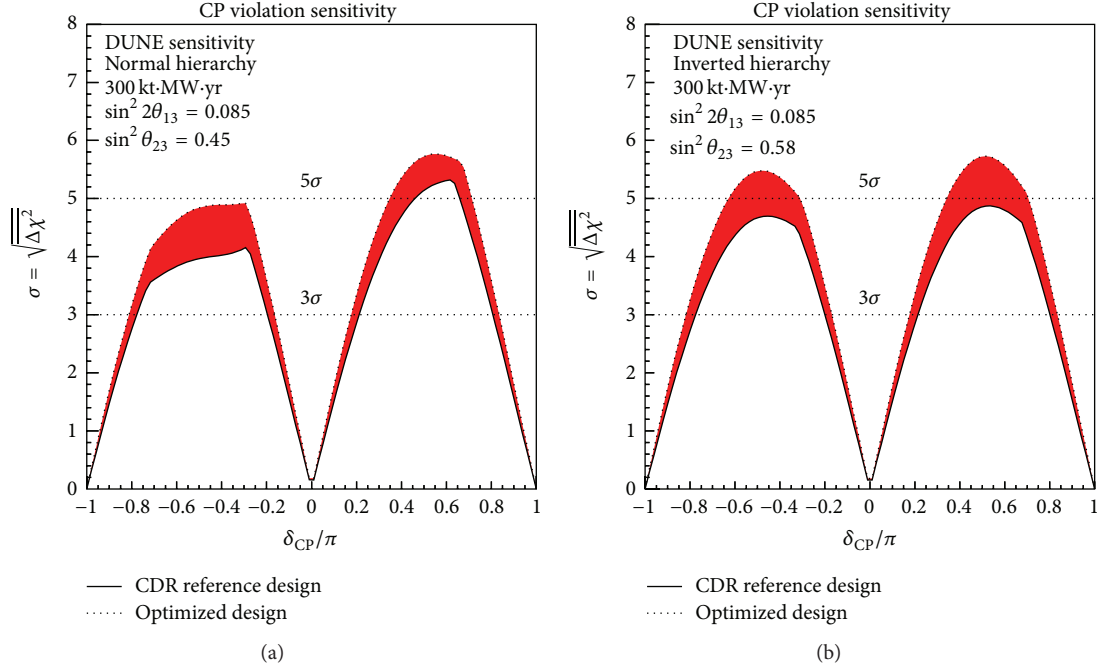


FIGURE 5: These figures show the sensitivity with which CP violation can be established using the LBNF beam as a function of  $\delta_{\text{CP}}$  for the NO (a) and IO (b). The shaded region shows the range between the CDR reference design and a possible optimized design of the beam.

asymmetry is larger. The value of  $\theta_{23}$  is important, affecting both the statistics and the sensitivity (in opposite directions) to the ordering and to CP violation. Nevertheless, DUNE will be able to unequivocally measure the mass ordering in the three-neutrino paradigm for any values of neutrino oscillation parameters. Note that a conversion of  $\Delta\chi^2$  to significance takes some care, as discussed in [8].

The magnitude of CP violation in the neutrino sector depends on a combination of neutrino oscillation parameters known as the Jarlskog invariant:

$$J_{\text{CP}}^{\text{PMNS}} \equiv \sin 2\theta_{12} \sin 2\theta_{13} \sin 2\theta_{23} \cos \theta_{13} \sin \delta_{\text{CP}}. \quad (1)$$

Since the value of  $\theta_{13}$  is now known, the minimal conditions required for measuring  $\delta_{\text{CP}}$  in the three-neutrino paradigm have been met; all three mixing angles and both mass splittings have been measured and are nonzero. This will introduce an asymmetry between neutrino and antineutrino oscillations unless  $\delta_{\text{CP}} = 0$  or  $\pi$ . Even then, the value of the parameter  $\delta_{\text{CP}}$  can be well measured, but CP violation in the neutrino sector can only be measured if those two possible values are ruled out. Either a precise measurement of or a stringent limit on CP violation would be quite interesting and challenging for theorists who believe that CP violation in the lepton sector may be related to the baryon-antibaryon asymmetry in the universe.

Figure 5 shows the significance with which the CP violation can be measured as a function of  $\delta_{\text{CP}}$  for an exposure of 300 kt·MW·yr assuming the NO and the IO. The shaded region represents a range in possible sensitivity from the reference design (pessimistic) to an optimized design

(optimistic). Using the reference design, DUNE will achieve a greater than  $3\sigma$  measurement of CP violation for 75% of  $\delta_{\text{CP}}$  values in 1320 kt·MW·yr, and a  $5\sigma$  measurement of CP violation for 50% of  $\delta_{\text{CP}}$  values in 810 kt·MW·yr. An exposure of 1320 kt·MW·yr is the suggested goal from the P5 report [1], an ambitious but achievable exposure for this facility in the long term.

A value of  $\theta_{23}$  of exactly  $45^\circ$  would indicate that  $\nu_\mu$  and  $\nu_\tau$  have equal contributions from  $\nu_3$ , which would be evidence for a new symmetry. A value greater than  $45^\circ$  would indicate mixing among the generations of the neutrino sector qualitatively different than in the quark sector (in addition to the different mixing angles). Thus, it is important to measure  $\theta_{23}$  with enough precision to determine the octant or the nondeviation from  $45^\circ$ . The measurement of  $\nu_\mu \rightarrow \nu_e$  is sensitive to  $\sin^2(\theta_{23})$  while  $\nu_\mu$  disappearance is sensitive to  $\sin^2(2\theta_{23})$ . DUNE will measure both of these and will probe the  $\theta_{23}$  octant precisely. The sensitivity as a function of the true value of  $\theta_{23}$  is shown in Figure 6. A strong indication of the octant can be found over most of its currently allowed range.

Systematic uncertainties in the accelerator neutrino measurements with DUNE will come from uncertainties in the neutrino flux after near/far extrapolation, the interaction model, the  $\nu_\mu$  and  $\nu_e$  reconstructed energy scales, and the fiducial volume. DUNE plans to take advantage of spectral analysis, meaning that absolute and relative flux normalization is required. Based on previous experience from the NuMI beam, a goal uncertainty of 2% has been set on  $\nu_e$  signal normalization relative to the  $\nu_\mu$  rate, added in quadrature

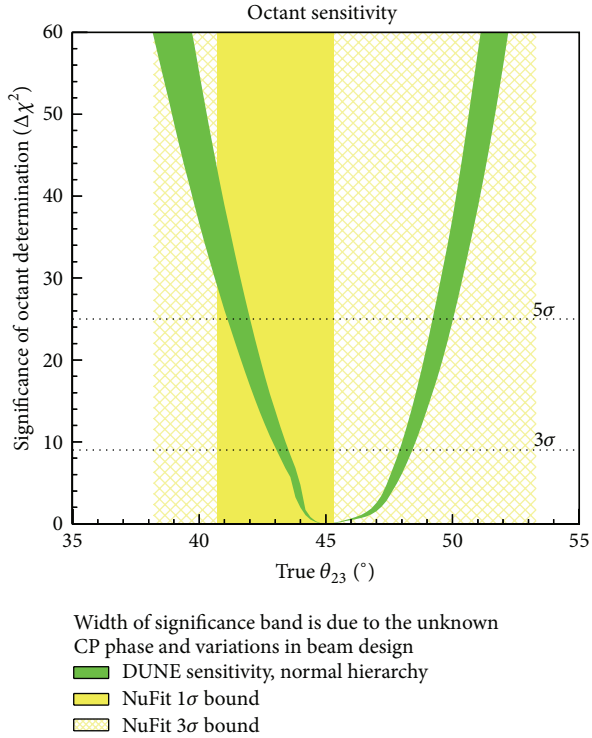


FIGURE 6: This figure shows the sensitivity with which the quadrant of  $\theta_{23}$  can be determined using the LBNF beam as a function of its true value. The green shaded region shows the range due to variations in beam design and the true value of  $\delta_{CP}$ . The yellow region shows the current best fit value for NO from a global fit from the NuFit collaboration.

with an overall 5% normalization. Uncertainty in neutrino interaction models comes from the relative rates of quasi-elastic, resonance, and deep inelastic scattering in nuclei, together with final state interactions. Significant improvements to neutrino interaction models are anticipated as a result of the intermediate neutrino program [9] and the goal for the effect of uncertainties is 2% after cancellation from the near/far comparison. Previous experiments have achieved uncertainties in the energy scale below 3%, and DUNE will take advantage of a number of liquid argon detectors being studied in test beams, in neutrino beams for the short-baseline program [10] and in the intermediate neutrino program [9]. The effect of fiducial volume uncertainty is reduced in large detectors such as DUNE and will be about 1%. The total systematic error on the  $\nu_e$  appearance rate is estimated at 3.6% and should be reduced by the time the statistical error gets down to that level.

The high-precision near detector of DUNE will be able to make a number of cross section measurements that will help in the extrapolation of the neutrino flux to the far detector. Should any anomalies remain after the SBN program and its search for sterile neutrinos [10], the near and far detectors together will be able to provide further understanding of the effects or constrain the physics involved. There are a variety of other new physics possibilities, such as nonstandard interactions, neutrino decay, and Lorentz violation that DUNE

will be able to investigate or constrain. While these are not the primary goals of DUNE and they entail no additional requirements on the detector, the remarkable capabilities of DUNE allow for the study of many possible extensions of the three-neutrino paradigm, should any exist.

### 3. Neutrino Oscillation Physics Capabilities Using Atmospheric Neutrinos

Atmospheric neutrinos come in all flavors and in a wide range of baseline, neutrino energy, and hence  $L/E_\nu$ . They are particularly sensitive to  $\theta_{23}$  and were the source of the atmospheric neutrino anomaly leading to the discovery of neutrino mass and oscillations by Super-Kamiokande in 1998 [11].

The transitions between electron neutrinos and muon neutrinos are affected by MSW transitions for the longest traveling atmospheric neutrinos  $\cos\theta_z \sim -1$ , where  $\theta_z$  is the zenith angle. There is an enhancement for neutrinos in the normal mass ordering and antineutrinos in the inverted mass ordering. From [4] the rates of fully contained  $\nu_e$ , fully contained  $\nu_\mu$ , and partially contained  $\nu_\mu$  are shown as a function of zenith angle for no oscillations, normal ordering, and inverted ordering (Figure 7). Differences in the event rates as a function of  $\theta_z$  are observed in comparing the NO and IO predictions at low values of  $\cos\theta_z$ .

Since the enhancement occurs for neutrinos (antineutrinos) in the NO (IO), the sensitivity is enhanced if neutrino and antineutrino events are separated. There are no current plans to magnetize DUNE; however, its high-resolution imaging capabilities provide the ability to measure recoil protons and decay electrons that can be used to statistically tag neutrinos and antineutrinos. Recoil protons occur more often in neutrino interactions and can be tagged with 100% efficiency if the kinetic energy is greater than 50 MeV. Decay electrons in  $^{40}\text{Ar}$  occur for  $\mu^+$  made by antineutrinos, but only 25% of the time for neutrino-induced  $\mu^-$ .

For atmospheric neutrinos, the ordering sensitivity is essentially independent of  $\delta_{CP}$ , in contrast to the beam neutrinos. This provides complementarity. In the three-neutrino paradigm, a joint fit of the atmospheric and beam neutrinos for the mass ordering increases the significance of the ordering measurement for those values of  $\delta_{CP}$  in Figure 4 where the significance is lowest. For all regions of  $\delta_{CP}$  atmospheric neutrinos provide a consistency check of the ordering determination which can be used as a test for new physics.

### 4. Status of the DUNE Collaboration

The international context and motivation for a long-baseline neutrino experiment is well described in [3] from the last special issue on neutrino physics and oscillations. In that document, ideas for approaches to future long-baseline neutrino facilities in the US, Europe, and Japan are described. Since that time, the P5 report in the United States [1] and the strategy document for particle physics in Europe [12] have helped to shape the direction of the field. In particular, a

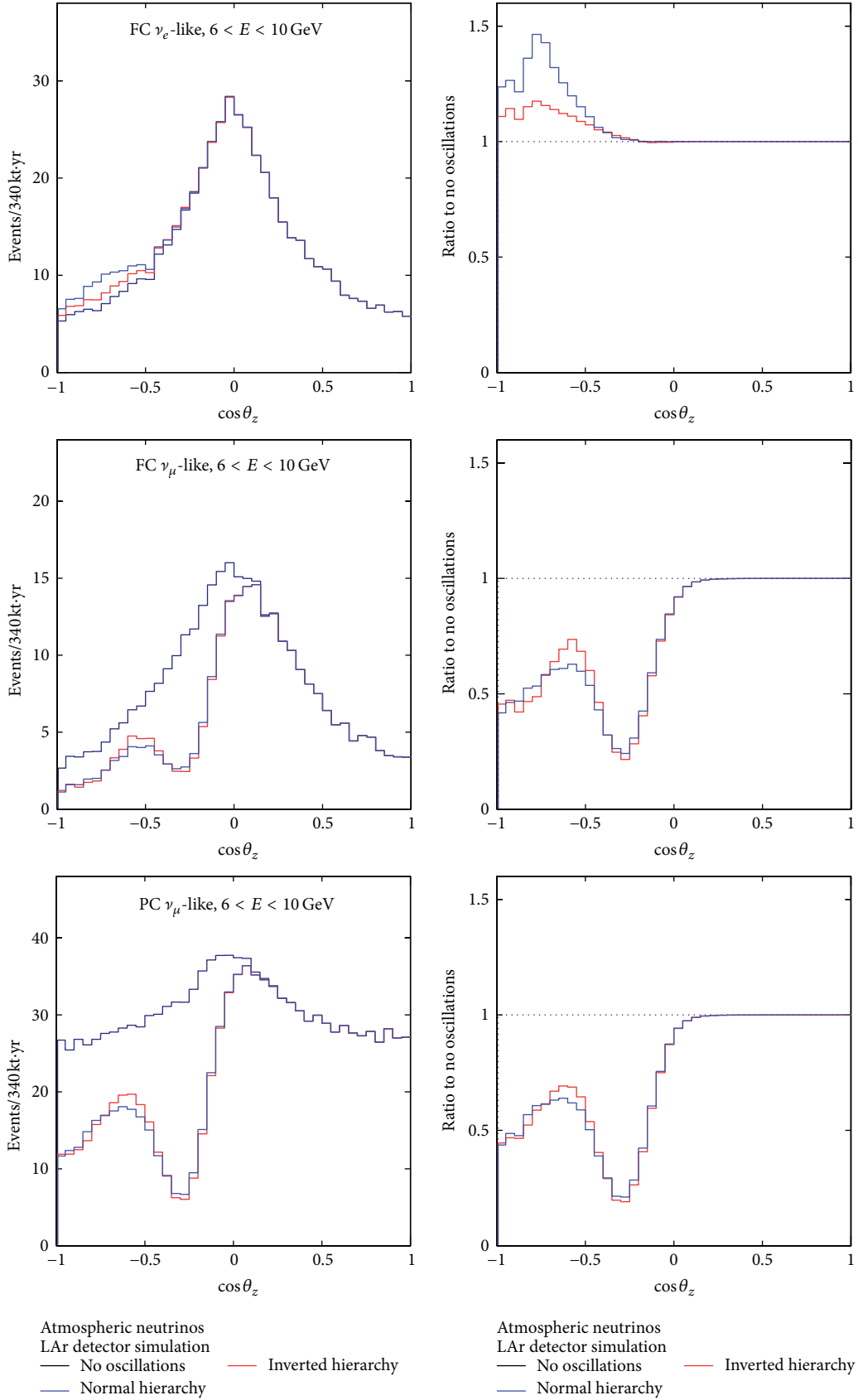


FIGURE 7: Reconstructed angles of atmospheric neutrinos in DUNE for 6 to 10 GeV fully contained  $\nu_e$  and  $\nu_\mu$  and partially contained  $\nu_\mu$  events. Distributions and ratios to the no oscillation case are shown for normal and inverted mass orderings.

conclusion of the European report was that CERN should help the European neutrino community participate in a long-baseline neutrino project outside of Europe. DUNE is made up of many former members from the LBNE and LBNO collaborations as well as many additional interested parties. It seems likely to grow to well over 1000 scientists during its phases of construction, installation, and operation. The collaboration formally adopted its rules in April of 2015. (Between the time of the P5 report and the formal start of the DUNE collaboration, it used the name ELBNF, for Experiment at the Long-Baseline Neutrino Facility.) It presently consists of 773 scientists from 144 institutions in 26 countries.

The P5 report specifically recommended that the previous efforts for a Fermilab-to-SURF long-baseline experiment be reformulated as an international collaboration [1]. The US involvement in the LHC at CERN has been seen as a successful example of international collaboration. A management structure paralleling those used at the LHC experiments has thus been established, a host lab providing the facilities, together with an international collaboration to build and operate the detector(s). The management structure of the collaboration includes two spokespersons elected by the collaboration, a technical coordinator, and a resource coordinator jointly appointed by the spokespersons and the Fermilab Management. An International Advisory Committee (IAC) consists of representatives from regional partners (such as CERN) and funding agencies that make major contributions to LBNF/DUNE. It advises the Department of Energy (DOE) and Fermilab and provides high-level global coordination. The Resources Review Board (RRB) has representatives from all the funding agencies. It provides focused monitoring and oversight of the projects. The Long-Baseline Neutrino Committee (LBNC) provides scientific peer review as an adjunct to the Fermilab Physics Advisory Committee (PAC). The Experiment-Facility Interface Group (EFIG) helps to ensure coordination between the detector systems from DUNE and technical infrastructure from LBNF for both the near and far detectors.

A letter of intent for DUNE was prepared and submitted to Fermilab in January of 2015 [13]. As mentioned above, the collaboration was formally established in April of 2015, it elected leaders, and core project leaders were appointed in parallel. A Conceptual Design Report was prepared and reviewed in July of 2015 by the Department of Energy in a process called CD-1 refresh (details of presentations can be found at <https://web.fnal.gov/project/LBNF/ReviewsAndAssessments/SitePages/Home.aspx> under “DOE reviews”). A high-level schedule for both the facility (LBNF) and detector (DUNE) construction and operation is shown in the CDR. At the request of the collaboration, early priority has been given to work at the far site. Site preparation will be complete in time coincidence with the completion at SURF of the rehabilitation of the Ross Shaft in late 2017. Four 10 kt fiducial mass liquid argon modules are scheduled to become operational between 2024 and 2027.

As DUNE is being developed, a multipronged short-baseline neutrino program will be carried out at Fermilab [10]. That is part of the response to the P5 call for a coherent

short- and long-baseline program of neutrino experiments. The three detectors, SBND, MicroBooNE, and ICARUS, all use liquid argon time projection chambers and provide an opportunity to test both the hardware and software that is envisaged for DUNE. The intermediate neutrino program [9] includes other neutrino measurements that will help in the precise understanding of neutrino cross sections and the measurements of other possible backgrounds [9]. And the CERN Neutrino Platform will include tests of present and possible future designs for the liquid argon readout in realistic conditions.

## 5. Summary

It could be claimed that, so far, nature has been kind to the neutrino physics community since, despite the smallness of the neutrino cross sections, it has been possible to measure the mixing angles and  $\Delta m^2$  values robustly in multiple ways [14]. Perhaps this favor will persist and CP-violating effects in neutrinos will be large and DUNE will have a long program of precisely measuring  $\delta_{CP}$  and searching for new physics beyond the three-neutrino paradigm. But whatever nature has in store for us, the 25+ year DUNE/LBNF physics program has been designed to provide a detailed, careful, and fruitful look at the properties of neutrinos, long considered the least understood element of the Standard Model, and exploit the large, high-resolution underground far detector for nonaccelerator physics topics such as atmospheric neutrinos, the search for nucleon decay, and the measurement of astrophysical neutrinos, especially those from a core-collapse supernova.

## Conflict of Interests

The author declares that there is no conflict of interests regarding the publication of this paper.

## References

- [1] Building for Discovery, Strategic Plan for U.S. Particle Physics in the Global Context, May 2014, [http://science.energy.gov/~media/hep/hepap/pdf/May%202014/FINAL\\_P5\\_Report\\_Interactive\\_060214.pdf](http://science.energy.gov/~media/hep/hepap/pdf/May%202014/FINAL_P5_Report_Interactive_060214.pdf).
- [2] Long-Baseline Neutrino Facility (LBNF) and Deep Underground Neutrino Experiment (DUNE) Conceptual Design Report, 4 Volumes, June 2015, <http://www.dunescience.org/>.
- [3] M. Diwan, R. Edgecock, T. Hasegawa, T. Patzak, M. Shiozawa, and J. Strait, “Future long-baseline neutrino facilities and detectors,” *Advances in High Energy Physics*, vol. 2013, Article ID 460123, 35 pages, 2013.
- [4] The LBNE Collaboration, “The long-baseline neutrino experiment: exploring fundamental symmetries of the universe,” <http://arxiv.org/abs/1307.7335>.
- [5] M. Bass, M. Bishai, D. Cherdack et al., “Baseline optimization for the measurement of CP violation, mass hierarchy, and  $\theta_{23}$  octant in a long-baseline neutrino oscillation experiment,” *Physical Review D*, vol. 91, no. 5, Article ID 052015, 2015.
- [6] <http://www-nova.fnal.gov/>.
- [7] <http://t2k-experiment.org/>.

- [8] M. Blennow, P. Coloma, P. Huber, and T. Schwetz, “Quantifying the sensitivity of oscillation experiments to the neutrino mass ordering,” *Journal of High Energy Physics*, vol. 2014, no. 3, article 28, 2014.
- [9] C. Adams, J. A. Alonso, A. M. Ankowski et al., “The Intermediate Neutrino Program,” <http://arxiv.org/abs/1503.06637>.
- [10] R. Acciarri, C. Adams, R. An et al., “A proposal for a three detector short-baseline neutrino oscillation program in the Fermilab booster neutrino beam,” <http://arxiv.org/abs/1503.01520>.
- [11] Y. Fukuda, T. Hayakawa, E. Ichihara et al., “Evidence for oscillation of atmospheric neutrinos,” *Physical Review Letters*, vol. 81, no. 8, pp. 1562–1567, 1998.
- [12] M. Krammer, “The update of the European strategy for particle physics,” *Physica Scripta T*, vol. 158, Article ID 014019, 2013.
- [13] Letter of Intent Submitted to the Fermilab PAC, P-1062, January 2015, [http://www.fnal.gov/directorate/program planning/Jan2015Public/LOI-LBNE.pdf](http://www.fnal.gov/directorate/program%20planning/Jan2015Public/LOI-LBNE.pdf).
- [14] M. Goodman, *Proceedings of the 16th Lomonosov Conference on Elementary Particle Physics*, World Scientific, 2015.

## Research Article

# Partial Quark-Lepton Universality and Neutrino CP Violation

Jiajun Liao,<sup>1,2</sup> D. Marfatia,<sup>1</sup> and K. Whisnant<sup>2</sup>

<sup>1</sup>Department of Physics and Astronomy, University of Hawaii at Manoa, Honolulu, HI 96822, USA

<sup>2</sup>Department of Physics and Astronomy, Iowa State University, Ames, IA 50011, USA

Correspondence should be addressed to Jiajun Liao; [liao@hawaii.edu](mailto:liao@hawaii.edu)

Received 1 June 2015; Accepted 29 July 2015

Academic Editor: Vincenzo Flaminio

Copyright © 2015 Jiajun Liao et al. This is an open access article distributed under the Creative Commons Attribution License, which permits unrestricted use, distribution, and reproduction in any medium, provided the original work is properly cited. The publication of this article was funded by SCOAP<sup>3</sup>.

We study a model with partial quark-lepton universality that can naturally arise in grand unified theories. We find that constraints on the model can be reduced to a single condition on the Dirac CP phase  $\delta$  in the neutrino sector. Using our current knowledge of the CKM and PMNS mixing matrices, we predict  $-32.4^\circ \leq \delta \leq 32.0^\circ$  at  $2\sigma$ .

## 1. Introduction

Our understanding of neutrinos has progressed steadily in the last two decades. After the observation of nonzero  $\theta_{13}$  by the Daya Bay [1, 2], RENO [3], and Double Chooz [4] experiments, we now know the three mixing angles  $\theta_{12}$ ,  $\theta_{23}$ , and  $\theta_{13}$  and the two mass squared differences to good precision. For the normal hierarchy, the current  $2\sigma$  ranges of the three mixing angles from a global three-neutrino oscillation analysis are [5]

$$\begin{aligned}\theta_{12} &= 33.7^{+2.1}_{-2.1} (^\circ), \\ \theta_{23} &= 41.4^{+6.6}_{-2.6} (^\circ), \\ \theta_{13} &= 8.80^{+0.73}_{-0.77} (^\circ).\end{aligned}\tag{1}$$

The focus of next generation neutrino oscillation experiments is shifted to the Dirac CP phase  $\delta$  and the neutrino mass hierarchy. Predictions of many theoretical models designed to explain the observed mixing patterns await verification. Among these models, quark-lepton universality (QLU) [6] is well motivated. It is based on simple relations in grand unified theories (GUT) and connects the mixing matrices of quarks and leptons. Exact quark-lepton universality leads to a symmetric PMNS mixing matrix. However,

using the current  $3\sigma$  ranges of the oscillation parameters [5], we find the moduli of the neutrino mixing matrix elements are

$$\begin{aligned}|V_{\text{PMNS}}| \\ = \begin{pmatrix} 0.789 - 0.853 & 0.501 - 0.594 & 0.133 - 0.172 \\ 0.195 - 0.556 & 0.410 - 0.733 & 0.602 - 0.784 \\ 0.196 - 0.557 & 0.411 - 0.733 & 0.602 - 0.784 \end{pmatrix}.\end{aligned}\tag{2}$$

We see that the exactly symmetric PMNS mixing matrix is disfavored by the current data. This aspect of the PMNS matrix with  $V_{\text{PMNS}} = V_{\text{PMNS}}^T$  or  $V_{\text{PMNS}} = V_{\text{PMNS}}^\dagger$  has been studied in [7–9].

In this paper, we discuss partial quark-lepton universality [6], which does not require the unitary matrices that diagonalize the upper and lower components of the weak doublets to be the same. We find that partial QLU fits the current data very well and we can make a prediction for the unknown Dirac CP phase.

In Section 2, we review partial quark-lepton universality and discuss renormalization group effects on the model. In Section 3, we discuss the phenomenological results of this model and predict the Dirac CP phase. We conclude in Section 4.

## 2. Partial Quark-Lepton Universality

Partial quark-lepton universality can be derived from some simple relations in grand unified theories [6]. We start with the SU(5) relation

$$M_l = M_d^T, \quad (3)$$

obtainable in lopsided models [10], and

$$M_u = M_u^T, \quad (4)$$

where  $M_l$ ,  $M_u$ , and  $M_d$  are the mass matrices of the charged-leptons, up-type quarks, and down-type quarks, respectively. If we assume  $M_d$  is Hermitian, which can be achieved by imposing left-right symmetry [6]<sup>1</sup>, then from (3) we find that both the down-type quarks and charged-leptons can be diagonalized by a unitary matrix  $V$

$$\begin{aligned} V^\dagger M_d V &= D_d, \\ V^T M_l V^* &= D_l. \end{aligned} \quad (5)$$

Also, from (4), we know that the up-type quarks can be diagonalized by a unitary matrix  $V'$

$$V'^\dagger M_u V'^* = D_u. \quad (6)$$

If the Dirac neutrino matrix  $M_{\nu D}$  and the right-handed Majorana neutrino mass matrix  $M_R$  are also diagonalized by  $V'$  (as in some SO(10) models [6]),

$$\begin{aligned} V'^\dagger M_{\nu D} V'^* &= D_{\nu D}, \\ V'^\dagger M_R V'^* &= D_R, \end{aligned} \quad (7)$$

Then, below the seesaw scale, the light neutrino mass matrix,  $M_\nu = -M_{\nu D} M_R^{-1} M_{\nu D}^T$ , is diagonalized by  $V'$  as well. Consider

$$V'^\dagger M_\nu V'^* = D_\nu. \quad (8)$$

From (5), (6), and (8), we can find that the observable mixing matrices are related to

$$V_{\text{CKM}} = V'^\dagger V, \quad (9)$$

$$V_{\text{PMNS}} = V^T V'. \quad (10)$$

Note that, for exact quark-lepton universality, we must have  $V' = V$ , which indicates that  $V_{\text{CKM}} = I$  and the  $V_{\text{PMNS}}$  mixing matrix is symmetric. This is disfavored by the current data. In the next section, we show that partial quark-lepton universality is still allowed by current data. A caveat to partial QLU is that small perturbations to the leading order relations of (9) and (10) are needed to reproduce the measured fermion masses. In [6], it was shown that, with a specific form for the perturbations, the measured fermion masses can be obtained while keeping the mixing matrices unchanged. Consequently, we focus on the connection between the mixing matrices of quarks and leptons.<sup>2</sup>

The current data that determine the CKM and PMNS mixing matrices are measured at low energies, while the

quark-lepton universality relations are realized at the grand unification scale. In order to use the current data to analyze the model, we must consider renormalization group (RG) effects. For the CKM matrix, the RG effects are very small; that is, the next order relative corrections to the CKM matrix are of the order  $\lambda^5$  [11, 12], where  $\lambda = 0.225$ . The RG effects in the neutrino sector are strongly dependent on the mass spectrum of the light neutrinos. For the inverted and quasi-degenerate mass hierarchies, the effects can be large [13–16]. However, with quark-lepton universality it is more natural to assume that the light neutrinos are very hierarchical with the normal mass spectrum. In this case, RG effects on the three angles are very small [17, 18]; for example,  $\delta\theta_{23} \sim 0.6^\circ$ ,  $\delta\theta_{13} \sim 0.2^\circ$  and  $\delta\theta_{12} \sim 0.8^\circ$  in the MSSM with  $\tan\beta = 20$  if the lightest neutrino mass is 0.01 eV. Since the current uncertainties in the three angles are larger than the RG effects, we neglect the RG effects in our analysis.

## 3. Phenomenology

In this section, we introduce a simple approach based on the properties of unitary matrices to reduce the constraints on the model to a single condition, which allows us to easily constrain the Dirac CP phase.

Partial QLU predicts the two observable mixing matrices to have the form of (9) and (10), which can be rewritten as

$$V_{\text{PMNS}} V_{\text{CKM}} = V^T V, \quad (11)$$

$$V_{\text{CKM}}^* V_{\text{PMNS}} = V'^T V'. \quad (12)$$

Hence, in order for the model to work, both  $V_{\text{PMNS}} V_{\text{CKM}}$  and  $V_{\text{CKM}}^* V_{\text{PMNS}}$  should be symmetric. However, the two constraints are not independent. Since (9) implies  $V' = V V_{\text{CKM}}^\dagger$ , (11) follows from (12).

Solutions for  $V$  and  $V'$  will always exist because if  $V_{\text{CKM}}^* V_{\text{PMNS}}$  is symmetric, then it can be diagonalized by a unitary matrix  $U_s$ ; that is,  $U_s^T V_{\text{CKM}}^* V_{\text{PMNS}} U_s = D$ , where  $D$  is diagonal. This means that we can find the solution,  $V' = \sqrt{D} U_s^\dagger$ . Once  $V'$  is known, the solution for  $V$  can be obtained from (9). Although solutions for  $V$  and  $V'$  exist, they are not unique. We can always insert a combination of a real rotation matrix  $R^T R$  into the middle of the right-handed side of (11) or (12). And since  $R^T R = I$ , the equation will not change. This can also be seen from (9) and (10). For any real rotation matrix  $R$ ,  $R V$  and  $R V'$  are also unitary; hence if we let  $V \rightarrow R V$  and  $V' \rightarrow R V'$ , the two observable mixing matrices will remain the same.

Now, if we define

$$U = V_{\text{CKM}}^* V_{\text{PMNS}}, \quad (13)$$

then the only constraint from the model is that  $U$  is symmetric. Since both  $V_{\text{CKM}}$  and  $V_{\text{PMNS}}$  are unitary matrices,  $U$  is also unitary. For a  $3 \times 3$  unitary matrix, it can be shown that  $U$  being symmetric is equivalent to the moduli of  $U$  being symmetric under phase redefinition [19]. This constraint still imposes three conditions:  $|U_{12}| = |U_{21}|$ ,  $|U_{13}| = |U_{31}|$ , and  $|U_{23}| = |U_{32}|$ . However, the conditions are not independent.

Since  $U$  is unitary,  $|U_{11}|^2 + |U_{12}|^2 + |U_{13}|^2 = |U_{11}|^2 + |U_{21}|^2 + |U_{31}|^2$ . Hence,  $|U_{12}| = |U_{21}|$  indicates  $|U_{13}| = |U_{31}|$  and vice versa. Similarly,  $|U_{23}| = |U_{32}|$  is equivalent to  $|U_{13}| = |U_{31}|$ . Therefore, there is only one independent condition that constrains the model. Here, we choose it to be  $|U_{13}| = |U_{31}|$ .

The CKM matrix can be written in terms of the Wolfenstein parameters [20] as follows:

$$V_{\text{CKM}} = \begin{bmatrix} 1 - \frac{\lambda^2}{2} & \lambda & A\lambda^3(\rho - i\eta) \\ -\lambda & 1 - \frac{\lambda^2}{2} & A\lambda^2 \\ A\lambda^3(1 - \rho - i\eta) & -A\lambda^2 & 1 \end{bmatrix} \quad (14)$$

$$+ \mathcal{O}(\lambda^4),$$

and the PMNS matrix can be written in the standard form, which is

$$V_{\text{PMNS}} = \begin{bmatrix} c_{13}c_{12} & c_{13}s_{12} & s_{13}e^{-i\delta} \\ -s_{12}c_{23} - c_{12}s_{23}s_{13}e^{i\delta} & c_{12}c_{23} - s_{12}s_{23}s_{13}e^{i\delta} & s_{23}c_{13} \\ s_{12}s_{23} - c_{12}c_{23}s_{13}e^{i\delta} & -c_{12}s_{23} - s_{12}c_{23}s_{13}e^{i\delta} & c_{23}c_{13} \end{bmatrix}, \quad (15)$$

where  $c_{ij}$ ,  $s_{ij}$  denote  $\cos\theta_{ij}$  and  $\sin\theta_{ij}$ , respectively, and Majorana phases are not included. From (13), we see that the condition  $|U_{13}| = |U_{31}|$  becomes

$$\left| \left( 1 - \frac{\lambda^2}{2} \right) s_{13}e^{-i\delta} + \lambda s_{23}c_{13} + c_{23}c_{13}A\lambda^3(\rho + i\eta) \right|$$

$$= \left| A\lambda^3(1 - \rho + i\eta)c_{13}c_{12} \right. \quad (16)$$

$$\left. + A\lambda^2(s_{12}c_{23} + c_{12}s_{23}s_{13}e^{i\delta}) + s_{12}s_{23} - c_{12}c_{23}s_{13}e^{i\delta} \right|.$$

Note that (16) cannot be satisfied when  $\theta_{13} = 0$ . Keeping in mind that  $\sin\theta_{13} < \lambda$ , the  $\lambda^2 s_{13}^2$  and  $\lambda^3 s_{13}$  terms can be neglected since they are of the same order of magnitude as the terms dropped in the Wolfenstein parametrization. Then, we get a simple expression for the cosine of the Dirac CP phase:

$$\cos\delta = \frac{s_{12}^2 s_{23}^2 + c_{12}^2 c_{23}^2 s_{13}^2 - s_{13}^2 - \lambda^2 B}{2s_{23}c_{23}s_{12}c_{12}s_{13} + 2\lambda s_{23}c_{13}s_{13} + 2A\lambda^2 s_{12}c_{12}(c_{23}^2 - s_{23}^2)s_{13}} \quad (17)$$

$$+ \mathcal{O}(\lambda^4),$$

where  $B = s_{23}^2 c_{13}^2 - 2As_{12}^2 c_{23} s_{23} - 2A\lambda(1 - \rho)c_{12}s_{12}c_{13}s_{23}$ . We see that for very small  $\theta_{13}$  the numerator of the above equation is always larger than the denominator, so that there is no solution for  $\delta$ .

Using the currently favored CKM [21] and PMNS [5] parameters with their respective uncertainties and solving the condition  $|U_{13}| = |U_{31}|$  numerically without any approximation, we find that the Dirac CP phase  $\delta$  in the PMNS matrix lies between  $-32.4^\circ$  and  $32.0^\circ$  at  $2\sigma$ . The asymmetry around 0 is due to the small CP violation in the CKM matrix, which does not enter the approximate result in (17).

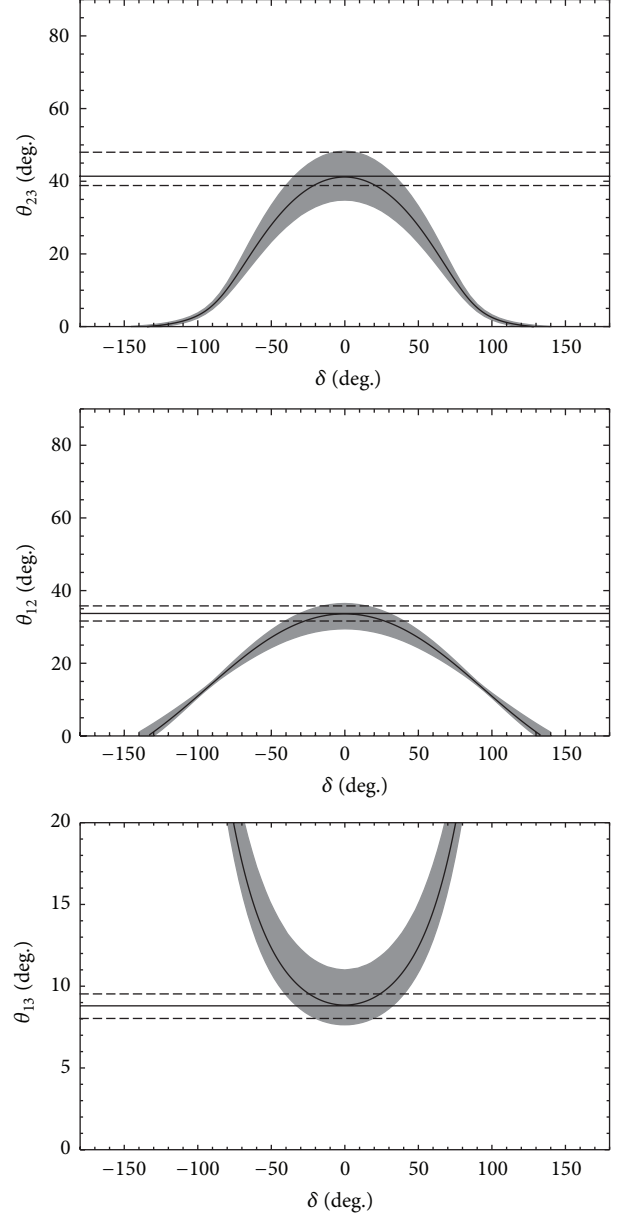


FIGURE 1: The  $2\sigma$  allowed regions (shaded bands) in the  $(\delta, \theta_{13})$ ,  $(\delta, \theta_{12})$ , and  $(\delta, \theta_{23})$  planes using measurements (with uncertainties) of the other two neutrino mixing angles and the CKM parameters. The solid curves within the shaded bands are the model predictions for the best-fit values of the other two mixing angles and the CKM parameters. The horizontal solid lines mark the best-fit values and the horizontal dashed lines mark the  $2\sigma$  limits of  $\theta_{23}$ ,  $\theta_{12}$ , and  $\theta_{13}$ .

We also find predictions for each mixing angle versus  $\delta$  given the best-fit values and  $2\sigma$  allowed regions of the other two mixing angles and the CKM parameters. The results are shown in Figure 1. With the constraints from the other two mixing angles and the CKM parameters, we find that  $\theta_{23} < 48.3^\circ$ ,  $\theta_{12} < 36.3^\circ$  and  $\theta_{13} > 7.64^\circ$  at  $2\sigma$ . The partial QLU model is perfectly consistent with the current data, and rather large  $\theta_{13}$  is strongly favored for the measured solar and

atmospheric mixing angles. Note that the relevant neutrino mass squared differences are trivially accommodated.

A measurement of  $\delta$  by future long baseline neutrino oscillation experiments will provide a stringent test of the viability of the partial quark-lepton universality model.

#### 4. Conclusion

We studied partial quark-lepton universality, which can naturally arise in grand unified theories. Constraints on the model can be reduced to one simple condition,  $|U_{13}| = |U_{31}|$ . Dropping terms of order  $\lambda^4$  from this condition, we find a simple expression for the Dirac CP phase  $\delta$  in the neutrino sector. We also studied the allowed parameter regions of the model numerically. Our prediction that  $\delta$  lies within the range  $[-32.4^\circ, 32.0^\circ]$  at the  $2\sigma$  level will be tested by future long baseline neutrino experiments.

#### Conflict of Interests

The authors declare that there is no conflict of interests regarding the publication of this paper.

#### Acknowledgment

This research was supported by the U.S. Department of Energy Grant no. DE-SC0010504.

#### Endnotes

1. Implementing a Hermitian  $M_d$  in a GUT is difficult because SU(5) does not incorporate left-right symmetry, and, in SO(10), the mass matrices arising from the couplings of fermions to Higgs fields in the 10 and 126 representations are complex symmetric (and not Hermitian), while those arising from couplings to 120 are complex antisymmetric.
2. An example in which (3), (4), (7), and the Hermiticity of  $M_d$  naturally arise is an SO(10) scheme with the superpotential terms [6]

$$W_d = \frac{f_{ij}}{M} (16_i^T B \Gamma_\mu H) (H^{T T} B \Gamma_\mu 16_j) + \frac{f'_{ij}}{M} (16_i^T B \Gamma_\mu H') (H^T B \Gamma_\mu 16_j), \quad (*)$$

$$W_u = g_{ij} (16_i^T B \Gamma_{\mu\nu\lambda\sigma\rho} 16_j) \Phi^{\mu\nu\lambda\sigma\rho},$$

where  $H, H'$  are 16-plet Higgs,  $\Phi$  is a  $\overline{126}$ -plet Higgs,  $B$  is a charge conjugation matrix in SO(10),  $i$  and  $j$  are generation indices, and  $\mu, \nu, \lambda, \sigma,$  and  $\rho$  are SO(10) indices. The Lorentz indices and the standard charge conjugation matrix are suppressed.  $H$  and  $H'$  contain neutral fields with the quantum numbers of  $\nu$  and  $\nu^c$ , so that the vacuum expectation value for  $\nu^c$  breaks SO(10) while SU(5) is preserved. We take the  $\overline{126}$  contribution to  $H_d$  to be zero or subdominant compared to  $H$  and

$H'$ , so  $M_d$  is only generated from  $W_d$ . By imposing an additional symmetry,  $16 \rightarrow 16^*, H \rightarrow H'^*$ , which leads to  $f_{ij} \rightarrow f'_{ij}$ , a Hermitian  $M_d$  can be obtained.

#### References

- [1] F. P. An, J. Z. Bai, A. B. Balantekin et al., "Observation of electron-antineutrino disappearance at Daya Bay," *Physical Review Letters*, vol. 108, no. 17, Article ID 171803, 7 pages, 2012.
- [2] F. P. An, Q. An, J. Z. Bai et al., "Improved measurement of electron antineutrino disappearance at Daya Bay," *Chinese Physics C*, vol. 37, no. 1, Article ID 011001, 2013.
- [3] J. K. Ahn, S. Chebotaryov, J. H. Choi et al., "Observation of reactor electron antineutrinos disappearance in the RENO experiment," *Physical Review Letters*, vol. 108, no. 19, Article ID 191802, 6 pages, 2012.
- [4] Y. Abe, C. Aberle, J. C. dos Anjos et al., "First measurement of  $\theta_{13}$  from delayed neutron capture on hydrogen in the Double Chooz experiment," *Physics Letters B*, vol. 723, no. 1-3, pp. 66–70, 2013.
- [5] F. Capozzi, G. L. Fogli, E. Lisi, A. Marrone, D. Montanino, and A. Palazzo, "Status of three-neutrino oscillation parameters, circa 2013," *Physical Review D*, vol. 89, no. 9, Article ID 093018, 2014.
- [6] A. S. Joshipura and A. Y. Smirnov, "Quark-lepton universality and large leptonic mixing," *Nuclear Physics B*, vol. 750, no. 1-2, pp. 28–44, 2006.
- [7] K. A. Hochmuth and W. Rodejohann, "On symmetric lepton mixing matrices," *Physics Letters B*, vol. 644, pp. 147–152, 2007.
- [8] Y. BenTov and A. Zee, "The neutrino mixing matrix could (almost) be diagonal with entries  $\pm 1$ ," *Physics Letters B*, vol. 714, no. 1, pp. 80–84, 2012.
- [9] W.-Z. Guo and M. Li, "A possible symmetric neutrino mixing ansatz," *Physics Letters B*, vol. 718, no. 4-4, pp. 1385–1389, 2013.
- [10] C. H. Albright, K. S. Babu, and S. M. Barr, "Minimality condition and atmospheric neutrino oscillations," *Physical Review Letters*, vol. 81, no. 6, pp. 1167–1170, 1998.
- [11] P. Kielanowski, S. R. Juarez Wyszoka, and H. J. G. Mora, "Theorems on the renormalization group evolution of quark Yukawa couplings and CKM matrix," *Physics Letters B*, vol. 479, no. 1-3, pp. 181–189, 2000.
- [12] M. Lindner, M. Ratz, and M. A. Schmidt, "Renormalization group evolution of Dirac neutrino masses," *Journal of High Energy Physics*, vol. 2005, no. 9, article 081, 2005.
- [13] J. A. Casas, J. R. Espinosa, A. Ibarra, and I. Navarro, "General RG equations for physical neutrino parameters and their phenomenological implications," *Nuclear Physics B*, vol. 573, no. 3, pp. 652–684, 2000.
- [14] K. R. S. Balaji, A. S. Dighe, R. N. Mohapatra, and M. K. Parida, "Radiative magnification of neutrino mixings and a natural explanation of the neutrino anomalies," *Physics Letters B*, vol. 481, no. 1, pp. 33–38, 2000.
- [15] N. Haba, Y. Matsui, and N. Okamura, "The effects of Majorana phases in three-generation neutrinos," *The European Physical Journal C—Particles and Fields*, vol. 17, no. 3, pp. 513–520, 2000.
- [16] P. H. Chankowski and S. Pokorski, "Quantum corrections to neutrino masses and mixing angles," *International Journal of Modern Physics A*, vol. 17, no. 5, pp. 575–614, 2002.
- [17] S. Antusch, J. Kersten, M. Lindner, M. Ratz, and M. A. Schmidt, "Running neutrino mass parameters in see-saw scenarios," *Journal of High Energy Physics*, vol. 2005, no. 3, article 024, 2005.

- [18] M. A. Schmidt and A. Y. Smirnov, “Quark lepton complementarity and renormalization group effects,” *Physical Review D*, vol. 74, Article ID 113003, 2006.
- [19] G. C. Branco and P. A. Parada, “Is the Cabibbo-Kobayashi-Maskawa matrix symmetric?” *Physical Review D*, vol. 44, no. 3, pp. 923–926, 1991.
- [20] L. Wolfenstein, “Parametrization of the kobayashi-maskawa matrix,” *Physical Review Letters*, vol. 51, no. 21, pp. 1945–1947, 1983.
- [21] M. Bona, M. Ciuchini, E. Franco et al., “The 2004 UTfit collaboration report on the status of the unitarity triangle in the standard model,” *Journal of High Energy Physics*, vol. 2005, no. 7, article 028, 2005, <http://www.utfit.org/>.

## Research Article

# Quasi-Classical Gravity Effect on Neutrino Oscillations in a Gravitational Field of a Heavy Astrophysical Object

Jonathan Miller<sup>1</sup> and Roman Pasechnik<sup>2</sup>

<sup>1</sup>*Departamento de Física, Universidad Técnica Federico Santa María, Casilla 110-V, 2930123 Valparaíso, Chile*

<sup>2</sup>*Theoretical High Energy Physics, Department of Astronomy and Theoretical Physics, Lund University, Sölvegatan 14A, 223-62 Lund, Sweden*

Correspondence should be addressed to Jonathan Miller; [jonathan.miller@usm.cl](mailto:jonathan.miller@usm.cl)

Received 1 December 2014; Revised 4 March 2015; Accepted 1 May 2015

Academic Editor: Srubabati Goswami

Copyright © 2015 J. Miller and R. Pasechnik. This is an open access article distributed under the Creative Commons Attribution License, which permits unrestricted use, distribution, and reproduction in any medium, provided the original work is properly cited. The publication of this article was funded by SCOAP<sup>3</sup>.

In the framework of quantum field theory, a graviton interacts locally with a quantum state having definite mass, that is, the gravitational mass eigenstate, while a weak boson interacts with a state having definite flavor, that is, the flavor eigenstate. An interaction of a neutrino with an energetic graviton may trigger the collapse of the neutrino to a definite mass eigenstate with probability expressed in terms of PMNS mixing matrix elements. Thus, gravitons would induce quantum decoherence of a coherent neutrino flavor state similarly to how weak bosons induce quantum decoherence of a neutrino in a definite mass state. We demonstrate that such an essentially quantum gravity effect may have strong consequences for neutrino oscillation phenomena in astrophysics due to relatively large scattering cross sections of relativistic neutrinos undergoing large angle radiation of energetic gravitons in gravitational field of a classical massive source (i.e., the quasi-classical case of gravitational Bethe-Heitler scattering). This graviton-induced *decoherence* is compared to *decoherence* due to propagation in the presence of the Earth matter effect. Based on this study, we propose a new technique for the indirect detection of energetic gravitons by measuring the flavor composition of astrophysical neutrinos.

## 1. Introduction

A theoretical extrapolation of the fundamental quantum mechanics concepts to Einstein's gravity suffers from major difficulties with quantization of space-time, ultraviolet behavior and nonrenormalizability of the resulting theory (for more details, see [1, 2] and references therein). A wealth of theoretical studies have been presented in the literature and many different quantum gravity models have been developed. However, no conclusive statement about the true quantum nature of gravity has been made. Only a real experiment can settle the longstanding confusion between the different approaches and provide guidance in developing the correct underlying theory.

Typically, in the standard quantum field theory framework which unifies three of four basic forces of nature, the quantum gravity effects are disregarded as being phenomenologically irrelevant at energy scales much smaller

than the Planck scale,  $M_{\text{pl}} \sim 10^{19}$  GeV. Moreover, due to enormous suppression, quantum gravity effects are often referred to as nearly unobservable [3–5]. While observing a single graviton directly may be impossible, it is not impossible to find an indirect evidence for quantum gravity. For an overview of potential phenomenological opportunities for indirect signatures of quantum gravity, see [6–9]. Nevertheless, our understanding of the quantum nature of gravity suffers from the lack of accessible sources of information.

In this paper, we propose a new approach for indirect experimental studies of (local) quantum gravity interactions based upon an effect of the large angle energetic gravitational Bremsstrahlung (or Gravi-strahlung, in short) off an astrophysical neutrino passing through an external classical gravitational potential on neutrino oscillation observables. This process, known as the gravitational Bethe-Heitler (GBH) process, can be considered in the quasi-classical approximation for large angle and/or large energy graviton emission;

that is, the Born approximation is sufficient. Such a process may happen with a rather high probability, such as in the case of an astrophysical neutrino scattering off a massive source of classical gravitational field (like a star, black hole, dark matter distribution, or galaxy). In quantum mechanics, the latter process may serve as a direct *quantum measurement* of the microscopic properties of the gravitational field at astrophysical scales.

*Quasi-Classical Gravity.* In the limit of weak gravity, the quasi-classical approximation to quantum gravity is a valid framework. In this case, the graviton field is a correction determined on the flat Minkowskian background and the metric operator in the Heisenberg representation is given by  $\hat{g}_{\mu\nu} = \eta_{\mu\nu} + \hat{h}_{\mu\nu}$ . Here, the  $c$ -number part  $\eta_{\mu\nu}$  is the Minkowski metric and  $\hat{h}_{\mu\nu}$  is the graviton arising after the quantization procedure. The Einstein-Hilbert action provides the mechanism for *virtual gravitons* to propagate in the flat space-time and to interact with one another in the quantum case as an analog of the standard QED picture of the Coulomb field around an electric charge. These virtual gravitons should be distinguished from *real gravitons* which are radiated off an accelerated massive body and their coherent wave packets correspond to gravitational waves in the classical limit. A “cloud” of virtual gravitons around a static massive body can be reinterpreted geometrically in terms of a deviation from the flat metric (or curvature) in Einstein’s classical relativity [10, 11] (the background must be chosen to be flat since only in this case is it possible to use the Casimir operators of the Poincaré group and show that the quanta have spin two and rest mass zero, thus being identified as gravitons).

A graviton couples to the full energy-momentum tensor. From the quantum mechanical point of view, we work in the mass eigenstate basis where the Hamiltonian of local quantum gravitational interactions has a diagonal form and identify the particle mass eigenstates with gravitational eigenstates (due to equivalence of gravitational and inertial mass). In this approach, higher Fock states are created by the graviton creation operator acting on a particle mass eigenstate. By measuring the quasi-classical graviton cross section and deviations from it, we would be engaging in the first investigations of the deeper quantum gravity theory similar to how electroweak  $\nu$ - $A$  measurements provided the first investigation of the deeper quantum Weinberg-Salaam theory.

## 2. Decoherence of Neutrino State

Generically, weakly interacting neutrinos can be considered as an efficient carrier of information across the universe as they are not absorbed or scattered by interstellar mediums. In practice, this unique property of neutrinos enables us to utilize them for large-scale astrophysical “experiments,” such as searching for possible tiny signatures of Lorentz invariance violation [12], testing general relativity [13] and quantum mechanics [14–16], testing the equivalence principle [17, 18], and testing minimal length models [19, 20]. Ultimately, it is possible to identify an *extraterrestrial large-scale quantum experiment* where neutrinos “change” their quantum state

due to a local quantum gravity process (in terms of local graviton coupling to a fundamental matter particle) and further convey information about such a process unchanged through the cosmological medium to the Earth.

*2.1. Propagation Decoherence.* The traditional source of decoherence typically referred to in astrophysical neutrino oscillations studies can be called *propagation decoherence*. This is when the distance that a neutrino travels exceeds the neutrino oscillation length. In this case, the neutrino mass states have separated so that they no longer interfere at large distances from the production point. This source of decoherence depends on the energy resolution of the detection process, the energy of the neutrino, the masses of the neutrino mass states, and other details of the production and detection processes. In neutrino experiments, the time between neutrino production and detection is normally not measured. In a real experiment, this means that beyond the neutrino oscillation length the propagating neutrino mass states no longer interfere during the interaction process in a detector [21, 22]. For cosmic/astrophysical neutrinos, in some cases and for some processes, this decoherence effect is irrelevant [23, 24].

*2.2. Classical Diósi-Penrose Decoherence.* The role of classical Einstein’s gravity in quantum mechanics is under extensive consideration in the literature and may be sizeable under certain conditions. As was claimed in [25], the gravity-induced quantum state reduction can be tested by observing the neutrino flavor oscillations at cosmological distances, while in [26] it was regarded as practically undetectable. This classical gravity effect on real-time evolution of a quantum state composed of several mass eigenstates was initially considered by Diósi [27–29] and Penrose [30]. In the classical gravity limit, the latter can be approximated by a change in the phase of the flavor wave function which appears mainly due to a nondegeneracy of neutrino mass eigenstates; that is,  $\Delta m_{ij}^2 \equiv m_j^2 - m_i^2 \neq 0$ , where  $m_j$  is the mass of the mass eigenstate  $j$ . This is caused by different mass states traveling along different geodesics in curved space-time and the whole effect gradually accumulates over large cosmological distances [31]. This is the essence of *classical decoherence* of a neutrino flavor state which is typically regarded as a probe for neutrino wave function collapse models and, more generally, alternatives to conventional (linear) quantum mechanics [32]. Instead, we consider another possible decoherence mechanism of a neutrino flavor state triggered *at the quantum level* by a single local graviton-neutrino interaction. Let us discuss this phenomenon in detail.

*2.3. Quantum Decoherence.* We expect elementary particles in the mass basis to be gravitational eigenstates of the Hamiltonian of quantum gravitational interactions in the same way as leptons and quarks are weak eigenstates in the flavor and CKM basis, respectively. The advantage of the neutrinos which we exploit here is that they interact via the weak force and that neutrino mass and flavor eigenstates are not the same and that they propagate at cosmological

distances/times. For particles whose flavor and mass eigenstates are identical this technique would not work to identify that a graviton induced quantum mechanical interaction had happened, which means that the neutrino is a unique carrier of astrophysical quantum gravity interactions.

Consider first a relativistic neutrino state propagating in the gravitational potential of a supermassive black hole, dark matter halo, or another massive system. These not only are sources of strong gravitational fields but could also be significant sources of astrophysical neutrinos. Suppose now that at the quantum level a graviton interacts only with a definite mass state (or gravitational mass eigenstate)  $a = 1, 2$  or  $3$ . This is equivalent to saying that definite mass eigenstates (the propagating states) are conserved by the quantum gravity Hamiltonian while superpositions, such as the flavor eigenstates, are not [33]. Note, the astrophysical neutrinos are initially produced in electroweak processes (e.g., in SNe processes) in a definitive flavor state,  $f = e, \mu$  or  $\tau$ , which are coherent superpositions of mass eigenstates. In an astrophysical environment, a high-energy graviton can interact only with a definite mass component of the neutrino wave function, thus causing *quantum decoherence* of the neutrino which is in a superposition of mass states, effectively “converting” it into a definitive mass eigenstate. This neutrino is quantum mechanically observed as being in a definite mass state. This means that between the production in an AGN or supernova (SNe) or other astrophysics source and the detection in an Earth based detector, the neutrino which was observed by the graviton exists in a definite mass state. This is independent from propagation decoherence.

The neutrino is “converted” to mass state with a probability  $P_{\nu_f \rightarrow \nu_a} = |\Psi_{\nu_f \rightarrow \nu_a}|^2$ , given in terms of the corresponding wave function  $\Psi_{\nu_f \rightarrow \nu_a}$  which projects out a flavor state  $\nu_f$  onto a mass state  $\nu_a$  and is typically expressed in terms of the corresponding PMNS mixing matrix element,  $\Psi_{\nu_f \rightarrow \nu_a} \equiv V_{af}$ . The considered effect is different from other known classical decoherence sources emerging due to a mere propagation (without a hard graviton radiation) in classical gravitational potential and/or neutrino propagation in flat space-time. The effect under consideration is a straightforward consequence of fundamental time-energy uncertainty relation for the real hard Gravi-strahlung and should be taken into account in studies of astrophysical neutrino oscillations.

The amplitudes of typical quasi-classical gravity scattering processes which may lead to the quantum decoherence effect under certain conditions can be represented as follows:

$$\begin{aligned} A_{\nu_f \rightarrow \nu_a}^{(G),1} &= \Psi_{\nu_f \rightarrow \nu_a} A^{(G)}(\nu_a + G \longrightarrow \nu_a + G), \\ A_{\nu_f \rightarrow \nu_a}^{(G),2} &= \Psi_{\nu_f \rightarrow \nu_a} A^{(G)}(\nu_a + M \longrightarrow \nu_a + G + M). \end{aligned} \quad (1)$$

Here,  $M$  is a source of strong classical gravitational fields, such as a massive star or a black hole. The first amplitude corresponds to the gravitational Compton scattering of a neutrino mass state off a real graviton in the medium, the second amplitude represents the GBH scattering of a neutrino in gravitational mass state off a classical heavy source  $M$  (with energetic graviton radiation). Clearly, a mass eigenstate  $\nu_a$  “produced” in this interaction due to decoherence

does not undergo oscillation until it interacts weakly with normal matter (e.g., in an Earth detector) by means of  $W, Z$ -exchange. Therefore, quantum decoherence may have a nonnegligible effect on neutrino oscillation observables, along with other existing sources of classical decoherence and medium matter effects [34, 35]. Explicitly, oscillation characteristics of neutrinos coming from, for example, a vicinity of the Galactic Center, may differ from vacuum oscillations. The latter case could be where a source of neutrinos is “nearby” but where there is no massive objects between the source and the Earth (nor significant variations in dark matter density). Such neutrinos, if identified, could be used as a control sample.

In a sense, the quantum gravity-induced decoherence of a definite flavor state described above is in close analogy to the weak-induced decoherence of a definite mass state. For example,  $W, Z$  bosons interact only with a coherent flavor state inducing a “conversion” of a definite mass state into a definite flavor state. Namely, a neutrino in a mass eigenstate  $\nu_a$  turns into a flavor eigenstate  $\nu_f$  through an interaction with the virtual  $Z, W$ -bosons propagating in the  $t$ -channel, that is, four different reactions, are possible as follows:

$$\begin{aligned} A_{\nu_a \rightarrow \nu_f}^{(w),1} &= \Psi_{\nu_a \rightarrow \nu_f} A^{(w)}(\nu_f + l'_f \longrightarrow \nu'_f + l_f), \\ A_{\nu_a \rightarrow \nu_f}^{(w),2} &= \Psi_{\nu_a \rightarrow \nu_f} A^{(w)}(\nu_f + l'_f \longrightarrow \nu_f + l'_f), \\ A_{\nu_a \rightarrow \nu_f}^{(w),3} &= \Psi_{\nu_a \rightarrow \nu_f} A^{(w)}(\nu_f + N \longrightarrow \nu_f + X), \\ A_{\nu_a \rightarrow \nu_f}^{(w),4} &= \Psi_{\nu_a \rightarrow \nu_f} A^{(w)}(\nu_f + N \longrightarrow l_f + X), \end{aligned} \quad (2)$$

such that  $\Psi_{\nu_a \rightarrow \nu_f} = \Psi_{\nu_f \rightarrow \nu_a}^*$ . Here, a definitive mass state which may exist due to previous hard neutrino-graviton interaction or due to the resonance MSW effect [34, 35] is “converted” back into a flavor state which may undergo oscillation. It is important to note that because the neutrino is not likely to interact weakly between the source and the Earth, if the neutrino is in a definitive mass state induced by the hard neutrino-graviton scattering event which occurred long before it arrives at the Earth it will still be in the definitive mass state at the Earth. The distance between a hard neutrino-graviton scattering event and detection event is not important.

In the case of vacuum neutrino oscillations, the traveling neutrino is not in a definitive mass eigenstate but is rather in a superposition of mass eigenstates which evolves when the neutrino travels in space-time. Then, with respect to the weak interactions, the nondiagonal  $\Psi_{\nu_f \rightarrow \nu_{f'}}$  transition amplitude between two flavor states  $f$  and  $f'$  is given by [36]

$$\Psi_{\nu_f \rightarrow \nu_{f'}} = \sum_j V_{f'j} e^{-i(m_j^2/2E_\nu)L} V_{fj}^*, \quad (3)$$

here  $L$  is the distance from where the neutrino was created in a definite flavor eigenstate  $\nu_f$ , and  $E_\nu$  is the energy of the neutrino. Analogously, for neutrino-graviton interactions

the  $\Psi_{\nu_f \rightarrow \nu_a}$  transition amplitude between a flavor state  $f$  and a mass state  $a$  can be written as

$$\Psi_{\nu_f \rightarrow \nu_a} = e^{-i(m_a^2/2E_\nu)L} V_{af} \quad (4)$$

which means that the probability for a given flavor neutrino state  $f$  to decohere by transforming into a mass state  $a$  due to a hard graviton-neutrino interaction, given by  $P_{\nu_f \rightarrow \nu_a}^{(G)} \sim |A_{\nu_f \rightarrow \nu_a}^{(G)}|^2 = |\Psi_{\nu_f \rightarrow \nu_a}|^2 |A^{(G)}|^2$ , is independent of the neutrino mass,  $m_a$ , the mass splitting,  $\Delta m_{ab}$ , and the distance from the neutrino source,  $L$ . The dependence on the relativistic neutrino energy,  $E_\nu \gg m_a$ , for a given scattering comes from the neutrino mass state scattering amplitude squared,  $|A^{(G)}|^2$  (for more details, see the next section).

**2.3.1. Differences from Other Sources of Decoherence.** Contrary to the Penrose-Diósi effect of classical decoherence [27–30], the quantum decoherence of a neutrino flavor state happens at small space-time scales,  $\Delta l_{\text{dec}}$ , which are much smaller than the neutrino wave length scale:  $\Delta l_{\text{dec}} \ll L_\nu$ , due to the quantum nature of the tree-level graviton-neutrino interaction. As an additional significant difference, the quantum decoherence effect is not sensitive to the mass differences of the mass eigenstates, or to  $\Delta m_{ij}^2$ , while they are crucial for and determine the classical decoherence of the neutrino flavor state at large separations,  $\Delta l_{\text{dec}} \gg L_\nu$ . Most importantly, quantum decoherence provides us with a key for phenomenological verification of quantum gravity models with possible deviations from quasi-classical gravity through measurement of neutrino oscillation characteristics.

The proposed effect is also different from the standard propagation decoherence (see Figure 2). In propagation decoherence, the neutrino mass states are separated in time and/or space and so the local weak interaction (the detection process) *observes* an incoherent sum of the propagating mass states in a given space-time point. In quantum decoherence, the neutrino exists only within a given mass eigenstate after being “observed” by the hard graviton (e.g., in the quantum processes of hard GBH or Compton scattering; see below). This difference is important. Indeed, while a flux of neutrinos which have undergone quantum decoherence is *observed* by a weak interaction in an Earth-based detector as an incoherent sum of the mass states, they do not experience a change of potential induced by matter (e.g., the MSW effect) as an incoherent sum of mass states. Namely, the neutrino which has not undergone quantum decoherence experiences matter as a superposition of mass states, while the neutrino which has undergone quantum decoherence would not experience matter as a superposition of mass states. Also, it is possible that a neutrino passing through densities which change nonadiabatically might demonstrate interference phenomena as presented in [23]. As we will explicitly demonstrate below, such a difference between the quantum and propagational decoherence in the presence of the Earth matter effect may be observable and is important in studies of astrophysical neutrino oscillations.

**2.4. Decoherence in the Presence of the Earth Matter Effect.** We would like to note that while the flux from quantum (gravitational) decoherence is a flux of pure mass eigenstates as noted, the important difference is that in the propagation decoherence case the flux is not of pure mass eigenstates, but rather decoherent (spatially separated) mass eigenstates. No quantum measurement of the state of these neutrinos has taken place, and the neutrino still exists as a superposition of mass states (just no longer with off diagonal elements in the density matrix). While these two situations are exactly the same when detected in the case where the flux is detected without passing through matter, in the case where the flux passes through matter, the regeneration which the neutrino flux experiences is different for the two cases. In the quantum gravitational decoherence case, the neutrino flux experiences regeneration as fluxes of neutrinos in pure mass eigenstates. However, in the propagation decoherence case, the neutrino flux experiences regeneration as a superposition of mass eigenstates; individual actual neutrinos continue to exist in a spatially separated quantum superposition of mass eigenstates. These spatially separated quantum superpositions experience the potential of the Earth. Simulation was done to demonstrate the possible size of this effect due to the difference in regeneration in the two cases (details below). In the simulation the neutrino is considered to have experienced propagation decoherence and the exact distance the neutrino travelled is not important (as long as it fulfils the conditions in [24]); in this work we consider relatively small distances ( $<1000$  kpc) since we do not explicitly consider differentiating quantum decoherence from potentially very long distance effects, for example, classical decoherence.

The simulation presented here operates in the S-matrix oscillations formalism [37] and was realised in Python, but for the neutrino propagation the code gives the same results as the Fortran simulation found in [38]. In the case of quantum decoherence where the neutrino exists as a single mass eigenstate, the neutrino is not coherent and the Earth matter effect causes no significant change to the measured flavor composition at low energies. For the case of propagational decoherence, the neutrino is a decoherent superposition of mass states where the description of the neutrino in the flavor basis is given by constant phase differences between the mass eigenstates and an effect may be seen. While many models for supernova neutrino spectra, see, for example, [39, 40], and other astrophysical neutrino sources may be interesting, for simplicity, we adopt an initial uniform electron neutrino flux with energies between 0.5 and 20 MeV. We are interested in a significant measurement so incorporated propagation of the neutrino directly through the Earth and have obtained a maximal difference between propagation decoherence and the quantum decoherence effect at greater than 100%. The latter is important for next generation neutrino measurements.

**2.5. Analytic Illustration: Two-Flavour Case without Core.** The theory of neutrino propagation, including neutrino propagation in medium and neutrino propagation when the neutrino experiences propagation decoherence, is well presented in the papers by Beuthe [22] and Akhmedov

and collaborators [41, 42] and Blennow and Smirnov [43]. These papers give the essential understanding of neutrino propagation in matter and propagation decoherence, but no explicit formula is given for a neutrino which undergoes propagation decoherence and then experiences the Earth matter effect.

For ease of discussion we will consider just two regimes, the vacuum and the Earth (with constant density) and two neutrino flavors. Due to the discontinuity at the Earth's surface, the adiabatic formulas do not describe the neutrino propagation. However, the solution is to match the flavor conditions between the two regimes. The flavor at the point before the density jump is used to determine the initial state after the jump [43, 44].

Propagation decoherence was studied in detail by Beuthe [22] but unfortunately only in the vacuum case. Akhmedov and Wilhelm [41] explicitly consider decoherence due to production or detection conditions but only note that finite coherence length is recovered during the integration over energy. Beuthe [22] goes into great detail about the physics, which is that the wave packets separate or that the wave packet spatial spread is so large that the phase varies over the wave packet and the information is lost. These are changes of the relationship between the states which make up the neutrino and the changes can be accounted for by integrating the phase in the vacuum transition probability. In the case of two regimes with a sharp transition, as we consider here, it is necessary to find the flavor states at the transition.

The condition for the wave packet separation to be complete is given explicitly by Farzan and Smirnov [24]. They explicitly note that this is different than the effect due to averaging (Section 2.1 in [24]) over the energy, despite the effect being computationally the same for the vacuum (and adiabatic) case [22]. As noted by [24], once the phase difference becomes large, the phase difference between the mass eigenstates can be expressed as a constant. This happens once [24]; consider

$$\begin{aligned} \sigma_x &\ll d_L \\ &= 3 \\ &\times 10^{-3} \text{ cm} \frac{L}{100 \text{ Mpc}} \frac{\Delta m^2}{2.5 \times 10^{-3} \text{ eV}^2} \left( \frac{10 \text{ TeV}}{E} \right)^2, \end{aligned} \quad (5)$$

which is achieved for both  $\Delta m_{12}^2 < 1 \text{ eV}$  and  $\Delta m_{23}^2 < 1 \text{ eV}$  for  $L = 10 \text{ kpc}$  since we expect  $\sigma_x$  to be less than  $10^{-10}$ .

To determine the proper state we must consider the proper normalisation and phase for the states. In the two-flavor approximation, the probability is given by

$$\begin{aligned} P_{ee} &= \frac{1}{2} (1 + \cos^2(2\theta)), \\ P_{e\mu} &= \frac{1}{2} \sin^2(2\theta), \end{aligned} \quad (6)$$

where  $\theta$  is the neutrino two-flavor mixing angle in vacuum and  $e$  and  $\mu$  are the two neutrino flavors. The amplitude can then be given by

$$\begin{aligned} A_{ee}^{\text{dec}} &= \cos^2(\theta) e^{i(3\pi/4)} + \sin^2(\theta) e^{-i(3\pi/4)}, \\ A_{e\mu}^{\text{dec}} &= \sin(\theta) \cos(\theta) (e^{-i(3\pi/4)} - e^{i(3\pi/4)}). \end{aligned} \quad (7)$$

These give the correct flavor amplitudes of a neutrino produced in a  $\nu_e$  state which has travelled through vacuum and experienced wave packet separation when it reaches the earth-to-vacuum transition. There is an overall phase, but for length scales (such as the earth-to-vacuum transition) much smaller than the distance between the wave packets (which can be 1 km or more) the phase difference between the wave packets is a constant as expressed above. An amplitude where the phase between the wave packets changes with distance would be incorrect for large wave packet separations.

This allows us to give a clear description of a produced  $\nu_e$  which experiences propagation decoherence, travels through the mantle of the earth, and then is detected as a  $\nu_e$ . This is

$$P_{ee}^{\text{prop}} = |A_{ee}^{\text{dec}} A_{ee}^{\text{mat}} + A_{e\mu}^{\text{dec}} A_{\mu e}^{\text{mat}}|^2 \quad (8)$$

which for the standard description in terms of a matter mixing angle  $\theta_m$  and the matter phase  $x_m$  is

$$\begin{aligned} P_{ee}^{\text{prop}} &= \frac{1}{8} (2\cos^2(x_m) (3 + \cos(4\theta)) + \sin^2(x_m) (4 \\ &+ \cos(4\theta_m) + \cos(4\theta_m - 8\theta) + 2\cos(4\theta_m - 4\theta) \\ &+ \sqrt{8}\sin^2(\theta) \sqrt{3 + \cos(4\theta)} \sin(4\theta_m - 4\theta)), \end{aligned} \quad (9)$$

where [37]

$$\begin{aligned} \sin(2\theta_m)^2 &= \frac{\sin(2\theta)^2}{\sin(2\theta)^2 + (\cos(2\theta) - 2AE_\nu/\Delta m^2)^2}, \\ x_m &= x \sqrt{\sin(2\theta)^2 + (\cos(2\theta) - 2AE_\nu/\Delta m^2)^2}, \quad (10) \\ x &= \frac{\Delta m^2 L}{4E_\nu}, \end{aligned}$$

and  $A$  is a constant density. This formula is different from that which is given for solar neutrinos and which is presented in the paper by Dighe et al. [45]. They give the calculation for an incoherent mixture of mass eigenstates originating in the sun, but this important paper does not explicitly consider propagation decoherence (decoherence due to wave packet separation) but rather the effects of coherent neutrino propagation at long baselines in addition to the known solar MSW resonance effect where neutrinos which leave the sun exist in only a single mass eigenstate. Farzan and Smirnov [24] explicitly give the condition to have the phase change for decoherent, and also for detection to restore coherence. The condition is that the measurement takes place over large enough time scales (or small enough energy resolutions) for both wave packets to be measurable [46].

In the case of quantum decoherence we have the emission of a graviton off a neutrino mass state in the vacuum. An interaction of a neutrino with the graviton serves essentially as a measurement of the neutrino state, both its detection and production in quantum mechanical language. This tells us the condition on the graviton which must be true for the effect presented in this work; it is the condition of coherent production/detection of a neutrino as presented in [22, 41]. The formulation can be considered in the framework of [41] but where the  $\tilde{U}$  matrix elements represent the mass eigenstates and not the matter eigenstates (so the identity since we are assuming propagation in the vacuum). Then the relationship for neutrinos which have undergone quantum gravity decoherence is simply (for two flavours)

$$P_{\alpha\beta} = P_{\alpha 1} P_{1\beta}^{\text{earth}} + P_{\alpha 2} P_{2\beta}^{\text{earth}}. \quad (11)$$

This is equivalent, as discussed in [45], to a coherent neutrino being observed a long distance from the neutrino source

$R_p$

$$= \frac{(\cos(x_m))^2 (3 + \cos(4\theta)) + (2 + \cos(4\theta_m - 8\theta) + \cos(4\theta_m - 4\theta)) \sin(x_m)^2 - 2 \sin(2x_m) \sin(2\theta_m - 2\theta) \sin(2\theta)}{(3 + \cos(4\theta))}. \quad (13)$$

Analogously, the ratio of neutrinos which have undergone *quantum decoherence* in the presence of matter effect in

$$R_q = \frac{5 + \cos(4\theta_m) + \cos(4\theta_m - 4\theta) + \cos(4\theta) + 4 \cos(2x_m) \cos(2\theta) \sin(2\theta_m - 2\theta)}{6 + 2 \cos(4\theta)}. \quad (14)$$

A difference between the ratios  $R_p$  and  $R_q$ , in principle, could be measurable and indicates the principal difference between propagation and quantum decoherence emerging in the presence of matter effect. Measurement of such a difference could therefore serve as a clear example of graviton detection.

### 3. Graviton-Neutrino Scattering

Now consider which quantum gravity processes the neutrino could possibly experience so as to experience the quantum decoherence effect in the astrophysical medium. As mentioned we will be considering quasi-classical gravity processes.

As is known the Coulomb field is measured by inserting a charged probe into it. From the quantum electrodynamics (QED) point of view, an electromagnetic scattering of a charged particle off the Coulomb field is due to an exchange of virtual photons (with small negative momentum transfer squared  $-q^2 = Q^2 > 0$  in the  $t$ -channel) between the probe and the source. Analogically, it is correct to discuss multiple exchange of virtual  $t$ -channel gravitons in a scattering event

by an experiment without arbitrary energy resolution. The probability is then given by

$$P_{ee}^{\text{grav}} = \frac{1}{16} \left( 10 + 2 \cos(4\theta_m) - \cos(4\theta_m - 2x_m) + 2 \cos(2x_m) - \cos(4\theta_m + 2x_m) + 4 \cos(4\theta) (\cos^2(2\theta_m) + \cos(2x_m) \sin^2(2\theta_m)) + 4 \sin(4\theta_m) \sin^2(x_m) \sin(4\theta) \right), \quad (12)$$

where  $x_m$  and  $\theta_m$  are as mentioned before.

The ratio of neutrinos which have undergone *propagation decoherence* and at the same time propagated through a region of constant density to those which have only propagated through the vacuum is given by the following expression:

a constant density medium to those which have propagated through the vacuum takes a different form:

as a signature of non-zeroth curvature itself (for more detailed discussions of the principles, see, for example, [47]).

Generically, in quantum electrodynamics (QED) the virtual photons may become real (produced on mass-shell) if one disturbs the field pumping energy into it. This is the physical reason for photon Bremsstrahlung in QED. Specifically, the standard Bethe-Heitler scattering in electrodynamics demonstrates that only an accelerated charge emits real photons (corresponding to electromagnetic wave in the classical limit of multiple soft photon radiation). Likewise, in the quasi-classical gravity framework, the virtual graviton, as a quantum of the gravitational field of a static massive object, may turn into the real one (corresponding to gravitational wave in the classical limit of multiple soft graviton radiation) if the source of the gravitational field is accelerated or, in general, when the energy-momentum tensor experiences disturbances.

Possible sources of real gravitons in the universe include active galactic nuclei (AGN), binary systems, supernova explosions (SNe), primordial black holes collisions, compact star/black holes binaries, quantum bremsstrahlung of gravitons of particles scattering off a massive object, black hole

(BH) evaporation, relic isotropic gravitational background from the early universe, inflation, phase transitions in the primordial plasma, and the decay or interaction of topological defects (e.g., cosmic strings). For details and references, see [48].

Consequently, in the cosmological medium a neutrino can scatter either off a classical gravitational potential with accompanying radiation of an energetic real graviton off the scattered neutrino (e.g., Bethe-Heitler-type scattering) or off real graviton in the astrophysical medium (e.g., Compton-type scattering). Let us consider both cases and conditions for initiation of the quantum neutrino decoherence in more detail.

**3.1. Gravitational Bethe-Heitler Scattering.** In fact, all elementary particles, including neutrinos, when traveling in the vicinity of massive objects (sources of classical gravitational field) can emit real gravitons with a certain energy spectrum. This process has a straightforward QED analog of a photon emission in relativistic electron scattering off the Coulomb field of a heavy nucleus mentioned above, the Bethe-Heitler process at the Born level. Even though the energy spectrum of radiated real gravitons is peaked in the forward direction and in the infrared limit (corresponding to forward radiation of classical gravitational waves), there is a nonnegligible probability to radiate *hard or energetic gravitons*, namely, with energies comparable to the incoming relativistic neutrino energy. Due to the quantum nature of the neutrino and graviton, the latter process can trigger a dramatic decoherence of an incoming neutrino flavor state at the quantum level during a very short time scale (inversely proportional to the energy of the radiated hard graviton).

The decoherence of the neutrino at the quantum level can only be initiated by hard energetic interactions with relatively hard gravitons whose energies exceed the mass difference between different mass states  $E_G \gtrsim \Delta m_{ij}$  and therefore requires hard real graviton emission. In this case, the hard graviton probe has a small wave length and thus can resolve separate mass states in a coherent or incoherent neutrino flavor state in the quantum mechanical sense (likewise a hard enough photon can resolve an internal substructure of the proton wave function and interacts with the separate quarks it is composed of while a soft one “sees” a proton as a whole only).

A soft graviton with energy lower than the difference between mass states will be unable to resolve the individual mass eigenstates in this superposition and will instead couple to the whole energy-momentum tensor of the flavor state, nonlocally, which is the classical general relativity limit. In the latter case quantum decoherence is not triggered, and the effect will be as discussed in [31].

The Born-level calculation is good first order approximation in the case of off-forward hard graviton emissions at large angles relevant for the quantum decoherence effect; this is the reason why one can disregard higher-order radiative corrections which are highly suppressed (by extra powers of the Planck mass) as long as one cuts off the problematic but uninteresting infrared/collinear parts of phase space. As was previously shown in [49], the radiative corrections can only

be relevant in the deep infrared limit of soft real gravitons  $E_G \rightarrow 0$  emitted in the forward direction where they will cancel the soft/collinear divergences. The latter classical limit represents classical gravitational waves emitted off a neutrino state with very small or no impact on it.

In the considered GBH case, shown in Figure 1(a), one deals with the graviton exchange with negative momentum transfer squared  $t = -q^2 < 0$  in the  $t$ -channel with the propagator stretched between the relativistic neutrino of mass  $m_\nu$  and energy  $E_\nu \gg m_\nu$ , and a massive classical gravitational field source with mass  $M \gg E_\nu$ . The wave function,  $\Psi_{\nu_f \rightarrow \nu_a}$ , describes a projection of a given flavor state  $f$  onto a fixed mass state  $a$  denoted as a dark ellipse, while the heavy classical source of the gravitational field is shown by a shaded circle.

The GBH cross section has initially been calculated for the gravitational scattering of scalar particles with  $M \gg m$  in [49]. In the soft graviton limit, the graviton-neutrino coupling is not sensitive to the spin of an incident relativistic particle to leading order, while the classical nonrelativistic source can be considered spineless in this first discussion for simplicity (in principle, helicity dependence of hard graviton-neutrino interactions can be a relevant topic for further studies). We therefore use their formula as a sufficiently good approximation to estimate the neutrino-solar mass cross section with graviton radiation numerically. In this case, as an order-of-magnitude estimate, the GBH cross section at the Born level behaves as

$$\sigma_{\text{GBH}} \sim \frac{M^2 E_\nu^2}{M_{\text{Pl}}^6}, \quad M \gg E_\nu \gg m_\nu, \quad (15)$$

and thus may not always be very small since the Planck scale suppression can be largely eliminated by having a mass  $M$  of a heavy classical source in numerator. In particular, for a solar mass object  $M \sim 10^{33}$  GeV, we have  $M^2/M_{\text{Pl}}^6 \sim 1 \text{ GeV}^{-4}$ , so there is no significant suppression of the cross section for relativistic neutrinos. This is a particle physics magnitude cross section which naively implies particle physics size impact parameters. Larger impact parameters would exist for larger masses, such as the dark matter halo. The above cross section is integrated over impact parameter, and it may be instructive to look into differential cross section in order to find the probability of this process as a function of distance to the massive astrophysical body. For the current study it suffices to note that such probability can potentially be significant.

It is worth noticing that the Bethe-Heitler calculation in QED to first order gives the correct cross section for the photon Bremsstrahlung for extended objects such as a nucleus as shown in [50] ([51] demonstrates that after advances it is still correct to first order in the hard photon limit). Similarly, one may expect that the GBH result for a point-like classical source of gravitational potential should be roughly correct to first order for extended objects as well, like a star or even a dark matter distribution in the quasi-classical gravity case. The QED calculations are provided in the above references for scattering due to the field surrounding the nucleus; the nucleus is small compared to the total size of the field and scattering off the nucleus via other processes can be

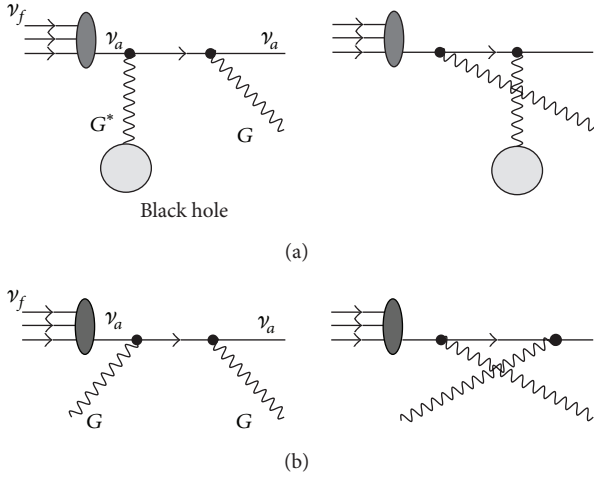


FIGURE 1: The quasi-classical gravity processes which destroy the coherence of the neutrino flavor eigenstate ( $f = e, \mu, \tau$ ) at the quantum level effectively turning it to a mass eigenstate ( $a = 1, 2, 3$ ), the gravitational Bethe-Heitler-type scattering of neutrino off a massive object, for example, a black hole (a) and the gravitational Compton scattering (b). The dark ellipse is a projection to a fixed mass state and the shaded circle is a classical source of the gravitational field.

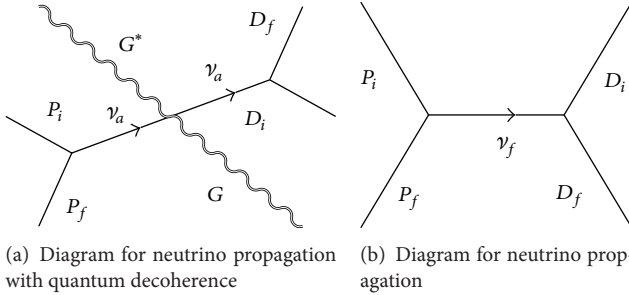


FIGURE 2: Shown are diagrams of neutrino propagation in the quantum field theoretical description (such as found in [22]). The neutrino is described as a stretched propagator between the production (P) and detection (D) (b) weak processes (with initial and final states denoted by subscripts  $i$  and  $f$ ). In the case of quantum decoherence (a), the emission of a graviton in between the production and detection processes means that the neutrino exists in a definitive mass state since both the propagation Hamiltonian and graviton interaction Hamiltonian conserve mass. The quantum decoherence effect described here follows from the discussion in Section 2 of [22].

safely ignored. Most of the cross section is thus not due to trajectories where the electron passes through the nucleus. We expect that this is also true for the GBH scattering, where most of the flux which scatters off the star or other massive object will not pass through the star, and the point-like estimation (15) remains valid.

In Figure 3 we have presented the differential (in radiated graviton energy  $E_G$  and neutrino angle  $\theta_\nu$ ) and integrated cross sections of the GBH process for typical MeV-scale astrophysical neutrinos and a solar mass scale source of the

gravitational field. As expected, the main bulk of the cross section comes from the soft gravitons (gravitational waves) emission in the forward limit. It is remarkably important, however, that there is a long nonnegligible tail in the differential distributions of the GBH cross section in the single real graviton energy  $E_G$  and emission angle  $\theta$ . It turns out that such a tail to harder/off-forward gravitons is not very strongly suppressed; typical GBH scattering cross sections for SNe neutrino energies of  $E_\nu \sim 10\text{--}100$  MeV and a solar-mass classical source are found to be around  $\sigma \sim 0.1\text{--}10$  millibarns, which are some 16–18 orders of magnitude larger than typical neutrino-electron scattering cross sections (less than an attobarn at the same energies).

This observation strongly suggesting the importance of the quantum decoherence initiated by interactions with such energetic real gravitons. The latter source of decoherence does not have a classical interpretation. As we have already mentioned, due to a quantum mechanical nature of a *single hard graviton* emission at energies  $E_G \geq \Delta m_{ij}$  (with local coupling to a gravitational mass eigenstate) and universal quantum mechanical time-energy uncertainty arguments, the considered effect of neutrino flavor decoherence is a purely *quantum effect*. The hard Gravi-strahlung effect is thus relevant for a broad range of neutrino energies, and one can utilize the SNe neutrinos as a clear sample since (1) fluxes of SNe neutrinos are the largest among astrophysical neutrinos and (2) SNe neutrino emission mechanisms are the best understood among other possible astrophysical sources.

Of course, the  $t$ -channel gravitons are extremely soft and form classical gravitational potential of a classical massive source and they do not trigger a decoherence of the neutrino state; only the hard real graviton emissions are relevant.

**3.2. Probability for Quantum Gravitational Decoherence.** The cross section of the considered GBH process can be enhanced for the galactic center ( $\sim 10^6\text{--}10^9$  solar masses) or the dark matter halo ( $\sim 10^{20}\text{--}10^{24}$  solar masses). It can also be enhanced for ultra-relativistic neutrinos which are potentially detectable at neutrino observatories such as IceCube and Super-K. As is our main result, we notice that the GBH scattering may cause the quantum decoherence of astrophysical neutrinos and this effect can be measured via neutrino flavor composition measurements. A massive classical source of the gravitational field may not necessarily be a black hole, but any compact star or, in general, any bound gravitational potential induced by continuous matter distribution in the galactic disk and halo.

Due to rather large cross sections it can be that most of the astrophysical neutrinos which are observed at the Earth from a given direction and have passed in close vicinity of a massive object would have experienced the quantum decoherence due to a graviton-induced scattering. In other words, the probability for a given neutrino in a superposition of mass states  $f$  to decohere, being “transformed” into one of the mass states  $a = 1, 2$  or 3 in the GBH process,  $P_G \sim |A^{(G)}|^2$ , may be large for possible (massive) astrophysical sources of classical gravitational fields, depending on details of astrophysics and quasi-classical gravity. Deviations from quasi-classical gravity

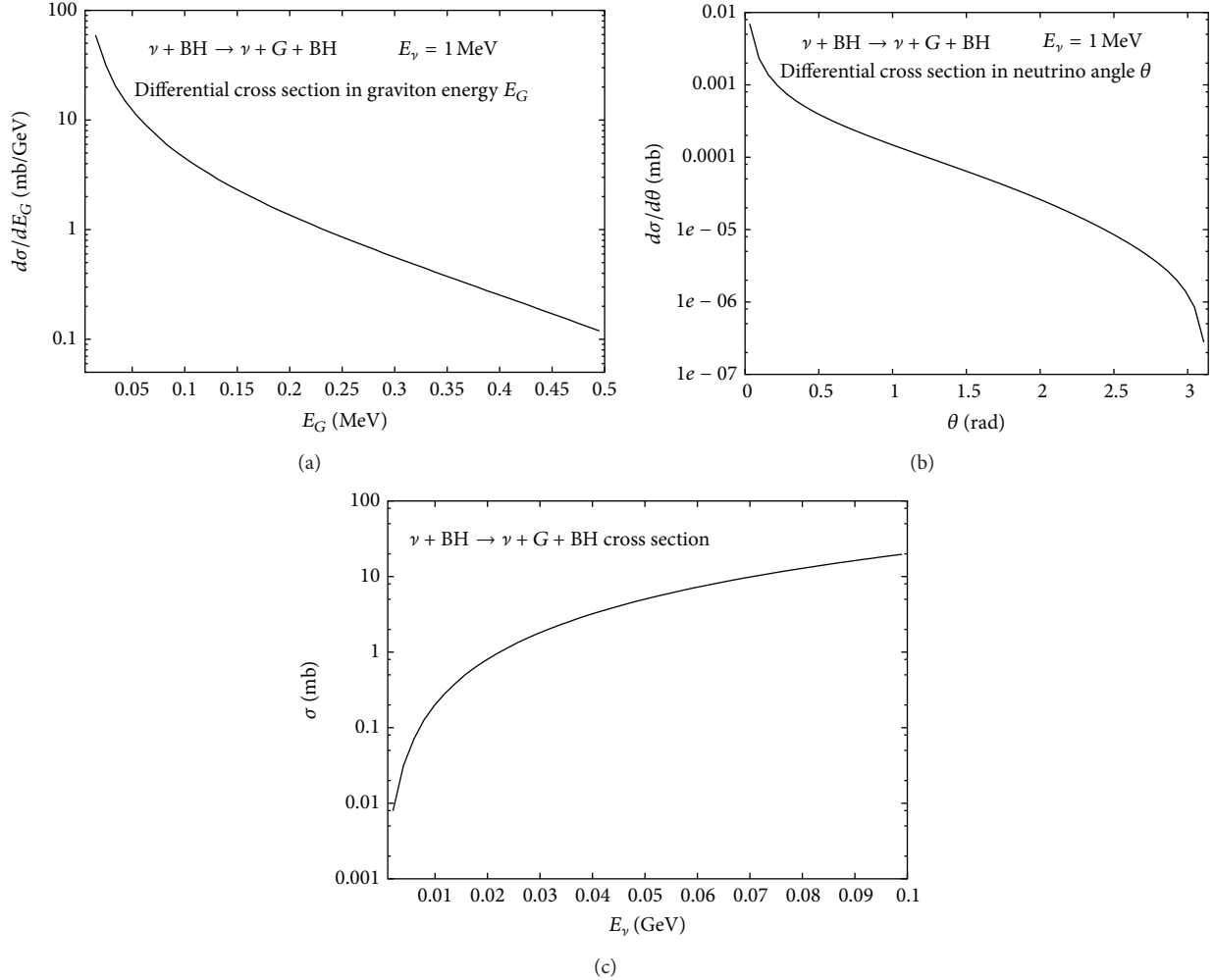


FIGURE 3: Differential cross section of the gravitational Bethe-Heitler scattering of neutrino off a massive object, for example, a black hole (BH) in radiated graviton energy  $E_G$  (a), in polar angle of the final-state neutrino  $\theta_\nu$  (b), and the integrated cross section as a function of incoming neutrino energy  $E_\nu$  typical for astrophysical sources, for example, see [69], (c).

which illuminate the fundamental quantum gravity theory may also be relevant. To parameterise this we can define

$$P_G \equiv \frac{N_{G\nu}}{N_{\text{init}}}, \quad (16)$$

where  $N_{G\nu}$  is the number of neutrinos which have radiated off an energetic graviton with  $E_G \geq \Delta m_{ij}$  while being scattered off a massive object (on the way to the Earth, a produced mass state may experience more graviton-induced rescatterings in classical gravitational potentials which do not affect the coherence of the neutrino state any longer but may cause an additional energy loss of the propagating neutrino into the gravitational radiation) and  $N_{\text{init}}$  is the total number of neutrinos which have been emitted off an astrophysical source. As we will demonstrate below, the  $P_G$  value can be measured via neutrino flavor composition observations leading to a promising opportunity for experimental tests of quantum gravity induced interactions.

A precise theoretical calculation for  $P_G$  is influenced by many potentially relevant aspects. First, it depends on

a quantum gravity model through model-dependent local neutrino-graviton couplings, thus offering a good opportunity for experimental tests of quantum gravity. Due to the extended nature of many of the sources, there might be strong differences for models with some nonlocality. Second, it may be influenced by yet unknown higher-order corrections and by multiple rescatterings of a neutrino off a massive source, multiple massive sources, or a diffuse source such as the dark matter halo which the neutrino passes through on its path to the Earth (in this case, the Eikonal approximation for neutrino-graviton rescattering can be used [52]). Thus, the actual cross sections may significantly vary depending on environment a neutrino propagates in. Thirdly, the astrophysical neutrino flavor composition may depend on production processes which may currently be unknown. Also, energy loss of the neutrino due to the hard Gravi-strahlung in each scattering event should be taken into consideration, together with other effects which change the coherence of the neutrino state. This could also be used to identify a graviton interaction, if, for example, this lower energy flux comes

some short time later than the initial flux. Finally, including possible dense astrophysical media might be important as the neutrino may have additional weak rescatterings off normal matter acting on the neutrino leaving the neutrino in a superposition of mass eigenstates when it arrives at the Earth. Therefore, additional astrophysical information is desired to constrain these uncertainties. All of the above aspects are the major unknowns in making predictions for the  $P_G$  quantity which require a further effort of the quantum gravity, neutrino, and astrophysics communities.

**3.3. Gravitational Compton Scattering.** Another possibility for quasi-classical gravity induced interactions with neutrino participation is shown in Figure 1(b). This is the (tree level) gravitational Compton scattering of a neutrino off a real graviton in cosmological medium. The latter process has been previously studied in [53] and in many other papers. The cross section in this case is always extremely small  $\sigma \sim E_\nu^2/M_{\text{Pl}}^2$  for a MeV neutrino, and real graviton fluxes are not expected to compensate for such a huge suppression. This process seems less interesting when applied to astrophysical neutrino flavor composition. Hypothetically, this effect could be considered in exotic cases of ultra-relativistic neutrinos and/or in the very early universe where the graviton fluxes might have been rather intense.

#### 4. Quasi-Classical Gravity Measurement Proposal

As presented above, the neutrino in a mass eigenstate does not oscillate unless it scatters off ordinary matter via a weak channel which will cause it to be in a flavor eigenstate. It is likely that the  $Z, W$ -mediated scattering happens only in the Earth-based detector enabling us to access information about the graviton-neutrino scattering which might have happened far away from the solar system. In the considered situation, the neutrino plays an analogical role of an electric charge in a quantum measurement of the microscopic Coulomb field properties. From the quantum mechanical point of view, a massive object (e.g., dark matter distribution or the galactic center) vicinity can then be viewed as a macroscopic “detector” of gravitons. The neutrino scattering off a massive object and radiating an energetic graviton by means of the local graviton-neutrino coupling would be an elementary act of quantum mechanical measurement, and the neutrino conveys the quantum information about the act of graviton measurement to the Earth (see Figure 2). The neutrino does not undergo oscillation or demonstrate properties consistent with being a superposition of mass eigenstates since it is in a definitive mass state during the propagation and graviton interaction. The neutrino not interacting weakly as it travels is a good approximation due to extremely weak interactions of neutrinos with ordinary matter. Then an Earth-based detector will “read off” the results of the “graviton measurement” which has taken place at the massive object.

Previously, in [5], it has been claimed that it is not possible to detect a single graviton with a planet-scale detector. Our proposal is to measure the described graviton-neutrino

scattering effect (specifically, the gravitational Bethe-Heitler scattering of neutrino off a massive object) experimentally, which is the best possibility for indirect graviton detection proposed. Remarkably, we consider a super massive-scale “detector” of energetic gravitons, with neutrinos serving as the most efficient carrier of the information about such a measurement to the Earth.

**4.1. Quantum Gravitational Decoherence Effect on Neutrino Oscillations.** Here we consider a very massive source of strong gravitational fields like cluster of stars (e.g., the center of our Galaxy) or a dark matter halo as a good example of a graviton “detector.” This section provides predictions for such an extreme large-scale quasi-classical gravity measurement.

As we have demonstrated above, the probability of an individual (elementary) act of the “quantum gravity measurement” defined by the graviton-neutrino cross section can be rather large due to a large GBH cross section and there may be scenarios where it should not be neglected. In particular, utilizing the dense region of stars and black holes in the galactic center (GC) as our “graviton detector” in the above sense, one could expect that a significant fraction of neutrinos passing by the dense region would have experienced the GBH scattering. Then since many of the neutrinos are now in a mass eigenstate, they will no longer undergo flavor oscillation. Due to the neutrino existing in a mass eigenstate during propagation, further graviton rescattering would not constitute additional quantum measurements of an “undetermined” quantum state. Depending on the astrophysical process, one might favor energies of neutrinos where the neutrino oscillation may not be suppressed due to the MSW effect where the neutrino exists in a single mass eigenstate, so that the graviton-induced effect would be cleaner. We suggest that this effect could be tested in neutrino telescopes and observatories by looking at the galactic center neutrino flavor composition and comparing it to the composition expected without quantum gravitational decoherence. It might be possible that close, “standard candle,” neutrino emitters in other parts of the sky provide a flux of neutrinos which have not undergone quantum gravitational decoherence (note: a very similar effect should take place in flavor oscillations in the neutral kaons  $K_L, K_S$  system as well).

The general formula for the number of electron type neutrinos observed from an electron type source in the vacuum is

$$\frac{N_{e,\text{det}}}{N_{e,\text{init}}} \propto P_{ee,\text{co}}^{\text{vac}} (1 - P_G) + P_G \sum_{i=1,2,3} V_{ei} V_{ie}^* V_{ei} V_{ie}^*. \quad (17)$$

Here  $P_{ee,\text{co}}^{\text{vac}}$  is the standard vacuum oscillation probability [36] far away from the neutrino source and  $P_G$  is the probability for neutrino in a flavor state to interact with at least one graviton (16) which will depend on the graviton-neutrino scattering cross section. Every mass eigenstate of the (relativistic) neutrino shares the same energy so  $P_G$  takes the same value.

If all neutrinos have interacted with at least one graviton, that is, fixing  $P_G = 1$ , than the expression for the total  $\nu_e \rightarrow \nu_e$  transition probability becomes

$$P_{ee}^G = \cos^4 \theta_{12} \cos^4 \theta_{13} + \cos^4 \theta_{13} \sin^4 \theta_{12} + \sin^4 \theta_{13}, \quad (18)$$

where  $\theta_{12}$ ,  $\theta_{13}$ , and  $\theta_{23}$  are the standard neutrino vacuum mixing angles. This basic formula is our prediction (in vacuum) for the “maximal decoherence” scenario valid for  $P_G \approx 1$ . In the standard Large mixing angle (LMA) global fit with  $\sin^2\theta_{13} = 0.025$ ,  $\sin^2\theta_{12} = 0.31$ , and  $\sin^2\theta_{23} = 0.60$  (but with  $\delta_{CP} = 0$ ) [54], the value for the transition probability throughout a range of neutrino energies is shown in Figure 4. The difference between the predictions for  $P_G = 1$  and  $P_G = 0$  is that a neutrino which has experienced propagation decoherence will have a constant phase difference in the flavor basis at the earth/vacuum boundary, possibly resulting in a greater than 100% change in the survival probability depending on neutrino energy, the detector resolution, and the detector location. Further detail is available in the Appendix. Here the simulation for neutrino propagation in matter and vacuum was based on [38].

As one notices in Figure 4, the relative effect ranges from a few percent at  $E_\nu \approx 2$  MeV to about 350% at  $E_\nu \approx 20$  MeV. This is expected because the electron type component of the super position of three decoherent mass states is larger than the electron type component of the single mass states. The Earth matter effect depends on neutrino energy and so the effect will be larger at higher energy (20 MeV and above) than at smaller energies (2 MeV). This gives a quite noticeable difference between the case where the neutrino undergoes *propagational decoherence* relative to the case where the neutrino experienced *quantum decoherence*.

For illustration in this calculation we use a constant, maximal probability for quantum decoherence case,  $P_G = 1$ . In practice we expect this to be less than one and to depend on the neutrino energy  $E_\nu$ . The  $P_G(E_\nu)$  value can be considered as an observable and extracted from the flavor composition data and further compared to theoretical calculations. Possible sources of neutrinos in extreme astrophysical environments include the aforementioned dense galactic center, but also ordinary stars, SNe, GRB, AGN, and other galactic or extragalactic sources [55, 56]. Quantum gravity models should aim at predicting the  $P_G$  in these extreme environments as a function of astrophysical parameters and neutrino energy so that favored models can be constrained by the neutrino flavor data.

The neutrino flux spectrum from astrophysical sources is still being modeled [57–59]. By comparing observed neutrino flavor composition for neutrinos passing through the Earth to that of neutrinos which have not passed through the Earth, the flux can be divided out and a possibly large effect may be observed (for the above LMA global fit). This could be visible in flavor data at large statistics.

This is our prediction for the quantum gravity-induced effect on the detected flavor composition in the “maximal quantum decoherence” scenario. While numerically the effect can be very large, one would certainly need to have a good understanding of all the other statistical and systematical uncertainties for a possible measurement of the dependence of  $P_G$  on neutrino energy. Current generation neutrino observatories can observe approximately ten thousand total events from nearby ( $\sim 10$  kpc) SNe; however, next generation neutrino observatories (such as Hyper-K) can provide statistics to reduce systematical uncertainties [60]. Additionally,

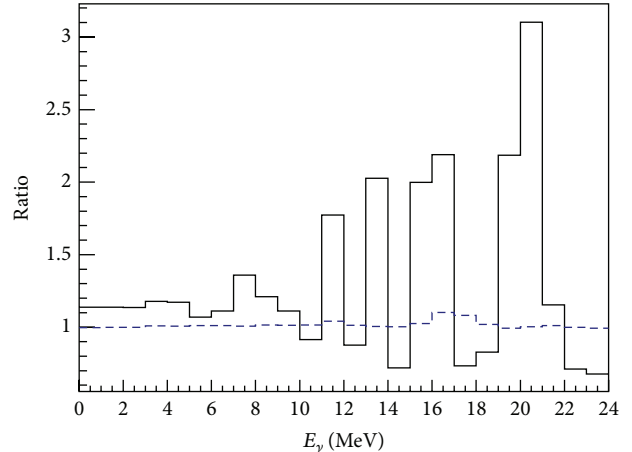


FIGURE 4: Here the difference due to the Earth matter effect in the observed number of electrons is plotted (assuming an initial flux that only contains electron neutrinos). The difference is defined to be the ratio of the observed number of electron type neutrinos for the case where there is a maximal Earth matter effect (impact parameter is  $\sin(.576)$ ) and the case where there is no earth matter effect. Shown are two curves, black solid for  $P_G = 0$  (propagational decoherence case) and blue dotted for the  $P_G = 1$  (quantum decoherence case). This calculation was done with a uniform distribution of decoherent electron neutrinos. The difference due to the Earth matter effect may be higher than 300%. In the case of fixed  $P_G = 1$ , the flavor composition of the neutrino flux is minimally affected by the Earth at low energies.

improvements are needed in current neutrino flavor reconstruction technologies, which can reconstruct the neutrino flavor to the percentage level [61]. It has been pointed out that sensitive neutrino detectors should be placed in North America (Sudbury), Japan (Hyper-K), Chile (ANDES), and Antarctica (Beyond DeepCore) to best observe SNe neutrinos and the effect that the Earth has on SNe neutrinos [62].

## 5. Conclusion

In conclusion, we have considered a quasi-classical gravity process, the gravitational Bethe-Heitler scattering of a neutrino off a massive object accompanied by an energetic graviton radiation, which can have a rather large cross section proportional to the mass squared of the classical source. Due to hard gravitons interacting with a neutrino mass eigenstate only, opposite to weak bosons which interact with a flavor eigenstate only, the considered process is a measurement of the incoming neutrino flavor state at the quantum level, causing its decoherence in a diffractive manner than the process which can be called propagational decoherence or other sources of decoherence. This quantum decoherence affects astrophysical neutrino behavior. Namely, quantum decoherence can be considered as a specific quasi-classical gravitational measurement of the neutrino propagating state, which changes the behavior of the neutrino in the presence of a potential (such as the Earth matter effect) compared to the traditional source of decoherence known as propagation

decoherence, which can be observed in the neutrino flavor composition in an Earth based detector (see the Appendix).

This enables the utilization of neutrinos traveling across the Galaxy as a source of information about the graviton-induced interactions they might have experienced on their journey to Earth. Specifically, the measured probability to find a given flavor component in the neutrino flux coming from a vicinity of a super massive black hole or another super massive object (galactic center or dark matter halo) will be different from the corresponding probability measured from a source of neutrinos where the neutrinos never pass near a massive system. In the case where no astrophysical neutrinos can be identified which have not interacted with a gravitational potential, the flavor composition can be compared to the expectation for the Earth matter effect which can be determined using reactor, atmospheric, and accelerator neutrinos. We have explicitly demonstrated that the maximal difference corresponding to an assumption that all of the detected neutrinos have experienced an interaction with a graviton, that is,  $P_G = 1$ , is large and can be measurable at high statistics. Assuming that the required astrophysical conditions are met for large  $P_G$ , this would provide a first measurement of quasi-classical gravity. Further discrimination of quantum gravity models would require more statistics and detailed calculations using these models. Additionally, we note that the energetic graviton bremsstrahlung would cause a significant decrease in energy of the neutrinos which are scattered at large angles. Since the galactic center is not only massive but is a source of neutrinos, it might be possible that a large enough SNe in the galactic center would produce enough neutrinos so that the existence of graviton bremsstrahlung could be induced by a group of neutrinos arriving a short time after the initial group with a lower median energy. This could be used in addition to the flavor to investigate quantum gravity models.

Thus, the probability for a neutrino state to interact with at least one energetic graviton,  $P_G$ , is considered to be a new observable containing information about the quantum gravity scattering process. An estimate of the  $P_G$  value from neutrino flavor composition data with good angular resolution would provide an important experimental test for quantum gravity models. This is the major proposal we make in our paper. We do not expect  $P_G \sim 1$  in most scenarios and a realistic theoretical estimate for  $P_G$  depends on many factors and is not well-constrained yet. For a distant enough source, there are many potential scatterers which may provide the maximal case of  $P_G = 1$ .

The difference between propagation decoherence and quantum gravitational decoherence is a crucial component in our study and so we provide short summary. In the classical case [22] the neutrino is produced and detected in distinct flavor states (at the astrophysical source and the earth detector) and exists as a quantum mechanical superposition of mass states due to the mass states being indistinguishable to the detection process. If the neutrino passes near a massive object, then it might undergo what we described as *classical decoherence* [25, 27–30]. The different mass states continue to exist and make up the neutrino even if they cease to overlap due to what we describe as *propagation decoherence* [22].

In the quasi-classical gravity case (this study), the neutrino is produced and detected in distinct flavor (at the astrophysical source and the earth detector); however, the neutrino exists in a single mass state due to being “observed” by the emitted graviton which distinguishes which mass state the neutrino exists in. We describe this effect as *quantum decoherence*. Since only a single mass state exists, the demonstrated phenomena are different such as that which is described by the Earth matter effect where the electron type component of the neutrino experiences the electromagnetic potential of the Earth differently than the other components. For low energy neutrinos in a single mass state, the Earth matter effect is less than 1%; in contrast to the Earth matter effect for a decoherent (due to propagation) superposition of mass states which have a stronger electron type neutrino component and experience a stronger Earth matter effect depending on neutrino energy.

While we give an explicit calculation of the GBH process to demonstrate that the emission of a hard graviton via gravitational Bremsstrahlung is relatively large and used this fact to motivate discussion of a maximal possible signature, that is,  $P_G = 1$ , we expect the calculation of gravitational Bremsstrahlung to require corrections similar to that of photon Bremsstrahlung [50, 51] for an extended source in addition to the loop-induced corrections for a full theory of quantum gravity. Additionally, in many considered astrophysical scenarios, the astrophysical distances involved would cause  $P_G$  to be small. This requires further work.

Having all that in mind, as a natural starting point in this very first paper we would like to present the basic concept/idea of quantum decoherence due to large angle neutrino-graviton interactions (Gravi-strahlung) in strong gravitational fields and its possible effect on neutrino flavor observables. In this paper we report on our preliminary study of such a graviton-induced effect on neutrino oscillations and motivate future studies in this direction. We plan to improve our simulation with fluxes and the astrophysical medium in a future study. The possibility that  $P_G$  is not zero in the vicinity of the Sun should be considered as well. For example, using the same simulation as used to produce Figure 4 we find a preliminary effect for solar neutrino of approximately 3% for  $P_G = 0$  in the integrated  $B_8$  spectrum while we see an asymmetry of  $\sim 0\%$  for  $P_G = 1$ . Explicitly, the length and energy dependence of neutrino flavor oscillation will depend on the relative strengths of the graviton-neutrino interactions, the matter properties, and the vacuum oscillation parameters. Inclusion of these possibilities in the global neutrino oscillation parameter fit will be left for a later paper. Additionally, extragalactic neutrinos should be considered with additional care as GBH scattering of the neutrino off the diffuse dark matter halo may play a role. Finally, the issue of coherent production of neutrinos is not considered in this study and should be studied in detail in a future work.

The program used to produce Figure 4 can be found on the arxiv [63]. For further information about semiclassical quantum gravity see [64] and for further information about graviton bremsstrahlung see [65–67].

In the review process, [68] was brought to the attention of the authors. Here the idea that a neutrino in a superposition

of mass eigenstates may be projected to a single mass eigenstate by a gravitational couplings was presented.

## Appendix

### Note on Measuring Graviton Induced Decoherence

The central effect of the graviton observation of the neutrino which is utilised in this proposed measurement is that a superposition is different than a classical ensemble of states. Distinguishing these two things is of key interest to the Quantum Information and Quantum Foundations communities and they have been shown to be different in experiments which investigate Bell Inequalities. To quote a member of the Quantum Foundations community who are also interested in distinguishing the situation where the particle is in a superposition (neutrino which has not undergone an interaction with a graviton, in our case) and those where the wave function has collapsed (in the mass basis in our case, where the neutrino has undergone an interaction with a graviton) [70]:

*It is a well-known and important property of quantum mechanics that a superposition of states is fundamentally different from a classical ensemble of states, where the system actually is in only one of the states but we simply do not know in which (this is often referred to as an ignorance-interpretation, or proper ensemble).*

What is required to distinguish these two cases is for the phase between the states to not be rapidly varying. In the case where interference phenomena may be observed (the phenomena of neutrino oscillation for neutrinos) this is obviously the case. For the case where the particle is still coherent but the phase difference between states is rapidly varying, it is obvious that it is impossible to differentiate a classical ensemble from a superposition. For neutrinos this is the situation where there is still overlap between the states but the energy resolution of the detector is not good enough to observe the oscillation and has been talked about in [22, 24].

However, there is an additional case where the neutrino in the flavor basis ceases to oscillate. The states no longer overlap. This is the case of propagation decoherence and generally the case for astrophysical neutrinos. In this case, in the flavor basis, the neutrino has a constant phase difference between (matter) states. If we measure this state without making any changes to it based on the phase difference we get the same result as if we measure a classical ensemble of states (the quantum gravity decoherence case). However, if we modify this (flavor) state by sending it through matter, the constant phase difference is changed differently than the classical ensemble of states and the neutrino can be distinguished as being in a classical ensemble of states (or having undergone quantum gravity decoherence) rather than a separated superposition. The boundary between matter regimes has a finite width and so the (flavor) state is going to have a constant phase difference (for large enough

separations), independent of the energy resolution of the final (flavor) detector which collapses the wave function.

This can be clearly described in the density matrix formalism. In the formalism, the evolution of the density matrix is given by

$$\dot{\rho} = -i[H, \rho], \quad (\text{A.1})$$

where  $\rho$  is the density matrix and  $H$  is the Hamiltonian. It has been shown [71] that if  $\dot{\rho} = 0$ , knowledge about the particulars of the wave packet is unnecessary and as a consequence you can not distinguish wave packet separation from the case where you have a measurement at large distances (or you have a graviton interaction leaving the neutrino in a distinct mass eigenstate). However, we are considering the case where wave packet separation has occurred and then the neutrino passes through jump in the potential. We can describe change of basis from flavor to vacuum as  $C_1$  and the change of basis from flavor to matter as  $C_2$ . We can describe the decoherence process as  $D$ , which nullifies the off diagonal components of the density matrix (e.g., [72]). Note that  $D$  does not commute with  $C$ . We can also describe the adiabatic process of the neutrino passing through the earth as  $H_m$ . We then consider

$$[C_2^{-1}H_mC_2C_1^{-1}DC_1, \rho] \quad (\text{A.2})$$

and note that it is not 0. Thus  $\dot{\rho} \neq 0$  and wave packet information is relevant and furthermore, as presented in this study, you may distinguish wave packet separation from graviton induced decoherence.

For the case of 2 neutrinos flavours, the constant phase difference for a neutrino in a separated superposition is obvious and is given by  $\pi/2$ . For the case of 3 neutrino flavours, it is more difficult, and by brute force phase differences which work for the neutrino parameters used in this study are  $0.756253i$  and  $1.477224i$ , the results of which are plotted in Figure 4.

## Conflict of Interests

The authors declare that there is no conflict of interests regarding the publication of this paper.

## Acknowledgments

Stimulating discussions and helpful correspondence with Sabine Hossenfelder and Alexei Vladimirov are gratefully acknowledged. Jonathan Miller was supported in part by PROYECTO BASAL FB 0821 CCTVal and Fondecyt (Grant no. 11130133). Roman Pasechnik was supported in part by Fondecyt (Grant no. 1090291) and the Crafoord Foundation (Grant no. 20120520). Roman Pasechnik is grateful to the "Beyond the LHC" Program at Nordita (Stockholm) for support and hospitality during a portion of this work. This research was supported in part by the National Science Foundation under Grant no. NSF PHY11-25915.

## References

- [1] J. Christian, “Why the quantum must yield to gravity,” in *Physics Meets Philosophy at the Planck Scale*, C. Callender and N. Huggett, Eds., Cambridge University Press, Cambridge, UK, 2001.
- [2] R. P. Woodard, “How far are we from the quantum theory of gravity?” *Reports on Progress in Physics*, vol. 72, no. 12, Article ID 126002, 2009.
- [3] F. Dyson, “The world on a string,” in *The Fabric of the Cosmos: Space, Time, and the Texture of Reality*, B. Greene, Ed., vol. 51, no. 8, Review of Books, New York, NY, USA, 2004.
- [4] F. Dyson, “Is a graviton detectable?” in *Proceedings of the Poincare Prize Lecture International Congress of Mathematical Physics*, Aalborg, Denmark, August 2012.
- [5] T. Rothman and S. Boughn, “Can gravitons be detected?” *Foundations of Physics*, vol. 36, no. 12, pp. 1801–1825, 2006.
- [6] G. Amelino-Camelia, “Introduction to quantum-gravity phenomenology,” in *Planck Scale Effects in Astrophysics and Cosmology*, vol. 669 of *Lecture Notes in Physics*, pp. 59–100, Springer, Berlin, Germany, 2005.
- [7] T. Damour and M. Lilley, “String theory, gravity and experiment,” in *Proceedings of the 87th Session of the Summer School in Theoretical Physics: String Theory and the Real World: From Particle Physics to Astrophysics*, Les Houches, France, July 2007.
- [8] S. Hossenfelder, “Experimental search for quantum gravity,” in *Classical and Quantum Gravity: Theory, Analysis and Applications*, V. R. Frignanni, Ed., chapter 5, Nova Publishers, 2011.
- [9] L. M. Krauss and F. Wilczek, “Using cosmology to establish the quantization of gravity,” *Physical Review D*, vol. 89, Article ID 047501, 2014.
- [10] S. Weinberg, “Photons and gravitons in S-matrix theory: derivation of charge conservation and equality of gravitational and inertial mass,” *Physical Review B*, vol. 135, pp. B1049–B1056, 1964.
- [11] S. Weinberg, “Photons and gravitons in perturbation theory: derivation of Maxwell’s and Einstein’s equations,” *Physical Review B*, vol. 138, pp. 988–1002, 1965.
- [12] J. S. Díaz, “Neutrinos as probes of Lorentz invariance,” *Advances in High Energy Physics*, vol. 2014, Article ID 962410, 11 pages, 2014.
- [13] G. L. Fogli, E. Lisi, A. Marrone, and G. Scioscia, “Testing violations of special and general relativity through the energy dependence of  $\nu_\mu \leftrightarrow \nu_\tau$  oscillations in the Super-Kamiokande atmospheric neutrino experiment,” *Physical Review D*, vol. 60, Article ID 053006, 1999.
- [14] M. Bahrami, S. Donadi, L. Ferialdi et al., “Are collapse models testable with quantum oscillating systems? The case of neutrinos, kaons, chiral molecules,” *Scientific Reports*, vol. 3, article 1952, 2013.
- [15] F.-C. Ma and H.-M. Hu, “Testing quantum mechanics in neutrino oscillation,” <http://arxiv.org/abs/hep-ph/9805391>.
- [16] R. S. Raghavan, D. Minic, T. Takeuchi, and C. H. Tze, “Using neutrinos to test the time-energy uncertainty relation in an extreme regime,” <http://arxiv.org/abs/1210.5639>.
- [17] M. M. Guzzo, H. Nunokawa, and R. Tomàs, “Testing the principle of equivalence by supernova neutrinos,” *Astroparticle Physics*, vol. 18, no. 3, pp. 277–286, 2002.
- [18] L. Anchordoqui and F. Halzen, “IceHEP high energy physics at the South Pole,” *Annals of Physics*, vol. 321, no. 11, pp. 2660–2716, 2006.
- [19] M. Sprenger, P. Nicolini, and M. Bleicher, “Quantum gravity signals in neutrino oscillations,” *International Journal of Modern Physics E*, vol. 20, no. S2, 2011.
- [20] M. Sprenger, M. Bleicher, and P. Nicolini, “Neutrino oscillations as a novel probe for a minimal length,” *Classical and Quantum Gravity*, vol. 28, Article ID 235019, 2011.
- [21] C. Giunti and C. W. Kim, “Coherence of neutrino oscillations in the wave packet approach,” *Physical Review D*, vol. 58, Article ID 017301, 1998.
- [22] M. Beuthe, “Oscillations of neutrinos and mesons in quantum field theory,” *Physics Reports A*, vol. 375, no. 2-3, pp. 105–218, 2003.
- [23] J. Kersten, “Coherence of supernova neutrinos,” *Nuclear Physics B—Proceedings Supplements*, vol. 237–238, pp. 342–344, 2013.
- [24] Y. Farzan and A. Y. Smirnov, “Coherence and oscillations of cosmic neutrinos,” *Nuclear Physics B*, vol. 805, no. 1-2, pp. 356–376, 2008.
- [25] J. Christian, “Testing gravity-driven collapse of the wave function via cosmogenic neutrinos,” *Physical Review Letters*, vol. 95, Article ID 160403, 2005.
- [26] S. Donadi, A. Bassi, L. Ferialdi, and C. Curceanu, “The effect of spontaneous collapses on neutrino oscillations,” *Foundations of Physics*, vol. 43, no. 9, pp. 1066–1089, 2013.
- [27] L. Diósi, “Gravitation and quantum-mechanical localization of macro-objects,” *Physics Letters A*, vol. 105, no. 4-5, pp. 199–202, 1984.
- [28] L. Diósi, “A universal master equation for the gravitational violation of quantum mechanics,” *Physics Letters A*, vol. 120, pp. 377–381, 1987.
- [29] L. Diósi, “Models for universal reduction of macroscopic quantum fluctuations,” *Physical Review A*, vol. 40, no. 3, pp. 1165–1174, 1989.
- [30] R. Penrose, “On gravity’s role in quantum state reduction,” *General Relativity and Gravitation*, vol. 28, no. 5, pp. 581–600, 1996.
- [31] D. V. Ahluwalia and C. Burgard, “Interplay of gravitation and linear superposition of different mass eigenstates,” *Physical Review D*, vol. 57, pp. 4724–4727, 1998.
- [32] A. Bassi and G. C. Ghirardi, “Dynamical reduction models,” *Physics Reports*, vol. 379, no. 5-6, pp. 257–426, 2003.
- [33] C. Corianò, L. Delle Rose, E. Gabrielli, and L. Trentadue, “Mass corrections to flavor-changing fermion-graviton vertices in the standard model,” *Physical Review D*, vol. 88, no. 8, Article ID 085008, 12 pages, 2013.
- [34] S. P. Mikheev and A. Y. Smirnov, “Resonant amplification of  $\nu$  oscillations in matter and solar-neutrino spectroscopy,” *Il Nuovo Cimento C*, vol. 9, pp. 17–26, 1986.
- [35] L. Wolfenstein, “Neutrino oscillations in matter,” *Physical Review D*, vol. 17, no. 9, pp. 2369–2374, 1978.
- [36] J. Beringer, J.-F. Arguin, R. M. Barnett et al., “Review of particle physics,” *Physical Review D*, vol. 86, Article ID 010001, 2012.
- [37] T. Ohlsson and H. Snellman, “Three flavor neutrino oscillations in matter,” *Journal of Mathematical Physics*, vol. 41, no. 5, pp. 2768–2788, 2000, Erratum in *Journal of Mathematical Physics*, vol. 42, p. 2345, 2001.
- [38] J. Edsjo, WimpSim Neutrino Monte Carlo, <http://www.fysik.su.se/~edsjo/wimpsim>.
- [39] J. Gava, J. Kneller, C. Volpe, and G. C. McLaughlin, “Dynamical collective calculation of supernova neutrino signals,” *Physical Review Letters*, vol. 103, Article ID 071101, 2009.

- [40] D. Vaananen and C. Volpe, "The neutrino signal at HALO: learning about the primary supernova neutrino fluxes and neutrino properties," *Journal of Cosmology and Astroparticle Physics*, vol. 2011, article 019, 2011.
- [41] E. K. Akhmedov and A. Wilhelm, "Quantum field theoretic approach to neutrino oscillations in matter," *Journal of High Energy Physics*, vol. 2013, article 165, 2013.
- [42] E. K. Akhmedov and J. Kopp, "Neutrino oscillations: quantum mechanics vs. quantum field theory," *Journal of High Energy Physics*, vol. 2010, no. 4, article 008, 2010, Erratum in: *Journal of High Energy Physics*, vol. 2013, no. 10, article 052, 2013.
- [43] M. Blennow and A. Y. Smirnov, "Neutrino propagation in matter," *Advances in High Energy Physics*, vol. 2013, Article ID 972485, 33 pages, 2013.
- [44] A. B. Balantekin and J. F. Beacom, "Semiclassical treatment of matter-enhanced neutrino oscillations for an arbitrary density profile," *Physical Review D*, vol. 54, pp. 6323–6337, 1996.
- [45] A. S. Dighe, Q. Y. Liu, and A. Y. Smirnov, "Coherence and the day–night asymmetry in the solar neutrino flux," <http://arxiv.org/abs/hep-ph/9903329>.
- [46] K. Kiers, S. Nussinov, and N. Weiss, "Coherence effects in neutrino oscillations," *Physical Review D*, vol. 53, pp. 537–547, 1996.
- [47] D. G. Boulware and S. Deser, "Classical general relativity derived from quantum gravity," *Annals of Physics*, vol. 89, pp. 193–240, 1975.
- [48] A. D. Dolgov and D. Ejlli, "Relic gravitational waves from light primordial black holes," *Physical Review D*, vol. 84, Article ID 024028, 2011.
- [49] B. M. Barker, S. N. Gupta, and J. Kaskas, "Graviton bremsstrahlung and infrared divergence," *Physical Review*, vol. 182, no. 5, pp. 1391–1396, 1969.
- [50] H. K. Tseng and R. H. Pratt, "Electron bremsstrahlung energy spectra above 2 MeV," *Physical Review A*, vol. 19, no. 4, pp. 1525–1528, 1979.
- [51] D. H. Jakubassa-Amundsen, "High-energy bremsstrahlung from polarized electrons colliding with spin-1/2 nuclei," *Physical Review C*, vol. 87, Article ID 064609, 2013.
- [52] D. N. Kabat and M. Ortiz, "Eikonal quantum gravity and planckian scattering," *Nuclear Physics B*, vol. 388, no. 2, pp. 570–592, 1992.
- [53] N. A. Voronov, "Gravitational Compton effect and photoproduction of gravitons by electrons," *Zhurnal Éksperimental'noi i Teoreticheskoi Fiziki*, vol. 64, pp. 1889–1901, 1973.
- [54] M. C. Gonzalez-Garcia, M. Maltoni, J. Salvado, and T. Schwetz, "Global fit to three neutrino mixing: critical look at present precision," *Journal of High Energy Physics*, vol. 2012, no. 12, article 123, 2012.
- [55] A. Strumia and F. Vissani, "Neutrino masses and mixings and...", <http://arxiv.org/abs/hep-ph/0606054>.
- [56] C. W. Kim and A. Pevsner, *Neutrinos in Physics and Astrophysics*, Harwood Academic, New York, NY, USA, 1993.
- [57] K.-C. Lai, G.-L. Lin, and T. C. Liu, "Flavor transition mechanisms of propagating astrophysical neutrinos: a model independent parametrization," *Physical Review D*, vol. 82, Article ID 103003, 2010.
- [58] S. Choubey and W. Rodejohann, "Flavor composition of ultra-high energy neutrinos at source and at neutrino telescopes," *Physical Review D*, vol. 80, Article ID 113006, 2009.
- [59] A. Esmaili and Y. Farzan, "An analysis of cosmic neutrinos: flavor composition at source and neutrino mixing parameters," *Nuclear Physics B*, vol. 821, pp. 197–214, 2009.
- [60] K. Scholberg, "Supernova neutrino detection," *Annual Review of Nuclear and Particle Science*, vol. 62, pp. 81–103, 2012.
- [61] T. Akiri, D. Allspach, M. Andrews et al., "The 2010 interim report of the long-baseline neutrino experiment collaboration physics working groups," <http://arxiv.org/abs/1110.6249>.
- [62] P. A. N. Machado, T. Muhlbeier, H. Nunokawa, and R. Z. Funchal, "Potential of a neutrino detector in the ANDES underground laboratory for geophysics and astrophysics of neutrinos," *Physical Review D*, vol. 86, no. 12, Article ID 125001, 19 pages, 2012.
- [63] J. Miller and R. Pasechnik, "Quantum gravity effect on neutrino oscillations in a strong gravitational field," <http://arxiv.org/abs/1305.4430>.
- [64] R. Paszko and A. Accioly, "Equivalence between the semiclassical and effective approaches to gravity," *Classical and Quantum Gravity*, vol. 27, no. 14, Article ID 145012, 2010.
- [65] R. J. Gould, "The graviton luminosity of the sun and other stars," *The Astrophysical Journal*, vol. 288, pp. 789–794, 1985.
- [66] B. M. Barker and S. N. Gupta, "High-energy graviton bremsstrahlung," *Physical Review D*, vol. 9, no. 2, pp. 334–338, 1974.
- [67] P. C. Peters, "Relativistic gravitational bremsstrahlung," *Physical Review D*, vol. 1, no. 6, pp. 1559–1571, 1970.
- [68] D. V. Ahluwalia, "On reconciling atmospheric, lsnd, and solar neutrino-oscillation data," *Modern Physics Letters A*, vol. 13, no. 28, pp. 2249–2264, 1998.
- [69] H.-T. Janka, "Explosion mechanisms of core-collapse supernovae," *Annual Review of Nuclear and Particle Science*, vol. 62, pp. 407–451, 2012.
- [70] M. Schlosshauer, "Decoherence, the measurement problem, and interpretations of quantum mechanics," *Reviews of Modern Physics*, vol. 76, p. 1267, 2005.
- [71] L. Stodolsky, "When the wavepacket is unnecessary," *Physical Review D*, vol. 58, Article ID 036006, 1998.
- [72] E. Akhmedov, J. Kopp, and M. Lindner, "Decoherence by wave packet separation and collective neutrino oscillations," <http://arxiv.org/abs/1405.7275>.

## Research Article

# Constraints on the Nonstandard Interaction in Propagation from Atmospheric Neutrinos

Shinya Fukasawa and Osamu Yasuda

Department of Physics, Tokyo Metropolitan University, Minami-Osawa, Hachioji, Tokyo 192-0397, Japan

Correspondence should be addressed to Osamu Yasuda; yasuda@phys.se.tmu.ac.jp

Received 3 May 2015; Accepted 5 August 2015

Academic Editor: Vincenzo Flaminio

Copyright © 2015 S. Fukasawa and O. Yasuda. This is an open access article distributed under the Creative Commons Attribution License, which permits unrestricted use, distribution, and reproduction in any medium, provided the original work is properly cited. The publication of this article was funded by SCOAP<sup>3</sup>.

The sensitivity of the atmospheric neutrino experiments to the nonstandard flavor-dependent interaction in neutrino propagation is studied under the assumption that only nonvanishing components of the nonstandard matter effect are the electron and tau neutrino components  $\epsilon_{ee}$ , and  $\epsilon_{e\tau}$ ,  $\epsilon_{\tau\tau}$  and that the tau-tau component satisfies the constraint  $\epsilon_{\tau\tau} = |\epsilon_{e\tau}|^2/(1 + \epsilon_{ee})$  which is suggested from the high energy behavior for atmospheric neutrino data. It is shown that the Super-Kamiokande (SK) data for 4438 days constrains  $|\tan\beta| \equiv |\epsilon_{e\tau}/(1 + \epsilon_{ee})| \leq 0.8$  at  $2.5\sigma$  (98.8%) CL whereas the future Hyper-Kamiokande experiment for the same period of time as SK will constrain as  $|\tan\beta| \leq 0.3$  at  $2.5\sigma$  CL from the energy rate analysis and the energy spectrum analysis will give even tighter bounds on  $\epsilon_{ee}$  and  $|\epsilon_{e\tau}|$ .

## 1. Introduction

From the experiments with solar, atmospheric, reactor, and accelerator neutrinos it is now established that neutrinos have masses and mixing [1]. Neutrino oscillations in the standard three-flavor scheme are described by three mixing angles,  $\theta_{12}$ ,  $\theta_{13}$ , and  $\theta_{23}$ , one CP phase  $\delta$ , and two independent mass-squared differences,  $\Delta m_{21}^2$  and  $\Delta m_{31}^2$ . The sets of the parameters  $(\Delta m_{21}^2, \theta_{12})$  and  $(|\Delta m_{31}^2|, \theta_{23})$  were determined by the solar neutrino experiments and the KamLAND experiment and by atmospheric and long baseline neutrino experiments, respectively.  $\theta_{13}$  was determined by the reactor experiments and the long baseline experiments [1]. The only oscillation parameters which are still undetermined are the value of the CP phase  $\delta$  and the sign of  $\Delta m_{31}^2$  (the mass hierarchy). In the future neutrino long-baseline experiments with intense neutrino beams the signs of  $\Delta m_{31}^2$  and  $\delta$  are expected to be determined [2, 3]. As in the case of B factories [4, 5], such high precision measurements will enable us to search for deviation from the standard three-flavor oscillations (see, e.g., [6]). Among such possibilities, in this paper, we will discuss

the effective nonstandard neutral current flavor-dependent neutrino interaction with matter [7–9], given by

$$\mathcal{L}_{\text{eff}}^{\text{NSI}} = -2\sqrt{2}\epsilon_{\alpha\beta}^{fP} G_F (\bar{\nu}_\alpha \gamma_\mu P_L \nu_\beta) (\bar{f} \gamma^\mu P f'), \quad (1)$$

where  $f$  and  $f'$  stand for fermions (the only relevant ones are electrons,  $u$  and  $d$  quarks),  $G_F$  is the Fermi coupling constant, and  $P$  stands for a projection operator that is either  $P_L \equiv (1 - \gamma_5)/2$  or  $P_R \equiv (1 + \gamma_5)/2$ . If the interaction (1) exists, then the standard matter effect [7, 10] is modified. We will discuss atmospheric neutrinos which go through the Earth, so we make an approximation that the number densities of electrons ( $N_e$ ), protons, and neutrons are equal (this assumption is not valid in other environments, e.g., in the Sun.). Defining  $\epsilon_{\alpha\beta} \equiv \sum_P (\epsilon_{\alpha\beta}^{eP} + 3\epsilon_{\alpha\beta}^{uP} + 3\epsilon_{\alpha\beta}^{dP})$ , the Hermitian  $3 \times 3$  matrix of the matter potential becomes

$$\mathcal{A} \equiv A \begin{pmatrix} 1 + \epsilon_{ee} & \epsilon_{e\mu} & \epsilon_{e\tau} \\ \epsilon_{\mu e} & \epsilon_{\mu\mu} & \epsilon_{\mu\tau} \\ \epsilon_{\tau e} & \epsilon_{\tau\mu} & \epsilon_{\tau\tau} \end{pmatrix}, \quad (2)$$

where  $A \equiv \sqrt{2}G_F N_e$  stands for the matter effect due to the charged current interaction in the standard case. With this matter potential, the Dirac equation for neutrinos in matter becomes

$$i \frac{d}{dx} \begin{pmatrix} \nu_e(x) \\ \nu_\mu(x) \\ \nu_\tau(x) \end{pmatrix} = [U \text{diag}(0, \Delta E_{21}, \Delta E_{31}) U^{-1} + \mathcal{A}] \begin{pmatrix} \nu_e(x) \\ \nu_\mu(x) \\ \nu_\tau(x) \end{pmatrix}, \quad (3)$$

where  $U$  is the leptonic mixing matrix defined by

$$U \equiv \begin{pmatrix} c_{12}c_{13} & s_{12}c_{13} & s_{13}e^{-i\delta} \\ -s_{12}c_{23} - c_{12}s_{23}s_{13}e^{i\delta} & c_{12}c_{23} - s_{12}s_{23}s_{13}e^{i\delta} & s_{23}c_{13} \\ s_{12}s_{23} - c_{12}c_{23}s_{13}e^{i\delta} & -c_{12}s_{23} - s_{12}c_{23}s_{13}e^{i\delta} & c_{23}c_{13} \end{pmatrix}, \quad (4)$$

and  $\Delta E_{jk} \equiv \Delta m_{jk}^2/2E \equiv (m_j^2 - m_k^2)/2E$ ,  $c_{jk} \equiv \cos\theta_{jk}$ , and  $s_{jk} \equiv \sin\theta_{jk}$ .

Constraints on  $\epsilon_{\alpha\beta}$  have been discussed by many authors, from atmospheric neutrinos [11–15], from  $e^+e^-$  colliders [16], from the compilation of various neutrino data [17], from solar neutrinos [18–20], from  $\nu_e e$  or  $\bar{\nu}_e e$  scatterings [21, 22], from solar and reactor neutrinos [23], and from solar, reactor, and accelerator neutrinos [24]. Since the coefficients  $\epsilon_{\alpha\beta}$  in (2) are given by  $\epsilon_{\alpha\beta} \sim \epsilon_{\alpha\beta}^e + 3\epsilon_{\alpha\beta}^\mu + 3\epsilon_{\alpha\beta}^d$ , considering the constraints in these references, we have the following limits [25] at 90%CL:

$$\begin{pmatrix} |\epsilon_{ee}| < 4 \times 10^0 & |\epsilon_{e\mu}| < 3 \times 10^{-1} & |\epsilon_{e\tau}| < 3 \times 10^0 \\ & |\epsilon_{\mu\mu}| < 7 \times 10^{-2} & |\epsilon_{\mu\tau}| < 3 \times 10^{-1} \\ & & |\epsilon_{\tau\tau}| < 2 \times 10^1 \end{pmatrix}. \quad (5)$$

From (5) we observe that the bounds on  $\epsilon_{ee}$ ,  $\epsilon_{e\tau}$ , and  $\epsilon_{\tau\tau}$  are much weaker than those on  $\epsilon_{\alpha\mu}$  ( $\alpha = e, \mu, \tau$ ).

On the other hand, the nonstandard interaction (NSI) with components  $\epsilon_{\alpha\beta}$  ( $\alpha, \beta = e, \tau$ ) must be consistent with the high-energy atmospheric neutrino data. It was pointed out in [26, 27] that the relation

$$|\epsilon_{e\tau}|^2 \simeq \epsilon_{\tau\tau} (1 + \epsilon_{ee}) \quad (6)$$

should hold for the matter potential (2) to be consistent with the high-energy atmospheric neutrino data, which suggest the behavior of the disappearance oscillation probability

$$1 - P(\nu_\mu \rightarrow \nu_\mu) \sim \sin^2 2\theta_{\text{atm}} \sin^2 \left( \frac{\Delta m_{\text{atm}}^2 L}{4E} \right) \propto \frac{1}{E^2}, \quad (7)$$

where  $\sin^2 2\theta_{\text{atm}}$  and  $\Delta m_{\text{atm}}^2$  are the oscillation parameters in the two-flavor formalism. In [28] it was shown that, in the high-energy behavior of the disappearance oscillation probability

$$1 - P(\nu_\mu \rightarrow \nu_\mu) \simeq c_0 + \frac{c_1}{E} + \mathcal{O}\left(\frac{1}{E^2}\right) \quad (8)$$

in the presence of the matter potential (2),  $|c_0| \ll 1$  and  $|c_1| \ll 1$  imply  $\epsilon_{e\mu} \simeq \epsilon_{\mu\mu} \simeq \epsilon_{\mu\tau} \simeq 0$  and  $\epsilon_{\tau\tau} \simeq |\epsilon_{e\tau}|^2/(1 + \epsilon_{ee})$ .

Taking into account the various constraints described above, in the present paper we take the ansatz

$$\mathcal{A} = A \begin{pmatrix} 1 + \epsilon_{ee} & 0 & \epsilon_{e\tau} \\ 0 & 0 & 0 \\ \epsilon_{e\tau}^* & 0 & \frac{|\epsilon_{e\tau}|^2}{(1 + \epsilon_{ee})} \end{pmatrix} \quad (9)$$

and analyze the sensitivity to the parameters  $\epsilon_{\alpha\beta}$  ( $\alpha, \beta = e, \tau$ ) of the atmospheric neutrino experiment at Super-Kamiokande and the future Hyper-Kamiokande (HK) facility [29] (as far as  $\epsilon_{\tau\tau}$  is concerned, the ansatz (9) is believed to be the best fit of the high energy atmospheric neutrino data at present. So as long as the true value of  $\epsilon_{\tau\tau}$  satisfies the relation (6), even if we analyze the data assuming that  $\epsilon_{\tau\tau}$  is a free parameter, the allowed region in  $(\epsilon_{ee}, |\epsilon_{e\tau}|)$  and the sensitivity to NSI are not expected to change very much, because the region of  $\epsilon_{\tau\tau}$ , which does not satisfy (6), gets an additional contribution of  $\chi^2$  and is not supposed to contribute to enlarge the allowed region or to increase the sensitivity to NSI).

The constraints on  $\epsilon_{ee}$  and  $\epsilon_{e\tau}$  from the atmospheric neutrino have been discussed in [30] along with those from the long-baseline experiments, in [31] by the Super-Kamiokande Collaboration, in [32–34] on the future extension of the IceCube experiment, and in [35] in the global analysis, with the ansatz different from ours.

The sensitivity of the ongoing accelerator experiments to the nonstandard interaction in propagation was studied by various authors. The constraints have been obtained from the MINOS experiment in [36], from the MINOS data using the same ansatz as the present paper in [37, 38], from the MINOS data from the viewpoint of degeneracy of  $\theta_{13}$  and NSI in [39], from  $\nu_e$  appearance in MINOS and T2K in [40], from the OPERA experiment in [41, 42], and from the LHC experiment in [43]. As for the future long-baseline experiments, the sensitivity of the INO experiment was discussed in [44], that of the reactor and superbeam experiments was discussed in [45], that of the T2KK experiment was studied in [28, 46], and that of the LBNE experiment was discussed in [43, 47]. The sensitivity of neutrino factories [6] was studied in various contexts: the sensitivity to NSI [48–50], the confusion with the effect of  $\theta_{13}$  [51], the optimization [52], resolving degeneracy with two baselines [53, 54], and the relation with nonunitary mixing [55].

The paper is organized as follows. In Section 2, we analyze the SK atmospheric neutrino data and give the constraints on the parameters  $\epsilon_{\alpha\beta}$  ( $\alpha, \beta = e, \tau$ ) from the SK atmospheric neutrino data. In Section 3, we discuss the sensitivity to  $\epsilon_{\alpha\beta}$  ( $\alpha, \beta = e, \tau$ ) of the future Hyper-Kamiokande atmospheric neutrino experiment. In Section 4, we draw our conclusions.

## 2. The Constraint of the Super-Kamiokande Atmospheric Neutrino Experiment on $\epsilon_{ee}$ and $|\epsilon_{e\tau}|$

In this section we discuss the constraint of the SK atmospheric neutrino experiment on the nonstandard interaction in propagation with the ansatz (9). The independent degrees of freedom in addition to those in the standard oscillation scenario are  $\epsilon_{ee}$ ,  $|\epsilon_{e\tau}|$  and  $\arg(\epsilon_{e\tau})$ .

The SK atmospheric neutrino data we analyze here is those in [56] for 4438 days. In [56], the contained events, the partially contained events, and the upward going  $\mu$  events are divided into a few categories. Since we have been unable to reproduce all their results of the Monte Carlo simulation, we have combined the two sub-GeV  $\mu$ -like data set in one, the two multi-GeV  $e$ -like in one, the two partially contained

event data set and the multi-GeV  $\mu$ -like in one, and the three upward going  $\mu$  in one. Reference [56] gives information on the ten zenith angle bins, while that on the energy bins is not given, so we perform analysis with the ten zenith angle bins and one energy bin; that is, we perform the rate analysis as far as the energy is concerned.

The analysis was performed with the codes which were used in [57–59].  $\chi^2$  is defined as

$$\chi^2 = \min_{\theta_{23}, |\Delta m_{32}^2|, \delta, \arg(\epsilon_{e\tau})} \left( \chi_{\text{sub-GeV}}^2 + \chi_{\text{multi-GeV}}^2 + \chi_{\text{upward}}^2 \right). \quad (10)$$

In (10)  $\chi^2$  for the sub-GeV, multi-GeV, and upward going  $\mu$  events are defined by

$$\begin{aligned} \chi_{\text{sub-GeV}}^2 &= \min_{\alpha_s, \beta_{s1}, \beta_{s2}} \left[ \frac{\beta_{s1}^2}{\sigma_{\beta_{s1}}^2} + \frac{\beta_{s2}^2}{\sigma_{\beta_{s2}}^2} \right. \\ &+ \sum_{j=1}^{10} \left\{ \frac{1}{n_j^s(e)} \left[ \alpha_s \left( 1 - \frac{\beta_{s1}}{2} + \frac{\beta_{s2}}{2} \right) N_j^s(\nu_e \rightarrow \nu_e) + \alpha_s \left( 1 + \frac{\beta_{s1}}{2} + \frac{\beta_{s2}}{2} \right) N_j^s(\nu_\mu \rightarrow \nu_e) + \alpha_s \left( 1 - \frac{\beta_{s1}}{2} - \frac{\beta_{s2}}{2} \right) N_j^s(\bar{\nu}_e \rightarrow \bar{\nu}_e) + \alpha_s \left( 1 + \frac{\beta_{s1}}{2} - \frac{\beta_{s2}}{2} \right) N_j^s(\bar{\nu}_\mu \rightarrow \bar{\nu}_e) - n_j^s(e) \right]^2 \right. \\ &+ \left. \frac{1}{n_j^s(\mu)} \left[ \alpha_s \left( 1 - \frac{\beta_{s1}}{2} + \frac{\beta_{s2}}{2} \right) N_j^s(\nu_e \rightarrow \nu_\mu) + \alpha_s \left( 1 + \frac{\beta_{s1}}{2} + \frac{\beta_{s2}}{2} \right) N_j^s(\nu_\mu \rightarrow \nu_\mu) + \alpha_s \left( 1 - \frac{\beta_{s1}}{2} - \frac{\beta_{s2}}{2} \right) N_j^s(\bar{\nu}_e \rightarrow \bar{\nu}_\mu) + \alpha_s \left( 1 + \frac{\beta_{s1}}{2} - \frac{\beta_{s2}}{2} \right) N_j^s(\bar{\nu}_\mu \rightarrow \bar{\nu}_\mu) - n_j^s(\mu) \right]^2 \right\}, \\ \chi_{\text{multi-GeV}}^2 &= \min_{\alpha_m, \beta_{m1}, \beta_{m2}} \left[ \frac{\beta_{m1}^2}{\sigma_{\beta_{m1}}^2} + \frac{\beta_{m2}^2}{\sigma_{\beta_{m2}}^2} \right. \\ &+ \sum_{j=1}^{10} \left\{ \frac{1}{n_j^m(e)} \left[ \alpha_s \left( 1 - \frac{\beta_{m1}}{2} + \frac{\beta_{m2}}{2} \right) N_j^m(\nu_e \rightarrow \nu_e) + \alpha_s \left( 1 + \frac{\beta_{m1}}{2} + \frac{\beta_{m2}}{2} \right) N_j^m(\nu_\mu \rightarrow \nu_e) + \alpha_s \left( 1 - \frac{\beta_{m1}}{2} - \frac{\beta_{m2}}{2} \right) N_j^m(\bar{\nu}_e \rightarrow \bar{\nu}_e) + \alpha_s \left( 1 + \frac{\beta_{m1}}{2} - \frac{\beta_{m2}}{2} \right) N_j^m(\bar{\nu}_\mu \rightarrow \bar{\nu}_e) - n_j^m(e) \right]^2 \right. \\ &+ \left. \frac{1}{n_j^m(\mu)} \left[ \alpha_s \left( 1 - \frac{\beta_{m1}}{2} + \frac{\beta_{m2}}{2} \right) N_j^m(\nu_e \rightarrow \nu_\mu) + \alpha_s \left( 1 + \frac{\beta_{m1}}{2} + \frac{\beta_{m2}}{2} \right) N_j^m(\nu_\mu \rightarrow \nu_\mu) + \alpha_s \left( 1 - \frac{\beta_{m1}}{2} - \frac{\beta_{m2}}{2} \right) N_j^m(\bar{\nu}_e \rightarrow \bar{\nu}_\mu) + \alpha_s \left( 1 + \frac{\beta_{m1}}{2} - \frac{\beta_{m2}}{2} \right) N_j^m(\bar{\nu}_\mu \rightarrow \bar{\nu}_\mu) - n_j^m(\mu) \right]^2 \right\}, \\ \chi_{\text{upward}}^2 &= \min_{\alpha_u} \left\{ \frac{\alpha_u^2}{\sigma_{\alpha_u}^2} + \sum_{j=1}^{10} \frac{1}{n_j^u(\mu)} \left[ \alpha_u N_j^u(\nu_e \rightarrow \nu_\mu) + \alpha_u N_j^u(\nu_\mu \rightarrow \nu_\mu) + \alpha_u N_j^u(\bar{\nu}_e \rightarrow \bar{\nu}_\mu) + \alpha_u N_j^u(\bar{\nu}_\mu \rightarrow \bar{\nu}_\mu) - n_j^u(\mu) \right]^2 \right\}. \end{aligned} \quad (11)$$

The summation on  $j$  runs over the ten zenith angle bins for each  $\chi^2$ ,  $n_j^a(\alpha)$  ( $a = s, m, u$ ;  $\alpha = e, \mu$ ) stands for the neutrino and antineutrino data of the numbers of the sub-GeV, multi-GeV, and upward going  $\mu$  events,  $N_j^a(\nu_\alpha \rightarrow \nu_\beta)$  ( $N_j^a(\bar{\nu}_\alpha \rightarrow \bar{\nu}_\beta)$ ) stands for the theoretical prediction for the number of  $\ell_\beta$ -like events ( $\ell_\beta = e, \mu$ ) which is produced from  $\nu_\beta$  ( $\bar{\nu}_\beta$ ) that originates from  $\nu_\alpha$  ( $\bar{\nu}_\alpha$ ) through the oscillation process  $\nu_\alpha \rightarrow \nu_\beta$  ( $\bar{\nu}_\alpha \rightarrow \bar{\nu}_\beta$ ), and it is expressed as the product of the oscillation probability  $P(\nu_\alpha \rightarrow \nu_\beta)$  ( $P(\bar{\nu}_\alpha \rightarrow \bar{\nu}_\beta)$ ), the flux  $F(\nu_\alpha)$  ( $F(\bar{\nu}_\alpha)$ ), the cross section, the number of the targets, and the detection efficiency.  $\alpha_a$  ( $a = s, m, u$ ) stands for the uncertainty in the overall flux normalization for the sub-GeV, multi-GeV, and upward going  $\mu$  events and  $\beta_{a1}$  ( $\beta_{a2}$ ) stands for the uncertainty in the relative normalization between  $\nu_e - \nu_\mu$  flux ( $\bar{\nu}_e - \bar{\nu}_\mu$  flux) for the sub-GeV ( $a = s$ ) and multi-GeV ( $a = m$ ) events, respectively. It is understood that  $\chi^2$  is minimized with respect to  $\alpha_s$ ,  $\beta_{sk}$  ( $k = 1, 2$ ),  $\alpha_m$ ,  $\beta_{mk}$  ( $k = 1, 2$ ), and  $\alpha_u$ . We have put the systematic errors

$$\sigma_{\beta_{s1}} = \sigma_{\beta_{m1}} = 0.03,$$

$$\sigma_{\beta_{s2}} = \sigma_{\beta_{m2}} = 0.05,$$

$$\sigma_\alpha = 0.2$$

(12)

and we have assumed that  $\alpha_s$  and  $\alpha_m$  for the contained events are free parameters as in [60]. We have omitted the other uncertainties, like the  $E_\nu$  spectral index, the relative normalization between PC and FC and up-down correlation, and so forth, for simplicity. In (10) the sum of each  $\chi^2$  is optimized with respect to the mixing angle  $\theta_{23}$ , the mass squared difference  $|\Delta m_{32}^2|$ , the Dirac CP phase  $\delta$ , and the phase  $\arg(\epsilon_{e\tau})$  of the parameter  $\epsilon_{e\tau}$ . The other oscillation parameters give little effect on  $\chi^2$ , so we have fixed them as  $\sin^2 2\theta_{12} = 0.86$ ,  $\sin^2 2\theta_{13} = 0.1$ , and  $\Delta m_{21}^2 = 7.6 \times 10^{-5} \text{ eV}^2$ .

The result for the Super-Kamiokande data for 4438 days is given in Figure 1. The best-fit point for the normal (inverted) hierarchy is  $(\epsilon_{ee}, |\epsilon_{e\tau}|) = (-1.0, 0.0)$   $((3.0, 1.7))$  and the value of  $\chi^2$  at this point is 79.0 (78.6) for 50 degrees of freedom, and goodness of fit is 2.8 (2.7)  $\sigma$ CL, respectively. The best-fit point is different from the standard case  $(\epsilon_{ee}, |\epsilon_{e\tau}|) = (0, 0)$ , and this may be not only because we have been unable to reproduce the Monte Carlo simulation by the Super-Kamiokande group, but also because we use only the information on the energy

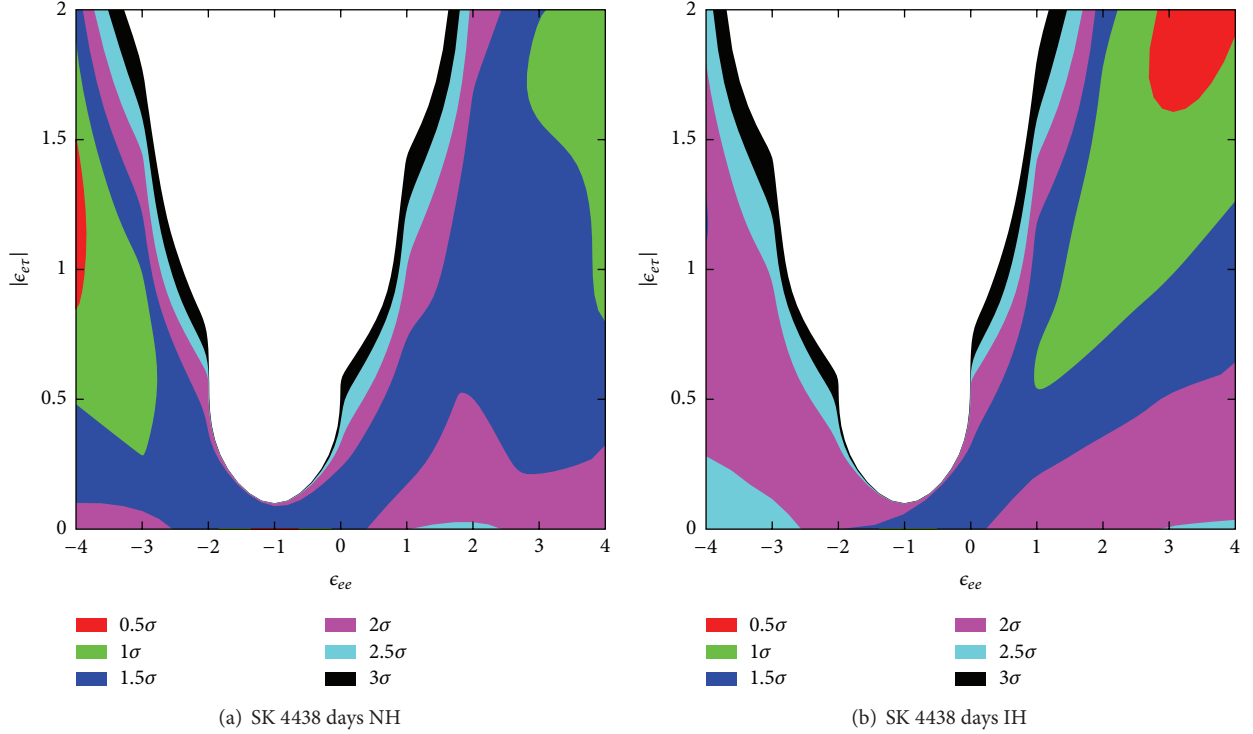


FIGURE 1: The allowed region in the  $(\epsilon_{ee}, |\epsilon_{e\tau}|)$  plane from the SK atmospheric neutrino data for a normal mass hierarchy (a) and for an inverted mass hierarchy (b). In the left panel, the best-fit point is  $(\epsilon_{ee}, |\epsilon_{e\tau}|) = (-1.0, 0.0)$ , although it is difficult to see from the figure that there is a very narrow region with CL less than  $0.5\sigma$  near this point.

rate and the sensitivity to NSI is lost due to the destructive phenomena between the lower and higher energy bins (see the discussions in Section 3.1). The difference of the value of  $\chi^2$  for the standard case and that for the best-fit point for the normal (inverted) hierarchy is  $\Delta\chi^2 = 2.7$  (3.4) for 2 degrees of freedom ( $1.1\sigma$ CL ( $1.3\sigma$ CL)), respectively, and the standard case is certainly acceptable for the both mass hierarchies in our analysis. From Figure 1 we can read off the allowed region for  $|\tan\beta| \equiv |\epsilon_{e\tau}|/|1 + \epsilon_{ee}|$ , and we conclude that the allowed region for  $|\tan\beta|$  is approximately

$$|\tan\beta| \equiv \frac{|\epsilon_{e\tau}|}{|1 + \epsilon_{ee}|} \lesssim 0.8 \quad \text{at } 2.5\sigma\text{CL}. \quad (13)$$

### 3. Sensitivity of the Hyper-Kamiokande Atmospheric Neutrino Experiment to $\epsilon_{ee}$ and $|\epsilon_{e\tau}|$

In this section we discuss the potential sensitivity of HK to  $\epsilon_{ee}$  and  $|\epsilon_{e\tau}|$ . Here we assume for simplicity that the Hyper-Kamiokande detector has the same detection efficiencies as those of SK and that the fiducial volume of HK is twenty times as large as that of SK. Since HK is a future experiment, the simulated numbers of events are used as “the experimental data,” and we vary  $\epsilon_{ee}$  and  $\epsilon_{e\tau}$  as well as the standard oscillation parameters trying to fit to “the experimental data.” Here we perform an analysis on the assumption that we know the mass hierarchy, because some hint on the mass hierarchy

is expected to be available at some confidence level by the time HK will accumulate the atmospheric neutrino data for twenty years.

Since “the experimental data” are the simulated numbers of events, we can perform an energy spectrum analysis, assuming that the detection efficiency and so forth are all equal among neutrinos and antineutrinos. Before we study the sensitivity to NSI, as a benchmark of our analysis, we have investigated the significance of the wrong mass hierarchy with our code, assuming the standard oscillation scenario and using different numbers of the energy bins. By comparing our result with the one in [29], we have found that our analysis on the mass hierarchy gives a result similar to that in [29], when we work with two energy bins in the contained events (the sub-GeV and multi-GeV events) and the systematic errors which are slightly different from those in [29] (when we have more than two energy bins, our results would lead to too large significance of the wrong mass hierarchy in the case of the standard oscillation scenario, compared with the one in [29]). Also in the presence of NSI, our study with more than two energy bins would give allowed regions which are smaller than those by the two-energy-bin analysis. So we will take two energy bins in the energy spectrum analysis to be conservative throughout this paper). We have checked that the sensitivity to NSI is not affected significantly by changing the systematic errors. As for the upward going  $\mu$  events, since our ansatz (9) is taken in such a way that the oscillation probability with  $\epsilon_{\alpha\beta}$  ( $\alpha, \beta = e, \tau$ ) approaches to the one with the standard scenario in the high energy limit, the upward

going  $\mu$  events are expected to give a small contribution to the significance of NSI. So in the case of the energy spectrum analysis we will work with two energy bins in the contained events and a single energy bin in the upward going  $\mu$  events.

**3.1. The Case with the Standard Oscillation Scenario.** First of all, let us discuss the case where “the experimental data” is the one obtained with the standard oscillation scenario. The values of the oscillation parameters which are used to obtain “the experimental data” are the following (to distinguish the oscillation parameters for the “the experimental data” ( $n_{Aj}^a(\ell)$  ( $j = 1, \dots, 10$ ;  $A = L, H$ ;  $a = s, m$ ;  $\ell = e, \mu$ ), etc.) and those for the numbers of events ( $N_{Aj}^a(\nu_\alpha \rightarrow \nu_\beta)$  ( $j = 1, \dots, 10$ ;  $A = L, H$ ;  $a = s, m$ ;  $\alpha, \beta = e, \mu$ ), etc.) for fitting, the parameters with a bar denote those for “the experimental data,” whereas those without a bar denote the parameters for the numbers of events for fitting):

$$\begin{aligned}\Delta\bar{m}_{31}^2 &= 2.5 \times 10^{-3} \text{ eV}^2, \\ \sin^2\bar{\theta}_{23} &= 0.5, \\ \bar{\delta} &= 0, \\ \sin^2 2\bar{\theta}_{12} &= 0.86, \\ \sin^2 2\bar{\theta}_{13} &= 0.1, \\ \Delta\bar{m}_{21}^2 &= 7.6 \times 10^{-5} \text{ eV}^2.\end{aligned}\tag{14}$$

As in the case of the analysis of the SK data, we vary the oscillation parameters  $\theta_{23}$ ,  $|\Delta m_{32}^2|$ ,  $\delta$ , and  $\arg(\epsilon_{e\tau})$  while fixing the other oscillation parameters  $\sin^2 2\theta_{12} = 0.86$ ,  $\sin^2 2\theta_{13} = 0.1$ , and  $\Delta m_{21}^2 = 7.6 \times 10^{-5} \text{ eV}^2$ .

In the energy rate analysis,  $\chi^2$  is the same as (10) where the numbers of events are calculated with the standard oscillation scenario with  $\bar{\theta}_{jk}$ ,  $\Delta\bar{m}_{jk}^2$ , and  $\bar{\delta}$  given by (14), and we have assumed that all the systematic errors except  $\sigma_{\beta m2}$  are the same as those in (12) in the analysis of SK data.  $\sigma_{\beta m2} = 0.16$ , which is the uncertainty in the relative normalization between the  $\nu - \bar{\nu}$  flux, was chosen because this value was used in the energy spectrum analysis on the significance of the wrong mass hierarchy to give the result close to that in [29] (see the discussions below).

In the spectrum analysis, on the other hand,  $\chi_{\text{sub-GeV}}^2$  and  $\chi_{\text{multi-GeV}}^2$  are replaced by

$$\begin{aligned}\chi_{\text{sub-GeV}}^2 &= \min_{\alpha_s, \beta', s, \gamma', s} \left[ \frac{\beta_{s1}^2}{\sigma_{\beta s1}^2} + \frac{\beta_{s2}^2}{\sigma_{\beta s2}^2} + \frac{\gamma_{L1}^2}{\sigma_{\gamma L1}^2} + \frac{\gamma_{L2}^2}{\sigma_{\gamma L2}^2} \right. \\ &+ \frac{\gamma_{H1}^2}{\sigma_{\gamma H1}^2} + \frac{\gamma_{H2}^2}{\sigma_{\gamma H2}^2} \\ &+ \left. \sum_{A=L,H} \sum_{j=1}^{10} \left\{ \frac{1}{n_{Aj}^s(e)} \right\} \right]\end{aligned}$$

$$\begin{aligned}&\cdot \left[ \alpha_s \left( 1 - \frac{\beta_{s1}}{2} + \frac{\beta_{s2}}{2} + \frac{\gamma_{A1}^j}{2} \right) N_{Aj}^s(\nu_e \rightarrow \nu_e) \right. \\ &+ \alpha_s \left( 1 + \frac{\beta_{s1}}{2} + \frac{\beta_{s2}}{2} + \frac{\gamma_{A1}^j}{2} \right) N_{Aj}^s(\nu_\mu \rightarrow \nu_e) \\ &+ \alpha_s \left( 1 - \frac{\beta_{s1}}{2} - \frac{\beta_{s2}}{2} + \frac{\gamma_{A1}^j}{2} \right) N_{Aj}^s(\bar{\nu}_e \rightarrow \bar{\nu}_e) \\ &+ \alpha_s \left( 1 + \frac{\beta_{s1}}{2} - \frac{\beta_{s2}}{2} + \frac{\gamma_{A1}^j}{2} \right) N_{Aj}^s(\bar{\nu}_\mu \rightarrow \bar{\nu}_e) \\ &\left. - n_{Aj}^s(e) \right]^2 \\ &+ \frac{1}{n_{Aj}^s(\mu)} \\ &\cdot \left[ \alpha_s \left( 1 - \frac{\beta_{s1}}{2} + \frac{\beta_{s2}}{2} + \frac{\gamma_{A2}^j}{2} \right) N_{Aj}^s(\nu_e \rightarrow \nu_\mu) \right. \\ &+ \alpha_s \left( 1 + \frac{\beta_{s1}}{2} + \frac{\beta_{s2}}{2} + \frac{\gamma_{A2}^j}{2} \right) N_{Aj}^s(\nu_\mu \rightarrow \nu_\mu) \\ &+ \alpha_s \left( 1 - \frac{\beta_{s1}}{2} - \frac{\beta_{s2}}{2} + \frac{\gamma_{A2}^j}{2} \right) N_{Aj}^s(\bar{\nu}_e \rightarrow \bar{\nu}_\mu) \\ &+ \alpha_s \left( 1 + \frac{\beta_{s1}}{2} - \frac{\beta_{s2}}{2} + \frac{\gamma_{A2}^j}{2} \right) N_{Aj}^s(\bar{\nu}_\mu \rightarrow \bar{\nu}_\mu) \\ &\left. - n_{Aj}^s(\mu) \right]^2 \Bigg],\end{aligned}\tag{15}$$

$\chi_{\text{multi-GeV}}^2$

$$\begin{aligned}&= \min_{\alpha_m, \beta', s, \gamma', s} \left[ \frac{\beta_{m1}^2}{\sigma_{\beta m1}^2} + \frac{\beta_{m2}^2}{\sigma_{\beta m2}^2} \right. \\ &+ \frac{\gamma_1^2}{\sigma_{\gamma 1}^2} + \frac{\gamma_2^2}{\sigma_{\gamma 2}^2} \\ &+ \left. \sum_{A=L,H} \sum_{j=1}^{10} \left\{ \frac{1}{n_{Aj}^m(e)} \right\} \right. \\ &\cdot \left[ \alpha_s \left( 1 - \frac{\beta_{m1}}{2} + \frac{\beta_{m2}}{2} + \frac{\gamma_1^j}{2} \right) N_{Aj}^m(\nu_e \rightarrow \nu_e) \right. \\ &+ \alpha_s \left( 1 + \frac{\beta_{m1}}{2} + \frac{\beta_{m2}}{2} + \frac{\gamma_1^j}{2} \right) N_{Aj}^m(\nu_\mu \rightarrow \nu_e) \\ &+ \alpha_s \left( 1 - \frac{\beta_{m1}}{2} - \frac{\beta_{m2}}{2} + \frac{\gamma_1^j}{2} \right) N_{Aj}^m(\bar{\nu}_e \rightarrow \bar{\nu}_e) \\ &\left. - n_{Aj}^m(e) \right]^2 \Bigg],\end{aligned}$$

$$\begin{aligned}
& + \alpha_s \left( 1 + \frac{\beta_{m1}}{2} - \frac{\beta_{m2}}{2} + \frac{\gamma_1^j}{2} \right) N_{Aj}^m (\bar{\nu}_\mu \rightarrow \bar{\nu}_e) \\
& - n_{Aj}^m(e) \Big]^2 \\
& + \frac{1}{n_{Aj}^m(\mu)} \\
& \cdot \left[ \alpha_s \left( 1 - \frac{\beta_{m1}}{2} + \frac{\beta_{m2}}{2} + \frac{\gamma_2^j}{2} \right) N_{Aj}^m (\nu_e \rightarrow \nu_\mu) \right. \\
& + \alpha_s \left( 1 + \frac{\beta_{m1}}{2} + \frac{\beta_{m2}}{2} + \frac{\gamma_2^j}{2} \right) N_{Aj}^m (\nu_\mu \rightarrow \nu_\mu) \\
& + \alpha_s \left( 1 - \frac{\beta_{m1}}{2} - \frac{\beta_{m2}}{2} + \frac{\gamma_2^j}{2} \right) N_{Aj}^m (\bar{\nu}_e \rightarrow \bar{\nu}_\mu) \\
& + \alpha_s \left( 1 + \frac{\beta_{m1}}{2} - \frac{\beta_{m2}}{2} + \frac{\gamma_2^j}{2} \right) N_{Aj}^m (\bar{\nu}_\mu \rightarrow \bar{\nu}_\mu) \\
& \left. - n_{Aj}^m(\mu) \Big]^2 \right]. \tag{16}
\end{aligned}$$

In (16) we have introduced the relative normalization, which in general depends on the flavor and the energy of the events, between the upward and downward going bins:

$$\begin{aligned}
\gamma_{A1,2}^j &= \begin{cases} \gamma_{A1,2} & (j \leq j_{\text{th}}; A = L, H) \\ -\gamma_{A1,2} & (j > j_{\text{th}}; A = L, H), \end{cases} \\
\gamma_{1,2}^j &= \begin{cases} \gamma_{1,2} & (j \leq j_{\text{th}}) \\ -\gamma_{1,2} & (j > j_{\text{th}}), \end{cases} \tag{17}
\end{aligned}$$

and  $j_{\text{th}} = 3$  is the index which separates the upward and downward bins. The indices  $L$  and  $H$  stand for the lower ( $E < E_{\text{th}}$ ) and higher ( $E > E_{\text{th}}$ ) energy bins, and the threshold energy  $E_{\text{th}}$  is chosen so that the numbers of events for the lower and higher energy bins are approximately equal, and in the case of the sub-GeV events,  $E_{\text{th}} = 0.5$  GeV, and in the case of the multi-GeV events, the threshold energy is  $E_{\text{th}} = 3.2$  GeV, respectively, for all the zenith angle bins. We have put the systematic errors as follows:

$$\begin{aligned}
\sigma_{\beta s1} &= \sigma_{\beta m1} = 0.03, \\
\sigma_{\beta s2} &= 0.05, \\
\sigma_{\beta m2} &= 0.16, \\
\sigma_\alpha &= 0.2, \tag{18}
\end{aligned}$$

$$\begin{aligned}
\sigma_{\gamma L1} &= 0.005, \\
\sigma_{\gamma L2} &= 0.008, \\
\sigma_{\gamma H1} &= 0.021, \\
\sigma_{\gamma H2} &= 0.018, \\
\sigma_{\gamma 1} &= 0.015, \\
\sigma_{\gamma 2} &= 0.025. \tag{19}
\end{aligned}$$

All the systematic errors in (18) except  $\sigma_{\beta m2}$  and  $\sigma_{\gamma 2}$  are the same as those in (12) in Section 2 and those used in [60].  $\sigma_{\beta m2} = 0.16$  is the uncertainty in the relative normalization between the multi-GeV  $\nu - \bar{\nu}$  flux and it was 0.05 in (12).  $\sigma_{\gamma 2} = 0.025$  is the uncertainty in the relative normalization between the upward and downward going multi-GeV  $\mu$ -like events and it was 0.008 in the analysis of SK data [60]. The choice of these systematic errors (18) and (19) and the index  $j_{\text{th}} = 3$  has been made so that the result of our analysis on the mass hierarchy is close to that in [29], and we have checked that the choice of (18) and (19) and the index  $j_{\text{th}} = 3$  do not affect the sensitivity to NSI significantly. Notice that we have included the systematic uncertainty for the up-down correlation, unlike our analysis of the Super-Kamiokande data in Section 2. We have omitted the other systematic uncertainties, such as the  $E_\nu$  spectral index, for simplicity. The systematic error for the spectral index affects all the numbers of events for each energy universally, and it is not expected to affect the sensitivity to NSI very much.

The results from the energy rate (spectrum) analysis are given by the upper (lower) panel in Figure 2. From the energy rate analysis we have  $|\epsilon_{e\tau}/(1 + \epsilon_{ee})| \lesssim 0.3$  at  $2.5\sigma$  CL. On the other hand, from the energy spectrum analysis we get  $-0.1 \lesssim \epsilon_{ee} \lesssim 0.2$  and  $|\epsilon_{e\tau}| < 0.08$  at  $2.5\sigma$  (98.8%) CL for the normal hierarchy and to  $-0.4 \lesssim \epsilon_{ee} \lesssim 1.2$  and  $|\epsilon_{e\tau}| < 0.34$  at  $2.5\sigma$  (98.8%) CL for the inverted hierarchy.

From Figure 2 we note two things. Firstly, the allowed regions from the energy spectrum analysis (the lower panel) are much smaller than those from the energy rate analysis (the upper panel) for both mass hierarchies. Secondly, the allowed regions (the right panel) for the inverted hierarchy are wider than those (the left panel) for the normal hierarchy for both rate and spectrum analyses.

To understand these phenomena, we have plotted in Figure 3  $\chi_{\text{multi-GeV}}^2$  for the multi-GeV events, which are expected to be sensitive to the matter effect and therefore to  $\epsilon_{ee}$ , as a function of  $\epsilon_{ee}$  in the case of  $\epsilon_{e\tau} = 0$ . In plotting the figures in Figure 3, we have taken into account only the statistical errors for simplicity, and we assume that the HK detector could distinguish neutrinos and antineutrinos for both  $e$ -like and  $\mu$ -like events in all the energy ranges of the multi-GeV events and that the detection efficiency is the same for both neutrinos and antineutrinos. Since the SK collaboration distinguish neutrinos and antineutrinos only for the multi-GeV  $e$ -like events [56], our assumption here may not be realistic, and the separate plots for neutrinos or for antineutrinos except for the  $e$ -like events should be regarded as information for theoretical consideration. The two figures

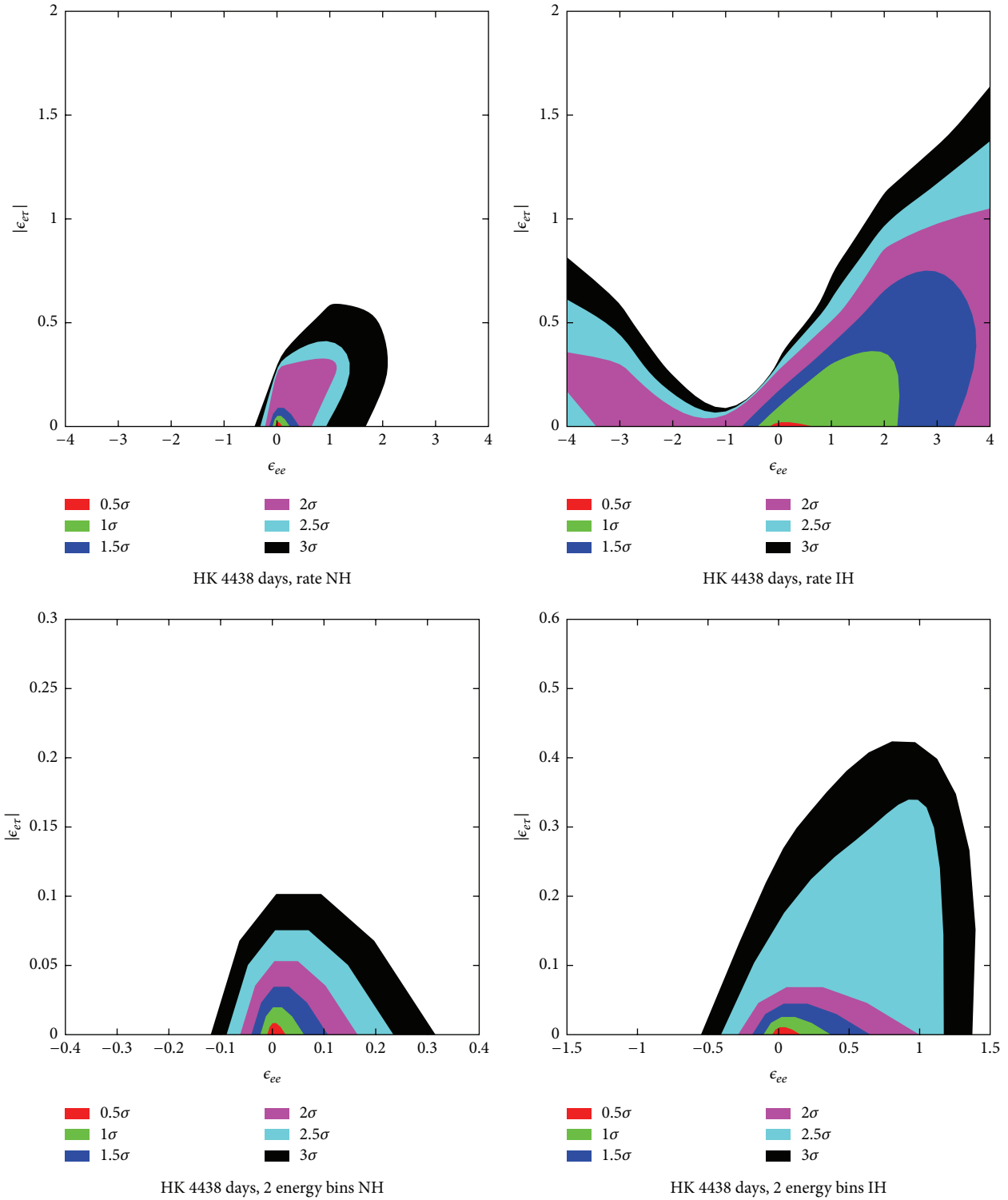


FIGURE 2: Upper panel: the allowed region in the  $(\epsilon_{ee}, |\epsilon_{e\tau}|)$  plane from the HK atmospheric neutrino data for a normal mass hierarchy (left panel) and for an inverted mass hierarchy (right panel) from the energy-rate analysis. Lower panel: the same allowed region as the upper panel from the two energy-bin analysis. Notice that the vertical scales in the lower panel are different for both mass hierarchies from the one in the upper panel.

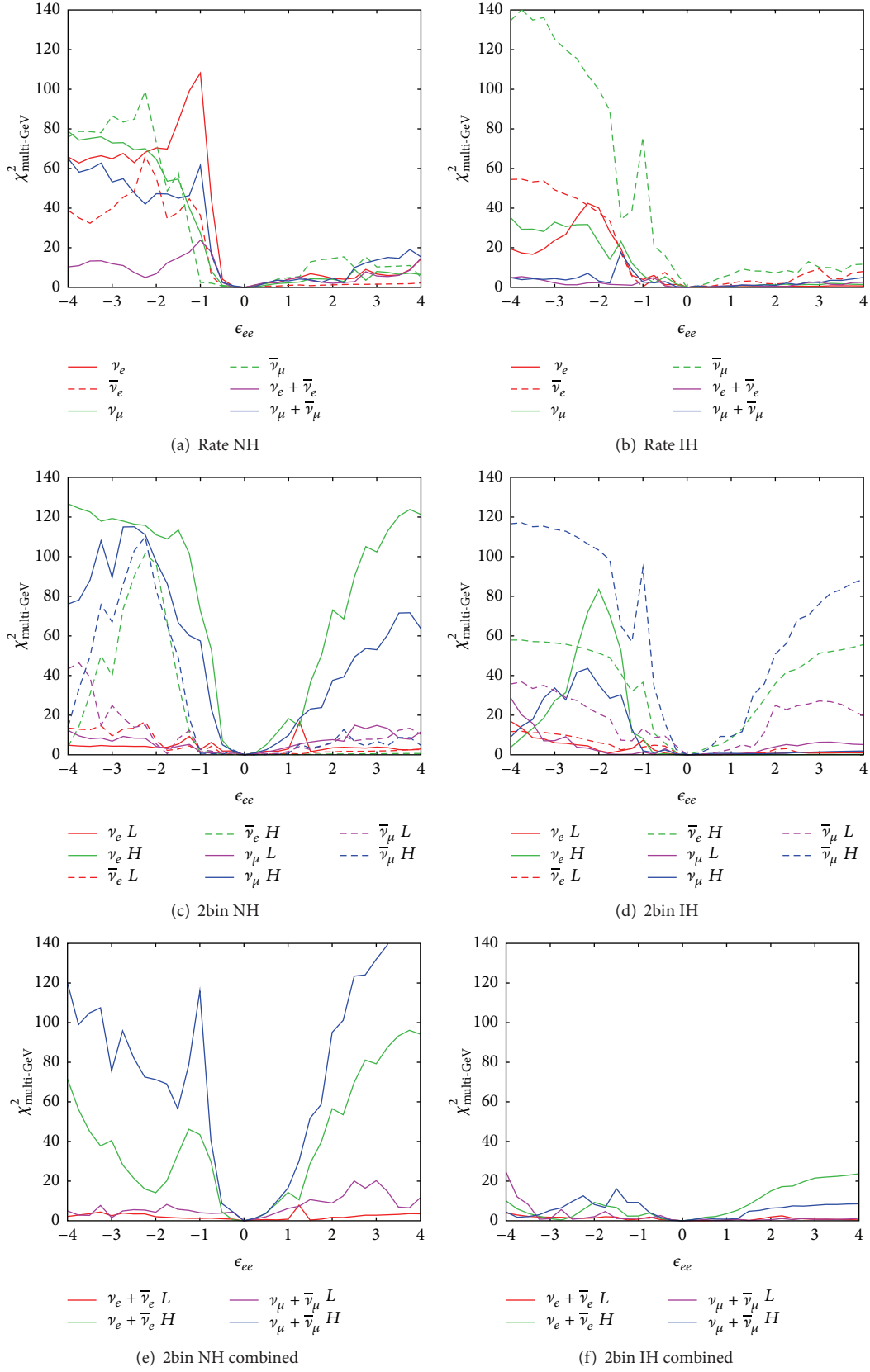


FIGURE 3: The behaviors of  $\chi_{\text{multi-GeV}}^2$  for  $\epsilon_{\text{cr}} = 0$  as a function of  $\epsilon_{ee}$ . ((a), (b)) Energy rate analysis for NH (a) and IH (b). ((c), (d)) Energy spectrum analysis for NH (c) and IH (d) for the separate neutrino or antineutrino events. ((e), (f)) Energy spectrum analysis for NH (e) and IH (f) using only the combined numbers of events of  $\nu_e + \bar{\nu}_e$  and  $\nu_\mu + \bar{\nu}_\mu$ . In (a), (b), (c), and (d), the plots for the separate neutrino or antineutrino events are created based on the assumption that HK could distinguish neutrinos and antineutrinos.

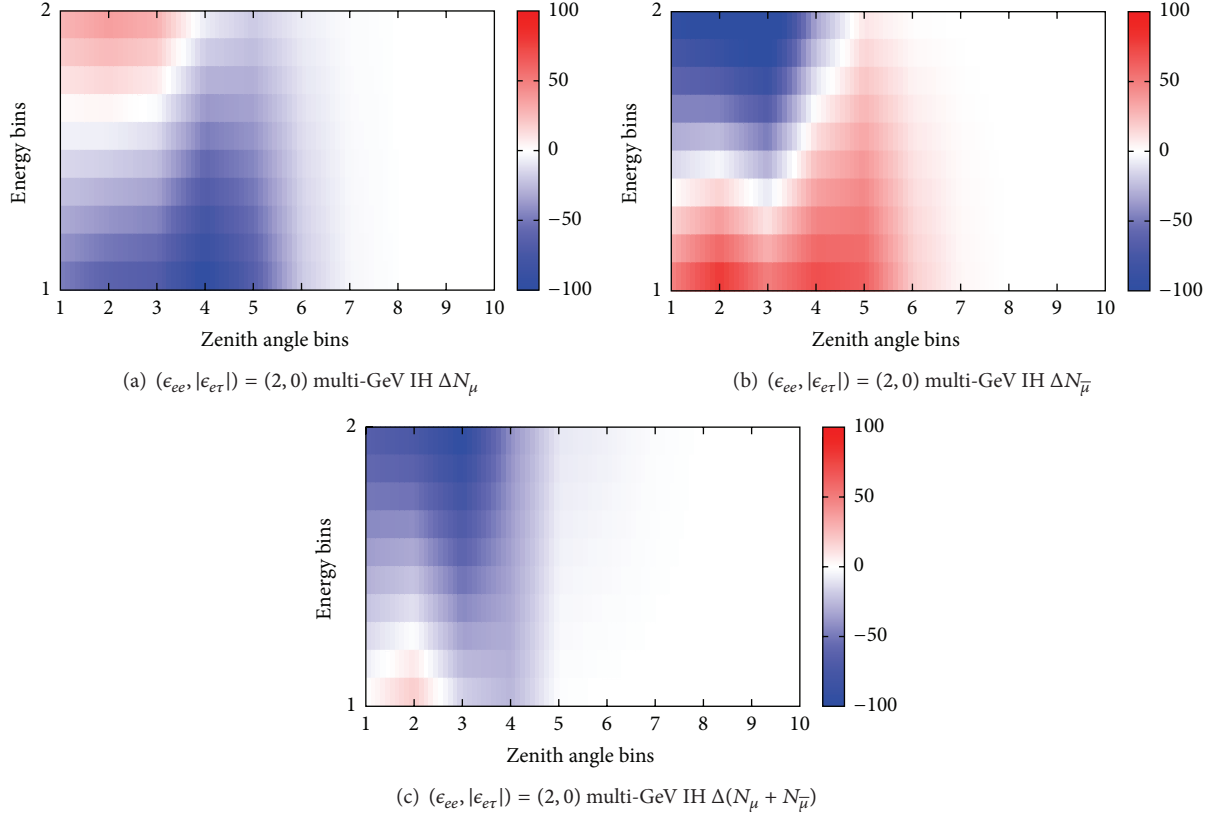


FIGURE 4: The behaviors of the difference of the numbers of the multi-GeV  $\mu$ -like events with the standard scenario and those with NSI  $(\epsilon_{ee}, |\epsilon_{e\tau}|) = (2, 0)$ . The vertical axis stands for the energy bin (1 for the lower energy and 2 for the higher energy), and the horizontal axis is the zenith angle bin (1 for  $-1.0 < \cos \Theta < -0.8, \dots, 10$  for  $0.8 < \cos \Theta < 1.0$ ). (a) The difference of the numbers of the multi-GeV  $\nu_{\mu}$ -like events. (b) The difference of the numbers of the multi-GeV  $\bar{\nu}_{\mu}$ -like events. (c) The difference of the numbers of the multi-GeV  $\nu_{\mu}$ -like and  $\bar{\nu}_{\mu}$ -like events.

((a) and (b)) in the top row are the results of the energy rate analysis. The two figures ((c) and (d)) in the middle row are the results of the energy spectrum analysis with two energy bins for the separate neutrino or antineutrino events. The two figures ((e) and (f)) in the bottom row are the results of the energy spectrum analysis with two energy bins of neutrinos and antineutrinos combined. Comparing the figures ((a) and (b)) in the top row and those ((e) and (f)) in the bottom row, we see that, even if some of the data set in the spectrum analysis have a sensitivity to the effect of  $\epsilon_{ee}$ , the data in the rate analysis does not necessarily have a sensitivity to  $\epsilon_{ee}$  particularly for  $\epsilon_{ee} > 0$ , for both mass hierarchies. While it is not clear to us why the sensitivity is lost only for  $\epsilon_{ee} > 0$ , we have found that, if we try to fit the same data with the numbers of events with the wrong mass hierarchy, then the plot becomes left-right reversed, that is, the sensitivity is lost only for  $\epsilon_{ee} < 0$ . On the other hand, by comparing the figures ((c) and (d)) in the middle row and those ((e) and (f)) in the bottom row, we see that, in the case of the inverted mass hierarchy, even though the separate  $\bar{\nu}_{\mu}$  data has a sensitivity to  $\epsilon_{ee}$ , the combined data  $\nu_{\mu} + \bar{\nu}_{\mu}$  loses a sensitivity. We could not explain these phenomena using the analytic expression for the oscillation probability, but we interpret this loss of sensitivity as a destructive phenomenon between neutrinos

and antineutrinos in the rate analysis and between the lower and higher energy bins in the spectrum analysis for the inverted mass hierarchy.

To visualize how this destructive phenomenon happens in terms of the numbers of events, we have plotted in Figure 4 the difference of the numbers of the multi-GeV  $\mu$ -like events with standard scenario and those with NSI for a typical case:  $(\epsilon_{ee}, |\epsilon_{e\tau}|) = (2, 0)$ . From Figure 4 we see that each positive and negative contribution to the difference in the  $\nu_{\mu}$  events (Figure 4(a)) is almost cancelled by negative and positive contribution in the  $\bar{\nu}_{\mu}$  events in Figure 4(b), so significance is reduced in the combined events (Figure 4(c)).

Although we have not thoroughly investigated, according to our investigation for a specific case ( $\epsilon_{ee} = 0$ ), this destructive phenomenon does not happen for  $|\epsilon_{e\tau}|$ ; that is, distinction between neutrinos and antineutrinos does not make much difference on the sensitivity to  $|\epsilon_{e\tau}|$ . This conclusion is consistent with the result of [44], in which the sensitivity to  $|\epsilon_{e\tau}|$  was studied, although they took a set of assumptions different from ours. This destructive phenomenon seems to be characteristic to the sensitivity to  $\epsilon_{ee}$  because of the asymmetry between the cases for  $\epsilon_{ee} + 1 > 0$  and for  $\epsilon_{ee} + 1 < 0$ .

It is expected that the HK experiment will be able to use information on the energy spectrum, so we believe that the

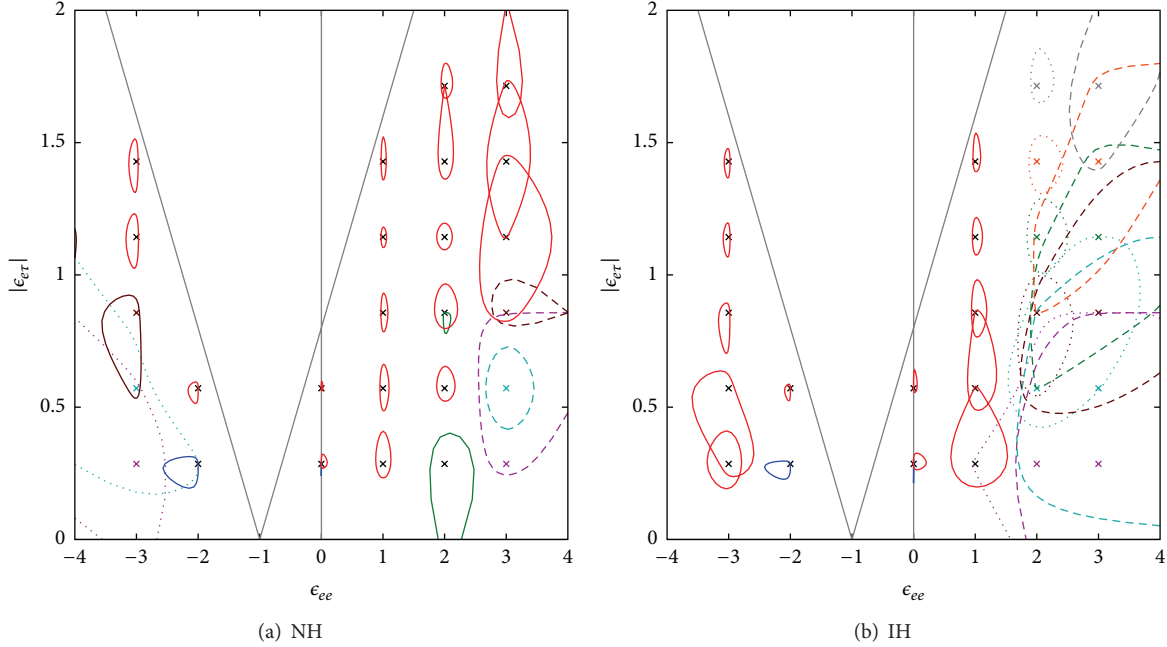


FIGURE 5: The allowed region at  $2.5\sigma$ CL around the point  $(\epsilon_{ee}, |\epsilon_{e\tau}|) \neq (0, 0)$ , where  $\bar{\delta} = \arg(\bar{\epsilon}_{e\tau}) = 0$  is assumed. Most of the allowed regions are connected, but those around a few points have an isolated island, and they are depicted in different colors: In (a), the blue curves around  $(\epsilon_{ee}, |\epsilon_{e\tau}|) = (-2, 2/7)$  and  $(0, 2/7)$  correspond to the degenerate allowed regions for the true values of  $(-2, 2/7)$ , the green curves around  $(2, 2/7)$  and  $(2, 6/7)$  are the degenerate allowed regions for the true values of  $(2, 2/7)$ , and the brown curves around  $(-3, 6/7)$  and  $(-4, 8/7)$  are the degenerate allowed regions for the true values of  $(-3, 6/7)$ . In (b), the blue curves around  $(-2, 2/7)$  and  $(0, 2/7)$  correspond to the degenerate allowed regions for the true values of  $(-2, 2/7)$ . The allowed regions at  $\epsilon_{ee} = \pm 3$  for the normal mass hierarchy and at  $\epsilon_{ee} = 2, 3$  for the inverted mass hierarchy are much wider compared with other cases, so their boundary is shown with dashed lines for  $\epsilon_{ee} = 3$  (NH and IH) and with dotted lines for  $\epsilon_{ee} = -3$  (NH) and  $\epsilon_{ee} = 2$  (IH). Also these boundary and their centers are shown in different colors: purple for  $|\epsilon_{e\tau}| = 2/7$ , light blue for  $|\epsilon_{e\tau}| = 4/7$ , brown for  $|\epsilon_{e\tau}| = 6/7$ , green for  $|\epsilon_{e\tau}| = 8/7$ , orange for  $|\epsilon_{e\tau}| = 10/7$ , and grey for  $|\epsilon_{e\tau}| = 12/7$ .

allowed region in the lower panel in Figure 2 with the energy spectrum analysis reflects the true HK sensitivity more than that in the upper panel does.

**3.2. The Case in the Presence of NSI.** Next let us discuss the case where “the experimental data” is the one obtained with  $(\epsilon_{ee}, \epsilon_{e\tau}) \neq (0, 0)$ . The analysis is the same as the one in Section 3.1, except that the “the experimental data” is produced assuming the presence of NSI, and here we perform only an energy spectrum analysis with two energy bins. The results are shown in Figure 5, where the allowed regions at  $2.5\sigma$ CL ( $\Delta\chi^2 = 8.8$  for 2 degrees of freedom) around the true points are depicted. The straight lines  $|\epsilon_{e\tau}| = 0.8 \times |1 + \epsilon_{ee}|$  in Figure 5 stand for the approximate bound from the SK atmospheric neutrinos in Figure 1, and we have examined only the points below these straight lines. As seen from Figure 5, the errors in  $\epsilon_{ee}$  and  $|\epsilon_{e\tau}|$  are small for  $|\epsilon_{ee}| \leq 2$  in the case of the normal hierarchy and for  $-3 \leq \epsilon_{ee} \leq 1$  in the case of the inverted hierarchy. The errors are large otherwise, and the reason that the errors are large is because a sensitivity is lost due to a destructive phenomenon between neutrinos and antineutrinos as was discussed in Section 3.1.

We note in passing that there are a couple of points in Figure 5, where the allowed region has an additional isolated island. This is regarded as so-called parameter degeneracy,

which is classified into the intrinsic degeneracy [61], the sign degeneracy [62], and the octant degeneracy [63, 64] in the standard three-flavor framework, in the presence of the NSI. Since little is known about parameter degeneracy in the presence of the new physics and since the study of the subject is beyond the scope of this paper, we do not discuss parameter degeneracy here.

## 4. Conclusions

In this paper we have studied the constraint of the SK atmospheric neutrino data on the nonstandard flavor-dependent interaction in neutrino propagation with the ansatz (9). From the SK atmospheric neutrino data for 4438 days, we have obtained the bound  $|\epsilon_{e\tau}|/|1 + \epsilon_{ee}| \leq 0.8$  at  $2.5\sigma$ CL, while we have little constraint on  $\epsilon_{ee}$ .

We have also discussed the sensitivity of the future HK atmospheric neutrino experiment to NSI by analyses with the energy rate and with the energy spectrum. If nature is described by the standard oscillation scenario, then the HK atmospheric neutrino data will give us the bound  $|\epsilon_{e\tau}|/|1 + \epsilon_{ee}| \leq 0.3$  at  $2.5\sigma$ CL from the energy rate analysis, and from the energy spectrum analysis it will restrict  $\epsilon_{ee}$  to  $-0.1 \leq \epsilon_{ee} \leq 0.2$  and  $|\epsilon_{e\tau}| < 0.08$  at  $2.5\sigma$  (98.8%) CL for the normal hierarchy and to  $-0.4 \leq \epsilon_{ee} \leq 1.2$  and  $|\epsilon_{e\tau}| < 0.34$  at  $2.5\sigma$  (98.8%) CL for the inverted hierarchy. On the other hand,

if nature is described by NSI with the ansatz (9), then HK will measure the NSI parameters  $\epsilon_{ee}$  and  $|\epsilon_{e\tau}|$  relatively well for  $|\epsilon_{ee}| \lesssim 2$  in the case of the normal hierarchy and for  $-3 \lesssim \epsilon_{ee} \lesssim 1$  in the case of the inverted hierarchy.

We have shown that it is important to use information on the energy spectrum to obtain strong constraint, because a sensitivity to NSI would be lost due to destructive phenomena between the low and high energy events. If there is a way to distinguish between neutrinos and antineutrinos, as is done by the SK collaboration [56] for the  $e$ -like multi-GeV events, also for the multi-GeV  $\mu$ -like events, then the sensitivity to NSI would be greatly improved, because in this case we can avoid destructive phenomena between neutrinos and antineutrinos.

Finally let us discuss some prospects for the global analysis with these future atmospheric results and the solar neutrino results. In [35] the global analysis was performed with all the data presently available, and the conclusion was that the constraints from the solar and KamLAND data are stronger than those from the atmospheric and long baseline experiments. Furthermore, because of the slight difference between the best fit values for the solar and KamLAND data in the standard scenario, their result may suggest a nonzero value for the NSI parameter  $\epsilon_D^f$ , which is a function of  $\epsilon_{\alpha\alpha}^f$  ( $\alpha = e, \mu, \tau$ ),  $\epsilon_{\mu\alpha}^f$  ( $\alpha = e, \mu, \tau$ ), and  $\epsilon_{\tau\tau}^f$ . From our results in Section 3, if the mass hierarchy is normal, then we see that the errors of the parameters  $\epsilon_{ee}$  and  $|\epsilon_{e\tau}|$  obtained in the future Hyper-Kamiokande experiment may be comparable to or even smaller than the present error of  $\epsilon_D^f$ . So HK may be able to contribute to give further constraints on the  $\epsilon_D^f$  parameter, although more detailed study will be required to be conclusive.

While HK is expected to play an important role in measurement of  $\delta$  in the standard three-flavor scenario using the JPARC beam, HK has also a potential for new physics with atmospheric neutrinos. Search for NSI may lead to physics beyond the Standard Model, and the effects of NSI at HK deserves further studies.

## Conflict of Interests

The authors declare that there is no conflict of interests regarding the publication of this paper.

## Acknowledgment

This research was partly supported by a Grant-in-Aid for Scientific Research of the Ministry of Education, Science and Culture, under Grants no. 24540281 and no. 25105009.

## References

- [1] Particle Data Group, "Review of particle physics," *Chinese Physics C*, vol. 38, no. 9, Article ID 090001, 2014.
- [2] K. Abe, H. Aihara, C. Andreopoulos et al., "A long baseline neutrino oscillation experiment using J-PARC neutrino beam and hyper-kamiokande," <http://arxiv.org/abs/1412.4673>.
- [3] C. Adams, D. Adams, T. Akiri et al., "The long-baseline neutrino experiment: exploring fundamental symmetries of the universe," <http://arxiv.org/abs/1307.7335>.
- [4] Belle experiment, <http://belle.kek.jp/>.
- [5] Babar experiment, <http://www-public.slac.stanford.edu/babar/>.
- [6] A. Bandyopadhyay, S. Choubey, R. Gandhi et al., "Physics at a future Neutrino Factory and super-beam facility," *Reports on Progress in Physics*, vol. 72, no. 10, Article ID 106201, 2009.
- [7] L. Wolfenstein, "Neutrino oscillations in matter," *Physical Review D*, vol. 17, no. 9, pp. 2369–2374, 1978.
- [8] M. M. Guzzo, A. Masiero, and S. T. Petcov, "On the MSW effect with massless neutrinos and no mixing in the vacuum," *Physics Letters B*, vol. 260, no. 1-2, pp. 154–160, 1991.
- [9] E. Roulet, "Mikheyev-Smirnov-Wolfenstein effect with flavor-changing neutrino interactions," *Physical Review D*, vol. 44, Article ID R935(R), 1991.
- [10] S. P. Mikheev and A. Y. Smirnov, "Resonance amplification of oscillations in matter and spectroscopy of solar neutrinos," *Soviet Journal of Nuclear Physics*, vol. 42, pp. 913–917, 1985, *Yadernaya Fizika*, vol. 42, p. 1441, 1985.
- [11] M. C. Gonzalez-Garcia, M. M. Guzzo, P. I. Krastev et al., "Atmospheric neutrino observations and flavor changing interactions," *Physical Review Letters*, vol. 82, no. 16, pp. 3202–3205, 1999.
- [12] P. Lipari and M. Lusignoli, "Exotic solutions of the atmospheric neutrino problem," *Physical Review D*, vol. 60, Article ID 013003, 1999.
- [13] N. Fornengo, M. C. Gonzalez-Garcia, and J. W. F. Valle, "On the interpretation of the atmospheric neutrino data in terms of flavor changing neutrino interactions," *Journal of High Energy Physics*, vol. 2000, no. 7, article 006, 2000.
- [14] N. Fornengo, M. Maltoni, R. Tomas, and J. W. F. Valle, "Probing neutrino nonstandard interactions with atmospheric neutrino data," *Physical Review D*, vol. 65, Article ID 013010, 2002.
- [15] M. C. Gonzalez-Garcia and M. Maltoni, "Atmospheric neutrino oscillations and new physics," *Physical Review D*, vol. 70, Article ID 033010, 2004.
- [16] Z. Berezhiani and A. Rossi, "Limits on the non-standard interactions of neutrinos from  $e^+e^-$  colliders," *Physics Letters B*, vol. 535, pp. 207–218, 2002.
- [17] S. Davidson, C. Pena-Garay, N. Rius, and A. Santamaria, "Present and future bounds on non-standard neutrino interactions," *Journal of High Energy Physics*, vol. 2003, no. 3, article 011, 2003.
- [18] A. Friedland, C. Lunardini, and C. Pena-Garay, "Solar neutrinos as probes of neutrino-matter interactions," *Physics Letters B*, vol. 594, no. 3-4, pp. 347–354, 2004.
- [19] O. G. Miranda, M. A. Tortola, and J. W. F. Valle, "Are solar neutrino oscillations robust?" *Journal of High Energy Physics*, vol. 2006, no. 10, article 008, 2006.
- [20] A. Palazzo and J. W. F. Valle, "Confusing nonzero  $\theta_{13}$  with nonstandard interactions in the solar neutrino sector," *Physical Review D*, vol. 80, Article ID 091301, 2009.
- [21] J. Barranco, O. G. Miranda, C. A. Moura, and J. W. F. Valle, "Constraining nonstandard interactions in  $\nu_e e$  or  $\bar{\nu}_e e$  scattering," *Physical Review D*, vol. 73, Article ID 113001, 2006.
- [22] J. Barranco, O. G. Miranda, C. A. Moura, and J. W. F. Valle, "Constraining nonstandard neutrino-electron interactions," *Physical Review D*, vol. 77, no. 9, Article ID 093014, 10 pages, 2008.

- [23] A. Bolanos, O. G. Miranda, A. Palazzo, M. A. Tortola, and J. W. F. Valle, “Probing nonstandard neutrino-electron interactions with solar and reactor neutrinos,” *Physical Review D*, vol. 79, Article ID 113012, 2009.
- [24] F. J. Escrivuela, O. G. Miranda, M. A. Tórtola, and J. W. F. Valle, “Constraining nonstandard neutrino-quark interactions with solar, reactor, and accelerator data,” *Physical Review D*, vol. 80, Article ID 105009, 2009, Erratum in: *Physical Review D*, vol. 80, Article ID 129908, 2009.
- [25] C. Biggio, M. Blennow, and E. Fernandez-Martinez, “General bounds on non-standard neutrino interactions,” *Journal of High Energy Physics*, vol. 2009, no. 8, article 090, 2009.
- [26] A. Friedland, C. Lunardini, and M. Maltoni, “Atmospheric neutrinos as probes of neutrino-matter interactions,” *Physical Review D*, vol. 70, Article ID 111301, 2004.
- [27] A. Friedland and C. Lunardini, “Test of tau neutrino interactions with atmospheric neutrinos and K2K data,” *Physical Review D*, vol. 72, Article ID 053009, 2005.
- [28] H. Oki and O. Yasuda, “Sensitivity of the T2KK experiment to the nonstandard interaction in propagation,” *Physical Review D*, vol. 82, Article ID 073009, 2010.
- [29] K. Abe, T. Abe, H. Aihara et al., “Letter of intent: the hyper-Kamiokande experiment—detector design and physics potential,” <http://arxiv.org/abs/1109.3262>.
- [30] M. C. Gonzalez-Garcia, M. Maltoni, and J. Salvado, “Testing matter effects in propagation of atmospheric and long-baseline neutrinos,” *Journal of High Energy Physics*, vol. 2011, no. 5, article 075, 2011.
- [31] G. Mitsuka, K. Abe, Y. Hayato et al., “Study of nonstandard neutrino interactions with atmospheric neutrino data in Super-Kamiokande I and II,” *Physical Review D*, vol. 84, Article ID 113008, 2011.
- [32] T. Ohlsson, H. Zhang, and S. Zhou, “Effects of nonstandard neutrino interactions at PINGU,” *Physical Review D*, vol. 88, no. 1, Article ID 013001, 2013.
- [33] A. Esmaili and A. Y. Smirnov, “Probing non-standard interaction of neutrinos with IceCube and DeepCore,” *Journal of High Energy Physics*, vol. 2013, no. 6, article 026, 2013.
- [34] S. Choubey and T. Ohlsson, “Bounds on non-standard neutrino interactions using PINGU,” *Physics Letters B*, vol. 739, pp. 357–364, 2014.
- [35] M. C. Gonzalez-Garcia and M. Maltoni, “Determination of matter potential from global analysis of neutrino oscillation data,” *Journal of High Energy Physics*, vol. 2013, no. 9, article 152, 2013.
- [36] A. Friedland and C. Lunardini, “Two modes of searching for new neutrino interactions at MINOS,” *Physical Review D*, vol. 74, Article ID 033012, 2006.
- [37] O. Yasuda, “New physics effects in long baseline experiments,” *Acta Physica Polonica B*, vol. 38, pp. 3381–3388, 2007.
- [38] H. Sugiyama, “More on non-standard interaction at MINOS,” *AIP Conference Proceedings*, vol. 981, article 216, 2008.
- [39] M. Blennow, T. Ohlsson, and J. Skrotzki, “Effects of non-standard interactions in the MINOS experiment,” *Physics Letters B*, vol. 660, no. 5, pp. 522–528, 2008.
- [40] J. A. B. Coelho, T. Kafka, W. A. Mann, J. Schneps, and O. Altinok, “Constraints for nonstandard interaction  $\epsilon_{\text{e}\tau} V_e$  from  $\nu_e$  appearance in MINOS and T2K,” *Physical Review D*, vol. 86, Article ID 113015, 2012.
- [41] A. Esteban-Pretel, J. W. F. Valle, and P. Huber, “Can OPERA help in constraining neutrino non-standard interactions?” *Physics Letters B*, vol. 668, no. 3, pp. 197–201, 2008.
- [42] M. Blennow, D. Meloni, T. Ohlsson, F. Terranova, and M. Westerberg, “Non-standard interactions using the OPERA experiment,” *The European Physical Journal C*, vol. 56, no. 4, pp. 529–536, 2008.
- [43] A. Friedland, M. L. Graesser, I. M. Shoemaker, and L. Vecchi, “Probing nonstandard standard model backgrounds with LHC monojets,” *Physics Letters B*, vol. 714, no. 2–5, pp. 267–275, 2012.
- [44] A. Chatterjee, P. Mehta, D. Choudhury, and R. Gandhi, “Testing non-standard neutrino matter interactions in atmospheric neutrino propagation,” <http://arxiv.org/abs/1409.8472>.
- [45] J. Kopp, M. Lindner, T. Ota, and J. Sato, “Non-standard neutrino interactions in reactor and superbeam experiments,” *Physical Review D*, vol. 77, no. 1, Article ID 013007, 23 pages, 2008.
- [46] N. C. Ribeiro, H. Nunokawa, T. Kajita, S. Nakayama, P. Ko, and H. Minakata, “Probing nonstandard neutrino physics by two identical detectors with different baselines,” *Physical Review D*, vol. 77, Article ID 073007, 2008.
- [47] A. Friedland and I. M. Shoemaker, “Searching for novel neutrino interactions at NOvA and beyond in light of large  $\theta_{13}$ ,” <http://arxiv.org/abs/1207.6642>.
- [48] A. M. Gago, M. M. Guzzo, H. Nunokawa, W. J. C. Teves, and R. Zukanovich Funchal, “Probing flavor changing neutrino interactions using neutrino beams from a muon storage ring,” *Physical Review D*, vol. 64, Article ID 073003, 2001.
- [49] T. Ota, J. Sato, and N.-A. Yamashita, “Oscillation enhanced search for new interactions with neutrinos,” *Physical Review D*, vol. 65, Article ID 093015, 2002.
- [50] M. Campanelli and A. Romanino, “Effects of new physics in neutrino oscillations in matter,” *Physical Review D*, vol. 66, Article ID 113001, 2002.
- [51] P. Huber, T. Schwetz, and J. W. F. Valle, “How sensitive is a neutrino factory to the angle  $\theta_{13}$ ?” *Physical Review Letters*, vol. 88, Article ID 101804, 2002.
- [52] J. Kopp, T. Ota, and W. Winter, “Neutrino factory optimization for non-standard interactions,” *Physical Review D*, vol. 78, no. 5, Article ID 053007, 17 pages, 2008.
- [53] N. C. Ribeiro, H. Minakata, H. Nunokawa, S. Uchinami, and R. Zukanovich-Funchal, “Probing non-standard neutrino interactions with neutrino factories,” *Journal of High Energy Physics*, vol. 2007, no. 12, article 002, 2007.
- [54] A. M. Gago, H. Minakata, H. Nunokawa, S. Uchinami, and R. Z. Funchal, “Resolving CP violation by standard and non-standard interactions and parameter degeneracy in neutrino oscillations,” *Journal of High Energy Physics*, vol. 2010, no. 1, article 49, 2010.
- [55] D. Meloni, T. Ohlsson, W. Winter, and H. Zhang, “Non-standard interactions versus non-unitary lepton flavor mixing at a neutrino factory,” *Journal of High Energy Physics*, vol. 2010, no. 4, article 041, 2010.
- [56] K. Abe, Y. Haga, Y. Hayato et al., “Limits on sterile neutrino mixing using atmospheric neutrinos in Super-Kamiokande,” *Physical Review D*, vol. 91, no. 5, Article ID 052019, 22 pages, 2008.
- [57] R. Foot, R. R. Volkas, and O. Yasuda, “Comparing and contrasting the  $\nu_\mu \rightarrow \nu_\tau$  and  $\nu_\mu \rightarrow \nu_s$  solutions to the atmospheric neutrino problem with SuperKamiokande data,” *Physical Review D*, vol. 58, Article ID 013006, 1998.
- [58] O. Yasuda, “Three flavor neutrino oscillation analysis of the SuperKamiokande atmospheric neutrino data,” *Physical Review D*, vol. 58, Article ID 091301, 1998.

- [59] O. Yasuda, “Four neutrino oscillation analysis of the Superkamiokande atmospheric neutrino data,” <http://arxiv.org/abs/hep-ph/0006319>.
- [60] Y. Ashie, J. Hosaka, K. Ishihara et al., “Measurement of atmospheric neutrino oscillation parameters by Super-Kamiokande I,” *Physical Review D*, vol. 71, Article ID 112005, 2005.
- [61] J. Burguet-Castell, M. B. Gavela, J. J. Gómez Cadenas, P. Hernández, and O. Mena, “On the measurement of leptonic CP violation,” *Nuclear Physics B*, vol. 608, no. 1-2, Article ID 0103258, pp. 301–318, 2001.
- [62] H. Minakata and H. Nunokawa, “Exploring neutrino mixing with low energy superbeams,” *Journal of High Energy Physics*, vol. 2001, no. 10, article 001, 2001.
- [63] G. L. Fogli and E. Lisi, “Tests of three-flavor mixing in long-baseline neutrino oscillation experiments,” *Physical Review D*, vol. 54, no. 5, pp. 3667–3670, 1996.
- [64] V. Barger, D. Marfatia, and K. Whisnant, “Breaking eightfold degeneracies in neutrino CP violation, mixing, and mass hierarchy,” *Physical Review D*, vol. 65, Article ID 073023, 2002.